



CURRENT DEBATES ON NATURAL AND ENGINEERING SCIENCES



HİKMET Y. ÇOĞUN
İŞHAK PARLAR

All Rights Reserved

It may not be reproduced in any way without the written permission of the publisher and the editor, except for short excerpts for promotion by reference.

ISBN:

1st Edition

25 Aralık 2022

Current Debates on Natural and Engineering Sciences 5

Bilgin Kùltür Sanat Yayın Dağıtım Pazarlama Ltd. Şti. pursuant to the law of intellectual and artistic works, it may not be quoted, copied, reproduced or published in any way without written permission.

Editors

Hikmet Y. ÇOĞUN

İshak PARLAR

Publisher

Engin DEVREZ

Bilgin Kùltür Sanat Yayınları

Certificate No: 20193

Selanik Cd. No: 68/10 06640 Kızılay / Ankara

Phone: 0 (312) 419 85 67 – Fax: 0 (312) 419 85 68

www.bilginkultursanat.com

bilginkultursanat@gmail.com



Contents

Automatic Classification of Neuromuscular Diseases With Random Forest (Rf) Algorithm	7
Erdem TUNCER.....	7
Performing Heart Rhythm With Iot Using Ecg Sensor	12
Çağatay ERSİN.....	12
Mehmet KARAYEL.....	12
Improvement of Satellite Optimization Parameters with Lagrange Multipliers	20
Enes ÇELİK.....	20
Potent Matrices.....	27
Hasan KELEŞ.....	27
Rised Co ₂ And Climate Change Effects On Wheat.....	44
Uğur KEKEÇ.....	44
Burçak KAPUR.....	44
Levent KOÇ.....	44
Müge Erkan CAN.....	44
Petrographic Features Of The Upper Triassic-Lower Jurassic Kızılören Formation Dolostones (Konya Northwest, Turkey).....	64
Ali Müjdat Özkan.....	64
Levent Kenan Kibar.....	64
Geocemical Properties Of The Saytepe Formation (Upper Cretaceous) Carbonates Around Hadım And North (Konya, Turkey)	79
Ali Müjdat Özkan.....	79
Görkem Kırkan.....	79
Bearing Capacity And Elastic Settlement Of Shallow Foundations	101
Mustafa AYTEKİN.....	101
Evidential Fuzzy Multi-Criteria Decision Making Based On Belief Entropy	124
Galip Cihan YALÇIN.....	124
Pandemics.....	133
Cihat Furkan Göv.....	133
Hulya Celik.....	133
An Application of Distributed Order Differential Equations to a HIV Infection Model	149
Mehmet KOCABIYIK.....	149
Mevlûde YAKIT ONGUN.....	149
İlkem TURHAN ÇETİNKAYA.....	149
Analysis of the Charge Transport Properties of Bis Chalcone Derivative from the Reorganization Energy, Band Gap under the Different Electric Fields and Results of Bond Length Alternation for Efficient Organic Field Effect Transistors.....	163
Gül YAKALI.....	163

<i>Abdullah BİÇER</i>	163
Günseli TURGUT CİN	163
Assembly Line Balancing using Lean Techniques and Mathematical Modeling: A Case Study..	173
Betül KAYIŞOĞLU	173
İsmet SÖYLEMEZ	173
Özgül DEMİREL	173
Gamzenur ARIKAN	173
Kübra KURTOĞLU	173
Nonlinear Deformation Capacities of RC Frames Under Seismic Loads and Pushover Analysis.	
.....	182
Mehmet Fatih Yılmaz	182
Impacts of Remote Working on Productivity of Civil Engineers during the COVID-19 Pandemic	
.....	191
Ayşegül TEPE	191
Bengi AYKAÇ	191
Murat AYHAN.....	191
Investigation of Energy Management Studies in Specified Microgrid Applications	203
Fatma Yaprakdal	203
The effect of the use of different materials and design optimization in the connecting rod on	
fatigue analysis	218
Berkay KARAÇOR.....	218
Ali Kemal DUMAN	218
Mustafa ÖZCANLI	218
Ballistic evaluation of armor plates at different angles	229
Umut KUMLU	229
Mustafa Atakan AKAR	229
Doğukan BAŞER	229
Ömer HÜKÜMDAR	229
Berkay KARAÇOR	229
Does Hardun Change Colors?: A Preliminary Study on Ventral Color Alterations of Anatolian	
Harduns	240
Melodi YENMİŞ.....	240
Yusuf BAYRAKCI	240
Software-Defined Network Application With AI Techniques.....	247
Fatih Şahin.....	247
Machine Learning Applications on COVID-19 Pandemic: A Systematic Literature Review.....	265
Kübra KÖKSAL.....	265
Buket DOĞAN.....	265

Zehra Aysun ALTIKARDEŞ	265
Using Various Renewable Energy Sources In Commercial Kitchens And Ensuring Energy Efficiency.....	285
Zafer KAHRAMAN	285
Murat HACI.....	285
Hakan Serhad SOYHAN.....	285
Evaluation of Grapefruit Peel Extract for Control of <i>Meloidogyne Incognita</i> on Tomato.....	296
Fatma Gül GÖZE ÖZDEMİR.....	296
Convergence by Modified Post-Widder Operators Preserving e^{2ax} ; $a > 0$	304
Gülten TORUN.....	304
Yunus Hüseyin Erkendirici.....	318
Selim Hartomacıoğlu ¹	318
Metin Yüksek ²	318
Flexible Photovoltaic Applications for Non-Planar Surfaces Geometry.....	327
İbrahim GÜNEŞ.....	327
Investigation of the Effects of Third Generation Biofuel/Alcohol Mixtures on Emission and Combustion Behaviors	340
Erdal ÇILGIN	340
Application of the Rescheduling Approach in Manufacturing Systems	358
Ediz ATMACA	358
Irrigation and Salt Relations in Citrus	366
Uğur KEKEÇ.....	366
Burçak KAPUR.....	366
Rasim CEKİK	373
Abdullah TURAN.....	373
Certain Curvature Tensor Fields on α -Kenmotsu Pseudo Metric Manifolds	383
Hakan ÖZTÜRK.....	383
Sermin ÖZTÜRK.....	383
Adaptive Fuzzy Logic Based Vector Controlled Permanent Magnetic Synchronous Motor Speed Control.....	395
Mehmet . KARAYEL.....	395
Ç. ERSİN	395
Zinc Oxide (ZnO) – Fundamental Properties and Applications	411
E. Asıkuzun Tokeser	411
The Story of a Superconductor	418
E. Asıkuzun Tokeser	418
Effect of Volcanic Basalt Fiber on Physical and Mechanical Behaviors in Mg Alloy Produced by Powder Metallurgy	426

Bünyamin ÇİÇEK.....	426
Tuna AYDOĞMUŞ	426
Highway Vertical Curve Optimization with Meta- Heuristic Algorithm	442
Sina ASHERLOU	442
Aref YELGHİ	442
Erhan Burak PANCAR.....	442
Şeref ORUÇ.....	442
Liquid Chromatography Methods for the Determination of Beta-Carotene in Vegetable and Fruit Samples- an Evaluation of the Last Decade.....	459
F. A. Özdemir Olgun ¹	459
Data: Concepts and Processing.....	473
Ahmet YÜCEL.....	473
K. Eren	493
N. Taktakoğlu	493
İ. Pirim	493

Automatic Classification of Neuromuscular Diseases With Random Forest (Rf) Algorithm

Erdem TUNCER

Introduction

Neuromuscular diseases; It is a disease that affects the peripheral nervous system, is acquired or develops genetically, and is characterized by muscle wasting or weakness later on. Electromyography (EMG), one of the most important tools for the correct diagnosis of neuromuscular diseases, is used. (Bekiroglu & et al. 2016). Separation of EMG signs and classification of similarly shaped ones by grouping provide valuable information in terms of neuromuscular pathology evaluation. Neuromuscular disorder is a general term that refers to diseases that affect any part of the nerve or muscle. Myopathy and neuropathy are two important types of neuromuscular diseases. The symptoms of these two diseases can be very similar to each other. In the complaint of not being able to move the muscles, this movement disorder in neuropathy is caused by the nerves going to the muscle, while in myopathy, movement disorder occurs due to a problem in the muscle. The purpose of electromyography in the diagnosis of these diseases is to support the clinical diagnosis. EMG signals, which have a complex structure, do not contain easily understandable information. Therefore, these signs need to be classified by computer (Lee & et al. 2021, Kucuk & et al. 2019).

In this study, a classification structure consisting of five processing steps was arranged for the diagnosis of neuropathy and myopathy, which are the most common types of neuromuscular diseases. EMG signals were preprocessed, windowed, feature extraction and classification stages before being classified. 80% of the EMG signals analyzed in 0,2 second windows were used for training and the rest for testing. Afterwards, 10 features were calculated and the feature vector was obtained. Finally, the data were classified with the Random Forest (RF) algorithm. With the proposed features and classification algorithm, a success rate of 96,6% was achieved in the classification of normal, myopathy and neuropathy EMG data.

Materials and Method

The open access PhysioNet EMG dataset was used in this study. Data were collected with the Medelec Synergy N2 EMG Monitoring System (Oxford Instruments Medical) by placing a 25 mm. concentric needle electrode on the tibialis anterior muscle of all subjects. Two analog filters, 20 Hz. high-pass and 5 KHz. low-pass filters, were used during the recording process. Figure 1 shows three 0,2 second samples of EMG data. Figure 1(a) a 44 year old man with no history of neuromuscular disease; Figure 1(b) 57 year old man with myopathy due to a long-standing history of polymyositis; male subject EMG. Data were recorded at 50 KHz. and then downsampled to 4 KHz. (Goldberger & et al. 2000).

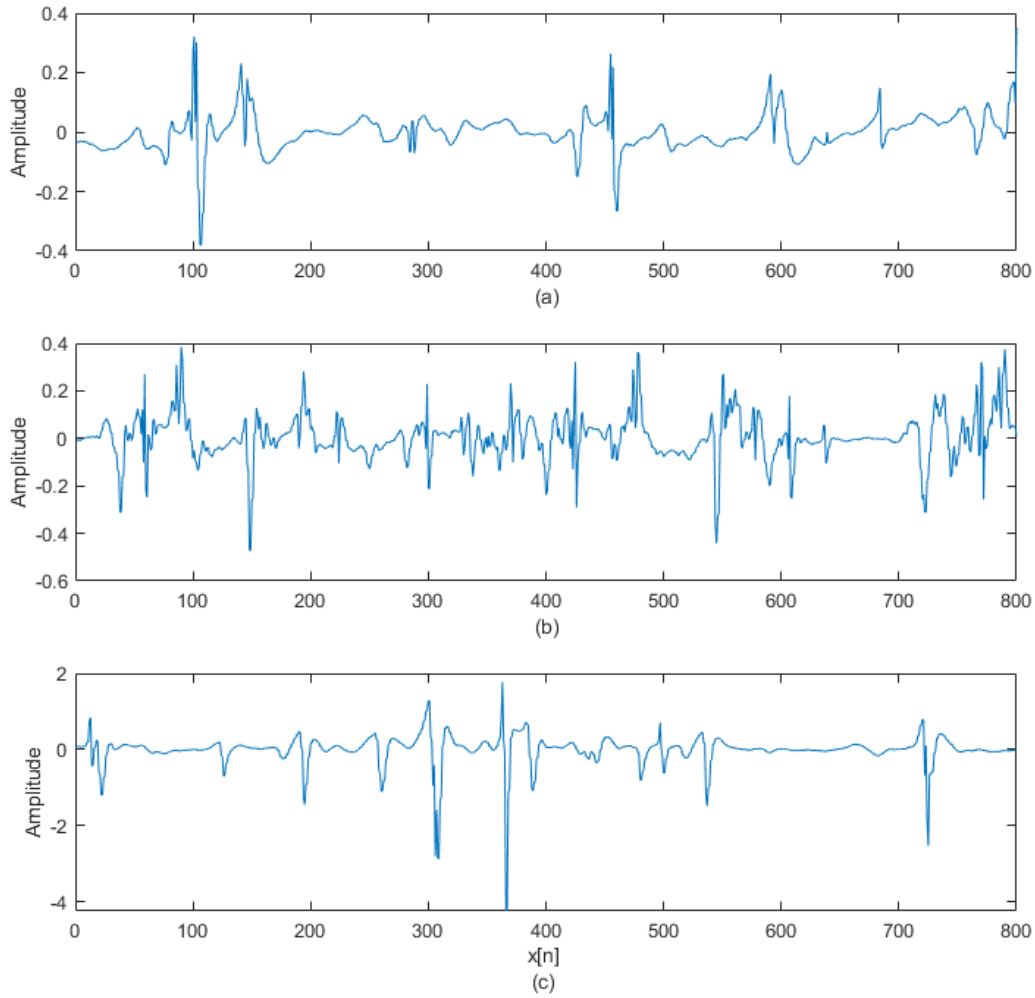


Fig 1. Typical EMG patterns of Normal (a), Myopathic (b) and Neuropathy (c) with 800 samples.

The data are split in 0,2 second windows with no overlap. The number of windows and data set information obtained from the data are given in Table 1.

Table 1. Information about the EMG dataset

Data type	Number of epochs	Total time (Second)
Normal	63	12,6
Myopathy	137	27,4
Neuropaty	184	36,8
Total	384	384

Various features are extracted for each window using the discrete wavelet method. 7-level wavelet transform is used to separate the EMG signal into lower frequency bands. The wavelet transform structure using the Symlets (Sym) 2 wavelet is shown in Figure 2.

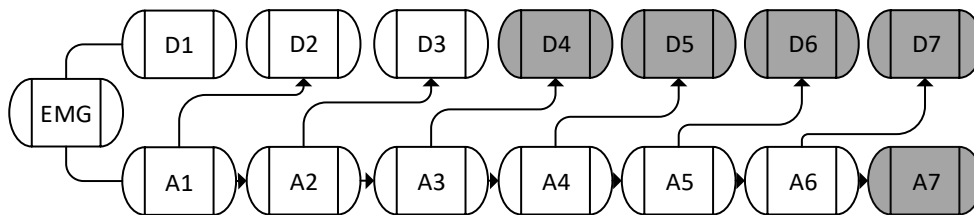


Fig. 2. Wavelet decomposition tree

Detail (D) and Approximation (A) coefficients were obtained from the EMG signal using the discrete wavelet transform. The approximation coefficients are obtained by calculating the low frequency components, and the detail coefficients are obtained by calculating the other frequency components (Tuncer E. 2022). 10 different features of these wavelet coefficients are extracted. In Figure 2, the wavelet coefficients from which the features are extracted are shown in bold. The list of obtained features is given in Table 2. With 2 features obtained from 5 different wavelet coefficients, a feature matrix was created for each window data.

Table 2. Feature list obtained from each window

No.	Feature Name	The wavelet coefficient from which the feature is obtained	No.	Feature Name	The wavelet coefficient from which the feature is obtained
1	Shanon Entropy	A7	6	Standard deviation	D4
2	Shanon Entropy	D7	7	Standard deviation	D5
3	Shanon Entropy	D6	8	Standard deviation	D6
4	Shanon Entropy	D5	9	Standard deviation	D7
5	Shanon Entropy	D4	10	Standard deviation	A7

The created feature matrix is given as input to the classifier algorithm. 80% of the data was used as training and the rest as testing. RF algorithm was used as the classifier algorithm. The RF algorithm is an improved version of the bagging method. Instead of branching out each node using the best branch among all the variables, it branches each node using the best among the randomly selected variables at each node. Each dataset is generated by displacement from the original dataset. Trees are then developed using random feature selection. Developed trees are not pruned (Archer & et al. 2008, Breiman & et al. 2001). With this strategy, the RF algorithm achieves successful results. RF is also very fast, resistant to overfitting and can work with as many trees as desired. Two parameters are defined by the user to start the RF algorithm. These parameters are the number of variables used at each node and the number of trees to be developed to determine the best split (Breiman & et al., Edla & et al. 2018).

Results and Discussion

In this study, a machine learning technique has been proposed to help the correct diagnosis of neuromuscular diseases from EMG data. In this study using the PhysioNet data set, normal-myopathy-neuropty data were classified.

EMG data are divided into windows and classified by calculating 2 features from 5 different wavelet coefficients. Data are classified with the RF algorithm. From the RF algorithm parameters; Batch size 40, max. depth 10 and number of trees 50. As a result of the study, 96,10% success was achieved with the RF algorithm in the correct classification of neuromuscular diseases. In terms of misdiagnosis rate, the error rate was again determined as 3,90%. The comparison of this study and the studies in the literature is given in Table 3.

Kucuk H. et al. focused on 2-class study rather than 3-class study. According to the results of binary classification using 25 features, they achieved an average success rate of 92,9%. Belkhou A. et al. similarly made a 2-class classification in their study. As a result of classification, they achieved a high success rate by using 55 features. However, the proposed model was used only to differentiate normal-disease data. Istenic R. et al. achieved a success rate of 70,4% with 40 features using SVM. Subasi A. et al. achieved a success rate of 99% using 47 features in their study. In this study, 10 features were used. Compared to the studies in the literature, the number of features used is quite low. This provides advantages with faster classification performance and less processing overhead. The success rate obtained was close to or higher than the success rates in the literature.

Considering the number of features used with success rates, it is understood that the model can be classified with few features and high accuracy.

Table 3. Accuracy comparison

Author	Dataset	Class types	Classifier	Number of Features	Acc.
Kucuk H. et al.	EMGLAB	Neuropathic -Normal Neuropathic -Myopathic Myopathic - Normal	SVM	25	97,39% 94,57% 86,74% Avg. 92,9%
Subasi A. et al.	EMGLAB	Myopathic-Neuropathic-Normal	Bagging Ensemble with SVM	47	99%
Istenic R. et al.	-	Myopathic-Neuropathic-Normal	SVM	40	70,4%
Belkhou A. et al.	EMGLAB	Normal- Neuropathic Normal-Miyopati	SVM KNN	55	99.34% 99.07%
This work	PhysioNet	Myopathic-Neuropathic-Normal	RF	10	96,10%

Although artificial intelligence is used in many sectors, its use in the health sector is increasing day by day. Expanding the use of machine learning algorithms, especially in the early diagnosis of high-cost chronic diseases, will positively affect the quality and cost of the delivery of health services. By using the created model on different data sets and increasing the data volume and size, it can give priority to the diagnosis and treatment process studies of diseases.

REFERENCES

- Archer, K. J. (2008) Empirical characterization of random forest variable importance measure, computational statistical data analysis. *Computational Statistics & Data Analysis*, 52 (4), 2249-2260.
- Bekiroglu, S., Cifci, E. G. (2016) The Evaluation Concerning Patient Complaint Systems Depend On General Secretary Hospitals. *Journal of Medical Social Work*, 0 (7), 32-42.
- Belkhou, A., Jbari, A., Badlaoui, O. E. (2021) A computer-aided-diagnosis system for neuromuscular diseases using Mel frequency Cepstral coefficients. *Scientific African*, 13, e00904.
- Breiman, L. (2001) Random forests, machine learning. *Kluwer Academic Publishers*, 45 (1), 5-32.
- Edla, D. R. Mangalorekar, K., Dhavalikar, G., Dodia, S. (2018) Classification of EEG data for human mental state analysis using Random Forest Classifier. *Procedia Computer Science*, 132, 1523-1532.
- Goldberger, A., Amaral, L., Glass, L., Hausdorff, J., Ivanov, P. C., Mark, R., ... & Stanley, H. E. (2000) PhysioBank, PhysioToolkit, and PhysioNet: Components of a new research resource for complex physiologic signals. *Circulation*, 101 (23), e215–e220.
- Istemic, R., Kaplanis, P. A. (2010) Multiscale entropy-based approach to automated surface EMG classification of neuromuscular disorders. *Med Biol Eng Comput*, 48, 773–781.
- Kucuk, H., Eminoglu, I., Balci, K. (2019) Classification of neuromuscular diseases with artificial intelligence methods. *Journal of the Faculty of Engineering and Architecture of Gazî University*, 34 (4), 1725-1741.
- Lee, J. W., Shin, M.J., Jang, M.H., Jeong, W.B., Ahn, S. J. (2021) Two-stage binary classifier for neuromuscular disorders using surface electromyography feature extraction and selection. *Medical Engineering and Physics*, 98, 65-72.
- Subasi, A., Yaman, E., Somaily, Y., Alynabawi, H.A., Alobaidi, F., Altheibani, S. (2018) Automated EMG Signal Classification for Diagnosis of Neuromuscular Disorders Using DWT and Bagging. *Procedia Computer Science*, 140, 230-237.
- Tuncer, E. (2022) Ictal-Interictal Epileptic State Classification with Traditional and Deep Learning Architectures. *International Journal of Research Publication and Reviews*, 3 (9), 1972-1977.

Performing Heart Rhythm With Iot Using Ecg Sensor

Çağatay ERSİN
Mehmet KARAYEL

Introduction

Today, cardiovascular diseases have become widespread due to unhealthy diets and sedentary lifestyles. Detection of cardiovascular diseases can be done with EKG devices in health institutions. In this study, a device that can measure and remotely monitor heart rhythm was designed and realized for individuals with cardiovascular disease. In the study, the ESP8266 wifi module was used for remote monitoring of the ECG heart sensor, microcontroller development board, and IoT (Internet of Things) channels over the internet. When the individual with heart disease or heart rhythm disorder places the probes of the ECG sensors in the heart region, instant measurements are made with the controller and sent to the previously opened channels on the thingspeak internet address, which is an IoT interface. Thanks to this study, the healthcare team will be able to follow the heart rhythm even when the patient is away. Cardiovascular diseases commonly cause death worldwide [1,3,4] Deaths due to heart diseases in Turkey constitute 45% of total deaths. Time is of the essence in any disease that occurs in the cardiovascular system. Anomalies occurring in the patient should be identified quickly and communicated to healthcare professionals. For this reason, continuous timed ECG recordings are of vital importance in patients with heart disease who have problems in the cardiovascular system [1].

Early diagnosis or preliminary inference is very important in the health sector. While this is important for the quality and effectiveness of the treatment, it also means vital interventions for critical diseases. The most important step necessary for the realization of preliminary inference and early diagnosis is the continuous monitoring of the data. Continuous monitoring and analysis of people's data can enable immediate detection of abnormal situations [2].

cardiovascular diseases occur due to dangerous factors such as smoking, hypertension, blood lipids, hereditary heart disease from the family, obesity and diabetes. To reduce the mortality rates brought about by these disorders, an Electro Cardiograph device was made. With this device, electrical activities occurring in the heart are observed, and with the data received, diseases in the heart can be detected beforehand and necessary precautions can be taken. With the EKG device, the flow rate and pulse of the heart can be easily measured [4]. The ECG is one of the most widely available and routinely performed diagnostic tools in modern medicine for non-invasive cardiovascular diseases [5]. Instant display of ECG data is of great importance for patients with heart disease [1]. In this study, a system that can send instant data to the thingspeak IoT interface with an ECG sensor has been designed. The heart rate graphs of the sick individual were monitored remotely with this system.

Material and Method

Heart signals are an important and effective biological signal used in the diagnosis of cardiovascular diseases [6]. The EKG, which is used for the diagnosis of cardiovascular diseases, is a device that provides a graphical recording of the electrical activity that occurs during the contraction of the heart. A weak electrical activity occurs during the contraction and relaxation of the atria and ventricles, also known as the heartbeat. This activity contains a lot of data on heart rhythm, frequency and spread. Electrocardiography, or in other words, an EKG device, is used to measure electrical activity. Electrodes attached to the skin on the chest, arms and legs allow the electrical activity of the heart to be measured [7]. In this study, the heart rhythm data from the ECG sensor were instantly measured and sent to the Thingspeak IoT interface via the ESP82266 wifi module. Arduino Uno microcontroller development board was used in the study and the ECG sensor was connected to the microcontroller development board. The power of the study was provided by a lithium-polymer battery with a voltage of 7.4 volts. The ESP8266 wifi module is connected to Arduino's microcontroller development board to send instantaneous data measured from the ECG sensor to the Thingspeak IoT interface. The block diagram of the study is shown in figure 1.

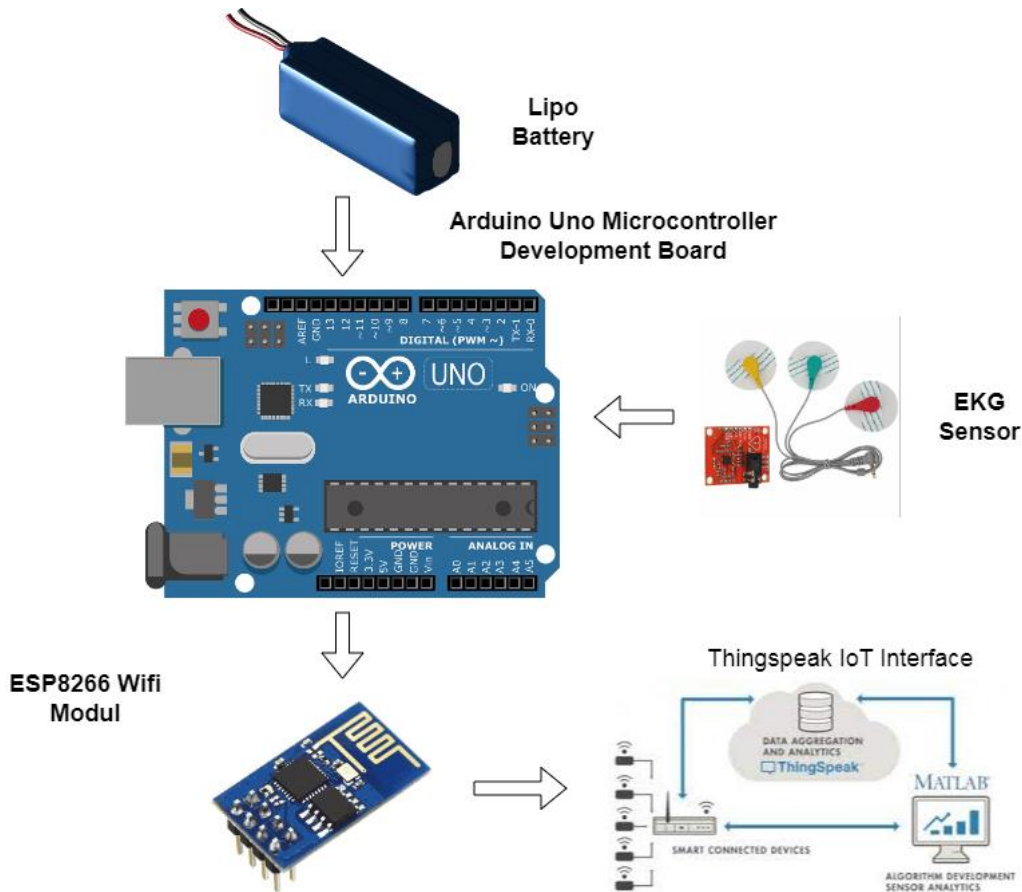


Figure 1. Block diagram of the system

2.1. Internet of Things

The detection provided by Wireless Sensor Network (WSN) technologies, which is the main area of use of IoT (Internet of Things), is encountered in many areas of today's life. This offers the ability to measure, infer and understand environmental indicators from sensitive natural resources

to urban environments. The proliferation of these devices in a communicative network creates the Internet of Things (IoT). Here, sensors and actuators seamlessly interact with the environment and enable information to be shared across platforms to develop a common language of communication. Fueled by the adoption of various wireless technologies such as RFID tags and embedded sensor and actuator nodes, IoT has evolved day by day from the beginning [8] The Internet of Things (IoT) allows physical objects to see, hear, and think, It allows coming together and "talk". IoT is the transformation of basic technologies such as embedded devices, communication protocols, sensor networks, internet protocols and applications from traditional to smart ones [9,10]. The concept of the Internet of Things was first used by Kevin Ashton in 1999 in a presentation on the benefits of Radio Frequency Identification (RFID) technology for P&G [11]. Internet of Things; It is used in applications such as e-health, home automation, smart environment, smart water, smart agriculture, smart livestock, smart energy, smart cities, smart measurement, industrial control, security and emergencies, shopping, and logistics. Relevant data are collected from sensors to provide better quality service in these areas and to increase efficiency and productivity. These data are stored in Cloud Computing systems, creating "Big Data". They are analyzed by machine learning methods and contribute to making related improvements. The most prominent application areas include the smart industry, where the development of smart manufacturing systems and connected manufacturing spaces is often discussed under the heading Industry 4.0. While smart energy applications focus on smart electricity, gas and water meters; In the smart home or building field, smart thermostats and security systems are attracting a lot of attention in the context of the Internet of Things applications [12]. In the study, the heart rate data was sent to the thingspeak internet of things interface by using the internet of things technology. Thanks to the study, the heart rate data of the patient, whose ECG sensor is attached to his body, will be able to be monitored remotely.

2.2. Thingspeak IoT Interface

Thingspeak is a free data platform for the Internet of Things (IoT) that remains popular today. Thingspeak is also a web-based open API IoT-based information platform that converts external components used for IoT into their data and is used to store sensor data. Thingspeak communicates between the internet connection and the cloud as a 'data packet' carrier and takes the detected graphic from the connected sensor to the main microcontroller, records, analyzes, observes and works. Thingspeak Arduino, TI CC3200 module, Raspberry-pi etc. It helps build the social network of development photos, sensor-based daily apps, location/location tracking apps, and updated objects. The main feature of the Thingspeak function is the Data field, location field, and Channel field, which is the status field. Thingspeak, mechanical mechanisms can be created, and the information you choose and information can be processed and visualized alternately and matched with MATLAB's use of tweets and other warning forms. It also offers the ability to create a general channel for general analysis and forecasting. It takes advantage of graphic visualization operations for sensors/actuators and can be used for objects. IoT helps bring everything together and allows us to communicate with our things, and more interestingly, allows objects to interact with other objects. This is the platform. Thingspeak offers the use of real data, graphic visualization, as well as plug-ins used to collaborate with web services, social networks or API. The main feature of Thingspeak is the Thingspeak Channel. On a page that will send the channel to Thingspeak for channelling. Programs loaded on the microcontroller transmit to the thingspeak channel within a certain period on the sensor screen. Programs uploaded to the microcontroller have a 15-second period to transmit the latest sensor values to the Thingspeak Channel. As the internet of things progressed, the wireless sensor network became more and more acceptable. As the Internet of Things progresses, the wireless sensor network is used. [13].

In this study, heart rate data is taken with a microcontroller development board and sent to the thingspeak channel with ESP8266. By opening an account in the Thingspeak IoT interface, a channel was created and heart rate data was sent to this channel. In addition, the position of the patient with an ECG sensor is entered in thingspeak, the channel is opened and the position information is shown in this channel.

2.3 Design of the System

In this study, a biomedical device was designed using a microcontroller development board. With this designed device, heart data can be obtained and monitored while the person with heart disease is away. ECG sensor pads (green, red, yellow) are placed on the person's body. The yellow electrode was placed on the heart of the patient, the red electrode was placed on the right side in line with the heart, and the green electrode was placed on the abdomen. The regions where the electrodes are placed are shown in figure 2.

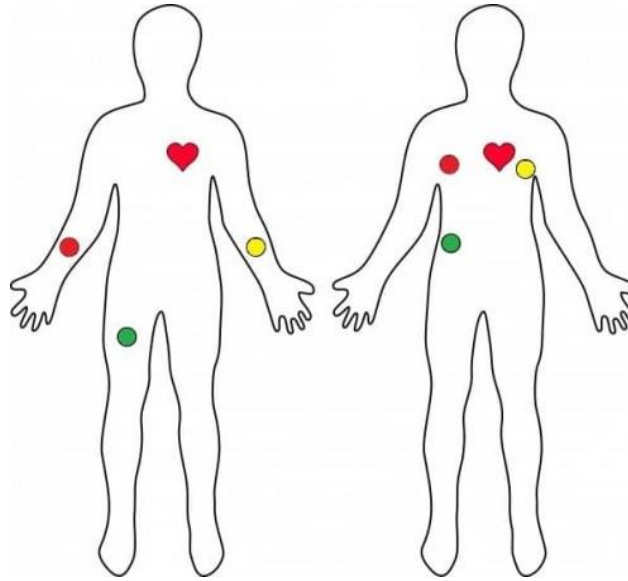


Figure 2. Areas where ECG electrodes are placed

The system is connected electronically and instant data is taken with the electrodes. The electronic circuit of the system in the study is shown in Figure 3.

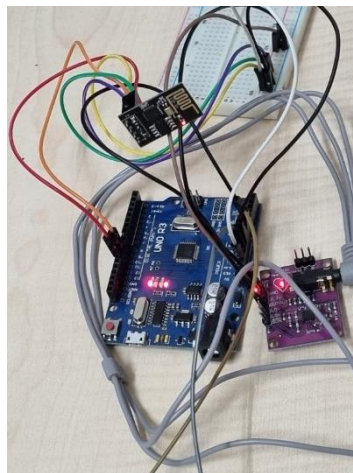


Figure 3. The electronic circuit of the system

Data from the system was received with the code written to the Arduino ide software. The data obtained with the electrodes attached to the person were instantly monitored on the serial monitor. The graphical representation of the data on the serial plotter is given in figure 4.

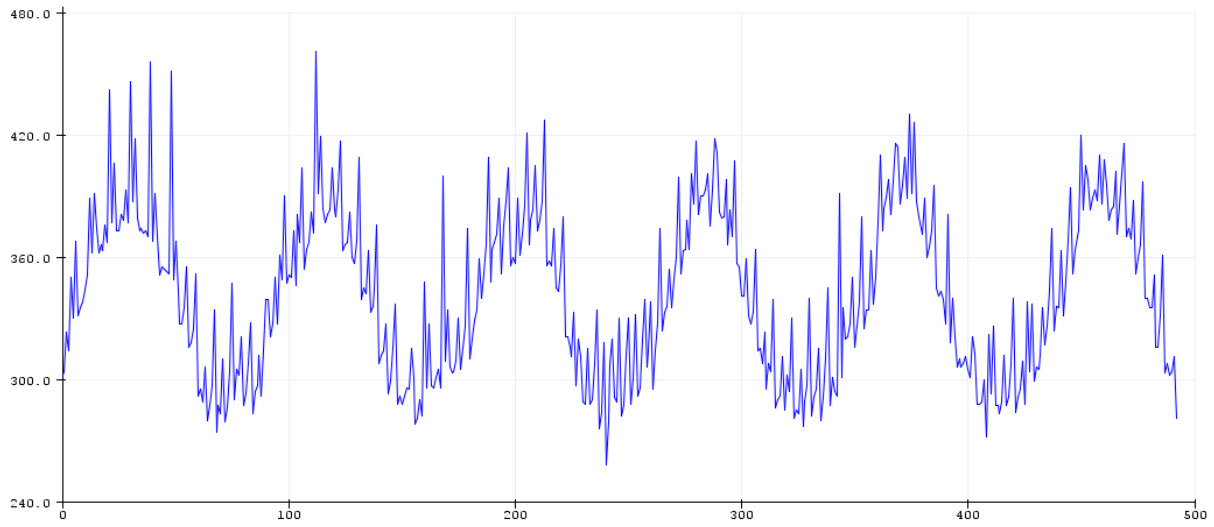


Figure 4. ECG graph

In the study, this instantaneous data was sent to the Thingspeak IoT channel using the ESP8266 wifi module. The device is connected to the internet with the wifi name and password and the data is sent to the thingspeak IoT interface IP address. The image of the sent data is shown in figure 5.

```
Data Send.  
112.33  
128.67  
GET https://api.thingspeak.com/update?api_key=1FNPNELLDGNUKX5B&field1=128.67
```

```
Data Send.  
98.67  
95.67  
GET https://api.thingspeak.com/update?api_key=1FNPNELLDGNUKX5B&field1=95.67
```

Figure 5. Data sent to Thingspeak IoT interface

These sent data were transferred to the Thingspeak IoT channel, which was opened before. It is shown graphically in the channel. In addition, the data of the person received through the electrodes are displayed on the screen by entering the location information. The location and graphical representation of the data sent to the Thingspeak IoT interface are shown in figure 6.

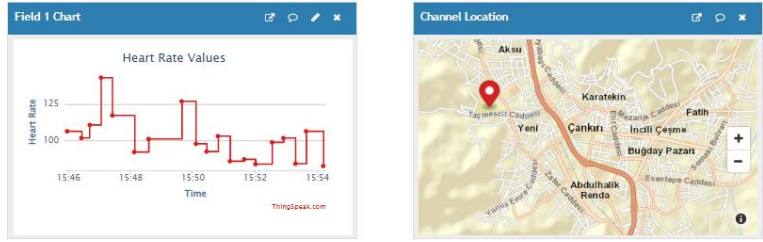
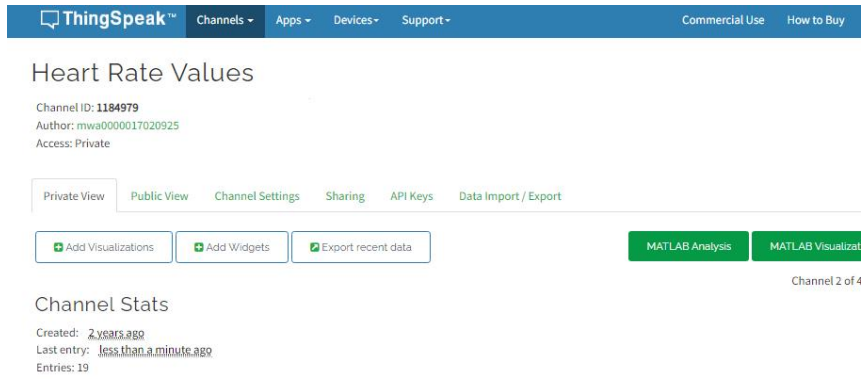


Figure 6. Thingspeak IoT interface, 2022

In the study, heart data was taken from the user and displayed as date and time on the thingspeak channels with an IoT interface. The location where the user's data is taken is also shown on a different screen. The display of the user's heart rate graphics and location over the channel is given in figure 7.

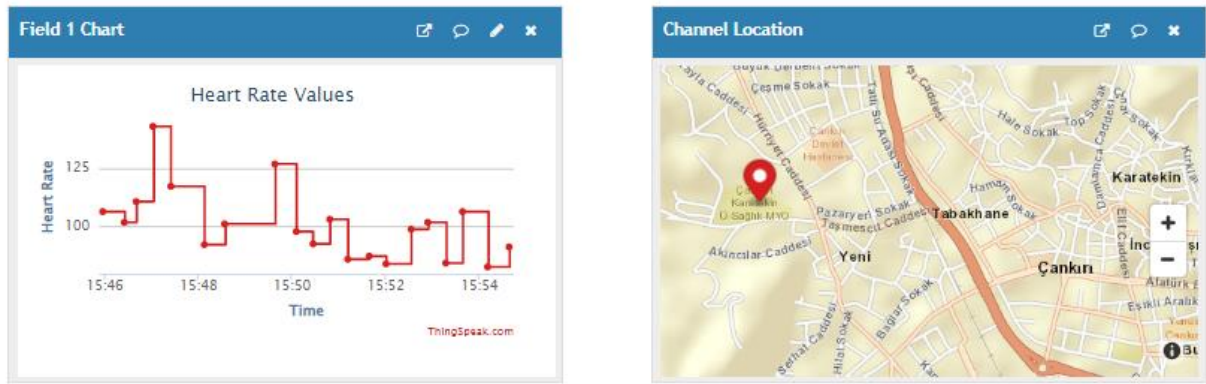


Figure 6. Data and location in the Thingspeak IoT interface channel

The healthcare team will be able to follow the patient remotely through this study. In addition, the thingview, which is an android software, is graphically shown in the interface for the tracking of the data sent to the Thingspeak interface with the android device. The graphical representation of the data coming to the Thingview interface is given in figure 7. Here, it is seen that the instantaneous heart rate is 106.33 and the maximum and minimum values are given.



Figure 7. Android IoT interface,

3. Results and Evaluation

In this study, a biomedical device was designed. The device received heart rate data with the ECG sensor and sent it to Thingspeak, which is used as an IoT interface with the internet of things technology. In the designed system, an ECG heart sensor, microcontroller development board for data acquisition and control, and EPS8266 wifi module are used to send data to the internet. With this study, the heart rhythm of the user can be monitored remotely with the Thingspeak internet address or android device. The study has been tested on the user and the data has been taken. The user's heart rate graph is shown in the system. In addition, with the location channel performed in this study, the information from which region the user's ECG data were obtained is also reached.

REFERENCES

Bilgin, SN, & Çamurcu, AY (2017). Wireless ECG and Pulse Oximeter Application System Design.

Akleyek, S., KILIÇ, E., Söylemez, B., Aruk, E., & Aksaç, C. (2020). A Study on Internet of Things Based Health Monitoring Systems. *Journal of Engineering Sciences and Design*, 8(5), 80-89.

İlhan, İ. (2017). Mobile device controlled EKG holter. *Dicle University Engineering Faculty Journal of Engineering*, 8(1), 101-110.

Farmer, B., Zeynep, S. EN, & AKKAS, M. (2021). Internet of Things Based Wireless Portable ECG Device. *European Journal of Science and Technology*, (26), 91-95.

Abdioğlu, S., Acar, B., & Kavsaoglu, AR (2021). Wireless ECG Device Design and Website Design for the Evaluation of Attributes Using Signal Processing Techniques. *European Journal of Science and Technology*, (26), 144-150.

Arslan, Ö., & Karhan, M. (2022). Effect of Hilbert-Huang transforms on classification of PCG signals using machine learning. *Journal of King Saud University-Computer and Information Sciences*.

medicalpark.com.tr

Ersin, C., Yaz, M., & Karhan, M. (2019). An Example IoT Application for the Defense Industry. *Electronic Letters on Science and Engineering*, 15(3), 66-73.

Aktaş, F., Ceken, C., & Erdemli, YE (2016). Applications of IoT technology in the field of biomedicine. *Düzce University Journal of Science and Technology*, 4(1), 37-54.

Gökrem, L., & Bozuklu, M. (2016). Internet of Things: Studies and current situation in our country. *Gaziosmanpaşa Journal of Scientific Research*, (13), 47-68.

Ercan, T., & Kutay, M. (2016). Internet of Things (IoT) applications in industry. *Afyon Kocatepe University Journal of Science and Engineering*, 16(3), 599-607.

Altınpulluk, H. (2018). The use of internet of things technology in educational environments. *Journal of Open Education Applications and Research*, 4(1), 94-111.

Ersin, C., & Ali, O. Z. (2020). IoT-based embedded system design and implementation for occupational health and safety. *European Journal of Science and Technology*, (18), 494-504.

Improvement of Satellite Optimization Parameters with Lagrange Multipliers

Enes ÇELİK¹

Introduction

With the beginning of the space age, satellites began to use in communication, earth observation and navigation. Satellite design, analysis, optimization, production, integration and operation have become essential areas. The problems that arise in satellite research and development are becoming increasingly complex. Satellite system design features, satellite orbiting and security design are still being developed today. Comprehensive design is to design and optimize at the system level. In this process, the design plan is according to the needs. Effective payload, reliability, launch and orbit are designed simultaneously in satellites. In addition, the effective load is limited for reliability reasons. Thus, the satellite system consists of many subsystems and becomes a problem involving a series of complex calculations. One of these subsystems is to optimize the design. Our limitations here may be parameters such as budget, lifespan and weight. The research aims to optimize the satellite performance and operation under the relevant rule constraints with the help of optimization subsystems of the overall satellite design (Larson & Wertz, 1999). The thrust of the satellites has increased thanks to the batteries with the latest technology (Dutta et al., 2013). In addition, mini, micro and nano satellites have developed. Earth's outermost satellites or satellites close to the Van Allen belt are exposed to severe radiation with long transfer times and sunrays causing damage to satellite devices (Dutta et al., 2014). To better model the satellite system, the transfer trajectory design should be calculated along with the station holding strategy, power, state control, thermal control, and outer construction material (Sobieszczanski-Sobieski, 1995). Therefore, multidisciplinary design optimization is preferred to deal with satellite system design problems (Sobieszczanski-Sobieski & Haftka, 1997).

Related Works

Shi et al. proposed a surrogate-assisted multidisciplinary design optimization framework for the multidisciplinary design optimization problem of electrified geostatic orbital satellites, consisting of multidisciplinary modeling, multidisciplinary analysis, and surrogate-assisted optimizer (Shi et al., 2017). Appel et al. were interested in the optimization problem of multi-satellite orbit transfer. The solution was carried out using functional optimization techniques. This algorithm is based on a combination of first-order gradient and neighbor-extremal algorithms (Appel et al., 2014). Conway, in a study, examined numerical optimization methods in the satellite optimal orbit problem. He proposed a solution to this optimization process with calculus of variations, nonlinear programming, parametric optimization and evolutionary algorithms (Conway, 2010). In one of his studies, George used a genetic algorithm and simulated annealing methods together to minimize the revisit time of constellation-shaped satellites (George, 1997). Wu et al. used the collaborative optimization method for the optimization problem of the remote sensing

¹ Instructor, Computer Science, Babaeski Vocational School, Kırklareli University, orcid: 0000-0002-3282-865X

satellite, which includes power, attitude control, thermal control and infrastructure systems (Wu et al., 2013). Huang et al. developed the nested cooperative optimization method to solve the optimization problem of manoeuvrable satellites (Huang et al., 2014).

Material and Methods

Lagrange multipliers are there to solve the constraints incrementally, incrementally. It is a precise method that optimizes the objective function to meet Kuhn-Tucker conditions (Luenberger & Ye, 1984). Since the main framework of the discrete Lagrange multipliers theory is similar to continuous lagrange multipliers, it is preferred for satellite optimization problems with continuous lagrange multipliers.

Continuous Lagrange Multipliers

Continuous Lagrange multipliers were initially developed to address constrained optimization problems. This method tries to find a local minimum by transforming an equality-constrained issue into an unconstrained problem space with the help of the Lagrangian function, where the objective function is expressed as follows.

$$\begin{aligned} &\text{Minimize } f(x) \\ &h_i(x) = 0 \quad i = 1, \dots, m \\ &x \in X \\ &L(x, \lambda) = f(x) + \lambda^T h(x) \end{aligned}$$

Then the x's are minimized to obtain an extreme point of the Lagrangian function (Avriel, 2003).

Discrete Lagrange Multipliers

Discrete Lagrange Multipliers provide a mathematical basis for handling discrete-constrained optimization. This theory extends the concept of a straight saddle point to discrete space. It provides the initial conditions for a saddle point to be a local minimum by defining a Lagrangian factorization formulation. Discrete Lagrange multipliers attempt to concentrate on generic theorems and lemmas related to discrete constrained optimization that do not answer according to the problem structure. Here d denotes a random set of discrete values. To find discrete Lagrangian factors, the generalized Lagrangian function defines in discrete space.

$$L_d(x, \lambda) = f(x) + \lambda^T H(h(x))$$

H is the continuous transformation function. The lambda equality constraints and $h(x)$ represent the corresponding vector of Lagrangian multipliers. Unlike straight Lagrange multipliers, it has been proven that the Discrete Lagrange Factors and the concept of the saddle point are intertwined. Thus, the conditions for a saddle point can change to be sufficient conditions for the local minimum solution (Wu, 1998).

Parameters of an available satellite system that need to be optimized; economy, outer shell, pneumatics, orbit, reliability, thermal control, thrust, weight, and electromagnetism. Numerical solutions for several representative cases are present for use in optimization processes. According to the weight function and constraint function consisting of impulse (x), budget (y), and electromagnetism (z) variables, what can be the x , y , and z variables to minimize the weight?

$$f(x, y, z) = x + y + 2z$$

$$g(x, y, z) = x^2 + y^2 + z^2 = 3$$

$$\nabla f = (1, 1, 2)$$

$$\nabla g = (2x, 2y, 2z)$$

$$1 = 2\lambda x$$

$$1 = 2\lambda y$$

$$2 = 2\lambda z$$

$$x^2 + y^2 + z^2 = 3$$

λ cannot be zero,

$$x = \frac{1}{2\lambda}$$

$$y = \frac{1}{2\lambda}$$

$$z = \frac{1}{\lambda}$$

substituting x, y, z in the equation,

$$\frac{1}{4\lambda^2} + \frac{1}{4\lambda^2} + \frac{1}{\lambda^2} = 3, \lambda = \pm \frac{\sqrt{2}}{2}$$

If λ substitute in the equations, in order of x, y, z,

$$(x, y, z) = \left(\frac{\sqrt{2}}{2}, \frac{\sqrt{2}}{2}, \sqrt{2}\right) \text{ or } (x, y, z) = \left(-\frac{\sqrt{2}}{2}, -\frac{\sqrt{2}}{2}, -\sqrt{2}\right)$$

substituting x, y, and z in the weight function,

$$f\left(\frac{\sqrt{2}}{2}, \frac{\sqrt{2}}{2}, \sqrt{2}\right) = x + y + 2z = 3\sqrt{2}$$

$$f\left(-\frac{\sqrt{2}}{2}, -\frac{\sqrt{2}}{2}, -\sqrt{2}\right) = x + y + 2z = -3\sqrt{2}$$

These critical points $\left(-\frac{\sqrt{2}}{2}, -\frac{\sqrt{2}}{2}, -\sqrt{2}\right)$ select to minimize the weight function.

According to the age function and constraint function consisting of the orbit (x) and thermal level (y) variables, what can be the x and y variables to maximize the age?

$$f(x, y) = xy$$

$$g(x, y) = 3x^2 + y^2 = 6$$

$$\nabla f = (y, x)$$

$$\nabla g = (6x, 2y)$$

$$y = 6\lambda x$$

$$x = 2\lambda y$$

$$3x^2 + y^2 = 6$$

x in the equation is substituted for x in the other equation,

$$y = 6\lambda(2\lambda y) = 12\lambda^2 y$$

x and y cannot be zero, simplifying the equation with y,

$$12\lambda^2 = 1$$

$$6 = 3x^2 + (6\lambda x)^2$$

$$6 = 3x^2 + 36\lambda^2 x^2$$

$$6 = 3x^2 + 3(12\lambda^2)x^2$$

$$6 = 3x^2 + 3x^2$$

$$x = \pm 1, y = \pm\sqrt{3}$$

Critical points are $(1, \sqrt{3})$, $(-1, \sqrt{3})$, $(1, -\sqrt{3})$, $(-1, -\sqrt{3})$. If x, y, pairs are written in place of the age function,

$$f(1, -\sqrt{3}) = xy = -\sqrt{3}$$

$$f(-1, \sqrt{3}) = xy = -\sqrt{3}$$

These critical points can select to minimize the age function.

$$f(1, \sqrt{3}) = xy = \sqrt{3}$$

$$f(-1, -\sqrt{3}) = xy = \sqrt{3}$$

These critical points can select to maximize the age function. Since we aim to maximize the age function $(1, \sqrt{3})$, $(-1, -\sqrt{3})$, these critical points are selected.

According to the cost function and constraint function consisting of pneumatic (x), outer shell (y), and weight by mass (z) variables, What can be the x, y, and z variables to minimize the cost?

$$f(x, y, z) = x^2 + y^2 + z^2$$

$$g(x, y, z) = x + y + z = 1$$

$$h(x, y, z) = x + 2y + 3z = 6$$

$$\nabla f = (2x, 2y, 2z)$$

$$\nabla g = (1, 1, 1)$$

$$\nabla h = (1, 2, 3)$$

$$x = \frac{\lambda + \mu}{2}$$

$$y = \frac{\lambda + 2\mu}{2}$$

$$z = \frac{\lambda + 3\mu}{2}$$

$$x + y + z = 1$$

$$x + 2y + 3z = 6$$

x, y, and z are substituted in the equation,

$$\frac{\lambda+\mu}{2} + \frac{\lambda+2\mu}{2} + \frac{\lambda+3\mu}{2} = 1, 3\lambda + 6\mu = 2$$

$$\frac{\lambda+\mu}{2} + 2\left(\frac{\lambda+2\mu}{2}\right) + 3\left(\frac{\lambda+3\mu}{2}\right) = 6, 3\lambda + 7\mu = 6$$

$\mu=4$ from the equations. If μ is substituted in the other equation,

$$3\lambda + 7(4) = 6, \lambda = -\frac{22}{3}$$

If λ and μ are substituted in the equations,

$$x = \frac{\lambda + \mu}{2} = \frac{-\frac{22}{3} + 4}{2} = -\frac{5}{3}$$

$$y = \frac{\lambda + 2\mu}{2} = \frac{-\frac{22}{3} + 8}{2} = \frac{1}{3}$$

$$z = \frac{\lambda + 3\mu}{2} = \frac{-\frac{22}{3} + 12}{2} = \frac{7}{3}$$

Thus, the critical points are $(-\frac{5}{3}, \frac{1}{3}, \frac{7}{3})$, respectively. Substituting the x, y, and z cost function,

$$f\left(-\frac{5}{3}, \frac{1}{3}, \frac{7}{3}\right) = x^2 + y^2 + z^2 = \frac{25}{3}$$

The value in the equation is the minimum point. There is no maximum point. These critical points $(-\frac{5}{3}, \frac{1}{3}, \frac{7}{3})$ choose to minimize the cost function.

Results

Satellite design, analysis, optimization, production, integration, and operation are critical subjects. Satellite systems consist of many subsystems and become a problem involving a series of complex calculations. Our primary constraints here are budget, life span, and weight parameters. In this study, satellite design optimization parameters were optimized under minimal possibilities. In this optimization process, the minimum and maximum points of the parameters related to Lagrange Multipliers have been determined. Since many parameters exist in satellite systems, successful results have been observed using Lagrange Multipliers in optimization processes. This study applied Lagrange Multipliers to artificial world data, not real-world data. In future studies, Lagrange Multipliers can be used in satellite optimization processes under constrained conditions.

References

- Appel, L. Guelman, M. & Mishne, D. (2014) Optimization of satellite constellation reconfiguration maneuvers. *Acta Astronautica*, 99, 166-174.
- Avriel, M. (2003) Nonlinear programming: analysis and methods. *Courier Corporation*.
- Conway, B. A. (2010) A brief survey of methods available for numerical optimization of spacecraft trajectories. In *61st International Astronautical Congress*, (pp. 1848-1862).
- Dutta, A. Libraro, P. Kasdin, N. J. Choueiri, E. & Fracken, P. (2013) Design of next-generation all-electric telecommunication satellites. In *31st AIAA International Communications Satellite Systems Conference* (pp. 5625).
- Dutta, A. Sreesawet, S. Vijayan, S. & Foster, A. (2014) On the design of power and propulsion subsystems of all-electric telecommunication satellites. In *32nd AIAA International Communications Satellite Systems Conference* (pp. 4243).
- George, E. R. (1997) Optimization of satellite constellations for discontinuous global coverage via genetic algorithms. *Astrodynamics*, (pp. 333-346).
- Huang, H. An, H. Wu, W. Zhang, L. Wu, B. & Li, W. (2014) Multidisciplinary design modelling and optimization for satellite with maneuver capability. *Structural and Multidisciplinary Optimization*, 50(5), 883-898.
- Larson, W. J. & Wertz, J. R. (1999) Space mission analysis and design. *Space*, 5(14), 110.
- Luenberger, D. G. & Ye, Y. (1984) Linear and nonlinear programming (Vol. 2). Reading, MA: Addison-wesley.
- Shi, R. Liu, L. Long, T. Liu, J. & Yuan, B. (2017) Surrogate assisted multidisciplinary design optimization for an all-electric GEO satellite. *Acta Astronautica*, 138, 301-317.
- Sobieszczanski-Sobieski, J. (1995) Multidisciplinary design optimization: an emerging new engineering discipline. In *Advances in structural optimization* (pp. 483-496) Springer.
- Sobieszczanski-Sobieski, J. & Haftka, R. T. (1997) Multidisciplinary aerospace design optimization: survey of recent developments. *Structural optimization*, 14(1), 1-23.
- Wu, Z. (1998) *Discrete Lagrangian methods for solving nonlinear discrete constrained optimization problems*. Doctoral dissertation, M. Sc. Thesis, University of Illinois, Urbana, IL.
- Wu, W. Huang, H. Chen, S. & Wu, B. (2013) Satellite multidisciplinary design optimization with a high-fidelity model. *Journal of Spacecraft and Rockets*, 50(2), 463-466.

Potent Matrices

Hasan KELEŞ¹

Giriş

This section is about the justification of (iii), which is one of the conditions for the algebraic structure that forms the basis of abstract algebra. The structure monoid of and how it is displayed on the structure is investigated. The definition of the idempotent element on a monoid structure is discussed. The algebraic structures according to the binary operation of multiplying square matrices in matrices, (\square, \cdot) and $(\square, +)$ are known that are monoids. The real numbers \square , with the usual operations of addition and multiplication, also form a field. In order to make the study more understandable, first the structures in \square and then the structures of square matrices according to the multiplication operation in the matrix are included. The situation of the equations that provide idempotent element formation in these structures in their own structures was examined. The solution of the equation $x^2 = x$ in real numbers is 0 and 1. Also, the solution of the equation $x^k = x$ in integer numbers is the number 0 and, If $k \in \square^+$ is odd, the set of solution to the equation $x^k = x$ is $\{0,1\}$, if k is even, it is $\{-1,0,1\}$.

The solution of the equation $x^2 = 1$ in real numbers is $x = \pm 1$. The solution of the equation $x^2 = x$ is 0 and 1. The solutions of this equation, 0 and 1, are idempotent numbers.

$$x^2 = x \Rightarrow x^2 - x = 0$$

$$x(x-1) = 0 \Rightarrow x = 0 \vee x = 1.$$

Let F be a field and $M_n(F) = \left\{ \left[a_{ij} \right]_n \mid a_{ij} \in F, n \in \square^+ \right\}$. Here $M_n(F)$ is considered as set of square matrices. The equation $AX = B$ is written for $A, X, B \in M_n(\square)$ matrices.

If $A = X = B$ matrix is taken in $AX = B$ equation, $X^2 = X$ equation is obtained. Necessary conditions in the solution of this equation necessitated the following definition.

$$X^2 - X = [0] \Rightarrow X(X - I_n) = [0]$$

$$X^2 - X = [0] \Rightarrow X = [0] \vee X = I_n.$$

Also, the solutions of the equation $X^2 = X$ are zero dividing matrices,

$$X(X - I_n) = [0] \Rightarrow X \neq [0] \vee X \neq I_n.$$

¹ Lecturer, Karadeniz Technical University, e-mail: hasankeles@ktu.edu.tr

In this section, the forces resulting from the multiplication of matrices and hence the forces of matrices are examined. For the special matrices existing in the literature, the conditions for being written for some orders are given.

Let us start with the row co-divisor definition that I gave in the study in [10-11].

Let A^T denote the transpose of $A \in M_n(F)$. Let A and B be two regular square matrices of order n . The determinant of the new matrix obtained by writing the i^{th} row of the matrix A on the j^{th} row of the matrix B is called the *co-divisor by row* of the matrix A by the row on the matrix B . It is denoted by AB_{ij} . Their number is n^2 . The matrix co-divisor by row is $\left[\left(AB_{ij} \right)_{ij} \right]$ [9].

For the two matrices satisfying the above conditions, the matrix division is also given by

$$\frac{A}{B} := \frac{1}{|B|} \left[\left(\begin{matrix} A_i \\ B_{ij} \end{matrix} \right)_{ji} \right] \text{ and at the same time, the solution of the equation } AX = B \text{ is } X = \frac{B}{A}.$$

The row co-divisor definition is related to the product XA , and the column co-divisor definition is related to the AX product. The same expression is written in terms of powers when the solutions of the expressions here are repeatedly divided into the same matrix.

Let $A \in \mathcal{M}(\mathbb{R})$ be a regular matrix then there are at least two regular matrices A_1 and A_2 which satisfies the following equation,

$$A = A_1 A_2 \text{ [12].}$$

Every regular matrix can be written as the product of an infinite number of regular matrices. Briefly, for any regular matrix A

$$A = \prod_{i=1}^{+\infty} A_i \text{ where } A_1, A_2, \dots \text{ are regular.}$$

An $n \times n$ matrix A is called involutory iff $A^2 = I_n$, where I_n is the $n \times n$ identity matrix [16].

The broader perspectives are presented for the involutive mind by taking , the periodic mind by taking and the the idempotent mind by taking in the equation .

Any power of a matrix other than an integer of 2 is equal to the unit matrix. To generalize this situation, the following definition is given.

Definition 1. An $n \times n$ matrix A is called k^{th} order involutive iff $A^k = I_n$, where $k \geq 2$.

Example 2. Let the matrix $A = \begin{bmatrix} 1 & 1 \\ -1 & 0 \end{bmatrix}$ be given. The matrix A is the 6th order infolutive matrix by

$$A^6 = \begin{bmatrix} 1 & 0 \\ 0 & 1 \end{bmatrix} = I_2.$$

$$X^k = \begin{cases} \text{idempotent, if } X^k = I_n \\ \text{involutive, if } X^k = X^{-1} \\ \text{nilpotent, if } X^k = [0] \\ \text{periyodik, if } X^{k+1} = X \end{cases}$$

There is sufficient information in the literature about nilpotent, periodic and involutive matrices.

Matrices Idempotent Degree k^{th}

Definition 1. A group is a set G equipped with a binary operation $\cdot : G \times G \rightarrow G$ that associates an element $ab \in G$ to every pair of elements $a, b \in G$, and having the following properties: \cdot is associative, has an identity element $e \in G$, and every element in G is invertible (w.r.t. \cdot). More explicitly, this means that the following equations hold for all $a, b, c \in G$:

1. $a.(b.c) = (a.b).c$. (associativity);
2. $a.e = e.a = a$. (identity);
3. For every $a \in G$, there is some $a^{-1} \in G$ such that $a.a^{-1} = a^{-1}.a = e$. (inverse) [11].

A set M together with an operation $\cdot : M \times M \rightarrow M$ and an element e satisfying only Conditions (G1) and (G2) is called a *monoid* [2, 17].

An element $a \in G$ is an idempotent (element) of G if $a * a = a$. We note $P(G)$ the set of idempotents of G in [1, 2, 17]. This set is the set of 2^{nd} order idempotent elements. Shortly,

$$P^2(G, *) = \{a * a = a, a \in G\}.$$

If a is element $P^2(G, *)$, then processing a , k – times is still equal to a , for a positive integer $k \geq 3$.

$$\underbrace{a * a \cdots * a}_{k\text{-times}} = a.$$

The set $P^k(G, *)$ is the set of *idempotent elements* of degree k^{th} . Likewise,

$$P^k(G, *) = \left\{ a \mid \underbrace{a * a \cdots * a}_{k\text{-times}} = a, a \in G \right\}.$$

The set $P^2(\square, +)$ of the monoid $(\square, +)$ is $\{0\}$ and the set $P^2(\square, \cdot)$ of the monoid (\square, \cdot) is $\{0, 1\}$.

The set of square matrices order n^{th} of a field F is denoted by $M_n(F)$. The set of idempotent elements of the monoid $M_n(F)$ is

$$P^k(M_n(F), \cdot) = \left\{ [a_{ij}]_n \mid A^k = A, A = [a_{ij}]_n \in M_n(F) \right\}$$

$$= \{[0]_n, I_n, \dots\}$$

If $n = 2$, this set is

$$P^2(M_2(F), \cdot) = \left\{ [a_{ij}]_2 \mid A^2 = A, A = [a_{ij}]_2 \in M_2(F) \right\}.$$

In this study, $F = \square$ is taken.

$$P^2(M_2(\square), \cdot) = \left\{ [a_{ij}]_2 \mid A^2 = A, A = [a_{ij}]_2 \in M_2(\square) \right\}.$$

Example 2. The matrix $A = \begin{bmatrix} 2 & -8 \\ \frac{1}{4} & -1 \end{bmatrix} \in P^2(M_2(\square), \cdot)$ is the idempotent elements of degree

2^{nd} . This matrix A is a second order second-degree idempotent matrix since this matrix provides the definition of idempotent,

$$A^2 = \begin{bmatrix} 2 & -8 \\ \frac{1}{4} & -1 \end{bmatrix} \begin{bmatrix} 2 & -8 \\ \frac{1}{4} & -1 \end{bmatrix} = \begin{bmatrix} 2 & -8 \\ \frac{1}{4} & -1 \end{bmatrix} = A.$$

Lemma 3. Let $A \in P^2(M_2(\square), \cdot)$. Then,

$$A^k = A, \text{ where } k \in \square^+.$$

Proof. The proof of this Lemma 3 is done by induction method. It is true for $k = 1$.

$$A = A.$$

Let us assume that lemma 1 for $k - 1$ is true.

$$A^{k-1} = A \Rightarrow (A^{k-1})A = AA = A$$

$$A^k = A.$$

Lemma 4. Let $A \in P^2(M_2(\square), \cdot)$. The elements in the positions of this matrix satisfying the conditions (i) and (ii) given below,

$$1. \quad a_{11} = \frac{1}{2} \pm \frac{1}{2} \sqrt{1 - 4a_{12}a_{21}} = a_{22}, a_{11} + a_{22} = 1.$$

$$2. \quad a_{21} \neq 0 \Rightarrow \begin{cases} a_{21} > 0 \Rightarrow \frac{1}{4a_{21}} > a_{12} \\ a_{21} < 0 \Rightarrow \frac{1}{4a_{21}} < a_{12} \end{cases}$$

$$a_{21} = 0 \Rightarrow A = \begin{bmatrix} 0 & 0 \\ 0 & 0 \end{bmatrix}.$$

Proof. If the matrix $A \in P^2(M_2(\square), \cdot)$, then $A^2 = A$.

$$A^2 = \begin{bmatrix} a_{11} & a_{12} \\ a_{21} & a_{22} \end{bmatrix} \begin{bmatrix} a_{11} & a_{12} \\ a_{21} & a_{22} \end{bmatrix} = \begin{bmatrix} a_{11} & a_{12} \\ a_{21} & a_{22} \end{bmatrix}$$

$$a_{11}^2 + a_{12}a_{21} - a_{11} = 0$$

$$a_{11}a_{12} + a_{12}a_{22} - a_{12} = 0$$

$$a_{11}a_{21} + a_{21}a_{22} - a_{21} = 0$$

$$a_{22}^2 + a_{12}a_{21} - a_{22} = 0$$

$$a_{11} = \frac{1}{2} \pm \frac{1}{2} \sqrt{1 - 4a_{12}a_{21}} = a_{22}$$

$$1 - 4a_{12}a_{21} \geq 0 \Rightarrow a_{12} \neq 0 \Rightarrow \begin{cases} \frac{1}{4a_{12}} > a_{21}, a_{12} > 0 \\ \frac{1}{4a_{12}} < a_{21}, a_{12} < 0 \end{cases}$$

$$a_{12} = 0, a_{11} + a_{22} = 1.$$

Lemma 5. Let $A \in P^3(M_2(\square), \cdot)$. The elements in the positions of this matrix satisfying the conditions (i), (ii) and (iii) given below,

$$1. \quad |a_{11}| \leq \frac{2}{\sqrt{3}} \sqrt{1 - a_{12}a_{21}}, 1 > a_{12}a_{21}.$$

$$2. \quad a_{12} = \frac{a_{11} - a_{11}^3}{a_{21}a_{22} + 2a_{11}a_{21}}, \text{ where } a_{21}a_{22} \neq -2a_{11}a_{21}.$$

$$3. \quad a_{11} = -\frac{1}{2}a_{11} \mp \frac{1}{2} \sqrt{4 - 3a_{11}^2 - 4a_{12}a_{21}}.$$

Proof. If the matrix A is the third-degree idempotent matrix, then $A^3 = A$.

$$A^3 = \begin{bmatrix} a_{11} & a_{12} \\ a_{21} & a_{22} \end{bmatrix} \begin{bmatrix} a_{11} & a_{12} \\ a_{21} & a_{22} \end{bmatrix} \begin{bmatrix} a_{11} & a_{12} \\ a_{21} & a_{22} \end{bmatrix} = \begin{bmatrix} a_{11} & a_{12} \\ a_{21} & a_{22} \end{bmatrix}.$$

$$a_{11} = \begin{cases} \square, a_{12} = 0 \\ -\frac{a_{22}}{2} \pm \frac{a_{22}}{2} \sqrt{4 - 3a_{22}^2 - 4a_{12}a_{21}}, a_{12} \neq 0 \end{cases}$$

$$a_{12} = \begin{cases} \frac{a_{11} - a_{11}^3}{2a_{11}a_{21} + a_{21}a_{22}} \vee \frac{a_{22} - a_{22}^3}{2a_{11}a_{21} + a_{21}a_{22}}, 2a_{11}a_{21} + a_{21}a_{22} \neq 0 \\ \square, a_{21}a_{22} = 0 \wedge a_{11} = 0 \\ \emptyset, a_{11} = 0 \wedge 2a_{11}a_{21} + a_{21}a_{22} = 0 \end{cases}$$

$$a_{12} = \begin{cases} \square, a_{12} = 0 \\ -\frac{a_{11}}{2} \pm \frac{1}{2} \sqrt{4 - 3a_{11}^2 - 4a_{12}a_{21}}, a_{12} \neq 0 \wedge -\frac{a_{11}}{2} \pm \frac{1}{2} \sqrt{4 - 3a_{11}^2 - 4a_{12}a_{21}} \in \square \\ -\frac{a_{11}}{2} + \frac{1}{2} \sqrt{4 - 3a_{11}^2 - 4a_{12}a_{21}}, a_{12} \neq 0 \wedge -\frac{a_{11}}{2} + \frac{1}{2} \sqrt{4 - 3a_{11}^2 - 4a_{12}a_{21}} \in \square \wedge -\frac{a_{11}}{2} - \frac{1}{2} \sqrt{4 - 3a_{11}^2 - 4a_{12}a_{21}} \in \square \setminus \square \\ -\frac{a_{11}}{2} - \frac{1}{2} \sqrt{4 - 3a_{11}^2 - 4a_{12}a_{21}}, a_{12} \neq 0 \wedge -\frac{a_{11}}{2} - \frac{1}{2} \sqrt{4 - 3a_{11}^2 - 4a_{12}a_{21}} \in \square \wedge -\frac{a_{11}}{2} + \frac{1}{2} \sqrt{4 - 3a_{11}^2 - 4a_{12}a_{21}} \in \square \setminus \square \\ \emptyset, a_{12} \neq 0 \wedge -\frac{a_{11}}{2} - \frac{1}{2} \sqrt{4 - 3a_{11}^2 - 4a_{12}a_{21}} \in \square \setminus \square \wedge -\frac{a_{11}}{2} + \frac{1}{2} \sqrt{4 - 3a_{11}^2 - 4a_{12}a_{21}} \in \square \setminus \square \end{cases}$$

$$a_{21} = \begin{cases} \left\{ 0, \frac{1 - a_{11}^2 - a_{22}^2 - a_{11}a_{22}}{a_{12}} \right\}, a_{12} \neq 0 \\ \square, 1 - a_{11}^2 - a_{22}^2 - a_{11}a_{22} = 0, a_{12} = 0 \\ \left\{ 0, a_{12} = 0, 1 - a_{11}^2 - a_{22}^2 - a_{11}a_{22} \neq 0 \right\} \end{cases}$$

Example 6. Conditions (i), (ii) and (iii) are fulfilled for $a_{11} = 1, a_{22} = -2$ and $a_{11} = 1, a_{22} = -2$. Indeed, the matrix $A \in P^3(\mathbf{M}_2(\square), \cdot)$ is, since

$$A^2 = \begin{bmatrix} 1 & 2 \\ -1 & -2 \end{bmatrix} \begin{bmatrix} 1 & 2 \\ -1 & -2 \end{bmatrix} = \begin{bmatrix} -1 & -2 \\ 1 & 2 \end{bmatrix} \neq A$$

The matrix A is not the matrix idempotent degree 2^{nd} .

$$A^3 = \begin{bmatrix} 1 & 2 \\ -1 & -2 \end{bmatrix} \begin{bmatrix} 1 & 2 \\ -1 & -2 \end{bmatrix} \begin{bmatrix} 1 & 2 \\ -1 & -2 \end{bmatrix} = \begin{bmatrix} 1 & 2 \\ -1 & -2 \end{bmatrix} = A.$$

But, matrix A is the matrix idempotent elements of 3^{th} degree.

Lemma 7. Let $A \in P^3(\mathbf{M}_2(\square), \cdot)$. Then,

$$A^{2k+1} = A, \text{ where } k \in \square^+.$$

Proof. The proof of this Lemma 7 is done by induction method. It is true for $k = 1$.

$$A^3 = A.$$

Let us assume that lemma 3 for $2k-1$ is true.

$$A^{2k-1} = A \Rightarrow (A^{2k-1})A^2 = AA^2 = A$$

$$A^{2k+1} = A^3 = A.$$

Theorem 8. An regular matrix $A \in P^3(M_n(\square), \cdot)$ if and only if the A matrix is involutive 2^{nd} degree.

Proof. \Rightarrow : If $A \in P^3(M_n(\square), \cdot)$, then

$$A^3 = A \Rightarrow A^2 = I_n.$$

\Leftarrow : If the A matrix is involutive 2^{nd} degree, then,

$$A^2 = I_n \Rightarrow A^3 = A.$$

CONCLUSIONS AND DISCUSSIONS

It is obvious that the concept of "idempotent elements of degree k^{th} ", which has just been defined, will find many application areas. The studies on the set of square regular matrices is carefully observed whether it adds a new feature to their algebraic structures. A more general expectation is the expansion of algebraic structures. For example, group, object, ring, etc.

REFERENCES

Herstein, I. N. (1975). Topics in Algebra 2nd Edition, , Wiley, International-Editions, John Wiley & Sons Inc, Printed in the United States of America.

Brawley, J. V., Gamble, R. O. (1978). Involutory Matrices over Finite Commutative Rings, Linear Algebra and Its Applications, 21, 175-188.

Gallier, J., and Quaintance, J. (2019). Algebra, Topology, Differential Calculus, and Optimization Theory For Computer Science and Engineering, University of Pennsylvania, PA 19104, USA.

Keleş, H. (2010). The Rational Matrices, New Trends in Nanotechnology and Nonlinear Dynamical Systems, Ankara, paper58.

Keleş, H. (, 2017). Different Approaches on the Matrix Division and Generalization of Cramer's Rule, Journal of Scientific and Engineering Research 4(3):105-108.

Keleş, H. (2015). Lineer Cebire Giriş-I-, Bordo Puplication, Trabzon, Turkiye.

Keleş, H. (2018). On Matrix Division and Rational Matrices, SOI: 1.1/IM DOI: 15863/IM, International Scientific Journal Intelligent Mathematics, 1(7).

Keleş, H. (2022). On Results Divisibility and Multipliers of Regular Matrices of Order n th, 8. International Istanbul Scientific Research Congress March 12-13, İstanbul, Turkiye, Pages 712-718.

Keleş, H. (2022). On The Relationship Between Transpose and Division, 8. International Istanbul Scientific Research Congress March 12-13, Pages 719-722, İstanbul, Turkiye.

Keleş, H. (2022). On Some Simplification and Extension of Rational Matrices, Türkiye.

Porter, Duane, A. (1976). Solvability of the Matric Equation $AX = B$, Linear Algebra and Its Applications 13. 164-177.

Rafael Bru., Maria T. Gassó., Isabel Giménez, and José A. S. ((2015)). The Hadamard Product of a Nonsingular General H-Matrix and Its Inverse Transpose is Diagonally Dominant, Hindawi Publishing Corporation Journal of Applied Mathematics Volume, Article ID 264680, 6 pages.

Volodymyr, P. Shchedryk. (2020). A greatest common divisor and a least common multiple of solutions of a linear matrix equation, Pidstryhach Institute for Applied Problems of Mechanics and Mathematics, National Academy of Sciences of Ukraine, Math. Gm.

Thabet KH. (2012). AL-Ghuribi SU., Matrix Multiplication Algorithms, IJCSNS International Journal of Computer Science and Network Security, 12(.2, 74-79.

Alvaro Rittatore. (1998). Algebraic Monoids And Group Embeddings, Arxiv:Math/9802073v1 [Math.Ag].

Keleş, H. (2023). On the Involutive Matrices of the k th Degree, Iraqi Journal for Computer Science and Mathematics, Vol. 4, No. 1, p. 10-14.

The Role Of Machine Learning Algorithms For Spam E-Mail Filtering

Bekir PARLAK¹

Introduction

Programs called MAILBOX on the Massachusetts Institute of Technology (MIT) computers dating back to 1965 are the first examples of electronic mail. A networked system was created by ARPANET and e-mail started to be used in 1972. Emails are defined as "username@computername". In a few years 75% of ARPANET traffic was sent via email. With the invention of e-mail, the world has moved from ARPANET to the Internet. With the discovery of the internet, e-mails have provided users with an easy way to exchange information on a global level. The simple message transfer protocol (SMTP: Simple Mail Transfer Protocol) is the e-mail standard that was first introduced. SMTP does not check whether the email sender is a contact. Because of this, some problems such as forgery and fraud arose in e-mail communication. This simplicity in the SMTP protocol is exploited by viruses, fraudsters and spammers.

The continuous increase in the number of e-commerce companies with the rise of e-commerce has led to an increase in the number of advertising emails(Cormack, 2008). Online shoppers receive emails from untrusted senders to hunt for their passwords or bank account information. These randomly sent unsolicited bulk e-mails are called spam. Symantec states that the total spam rates in 2015, 2016 and 2017 were 52.7%, 53.4% and 54.6%, respectively(Cleary et al., 2018). Kaspersky also reported the rate of spam emails as 53.49% at the end of the third quarter of 2018(Vergelis et al., 2019).

The ease of use of e-mails and the ability to reach thousands of people at the same time have brought some disadvantages. One of these disadvantages is unsolicited(spam) messages(Bhowmick and Hazarika, 2018). Thanks to its cost and speed advantage, e-mails are used for purposes such as advertising, promotion, marketing, creating public opinion, sharing inappropriate content, obtaining personal information by sending malicious software, and dozens of spam e-mails are sent to e-mail boxes every day. The rate of spam e-mail is increasing day by day in the researches conducted by most of the research companies. While this situation causes loss of time and effort for users, it also causes unnecessary occupation of network traffic. In addition, from the point of view of enterprises, it is seen that it causes huge financial losses. Many different methods and techniques are used to filter spam and successful results are obtained. Despite this, they continue to use their e-mail systems, developing new strategies and methods to overcome the filters or techniques applied to spam users. For this reason, it is essential to carry out current studies in this field, to develop different methods and techniques, to create different data sets and to support analyzes.

¹ Dr. Öğr. Üyesi, Amasya Üniversitesi

In order to solve many problems, computers aim to provide machines with abilities such as learning and interpretation inspired by the behavior of the human brain. Different methods and techniques are used to reveal spam. However, such studies are usually carried out with English datasets. Studies on Turkish datasets are not serious. The reason for this is the inadequacy of data sets or the scarcity of researchers working in this field. There are many techniques for detecting and removing spam. These techniques can be grouped into two groups, namely artificial intelligence and machine learning. Machine learning techniques are examined in two groups as supervised or unsupervised. However, it is supervised learning that is widely used. In order to detect whether an e-mail is spam or regular e-mail, a large data set must be prepared as spam and regular e-mail, with each document labeled according to its class.

In this study, it aims to contribute to the spam filtering studies and the literature by determining the most successful classification algorithms and feature selection methods using a Turkish and English datasets available in the literature. In order to classify Turkish and English e-mails as spam or normal, firstly, a Turkish and English e-mail datasets containing text-based spam and normal e-mail samples were used. Then, the content of each e-mail was analyzed and different words or terms appearing in each e-mail were found. After applying some preprocessing techniques to these words, scores were assigned with three successful feature selection methods, Gini-Index(GI), Max-Min Ratio(MMR), and Extensive Feature Selector (EFS). The feature vectors obtained by these methods are classified by two successful classifiers.

E-mail System and Spam E-mail

Electronic mail (e-mail) is the name given to an electronic message, usually in the form of a simple text, image or video, that a user sends to a computer and forwards it to another user who can read it over a computer network(Altunyaprak, 2006). Email messages consist of a header and a body. The title includes the sender, recipient, subject, and date. Spam are messages sent in bulk by strangers, malware, or bot accounts. These can also be defined as messages sent to e-mail accounts without the request of the person. Unwanted e-mails can be used for purposes such as advertising, promotion and propaganda, as well as for purposes such as stealing personal information and crashing companies' systems. When we look at our e-mail addresses in daily life, we encounter dozens of advertising messages every day, and some of them come from addresses we do not know. In addition, some spam messages may send viruses or computer-damaging links to capture our personal information and bank account information. They can steal our information when they copy trusted web addresses and make us trust them. Another reason why we face spam today is the email trade. Companies that offer e-mail services usually offer it for free. However, while providing this service, it can provide access to many data, especially an e-mail address. E-mail addresses belonging to millions of people are marketed to different businesses and cause us to receive unsolicited messages from companies we do not know. While companies are always looking for ways to communicate with their customers more accessible, cheaper or faster, they offer all three with the e-mail service available on the internet. In this case, the marketing of email addresses is one of the reasons for the increase in spam. Today, many different methods are used and new techniques are being developed to filter unsolicited (spam) e-mails. Some of these methods are Word Filtering, Rule-Based Filtering, Blacklists and Antivirus Scanning.

There are some common features when examining spam. These are;

- The contents are up to date.
- They can talk about human feelings and ask for the e-mail to be forwarded to many people.

- Often their content is misleading.
- It is sent for promotional purposes.

Related Works

Although there are many studies to filter spam written in English(Ahmed, 2020; Sharma and Kaur, 2016; Venkatraman et al., 2019), such studies are relatively few with Turkish(Dedeturk and Akay, 2020; Ergin et al., 2012; Ozgur et al., 2004), an agglutinative language with a much more complex morphological structure than English. For the Turkish language, Özgür et al.(Ozgur et al., 2004) used a rooting operator to classify Turkish emails and applied two different classifiers, with a success rate of approximately 90%. Tunga and Kitik(Güngör and Çıltık, 2007) proposed methods based on the n-gram method and the first n-word heuristic. The best success rates with their approach were about 97% for a Turkish dataset. In the study of Ates(Ates, 2014), two different content-based filtering methods were carried out using the supervised learning algorithm Support Vector Machines and the unsupervised learning algorithm Gaussian Mixture Models, using both Turkish and English datasets. Deniz et al.(Deniz et al., 2019) Attribute extraction was performed using the TurkishEmail e-mail dataset and algorithms belonging to the Doc2Vec library were used. Doc2Vec includes two different algorithms called Distributed Bag of Word (DBoW) and Distributed Memory (DM). Classification was made with six different pattern classifiers. The highest performance DBoW+DM feature selection and support vector machine machine learning resulted in a score of 78.75%. Karamollaoglu et al.(Karamollaoglu et al., 2018) aimed to analyze the content information of e-mails written in Turkish, to determine whether these e-mails are spam e-mails and to classify them with the help of Naive Bayes Classifier and Vector Space Model, one of the machine learning methods. Both methods were subjected to different evaluation criteria and their performances were compared. Experimental results showed higher performance of Naive Bayes Classifier method compared to Vector Space Model. Unlike other studies, Kaynar et al.(Kaynar et al., 2016) proposed an automatic encoder-based deep learning machine, which is one of the modern machine learning approaches for the classification of spam. Autoencoders are actually multilayer sensors where the inputs and outputs have the same dataset. The classifier using the automatic encoder deep learning machine has been shown to have an extremely high success rate of 98% accurate classification. Ergin et al.(Ergin et al., 2012) applied a Turkish anti-spam filter to identify text-based Turkish spam emails (junk or bulk email). In the study, a database containing spam and normal e-mail samples in Turkish was created. The content of each e-mail was analyzed and different words from all e-mails were identified. The content of each e-mail was analyzed and different words from all e-mails were identified. Then, a Turkish root extraction function was used to obtain the root forms of different words. Mutual Information (MI= Mutual Information) scores of different words were calculated, so that two types of feature vectors were created according to the MI scores. After this process, binary and probability based models of Bayesian classifier were tested and success rates of binary and probability based models were compared.

In addition to the Turkish spam filtering studies, there are also English e-mail filtering studies in the literature. In one study(Renuka et al., 2015), spam classification in the proposed system was carried out using the Naive Bayes classifier, which is a conditional probability-based probabilistic classifier applicable to more complex classification problems. The application of feature selection using Hybrid Ant Colony Optimization also serves to be efficient and yielding good results for the system proposed in this study. Venkatraman et al.(Venkatraman et al., 2020) proposed the integration of the Naive Bayes classification with the conceptual and semantic similarity technique to combat the uncertainty posed by polysemy in spam detection. To analyze the effectiveness of the approach, experiments were performed on comparative datasets such as Spambase, PU1, Enron1 and Lingspam. It is clear from the experimental results that the proposed system achieves

a higher accuracy of 98.89% than existing approaches. In another study (Bhuiyan et al., 2018), related to Machine Learning Techniques (MLT=Machine Learning Techniques) such as Naive Bayes, SVM, K-Nearest Neighborhood, Bayesian Additive Regression, KNN Tree and rules shows a survey of the different email spam filtering system available. However, this study presents the classification, evaluation and comparison of different spam filtering systems and summarizes the general scenario regarding the accuracy of the different approaches available. Bhowmick et al. (Bhowmick and Hazarika, 2018), presented a comprehensive review of the latest and successful content-based spam filtering techniques. Their focus is mainly on machine learning-based spam filters and their inspired derivatives. They came to the conclusion by examining techniques, evaluation criteria and exploring promising branches of the latest developments and making recommendations for future research. Subasi et al. (Subasi et al., 2018) proposed an approach for spam filtering based on simple and better accuracy decision tree algorithms. From the experimental results, the proposed random forest classifier outperformed other decision tree methods for public datasets.

Feature Extraction

The word bag-of-words (BoW) approach (Li et al., 2020) is one of the methods used for feature extraction in text classification studies. In this approach, the order of the terms in the documents is ignored, while the frequency of their occurrence is used. Therefore, each unique word in a text collection is considered a different attribute. As a result, a document is represented by a multidimensional feature vector (Parlak and Uysal, 2021). In a feature vector, each dimension corresponds to a value weighted by term frequency (TF) or term frequency-inverse document frequency (TF-IDF) (Parlak and Uysal, 2018).

In addition, it should not be forgotten that some pre-processing steps (Uysal and Gunal, 2014) are necessary for performance during feature extraction from text documents. Commonly used preprocessing steps are the "removal of stop-words" and the "stemming" algorithm. In this study, both pre-processing steps were applied. For stemming, Zemberek (Akin and Akin, 2007) and Porter stemmer (Porter, 1980) algorithm and term frequency-inverse document frequency (TF-IDF) were used as weighting approach.

Feature Selection

In addition, it should not be forgotten that some pre-processing steps (Uysal and Gunal, 2014) are necessary for performance during feature extraction from text documents. Commonly used preprocessing steps are the "removal of stop-words" and the "stemming" algorithm. In this study, both pre-processing steps were applied. For stemming, Zemberek (Akin and Akin, 2007) and Porter stemmer (Porter, 1980) algorithm and term frequency-inverse document frequency (TF-IDF) were used as weighting approach.

Feature selection techniques generally fall into three categories: filters, wrappers, and embedded methods. Filter techniques are computationally fast; however, they usually ignore attribute dependencies. Filter-based techniques are widely preferred especially for text classification field. There are many filter-based techniques for the selection of distinctive features in text classification. In this study, three different feature selection techniques, namely Gini Index (GI), Normalized Difference Measure (NDM) and Extensive Feature Selector (EFS) were used. Table 1 explains the notations in the formulas of these methods. Also, the methods are detailed below:

Table 1. Notations for feature selection methods

Notation	Meaning
$p(t C_j)$	Probability of term t when class C_j exists
$p(\bar{t} C_j)$	Probability of absence of term t when class C_j exists
$p(t \bar{C}_j)$	Probability of absence of of term t when class C_j does not exists
$p(\bar{t} \bar{C}_j)$	Probability of term t when class C_j does not exists
$p(C_j t)$	Probability of class C_j when t term is present
$p(\bar{C}_j t)$	Probability of absence of class C_j when t term is present
$p(C_j \bar{t})$	Probability of class C_j when t term is not present
$p(\bar{C}_j \bar{t})$	Probability of absence of class C_j when t term is not present

Gini Index(GI)

GI is an improved version of the method originally used to find the best feature distribution in decision trees(Singh et al., 2010). It is an accurate and fast method. The formula is as follows:

$$GI(t) = \sum_{j=1}^M P(t|c_j) * P(c_j|t) \quad (1)$$

Max-Min Ratio(MMR)

MMR(Rehman, Javed, Babri, & Asim, 2018) provides better performance on datasets including highly skewed classes. The method is a combination of true positives, false positives and their differences. According to the method, the feature score is calculated as follows:

$$MMR(t) = \sum_{j=1}^M \frac{|P(t|c_j) - P(t|\bar{c}_j)|}{\min(P(t|c_j), P(t|\bar{c}_j))} \cdot \max(P(t|c_j), P(t|\bar{c}_j)) \quad (2)$$

Extensive Feature Selector(EFS)

The EFS method(Parlak and Uysal, 2021) selects more important features by using both class-based and collection-based probabilities of the feature. Its formula is a bit more complex than other methods:

$$EFS(t) = \sum_{j=1}^M \left(\frac{P(t|C_j)}{P(\bar{t}|C_j) + P(t|\bar{C}_j) + 1} \right) \cdot \left(\frac{P(C_j|t)}{P(\bar{C}_j|t) + P(C_j|\bar{t}) + 1} \right) \quad (3)$$

Datasets

In this study, "TurkishEmail"(Ergin et al., 2012) and "Enron1"(Uysal and Gunal, 2014) datasets were used. There are a total of 800 e-mails in this dataset, which consists of normal and spam e-mails in the Turkish dataset. In the English dataset (Enron1), there are 5172 e-mails in total in this dataset, which consists of regular and spam e-mails. The distribution of training and test data of these datasets is given in Table 2-3 below.

Table 2. *Turkish Email Dataset*

	Train	Test
Ham	300	100
Spam	300	100

Table 3. *English Email Dataset*

	Train	Test
Ham	1836	1836
Spam	750	750

Classifiers

In this study, it is employed two successful classifiers. These classifiers Multinomial Naive Bayes(MNB) and Decision Tree(DT).

A particular naive Bayes classifier called MNB was created specifically for classifying texts. This naive Bayes classifier's event model was specifically represented by the multinomial term. For text categorization, multinomial and multi-variate Bernoulli event models are frequently used(Zhao et al., 2016). The way a portion of the formula is calculated varies across multinomial and multi-variate Bernoulli event models. Multi-variate Bernoulli event model employs document frequencies in this calculation, whereas multinomial model considers term frequencies.

The widely-used DT classifier(Quinlan, 1986) creates a hierarchy of decision rules from data automatically. Each path in the tree structure used to express these decision criteria leads to the assignment of a class label. After making Yes/No decisions along a path of nodes inside a tree structure, classification is carried out. One of the most effective decision tree classification methods is C4.5.

Experimental Study

Different sized vectors of the features selected by each selection method were fed with MNB and SVM classifiers. Stop-words removal and stemming were applied in the experiments. The widely known Zemberek algorithm has been implemented as a stemming algorithm for Turkish dataset. Also, Porter-stemmer algorithm has been employed as a stemming algorithm for English dataset. In this study, GI, MMR and EFS were used as feature selection methods. The total number of features was 18650 and 27521 for Turkish and English datasets, respectively. However, in terms of size; dimension reduction was performed by creating 100, 250, 500 and 1000 feature vectors. In addition, the F score(Goutte and Gaussier, 2005) was used as a measure of success. This score is presented predominantly, not in a class-specific form. The F-Scores obtained are listed in Table 4-7. The best ones in the results are shown in bold.

Given the highest weighted average F scores, it outperformed the GI, MMR, and EFS methods overall in most cases. In the Turkish dataset, GI has the highest performance in the MNB classifier, while MMR has the highest performance in the DT classifier. However, the methods are more successful when the feature size is low in the MNB classifier, while the methods are more successful when the feature size is high in the DT classifier. In the English dataset, EFS has the highest performance in the MNB classifier, while GINI has the highest performance in the DT classifier. However, the methods are more successful when the feature size is high in the MNB classifier, while the methods are more successful when the feature size is low in the DT classifier.

Table 4. F Scores for Turkish E-mail Dataset with MNB Classifier

Turkish E-mail	100	250	500	1000
GINI	0.977	0.940	0.930	0.930
MMR	0.970	0.925	0.935	0.915
EFS	0.970	0.940	0.915	0.930

Table 5. F Scores for Turkish E-mail Dataset with DT Classifier

Turkish E-mail	100	250	500	1000
GINI	0.950	0.960	0.970	0.965
MMR	0.955	0.965	0.975	0.970
EFS	0.960	0.965	0.970	0.965

Table 6. F Scores for English E-mail Dataset with MNB Classifier

English E-mail	100	250	500	1000
GINI	0.877	0.904	0.916	0.921
MMR	0.869	0.901	0.918	0.917
EFS	0.884	0.902	0.916	0.923

Table 7. F Scores for English E-mail Dataset with DT Classifier

English E-mail	100	250	500	1000
GINI	0.911	0.897	0.889	0.889
MMR	0.888	0.893	0.880	0.871
EFS	0.894	0.888	0.890	0.890

Conclusions

In this study, the performances of two widely known classifiers were extensively analyzed using three different feature selection methods. This analysis was carried out on datasets consisting of Turkish and English e-mail documents. Experimental results were obtained with the combination of MNB classifier and GI Feature Selector of the most successful scheme for the Turkish dataset. For the English dataset, the most successful schema was obtained with the combination of MNB classifier and EFS Feature Selector. As a future study, a new Turkish e-mail dataset in this field will be gained and analyzed with different attribute selection techniques.

REFERENCES

- Ahmed, B. (2020). Wrapper Feature Selection Approach Based on Binary Firefly Algorithm for Spam E-mail Filtering. *Journal of Soft Computing and Data Mining 1*, 44-52.
- Akın, A.A., Akın, M.D. (2007). Zemberek, an open source NLP framework for Turkic languages. *Structure 10*, 1-5.
- Altunyaprak, C. (2006). Bayes yöntemi kullanarak istenmeyen elektronik postaların filtrelenmesi. Yüksek Lisans Tezi, Muğla Üniversitesi Fen Bilimleri Enstitüsü.
- Ates, N. (2014) Support vector machine and gauss mixture model detection of unsolicited e-mails. Master's thesis, Suleyman Demirel Üniversitesi, Fen Bilimleri Enstitüsü, Bilgisayar Mühendisliği Anabilim Dalı.
- Bhowmick, A., Hazarika, S.M. (2018). E-Mail Spam Filtering: A Review of Techniques and Trends, *Advances in Electronics, Communication and Computing. Springer*, pp. 583-590.
- Bhuiyan, H., Ashiquzzaman, A., Juthi, T.I., Biswas, S., Ara, J. (2018). A survey of existing e-mail spam filtering methods considering machine learning techniques. *Global Journal of Computer Science and Technology*.
- Cleary, G., Corpin, M., Cox, O., Lau, H., Nahorney, B., O'Brien, D., O'Gorman, B., Power, J.-P., Wallace, S., Wood, P. (2018). Internet security threat report. Symantec Corporation, California, USA, Tech. Rep.
- Cormack, G.V. (2008). Email spam filtering: A systematic review. *Foundations and Trends® in Information Retrieval 1*, 335-455.
- Dedetürk, B.K., Akay, B. (2020). Spam filtering using a logistic regression model trained by an artificial bee colony algorithm. *Applied Soft Computing 91*, 106229.
- Deniz, E., Erbay, H., Coşar, M. (2019). Türkçe e-postaların Doc2Vec ile sınıflandırılması.
- Ergin, S., Sora Gunal, E., Yigit, H., Aydın, R. (2012). Turkish anti-spam filtering using binary and probabilistic models. *Global Journal on Technology 1*.
- Goutte, C., Gaussier, E. (2005). A probabilistic interpretation of precision, recall and F-score, with implication for evaluation, European conference on information retrieval. Springer, pp. 345-359.
- Güngör, T., Çıltık, A. (2007). Developing methods and heuristics with low time complexities for filtering spam messages, International Conference on Application of Natural Language to Information Systems. Springer, pp. 35-47.
- Karamollaoglu, H., Dogru, İ.A., Dorterler, M. (2018). Detection of Spam E-mails with Machine Learning Methods, 2018 Innovations in Intelligent Systems and Applications Conference (ASYU). IEEE, pp. 1-5.
- Kaynar, O., Görmez, Y., Işık, Y. (2016). Oto Kodlayıcı Tabanlı Derin Öğrenme Makinaları İle Spam Tespiti. Uluslararası Yönetim Bilişim Sistemleri Konferansı 44.

Li, P., Mao, K., Xu, Y., Li, Q., Zhang, J. (2020). Bag-of-Concepts representation for document classification based on automatic knowledge acquisition from probabilistic knowledge base. *Knowledge-Based Systems* 193, 105436.

Ozgur, L., Gungor, T., Gurgun, F. (2004). Adaptive anti-spam filtering for agglutinative languages: a special case for Turkish. *Pattern Recognition Letters* 25, 1819-1831.

Parlak, B., Uysal, A.K. (2018). On feature weighting and selection for medical document classification, *Developments and Advances in Intelligent Systems and Applications*. Springer, pp. 269-282.

Parlak, B., Uysal, A.K. (2021). A novel filter feature selection method for text classification: Extensive Feature Selector. *Journal of Information Science*, 0165551521991037.

Porter, M.F. (1980). An algorithm for suffix stripping. *Program* 14, 130-137.

Quinlan, J.R. (1986). Induction of decision trees. *Machine learning* 1, 81-106.

Renuka, D.K., Visalakshi, P., Sankar, T. (2015). Improving E-mail spam classification using ant colony optimization algorithm. *Int. J. Comput. Appl* 22, 26.

Sharma, R., Kaur, G. (2016). E-Mail Spam Detection Using SVM and RBF. *International Journal of Modern Education and Computer Science (IJMECS)* 8, 57.

Singh, S.R., Murthy, H.A., Gonsalves, T.A. (2010). Feature Selection for Text Classification Based on Gini Coefficient of Inequality. *Fsdm* 10, 76-85.

Subasi, A., Alzahrani, S., Aljuhani, A., Aljedani, M. (2018). Comparison of decision tree algorithms for spam e-mail filtering, 2018 1st International Conference on Computer Applications & Information Security (ICCAIS). IEEE, pp. 1-5.

Uysal, A.K., Gunal, S. (2014). The impact of preprocessing on text classification. *Information Processing & Management* 50, 104-112.

Venkatraman, S., Surendiran, B., Kumar, P.A.R. (2019). Spam e-mail classification for the Internet of Things environment using semantic similarity approach. *The Journal of Supercomputing*, 1-21.

Vergelis, M., Shcherbakova, T., Sidorina, T., Kulikova, T. (2019). Spam and phishing in 2018. *Secure List*.

Zhao, L., Huang, M., Yao, Z., Su, R., Jiang, Y., Zhu, X. (2016). Semi-supervised Multinomial Naive Bayes for text classification by leveraging word-level statistical constraint, *Proceedings of the Thirtieth AAAI Conference on Artificial Intelligence*. AAAI Press, pp. 2877-2883.

Rised Co₂ And Climate Change Effects On Wheat

Uğur KEKEÇ
Burçak KAPUR
Levent KOÇ
Müge Erkan CAN

Introduction

Short-wave radiation from the sun, retained as long-wave radiation in the earth and atmosphere; dispersed on earth by ocean circulation and given back to the atmosphere as ground radiation. Part of it absorbed by clouds and greenhouse gases in the atmosphere and released back to the atmosphere. In this way the earth's surface and the lower atmosphere are warming. Earth warming more than expected this process, which provides and regulates the heat balance, is called the natural greenhouse effect (Türkes, Sümer & Çetiner, 2000). Today, the aforementioned global climate change as a result of the strengthening the natural greenhouse effect of the rapid increase in greenhouse gas accumulations released into the atmosphere increase in the average surface temperature of the Earth and reveals changes in climate.

The average temperature of the earth and water bodies has been increasing since 1861. The increase is around 0.8 °C during the 20th century (IPCC, 2001). Globally, from 1861 to the 1990s was the warmest decade and 1998 was instrumental measurement It was recorded as the hottest year of the process. Every 10 years between 1950-1993 the average daily-nightly maximum surface air temperatures increased by 0.2 °C. The specified increase is 0.1°C higher than the 10-year increase in the daily maximum temperature is too much. The prolongation of frost-free seasons in many mid and high latitudes seen as a result of temperature increase. Since 1880, the temperature of the Earth has risen by 0.08 °C per decade, but since 1981, the pace of warming has increased by more than twice that, to 0.18 °C per decade (NOAA, 2022). According to NOAA's temperature data, 2021 was the sixth-warmest year ever. Nine years between 2013 and 2021 are among the ten warmest on record (NOAA, 2022). Clearly indicates that the negative effects of human actions on the climate in recent years shows its effects (Figure 1). The extraordinary development of the industry in recent years and increased use of fossil fuels, increasing CO₂ emissions; 120 years of the past the increase in temperature during the last 20 years of today.

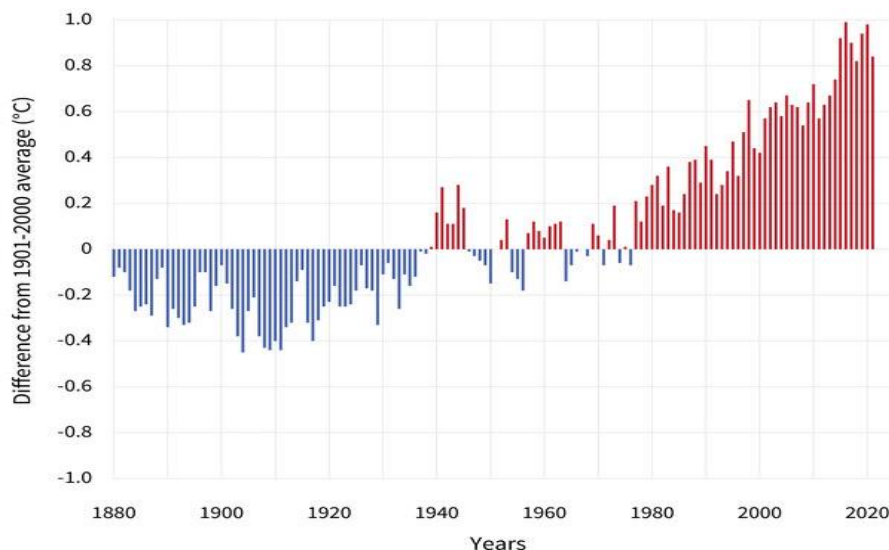


Figure 1. Annual surface temperature as compared to the average for the 20th century (1880–2021). Red bars reflect years that were warmer than normal, and blue bars show years that were cooler than usual. NOAA Climate.gov graph, based on data from the National Centers for Environmental Information. (NOAA, 2022).

In this context, Turkey is at risk for the potential effects of global warming group of countries. The most striking changes observed in Turkey characterized by increases in summer temperatures. Summer temperatures, mostly, increases in the western and southwestern regions. In addition, the last 50 years the amount of precipitation on the western provinces of Turkey in the winter season decreased (Karaca, Deniz & Tayanç, 2000).

The last 70 years, according to the data recorded at the meteorological stations, the increase in annual average temperatures in Turkey tends to; especially in the Mediterranean and Southeast Anatolian regions increase between 0.07-0.34 degrees every 10 years (WorldData, 2022). 1930-2003 in a study using Mann-Kendall trend analysis significant increases in annual average temperatures in the Çukurova region (Kapur et al., 2007) were detected.

Agro-economic systems (agriculture, forestry, fisheries and water resources) are vital to human development and is highly sensitive to climate change. The annual average increasing temperature will enhance desertification, salinization, erosion and thus, arid and semi-arid areas. The type of crop, yield and growth time and duration are determined by atmospheric conditions. Within this context, wheat is a crucial plant that needs to be protected from the harmful impacts of climate change. It occupies 15% of the world's agricultural areas and provides 25% of the protein and 20% of the calories needed for food. Turkey, which meets 3.6% of the world wheat production, is among the most important wheat producer and consumer countries in the world. Wheat is cultivated on an area of approximately 9.5 million hectares in our country. Although it changes from year to year in production, it is around 20 to 21 million tons. An average of 225 kg of wheat per year is required to feed one person considering that, for our 80 million population (OECD/FAO, 2021).

Possible effects of global climate change on wheat crop

In wheat, a positive effect could be seen due to the increase in CO₂ when it transfers the growth which affects positively to the expanding leaf area. Thus, the plant receives more light and CO₂, positively affecting its development. This positive development, in addition to CO₂, depends on the competition for light, water, temperature and plant nutrients (Gifford & Morrison, 1993).

However, in the field, such a high increase in yield should not be expected due to the competition in the field. The positive effect of CO₂ on the development of wheat decreased due to the limited water and plant nutrients, decreased aeration in the plant root zone and increased salinity levels. With these limitations, the plant negatively effected and could not responde to the positive effect of CO₂ and this is known as the plant's capacity to use assimilates (Sink Effect). Root development acts as a depot for photoassimilation and thus, the reason for the limitation of plant growth depends on the limited storage of roots. Stitt (1991), reveals that the limited phytosynthesis despite to the increasing CO₂ level attributed to the effect of deficit root storage capacity. Thus, plant responses determined by long-term, experimental studies could be explained according to the capacity of the plant, which depends on the plant variety, development process and growing conditions.

Due to the increase of CO₂, enhanced plant growth and leaf area also causes a rise in the loss of CO₂ by respiration. As a result of this, more larger plants, in other words, plants that grow faster, so that more respiration they do (Gifford & Morison, 1993). Another negative effect is the plant shading itself. Allows larger leaf surface area to benefit from more light however, increasing leaf sizes shade each other. Thus, this reduces the photosynthesis in the unit area. All these positive and negative factors combined effects reveals the actual vegetation growth rate was positive in the trials against the CO₂ increase (Reddy & Hodges 2000). Table 1 displays the anticipated effects on wheat yield under two fold CO₂ climatic scenarios developed using global circulation models, taking into account the studies that are currently published worldwide.

Table 1. *Wheat production with Global Circulation Model in conditions of double CO₂ increase (IPCC, 2001).*

Region	Yield Change(%)	Countries
Europe	-10 to +10	France, UK, and Northern Europe
South America	-61 to +5	Argentina, Brazil, Chile, and Mexico
Former Soviet Union	-19 to +41	---
North America	-100 to +234	USA and Canada
Africa	-65 to +6	Egypt, Kenya, South Africa, Zimbabwe
South Asia	-61 to +67	Bangladesh, India, Phillipine, Thailand, Indonesia
China	-78 to +28	---
Asia	-41 to +65	Australia and Japan

Effects of CO₂ and possible CO₂ increase on plant physiology and productivity

The effect of the rised CO₂ on the plant is varies from the microscopic level (at the cell level) to the macroscopic agro-ecosystem level. The study of the increase level of CO₂ in C3 crops such as wheat is complex to explain the physiology and the process. Photosynthesis, respiration and transpiration is one of the most important processes which the plants are directly affected by the increase in CO₂. Some of these primary effects is positive; some will have negative effects on wheat. The general effects of increased CO₂ on the plant are schematically illustreted in Figure 2. With increasing carbon dioxide, if plant nutrients and climatic factors are suitable an increase in yield could be possible. However, how plants respond to increased carbon dioxide under restrictive

conditions will depend on the level of negative conditions. Examining the level these interactions of possible changes are very important in determining the adaptation approaches.

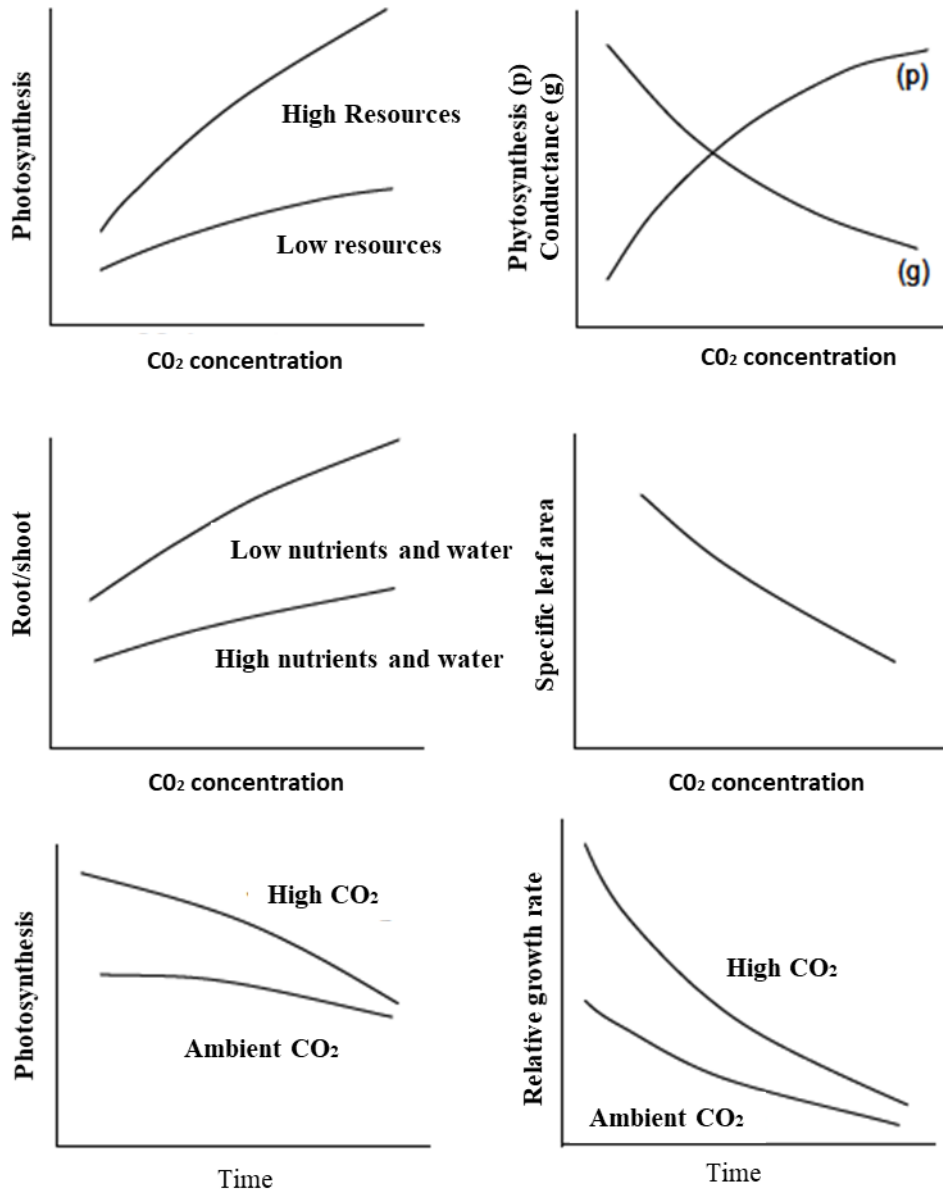


Figure 2. The response of plants to CO₂ concentration (Bazzaz, 1990).

Photosynthesis and respiration

The net relationship of photosynthesis and respiration between the atmosphere and terrestrial ecosystems which is clearly known that it affects the direction of carbon flow.

Photosynthesis: Despite the rise in atmospheric CO₂, it is thought that this increase may benefit agriculture if changes in temperature and precipitation regime do not actually occur. CO₂ is an absolute requirement for photosynthesis and life on earth. The increased CO₂ concentration in the atmosphere, enhance the CO₂ concentration differences between the atmosphere and inside

uptake of CO₂ by diffusion and thus, chloroplasts CO₂ diffusion increases in leaves and conversions of carbohydrates rised. In C₃ plants, including wheat, the increase in CO₂ increases the rate of photosynthesis at both leaf and vegetation levels (Lemon, 1983; Acock & Allen, 1985; Drake & Leadley, 1991).

Due to the different photosynthetic mechanisms of the plant species to CO₂ increases causes different respond. In some species, photosynthesis takes the C₃ pathway. The reason why this pathway is called the C₃ is because the first formed in the biochemical process phosphoglyceric acid which has three carbons. In other species, this path is conversely, since the first product has four carbons, the C₄ path and called C₄ plants. The C₄ plants affected less than C₃ plants versus CO₂ increase in photosynthesis action as reflected in Figure 3 (Akita & Moss, 1973).

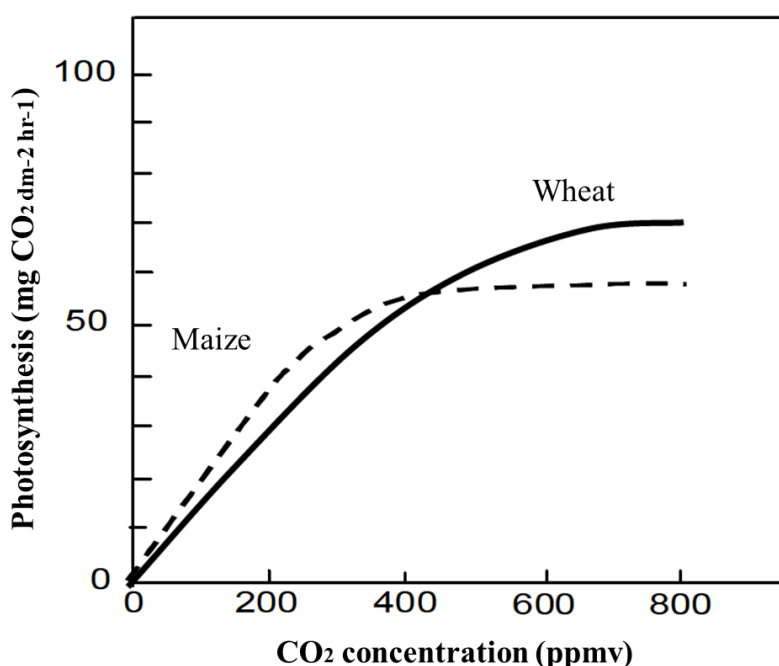


Figure 3. The rate of photosynthesis in maize and wheat change depending on CO₂ (Akita & Moss, 1973)

Respiration: Photosynthetic carbon uptake response to atmospheric CO₂ changes can be easily understood and modeled at many scales. However, the mechanism of respiration change versus to CO₂ increase (in a short time-second or minute; long in the process-seasonal) is less understood. Photosynthesis, growth and substrate increases in enhance the respiration rate per unit area. This situation could be explained as the higher biomass requires higher energy support to grow. On the other hand, increasing levels of CO₂ in the atmosphere could reduces the level of CO₂ that released via respiration (Amthor, 1989). So these two opposing effects interaction is unknown. Some researchers think twice the CO₂ concentration reversing the outward, net movement of CO₂ in plant tissue found to decrease. Some researchers also found that increased CO₂ concentrations increased CO₂ use efficiency on phytosynthesis (Gifford & Morrison, 1993). In addition, increasing CO₂ levels in wheat, in the long term, controlled-condition studies and field trials demonstrating reduced respiration Reddy & Hodges (2000). However, today short-term metabolic changes has not been fully determined with the relations in the long-term and permanent changes.

Climate adaptations of photosynthesis and respiration (aclimation): Depending on the increase of CO₂ level cause an increase in the rate of photosynthesis however, it is stated that this initial reaction will decrease in the long run (Stitt, 1991). An organism's adaptation to changing

environmental conditions is often inherited (Hale & Orcutt, 1987). Plants adapt the rate of photosynthesis and respiration to high CO₂ levels. However, adaptability of the plants is insufficiently defined today. Photosynthetic adaptation causes a decrease in Rubisco enzyme production. This process is more linked with the high levels of carbohydrates in the leaves (Stitt, 1991). Another important factor affecting the photosynthesis rate of the plant is depends on the effectively storing capacity of photosynthesis products as refered physiological capacity. In other words, higher persistence of photosynthesis at high levels, or continuous/stable formation depends on the biomass storages such as fruit, tuber and grain. These depots provide increasingly fixed carbohydrates. Even in the process of adaptation level, photosynthesis is generally increases as the CO₂ concentration increase in the atmosphere. On the other hand, long-term adaptation is necessary for photosynthetic capacity and respiration (Reddy & Hodges 2000).

Stoma resistance and water use efficiency

Another important physiological effect of CO₂ increase is on the movement of stomata is the effect. CO₂ absorption from stomatal pores on leaf surfaces and water vapor is released. In this context, due to atmospheric CO₂ increase, transpiration level may decrease. A 30% decrease in conductivity stoma was detected in a double CO₂ increase environment. (Cure & Acock, 1986) (Table 2).

Table 2. Percentage change in transpiration in plants against increased CO₂ (300 ppm CO₂ increase) (Cure & Acock, 1986).

Reaction Type	Wheat	Barley	Rice	Corn
Transpiration	-17 ± 17	-19 ± 6	-16 ± 9	-26 ± 6
Type Reaction	Sorghum	Soy Beans	Cotton	Potatoes
Transpiration	-27 ± 16	-23 ± 5	-18 ± 17	-51 ± 24

Thus, the water use efficiency (WUE) is increased by this two fold increase in CO₂ together, it will cause a decrease in transpiration. WUE is defined as the biomass rate to the water lost by the plant through evapotranspiration. Proportionality rise of CO₂ affects positively C3 crops such as wheat under limited irrigation conditions than the sufficient water conditions due to smaller stomatal openings of C3 plants. Increases between 70-100% in water use efficiency in wheat which was determined by Kimball & Idso (1983) and Morison (1985).

At the leaf level, in the conducted studies on fifty different plants, CO₂ increases effects C3 and in C4 plants on gymnosperms, angiosperms, monocotyledons and dicotyledons as different stoma responses (Morison, 1985). However, an increase in CO₂ or the stomatal behavior associated with the reduction and the related physiological mechanism not fully understood. Contrary to past information, the stomata of C3 and C4 plants in a linear relationship against the 2 fold CO₂ increase and that, on average, both C3 and C4 plants have showed a 40% decrease in stomatal opening to double CO₂ increase. (Figure 4.) (Rosenzweig & Hillel, 1998).

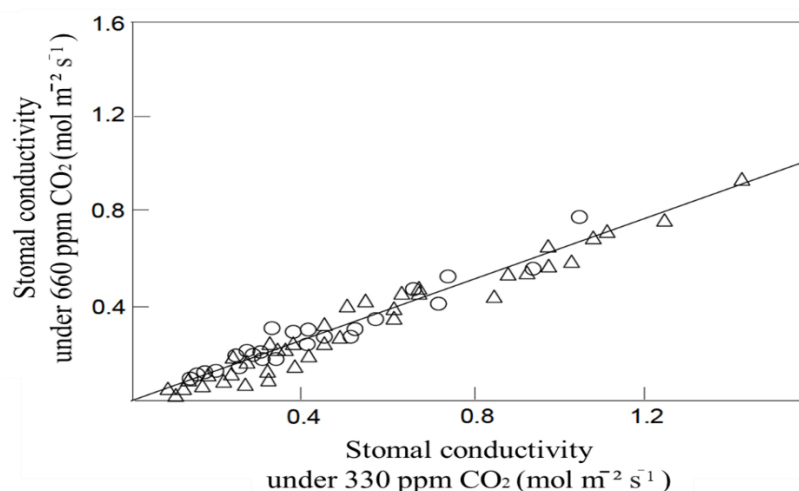


Figure 4. Change of stomatal conductivity due to CO₂ increase (Δ = C3 plant, O=C4 plant) (Morison, 1985).

The stomatal response to the increase in CO₂ varies according to many factors. These are leaves age, light intensity, atmospheric humidity, and temperature (Morison, 1985). Determining the stomatal response with the relationship between CO₂ is difficult because of the interaction between CO₂, temperature and plant hormones. The relationship between stomatal regulation and gas exchange also presents similar difficulties for the explanation.

The closure of stomata and the parallel as a result of decreased transpiration and latent heat loss associated with the leaf temperature increase is a well known aspect. Leaf and vegetation temperatures under controlled climate chambers increase 1-3 °C depending on the CO₂ increase (Chaudhuri et al., 1986; Idso, Kimball & Mauney, 1987). Reduction in transpiration associated with closure of stomata (25-35%), is not equal to the decrease in stomatal conduction (40%) (Allen, Jones & Jones, 1985; Morison, 1985). The reason for this is the increased vapor pressure inside the leaf, partial it increases the vapor pressure gradient from the leaf to the air in order to compensate for the decreasing conductivity. Thus, the leaf temperature is also increases the metabolism and leaves (including respiration and physiological development) causes tissue aging.

The relationship between photosynthesis and stomatal movements can be considered at three levels. These can be considered as leaves, plants and vegetation. At the leaf level, certain increased transpiration efficiency (photosynthetic water use) as a result of the increase in CO₂ increases net assimilation between 60% - 160% with a decrease in transpiration (Morison, 1985).

At the plant level, photosynthetic water use efficiency do not increase as much as water use efficiency during longer growth periods. This is caused due to the photosynthetic adaptation, adverse temperature effect, amount of product and transpiration. Under double CO₂ increased conditions, Morison (1985) reported a plant growth increase of about 30% together with a decrease in transpiration, in which case both factors mentioned (plant growth and transpiration) water use efficiency in the plant between 70% and 100% increases.

At the vegetation level, the water use efficiency in the field is planted per unit area biomass accumulation to the total water level used by plants in that area (E_{Tc}) ratio. The total amount of water used by the plant directly affected by CO₂ increase but by vegetation cover and plant water uptake both affected by stomatal inclusions and soil evaporation and transpiration.

Another change in the hydrological regime under increasing CO₂ conditions is the water balance interaction due to the increase of leaf area. In arid environments this cause a direct transpiration rise significantly. Thus, at the vegetation level at the field, on the water use efficiency more complex relationships and effects occur. With double CO₂ increase, the increases in WUE causes increase by approximately 30% to 50% in products and vegetation.

Biological yield and grain yield

Increased photosynthesis at high atmospheric CO₂ concentration provides increased biomass accumulation as expected (Kimball & Idso, 1983; Cure & Acock, 1986; Poorter, 1993). With a doubling of CO₂ in trials under controlled conditions (today 350 ppm), yield levels of plants such as wheat differs. Response (yield level) of most plants is positive, but small some of them were negative (Table 3). Some researchers have conducted their experiments to verify controlled conditions (Lawlor & Mitchell, 1991; Hendrey, 1993).

Table 3. The rate of the yield change in different crops against increasing CO₂ (%) change (300 ppm CO₂ increase) (Cure and Acock, 1986).

Wheat	Barley	Rice	Corn	Soy Beans	Cotton	Potato	Dessert potato	Weighted average
+35±14	+70±9	+15±3	+29±64	+29±8	+209±20	+51±11	+83±12	+41

Response to increased CO₂, different plants and even different varieties of the same plants varies. Varieties of the same cultivar different response to CO₂ is depending on the genetics of plant varieties, experimentation technique and to the pattern. C3 and C4 photosynthetic pathways seem to be the general variation reason for differences between plants.

Biomass formed in the crops is the difference between photosynthesis and respiration via accumulation in the form of carbon products, plus mineral accumulation. Therefore biomass increase parallels concurrent to net photosynthesis impact as expected. On the other hand, under real conditions, plant nutrients, the amount of soil water content and other factors, should also be at an optimum level. Example;the promotion of root and vegetative parts growth means additional resource use. This on the contrary, increased carbon assimilation makes nutrients more restrictive for growth. Growth at low temperatures is probably not by assimilation, rather it will be limited by its photosynthetic capacity. If these factors are sufficient CO₂ increase could rise the wheat yield from 0% to 40%. Earlier field studies found that doubling CO₂ could be increased to 30%, and an increase of 20% can be achieved by quadrupling. In trials simulating field temperature in England, The biomass value of winter wheat is between 15-27% with a doubling of CO₂ and if the CO₂ level is doubled in graduated temperature tunnels, the reaction was between 6-34% (Lawlor & Mitchell, 2000). Nine regions in Europe under Open Top Chambers (OTC) 25 studies were conducted with wheat, starting at 10% of CO₂ 320 µmol/mol encourage biomass production, the trials and regression analysis using all data reflects for each 100 µmol/mol 13% of the above-ground biomass increase detected (Lawlor & Mitchell, 2000).

Wheat's response to increased carbon assimilation is resilient and all plant organs could growth. The main stems are usually the least affected organs which is also mentioned by Kapur (2010) for the wheat under climate change effects. On the other hand, tiller growth and viability and root growth were the most encouraged are organs. However, the leaf area, the number of grains per spike and the grain weight was determined by the variety and environmental conditions. From rised CO₂ the grain yield increase is similar with the increase of the biomass. Reproductive

period in comparison to the vegetative growth period grain yield is more sensitive to biomass production, especially during flowering. Summer wheat variety Minaret in multi-site OTC trials reveals 11% grain weight increase per 100 $\mu\text{mol/mol}$ CO_2 enrichment. These results are similar which obtained on the wheat variety Mersia (Lawlor & Mitchell 2000).

Kimball (1983) investigated the effect of CO_2 on wheat in more than seventy studies on pot experiments, yield levels also increased around 90% of the studies. These increases are varies between 0-100%. Although a few negative results were mentioned, but the reason was not disclosed. Gifford and Morison (1993) stated that the negative results of the experiment are due to the mixing of CO_2 with other gases such as ethylene may be a decrease in yield. Kimball (1983) and Cure & Acock (1986) found that C3 plants on average yields were reported with a twofold increase in CO_2 an increase of 35% yield reported. On the other hand, this increase was detected as 10% in C4 plants. For C3 plants, this means biomass of 0.1%/ppmv increase to CO_2 rise. The increase in C4 plants is not directly related to photosynthesis, may be due to the improvement of the efficiency of water use. Despite several trials on yield quality, the increase in CO_2 appears to have little effect (Reddy & Hodges, 2000).

In general, the increase in wheat yield, tillering and more depends on the grain (Lawlor & Mitchell, 1991; Kapur, 2010). Experimental CO_2 increase also changes in organs were observed. These changes are related with the stem and root length, the increase in leaf area and thickness.

If not always also, generally increased leaf thickness, which is due to increased starch levels and the specific leaf surface area (Reddy & Hodges, 2000). These two effect could reduces the potential assimilation of unit leaf area via lowering the rise of photosynthesis (Rosenzweig & Hillel, 1998).

Temperature and possible temperature rise effect on plant physiology, growth and yield

High temperature stress processes in plant is the least understood subject. Soil and air temperatures although they are not simultaneously rise often show a high level of variation. Therefore the roots and branches grow in changing environments. The metabolism of field crops is highly affected by these environmental temperatures. Significantly the temperature affects the crop morphology, degradation of photosynthetic products and root-branch ratio. 'Critical Temperatures' that used in the empirical description of plant growth, covers the average minimum and maximum diurnal temperatures and the total temperature above a certain limit as well as in the growth period. Different physiological processes and plant development periods have different temperature responses (Reddy & Hodges, 2000).

The effect of CO_2 increase on plant growth has been studied extensively, however, the interaction of CO_2 with temperature increase in this regard has not been well studied. Generally the studies covering the effect of temperature change in controlled environments taking into account without nighttime changes. In the field, high temperatures are often associated with high radiation and increased water requirements and thus, it is difficult to understand the effects of climatic factors separately on the plant (Reddy & Hodges, 2000).

Global climate models over the growth period of any plant, gives the number of days in the season that the total temperature and tolerance limit value required will be exceeded. This reflects only the potential effects of high temperature on the amount of yield (Reddy & Hodges, 2000).

Effect of temperature on physiological processes

High temperatures mostly in moderate climatic regimes is expected to decrease the yield. This type of damage in plant production systems is difficult to detect and temperatures are generally within out of optimal ranges in many agricultural regions. For example, optimum growth of wheat temperature is 15 °C as the period average, however, in the Great Plains in the USA. It is also grown when the daily temperature maxima reaches 25 °C during the grain filling process (Paulsen, 1994).

Plants balance the temperature rise, long-wavelength radiation and heat energy by spreading through transpiration and close their stomata when exposed to drought stress (Gates, 1980). These closures reduce transpiration and, as a result, the cooling effect of water loss disappears, so plant temperatures increase. Thus, water and temperature stresses often occur together and they affect.

Hot dry winds (North African Sirocco or Middle East Chamsin) often increase high temperature damage. Temperatures between 45-55°C for at least 30 minutes are damage the leaves many environments. Even if temperatures of around 35 °C and 40 °C last longer, they show approximately the same effect (Fitter & Hay, 1987) and above 40 °C temperatures also affect the closure of stomata (Shibles, Anderson & Gibson 1975). Considering the effects of high temperatures on major crops such as wheat that vernalization is reversed in temperature periods of 30 °C and above for more than eight hours (Acock & Acock, 1993).

Root temperature is more effective than above soil surface temperature because the roots optimal temperature values are lower and to rapid temperature fluctuations shows less adaptations (Paulsen, 1994). Reduction of metabolic substrates, increase in the levels of respiration affects the root activity and the other physiological processes negatively. Therefore, root growth and function are highly affected under high temperature. Temperature affects the uptake of plant nutrients and water, as well as the displacement of root carbohydrates. Prolonged high temperatures ultimately result in completely stop the root growth.

The sensitivity of photosynthesis to temperature is higher than the respiration. The leaf photosystem II (PS2) reaction center in their chloroplasts and thylakoid membranes is very sensitive and responds quickly to high temperature and high luminous (especially during the grain filling process) (Paulsen, 1994).

In many studies, net photosynthesis in wheat is limited at 5 °C that it increases over a wide optimum range as the temperature increases (>25 °C) and stopped around 40 °C (Lawlor and Mitchell, 2000). Due to the nature of Rubisco, the sensitivity of net photosynthesis to CO₂ was found to increase significantly with temperature. Optimum temperature with elevated CO₂ increases by a few degrees. This is related with the kinetic parameters of Rubisco that due to temperature and the proportional solubility of CO₂ and oxygen (O₂). This means that photorespiration increases with temperature. The most important effect of the climate change is the higher temperature accelerates the leaf formation and aging, thus shortening the active photosynthesis period (Lawlor & Mitchell, 2000).

Above a minimum limit value, the plants' resistance to rising temperature tends to be positive up to the optimum temperature value. Optimum temperature value is the maximum rate of plant growth when all other variables are optimum. These other variables are humidity, aeration, plant nutrients (BBM), light and CO₂ of the environment (Fitter & Hay, 1987). When this optimal range is exceeded, plants react negatively and significant reduction in growth and yield occurs (Fig. 5). Different Optimal temperatures vary according to plants. For example, a semi-arid region plant optimal temperature required by corn for photosynthesis is higher than the wheat and grows in a

more temperate climate (Figure 6). Generally plants maintained the temperature of the leaves according to the ambient temperature, if the usable water level is sufficient.

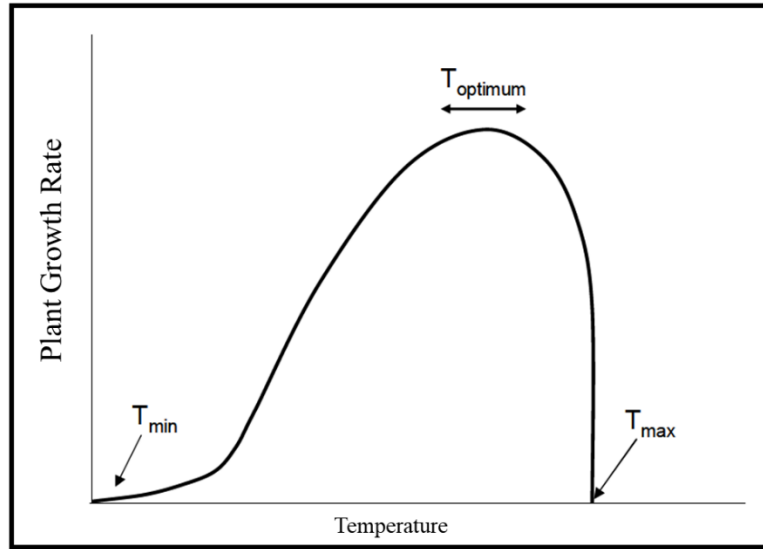


Figure 5. The relationship between plant growth rate and temperature (Rosenzweig & Hillel, 1998)

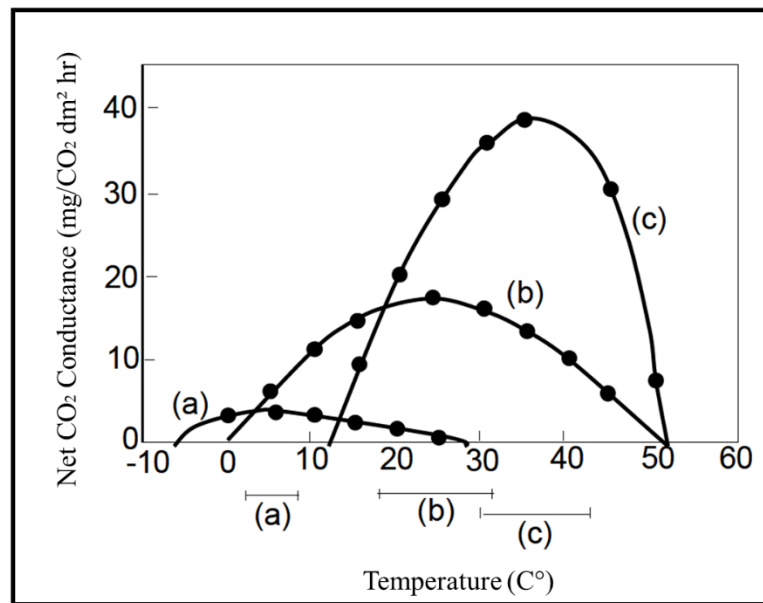


Figure 6. Relationship between net photosynthesis rate and temperature (a: grass; b: wheat, c: maize; horizontal lines indicate optimum range) (Rosenzweig & Hillel, 1998)

Rising temperatures increase the metabolic activities of plant cells, however, extremely high temperatures can damage enzymes (Fitter & Hay, 1987). Rapid reaction levels are useful up to a certain level, above which temperatures can damage some plant processes. Balancing both effects serves to determine the general response of the plant to the increase in temperature. Optimum temperature above the range photoplasmic proteins, cellular enzymes and membranes decompose and a cessation or decrease in the rate of cytoplasmic flow occurs.

In temperate zone varieties, respiration rates are 20 °C below the temperature is low and with the rise in temperature it reaches the 'equilibrium point' until 40 °C. At this temperature point, the respiration rate is equals the rate of photosynthesis; and a net carbon build-up does not occur

at this point which stops the growth. The net level of photosynthesis is obtained when the gross carbon is subtracted from the respiration carbon consumption. This relation were reflected in Figure 7 (Fitter & Hay,1987). Accelerated respiration reduces net biomass accumulation and lowers the efficiency of economical product. In an example given by Paulsen (1994), wheat grains was reduced by the increased respiratoion at high temperature levels. Under increased CO₂ conditions respiration rate changes may partly contribute to reduce the photosynthesis. On the other hand, plants have a certain respiration adaptation to warmer conditions, without an increase in rate (Reddy & Hodges, 2000).

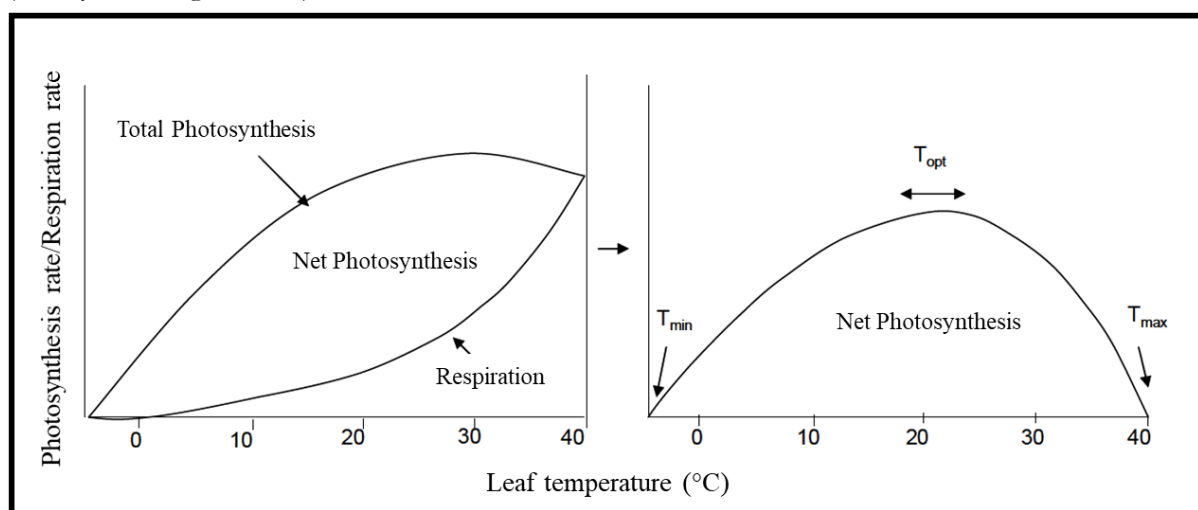


Figure 7. The effect of temperature on plant photosynthesis and respiration and net production (Pisek et al., 1973)

The susceptibility of plants to high temperature damage may be affected vegetative and reproductive development periods differently by their prolongation. Especially during the reproductive development of the plant the high temperatures could damage the plant. Possibly, it can affect grain filling in wheat. In the Anthesis process and just before, the changes that may cause many types of infertility, however, it was determined that wheat was less sensitive to this change (Paulsen, 1994).

Low yield depends on low assimilation rates, accelerated plant development and shortened daily temperature changes. High temperatures can accelerate ripening and effect the functional quality properties of wheat. After near-optimal temperatures in the main products negative effects of rised temperatures, will be higher. In the double CO₂ scenario when the predicted temperature rise reaches its upper limit, plant breeders must be to develop temperature-tolerant varieties (approximately 4 °C temperature rise).

The effects of temperature on wheat phenology are more than the effects of extreme temperatures. Extreme cold can damage wheat; or late frosts promote sterility. During flowering temperatures above freezing (lower than 5 °C) and extreme temperatures (more than 30 °C) can damage pollen formation. This, as a result, may reduce yield while reducing grain settling. Climate change is likely can lead to low yields due to extreme temperatures; because of climate change due to the frequency of extreme temperatures, especially in short development stages to which plant growth is sensitive, may change over time (Lawlor & Mitchell, 2000).

As the effects of changing climate, winter death, vernalization, respiration levels and high temperature stress may vary. High night temperatures can stop the accumulation of carbohydrates of plant organs (Hall & Allen, 1993), and thus, flowering and grain filling may be adversely affected.

In some field crops, the tissues are resistant to low temperatures and thus they become more resistant to the harmful effects of frost. Warmer or milder autumns reduce winter strength and infrequent cold could increase the yield damage sensitivity in these periods. Some studies reveal that 'Winter Deaths' may increase with warming scenarios (Mearns, Rosenzweig & Goldberg, 1992).

In some crops, such as winter wheat, 'full blooming' cannot occur without passing the cooling period. This process is called 'vernalization'. In winter as temperatures rise, vernalization is negatively affected. Farmers can adapt to the change by switching to the 'summer wheat variety' (Rosenzweig, 1985). This situation changes the marketing, processing and quality of wheat.

Rising temperatures during the night increase respiration so increase the use of plant carbohydrates storage and thus yield decreased. This effect, limits some tropical crop yields in agricultural areas. In a simulation study, the effects of the minimum and maximum temperature changes were investigated by Rosenzweig & Tubiello (1996) and they reveal, the minimum temperature increase negatively affects the wheat yield in the USA more than the maximum temperature rise. Plant responses to adverse effects of climate change are variable, however if a north-south section consideration, the southern part of USA has more negative effects due to decreases in vernalization on wheat Rosenzweig & Tubiello (1996).

Effect of temperature on growth and development period

In mid and high latitude areas increased warming could be beneficial as it increases the duration of the potential growth season. A prolonged potential growing season could provide early sowing in spring, accelerated growth and early ripening with the harvest. As a result, multiple cropping can take place.

The main environmental factor controlling plant growth is temperature. High temperatures generally affect the phenological development of plants and accelerate maturation (Ellis et al., 1990). Shortened growth period of time due to increased temperature can reduce the potential yield of annual crops (Rosenzweig, 1990; Butterfield & Morison, 1992). In this context, the length of the growth period and the total amount of light input are main determinants of the total dry matter and yield (Monteith, 1981). Early plant growth in warm environments affects the potential grain yield in the plant growth period (Paulsen, 1994).

With high temperature, the lengths of all developmental stages are shortened. Especially if the period from double ring formation at the apex to flowering is shortened more causes a decrease in the number of grains of each spike and a decrease in grain yield Reddy & Hodges (2000). High temperatures often reduce the number of leaves and spikes due to rapid growth (Paulsen, 1994). Optimum photosynthesis temperature for wheat is between 20-30 °C, whereas it is 15 °C on average for grain yield during the growing period. This temperature difference reveals the importance for maximum yield for temperate plant varieties via photosynthetic activity and temperature process in wheat (Paulsen, 1994). High temperature it also reduces the number and weight of grains that can be harvested. Figure 8 shows the effects of high and low temperatures (Acock & Acock, 1993).

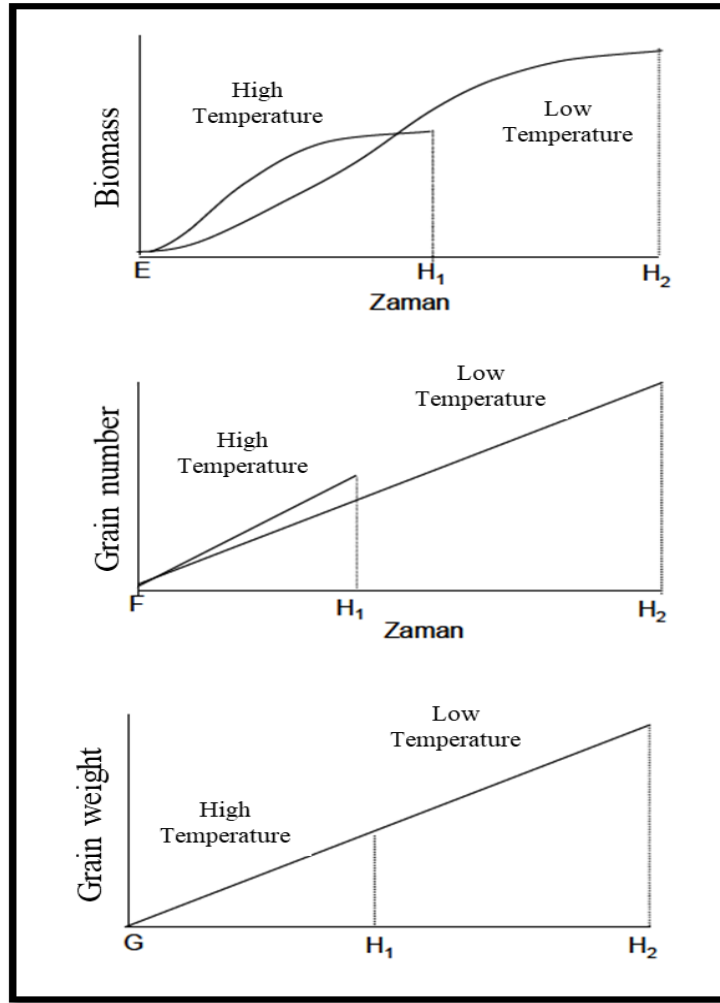


Figure 8. Effects of low and high temperatures on plant growth and yield (E: Germination, F: Beginning of development of plant organs for harvest, G: Beginning of Dry matter accumulation, H: End of dry matter accumulation) (Acock & Acock, 1993).

Researchers have determined the need for thermal time for a plant during its development period as various linear and nonlinear indices. Thermal indices are usually 'degree days of growth' (Thermal Time = Total Temperature defined as Growing Degree Days, GDD) and calculated based on total daily or monthly maximum and minimum temperatures. Some of these have been changed as day length, solar radiation and water stress. These indices are used in calculating the effects of seasonal temperatures according to plant growth, crop and geographical region.

Phenological development and growth processes of plants as seed germination, leaf formation, growth and the beginning of the spike period are directly related to the temperature. The plant total temperature need for each development period is called Thermal Time. Effective thermal process cannot accumulate and plant growth cannot progress below from a certain base or sub-temperature level. Thermal time, accumulation level and plant growth level are increasing with optimal temperature. A forementioned above this optimal temperature, basic process accumulation and plant growth decreases and with the increase in temperature, the accumulation inhibited and accordingly the development of the plant stops.

Effects of temperature on biological yield and grain yield

High temperatures shorten all development cycles. In this context, there is more limited time to obtain resources such as the light water and nutrients, and thus biomass production decreases with increasing temperature. The size of influence depends on which growth cycle is affected. Because the maximum shortening of the growth rate period compared to the shortening of the first growth period, has greater impact on biomass. In a study in England, a 3.5 °C increase throughout all growth periods reduces the biomass of winter wheat 16% and grain yield by 35% with greatly shortened growth period (Reddy & Hodges, 2000). Further more according to Kapur (2010), vegetative parts (leaf, stem and root weight) per plant, under warm conditions increased more rapidly than in cooler conditions with reached to the highest value early and consequently the weight is lower in hot conditions than in cool conditions. Generally, in the greenhouse trails where the ambient temperature changes, the effects of increasing temperature on biomass were more negatively detected. However, this situation varies greatly between seasons and varieties (Lawlor & Mitchell, 2000).

The negative effect of increasing temperature on grain yield is higher than on the biomass. So the harvest index decreases more in rised temperature. This means that particular the grain yield is sensitivity to grain filling period. During the grain filling period 1 °C increase in temperature shortens the time by 5% and thus, harvest index and grain yield reduced. If the high temperatures promote sterility in flowering period also this reduces yield. In open air growth chamber using minaret summer wheat variety trials at 9 different regions, statistical analysis, reflects 6% of grain yield and biomass decreased for each 1 °C increase throughout growing season (from emergence to maturity). Also these effects can be estimated very well with simulation models (Lawlor & Mitchell, 2000).

Water and possible drought effects on growth and yield

Precipitation is the primary source of soil moisture and in arid regions it is the major factor that influencing the plant yield. An overall average precipitation estimator global climate model results also reflect the potential changes of hydrological regimes in each location. A change in climate parameters affects the total seasonal precipitation. In addition, also this situation affects the seasonal distribution and inter-seasonal distribution change. For plant productivity, the seasonal distribution of precipitation degradation may be even more effective than the reduction in total precipitation. Yield, beside amount of water, is also sensitive to potential daily or seasonal 'ET' variation.

Crop water stress depends on the cellular water activity, reduced energy potential in plants, low cell turgor pressure, increased solution densities, decreased cell pressure and lost hydration of tissues (Hale & Orcutt, 1987). After all, the cell expansion and division, cell wall formation, protein and chlorophyll synthesis, and photosynthesis slows down. When significant water stress occurs, the respiratory level rises, sugar and proteins accumulate and metabolism is disrupted (Fitter & Hay, 1987).

As water stress increases, the potential osmotic pressure in plant cells decreases. This process adjusts the regulation of turgor. Osmotic regulation allows cell growth at low water levels (Kramer, 1983). Conservation of turgor features are the lowering osmotic pressure, deposition of solute capacity, and elasticity properties of cells (Hale & Orcutt, 1987).

In the initial stages of drought stress, crop could be protected via turgor osmotic regulation. If water stress persists, plants may lose their adaptive properties and yield levels are more likely to suffer from drought, especially during the reproductive development period. In water stress, leaves, which absorb water rapidly during the dry period can draw water from the grain (Rosenzweig &

Hillel, 1998). Drought in leaves accelerates aging and leaf fall. The water tension during the flowering, pollen release and grain filling phases affects the yield especially in wheat. In wheat, leaf formation and spike formation are affected by water stress.

Wheat studies on the interaction of CO₂ and drought under field conditions are quite a few and can be summarized as follows (Bauer,1972);

a) In elevated CO₂ application, the water use of the wheat plant is may decrease slightly in moist environment, however, in dry conditions could increase slightly

(b) Stimulation of biomass and grain yield with elevated CO₂ tends to be greater in dry conditions compared to humid conditions.

CO₂, climate change and wheat yield

CO₂ temperature and precipitation variations change the growing conditions of crops. The physiological effect of increased CO₂ on the plant may be beneficial to agriculture. Under changing conditions, in environments where plant nutrients and water are not limited, the water use efficiency and photosynthesis increased in the short periods. However, in field conditions, there is often a lack of water and plant nutrients and so productivity may not be an increase (Rosenzweig & Hillel, 1998).

A combination of changes in key factors in plant physiological processes, understanding of the reasons for the yield change is very powerful. In order to determine the effects of climate change realistically, with CO₂ more research is needed on the interaction between temperature and drought. Furthermore, conducting such studies for each agro-ecosystem could give reasonable results.

References

Acock, B. & Acock, M. C. (1993). Modeling approaches for predicting crop ecosystem responses to climate change. In D. R. Buxton, R. Shibles, R. A. Forsberg, B. L. Blad, K. H. Asay, G. M. Paulsen, and R. F. Wilson (eds.). *International Crop Science I*. Crop Science Society of America. Madison, WI. pp. 299-306.

Acock, B. & Alien, L. H. (1985). Crop responses to elevated CO₂ concentrations. In B. R. Strain and J. D. Cure (eds.). *Direct Effects of Increasing CO₂ on Vegetation*. DOE/ER-0238. U.S. Department of Energy. Washington, DC. pp. 53-97.

Akita, S. & Moss, D. N. (1973). Photosynthetic responses to CO₂ and light by maize and wheat leaves adjusted for constant stomatal apertures. *Crop Science* 13:234-237.

Allen, L. H., Jones, P. & Jones, J. W. (1985). Rising atmospheric CO₂ and evapotranspiration. In *Advances in Evapotranspiration*. Proceedings of the National Conference on Advances in Evapotranspiration. December 16-17, 1985. American Society of Agricultural Engineers. St. Joseph, MI. pp. 13-27.

Amthor, J. S. (1989). *Respiration and Crop Productivity*. Springer-Verlag. New York. 215 pp.

Bauer, A. (1972). Effect of Water Supply and Seasonal Distribution on Spring Wheat Yields. Bulletin 490. North Dakota Agricultural Experiment Station. Fargo, ND.

Bazzaz, F. A. (1990). The response of natural ecosystems to the rising global CO₂ levels. *Annual Review of Ecology and Systematics* 21: 167- 196.

Bulterfield, R. E. & Morison, J. I. L. (1992). Modeling the impact of climatic warming on winter cereal development. *Agriculture and Forest Meteorology* 62:241-261.

Chaudhuri, U. N., Burnelt, R. B., Kanemasu, E. T. & Kirkham, M. B. (1986). Effect of Elevated Levels of CO₂ on Winter Wheat Under Two Moisture Regimes. *Response of Vegetation to Carbon Dioxide*. 029. U.S. Department of Energy. Washington, DC. 71 pp.

Cure, J. D. & Acock, B. (1986). Crops responses to carbon dioxide doubling: A literature survey. *Agriculture and Forest Meteorology* 38: 127-145.

Drake, B. G. & Leadley, P. W. (1991). Canopy photosynthesis of crops and native plant communities exposed to long-term elevated CO₂. *Plant, Cell and Environment* 14:853-860.

Ellis, R. H., Hadley, P., Roberts, E. H. & Summerfield, R. J. (1990). Quantitative relations between temperature and crop development and growth. In M. T. Jackson, B. V. Ford-Lloyd, and M. L. Parry. (eds). *Climatic Change and Plant Genetic Resources*. Belhaven Press. London. pp. 85-115.

Fitter, A. H. & Hay, R. K. M. (1987). *Environmental Physiology of Plants*. Second Edition. Academic Press. London. 423 pp.

Gates, D. M. (1980). *Biophysical Ecology*. Springer-Verlag. New York. 611 pp.

Gifford, R. M. & Morison, J. I. L. (1993). Crop responses to the global increase in atmospheric CO₂ concentration. In *International Crop Science I*. Crop Science Society of America. Madison, WI. pp. 325-331.

Hale, M. G. & Orcutt, D. M. (1987). *The Physiology of Plants Under Stress*. Wiley. New York. 206 pp.

Hale, M. G. & Orcutt, D. M. (1987). *The Physiology of Plants Under Stress*. Wiley. New York. 206 pp.

Hall, A. E. & Alien, L. H. (1993). Designing cultivars for the climatic conditions of the next century. In *International Crop Science I*. Crop Science Society of America. Madison , WI. pp. 291-297.

Hendrey, G. R., (1993). *Free-air CO₂ Enrichment for Plant Research in the Field*. C. K. Smoley. Boca Raton, FL. 308 pp.

Idso, S. B., Kimball, B. A. & Mauney, J. R. (1987). Atmospheric carbon dioxide enrichment effects on cotton midday foliage temperature: Implications for plant water use and crop yield. *Agronomy Journal* 79:667-672.

IPCC, (2001). *Climate Change: Impacts, Adaptation and Vulnerability*. Contribution of Working Group II to the Third Assessment Report of Intergovernmental Panel on Climate Change. pp 398-400.

Kapur, B. (2010). *Enhanced CO₂ and Global Climate Change Effects on Wheat Yield in Çukurova Region*. Ph. D. Thesis, Çukurova University, Adana, Turkey (in Turkish).

Kapur, B., Topaloğlu, F., Özfidaner, M. & Koç, M. (2007). Çukurova bölgesinde Küresel İklim Değişikliği ve Buğday Verimliliği Üzerine Etkilerine Genel Bir Bakış. Küresel İklim Değişikliği ve Çevresel Etkiler Konferansı, 18-20 Ekim, 2007. Konya Büyükşehir Belediyesi, Bildiriler Kitabı, Konya, s. 35-45.

Karaca, M., Deniz A. & Tayanc, M. (2000). Cyclone Track Variability over Turkey in Association with Regional Climate, *Int. J. of Climatology*, No: 20.

Kimball, B. A. & Idso, S. B. (1983). Increasing atmospheric CO₂: Effects on crop yield, water use, and climate. *Agricultural Water Management* 7:55-72.

Kimball, B. A. (1983). Carbon dioxide and agricultural yield: An assemblage and analysis of 430 prior observations. *Agronomy Journal* 75:779-788.

Kramer, P. J. (1983). *Water Relations of Plants*. Academic Press. San Diego.

Lawlor, D. W. & Mitchell, R. A. C. (1991). The effects of increasing CO₂ on crop photosynthesis and productivity: A review of field studies. *Plant, Cell and Environment* 14:807-818.

Lawlor, D. W. & Mitchell, R. A. C. (2000). *Crop Ecosystem Responses to Climate Change: Wheat*. In: Reddy, K.R., Hodges, H.F. (eds), *Climate Change and Global Crop Productivity*. CABI Publishing, Cab International, Wallingford, UK, 57-80 pp.

Lemon, E. R., (1983). CO₂ and Plants: The Response of Plants to Rising Levels of Atmospheric Carbon Dioxide. Westview Press. Boulder, CO. 280 pp.

Mearns, L. O., Rosenzweig, C. & Goldberg, R. (1992). Effect of changes in interannual climatic variability on CERES-Wheat yields: Sensitivity and 2xCO₂ general circulation model studies. *Agricultural and Forest Meteorology* 62: 159-189.

Monteith, J. L. (1981). Climatic variation and the growth of crops. *Quarterly Journal of the Royal Meteorological Society* 107:749-774.

Morison, J. I. L. (1985). Sensitivity of stomata and water use efficiency to high CO₂. *Plant, Cell and Environment* 8:467-474.

NOAA. (2022). National Centers for Environmental Information, State of the Climate: Monthly Global Climate Report for 2021, published online January 2022, retrieved on September 22, 2022 from <https://www.ncei.noaa.gov/access/monitoring/monthly-report/global/202113/supplemental/page-3>.

OECD/FAO, (2021). OECD-FAO Agricultural Outlook 2021-2030, OECD Publishing, Paris, <https://doi.org/10.1787/19428846-en>.

Paulsen, G. M. (1994). High temperature responses of crop plants. In K. J. Boote, J. M. Bennett, T. R. Sinclair, and G. M Paulsen (eds.). *Physiology and Determination of Crop Yield*. American Society of Agronomy. Madison, WI. pp. 365-389.

Pisek, A., Larcher, W., Vegis, A. & Napp-Zinn, K. (1973). The Normal Temperature Range. In: *Temperature and Life*. Springer, Berlin, Heidelberg. https://doi.org/10.1007/978-3-642-65708-5_4

Poorter, H. (1993). Interspecific variation in the growth response of plants to an elevated ambient CO₂ concentration. *Vegetation* 104/105:77-97.

Reddy, K. R., & Hodges, H. (2000). *Climate Change and Global Crop Productivity*. Wallingford: CABI. <https://doi.org/10.1079/9780851994390.0007>

Rosenzweig, C. (1990). Crop response to climate change in the Southern Great Plains: A simulation study. *Professional Geographer* 42:20-37.

Rosenzweig, C. & Tubiello, F. N. (1996). Effects of changes in minimum and maximum temperature on wheat yields in the central U.S.: A simulation study. *Agricultural and Forest Meteorology* 80:215-230.

Rosenzweig, C. (1985). Potential CO₂-induced climate effects on North American wheat producing regions. *Climatic Change* 7:367-389.

Rosenzweig, C., & Hillel, D. (1998). *Climate Change and the Global Harvest: Potential Impacts of the Greenhouse Effect on Agriculture*. Oxford University Press. New York, N.Y.

Rosenzweig, C., & Hillel, D. (1998). *Climate Change and the Global Harvest: Potential Impacts of the Greenhouse Effect on Agriculture*. Oxford University Press. New York, N.Y.

Shibles, R. M., Anderson, I. C. & Gibson., A. H. (1975). Soybean. In L. T. Evans (ed.). Crop Physiology. Cambridge University Press. London. pp. 151-189.

Stitt, M. (1991). Rising CO₂ levels and their potential significance for carbon flow in photosynthetic cells. Plant, Cell and Environment 14:741-762.

Türkeş, M., Sümer, U. M. & Çetiner, G. (2000). 'Küresel iklim değişikliği ve olası etkileri', Çevre Bakanlığı, Birleşmiş Milletler İklim Değişikliği Çerçeve Sözleşmesi Seminer Notları (13 Nisan 2000, İstanbul Sanayi Odası), 7-24, ÇKÖK Gn. Md., Ankara.

WorldData, (2022). The Climate in Turkey. <https://www.worlddata.info/asia/turkey/climate.php> (Erişim: Ekim, 2022)

Petrographic Features Of The Upper Triassic-Lower Jurassic Kızılören Formation Dolostones (Konya Northwest, Turkey)

Ali Müjdat Özkan¹
Levent Kenan Kibar²

Introduction

The study area covers Ardıçlı District and its surroundings, located in the northwest of Konya province. Previous studies were mainly stratigraphic and mineral exploration, and the Kızılören Formation dolostones were not studied in detail. Özkan and Kibar (2015) studied the Kızılören Formation carbonates in detail (sedimentological and geochemical) in the study area. In this study, the petrographic features of Kızılören dolostones were studied in detail. In the study, thin sections were carried out under a polarizing microscope for all samples and a scanning electron microscope was performed for some samples. Alizarin red-s test was applied to separate dolomite and calcite minerals on thin sections of dolostone. Thus, the mineralogical compositions, textural properties, and depositional environments of the dolostones were determined.

In accordance with the purpose of the study, 3 measured stratigraphic sections were measured from the Kızılören Formation, samples were collected from appropriate levels and the measured sections were correlated (Özkan and Kibar, 2015).

According to the petrographic characteristics of the Kızılören Formation dolomites: (1) unimodal, very fine to fine crystalline planar-s (subhedral) mosaic dolomite, (2) medium to coarse crystalline planar-e (euhedral) mosaic dolomite, (3) medium crystalline planar-e (euhedral) replaced dolomite, (4) unimodal, medium to coarse crystalline non-planar-s-a (subhedral-anhedral) mosaic dolomite, (5) fine-crystalline planar-e-s (euhedral-subhedral) mosaic dolomite, (6) polymodal planar-e-s (euhedral-subhedral) mosaic dolomite, (7) coarse-very coarse crystalline non-planar-c (cement) saddle dolomite and (8) defined as microbrecciated dolomite (Özkan and Kibar, 2015).

Results

Petrographic Properties of the Samples Taken from Karagüneytepe Measured Stratigraphic Section (A)

The Kızılören carbonates at Karagüney Tepe start with dolomitic limestone at the bottom, continue as limestone-dolostone alternation in the middle sections and continue as dolostone towards the top after the dolomitic limestone, and end with limestone at the top. Considering the microscopic properties of the samples taken from the Karagüneytepe measured stratigraphic

¹ Assoc. Prof. Dr., Konya Technical University

²Geology M.Sc. Engineer, İş Sağlığı ve Güvenliği Genel Müdürlüğü

section, it was observed that they were dolomitic limestone, limestone (mudstone), dolomitic sparite, dolosparite, and crystalline limestone according to Dunham's (1962) classification (Table 1).

Table 1. Microscopic properties of samples taken from Karagüneytepe measured stratigraphic section

Sample	Calcite content%	Dolomite content %	Allochems				Orthochems		Name of the rock (Dunham,1962)
			Fossil %	Intraclast %	Ooid %	Pellet %	Sparite %	Micrite %	
A-1	82	18	10	5	-	7	25	53	dolomitic limestone
A-5	85	15	5	-	-	-	10	85	dolomitic limestone
A-9	92	8	9	-	-	-	7	84	limestone
A-20	94	6	7	5	-	-	15	73	limestone
A-25	80	20	-	-	-	-	100	0	dolomitic limestone
A-33	5	95	-	-	-	-	50	50	dolomitic sparite
A-41	91	9	-	-	-	-	0	100	mudstone
A-57	8	92	-	-	-	-	90	10	dolomitic sparite
A-67	95	5	-	-	-	-	-	100	mudstone
A-85	82	18	-	-	-	-	2	98	dolomitic limestone
A-120	7	93	-	-	-	-	100	0	Dolosparite
A-160	91	9	-	-	-	-	100	0	crystalline limestone

In thin sections, idiopic, hibidiopic, and xenopic textured dolomite crystals are observed in the form of euhedral-subhedral and anhedral grains in sizes varying from micro to coarse (Table 2).

Table 2. Textural properties of samples taken from Karagüneytepe measured stratigraphic section

Sample	Calcite content%	Dolomite content %	Primary texture preservation rate	Dolomite Crystal					Texture
				Size	Sorting	Shape			
						Eu	Su	Xe	
A-1	82	18	Mimetic	fine	good	yes	yes	yes	xenopic
A-5	85	15	Mimetic	fine	good	-	-	yes	xenopic
A-9	92	8	Mimetic	fine	good	-	-	yes	xenopic
A-20	94	6	Mimetic	fine	good	-	-	yes	xenopic
A-25	80	20	non-mimetic	fine	good	yes	yes	yes	subhedral
A-33	5	95	Mimetic	fine - coarse	kötü	yes	-	yes	euhedral
A-41	91	9	Mimetic	fine	good	yes	-	yes	xenopic
A-57	8	92	Mimetic	fine - coarse	poor	yes	yes	yes	subhedral
A-67	95	5	Mimetic	fine - coarse	poor	-	yes	yes	xenopic
A-85	82	18	Mimetic	fine	good	-	-	yes	xenopic
A-120	7	93	non-mimetic	fine-medium	good	yes	yes	-	euhedral
A-160	91	9	non-mimetic	fine	good	yes	yes	-	subhedral

Eu: euhedral, Su: subhedral, Xe: xenopic

As a result of petrographic examinations, it was observed that they were in the form of fine to very fine crystalline dolomite (Figure 1a), calcite-cemented brecciated dolomites (Figure 1b), fine-to-coarse crystalline (polymodal, Figure 2a) dirty, euhedral and subhedral dolomite rhombs, medium-crystalline, euhedral replaced dolomite (Figure 2b), subhedral, fine-to-very fine-crystalline dolomites (Figure 3a), subhedral-xenopic, medium-coarse crystalline and mostly in the form of dirty dolomites (Figure 3b), fine crystalline dolomitic limestone (Figure 4a) and crystalline limestone (Figure 4b).

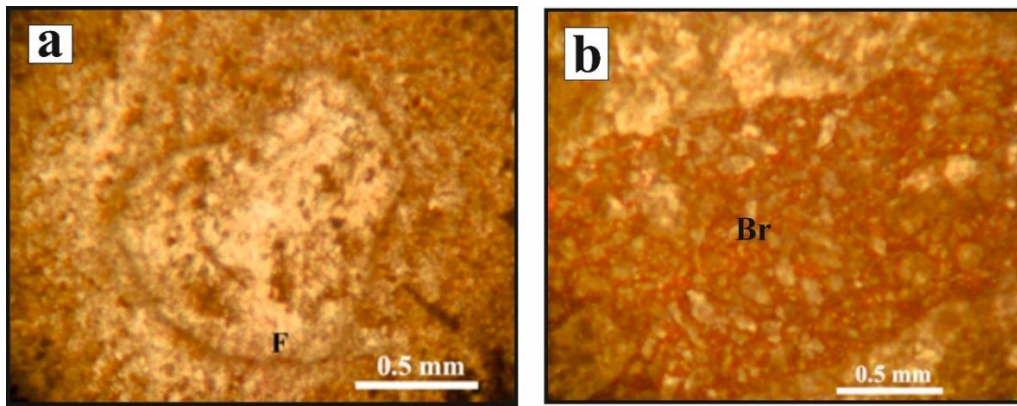


Figure 1. a) Very fine to fine crystalline, subbedral mosaic dolomite (df-1), fossiliferous dolomitic limestone. F: fossil (PPL, Sa:A-1; dolomitic limestone), b) Calcite-cemented brecciated (Br) dolomite (df-8) and dolomitic sparite (df-1) (PPL, Sa: A-57 dolomite)

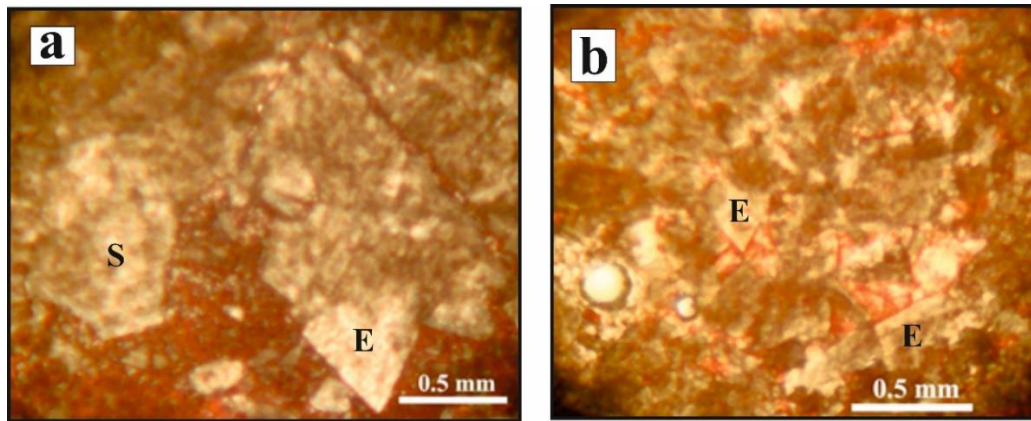


Figure 2. a) Thin-coarse crystalline (polymodal; df-6), euhedral (E) and subbedral (S) dolomite rhomboids (PPL, Sa: A-57 dolomite), b) Medium-crystalline (df-3), euhedral dolomite rhombs (PPL, Sa: A-33; dolomite)

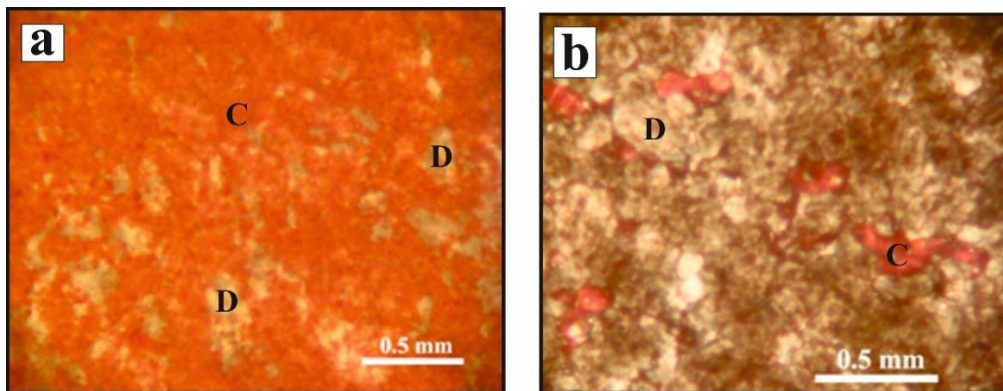


Figure 3. a) Fine-crystalline (df-1), xenotopic dolomite (PPL, Sa: A-85; dolomitic limestone) b) Subbedral-xenotopic, medium-coarse crystalline (df-4) and mostly dirty dolomite (PPL, Nu: A-120; dolomite), C: calcite, D: dolomite

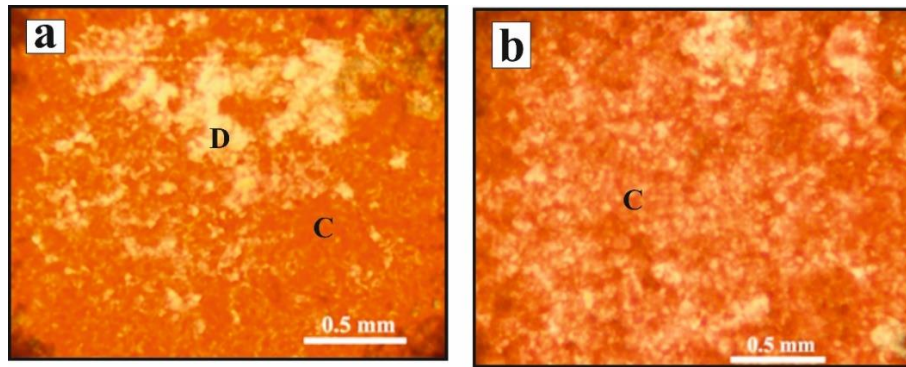


Figure 4. a) Fine crystalline dolomitic limestone (PPL, Sa: A-160; limestone), b) Crystalline limestone (PPL, Sa: A-160; limestone), C: calcite, D: dolomite

As a result of the SEM (scanning electron microscope) examination made from a sample (A-33) taken from the Karagüneytepe measured stratigraphic section, fine-medium crystalline subhedral dolomite crystals, and the EDX diagram is seen (Figures 5 and 6).

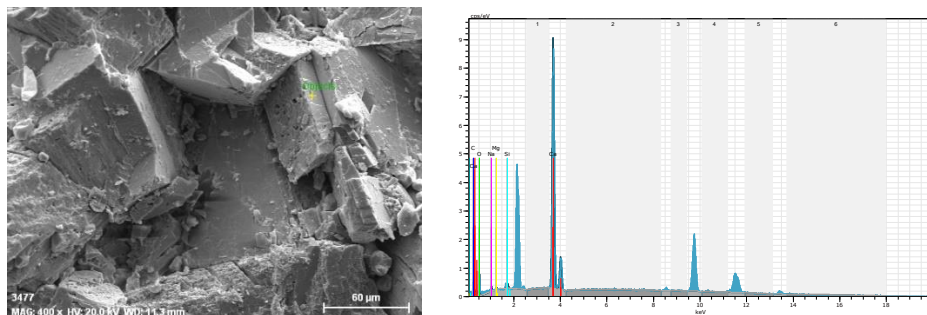


Figure 5. Fine-medium-crystalline, euhedral, subhedral dolomite crystals, intracrystalline and intercrystalline porosity (SEM) and energy dispersion X-Ray spectra (EDX)

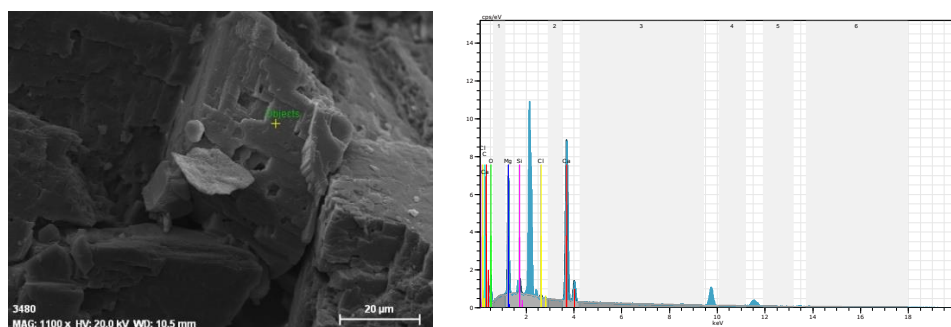


Figure 6. Fine-crystalline, euhedral dolomite crystals, intracrystalline and intercrystalline porosity (SEM), and energy dispersion X-Ray spectra (EDX)

Petrographic Properties of the Samples Taken from the Doğudağ Measured Stratigraphic Section (B)

The carbonates in the Doğudağ measured stratigraphy section begin with dolostone at the base, contain intercalations of calcitic dolomite upwards, and end with dolostones. Fossils (5-25%) are observed in some dolostones and calcite dolomites, and there are 0-90% micrite and 10-100% sparite in the dolostones (Table 3).

In thin sections, euhedral, subhedral, and anhedral dolomite crystals of varying sizes from micro to large are observed (Table 4).

Table 3. Microscopic properties of samples taken from Doğudağ measured stratigraphic section (B)

Sample	Calcite content %	Dolomite content %	Allochems				Orthochems		Name of the rock (Dunham,1962)
			Fossil %	Intraclast %	Ooid %	Pellet %	Sparite %	Micrite %	
B-1	3	97	25	-	-	-	100	0	dolosparite
B-15	2	98	5	-	-	-	55	40	dolomiesparite
B-33	1	99	15	3	-	5	17	60	dolomiesparite
B-60	4	96	-	-	-	-	10	90	dolomiesparite
B-80	35	65	14	-	-	-	86	0	calcitic dolomite
B-100	3	97	-	-	-	-	85	15	dolomiesparite
B-120	2	98	-	-	-	-	80	20	dolomiesparite
B-160	2	98	-	-	-	-	65	35	dolomiesparite
B-195	2	98	-	-	-	-	55	45	dolomiesparite
B-235	45	55	-	4	-	2	84	10	calcitic dolomite
B-257	6	94	-	14	-	-	60	26	dolomiesparite
B-300	8	92	-	15	-	-	70	15	dolomiesparite

Table 4. Textural properties of samples taken from Doğudağ measured stratigraphic section (B)

Sample	Calcite content %	Dolomite content %	Primary texture preservation rate	Dolomite Crystal					Texture
				Size	Sorting	Shape			
						Eu	Su	Xe	
B-1	3	97	non-mimetic	fine-coarse	kötü	yes	yes	-	euhedral
B-15	2	98	mimetic	fine-medium	good	yes	yes	yes	Subhedral
B-33	1	99	mimetic	fine-medium	good	yes	yes	yes	Subhedral
B-60	4	96	mimetic	fine	good	yes	yes	yes	xenotopic
B-80	35	65	non-mimetic	fine-medium	good	yes	yes	-	Subhedral
B-100	3	97	mimetic	fine-medium	good	yes	yes	yes	Subhedral
B-120	2	98	mimetic	fine-medium	good	yes	yes	yes	Subhedral
B-160	2	98	mimetic	fine-medium	good	yes	yes	yes	Subhedral
B-195	2	98	mimetic	fine-medium	good	yes	yes	yes	Subhedral
B-235	45	55	mimetic	fine-coarse	poor	yes	-	-	euhedral
B-257	6	94	mimetic	fine	good	yes	yes	yes	Subhedral
B-300	8	92	mimetic	fine-coarse	poor	yes	yes	yes	Subhedral

Eu: euhedral, Su: subhedral, Xe: xenotopic

As a result of the petrographic examination of the samples, it was observed that they were in the form of rhomboids of medium to coarse crystalline (df-2) euhedral dolomite (Figure 7a), dolomiesparitic (polymodal; df-6) dolomite (Figure 7b), fine crystalline (df-1) dolomiesparite (Figure 8a), fine crystalline (df-1) calcitic dolomite (Figure 8b), fine-crystalline (df-1) dolomiesparite and replacement with iron oxide (Figure 9a), dedolomitization in dolosparites (Figure 9b), intracrystalline dolomite and calcite cement (Figure 10a), fine-crystalline (Figure 9a) df-1)

dolomitic sparite with calcite veins and partially replaced by dolomite (10b), medium to coarse crystalline (df-2) euhedral, zoned dolomite rhomboids (Figure 11a) and fossiliferous dolomitic sparite (11b; df-1).

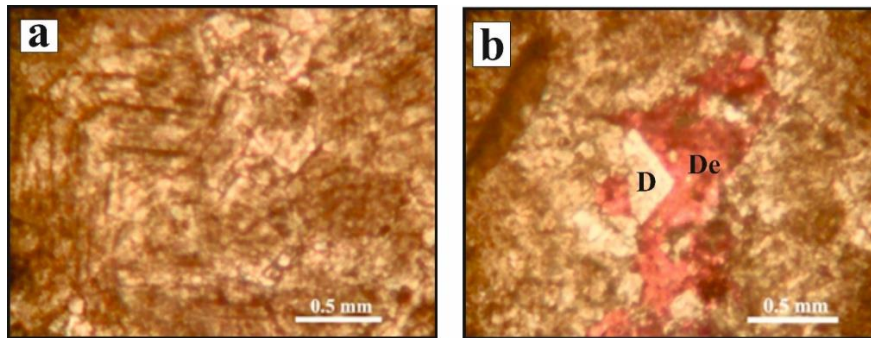


Figure 7. a) Euhedral, medium-coarse crystalline (df-2), dirty dolomite rhomboids (PPL, Sa: B-1; dolomite), b) Euhedral-subbedral, polymodal (df-6) dolomite crystals and dedolomite (PPL, Sa: B-15; dolomite), D: dolomite, De: dedolomite

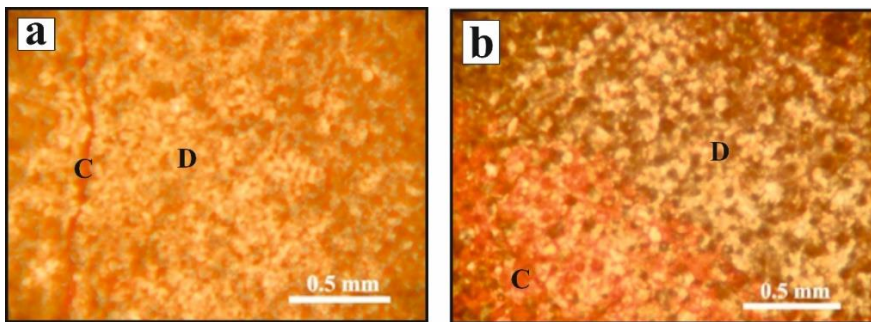


Figure 8. a) Fine-crystalline (df-1) dolomitic sparite and calcitic vein (PPL, Sa: B-60; dolomite) b) Fine-crystalline (df-1) calcitic dolomite (PPL, Sa: B-80; calcitic dolomite), C: calcite, D: dolomite

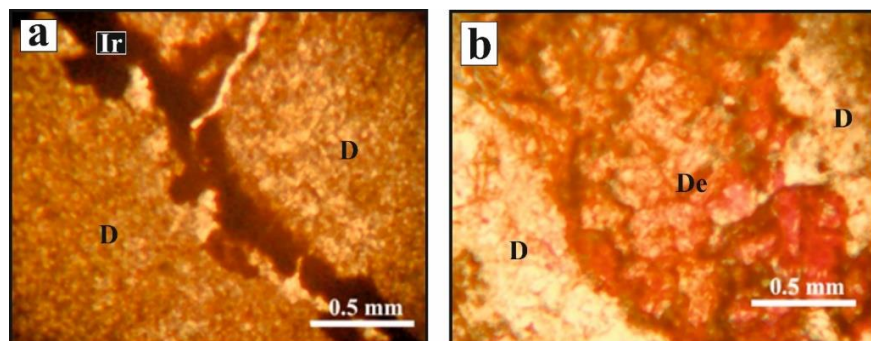


Figure 9. a) Replacement by fine crystalline (df-1) dolomitic sparite and iron oxide. De: iron oxide (PPL, Sa: B-100; dolomite), b) Dedolomitization in dolomitic sparite (PPL, Sa: B-160; dolomite), D: dolomite, De: dedolomite, Ir: iron oxide

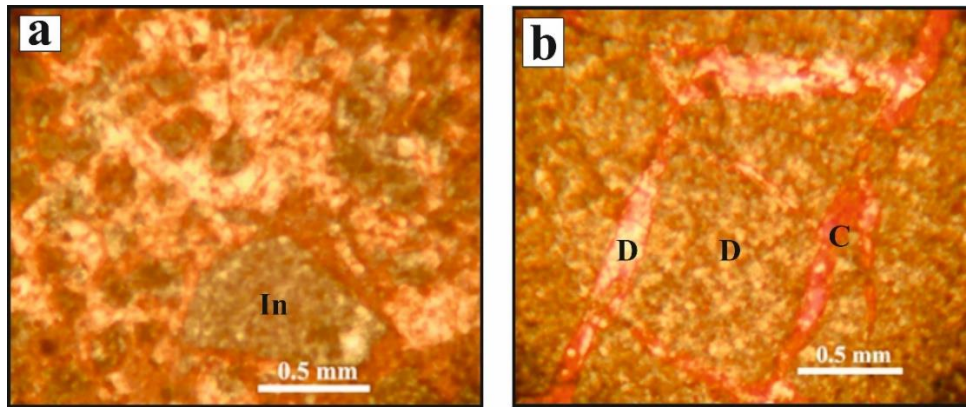


Figure 10. a) Intracrystalline dolomite and calcite cement (PPL, Sa: B-235; calcitic dolomite), b) Calcite vein in fine crystalline (df-1) dolomitic sparite and partially replaced by dolomite (PPL, Sa: B-257; dolomite), D: dolomite, C: calcite, In: intraclast

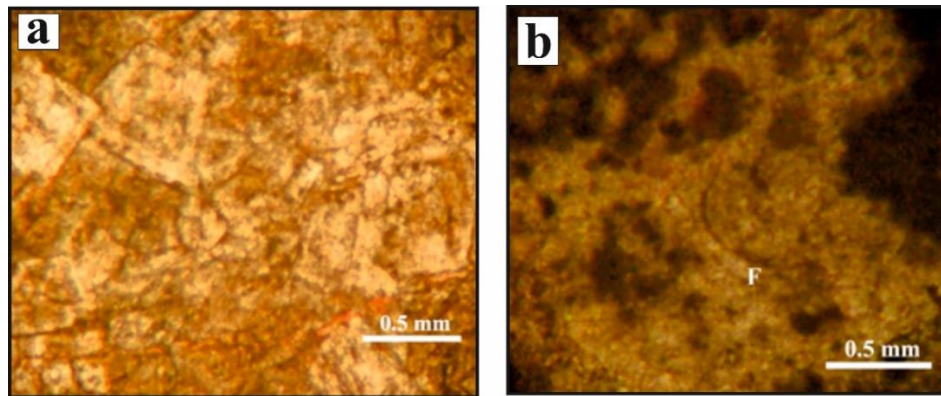


Figure 11. a) Medium-coarse crystalline (df-2), euhedral, zoned dolomite rhombs (PPL, Sa: B-300; dolomite), b) Fine-crystalline (df-1), fossiliferous dolomitic sparite. F: fossil (XPL, Sa: B-33; dolomite)

As a result of the SEM (scanning electron microscope) examination of two samples (B-1, B-120) taken from the Doğudağ measured stratigraphic section, fine crystalline, subhedral (Figure 12), and euhedral (Figure 13) dolomite crystals and EDX diagram are seen.

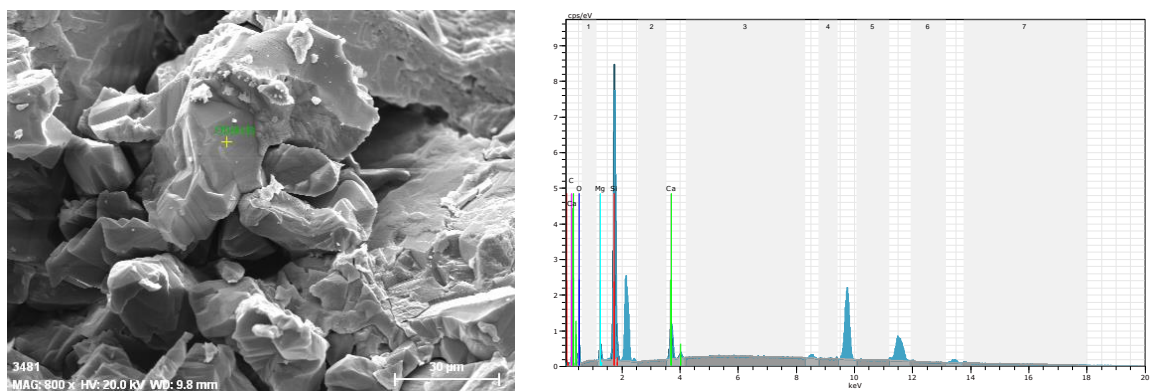


Figure 12. Fine-crystalline, subhedral dolomite crystals, intercrystalline porosity (SEM), and energy dispersion X-Ray spectra (EDX; B-1)

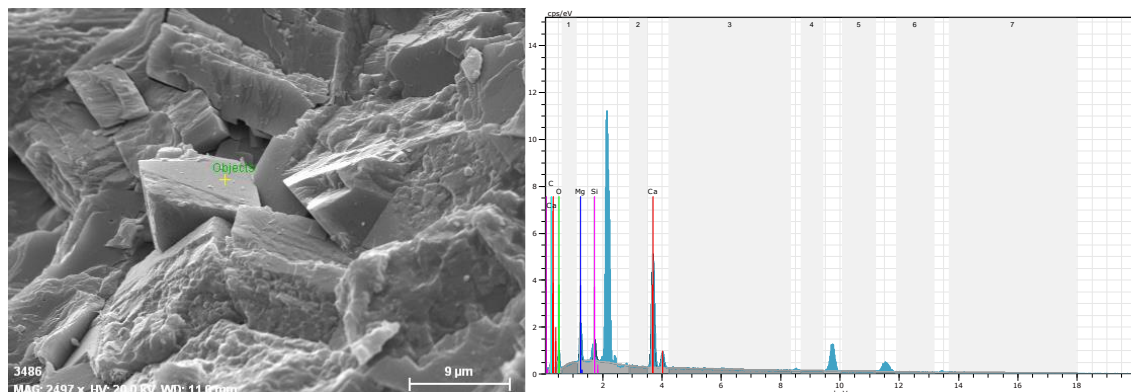


Figure 13. Fine-crystalline, euhedral dolomite crystals, intercrystalline porosity (SEM), and energy dispersion X-Ray spectra (EDX; B-120)

Petrographic Properties of the Samples Taken from the Sarıbayırsırtı Measured Stratigraphy Section (C)

The carbonates in the Sarıbayırsırtı measured stratigraphic section (C) start with dolostone at the base, continue with dolomitic limestone interbedded limestone in the middle sections, and end with dolostone at the top, after the alternation of calcitic dolomite-dolostone (Table 5). Thin-crystalline, subhedral and anhedral dolomite crystals with hibidiotopic and xenotopic textures are observed in thin sections (Table 6).

Table 5. Microscopic properties of samples taken from Sarıbayırsırtı measured stratigraphic section (C)

Sample	Calcite content %	Dolomite content %	Allochems				Orthochems		Name of the rock (Dunham,1962)
			Fossil %	Intraclast %	Ooid %	Pellet %	Sparite %	Micrite %	
C-7	9	91	10	8	-	-	60	22	dolomicsparite
C-17	25	75	-	-	-	-	85	15	calcitic dolomite
C-25	6	94	-	15	-	-	50	35	dolomicsparite
C-30	9	91	-	10	-	-	60	30	dolomicsparite
C-39	45	55	5	-	-	-	100	0	calcitic dolomite
C-50	100	0	8	-	-	-	44	48	mudstone
C-56	93	7	7	-	-	-	46	47	mudstone
C-62	60	40	-	-	-	-	85	15	dolomitic limestone
C-67	94	6	-	-	-	-	100	0	crystalline limestone
C-73	92	8	-	-	-	-	100	0	crystalline limestone
C-87	9	91	-	-	-	-	100	0	dolosparite
C-109	8	92	8	-	-	-	100	0	dolosparite

Table 6. Textural properties of samples taken from Sarbayırsırtı measured stratigraphic section (C)

Sample	Calcite content %	Dolomite content %	Primary texture preservation rate	Dolomite Crystal					Texture
				Size	Sorting	Shape			
						Eu	Su	Xe	
C-7	9	91	mimetic	fine	good	yes	yes	yes	subhedral
C-17	25	75	mimetic	fine	good	yes	yes	yes	subhedral
C-25	6	94	mimetic	fine-coarse	poor	yes	yes	yes	subhedral
C-30	9	91	mimetic	fine-coarse	poor	yes	yes	yes	subhedral
C-39	45	55	non-mimetic	fine	good	yes	yes	-	subhedral
C-50	100	0	mimetic	fine	good	-	-	-	xenotopic
C-56	93	7	mimetic	fine	good	-	yes	yes	xenotopic
C-62	60	40	mimetic	fine	good	-	yes	yes	subhedral
C-67	94	6	non-mimetic	fine	good	-	yes	-	subhedral
C-73	92	8	non-mimetic	fine	good	-	yes	-	subhedral
C-87	9	91	non-mimetic	fine	good	yes	yes	-	subhedral
C-109	8	92	non-mimetic	fine	good	yes	yes	-	subhedral

Eu: euhedral, Su: subhedral, Xe: xenotopic

As a result of the petrographic examination, it was observed that they were in the form of dolomitic sparite (Fig. 14a; df-1), calcitic dolomite (Fig. 14b), dolomitic limestone (Fig. 15a), euhedral-subhedral, fine-crystalline (df-5) sugary dolosparite and dedolomite (Fig. 15b, 16a), dolomitic limestone (Fig. 16b), euhedral-subhedral, fine-crystalline (df-5) dolomite crystals-dolomiticrite, calcite fossil and void fill calcite cement (Figure 17a) and coarse-very coarse crystalline (df-7) saddle (cement) dolomite (Fig. 17b).

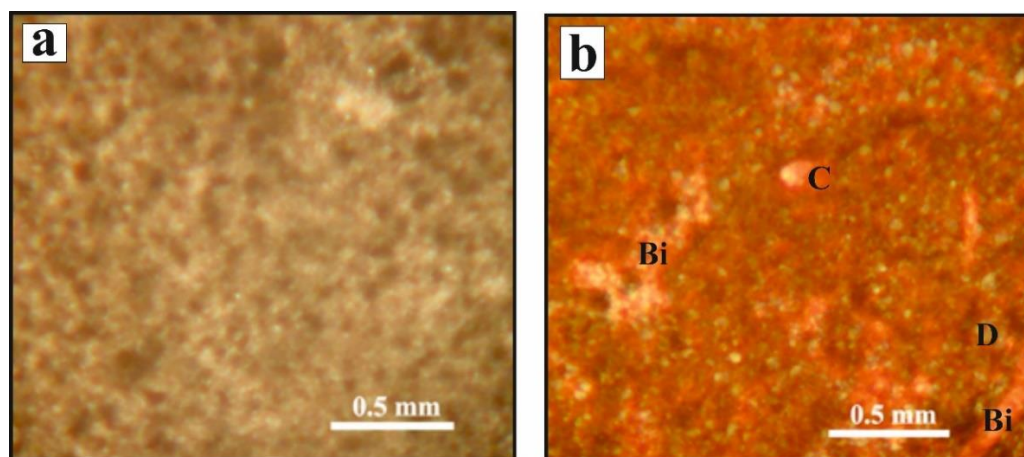


Figure 14. a) Fine to very fine crystalline (df-1), Dolomitic sparite (PPL, Sa: C-7; dolomite), b) Bioclast, fine crystalline (df-1) dolomitic sparite and calcite cement (PPL, Sa: C-7; dolomite), C: calcite, D: dolomite, Bi: bioclast

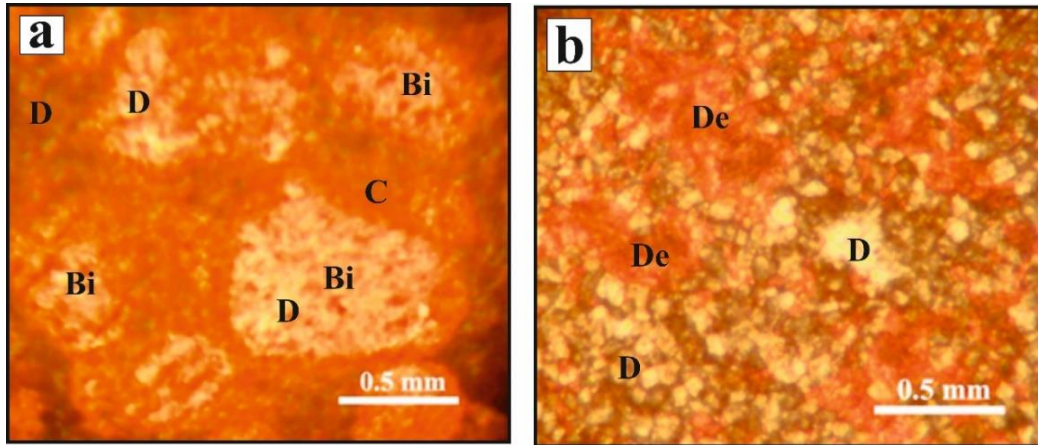


Figure 15. a) Bioclasted, calcite-cemented dolomitic sparite (df-1, PPL, Sa: C-7; dolomite), b) Euhedral-subhedral, fine-crystalline (df-5) dolosparite and dedolomite (PPL, Sa: C-39); calcitic dolomite, C: calcite, D: dolomite, De: dedolomite, Bi: bioclast

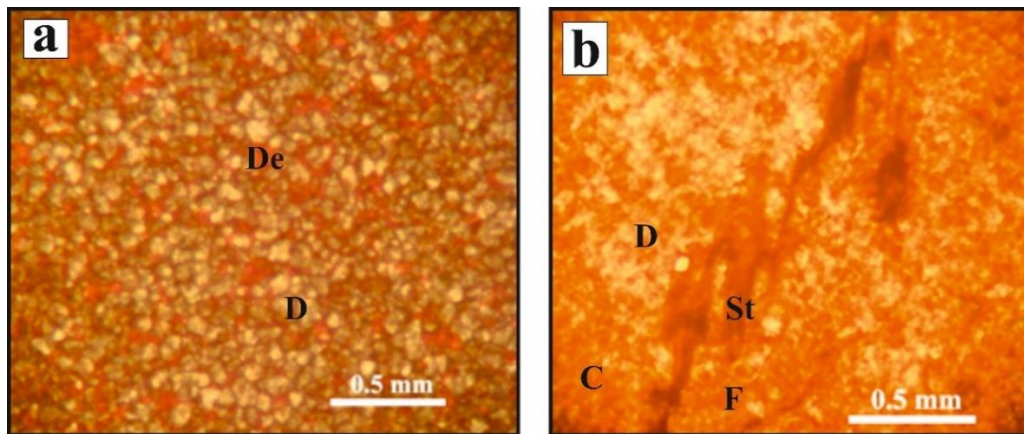


Figure 16. a) Euhedral to subhedral, fine crystalline (df-5) sugary dolosparite and dedolomite (PPL, Sa: C-39; calcitic dolomite), b) Sparicalcrite, fossil (F), stylolite, and dolomite crystals (PPL, Sa: C-67; limestone), C: calcite, D: dolomite, De: dedolomite, St: stylolite

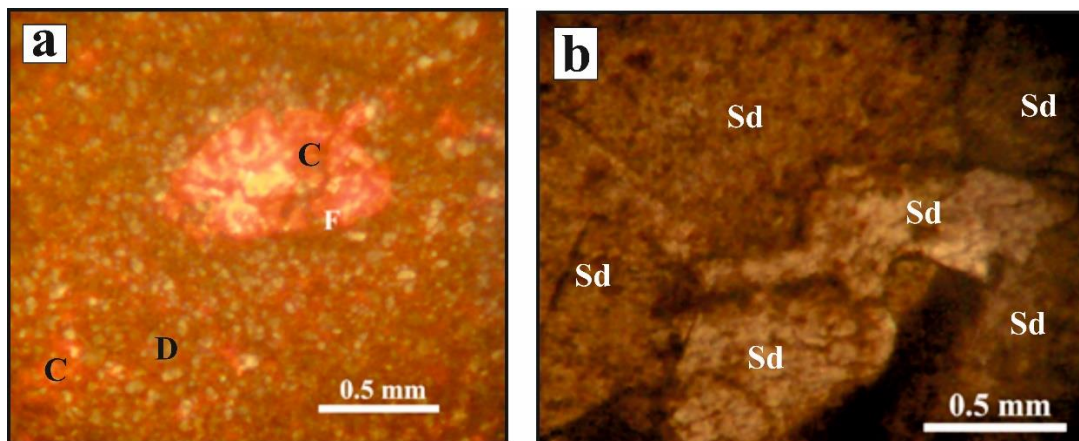


Figure 17. a) Euhedral-subhedral, fine-crystalline (df-5) dolomite crystals-dolomicrite, calcite fossil, and void-filling calcite cement, (PPL, Sa: C-109; dolomite) F: fossil, b) Coarse-very coarse crystalline (df-7), (nonplanar-c) saddle dolomite cement. (PPL, Sa: C-25; dolomite), C: calcite cement, D: dolomite, Sd: saddle dolomite

Discussion

Unimodal, very fine to fine crystalline planar-s (subhedral) dolomites (df-1); small crystal sizes ($<60\ \mu\text{m}$) indicate limited subtidal to supratidal environments (Amthor and Friedman, 1991). It may develop by early replacement of fine crystalline early diagenetic dolomite or concurrent neomorphic or original peritidal carbonate mudstones (Zenger, 1983; Amthor and Friedman, 1991). Crystal size is controlled by the ratio relationship of the two functions; nucleation and growth rate (Spry, 1969; Amthor and Friedman, 1991). Dolomite often selectively replaces fine crystalline CaCO_3 (Murray and Lucia, 1967; Sibley et al., 1987; Amthor and Friedman, 1991). The fine particles have a very large surface area compared to their volume and therefore the nucleation rate is fast. If the nucleation rate is high compared to the growth rate, the resulting crystal size will be small (Amthor and Friedman, 1991). This can be explained, among others, by selective dolomitization of finer crystalline calcium carbonate and early dolomitization of subtidal and supratidal carbonate muds (Amthor and Friedman 1991). We can emphasize that the fine crystalline dolomites in the Kızılören Formation were formed by early diagenetic replacement of carbonates in tidal and subtidal environments.

Medium to coarse crystalline planar-e (euhedral) mosaic dolomites (df-2); are often presented as evidence of pre-dolomitization texture. Because the crystal size in individual mosaics is unimodal and it can be stated that the nucleation sites for dolomite are homogeneously distributed (Sibley, 1982; Schofield, 1984; Amthor and Friedman, 1991). The fact that the dolomite crystals show the sharing of reconciled boundaries indicates that they are formed in situ. They develop simultaneously to form congruent crystal boundaries and the development of planar-e mosaics is achieved by the combined growth of zones in adjacent crystals (Schofield, 1984; Amthor and Friedman, 1991). The absence of intracrystalline chipping features, continuity, and zones of equal width indicate the continued development of the crystals. We can say that the medium-coarse crystalline planar-e (euhedral) mosaic dolomites (df-2) of the Kızılören Formation developed simultaneously and in situ.

Medium-crystalline planar-e (euhedral) replaced dolomites (df-3); dirty core and clean margin texture can be observed widely in rocks of all ages (Sibley, 1982; Amthor and Friedman, 1991). Intercrystalline chipping in dolomite rhombs indicates dissolution after dolomitization. Late diagenetic crack-filled dolomites are formed at high temperatures (burial origin). The crack fillings that cut the dolomite rhombs in the mid-crystalline euhedral replacement dolomites of the late diagenetic phase indicate a high temperature (burial origin) formation. The euhedral form of dolomite rhombs suggests formation at temperatures below $50\text{--}100^\circ\text{C}$ (approximately critical temperature), since higher temperatures develop anhedral forms (Sibley and Gregg, 1987; Ramadan, 2014). Also, planar dolomite crystals may form along chemical compaction dissolution wrinkles. We can state that the medium crystalline planar-e (euhedral) replaced dolomites (df-3) of the Kızılören Formation are of late diagenetic burial origin.

Unimodal, medium to coarse crystalline non-planar-s-a (subhedral-anhedral) replaced dolomites (df-4); it develops as a replacement for the original limestone or dolostone. This type of replacement usually completely destroys the original depositional tissues (Amthor and Friedman, 1991). This type of dolomite corresponds to the xenotopic-a dolomite described by Gregg and Sibley (1984) and Sibley and Gregg (1987) (Ramadan, 2014). They propose that the xenotopic dolomite texture results from the neomorphic recrystallization of pre-existing dolomite or the replacement of limestone at high temperatures. Folk (1959) described non-planar-a dolomite as the replacement of the original limestone in the burial setting. Such a replacement can occur only in certain zones and originally had high porosity and permeability. This coarse non-planar dolomite cement is generally called saddle dolomite (Radke and Mathis, 1980; Amthor and Friedman, 1991).

It has been emphasized that almost all of these dolomites consist of high temperatures (60-150°C; Radke and Mathis, 1980) and high salinity basinal waters (Ramadan, 2014). No conclusive evidence of saddle dolomite formation at low temperatures from marine or hyposaline waters has been demonstrated so far (Amthor and Friedman, 1991; Ramadan, 2014). We can say that the unimodal, medium to coarse crystalline non-planar-s-a (subhedral-anhedral) replacement dolomites (df-4) in the Kızılören Formation developed in a high-temperature burial environment.

Fine-medium crystalline planar-e-s (euhedral-subhedral) mosaic dolomites (df-5); fine crystalline matrix dolomite usually develops as a fabric destroyer (Lonnee, 1999). At this stage, the micritic matrix and fossil components in the mud-supported sediments are replaced. The fine crystalline matrix dolomite was restricted to formation after the initial chemical compaction but formed approximately simultaneously with the medium crystalline matrix dolomite. The mid-crystalline matrix dolomite in the Kızılören Formation developed as fabric-destructive replaced dolomite.

Polymodal planar-e-s (euhedral-subhedral) mosaic dolomites (df-6); are formed by mimetic and non-mimetic replacement of fossils and unimodal matrix (Sibley and Gregg, 1987). If the dolomitization solution is slightly less supersaturated with respect to dolomite, the matrix may become dolomitized but the fossils may remain undolomitized (Sibley and Gregg, 1987). The fossils remain undolomitized because at less saturation very few dolomite cores are formed on very coarse calcite. If these fossils remain as calcite, the resulting rock will be in the form of unimodal, planar-s dolomite with unreplaced allochemes (Sibley and Gregg, 1987). If allochemes are resistant to dolomitization, they then dolomitize above the critical temperature or critical saturation, and the resulting texture may be polymodal with non-planar dolomite, non-mimetic replacement allochemes, and planar-s matrix (Sibley and Gregg, 1987). Another possibility is that non-replaced fossils will dissolve leaving patterns either during or after dolomitization (Sibley and Gregg, 1987). If the non-dolomitized matrix and allochemes dissolve, the resulting dolomite will be unimodal, planar-e dolomite. This form of dolomite is commonly referred to as sugary. It may develop similarly to the situation described by Sibley and Gregg (1987), but the dolomite may continue to evolve until the void is completely filled, resulting in unimodal, planar-s dolomite (Sibley and Gregg, 1987; Ramadan, 2014). We can say that the Kızılören Formation was formed by the mimetic replacement of the original limestones in the polymodal planar-e-s (euhedral-subhedral) mosaic dolomites (df-6).

Coarse-very large anhedral cement dolomites (df-7) are generally referred to as saddle dolomite (Radke and Mathis, 1980). Almost all of these dolomites have been interpreted as formed by brines at elevated temperatures (60–150°C; Radke and Mathis, 1980) and high salinity (Amthor and Friedman, 1991). Saddle dolomites, for which conclusive evidence has not been provided so far, may form in hyposaline water, or at lower temperatures than seawater (Radke and Mathis, 1980; Machel, 1987). In this lack of evidence, anhedral cement dolomite has also been interpreted as being formed at higher salinities than seawater and elevated temperatures from brine (Amthor and Friedman, 1991). It is thought that the saddle dolomites observed in the Kızılören Formation dolomites are formed from basinal saline waters at elevated temperatures with medium-deep burial.

Microbrecciated dolomites (df-8); the time of formation of fractures and cracks reflect the state of the rock or sediment while providing evidence of local or regional tectonic events (Boillot et al., 1988). They are helpful in determining relative chronology and can sometimes determine the time, and they may also be important in restoring porosity (Boillot et al., 1988). Fractures and fissures are therefore of great importance in a diagenetic study. The chronological order establishes the relation of the original rock to the petrification state and its relation to the stylolitization. The crack line is used to distinguish two types of cracks: (1) zig-zag cracks with jagged or irregular edges

without specific geometries, (2) roughly linear cracks with zig-zag, smooth, or irregular (on close examination) edges (Boillot et al., 1988). We think that the Kızılören Formation developed as brecciated dolomites within the local and/or regional tectonic fractures in the microbrecciated dolomites (df-8).

The beginning of the stylolitization in the limestones is about 500 m (Dunnington, 1967; Lind, 1993; Duggan 2004). Horizontal stylolites with amplitudes of 10 cm or greater are found, although they are less than 1 cm in most lithofacies. It suggests that the larger amplitude stylolites cut the smaller amplitude stylolites, suggesting that the stylolitization in a given lithology occurred during the progressive middle and deep burial (Duggan, 2004). Since the amplitudes of the stylolites observed in the Kızılören Formation dolomites are <1 cm, they suggest shallow-medium burial. The dark coloration observed at the borders of the stylolites was thought to be probably of organic origin.

The characteristics of the Kızılören Formation dolostones suggest formation at low temperatures in the shallow-buried (in-tidal-subtidal) mixed water area in a shallow marine carbonate environment in the early diagenesis, and at high temperatures from altered seawater in the mid-deep burial area in the late diagenesis. Dedolomitization occurred by meteoric water affection in the Kızılören Formation.

REFERENCES

- Amthor, J. E. & Friedman, G. M. (1991) Dolomite-rocks textures and secondary porosity development in Ellenburger Group carbonates (Lower Ordovician), west Texas and southeastern New Mexico. *Sedimentology*, 38, 343-362.
- Boillot, G. Comas, M. C. Girardeau, J. Kornprobst, J. Loreau, J. P. Malod, J. Mougenot, D. Moullade, M. (1988) Preliminary results of the Galinaute Cruise: dives of the submersible *Nautile* on the western Galicia Margin, Spain. *Ocean Drilling Program*, 37-51.
- Duggan, J. P. (2004) Burial dolomites at Swan Hills Simonette NTEf, West-central Alberta Basin. *Can. Soc. Petrol. Geol., 2004 Dolomite Conference*, 29 p.
- Dunham, R. J. (1962) Classification of carbonate rocks according to depositional texture. In: classification of carbonate rocks, (ed. W. E. Ham). *Amer. Assoc. Petrol. Geol. Memoir*, 1, 108-121.
- Dunnington, H. V. (1967) Aspects of diagenesis and shape in stylolitic limestone reservoirs. In: origin of oil. *Geology and Geophysics, Proc. Seventh World Petroleum Congress*, 2, 339-352.
- Folk, R. L. (1959) Thin-section examination of pre-simpson Paleozoic rocks. In: stratigraphy of the pre-simpson Paleozoic subsurface rocks of Texas and southeast New Mexico (eds. V. E. Barnes, P. E. Cloud, Jr, L. P. Dixon, R. L. Folk, E. C. Jonas, A. R. Palmer & E. J. Tynan), University of Texas. *Bur. Econ. Geol. Publ.*, 5924, 95-130.
- Gregg, J. M. & Sibley, D. F. (1984) Epigenetic dolomitization and the origin of xenotopic dolomite texture. *Jour. Sedim. Petrol.*, 54, 908-931.
- Lind, I. L. (1993) Stylolites in chalk from leg 130, Ontong Java Plateau. *Proceedings of the Ocean Drilling Program, Scientific Results*, 130, 445-451.
- Lonnee, J. S. (1999) Sedimentology, dolomitization and diagenetic fluid evolution of the Middle Devonian Sulphur Point Formation, northwestern Alberta. *University of Windsor*, MSc. Thesis, p. 133.
- Murray R. C. & Lucia, F. J. (1967) Cause and control of dolomite distribution by rocks selectivity. *Bull. Geol. Soci. Amer.*, 78, 21-35.
- Özkan, A. M. & Kibar, L. K. (2015) Konya kuzeybatısındaki Kızılören formasyonundaki (Üst Triyas-Alt Jura) dolomitlerin sedimantolojik ve jeokimyasal incelenmesi. *Selçuk Üni. Fen Bil. Enst. Yüksek Lisans Tezi*, 93 s. (Unpublished)
- Radke, B. M. & Mathis, R. L. (1980) On the formation and occurrence of saddle dolomite. *Jour. Sedim. Petrol.*, 50, 1149-1168.
- Ramadan, F. S. (2014) Petrographic and diagenetic characteristics of the dolomites at Um Bogma Formation (Early Carboniferous), West-central Sinai, Egypt. *World Applied Sciences Journal*, 31, 12-30.
- Schofield, K. (1984) Are pressure solution, neomorphism and dolomitization genetically related? In: stylolites and associated phenomena—relevance to hydrocarbon reservoirs. *Spec. Publ. Abu Dhabi Nat. Reservoir Res. Found.*, 183-201.

Sibley, D. F. (1982) The origin of common dolomite fabrics, clues from the Pliocene. *Jour. Sedim. Petrol.*, 52, 1087-1100.

Sibley, D. F. & Gregg, J. M. (1987) Classification of dolomite rock textures. *Jour. Sedim. Petrol.*, 57, 967-975.

Sibley, D. F. Dedoes, R. E. Bartlett, T. R. (1987) Kinetics of dolomitization. *Geology*, 15, 1112-1114.

Spry, A. (1969) Metamorphic textures. Oxford, *Pergamon Press*.

Zenger, D. H. (1983) Burial dolomitization in the Lost Burro Formation (Devonian), east-central California, and the significance of late diagenetic dolomitization. *Geology*, 11, 519-522.

Geocemical Properties Of The Saytepe Formation (Upper Cretaceous) Carbonates Around Hadım And North (Konya, Turkey)

Ali Müjdat Özkan¹
Görkem Kırcan²

Introduction

The aim of the study is to study the geochemical properties of the Saytepe Formation (Upper Cretaceous) carbonates around Hadım (Konya, Türkiye) located in the Central Taurus Mountains. In this context, major, trace, and rare earth element analyzes were made from the Saytepe Formation carbonate samples, in which environment this formation was deposited, how it was altered in its diagenetic history, it was determined how the climate was during the deposition process, whether there was terrigenous material input to the basin during the deposition of carbonates, and which rocks were the origin of detrital.

Previous studies have shown that the distribution and amounts of some major and trace elements in fine-grained rocks can be used to determine paleoclimatic conditions (Cao et al., 2012; Wang et al., 2017; Ding et al., 2018). It has been stated by many researchers (Cao et al., 2012; Wang et al., 2017; Ding et al., 2018) that elements such as Fe, Mn, V, Cr, Co, and Ni show relative enrichment in humid climatic conditions. Ding et al. (2018) emphasized as a result of the increase in alkalinity of water due to evaporation in arid climate conditions, the storage of salty minerals increases, and elements such as Ca, Mg, Na, K, Ba, and Sr are concentrated.

The geochemical properties of the Saytepe Formation carbonates were tried to be revealed by making main, trace and rare earth element analyses of the samples taken at appropriate intervals along the lines of two measured stratigraphic sections (Büyükkaratepe ÖSK and Dedetepe ÖSK) selected around Bağbaşı-Hadım (Konya). In this framework, the determination of the environmental conditions (oxic to anoxic) in which the Saytepe Formation carbonates were deposited, whether there were continental detritus (stream and/or wind blow) development into the basin during the deposition, whether there were hydrothermal entrances to the basin, whether the original characteristics of the carbonate phase were preserved if there are terrestrial inputs, studies have been carried out to determine their source rock (felsic, mafic or mixed) types, to determine to what extent the limestones have been affected in the diagenetic process, whether they have undergone metamorphism and paleoclimatic conditions.

¹ Doç. Dr. Konya Teknik Üniversitesi

² Jeoloji Müh. Konya Teknik Üniversitesi,

Results

Major Element Geochemistry

The litho-geochemical results of Saytepe carbonates are given in Tables 1, 2, and 3. In some of the carbonate samples, the measurable element values that are very low or below the limit values may be due to the adsorbing of these elements to the clay minerals. Elements below the limit value were evaluated by taking the limit values in this study.

The Saytepe carbonate samples present, %0.10-1.03 SiO₂, %0.01-0.45 Al₂O₃, %0.04-0.48 Fe₂O₃, %0.01-0.12 K₂O, %0.01-0.02 TiO₂, %0.01-0.02 P₂O₅, %0.01 MnO, %0.01-0.03 Na₂O, %34.53-55.76 CaO ve %0.34-18.09 MgO (Table 1).

In the Saytepe samples, there is a strong positive correlation between SiO₂ and Al₂O₃, Fe₂O₃, Na₂O, K₂O, TiO₂, moderate negative correlation with CaO, moderate positive correlation with MgO, no correlation with P₂O₅ and MnO (Table 4).

Table 1. Major element (%) concentrations of the Saytepe Formation carbonates

Sample	SiO ₂	Al ₂ O ₃	Fe ₂ O ₃	MgO	CaO	Na ₂ O	K ₂ O	TiO ₂	P ₂ O ₅	MnO	Cr ₂ O ₃	LOI	SUM
B-80	0.16	0.02	0.06	0.71	55.02	<0.01	<0.01	<0.01	<0.01	<0.01	<0.002	44.0	99.69
B-68	0.22	0.04	0.11	1.46	53.74	<0.01	<0.01	<0.01	0.01	<0.01	0.002	44.3	99.96
B-55*	0.20	0.04	0.13	18.09	34.53	0.02	<0.01	<0.01	<0.01	<0.01	<0.002	46.7	99.95
B-49	0.32	0.15	0.04	0.55	54.80	<0.01	0.05	0.01	0.02	<0.01	0.002	44.0	99.96
B-43	0.40	0.19	0.08	0.61	54.48	<0.01	0.06	0.01	0.02	<0.01	0.002	44.1	99.95
B-30	0.16	<0.01	0.05	0.39	55.25	<0.01	<0.01	<0.01	<0.01	<0.01	<0.002	44.1	99.94
B-19	0.10	<0.01	0.04	0.34	55.76	<0.01	<0.01	<0.01	<0.01	<0.01	<0.002	43.7	99.96
B-15	0.20	<0.01	0.04	0.37	55.50	<0.01	<0.01	<0.01	<0.01	<0.01	<0.002	43.8	99.94
B-10	0.16	<0.01	0.07	0.41	55.34	<0.01	<0.01	<0.01	<0.01	<0.01	<0.002	44.0	99.67
B-6	0.19	0.03	0.11	0.56	55.06	<0.01	<0.01	<0.01	<0.01	<0.01	<0.002	44.0	99.92
B-1*	1.03	0.45	0.48	16.39	34.92	0.03	0.12	0.02	<0.01	<0.01	<0.002	46.3	99.95

*dolostone

Table 2. Trace element (ppm) concentrations of the Saytepe Formation carbonates

Sample	Ba	Rb	Sr	Zr	U	V	Th	Mo	Cu	Ni	Pb	Zn	Sc	Co	Cs
B-80	11	<0.1	263.3	5.6	1.5	<8	<0.2	<0.1	1.5	3.9	2.5	3	<1	<0.2	<0.1
B-68	16	0.3	357.0	4.8	2.4	20	<0.2	0.1	1.7	4.7	2.5	3	<1	0.2	<0.1
B-55*	7	<0.1	178.7	6.0	2.2	16	<0.2	0.2	2.4	4.4	2.3	12	<1	0.4	<0.1
B-49	10	1.4	311.2	8.4	0.3	<8	<0.2	<0.1	1.2	3.2	1.4	5	<1	<0.2	<0.1
B-43	5	1.9	240.2	6.2	0.6	<8	0.2	<0.1	1.5	4.1	1.6	4	<1	<0.2	<0.1
B-30	4	<0.1	307.5	5.2	1.1	8	<0.2	<0.1	1.4	3.6	2.0	4	<1	<0.2	<0.1
B-19	5	<0.1	320.7	3.9	0.5	<8	<0.2	<0.1	0.9	3.3	2.9	3	<1	<0.2	<0.1
B-15	6	<0.1	268.3	6.6	0.6	<8	<0.2	<0.1	1.3	3.1	2.0	3	<1	<0.2	<0.1
B-10	7	<0.1	367.8	3.5	0.6	<8	<0.2	<0.1	1.0	2.7	2.3	4	<1	<0.2	<0.1
B-6	9	0.2	211.6	4.2	0.9	<8	<0.2	0.2	1.5	2.7	10.6	11	<1	<0.2	<0.1
B-1*	7	4.2	142.7	5.4	3.4	24	0.4	9.2	3.9	9.1	12.5	21	<1	0.6	0.1

Table 2. Continued

Sample	Ga	Be	Hf	Nb	Ta	Sn	Hg	As	Tl	Se	Bi	Sb	Cd
B-80	<0.5	<1	0.1	<0.1	<0.1	<1	0.10	2.1	<0.1	<0.5	<0.1	0.1	0.3
B-68	<0.5	<1	0.1	<0.1	<0.1	<1	0.05	1.9	<0.1	<0.5	<0.1	0.3	0.4
B-55*	<0.5	<1	0.2	<0.1	<0.1	<1	0.06	2.6	<0.1	<0.5	<0.1	0.6	0.4
B-49	<0.5	<1	0.1	<0.1	<0.1	<1	0.05	1.9	<0.1	<0.5	<0.1	0.2	0.8
B-43	<0.5	<1	0.2	0.1	<0.1	<1	0.04	1.5	<0.1	<0.5	<0.1	0.1	0.4
B-30	<0.5	<1	<0.1	<0.1	<0.1	<1	0.08	2.5	<0.1	<0.5	<0.1	0.2	0.3
B-19	<0.5	<1	<0.1	<0.1	<0.1	<1	0.03	1.9	<0.1	<0.5	<0.1	0.5	0.3
B-15	<0.5	<1	0.2	<0.1	<0.1	<1	0.02	1.3	<0.1	<0.5	<0.1	0.4	0.3
B-10	<0.5	<1	<0.1	<0.1	<0.1	<1	0.09	1.3	<0.1	<0.5	<0.1	0.4	0.2
B-6	<0.5	<1	<0.1	0.2	<0.1	<1	0.29	3.0	<0.1	<0.5	<0.1	1.2	0.7
B-1*	<0.5	<1	0.1	0.3	<0.1	<1	2.62	9.3	<0.1	<0.5	<0.1	3.3	0.2

Table 3. Rare earth element (ppm) concentrations of the Saytepe Formation carbonates

Sample	La	Ce	Pr	Nd	Sm	Eu	Gd	Tb	Dy	Y	Ho	Er	Tm	Yb	Lu	TREE
B-80	<0.1	0.2	<0.02	<0.3	<0.05	<0.02	<0.05	<0.01	<0.05	0.2	<0.02	<0.03	<0.01	<0.05	<0.01	0.92
B-68	0.6	0.6	0.05	0.5	0.09	<0.02	0.10	0.01	0.10	1.7	0.02	0.08	<0.01	<0.05	<0.01	2.24
B-55*	0.1	0.2	<0.02	<0.3	<0.05	<0.02	<0.05	<0.01	<0.05	0.3	<0.02	<0.03	<0.01	<0.05	<0.01	0.92
B-49	0.3	0.9	0.07	0.4	<0.05	<0.02	0.07	<0.01	0.06	0.4	<0.02	0.04	<0.01	<0.05	<0.01	2.01
B-43	0.6	1.1	0.10	0.6	0.10	<0.02	<0.05	<0.01	0.08	0.6	<0.02	0.05	<0.01	<0.05	<0.01	2.80
B-30	0.2	0.2	<0.02	<0.3	<0.05	<0.02	<0.05	<0.01	<0.05	0.7	<0.02	0.03	<0.01	<0.05	<0.01	1.02
B-19	0.2	0.2	<0.02	<0.3	<0.05	<0.02	<0.05	<0.01	0.06	0.5	<0.02	<0.03	<0.01	<0.05	<0.01	1.03
B-15	0.1	0.3	<0.02	<0.3	<0.05	<0.02	<0.05	<0.01	<0.05	0.6	<0.02	0.04	<0.01	<0.05	<0.01	1.01
B-10	0.3	0.2	0.05	<0.3	<0.05	<0.02	<0.05	<0.01	0.06	0.8	<0.02	0.03	<0.01	<0.05	<0.01	1.16
B-6	0.4	0.5	0.02	0.3	<0.05	0.04	0.08	<0.01	0.09	1.1	<0.02	0.08	<0.01	<0.05	0.02	1.67
B-1*	0.9	1.9	0.18	0.8	0.14	<0.02	0.14	0.01	0.08	0.9	<0.02	0.07	<0.01	0.06	<0.01	4.34

Table 4. Major element (%) correlation of the Saytepe Formation carbonates

	SiO ₂	Al ₂ O ₃	Fe ₂ O ₃	MgO	CaO	Na ₂ O	K ₂ O	TiO ₂	P ₂ O ₅	MnO	TREE	LOI
SiO ₂	1											
Al ₂ O ₃	0.98	1										
Fe ₂ O ₃	0.93	0.86	1									
MgO	0.59	0.54	0.73	1								
CaO	-0.63	-0.58	-0.76	-0.99	1							
Na ₂ O	0.83	0.78	0.93	0.92	-0.93	1						
K ₂ O	0.96	0.99	0.81	0.47	-0.517	0.72	1					
TiO ₂	0.95	0.89	0.97	0.63	-0.66	0.89	0.86	1				
P ₂ O ₅	0.14	0.30	-0.19	-0.22	0.20	-0.21	0.37	-0.15	1			
MnO	.c	.c	.c	.c	.c	.c	.c	.c	.c	.c		
TREE	0.92	0.94	0.81	0.38	-0.43	0.63	0.92	0.81	0.31	.c	1	
LOI	0.57	0.53	0.71	0.99	-0.99	0.89	0.46	0.60	-0.19	.c	0.39	1

Trace Element Geochemistry

Trace element analysis results of the Saytepe Formation samples: Sr 143-368 ppm, Rb 0.1-4.2 ppm, Ba 4-16 ppm, Zr 3.5-8.4 ppm, U 0.3-3.4 ppm, V 8-24 ppm, Mo 0.1-9.2 ppm, Ni 2.7-9.1 ppm, Co 0.2-0.6 ppm, Th 0.2-0.4 ppm, Zn 3-21 ppm, Pb 1.4-12.5 ppm, Cu 0.9-3.9 ppm, Hf 0.1-0.2 ppm, Nb 0.1-0.3 ppm, Cs 0.1 ppm and Ga 0.5 ppm (Table 2).

In the Saytepe carbonate samples, strong positive correlation between Rb and K₂O (R=0.99), SiO₂ (R=0.97), Al₂O₃ (R=0.99), Fe₂O₃ (R=0.84), TiO₂ (R=0.88), Na₂O and Rb (R=0.74), strong positive correlation between Rb and Th (R=0.88), Mo (R=0.87), Ni (R=0.84), Hg (R=0.86), As (R=0.82), Rb a moderate positive correlation was observed between Na₂O (R=0.74), Cu (R=0.76), Zn (R=0.70), Co (R=0.74), Nb (R=0.75) (Table 5). Moderate positive correlation between Sr and CaO (R=0.74), SiO₂ (-0.61), Fe₂O₃ (R=-0.66), MgO (R=-0.73), Na₂O (R=-0.74), Cu (R=-0.77) moderate negative correlation between Pb (R=-0.64), Co (R=-0.74), Nb (R=-0.67), Hg (R=-0.61), As (R=-0.67), Sr and Zn (R=-0.82), a strong negative correlation is observed. Ba and Zr elements do not show strong or moderate correlations with any major or trace element (Table 5).

Özkan, Ali Müjdat & Kırkan, Görkem; Geocemical Properties Of The Saytepe Formation (Upper Cretaceous) Carbonates Around Hadım And North (Konya, Turkey)

Table 5. Major (%) and trace element (ppm) correlation of the Saytepe Formation carbonates

	Si O ₂	Al ₂ O ₃	Fe ₂ O ₃	Mg O	Ca O	Na ₂ O	K ₂ O	Ti O ₂	P ₂ O ₅	Mn O	Ba	Sr	Zr	U	V	Th	Mo	Cu	Ni	Pb	Zn	Co	Hf	Nb	Hg	As	Rb
Si O ₂	1																										
Al ₂ O ₃	0.81	1																									
Fe ₂ O ₃	0.75	0.75	1																								
Mg O	0.59	0.54	0.77	1																							
Ca O	0.65	0.58	0.67	0.77	1																						
Na ₂ O	0.65	0.78	0.67	0.67	0.67	1																					
K ₂ O	0.77	0.77	0.77	0.77	0.77	0.77	1																				
Ti O ₂	0.71	0.71	0.71	0.71	0.71	0.71	0.71	1																			
P ₂ O ₅	0.14	0.30	0.10	0.22	0.20	0.22	0.37	0.15	1																		
Mn O	0.65	0.65	0.65	0.65	0.65	0.65	0.65	0.65	0.65	1																	
Ba	0.06	0.08	0.09	0.09	0.08	0.12	0.13	0.09	0.06	0.06	1																
Sr	0.25	0.25	0.25	0.25	0.25	0.25	0.25	0.25	0.25	0.25	0.25	1															
Zr	0.19	0.27	0.10	0.11	0.11	0.11	0.31	0.01	0.02	0.05	0.05	0.21	1														
U	0.55	0.55	0.55	0.55	0.55	0.55	0.71	0.45	0.42	0.33	0.33	0.52	0.10	1													
V	0.68	0.68	0.68	0.68	0.68	0.68	0.72	0.53	0.27	0.37	0.37	0.40	0.05	0.10	1												
Th	0.15	0.15	0.15	0.15	0.15	0.15	0.15	0.15	0.15	0.15	0.15	0.15	0.15	0.15	0.15	1											
Mo	0.15	0.15	0.15	0.15	0.15	0.15	0.15	0.15	0.15	0.15	0.15	0.15	0.15	0.15	0.15	0.15	1										
Cu	0.03	0.03	0.03	0.03	0.03	0.03	0.03	0.03	0.03	0.03	0.03	0.03	0.03	0.03	0.03	0.03	0.03	1									
Ni	0.06	0.06	0.06	0.06	0.06	0.06	0.06	0.06	0.06	0.06	0.06	0.06	0.06	0.06	0.06	0.06	0.06	0.06	1								
Pb	0.06	0.06	0.06	0.06	0.06	0.06	0.06	0.06	0.06	0.06	0.06	0.06	0.06	0.06	0.06	0.06	0.06	0.06	0.06	1							
Zn	0.79	0.79	0.79	0.79	0.79	0.79	0.79	0.79	0.79	0.79	0.79	0.79	0.79	0.79	0.79	0.79	0.79	0.79	0.79	0.79	1						
Co	0.12	0.12	0.12	0.12	0.12	0.12	0.12	0.12	0.12	0.12	0.12	0.12	0.12	0.12	0.12	0.12	0.12	0.12	0.12	0.12	0.12	1					
Hf	0.05	0.05	0.05	0.05	0.05	0.05	0.05	0.05	0.05	0.05	0.05	0.05	0.05	0.05	0.05	0.05	0.05	0.05	0.05	0.05	0.05	0.05	1				
Nb	0.05	0.05	0.05	0.05	0.05	0.05	0.05	0.05	0.05	0.05	0.05	0.05	0.05	0.05	0.05	0.05	0.05	0.05	0.05	0.05	0.05	0.05	0.05	0.05	1		
Hg	0.17	0.17	0.17	0.17	0.17	0.17	0.17	0.17	0.17	0.17	0.17	0.17	0.17	0.17	0.17	0.17	0.17	0.17	0.17	0.17	0.17	0.17	0.17	0.17	0.17	1	
As	0.06	0.06	0.06	0.06	0.06	0.06	0.06	0.06	0.06	0.06	0.06	0.06	0.06	0.06	0.06	0.06	0.06	0.06	0.06	0.06	0.06	0.06	0.06	0.06	0.06	0.06	1
Rb	0.33	0.33	0.33	0.33	0.33	0.33	0.33	0.33	0.33	0.33	0.33	0.33	0.33	0.33	0.33	0.33	0.33	0.33	0.33	0.33	0.33	0.33	0.33	0.33	0.33	0.33	1

In the Saytepe Formation samples, strong positive correlation between rare earth elements La and SiO₂ (R=0.81), Al₂O₃ (R=0.81), moderate positive correlation between Fe₂O₃ (R=0.75), K₂O (R=0.78), TiO₂ (R=0.71) is observed. Strong positive correlation between La and Ce (R=0.88), Pr (R=0.87), Nd (R=0.92), Sm (R=0.93), Gd (R=0.84), La and Dy (R=0.79), a moderate positive correlation was observed between Er (R=0.75), Yb (R=0.71) (Table 6). Strong positive correlation between Ce and SiO₂ (R=0.95), Al₂O₃ (R=0.97), Fe₂O₃ (R=0.80), K₂O (R=0.97), TiO₂ (R=0.81), La (R=0.88) moderate positive correlation between Na₂O (R=0.65), Gd (R=0.79), strong positive correlation was observed between Ce and Pr (R=0.96), Nd (R=0.95), Sm (R=0.89), Yb (R=0.81) (Table 6). No strong or moderate correlation was observed between Eu and any major and trace element (Table 6).

Özkan, Ali Müjdat & Kırkan, Görkem; Geocemical Properties Of The Saytepe Formation (Upper Cretaceous) Carbonates Around Hadım And North (Konya, Turkey)

Table 6. Major (%) and rare earth element (ppm) correlation of the Saytepe Formation carbonates

	Si O ₂	Al ₂ O ₃	Fe ₂ O ₃	Mg O	Ca O	Na ₂ O	K ₂ O	Ti O ₂	P ₂ O ₅	Mn O	La	Ce	Pr	Nd	Sm	Eu	Gd	Tb	Dy	Y	Ho	Er	Tm	Yb	Lu	
SiO ₂	1																									
Al ₂ O ₃	0.5	1																								
Fe ₂ O ₃	0.5	0.86	1																							
MgO	0.59	0.54	0.75	1																						
CaO	0.6	-	0.58	0.76	1																					
Na ₂ O	0.5	0.78	0.95	0.9	0.9	1																				
K ₂ O	0.5	0.99	0.81	0.47	-	0.72	1																			
TiO ₂	0.5	0.89	0.97	0.65	0.6	0.89	0.8	1																		
P ₂ O ₅	0.14	0.30	-	0.22	0.2	0.21	0.57	0.15	1																	
MnO	.c	.c	.c	.c	.c	.c	.c	.c	.c	.c																
La	0.5	0.81	0.75	0.27	-	0.52	0.7	0.7	0.2	.c	1															
Ce	0.5	0.97	0.89	0.4	-	0.65	0.9	0.8	0.39	.c	0.8	1														
Pr	0.5	0.97	0.82	0.4	-	0.69	0.9	0.8	0.53	.c	0.8	0.9	1													
Nd	0.5	0.92	0.89	0.42	-	0.65	0.9	0.7	0.29	.c	0.9	0.9	0.9	1												
Sm	0.5	0.86	0.82	0.44	-	0.66	0.8	0.8	0.14	.c	0.9	0.8	0.9	0.9	1											
Eu	-	-	0	0.15	-	0.14	0.17	0.1	0.15	.c	0.07	-	-	-	-	1										
Gd	0.5	0.75	0.86	0.45	-	0.67	0.6	0.8	0.12	.c	0.8	0.7	0.7	0.7	0.7	0.1	1									
Tb	.c	.c	.c	.c	.c	.c	.c	.c	.c	.c	.c	.c	.c	.c	.c	.c	.c	.c	.c	.c	.c	.c	.c	.c	.c	.c
Dy	0.54	0.35	0.37	-	-	0.09	0.5	0.2	0.1	.c	0.7	0.5	0.4	0.5	0.5	0.4	0.6	.c								
Y	0.14	0.07	0.25	-	0.0	-	0.02	0.1	-	.c	0.59	0.23	0.18	0.33	0.4	0.5	0.5	.c	0.9	1						
Ho	.c	.c	.c	.c	.c	.c	.c	.c	.c	.c	.c	.c	.c	.c	.c	.c	.c	.c	.c	.c	.c	.c	.c	.c	.c	.c
Er	0.44	0.40	0.49	0.09	-	0.23	0.55	0.3	-	.c	0.75	0.55	0.4	0.55	0.58	0.5	0.7	.c	0.9	0.8	.c				1	
Tm	.c	.c	.c	.c	.c	.c	.c	.c	.c	.c	.c	.c	.c	.c	.c	.c	.c	.c	.c	.c	.c	.c	.c	.c	.c	.c
Yb	0.5	0.89	0.97	0.65	0.6	0.89	0.8	1.0	0.15	.c	0.7	0.8	0.8	0.7	0.8	-	0.8	.c	0.25	0.1	0.3	.c				
Lu	0.12	0.14	0	0.15	0.1	0.14	0.17	0.1	0.15	.c	0.07	0.0	0.2	0.2	0.1	1.0	0.1	.c	0.43	0.51	.c	0.54	.c	0.1	1	

Some elemental ratios such as Mo/U, V/Cr, Ni/Co, U/Th, and V/(V+Ni) are used to reveal redox conditions (Hatch and Leventhal, 1992; Jones and Manning, 1994) (Table 7). Mo/U, V/Cr, Ni/Co, U/Th, and V/(V+Ni) ratios of the Saytepe Formation samples vary between 0.04-2.71, 0.58-1.75, 11-23.5, 1.5-12, and 0.66-0.81, respectively. (Table 8; Figure 1).

Table 7. Some elemental concentrations used to evaluate paleoredox conditions

Element ratio	Oxic	Dysoxic	Anoxic	Euxinic	Writers
Ni/Co	<5	5-7	>7		Jones & Manning (1994)
V/Cr	<2	2-4.5	>4.5		
U/Th	<0.75	0.75-1.25	>1.25		
V/(V+Ni)	<0.46	0.46-0.60	0.54-0.82	>0.84	Hatch & Leventhal (1992)

Table 8. Redox susceptibility trace element concentrations and geochemical ratios of the Saytepe Formation carbonate samples (* dolostone)

Sample	Mo/U	V/Cr	Ni/Co	U/T	V/(V+Ni)	Mn/Sr	K/Rb	Si/Al	Al/Ti	Ce/Ce*	Eu/Eu*	Pr/Pr*	La/La*	(La/Sm) _N	(Dy/Sm) _N
B-80	0,07	0,58	19,5	7,5	0,67	0,29	0,083	7,047	1,77	0,70	1,88	0,399	-0,24	0,29	1,18
B-68	0,04	1,46	23,5	12	0,81	0,22	0,028	4,849	3,53	0,705	0,98	0,508	-1,25	0,97	1,32
B-55*	0,09	1,17	11	11	0,78	0,43	0,083	4,405	3,53	1,03	1,88	0,399	-0,24	0,29	1,19
B-49	0,33	0,58	16	1,5	0,71	0,25	0,029	1,883	13,23	0,96	1,54	0,686	42,74	0,87	1,42
B-43	0,16	0,58	20,5	3	0,66	0,32	0,026	1,859	16,75	1,02	1,29	0,678	-11,04	0,87	0,95
B-30	0,09	0,58	18	5,5	0,69	0,25	0,083	14,09	0,88	0,67	1,88	0,399	-0,48	0,58	1,19
B-19	0,2	0,58	16,5	2,5	0,71	0,24	0,083	8,811	0,88	0,67	1,88	0,398	-0,48	0,58	1,42
B-15	0,16	0,58	15,5	3	0,72	0,29	0,083	17,62	0,88	1,54	1,88	0,359	-0,24	0,29	1,19
B-10	0,16	0,58	13,5	3	0,75	0,21	0,083	14,09	0,88	0,37	1,88	0,997	-11,04	0,87	1,42
B-6	0,22	0,58	13,5	4,5	0,75	0,37	0,041	5,585	2,65	0,99	2,83	0,299	-0,96	1,16	2,13
B-1*	2,71	1,75	15,2	8,5	0,73	0,54	0,024	2,021	19,84	1,09	0,67	0,859	1,69	0,93	0,68

Table 8. Continued

Sample	Al ₂ O ₃ /TiO ₂	Y/Ho	Er/Nd	(Nd/Yb) _N	Eu/Sm	Rb/Sr	Sr/Ba	Sr/Rb	Ga/Rb	Sr/Cu	Th/Co	La/Sc	Mg/Ca	Fe/Al	K/Na	Th/U
B-80	2	10	0,10	0,50	0,4	0,0004	23,9	2633	5	175	1	0,1	0,011	3,962	1,119	0,133
B-68	4	85	0,16	0,83	0,22	0,0008	22,3	1190	1,7	210	1	0,6	0,023	3,627	1,119	0,083
B-55*	4	15	0,10	0,50	0,4	0,0006	25,5	1787	5	74	0,5	0,1	0,442	4,288	0,559	0,091
B-49	15	20	0,10	0,66	0,4	0,0045	31,1	222,3	0,4	259	1	0,3	0,008	0,353	5,594	0,667
B-43	19	30	0,08	0,99	0,2	0,0079	48,0	126,4	0,3	160	1	0,6	0,009	0,556	6,713	0,333
B-30	1	35	0,10	0,50	0,4	0,0003	76,9	3075	5	220	1	0,2	0,006	6,604	1,119	0,182
B-19	1	25	0,10	0,50	0,4	0,0003	64,1	3207	5	356	1	0,2	0,005	5,283	1,119	0,400
B-15	1	30	0,13	0,50	0,4	0,0004	44,7	2683	5	206	1	0,1	0,006	5,283	1,119	0,333
B-10	1	40	0,10	0,50	0,4	0,0003	52,5	3678	5	368	1	0,3	0,006	9,245	1,119	0,333
B-6	3	55	0,27	0,50	0,8	0,0009	23,5	1058	2,5	141	1	0,4	0,008	4,836	1,119	0,222
B-1*	22,5	45	0,08	1,11	0,14	0,0294	20,4	34,0	0,1	36	0,7	0,9	0,396	1,410	4,476	0,118

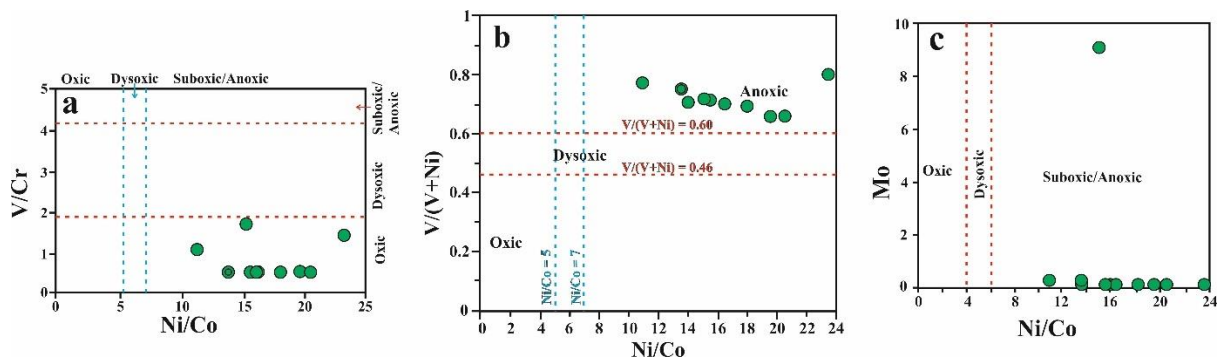
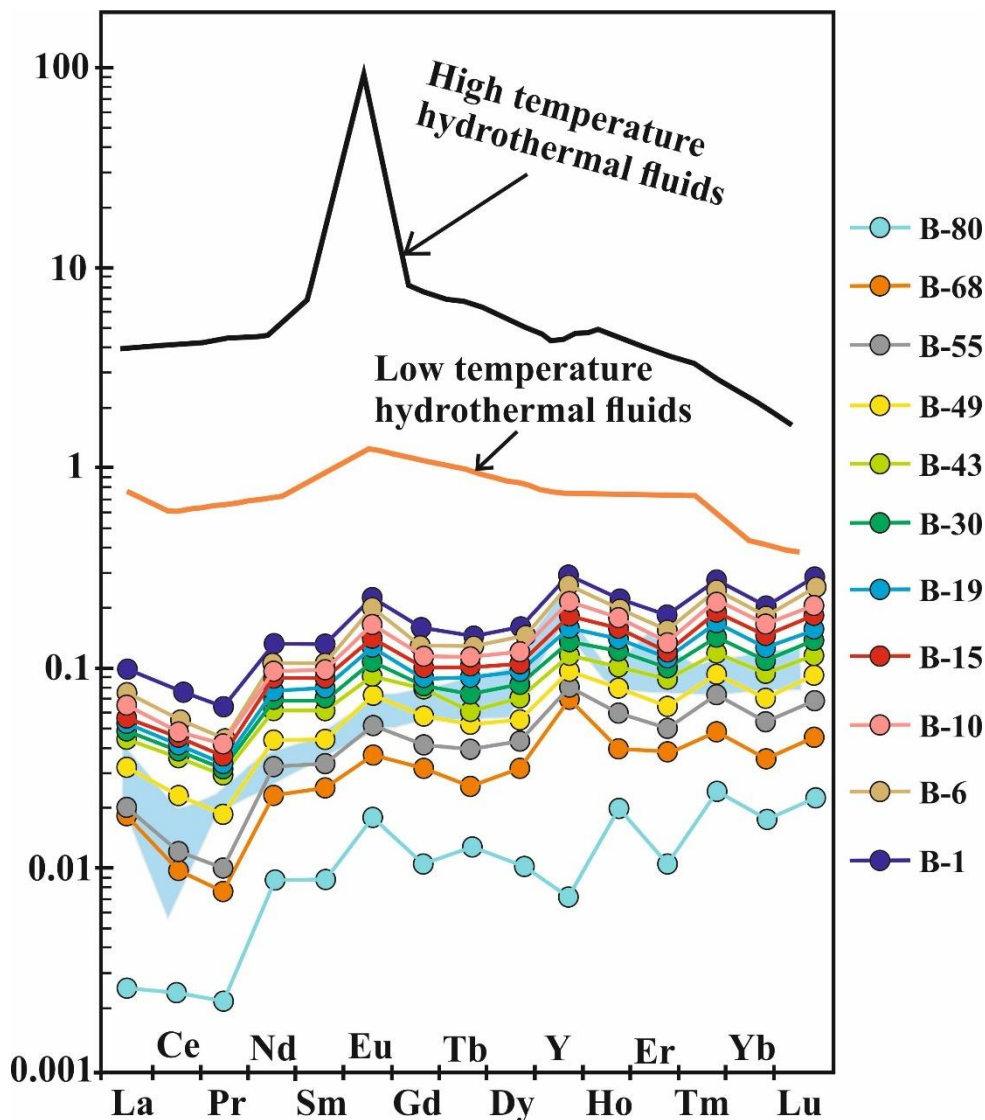


Figure 1. a) The Saytepe Formation samples fall into the suboxic-anoxic area in the V/Cr–Ni/Co diagram, b) The Saytepe Formation samples fall into the anoxic area in the V/(V+Ni)–Ni/Co diagram, c) Mo–Ni/Co In the diagram, the Saytepe Formation samples fall into the suboxic-anoxic area.

The total rare earth element values of the Saytepe carbonate samples are 0.92-4.34 ppm (average 1.74 ppm), which is very low compared to present-day marine sediments and Post-Archaean Average Australian Shale (PAAS). The values of the Saytepe carbonate samples normalized to Post-Archaean Australian Shale (McLennan, 1989) show depletion and moderate positive Y anomaly in all samples (Graph 1).



Graph 1. Shale normalized (PAAS) REE+Y diagram of the Saytepe carbonate samples. The blue area denotes present-day seawater

In addition, the REE+Y values of the Saytepe carbonate samples normalized to Post-Archaeon Australian Shale show that a small number of samples exhibit current seawater characteristics, most of them exhibit higher values than current seawater by light rare earth elements and a few samples show lower values than current seawater (Graph 1). Again, we can say in Graph 1 that Saytepe carbonate samples were not exposed to any hydrothermal fluid effects and present moderately negative Ce, positive Eu anomaly, and positive Y anomaly.

Discussion

Evaluation of Sample Conservation

During the diagenesis process, some elements show enrichment and some elements show depletion, so it becomes necessary to determine the degree of change in our samples. Some tests are used to determine the degree of this change.

The textural change in carbonate rocks is mostly in the form of the transformation of unstable minerals into stable minerals (Brand and Veizer, 1980; Wang et al., 2017). Micritic and/or sparitic calcite minerals can transform into neomorphic coarse sparicalcite as a result of diagenetic alteration. Although the Saytepe carbonate samples were deposited as micritic mudstone, they were metamorphized into microsparitic and sparitic limestones during the diagenetic change process, but it was observed that the primary texture was preserved in most samples.

Some elemental ions (such as Sr, Mg, Fe and Mn) can be incorporated into calcite mineral lattices. Meteoric waters contain low Sr^{+2} but high Fe^{+2} and Mn^{+2} elements (Brand and Veizer, 1980; Wang et al., 2017). Therefore, in the diagenetic alteration process, an increase in Fe^{+2} and Mn^{+2} content, a decrease in Sr^{+2} content, while a decrease or increase may be observed in Mg^{+2} depending on the nature of the primary carbonate mineral (Brand and Veizer, 1980; Wang et al., 2017). From this, we can say that the changes of trace elements are important markers and they can reflect the degree of diagenetic alteration (Wang et al., 2017) that took place after deposition.

Again, Wang et al. (2017) stated that Sr and Mn are important elements of diagenetic alteration. While meteoric diagenesis can remove Sr^{+2} from the carbonate mineral structure, it can ensure the incorporation of Mn^{+2} into the carbonate mineral structure (Brand and Veizer, 1980; Gilleaudeau and Kah, 2013; Wang et al., 2017). Therefore, we can state that Mn/Sr values are very useful indicators in determining the diagenetic alteration of carbonate rocks due to the contradictory properties of Sr and Mn elements.

If the Mn/Sr values are less than 3, it is stated by some researchers that the primary deposition feature of the rock is preserved, if it is between 3-10, it has undergone low diagenetic alteration, and if it is >10 , it indicates severe alteration (Kaufman and Knoll, 1995; Wang et al., 2017). Mn/Sr values of the Saytepe carbonate samples are between 0.21 and 0.54, and we can say that they preserve their primary deposition characteristics. Although it is known that hydrothermal effects show positive Eu and high Ba values, positive Eu (Graph 1) and low Ba values (Table 2) are observed in the Saytepe carbonate samples, and we can state that positive Eu values are caused by terrigenous feldspars rather than hydrothermal effect. Because no hydrothermal effect is observed in our samples in Graph 1.

The K/Rb values were high (≥ 500) in highly metamorphosed rocks, 230 in unmetamorphized igneous rocks (except oceanic tholeiites) and 200 in shales, Rudnick et al. (1985) and Bauernhofer et al. (2009) emphasized. Since the K/Rb values of the Saytepe samples vary between 0.024 and 0.083 (Table 8), we can state that they did not undergo metamorphism.

The Sr/Ca versus Na diagram of the Saytepe carbonate samples also shows some diagenetic alteration in the Saytepe Formation samples (Figure 2).

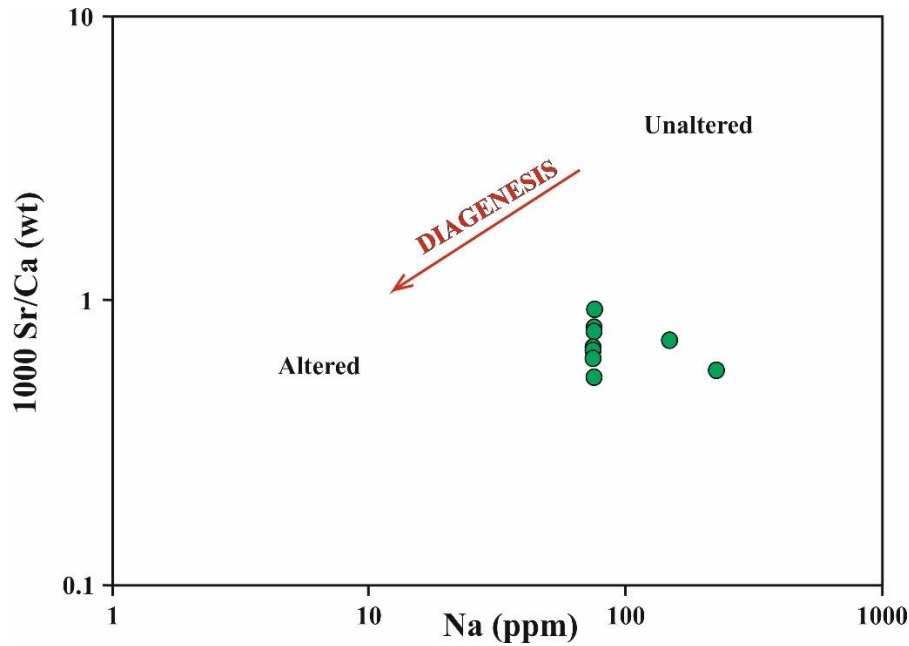


Figure 2. Sr/Ca vs. Na diagram of the Saytepe carbonate samples

Major and Trace Element Evaluation of the Saytepe Formation Carbonates

It has been emphasized by many researchers such as Garrels and Mackenzie (1971), Nesbitt ve ark. (1980), Taylor ve McLennan (1985), and Wronkiewicz ve Condie (1990) that the behavior of trace elements is complex depending on processes such as weathering, physical sorting, adsorption, provenance, diagenesis, and metamorphism.

It is known that the major and trace elements contained in the limestones are greatly affected by the terrigenous contribution (Kuchenbecker et al., 2016). It is observed that the terrigenous contribution of Si, K, Al, Ti, Rb, Sr, Ba, Nb, Ta, Th, U, and REEs in the Saytepe samples is generally low (Tables 1, 2, and 3; Figure 3). Again, the distribution of the Saytepe carbonate samples in the Si versus Zr diagram shows that Si is entire of terrestrial origin rather than biogenic (Figure 4).

Calcium is predominantly biogenic and strongly negatively correlated with almost all other major and trace elements (Zhang et al., 2017), it functions as a diluent of other components. This situation is clearly observed in the form of carbonate tendency in the $\text{SiO}_2\text{-Al}_2\text{O}_3\text{-CaO}$ diagram of the Saytepe samples (Figure 3). While Al_2O_3 values did not show any correlation with MnO and P_2O_5 in the Saytepe limestone samples, they were strongly positive correlation with SiO_2 ($R=0.98$), Fe_2O_3 ($R=0.86$), Na_2O ($R=0.78$), K_2O ($R=0.99$), TiO_2 ($R=0.97$) (Table 4) indicates that Si, Fe, Na, K, Ti are mostly provided by clay minerals.

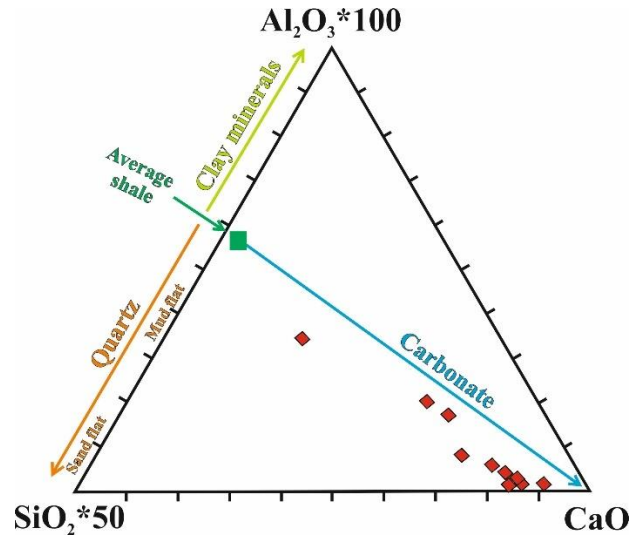


Figure 3. In the Al-Si-Ca triangular diagram, all the Saytepe Formation samples show a carbonate rock tendency

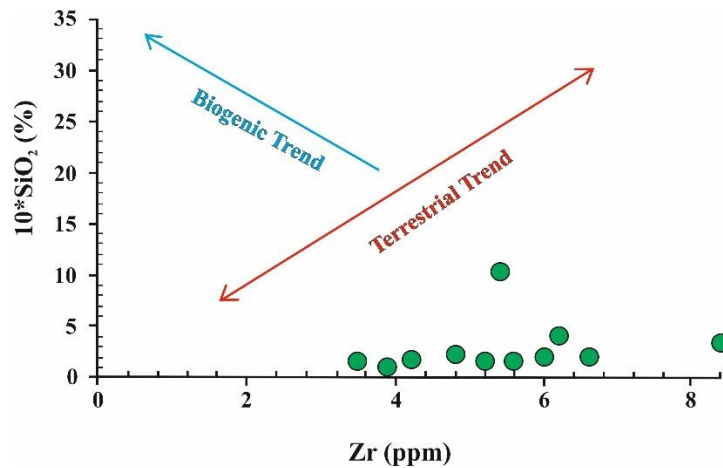


Figure 4. In the SiO_2 vs. Zr diagram, the silica in the Saytepe carbonates has a terrestrial tendency and is not of biogenic origin

Kuchenbecker et al. (2016) stated that Rb/Sr ratios reflect the relative abundance of terrigenous content and carbonate fraction. The Rb/Sr values of the Saytepe Formation samples are 0.0003-0.030 (mean 0.0042) (Table 5), indicating that some Sr loss has occurred as a result of diagenetic alteration. Because Kuchenbecker et al. (2016) are slightly higher than the expected 0.0008 Rb/Sr value in carbonate rocks.

It is emphasized that Th/U values are very useful indicators in determining the provenance of contamination in chemical sedimentary rocks. Chemically formed sedimentary rocks can contain debris such as volcanic ash, detrital material, and phosphate (Thurston et al., 2011).

Thurston et al. (2011) emphasized that the ratio of phosphate pollution in chemical rocks occurs when having a Th/U > 5 value, while other contaminations are represented by Th/U values between 3-5 (Condie, 1993; Thurston et al., 2011). Since the Th/U values observed in the Saytepe samples vary between 0.08 and 0.67, it indicates the absence of phosphate contamination.

Zhang et al. (2017) stated that using the Rb-Sr-Ba triangle diagram, it is possible to distinguish between freshwater limestones, shallow marine limestones, and open ocean limestones. When the Rb-Sr-Ba triangle diagram is used for the Saytepe samples, the samples show the offshore environment (Figure 5). Again, Zhang et al. (2017), the graph of Sr/Ba versus Sr/Rb can be used to distinguish between limestones deposited in fresh water and limestones deposited in shallow marine environments. When we reduced the Saytepe samples to the Sr/Ba versus Sr/Rb plot, all of the samples indicated deposition in the shallow marine (continental margin) environment (Figure 6).

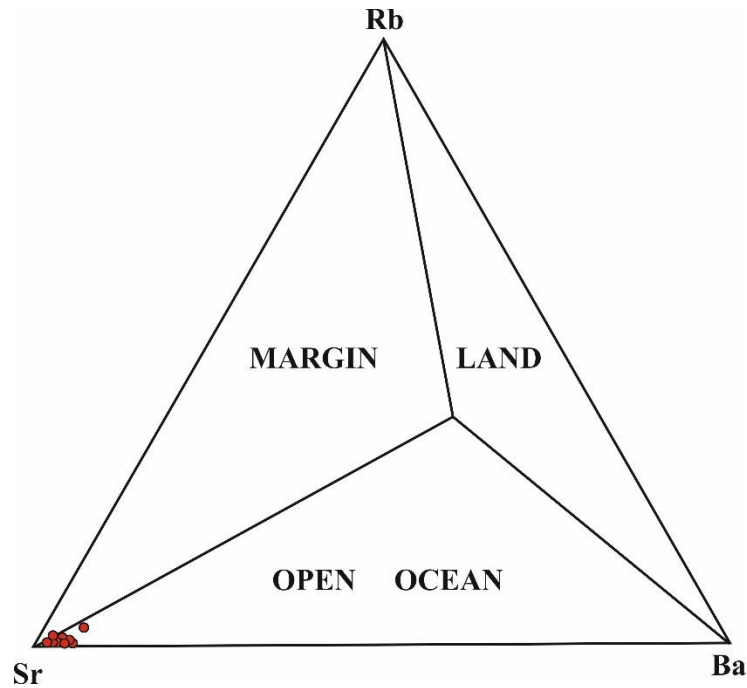


Figure 5. Rb-Sr-Ba triangular diagram of the Saytepe carbonate samples. Diagram showing various limestone depositional environments (from Zhang et al., 2017)

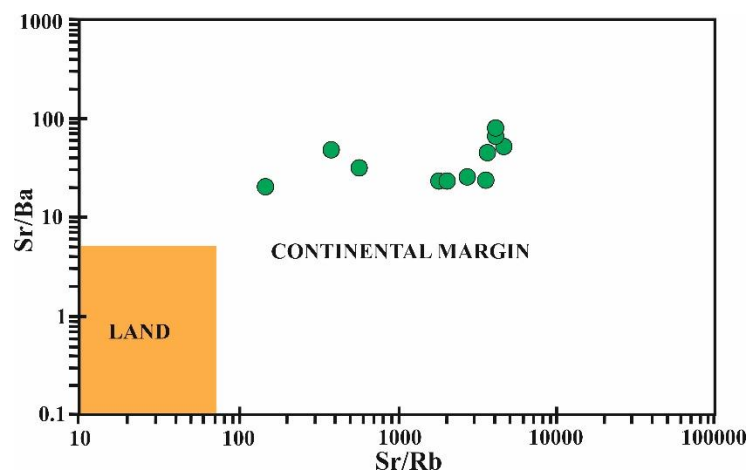


Figure 6. Sr/Ba versus Sr/Rb diagram of the Saytepe carbonates

Roy and Roser (2013), Yandoka et al. (2015), Xie et al. (2018), and Ding et al. (2018) stated that Sr/Cu and Ga/Rb values can also be used to determine the paleoclimate. Ga is mostly enriched in clay minerals (especially kaolinite) and indicates a warm-humid climate (Ding et al., 2018). Ding et al. (2018) emphasized that the Rb element is closely related to the illite mineral and reflects the cold and dry climate. The very low Ga/Rb values in the sediments indicate that the climate is cold and dry. Generally, in warm and humid climatic conditions, fine-grained sediments exhibit low Sr/Cu values and high Ga/Rb values (Ding et al., 2018). Ding et al. (2018) emphasized that Sr/Cu values between 1.3-5 indicate a warm humid environment, while values above 5 indicate hot-arid climate conditions.

Figure 7 shows the Ga/Rb vs. Sr/Cu graph of the Saytepe samples, with Ga/Rb 0.11-5 (mean 3.17), Sr/Cu 36-368 (average 200) values. Therefore, Sr/Cu values of the Saytepe samples indicate warm-arid climatic conditions.

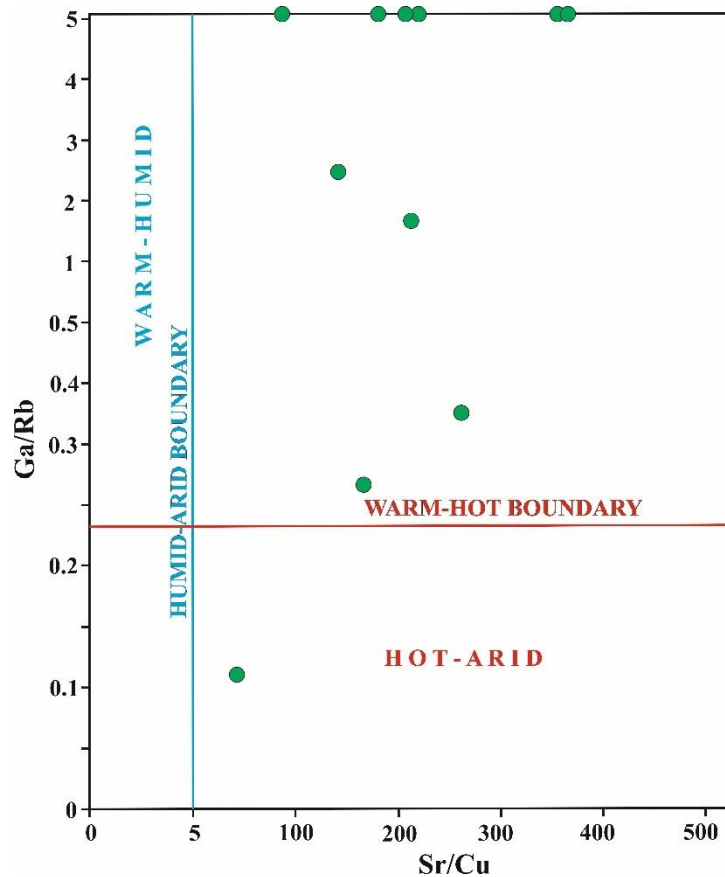


Figure 7. Ga/Rb versus Sr/Cu diagram of the Saytepe carbonate samples. Diagram shows paleoclimatic conditions (diagram from Ding et al., 2018)

The presence of rare earth elements in carbonates can be affected by many factors. (1) The introduction of terrigenous detrital into the basin (Piper, 1974; McLennan, 1989), (2) the biogenic deposition from the water column in the basin (Murphy and Dymond, 1984), and (3) the interaction process related to the depth, salinity, and oxygen content of the water in the basin (Elderfield, 1988; Piegras and Jacobsen, 1992; Bertram and Elderfield, 1993; Greaves et al., 1999), (4) eutigenic removal of rare earth elements from the water column in the basin and due to early diagenesis (Sholkovitz, 1988).

Seawater contributes very little REE to chemical sediments, but sediments that do not have marine water characteristics can have very high REE concentrations due to contamination by non-carbonate materials (Nothdurft et al., 2004) such as silicates, Fe-Mn oxides, phosphates and sulfides during the chemical filtration process (Zhao et al., 2009).

Positive correlation with total rare earth elements SiO_2 , Al_2O_3 , TiO_2 , and Fe_2O_3 ($R=0.62$, $R=0.48$, $R=0.67$, $R=0.45$, respectively) in terrestrial and shallow marine limestones indicates that REE is under the influence of siliciclastic input (Zhang et al. et al., 2017). The strong positive correlation between TREE of the Saytepe samples and SiO_2 ($R=0.92$), Al_2O_3 ($R=0.94$), TiO_2 ($R=0.81$), Fe_2O_3 ($R=0.81$) (Table 6) also highlights the effect of siliciclastic input on REE.

Zhang et al. (2017) stated that the size of the Ce anomaly of the limestones increased significantly from spreading ridges to continental coastal seas. In the graph of Ce/Ce^* versus Al_2O_3 and Fe_2O_3 (Figure 8) the Saytepe Formation samples mostly point to the terrestrial margin and partly to the open sea environment. However, in Figure 8a, two samples fall into the terrestrial environment, possibly indicating an intertidal or supratidal environment.

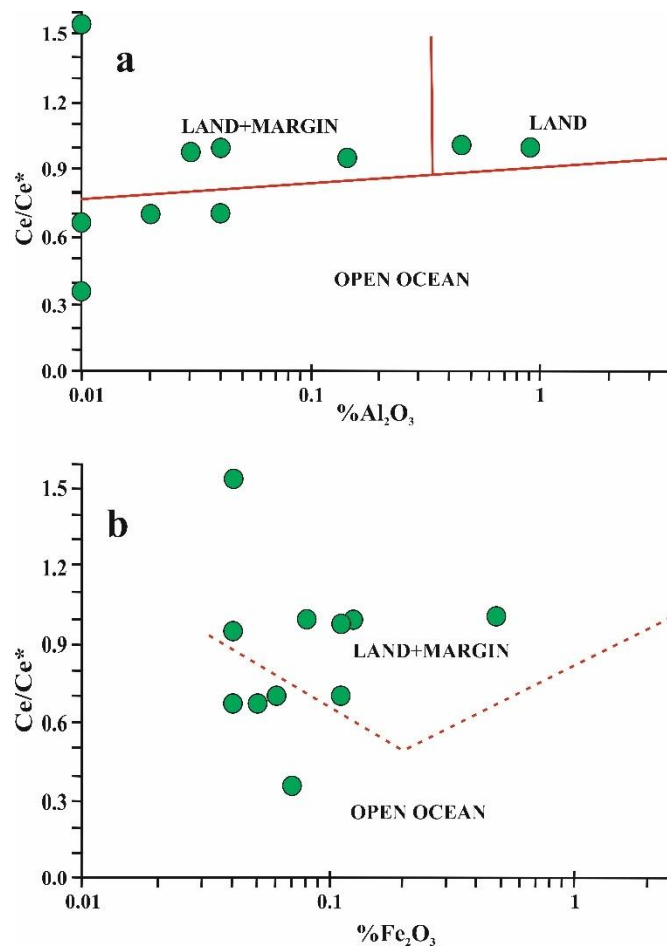


Figure 8. Ce/Ce^* versus Al_2O_3 and Fe_2O_3 diagram of the Saytepe carbonate samples. Limestones deposited in various storage environments (Taylor and McLennan, 1985)

Murray et al. (1990, 1991) stated that Ce anomaly depends on the deposition environment, high Ce values indicate oxic conditions, while low Ce values indicate anoxic conditions. During the transgression process, the bottom waters become anoxic and the whole rock Ce anomaly becomes negative (Wilde et al., 1996). In the regression process, any fixed point in the base becomes shallow; therefore, the bottom waters will be oxic and the whole rock Ce anomaly will be positive.

Since the characteristics of the Saytepe Formation sediments occur in a transgressive shallow marine (carbonate-dominated shelf) depositional environment, Wilde et al. (1996) suggest the applicability of the model proposed in this study. From this, we can say that the Ce values contained by the Saytepe carbonate samples are negative values (Graph 1), indicating transgressive and anoxic carbonate deposition. In the Ce/Ce* vs. Nd graph in Figure 9, all of the Saytepe samples fall into the anoxic area, and in the Ce/Ce* vs. La_N/Sm_N diagram in Figure 10, all the samples fall into the anoxic area, supporting the above interpretation. In addition, the fall of the Saytepe carbonate samples into the anoxic area in the Pr/Pr* versus Y/Ho diagram in Figure 11 also indicates the dominance of anoxic conditions during the deposition process.

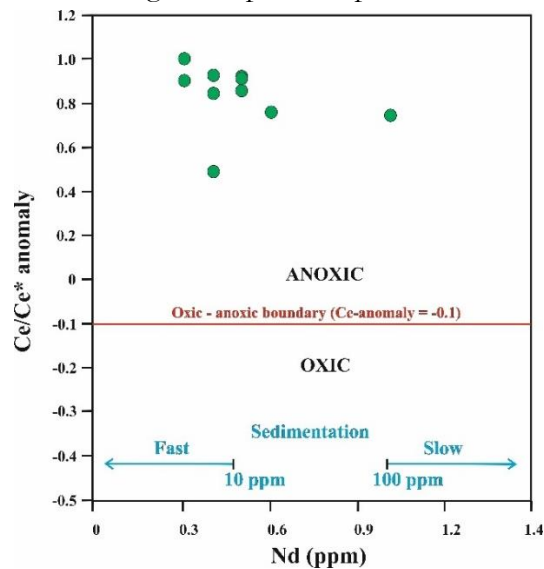


Figure 9. Ce/Ce* vs. Nd diagram of the Saytepe carbonates

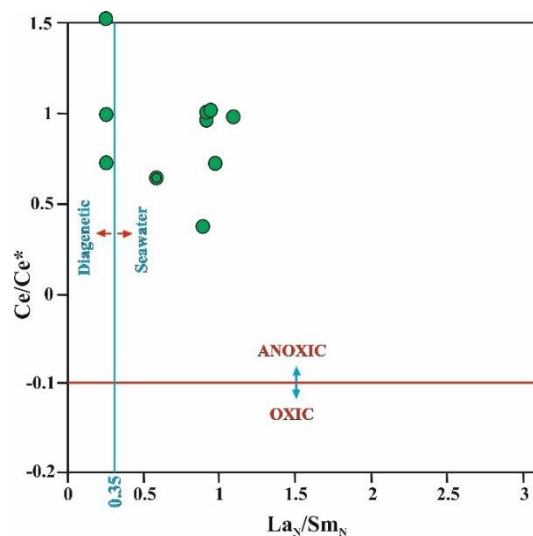


Figure 10. Ce/Ce* versus (La/Sm)_N diagram of the Saytepe carbonates

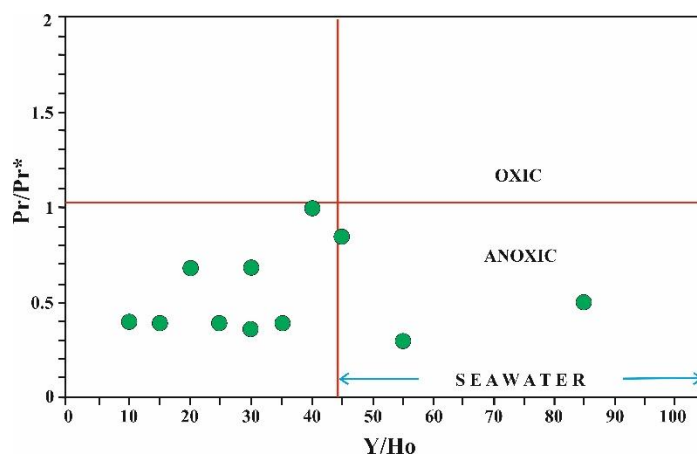


Figure 11. Pr/Pr^* vs. Y/Ho diagram of the Saytepe carbonate samples

Ali and Wagreich (2017) stated in their study that limestone Ce anomalies are close to 1 and differ from seawater (0.1-0.4) values. They stated that (1) the presence of small amounts of clay (from detrital input) minerals in pure and impure samples, (2) may have resulted from the increase in LREEs due to the degradation of Ce-containing organic matter a few cm deep in the sediment column below the seafloor. Ce anomaly values in the Saytepe carbonate samples vary between 0.37-1.54 (mean 0.88) (Table 8) and are higher than seawater values. We can say that the increase in Ce anomaly in the Saytepe samples is due to the presence of clay minerals in the limestones and/or the degradation of organic matter containing Ce in the seafloor sediments.

The redox potential of Eu/Eu^* in aqueous solutions is highly dependent on temperature and less on the variation of pressure, pH, and REE (Bau, 1996; Bau and Dulski, 1996), and positive Eu anomalies may be associated with acidic, reducing hydrothermal fluids.

Eu/Eu^* in the Saytepe carbonate samples vary between 0.67-2.83 (mean 1.69; Table 8), and they show great differences. In addition, although these samples show positive Eu anomaly, we cannot say that they indicate any hydrothermal fluid effect. Because positive Eu anomaly can be caused not only by hydrothermal fluids but also by the input of detrital feldspars. In addition, Graph 1 shows that Saytepe carbonate samples have not undergone hydrothermal alteration. Observation of >1 Eu anomaly in all Saytepe carbonate samples (except for two samples) indicates that this positivity originates from detrital feldspars. Positive Eu anomalies, which are not common in seawater, are mostly (1) an increased influx of hydrothermal fluids into the ocean at mid-ocean ridges (German et al., 1990); (2) a slight increase in the primary or detrital feldspar component (Madhavaraju et al., 2010); (3) due to diagenetic alteration of limestones (Brand and Veizer, 1980).

In the Eu/Eu^* vs. Ce/Ce^* graph of the Saytepe carbonate samples (Figure 12), our samples mostly show deposition in the marginal-offshore environment.

Bau (1996), and Bau and Dulski (1996) stated that the Y/Ho values (44-74) in seawater are high, while a constant chondritic Y/Ho value of ~ 28 is observed in terrigenous detrital and volcanic ash. The Y/Ho value is between 60-90 in open sea water and varies depending on the salinity (Lawrence et al., 2006). Recent seawater Y/Ho values are significantly higher than stream and estuary water (Nozaki et al., 1999; Lawrence et al., 2006).

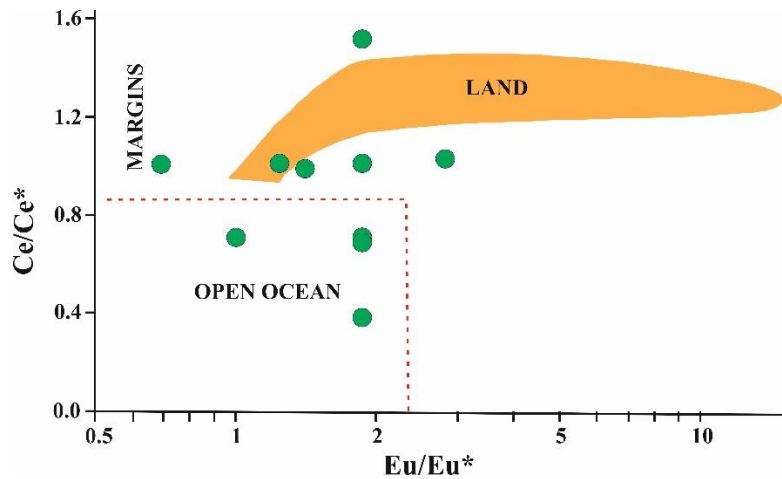


Figure 12. Positions of Saytepe carbonate samples in Ce/Ce* vs. Eu/Eu* diagram according to various storage environments. The diagram is taken from Zhang et al. (2017)

The Y/Ho ratios of the Saytepe Formation samples (Table 8) have an average value of 35 (between 10-85), which is considerably lower than the open sea water value (60-90), and it is observed that at some stages during the deposition of the carbonate, the freshwater suspension load and/or the eolian states that the powders are mixed effectively (Kuchenbecker et al., 2016). In addition, the low Y/Ho values of the Saytepe carbonate samples (10-85), Song et al. (2014) maintained the seawater values at a low rate (only 1 sample). This situation is observed in the Y/Ho versus TREE diagram in Figure 13, indicating predominantly terrestrial input for REE.

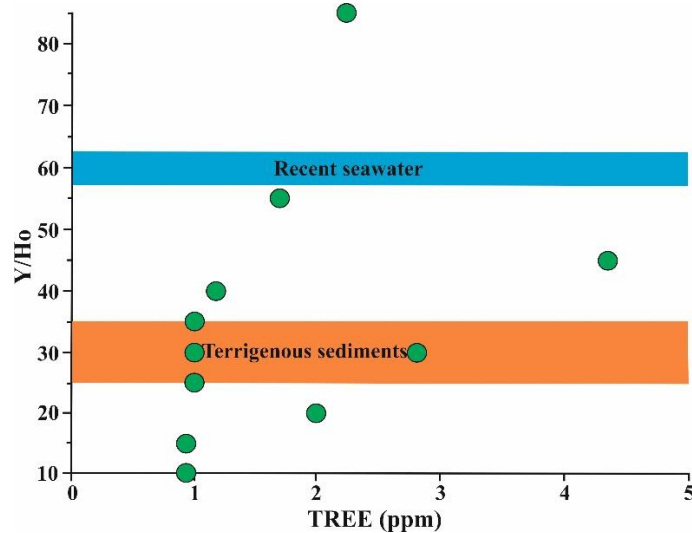


Figure 13. The Saytepe carbonate samples in the Y/Ho-TREE diagram indicate a high degree of siliciclastic contamination

Y/Ho values in the Saytepe samples were found to be low at levels with siliciclastic addition (in impure limestones) and higher at levels without siliciclastic additions (≥ 36 in relatively pure limestones) (Figure 13).

Ali and Wagreich (2017) stated that in previous studies, they found that the Y/Ho values in seawater were approximately two times higher than those of chondritic and shale values. Researchers believe that this value is affected by redox conditions; they stated that due to the

preferential adsorption of Ho to Y by Fe and Mn oxyhydroxide particles dissolved under anoxic conditions, it decreased from 102 in oxic waters to 67 in anoxic waters (Bau et al., 1997). We can say that during the deposition of the Saytepe carbonates, the oxic conditions on the shallow shelf turned into anoxic conditions on the deep shelf (offshore) and the Y/Ho values may have decreased from 102 to an average of 35 (between 10-85). This is also consistent with the fact that Saytepe carbonate samples show the development under anoxic conditions in Figures 9, 10, and 11.

Possible Sources of Detritic Materials in the Saytepe Formation Carbonates

Major oxides in sediments can be attributed to their origin, but some trace elements, including Na, K, Ca, Mg, and Fe, are not fully compatible with source rocks due to variable weathering and diagenetic processes (McLennan, 1989; Xing et al., 2021). Stable elements such as Ti, Si, Al, and Zr are relatively immobile during diagenetic processes and are often used as markers to reflect terrigenous input (Hatch and Leventhal, 1992; Xing et al., 2021). For instance, in sediments Ti is commonly found in the minerals ilmenite (FeTiO₃) or rutile (TiO₂), Si is most commonly associated with siliciclastics, including quartz, feldspar, and clay minerals (Kidder and Erwin, 2001; Xing et al., 2021), and in Al feldspars, clay minerals and other aluminum silicate minerals (Rimmer, 2004; Xing et al., 2021).

The strong (R=0.98) positive relationship between SiO₂ and Al₂O₃ in the Saytepe carbonate samples indicates that feldspar and quartz are derived from terrestrial input from the same source (Table 4).

Al₂O₃/TiO₂ values are used to reveal the provenance of clastic rocks, and these values range from 3-8 for mafic igneous rocks, 8-21 for intermediate rocks, and 21-70 for felsic igneous rocks (Hayashi et al., 1997). The Al₂O₃/TiO₂ ratios of the Saytepe samples are 3-8 (3 samples), 9-19 (2 samples), and 22 (one sample) (Table 8), with 5 samples <3 and emphasizing the source rock composition from mixed source rocks.

In addition, Al/Ti ratios are also used to determine whether the terrigenous input is of a stream or eolian origin. The Al/Ti ratios of the Saytepe carbonate samples range from 1 to 20 (average 6) (Table 8), and the fact that they are lower than the upper crust average value (27), indicates that terrigenous input to the basin during the deposition process is via wind transport rather than streams.

In addition, the source of terrigenous input in the Saytepe samples falls into the arid climate zone (Figures 7 and 14), and the terrigenous material arriving in the basin during the deposition of the Saytepe Formation shows a low level of input depending on the climate.

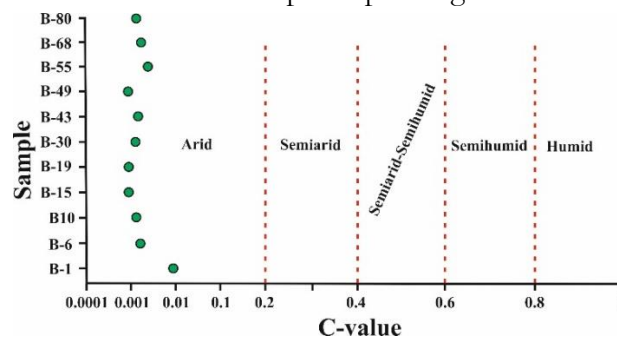


Figure 14. The Saytepe Formation samples show the arid climate zone according to the C-value $[\Sigma(Fe+Mn+Cr+Ni+V+Co) / \Sigma(Ca+Mg+Sr+Ba+K+Na)]$

Many authors (McLennan, 1989; McLennan and Taylor, 1991; McLennan et al., 1980; Wronkiewicz and Condie, 1990) have suggested Th and La elements as indicators of felsic origin, Sc and Cr elements as indicators of mafic origin, and used to make a distinction between felsic and mafic provenance.

In the La versus Th diagram (Figure 15a), the Saytepe carbonate samples fall into the mafic source area. The TiO_2/Zr ratio is another indicator of source rocks (McLennan et al., 1993; Xing et al., 2021), where TiO_2/Zr ratios of mafic rocks are higher than 200 and felsic rocks are lower than 55. Since the TiO_2/Zr ratios of Saytepe carbonate samples are $\ll 1$, it indicates that the terrigenous fragments were taken from the felsic source. In the TiO_2 vs. Zr diagram (Figure 15b), all of the Saytepe Formation samples fall into the source area of felsic rocks. Therefore, the detrital that came to the basin during the deposition of Saytepe carbonates was taken from mixed provenance.

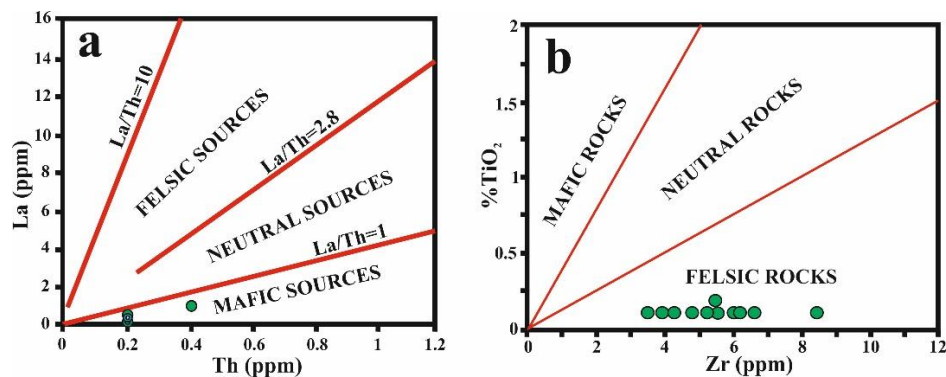


Figure 15. (a) Th versus La diagram for Saytepe carbonate samples, (b) TiO_2 versus Zr diagram

It was emphasized by Cullers (2002) that the provenance of detrital rocks can be determined in the plot of Th/Co versus La/Sc. When the Saytepe carbonate samples are reduced to the Th/Co versus La/Sc plot, it indicates that the detrital input originates from felsic rocks (Figure 16a).

The Na_2O versus K_2O separation diagram of the Saytepe Formation carbonates (Bhatia, 1983) indicates the high richness of quartz in the clastic inputs (Figure 16b). This situation is also consistent with the quartz abundance observed in the petrographic examinations of our samples.

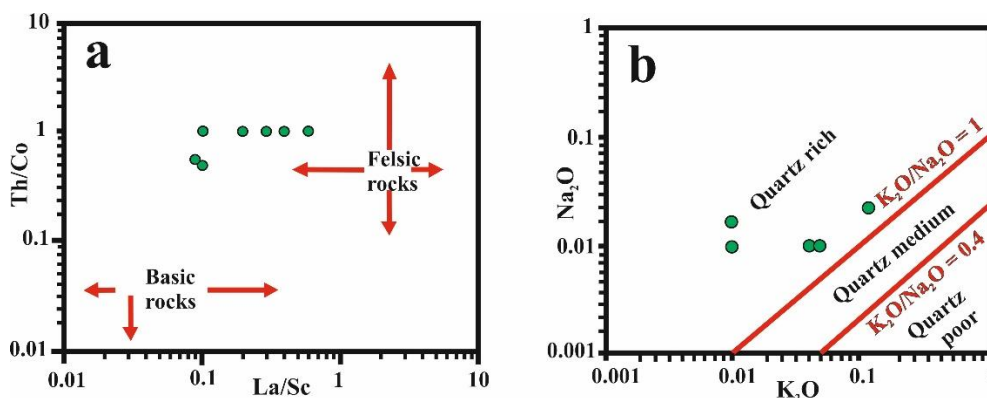


Figure 16. (a) La/Sc vs. Th/Co diagram for the Saytepe carbonate samples (diagram taken from Cullers, 2002), (b) Na_2O vs. K_2O diagram

REFERENCES

- Ali, A. & Wägrich, M. (2017) Geochemistry, environmental and provenance study of the Middle Miocene Leitha limestones (Central Paratethys). *Geologica Carpathica*, 68(3), 248-268.
- Bau, M. (1996) Controls on fractionation of isovalent trace element in magmatic and aqueous systems: evidence from Y/Ho, Zr/Hf, and lanthanide tetrad effect. *Contributions to Mineralogy and Petrology*, 123, 323-333.
- Bau, M. & Dulski, P. (1996) Distribution of yttrium and rare-earth elements in the Penge and Kuruman iron-formations, Transvaal Supergroup. *Precambrian Res.*, 79, 37-55.
- Bau, M. Möller, P. Dulski, P. (1997) Yttrium and lanthanides in eastern Mediterranean seawater and their fractionation during redox-cycling. *Mar. Chem.*, 56, 123-131.
- Bauernhofer, A. Hauzenberger, C. Wallbrecher, E. Muhongo, S. Hoinkes, G. Mogessie, A. Opiyo-Akech, N. Tenczer, V. (2009) Geochemistry of basement rocks from SE Kenya and NE Tanzania: Indications for rifting and early Pan-African subduction. *International Journal of Earth Sciences*, 98(8), 1809-1834.
- Bertram, C. J. & Elderfield, H. (1993) The geochemical balance of the rare earth elements and Nd isotopes in the oceans. *Geochim. Cosmochim. Acta*, 57, 1957-1986.
- Bhatia, M. R. (1983) Plate tectonics and geochemical composition of sandstones. *J Geol.*, 91, 611-627.
- Brand, U. & Veizer, J. (1980) Chemical diagenesis of a multi-component carbonate system: trace elements. *Jour. Sediment. Petrol.*, 50, 1219-1236.
- Cao, J. Wu, M. Chen, Y. Hu, K. Bian, L. Z. Wang, L. G. Zhang, Y. (2012) Trace and rare earth element geochemistry of Jurassic mudstones in the northern Qaidam Basin, northwest China. *Chem. Erde-Geochem.*, 72, 245-252.
- Condie, K. C. (1993) Chemical composition and evolution of the upper crust: Contrasting results from surface samples and shales. *Chem. Geol.*, 104, 1-37.
- Cullers, R. L. (2002) Implications of elemental concentrations for provenance, redox conditions, and metamorphic studies of shales and limestones near Pueblo, CO, USA. *Chemical Geology*, 191(4), 305-327.
- Ding, J. Zhang, J. Tang, X. Huo, Z. Han, S. Lang, Y. Zheng, Y. Li, X. Liu, T. (2018) Elemental Geochemical Evidence for Depositional Conditions and Organic Matter Enrichment of Black Rock Series Strata in an Inter-Platform Basin: The Lower Carboniferous Datang Formation, Southern Guizhou, Southwest China. *Minerals*, 8(11), 1-29.
- Elderfield, H. (1988) The oceanic chemistry of the rare earth elements. *Philos. Trans. R. Soc. Lond., A* 325, 105-126.
- Garrels, R. M. & Mackenzie, F. T. (1971). *Evolution of sedimentary rocks*. NY:W.W. Norton and Co.

German, C. R. Klinkhammer, G. P. Edmond, J. M. Mitra, A. Elderfield, H. (1990) Hydrothermal scavenging of rare earth elements in the ocean. *Nature*, *345*, 516-518.

Gilleaudeau, G. J. & Kah, L. C. (2013) Carbon isotope records in a Mesoproterozoic epicratonic sea: carbon cycling in a low-oxygen World. *Precambrian Res.*, *228*, 85-101.

Greaves, M. J. Elderfield, H. Sholkovitz, E. R. (1999) Aeolian sources of rare earth elements to the Western Pacific Ocean. *Marine Chemistry*, *68*, 31-38.

Hatch, J. R. & Leventhal, J. S. (1992) Relationship between Inferred Redox Potential of the Depositional Environment and Geochemistry of the Upper Pennsylvanian (Missourian) Stark Shale Member of the Dennis Limestone, Wabaunsee Country, Kansas, USA. *Chemical Geology*, *99*, 65-82.

Hayashi, K. I. Fujisawa, H. Holland, H. D. Ohmoto, H. (1997) Geochemistry of ~1.9 Ga sedimentary rocks from northeastern Labrador, Canada. *Geochim. Cosmochim. Acta*, *61*(19), 4115-4137.

Jones, B. & Manning, D. A. C. (1994) Comparison of Geochemical Indices Used for the Interpretation of Palaeoredox Conditions in Ancient Mudstones. *Chemical Geology*, *111*, 111-129.

Kaufman, A. J. & Knoll, A. H. (1995) Neoproterozoic variations in the C-isotopic composition of seawater: stratigraphic and biogeochemical implications. *Precambrian Research*, *73*, 27-49.

Kidder, D. L. & Erwin, D. H. (2001) Secular Distribution of Biogenic Silica through the Phanerozoic: Comparison of Silica-Replaced Fossils and Bedded Cherts at the Series Level. *The Journal of Geology*, *109*(4), 509-522.

Kuchenbecker, M. Babinski, M. Pedrosa-Soares, A. C. Lopes-Silva, L. Pimenta, F. (2016) Chemostratigraphy of the Lower Bambuí Group, Southwestern São Francisco Craton, Brazil: Insights on Gondwana Paleoenvironments. *Brazilian Journal of Geology*, *46*, 145-162.

Lawrence, M. G. Greig, A. Collerson, K. D. Kamber, B. S. (2006) Rare earth element and yttrium variability in South East Queens-land waterways. *Aquatic Geochemistry*, *12*(1), 39-72.

Madhavaraju, J. González-León, C. M. Lee, Y. I. Armstrong-Altrin, J. S. Reyes-Campero, L. M. (2010) Geochemistry of the Mural Formation (Aptian-Albian) of the Bisbee Group, Northern Sonora, Mexico. *Cretaceous Research*, *31*, 400-414.

McLennan, S. M. Nance, W. B. Taylor, S. R. (1980) Rare earth element-thorium correlations in sedimentary rocks, and the composition of the continental crust. *Geochim. Cosmochim. Acta*, *44*(11), 1833-1839.

McLennan, S. M. (1989) Rare Earth Elements in Sedimentary Rocks: Influence of Provenance and Sedimentary Process. *Review of Mineralogy*, *21*, 169-200.

McLennan, S. M. & Taylor, S. R. (1991) Sedimentary Rocks and Crustal Evolution: Tectonic Setting and Secular Trends. *The Journal of Geology*, *99*(1), 1-21.

McLennan, S. M. Hemming, S. McDaniel, D. K. Hanson, G. N. (1993) Geochemical approaches to sedimentation, provenance, and tectonics, in Processes Controlling the Composition of Clastic Sediments, edited by M. J. Johnsson, and A. Basu. *Spec. Pap. Geol. Soc. Am.*, 284, 21-40.

Murphy, K. & Dymond, J. (1984) Rare earth element fluxes and geochemical budget in the eastern equatorial Pacific. *Nature*, 307, 444-447.

Murray, R. W. Buchholz Ten Brink, M. R. Jones, D. L. Gerlach, D. C. Russ, G. P. (1990) Rare Earth Elements as Indicators of Different Marine Depositional Environments in Chert and Shale. *Geology*, 18, 268-271.

Murray, R. W. Brink, M. R. B. Brumsack, H. J. Gerlach, D. C. (1991) Rare earth elements in Japan Sea sediments and diagenetic behavior of Ce/Ce*: Results from ODP Leg 127. *Geochimica et Cosmochimica Acta*, 55(9), 2453-2466.

Nesbitt, H. W. Markovics, G. Price, R. C. (1980) Chemical processes affecting alkalies and alkaline earth during continental weathering. *Geochim. Cosmochim. Acta*, 44, 1659-1666.

Nothdurft, L. Webb, G. E. Kamber, B. S. (2004) Rare earth element geochemistry of Late Devonian reefal carbonates, Canning Basin, Western Australia: Confirmation of a seawater REE proxy in ancient limestones. *Geochimica et Cosmochimica Acta*, 68, 263-283.

Nozaki, Y. Alibo, D. S. Amakawa, H. Gamo, T. Hasumoto, H. (1999) Dissolved rare earth elements and hydrography in the Sulu Sea. *Geochim. Cosmochim. Acta*, 63, 2171-2181.

Piegras, D. J. & Jacobsen, S. B. (1992) The Behavior of Rare Earth Elements in Seawater: Precise Determination of Variations in the North Pacific Water Column. *Geochimica et Cosmochimica Acta*, 56, 1851-1862.

Piper, D. Z. (1974) Rare Earth Elements in the Sedimentary Cycle: A Summary. *Chemical Geology*, 14(4), 285-343.

Rimmer, S. M. (2004) Geochemical paleoredox indicators in Devonian–Mississippian black shales, central Appalachian Basin (U.S.A.). *Chem. Geol.* 206, 373-391.

Roy, D. K. & Roser, B. P. (2013) Climatic control on the composition of Carboniferous–Permian Gondwana sediments, Khalaspir basin, Bangladesh. *Gondwana Res.*, 23, 1163-1171.

Rudnick, R. L. McLennan, S.M. Taylor, S.R. (1985) Large iron lithophile elements in rocks from high-pressure granulite facies terrains. *Geochimica et Cosmochimica Acta*, 49,1645-1655.

Sholkovitz, E. R. (1988) Rare earth elements in the sediments of the North Atlantic Ocean, Amazon Delta, and the East China Sea: the reinterpretation of terrigenous input patterns to the oceans. *American Journal of Science*, 288(3), 236-281.

Song, C. Herong, G. Linhua, S. (2014) Geochemical characteristics of REE in the Late Neoproterozoic limestone from northern Anhui Province, China. *Chin. Jour. Geochem.*, 33, 187-193.

Taylor, S. R. & McLennan, S. M. (1985) The Continental Crust: Its Composition and Evolution. Cambridge: Blackwell.

Thurston, G. Ito, K. Lall, R. A. (2011) Source apportionment of U.S. fine particulate matter air pollution. *Atmos. Environ.*, 45(24), 3924-3936.

Wang, Z. W. Fu, X. G. Feng, X. L. Song, C. Wang, D. Chen, W. B. Zeng, S. Q. (2017) Geochemical features of the black shales from the Wuyu Basin, southern Tibet: Implications for palaeoenvironment and palaeoclimate. *Geol. Jour.*, 52, 282-297.

Wilde, P. Quinby-Hunt, M. S. Erdtmann, B. D. (1996) The Whole-rock Cerium Anomaly: a Potential Indicator of Eustatic Sea-level Changes in Shales of the Anoxic Facies. *Sediment. Geol.*, 101(1-2), 43-53.

Wronkiewicz, D. J. & Condie, K. C. (1990) Geochemistry and mineralogy of sediments from the Ventersdorp and Transvaal Supergroups, South Africa: Cratonic evolution during the early Proterozoic. *Geochim. Cosmochim. Acta*, 54, 343-354.

Xie, G. L. Shen, Y. L. Liu, S. G. Hao, W. D. (2018) Trace, and rare earth element (REE) characteristics of mudstones from Eocene Pinghu Formation and Oligocene Huagang Formation in Xihu Sag, East China Sea Basin: Implications for provenance, depositional conditions, and paleoclimate. *Mar. Petrol. Geol.*, 92, 20-36.

Xing, K. Shu, Q. Lentz, D. R. (2021) Constraints on the Formation of the Giant Daheishan Porphyry Mo Deposit (NE China) from Whole-Rock and Accessory Mineral Geochemistry. *J. Pet.* 62, 1-26.

Yandoka, B. M. S. Wan, H. A. Abubakar, M. B. Hakimi, M. H. Adegoke, A. K. (2015) Geochemical characterization of Early Cretaceous lacustrine sediments of Bima Formation, Yola Sub-basin, Northern Benue Trough, NE Nigeria: Organic matter input, preservation, paleoenvironment and palaeoclimatic conditions. *Mar. Petrol. Geol.*, 61, 82-94.

Zhang, K. J. Li, Q. H. Yan, L. L. Zeng, L. Lu, L. Zhang, Y. X. Hui, J. Jin, X. Tang, X. C. (2017) Geochemistry of limestones deposited in various plate tectonic settings. *Earth-Science Reviews*, 167, 26-47.

Zhao, Y. Zheng, Y. F. Chen, F. (2009) Trace element and strontium isotope constraints on the sedimentary environment of Ediacaran carbonates in southern Anhui, South China. *Chemical Geology*, 265, 345-362.

Bearing Capacity And Elastic Settlement Of Shallow Foundations

Mustafa AYTEKIN¹

Introduction

There are many methods proposed to estimate the bearing capacity and elastic settlement of shallow foundations. In author's opinion, a reliable method of bearing capacity estimation among all is the effective area method that is also known as Meyerhof's theory. For the settlement estimations, the Schmertmann Method is among others is the best estimation approaches. However, application of these methods as they have proposed originally are a little bit time consuming. In this chapter, you will find these methods are modified to overcome their shortages since these methods are modified by the author to be able to apply in an easy way.

In this chapter, the author has concentrated on the bearing capacity of two-way eccentric shallow foundations. In rectangular/square based and two-way loaded (two-way eccentric) shallow foundations, four zones in which the resultant load might act are defined in the effective area method. Three out of the four zones that are employed in the determination of the effective areas overlap around kern. Only one zone that has a triangular-shaped effective area (called as case 1 in the literature) out of the four zones has no overlap with the others. The resultant load will always be out of the kern for case 1, and also it might be out of the kern for the remaining three cases. Design of foundations is not acceptable in general if the resultant load acts out of the kern. In the present study, the four cases are reconsidered. The zones on which the resultant load can be acting for the four cases are modified because these zones are overlapped partly. The modification has been made to have clear borders between the zones. On top of that, zone 4 is divided into two. A new zone corresponding to the area of kern is defined as zone 5. The design will be accepted if the resultant load acts within zone 5 (the kern). Also, the graphs in use to determine the dimensions of the effective areas are eliminated since it is not precise. Formulae are derived to determine the dimensions of the effective areas instead of using the graphs. Two new criteria are discovered and proposed to check whether the resultant load acts outside, inside or on the borderline of zone 5 (the kern).

One of the methods intensively employed in many practical projects to estimate the immediate (elastic) settlement of shallow foundations is the Schmertmann-Hartman-Brown method (1978). In the method, two approaches are given as a function of type of the shallow foundation either a square/circular (axisymmetric condition) or a strip (plain strain condition) foundation. Thus, two sets of equations are provided to estimate the settlements for these types of shallow foundations. If a shallow foundation has a shape of rectangular, some approximations are suggested in the technical literature to estimate the elastic settlement of rectangular based shallow foundations. These approximations are tedious and time consuming. In this study, the Schmertmann – Hartman – Brown method (1978) is modified and only one set of equations used for any type (square, circular, rectangular, and strip) of shallow foundations is introduced. The

¹ Prof., University of Bahain, Department of Civil Engineering,

modified method estimates the immediate settlement as precise as the original form of the method that is more complicated. Also, some hypothetical cases are considered to figure out the effect of width and length/width ratios of foundations on elastic settlement.

Bearing Capacity

The bearing capacity estimation on the geotechnical design of two-way loaded (two-way eccentric) foundations are as follows:

- a. Determine the eccentricities of e_B and e_L seen in Fig.1 in both directions of B and L, respectively.

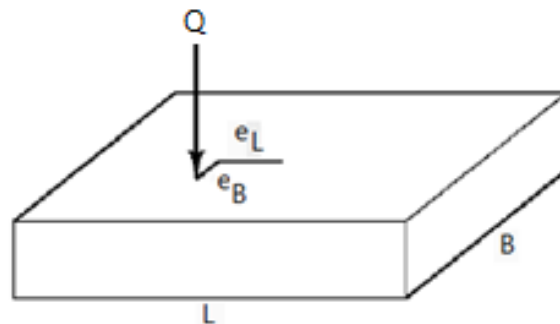


Fig.1 Two-way loaded square/rectangular foundation

- b. Determine the dimensions of the kern as seen in Fig.2 and check the location of the resultant load (Q) whether it acts inside, outside or on the border line of the kern.

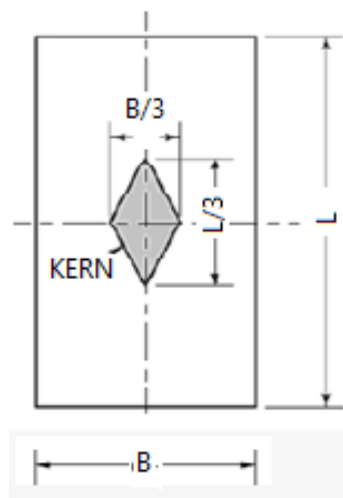


Fig.2 Dimensions of the kern

Use the criteria seen below to find out the location of the resultant load (Eq.1).

$$\left(\frac{6e_B}{B} + \frac{6e_L}{L}\right) \leq 1 \quad (1)$$

If Eq. (1), which is actually the last two terms of second parenthesis of Eq.(2) has the value equal to one, the minimum bearing pressure would be nil whereas if the value is more than one, it would be a negative number, which means the minimum bearing is tension. In other words, if Eq. (1) is satisfied, the minimum bearing pressure is either compression or nil. Otherwise, the minimum bearing is a negative value that reflects a gap between the base of the foundation and underlying

soil. Since no gap in the design is accepted under any foundation, there must be some solutions to avoid this situation like increasing dimensions of foundation or reducing the eccentricities physically.

c. Use the sign (+ or -) in Eq. (2) to calculate the maximum and minimum bearing pressures at the base of foundation according to the position of the load (inside, or on the border line of the kern).

$$q = \left(\frac{Q+W_f}{BL} - u_D \right) \left(1 \pm \frac{6e_B}{B} \pm \frac{6e_L}{L} \right) \quad (2)$$

where

Q: Load from superstructure

W_f : Weight of foundation

B and L: Width and length of foundation, respectively

U_{Df} : Pore water pressure at the base level of the foundation

e_B and e_L : eccentricities on B and L directions, respectively.

In the design, the maximum bearing pressure must be less than or equal to the allowable bearing capacity of soil, and at the same time the minimum bearing pressure must be compression or at least zero but not tension. Once, the maximum and minimum bearing pressures are estimated, allowable bearing capacity of the foundation must be determined too.

The bearing capacity of foundation can be estimated by a number of methods. Terzaghi's bearing capacity equation (Terzaghi, 1943) is widely used to estimate ultimate bearing capacity of foundations even it has many limitations in practical applications. In order to minimize these limitations, many proposals have been made by researchers (Meyerhof, 1963; Prakash and Saran, 1971; Saran and Agarwal, 1993; Vesic, 1973; Sawwaf and Nazir, 2012; Krabbenhoft and others, 2012; Loukidis and others, 2008). One of these methods has been proposed by Meyerhof (1963) and his proposed method is known as *Meyerhof Bearing Capacity Equation, General Bearing Capacity Equation, or The Effective Area Method*. Vesic, 1973 has also proposed an equation almost identical with Meyerhof's equation. Meyerhof's general bearing capacity equation is seen below:

$$q_u = c'N_c F_{cs} F_{cd} F_{ci} + qN_q F_{qs} F_{qd} F_{qi} + 0.5\gamma B' N_\gamma F_{\gamma s} F_{\gamma d} F_{\gamma i} \quad (3)$$

Then, the ultimate bearing load can be estimated as follows.

$$Q_{ult} = q_u A' \quad (4)$$

A procedure to determine the effective area (A') and effective width (B') that would be used in the Meyerhof's general bearing capacity equation was proposed by (Highter & Anders, 1985) in addition to one proposed by Meyerhof (1963).

It is the common practice to employ the proposed *effective area* determination on the design of two-way loaded foundations. In the determination of effective area, four cases are provided to design a square/rectangular based and two-way loaded foundations by Highter & Anders in 1985. In the determination of the four cases, the criteria are the ranges of the ratios of e_B/B , and e_L/L . In general, nothing is mentioned for these four cases about the application points of the resultant

loads whether it is in or out of the kern. However, anything may occur in terms of eccentricity. It means that the resultant force can be in, out or on the border line of the kern except case 1 in that eccentricity is always out of the kern.

Cases defined in the effective area method

When one has a closer look into the four cases mentioned in the effective area method, the resultant load is always out of the kern in case 1 seen in Fig. 3, mostly out of the kern in cases 2 (Fig.4), and 3 (Fig. 5), some area out of the kern even in case 4 (Fig.6). Thus, the cases should be modified in order to have a clear border between the cases. Only case 1 has the areas not overlap with the areas of the rest of the cases. There are overlaps of the areas in the cases of 2, 3, and 4 as seen in Figs. 4, 5, and 6. The zone 4 seen in Fig. 6 is the common zone in the cases of 2, 3, and 4. The shapes and borders of the effective areas are taken from Das, 2007.

CASE 1: $[(e_L/L) > (1/6) \text{ and } (e_B/B) > (1/6)]$ As it is seen in Fig. 3, the resultant acts within the zones 1.

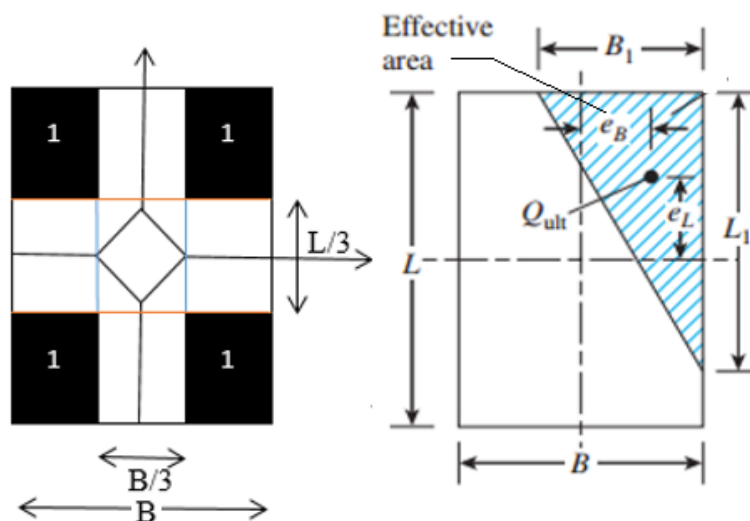


Fig. 3 Resultant load acts in zones 1 (Case 1)

It is obvious that the resultant acts out of the kern so that minimum bearing pressure would be tension and a gap between the base of foundation and the underlying soil would occur.

CASE 2: $[(e_L/L) < 0.5 \text{ and } 0 < (e_B/B) < (1/6)]$ As it is seen in Fig. 4, the resultant load acts within the zone 2. Again, it is obvious that the resultant load is not always acting within or border line but mostly out of the kern so that minimum bearing pressure would be tension mostly and a gap between the base of foundation and the underlying soil would occur.

CASE 3: $[(e_L/L) < (1/6) \text{ and } 0 < (e_B/B) < 0.5]$ As it is seen in Fig. 5, the resultant load acts within the zone 3. Again, it is obvious that the resultant load not always acting within or border line but mostly out of the kern so that minimum bearing pressure would be tension mostly and a gap between the base of foundation and the underlying soil would occur.

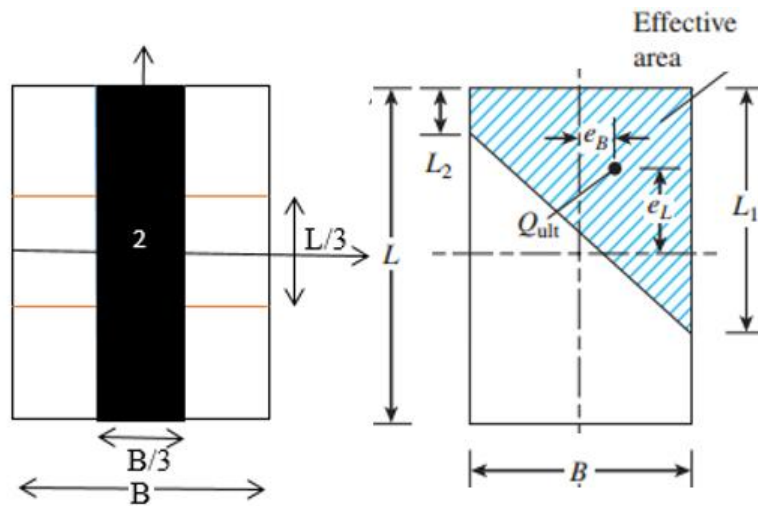


Fig. 4 Resultant load acts in zone 2 (Case 2)

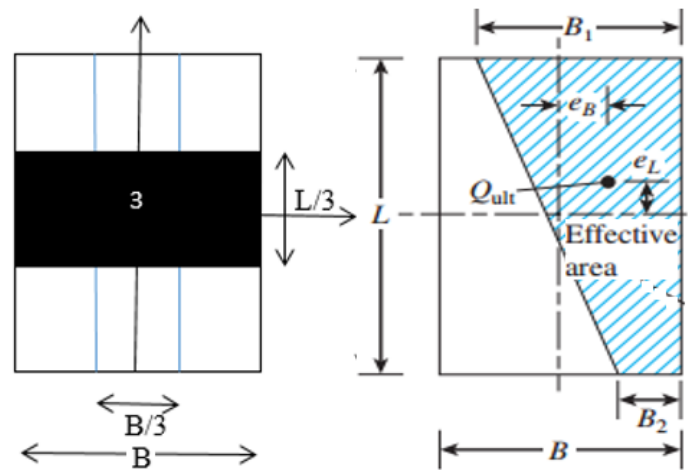


Fig. 5 Resultant load acts in zone 3 (Case 3)

CASE 4: $[(e_L/L) < (1/6) \text{ and } (e_B/B) < (1/6)]$

As it is seen in Fig. 6, the resultant load acts within the zone 4. The resultant load not always acting within or border line but it might be out of the kern so that minimum bearing pressure might be tension and a gap might occur between the base of foundation and the underlying soil.

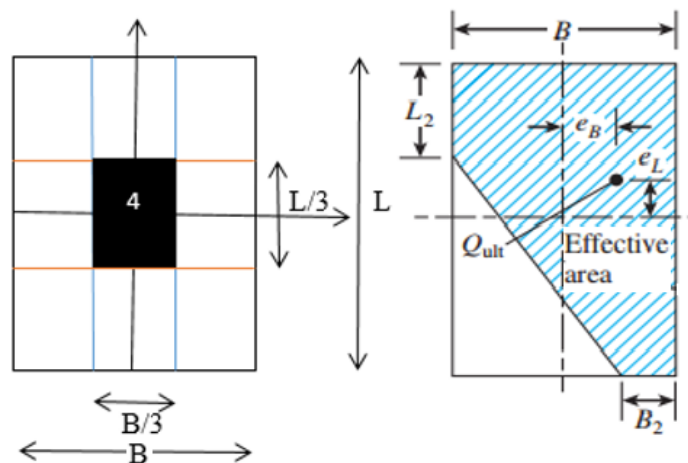


Fig. 6 Resultant load acts in zone 4 (Case 4)

Modified Cases

CASE 1 is not modified so that it will remain as it is. In the modified cases of 2, 3, 4, the resultant load is out of the kern mostly, and it is always out of the kern in case 1. Thus, these cases may be employed for any research or other purposes except the design that would be applied in the field because there would be tension between the base of foundation and underlying soil.

In this study, a new case is defined as *case 5* (Fig.11) that is actually representing the kern so that case 5 can be used to design foundations that would be applied in the field because the resultant load acts in the kern so that the minimum bearing pressure would be a positive value or at least nil.

Modified CASE 2: Modified and redefined as seen below

$[(1/6) < (e_L/L) < 0.5$ and $0 < (e_B/B) < (1/6)]$. When these ranges are applied to zone 2, it will become as seen in Fig.7. You can see the difference by comparing Figs.4 and 7.

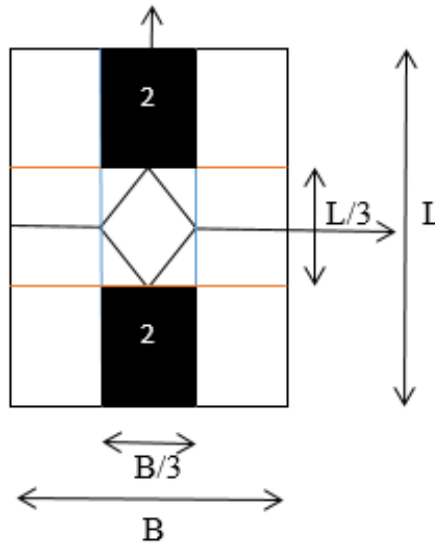


Fig. 7. Zone 2 to after the modification

The dimensions of the effective area seen in Fig. 4b can be calculated by the Eqs. (5 to 9) instead of using the graph generated in the original effective area method.

$$A_o = \frac{B-6e_B}{B+6e_B} \quad (5)$$

$$L_1 = \left(\frac{1.5-3e_L/L}{1+A_o+A_o^2} \right) (A_o + 1)L \leq L \quad (6)$$

$$L_2 = A_o L_1 \leq L \quad (7)$$

The effective area;

$$A' = \frac{1}{2}(L_1 + L_2)B \quad (8)$$

and the effective width;

$$B' = \frac{A'}{L_1 \text{ or } L_2 (\text{larger one})} \quad (9)$$

Modified CASE 3: Modified and redefined as seen below [$(e_t/L) < (1/6)$ and $(1/6) < (e_B/B) \leq 0.5$].

When these ranges are applied to zone 3, it will become as seen in Fig.8. The difference can be seen by comparing Figs.5 and 8.

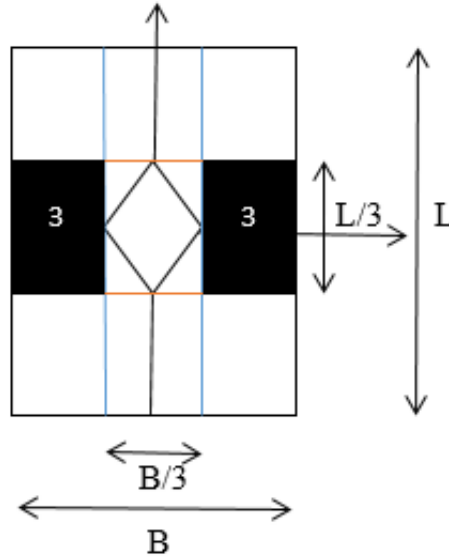


Fig. 8 Zone 3 to after the modification

The dimensions of the effective area seen in Fig. 4b can be calculated by the Eqs. (10 to 14) instead of using the graph generated in the original effective area method.

$$A_1 = \frac{L+6e_L}{L-6e_L} \quad (10)$$

$$B_1 = \left(\frac{1.5-3e_B/B}{1+A_1+A_1^2} \right) (A_1 + 1)B \leq B \quad (11)$$

$$B_2 = A_1 B_1 \leq B \quad (12)$$

The effective area;

$$A' = \frac{1}{2}(B_1 + B_2)L \quad (13)$$

and the effective width:

$$B' = \frac{A'}{L} \quad (14)$$

Modified CASE 4: The four dark triangular zones seen in Fig. 9 represent zone 4. The eccentricity of the resultant load would be within the following borders for this case.

$$e > e_{max}, \text{ and } \frac{e_B}{B} \leq \frac{1}{6} \text{ and } \frac{e_L}{L} \leq \frac{1}{6}$$

where e and e_{max} are calculated from Eqs.(19 & 18), respectively. The effective area and effective width for this case would be calculated just like the procedure given in case 5.

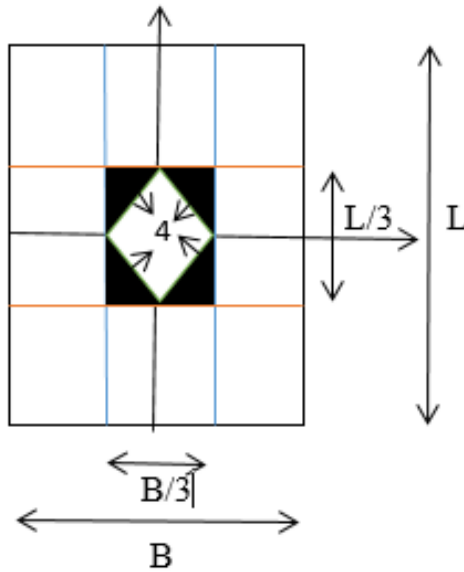


Fig. 9 Zone 4 to after the modification

CASE 5 (New): A newly considered case in that only the zone of kern will be considered (see Fig. 10). Two criteria for this zone have been determined by the author and given below. One of the criteria can be employed to determine whether the resultant load is in, on or out of the border line of kern.

Criteria 1:

The kern is seen in Fig, 11a (zone 5), and one of the four parts of the kern is shown in Fig. 11b. To create a criteria that would be employed for the case 5 in the effective area method, the steps are as follows.

1. Find angles α and β in Fig.11b as seen below.

$$\alpha = \tan^{-1} \left(\frac{B}{L} \right) \quad (15)$$

$$\beta = \tan^{-1} \left(\frac{e_B}{e_L} \right) \quad (16)$$

$$\gamma = 180 - \alpha - \beta \quad (17)$$

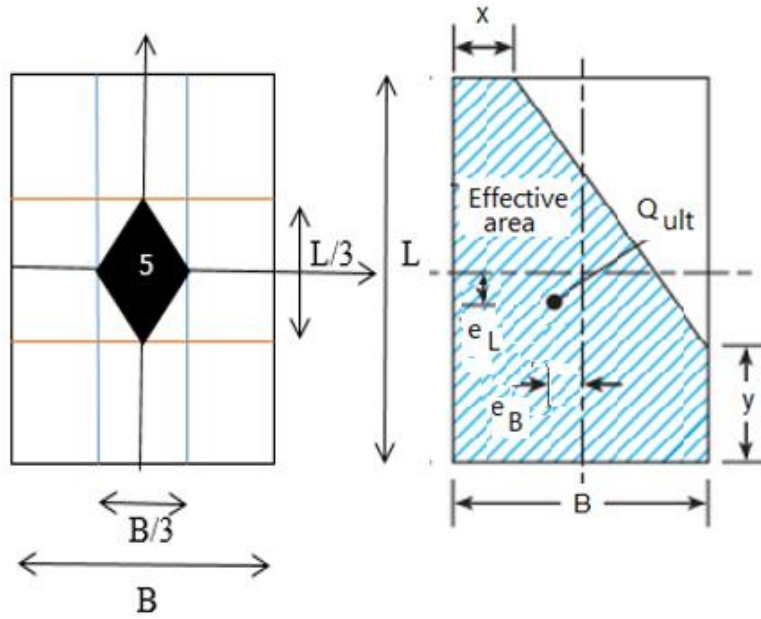


Fig. 10. Zone 5 newly defined

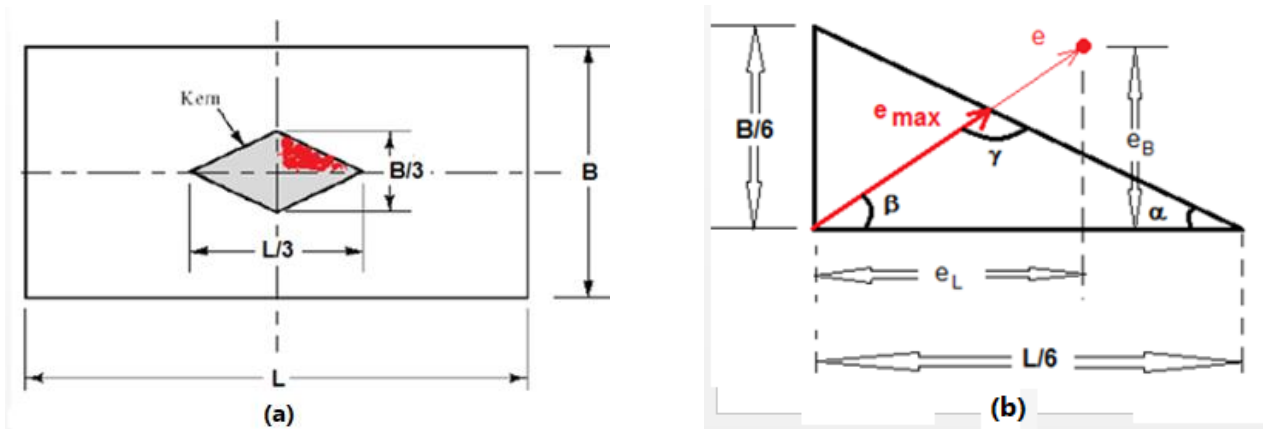


Fig. 11 The value of eccentricities on a foundation

2. Find maximum value of eccentricity within the kern:

$$e_{max} = \frac{\sin \alpha}{\sin \gamma} \cdot \frac{L}{6} \quad (18)$$

3. Find the existing eccentricity;

$$e = \sqrt{(e_L^2 + e_B^2)} \quad (19)$$

Application of resultant load is within the kern if

$$e < e_{max}$$

Application of resultant load is on the borderline of the kern if

$$e = e_{max}$$

Application of resultant load is outside of the kern if

$$e > e_{max}$$

Finally, check the criteria of the modified cases given here. If e is less than or equal to e_{max} , then, employ the procedure for case 5.

Criteria 2:

In order to have the application point of the resultant load within the kern, when the eccentricity on B-direction only, maximum value of $e_B = B/6$, the eccentricity on L-direction must be equal to zero ($e_L = 0$) or vice versa if the eccentricity on L-direction only (see Fig.12).

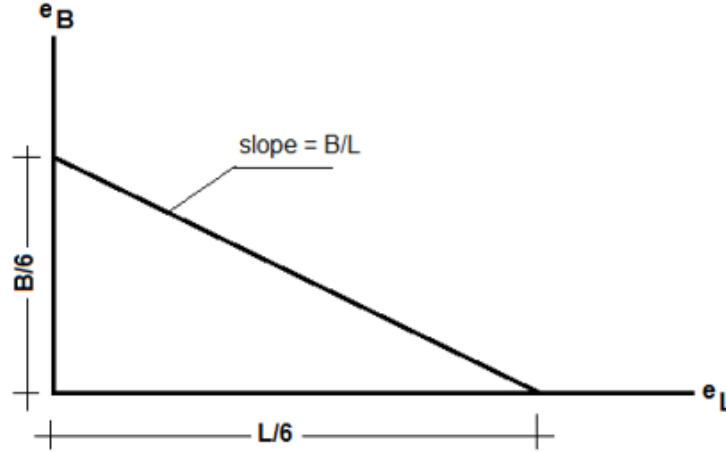


Fig. 12 One fourth of the kern

Thus, the following relationships can be written:

$$\left[0 \leq \frac{e_B}{B} \leq \left(\frac{1}{6} - \frac{e_L}{L} \right) \right] \quad (20)$$

Or

$$\left[0 \leq \frac{e_L}{L} \leq \left(\frac{1}{6} - \frac{e_B}{B} \right) \right] \quad (21)$$

If this is the case of eccentricities, the resultant load acts either in the kern or on the borderline of the kern. If this criterion is not satisfied, it means that the location of resultant load is out of the kern. In this case, minimum value of the bearing pressure would be tension so that the foundations with a tension under it should not be designed in general because there will be a gap between the base of the foundation and soil under lying instead tension stress.

If the resultant load acts in zone 5, which is actually the kern, the shape of the effective area would be similar to one seen in Fig. 13b. Coordinates of the effective area can be located from 0 to 5 that must be numbered clockwise as seen in Fig 13a. The coordinates of the points (0 to 5) are numbered as follows:

$$0(x_0, y_0), 1(x_1, y_1), 2(x_2, y_2), 3(x_3, y_3), 4(x_4, y_4), 5(x_5, y_5)$$

Actually, $x_0 = x_5$, and $y_0 = y_5$. From Fig. 13b:

$$0(0,0), 1(0, L), 2(x, L), 3(B, y), 4(B,0), 5(0,0) \text{ can be written.}$$

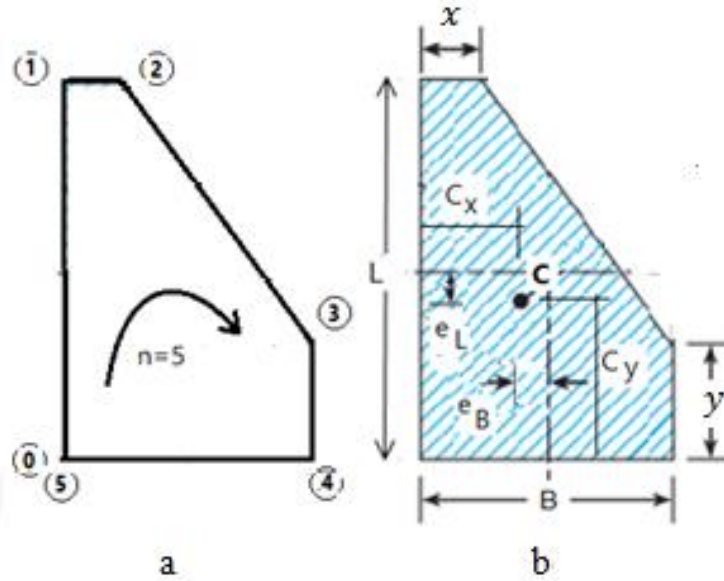


Fig.13 Coordinates of effective area

Coordinates (C_x , and C_y) of the centroid of effective area can be written as follows (see Fig.13b):

$$C_x = \frac{B}{2} - e_B \quad (22)$$

$$C_y = \frac{L}{2} - e_L \quad (23)$$

Also, these coordinates can be written as follows:

$$A = \frac{1}{2} \sum_{i=0}^{n-1} (x_i y_{i+1} - x_{i+1} y_i) \quad (24)$$

$$C_x = \frac{1}{6A} \sum_{i=0}^{n-1} (x_i + x_{i+1})(x_i y_{i+1} - x_{i+1} y_i) \quad (25)$$

$$C_y = \frac{1}{6A} \sum_{i=0}^{n-1} (y_i + y_{i+1})(x_i y_{i+1} - x_{i+1} y_i) \quad (26)$$

The right side of Eq. (25) is equal to the right side of Eq. (20), and Eq.(26) is equal to Eq.(23). Therefore, Eqs. (27) and (28) can be derived as follows:

$$-x^2 L + (x + B)(xy - BL) - 2B^2 y - 3 \left(\frac{B}{2} - e_B \right) (-xL + xy - BL - By) = 0 \quad (27)$$

$$2xL^2 + (L + y)(xy - BL) - By^2 - 3 \left(\frac{L}{2} - e_L \right) (-xL + xy - BL - By) = 0 \quad (28)$$

Eqs. (27), and (28) can be solved for unknowns of x and y numerically by a proper method. In this study, a MATLAB code has been developed to solve these equations and normalized values are given in Table 1. The effective area can be determined from:

$$A' = \frac{1}{2} (BL + xL + By - xy) \quad (29)$$

Or

$$A' = \frac{1}{2} (B + x)(L - y) + By \quad (30)$$

Or

$$A' = BL - \frac{1}{2}(B - x)(L - y) \quad (31)$$

And the effective width;

$$B' = \frac{A'}{L} \quad (32)$$

Tables 1 and 2 can be used to determine effective area for this case just like newly described case 5.

Table 1. x / B values

eL/L	0.027	0.053	0.080	0.107	0.133	0.160
eB/B	x/B values					
0.02	0.4614					
0.04	0.7380	0.3408	0.0625			
0.06	0.7323	0.5006	0.2389	0.0519		
0.08	0.6966	0.5352	0.3303	0.1491	0.0124	
0.10	0.6539	0.5250	0.3628	0.2027	0.0688	
0.12	0.6090	0.4982	0.3633	0.2244	0.1000	
0.14	0.5636	0.4642	0.3475	0.2259	0.1125	0.0144
0.16	0.5184	0.4272	0.3232	0.2150	0.1120	0.0204

Table 2. y / L values

eL/L	0.027	0.053	0.080	0.107	0.133	0.160
eB/B	y / L values					
0.02	0.7819	0.7823	0.7256	0.6634	0.6006	0.5386
0.04	0.3254	0.6211	0.6249	0.5830	0.5304	0.4747
0.06	0.0477	0.3894	0.4853	0.4812	0.4469	0.4021
0.08		0.1901	0.3303	0.3655	0.3540	0.3232
0.10		0.0467	0.1902	0.2495	0.2584	0.2419
0.12			0.0756	0.1439	0.1667	0.1623
0.14				0.0530	0.0833	0.0879
0.16					0.0100	0.0204

Elastic settlement

It has been a principal issue to estimate the settlement of foundations for civil engineers. Thus, many researchers have studied the problem to get a reliable solution of it. Terzaghi and Peck (1948) proposed an empirical relationship between the settlement (S_e) of a prototype foundation measuring $B \times B$ in plan and the settlement of a test plate. Bjerrum and Eggstad (1963) provided the results of 14 sets of load settlement tests. Bazaraa (1967) also provided several field tests results. Both gave correlation of settlements between with size of plate used in the tests and size of foundation that would be designed. Jeyapalan and Boehm (1986) and Papadopoulos (1992) summarized the case histories of 79 foundations. DeBeer and Martens (1957) and DeBeer (1965) proposed another formula to estimate the elastic settlement of a foundation. Burland and Burbidge (1985) proposed a method for calculating the elastic settlement of sandy soil using the field standard penetration number N_{60} .

The Schmertmann-Hartman-Brown method (1978) is commonly used for the estimation of elastic (immediate) settlement of shallow foundations. In the procedure on the estimation of immediate settlement, two approaches are used. One for axisymmetric (square and circular foundations) cases, and the other is for plane strain (strip foundations) condition as seen in Fig.14. In case of rectangular foundations, there is an approximation in the method by using both axisymmetric and plane strain conditions.

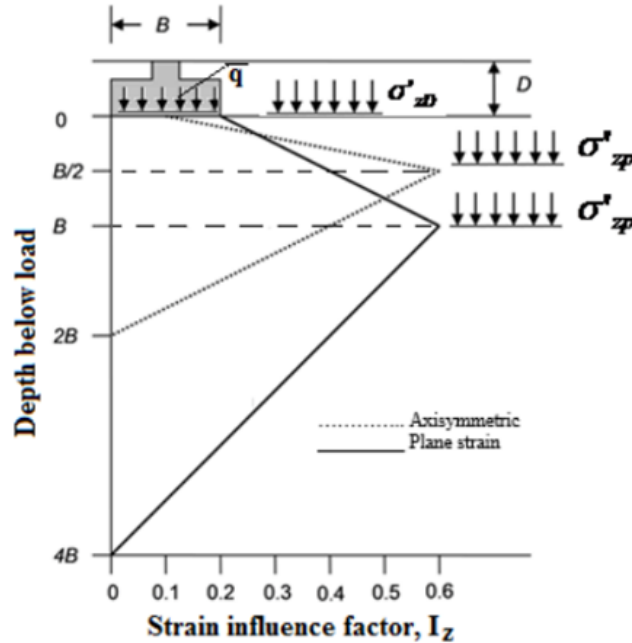


Fig. 14 Variation of stress influence factors (a) square/ circular based and strip foundations (Schmertmann, 1978), (b) Proposed variation of strain influence factor (u-line) for any shape of shallow foundation.

Schmertmann – Hartman - Brown Method (1978)

In this method, immediate (or elastic) settlements (S_e) of shallow foundations are calculated by Eq. (1) seen below.

$$S_e = C_1 C_2 C_3 (q - \sigma'_{zd}) \sum_{i=1}^n \frac{\Delta z_i I_{zi}}{E_{si}} \quad (33)$$

Where

$$C_1 = 1 - 0.5 \left(\frac{\sigma'_{zd}}{q - \sigma'_{zd}} \right) \quad (34)$$

Correction for strain relief due to excavation,

$$C_2 = 1 + 0.2 \log \left(\frac{t}{0.1} \right) \quad (35)$$

Correction for creep,

$$C_3 = 1.03 - 0.03 \left(\frac{L}{B} \right) \geq 0.73 \quad (36)$$

q = gross contact pressure of footing,

σ'_{zD} = Effective stress at the base level of footing before the construction

Δz_i = thickness of soil layer i .

I_{z_i} = strain influence factor of layer i .

E_{s_i} = elasticity modulus of layer i .

B = width of foundation

L = length of foundation

According to Fig.1a, the exact value of I_{z_i} at any depth can be determined as follows; For square and circular footings ($L/B=1$)

$$I_z = 0.1 + \frac{z}{B} (2I_{zp} - 0.2) \quad \text{if} \quad \left(0 \leq z \leq \frac{B}{2} \right) \quad (37)$$

$$I_z = 0.667I_{zp} \left(2 - \frac{z}{B} \right) \quad \text{if} \quad \left(\frac{B}{2} \leq z \leq 2B \right). \quad (38)$$

For strip (continuous) footings $\frac{L}{B} \geq 10$

$$I_z = 0.2 + \left(\frac{z}{B} \right) (I_{zp} - 0.2) \quad \text{if} \quad (0 \leq z \leq B) \quad (39)$$

$$I_z = 0.333I_{zp} \left(4 - \frac{z}{B} \right) \quad \text{if} \quad (B \leq z \leq 4B) \quad (40)$$

For rectangular footings in which the length is greater than ten times the width, the plane strain approach is used. For rectangular loads in which the length is less than ten times the width, a linear interpolation between the axisymmetric and plane strain case is performed, dependent on the length to width ratio. For the rectangular foundations $\left(1 < \frac{L}{B} \leq 10 \right)$

$$I_z = I_{zp} + 0.111(I_{zc} - I_{zs}) * \left(\frac{L}{B} - 1 \right) \quad (41)$$

where

I_{zc} = strain influence factor for strip footing that has a width of B ,

I_{zs} = strain influence factor for square footing that has a width of B , this value must be at least zero or larger

As it is seen above, the calculations of strain influence factors are complicated and time consuming. To avoid these problems, the method is modified and a procedure much simpler than the original Schmertmann et al. method.

Modification of the Schmertmann-Hartman-Brown (1978) Method

In this paper, the Schmertmann – Hartman - Brown (1978) method is modified by considering boundary conditions of the square/circular ($L/B = 1$) and strip ($L/B > 10$) foundations. Equations on the calculation of strain influence factors for any type of shallow foundation such as rectangular, square, circular, strip in Eq. (33) have been re-driven. Thus, the following procedure has been prepared to estimate immediate settlements of any type of shallow foundations. In the modified method, the assumed variation of the strain influence factor is seen in Fig. 15. The user should not be worried about the problem whether it is an axisymmetric or plane strain problem. The data that are needed to be used in the modified method are the size, depth of foundation, load (or bearing pressure), unit weight of soil, number and thickness of soil layers and their modulus of elasticity values under the foundation within the depth of $2B$ or maximum $4B$. The author suggests to users that consider the layers only within the depth of z_{max} that can be calculated by Eq. (18) from the base of foundation.

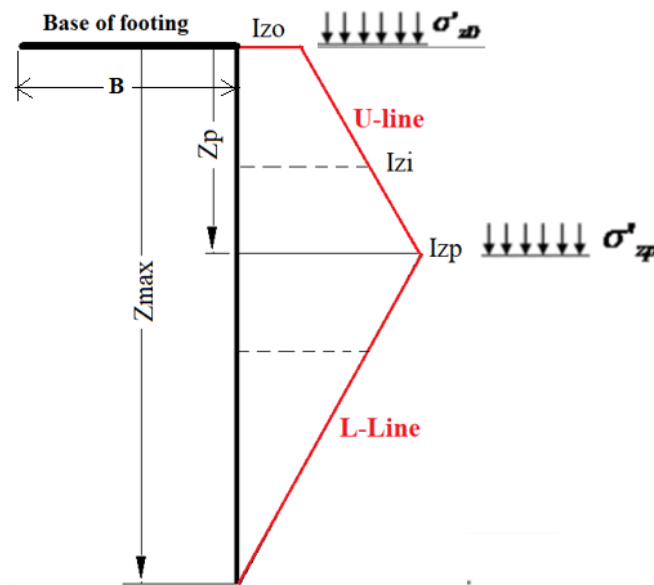


Fig. 15 Variation of the strain influence factor for any type (square, circular or rectangular) of shallow foundation in the modified method

Calculation steps of the modified approach for any type of shallow foundations:

1. Calculate the followings:
 1. Total bearing pressure (contact pressure):

$$q = \frac{P + W_f}{A} \quad (42)$$

Where

P = Column load

W_f = Weight of footing

A = Base area of footing (BxL)

2. Effective overburden pressure at the base level of foundation:

$$\sigma'_{zD} = \gamma D_f - u_D \quad (43)$$

3. Net bearing pressure

$$q_{net} = q - \sigma'_{zD} \quad (44)$$

Where

u_D = pore water pressure at base level of footing

C_1 , C_2 , and C_3 would be calculated from Eqs. 34, 35, and 36, respectively.

Up to this point, all the procedure and calculations are same as the original method. After this point the modifications would take place.

4. Depth of z_p at which the peak of the strain influence factor (I_{zp}) occurs (see Fig. 15). Its value must be $B/2$ and B for square/circular based footings and strip footings, respectively. The following equation can be used for any type of shallow foundations to get the depth of which peak strain influence factor occurs.

$$z_p = \left(\frac{L}{B} - 1\right) \frac{B}{18} + \frac{B}{2} \quad (B/2) \leq z_p \leq B \quad (45)$$

As an alternative, Fig. 16 can be used to get z_p value as follows.

$$z_p = B C_p \quad (46)$$

Where C_p is a coefficient that can be taken from Fig.16.

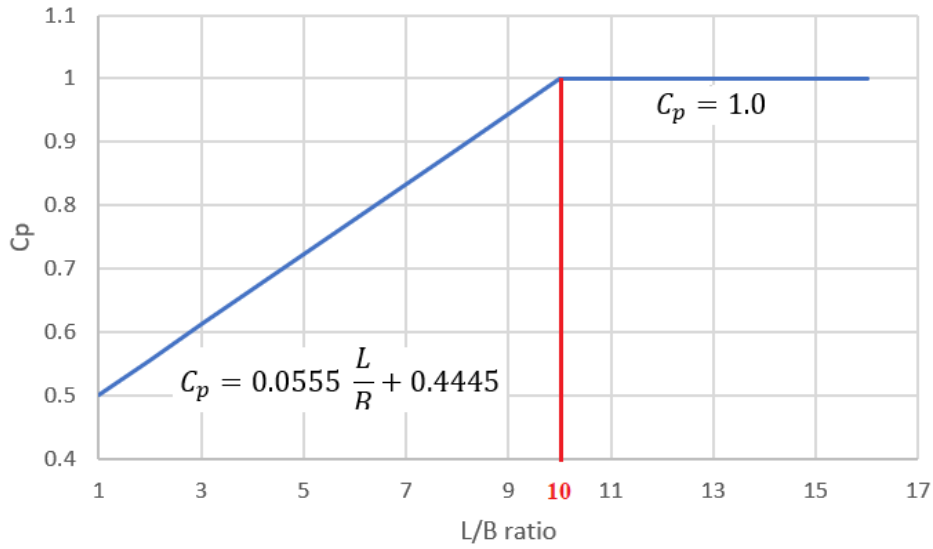


Fig. 16 C_p -coefficient as a function of L/B ratio

5. Effective overburden pressure at the depth of z_p , at which peak of strain influence factor takes place:

$$\sigma'_{z_p} = z_p \gamma' \quad (47)$$

Where

γ' = submerged unit weight of soil

6. The strain influence factor, I_{z_0} (at the base of any shape of a shallow foundation) is seen in Eq.16. Its value must be between 0.1 and 0.2 (Fig. 17).

$$I_{z_0} = \frac{8}{90} + \frac{1}{90} \left(\frac{L}{B} \right) \quad \frac{L}{B} \leq 10 \quad (48)$$

As an alternative, I_{z_0} can be taken from Fig.4 as a function of L/B ratio.

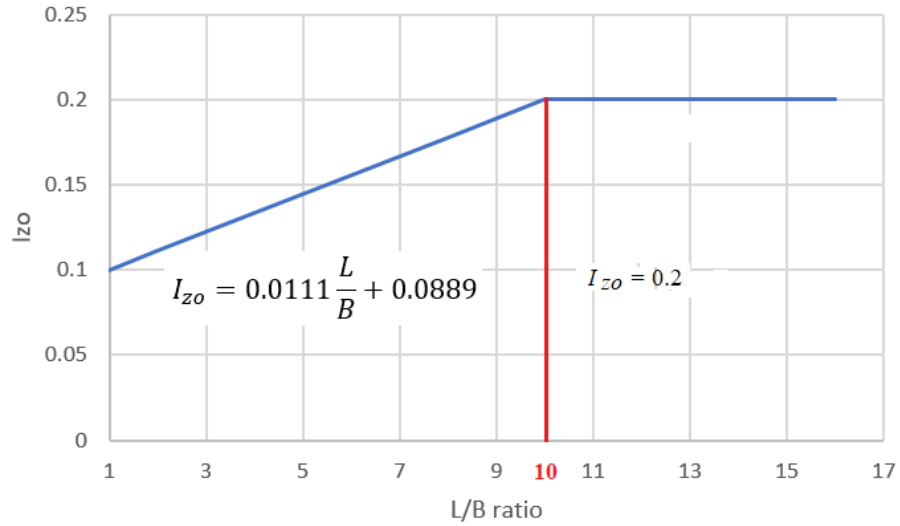


Fig. 17 Variation of I_{zo} as a function of L/B -ratio

7. The peak value of strain influence factor same as Schmertmann et al. (1978) method:

$$I_{zp} = 0.5 + 0.1 \sqrt{\frac{q_{net}}{\sigma'_{zp}}} \quad (49)$$

8. Depth z_{max} at which the strain influence factor would be reduced to zero.

$$z_{max} = \frac{2}{9}L + \frac{16}{9}B \quad (2B \leq z_{max} \leq 4B) \quad (50)$$

As an alternative Fig.5 can be used to get z_{max} value as follows.

$$z_{max} = B C_m \quad (51)$$

Where C_m is a coefficient that can be taken from Fig.18.

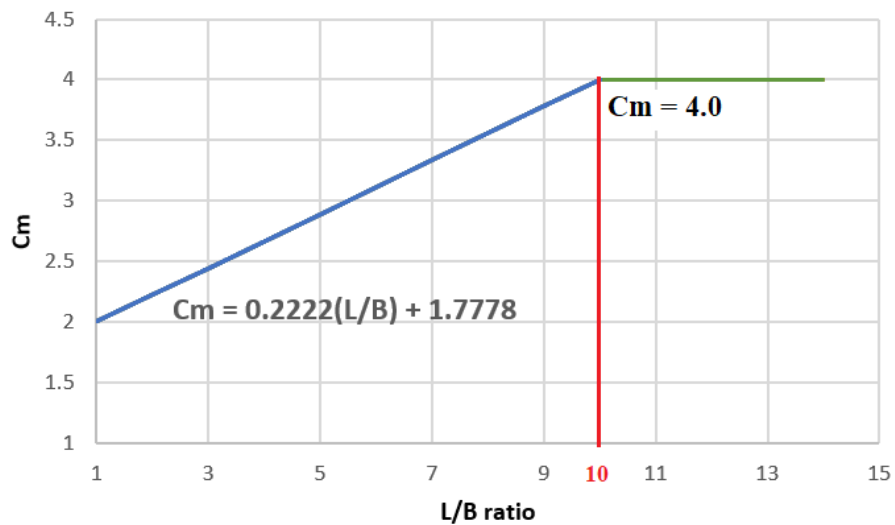


Fig. 18 Coefficient of C_m as a function of L/B ratio

9. Calculation of I_{zi} values on **U-line** in Fig. 15 by Eq. (52)

$$I_{zi} = I_{zo} + \left(\frac{I_{zp} - I_{zo}}{z_p} \right) z_i \quad \text{if } (0 \leq z_i \leq z_p) \quad (52)$$

10. Calculation of I_{zi} values on **L-line** in Fig. 15 by Eq. (53)

$$I_{zi} = I_{zp} - \left(\frac{I_{zp}}{z_{max} - z_p} \right) (z_i - z_p) \quad \text{if } (z_p \leq z_i \leq z_{max}) \quad (53)$$

2. Modulus of elasticity is estimated by tip resistance, q_c , of Cone Penetration Test, CPT, if E_s values are not known Eq. (54).

$$E_s = q_c \left(2.389 + 0.111 \frac{L}{B} \right) \quad \frac{L}{B} \leq 10 \quad (54)$$

Terzaghi, Peck and Mesri, 1996) suggest using the following equation.

$$\frac{E_{s(L/B)}}{E_{s(L/B=1)}} = 1 + 0.4 \log \left(\frac{L}{B} \right) \leq 1.4$$

$$\text{where } E_{s(L/B=1)} = 3.5q_c$$

Note: If the modulus of elasticity of soil layers are known, no need the estimation by Eq. (54).

Elastic (immediate) settlement calculation is same as Schmertmann, et all. (1978) method Eq. (1) seen below:

$$S_e = C_1 C_2 C_3 q_{net} \sum_{i=1}^n \frac{\Delta z_i I_{zi}}{E_{si}} \quad (1)$$

Hypothetical Cases:

Once modification of Schmertmann's method was completed, calculations of the elastic (immediate) settlements became quite simple with a simple computer code prepared. Then, the effect of L/B (length/width ratio) and B (width) on elastic settlement is investigated. For the hypothetical case, the foundation and soil profile seen in Fig. 19 are employed.

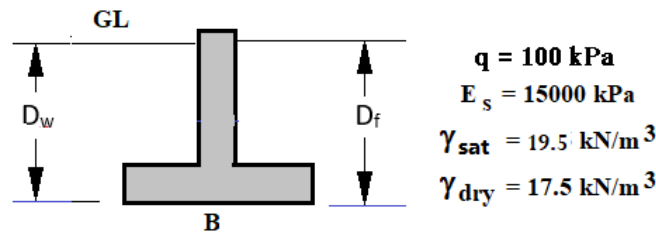


Fig.19 Soil profile and foundations in hypothetical cases

The variation of settlements with L/B starting from 1 to 12 for B = 1, 3, 5 meters have been estimated by the code and plots are given in Fig. 20. As it is seen in Fig. 7, when L/B is increased, settlement increases too until L/B=10. Then, there is no change on the settlement. Similarly, when B is increased, settlement increases too.

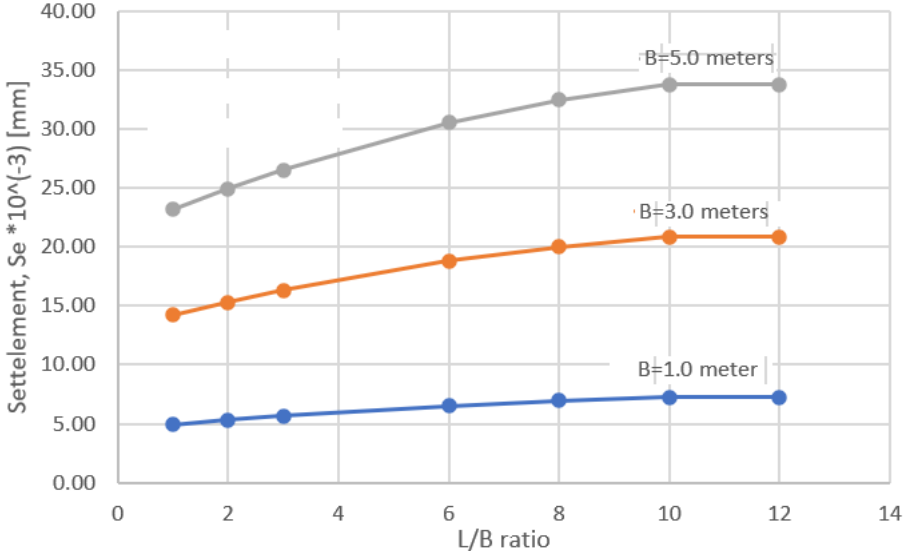


Fig. 20 Settlement/Width versus L/B ratios

However, once the settlements are normalized as $\left(\frac{S_e}{B}\right)$, it has been seen that when B is increased, $\left(\frac{S_e}{B}\right)$ ratios are decreased as seen in Fig. 21.

CONCLUSIONS

The following conclusions are drawn after the analytical and numerical work done in this study.

1. Clear borders among the four zones are established without overlaps. That means borders of the zones given in the technical literature are modified.
2. Zone 4 is divided into two. In other words, zone 4 has been modified and a new zone (zone 5) is defined.

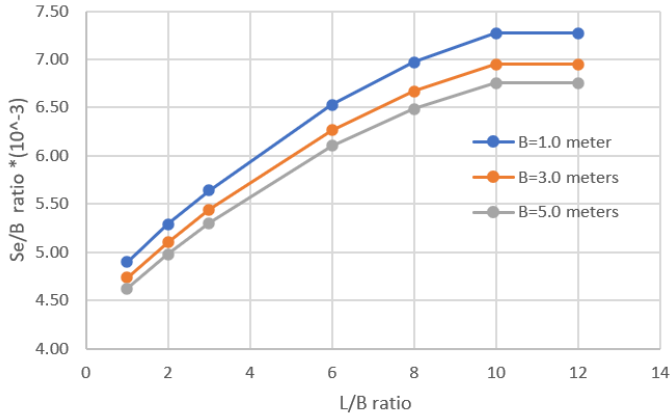


Fig. 21 Settlement/Width versus L/B ratios

1. To check whether the resultant load acts in zone 5 (kern), two more criteria have been derived in addition to one in use.
2. To calculate the effective areas for the defined five zones, formulas have been derived instead of employing the graphs in calculation of effective areas for all of the cases.
3. Since the hand solution of formulas for zone 4, and 5 is impossible, a MATLAB code is generated, and the equations are solved. However, any other numerical technique can be employed to solve the equations of (27) and (28).
4. The Schmertmann, et al (1978) method is modified, and a more convenient approach is proposed, so that there would be no worries about the foundation whether it is an axisymmetric problem or plain strain problem. Also, only two equations would be employed to calculate the strain influence values in place of five equations in the original method.
5. The settlements increase from $L/B = 1$ until it is 10, after that ($L/B > 10$) no more settlement would occur.
6. Settlement/width ratio would be decreasing while the width of footing is increased. This result shows that angular distortion of footings with larger width (B) would be less than the angular distortion of footings with smaller B .

REFERENCES

- Badakhshan E, Noorzad A (2017). A simplified method for prediction of ultimate bearing capacity of eccentrically loaded foundation on geogrid reinforced sand bed. *International Journal of Geosynthetics and Ground Engineering*, 3(2), 1-15.
- Bazaraa ARSS (1967). Use of the Standard Penetration Test for Estimating Settlements of Shallow Foundations on Sand. Ph.D. Thesis, University of Illinois, Champaign-Urbana, Illinois.
- Bjerrum L, Eggstad A (1963). Interpretation of load test on sand. *European Conference on Soil Mechanics and Foundation Engineering*, Weisbaden, West Germany, 1, 199.
- Burland JB, Burbidge MC (1985). Settlement of foundations on sand and gravel. *Institution of Civil Engineers*, 78(1), 1325-1381.
- Das BM, Atalar C, Shin FC (2009). Developments in elastic settlement estimation procedures for shallow foundations on granular soil. *2nd International Conference on New Developments in Soil Mechanics and Geotechnical Engineering*, Near East University, Nicosia, North Cyprus, 9-41.
- Das MB (2007). *Principles of Foundation Engineering*. 6th edition, CENGAGE Learning, Hampshire, UK.
- DeBeer E, Martens A (1957). Method of computation of an upper limit for the influence of heterogeneity of sand layers in the settlement of bridges. *4th International Conference on Soil Mechanics and Foundation Engineering*, London, 1, 275-281.
- DeBeer EE (1965). Bearing capacity and settlement of shallow foundations on sand. *Symposium on Bearing Capacity Settlement of Foundations*, Duke University, Durham, NC, 15-33.
- Highter WH, Anders JC (1985). Dimensioning footings subjected to eccentric loads. *Journal of geotechnical engineering*. *Journal of Geotechnical Engineering*, ASCE, 111(5), 659-665.
- Jeyapalan JK, Boehm R (1986). Procedures for predicting settlements in sands. In W.O. Martin (ed.), *Settlements of Shallow Foundations on Cohesionless Soils: Design and Performance*, ASCE, Seattle, 1-22.
- Krabbenhoft S, Damkilde L, Krabbenhoft H (2012). Lower-bound calculations of the bearing capacity of eccentrically loaded footings in cohesionless soil. *Canadian Geotechnical Journal*, 49(3), 298-310.
- Loukidis D, Chakraborty T, Salgado R (2008). Bearing capacity of strip footings on purely frictional soil under eccentric and inclined loads. *Canadian Geotechnical Journal*, 45(6), 768-787.
- Meyerhof GG (1953). The bearing capacity of foundations under eccentric and inclined loads. *Proceedings, 3rd International Conference on Soil Mechanics and Foundation Engineering*, Zurich, Vol. 1, 440-445.
- Meyerhof GG (1963). Some recent research on the bearing capacity of foundations. *Canadian Geotechnical Journal*, 1(1), 16-26.
- Papadopoulos BP (1992). Settlements of shallow foundations on cohesionless soils. *Journal of Geotechnical Engineering*, ASCE, 118(3), 377-393.

Prakash S, Saran S (1971). Bearing capacity of eccentrically loaded footings, Journal of the Soil Mechanics and Foundation Division, ASCE, 97(SM1), 95-117.

Sahu R, Patra CR, Sobhan K, Das BM (2019). Ultimate Bearing Capacity Prediction of Eccentrically Loaded Rectangular Foundation on Reinforced Sand by ANN. In: Meguid M, Guler E, Giroud J (eds) Advances in Geosynthetic Engineering. GeoMEast 2018. Sustainable Civil Infrastructures. Springer, Cham.

Schmertmann JH, Hartman JP, Brown PR (1978). Improved strain influence factor diagrams. Journal of Geotechnical Engineering Division, ASCE, 104(8), 1131-1135.

Terzaghi K (1943). Theoretical Soil Mechanics. Wiley, New York.

Terzaghi K, Peck RB (1948). Soil Mechanics in Engineering Practice. 1st Edition, John Wiley and Sons, New York.

Terzaghi K, Peck RB, Mesri G (1996). Soil Mechanics in Engineering Practice. 3rd Edition, John Wiley & Sons, New York.

Vesic AS (1973). Analysis of ultimate loads of shallow foundations. Journal of the Soil Mechanics and Foundation Division, ASCE, 99(SM1), 45-73

Evidential Fuzzy Multi-Criteria Decision Making Based On Belief Entropy

Galip Cihan YALÇIN¹

Introduction

The decision-making process is the process of selecting the best alternative by evaluating alternatives according to one or more criteria. The decision maker will need to combine the data at hand while evaluating the alternatives according to the criteria. Data aggregation is the process of obtaining information about different situations or events from various and different data sources and then integrating them from a single data source to reach final results with higher accuracy. In other words, data aggregation is an approach to handle various sources of information that are imperfect in various ways, and ultimately to obtain a clearer view of the situation, thus reducing uncertainty. Much of this data to be combined is uncertain. Common causes of uncertainty are imprecision, randomness and vagueness. We can express the errors arising from the measurements made as the state of being imprecise. The reason for ambiguity is the uncertainties arising from verbal or linguistic expressions such as "good", "bad" during decision making. There are many methods developed to combat situations such as incompleteness, uncertainty and inconsistency that negatively affect the decision-making process. The basis of these methods is Probability Theory, Fuzzy Set Theory and Dempster-Shafer Mathematical Proof Theory. And the main purpose of these methods is to combat the uncertainty in the decision-making process. Among these methods, Fuzzy Set Theory and DST are the strongest theories (Kalci, 2008). Fuzzy Set Theory helps to select the most appropriate evidence from different sources at different times, while DST helps consolidate evidence for the final assignment process (Chatterjee & Namin, 2021).

Fuzzy sets, rough sets, DST and many similar methods are used to identify information that is currently uncertain. And many of these methods can be translated into a framework on evidence theory. DST stands out because it can better represent information that is uncertain by using basic probability assignment (bpa) and applying uncertainty reasoning. DST not only provides a mathematical framework for modeling uncertainty, but also provides a method of combining data from different sources (Deng, Xiao & Deng, 2017). DST can effectively combine the uncertainty of conflict information, but it still has some shortcomings in conflict between different sources of evidence (Xiong, Su & Qian, 2021). DST offers several advantages, including the ability to transfer probabilistic measures to focal elements and assign probabilistic values to the proof-of-discrimination framework (Chatterjee & Namin, 2021).

Method

DST, which emerged with A.P.Dempster's work on determining the lower and upper limits of probability in 1967, was developed in 1976 with some additions in G.Shafer's book titled Mathematical Theory of Proof. At the beginning of these additions; opinion function (belief function) definition comes. For this reason, the theory was named DST, taking the name of both

¹ PhD. Student, Kirikkale University, Institute of Science and Technology, Mathematics Program, Kirikkale, Turkiye,

fathers of ideas. This theory is a numerical method and was developed to deal with incomplete and uncertain information. DST has successful applications in many areas from artificial intelligence to medical diagnosis, from statistical classification to data fusion, from face identification to risk assessment, from target identification to multi-criteria decision analysis (Çerçioğlu, 2004). DST has been widely studied and applied because of its advantage of effectively handling uncertainty problems in combining multi-source information. Many in-depth studies have been carried out with DST, which is presented as an effective method to solve the uncertainty problem (Zhu & Xiao, 2021).

As an extension of probability theory, proof theory can better handle unknown and imprecise information. Because of its advantages, evidence theory has more flexibility and efficiency for modeling and processing uncertain information. The uncertainty measurement plays an important role in both evidence theory and probability theory. In probability theory, Shannon entropy provides a new perspective for measuring uncertainty. Various entropies are available to measure the uncertainty of the bpa in proof theory (Deng, Xiao & Deng, 2017).

DST is an advanced version of Bayesian probability theory. It has the advantage of showing "uncertainty" by distributing probability to multiple event hypotheses rather than a single event (Zhu & Xiao, 2021). There are some features that distinguish Bayesian inference and DST, which has many common denominators. In Bayesian inference, the weights assigned to the situations are called "probability", while in DST they are called "mass". The most important distinguishing feature is; In DST, there is no obligation to give a clear value to the variables as in Bayesian inference. For example, in Bayesian inference, everything takes a net value such as "0" and "1", "black" and "white", while in DST it can take any value between 0 and 1 (Seçkin, 2015).

If Θ is a set containing all possible possible values of a variable and the elements in Θ are mutually exclusive, then Θ is referred to as the perceptual frame (Xiong, Su & Qian, 2021).

Considering Θ ($\Theta = \{A_1, A_2, \dots, A_i, \dots, A_N\}$) as the frame of discernment and 2^Θ ($2^\Theta = \{\emptyset, \{A_1\}, \{A_2\}, \dots, \{A_N\}, \{A_1, A_2\}, \dots, \{A_1, A_2, \dots, A_i\}, \dots, \Theta\}$) as all subsets of Θ , the function in $m: 2^\Theta \rightarrow [0,1]$ format is a bpa function if the following conditions are met (Büyükyazıcı & Sucu, 2009):

$$m(\emptyset) = 0$$

$$\sum_{x \in 2^\Theta} m(x) = 1$$

We can define the values of the bpa function here as the probabilities of each element in the frame of discernment Θ . The function m is called the function bpa and $m(x)$ is called the fundamental probability of x (Xiong, Su & Qian, 2021).

When x is treated as any subset of Θ and the fundamental probability value is different from 0, x is a focal element (Xiong, Su & Qian, 2021). The value received for any focus element belonging to the belief function is called the degree of belief (Büyükyazıcı & Sucu, 2009).

There are two confidence criteria: the belief function (bel) and the plausibility (pls) function. As the first confidence criterion, the one-to-one opinion function is defined as $bel: 2^\Theta \rightarrow [0,1]$

and this value is obtained from the sums of the propositions in question (Beynon, Curry & Morgan, 2000).

$$bel(A) = \sum_{B \subseteq A} m(B), \quad \forall A \subseteq \theta$$

Another of the confidence criteria, the one-to-one plausibility (pls) function, is defined as $pls: 2^\theta \rightarrow [0,1]$.

$$pls(A) = 1 - bel(\bar{B}) = \sum_{B \cap A \neq \emptyset} m(B), \quad \forall A \subseteq \theta$$

$bel(A)$ and $pls(A)$ are lower and upper limits of function A . The lower limit indicates the degree of support for the hypothesis, and the upper limit indicates the maximum degree of support expected to be assigned to the hypothesis (Xiao, 2020).

The relationships between the variables whose mass values are observed and their relationships with the values obtained from previous observations are made using Dempster's rule of combination (Çavdur, 2005). Information obtained from different information sources can be easily combined with the Dempster's rule of combination (Xiong, Su & Qian, 2021).

When the independent evidence sources m_1 and m_2 are combined, the $m = m_1 \oplus m_2: 2^\theta \rightarrow [0, 1]$ toa function is obtained (Xiao, 2020). The \oplus operator has commutation and union properties (Tong, Xu & Denœux, 2021).

$$m(A) = \begin{cases} 0 & A = \emptyset \\ \frac{\sum_{B,C \in 2^\theta | B \cap C = A} m_1(B)m_2(C)}{1 - K} & A \neq \emptyset \end{cases}$$

Here K can be expressed as the conflict coefficient (amount of conflict) between m_1 and m_2 and is calculated with the help of the following formula:

$$K = \sum_{B,C \in 2^\theta | B \cap C = \emptyset} m_1(B)m_2(C)$$

The operations in the DST method are shown below step by step:

Step-1: Alternatives are given values in line with the verbal expressions shown below by the decision makers (Shemshadi et al., 2011):

Table 1. Linguistic variables for the fuzzy rates of the alternatives

Linguistic Variables	Abbreviations	Fuzzy Number Values
Very Poor	VP	(0.0, 0.0, 0.1, 0.2)
Poor	P	(0.1, 0.2, 0.2, 0.3)
Medium Poor	MP	(0.2, 0.3, 0.4, 0.5)
Fair	F	(0.4, 0.5, 0.5, 0.6)
Medium Good	MG	(0.5, 0.6, 0.7, 0.8)
Good	G	(0.7, 0.8, 0.8, 0.9)
Very Good	VG	(0.8, 0.9, 1.0, 1.0)

Step-2: A decision matrix is created by assigning fuzzy number values to linguistic variables.

Step-3: The decision matrix of the criteria is created.

$$W = [w_1 \dots w_j \dots w_n]$$

In addition, the decision matrix containing the values taken by the *i th* alternative according to the *j th* criterion is prepared by the *k th* decision maker.

$$\tilde{X}_k = \begin{bmatrix} \tilde{x}_{11k} & \dots & \tilde{x}_{1jk} & \dots & \tilde{x}_{1nk} \\ \vdots & \dots & \vdots & \dots & \vdots \\ \tilde{x}_{i1k} & \dots & \tilde{x}_{ijk} & \dots & \tilde{x}_{ink} \\ \vdots & \dots & \vdots & \dots & \vdots \\ \tilde{x}_{m1k} & \dots & \tilde{x}_{mjk} & \dots & \tilde{x}_{mnk} \end{bmatrix}$$

Step-4: The elements of the weighted decision matrix are calculated with the following formulas

$$x_{ijk1}^w = x_{ijk1} * w_j$$

$$x_{ijk2}^w = x_{ijk2} * w_j$$

$$x_{ijk3}^w = x_{ijk3} * w_j$$

$$x_{ijk4}^w = x_{ijk4} * w_j$$

The weighted decision matrix is created as follows:

$$\tilde{D}_k = \begin{bmatrix} \tilde{x}_{11k}^w & \dots & \tilde{x}_{1jk}^w & \dots & \tilde{x}_{1nk}^w \\ \vdots & \dots & \vdots & \dots & \vdots \\ \tilde{x}_{i1k}^w & \dots & \tilde{x}_{ijk}^w & \dots & \tilde{x}_{ink}^w \\ \vdots & \dots & \vdots & \dots & \vdots \\ \tilde{x}_{m1k}^w & \dots & \tilde{x}_{mjk}^w & \dots & \tilde{x}_{mnk}^w \end{bmatrix}$$

Step-5: Aggregated weighted decision matrix elements are calculated with the following formulas.

$$x_{ij1}^w = \min_k \{x_{ijk1}^w\}$$

$$x_{ij2}^w = \frac{1}{t} \sum_{k=1}^t x_{ijk2}^w$$

$$x_{ij3}^w = \frac{1}{t} \sum_{k=1}^t x_{ijk3}^w$$

$$x_{ij4}^w = \max_k \{x_{ijk4}^w\}$$

The aggregated weighted decision matrix is created as follows:

$$\tilde{D} = \begin{bmatrix} \tilde{x}_{11}^w & \cdots & \tilde{x}_{1j}^w & \cdots & \tilde{x}_{1n}^w \\ \vdots & \cdots & \vdots & \cdots & \vdots \\ \tilde{x}_{i1}^w & \cdots & \tilde{x}_{ij}^w & \cdots & \tilde{x}_{in}^w \\ \vdots & \cdots & \vdots & \cdots & \vdots \\ \tilde{x}_{m1}^w & \cdots & \tilde{x}_{mj}^w & \cdots & \tilde{x}_{mn}^w \end{bmatrix}$$

Step-6: Combined fuzzy values are calculated separately for benefit and cost criteria. For this, the following formula is used:

$$x_{ij4}^{w+} = \max_i \{x_{ij4}^w\}, \text{ for benefit criteria } (BC_j)$$

$$x_{ij1}^{w-} = \min_i \{x_{ij1}^w\}, \text{ for cost criteria } (CC_j)$$

$$\tilde{x}_{ij}^w = \begin{cases} \left(\frac{x_{ij1}^w}{x_{ij4}^{w+}}, \frac{x_{ij2}^w}{x_{ij4}^{w+}}, \frac{x_{ij3}^w}{x_{ij4}^{w+}}, \frac{x_{ij4}^w}{x_{ij4}^{w+}} \right), \text{ for } BC_j \\ \left(\frac{x_{ij1}^w}{x_{ij1}^{w-}}, \frac{x_{ij2}^w}{x_{ij1}^{w-}}, \frac{x_{ij3}^w}{x_{ij1}^{w-}}, \frac{x_{ij4}^w}{x_{ij1}^{w-}} \right), \text{ for } CC_j \end{cases}$$

The normalized aggregated weighted decision matrix is created as follows:

$$\bar{\tilde{D}} = \begin{bmatrix} \bar{\tilde{x}}_{11}^w & \cdots & \bar{\tilde{x}}_{1j}^w & \cdots & \bar{\tilde{x}}_{1n}^w \\ \vdots & \cdots & \vdots & \cdots & \vdots \\ \bar{\tilde{x}}_{i1}^w & \cdots & \bar{\tilde{x}}_{ij}^w & \cdots & \bar{\tilde{x}}_{in}^w \\ \vdots & \cdots & \vdots & \cdots & \vdots \\ \bar{\tilde{x}}_{m1}^w & \cdots & \bar{\tilde{x}}_{mj}^w & \cdots & \bar{\tilde{x}}_{mn}^w \end{bmatrix}$$

Step-7: The elements of the normalized aggregated decision matrix are calculated with the help of the following formula:

$$Def(\bar{x}_{ij}^w) = \frac{\int \mu(x)xdx}{\int \mu(x)dx} = \frac{\int_{\bar{x}_{ij1}^w}^{\bar{x}_{ij2}^w} \left(\frac{x-\bar{x}_{ij1}^w}{\bar{x}_{ij2}^w-\bar{x}_{ij1}^w} \right) .xdx + \int_{\bar{x}_{ij2}^w}^{\bar{x}_{ij3}^w} xdx + \int_{\bar{x}_{ij3}^w}^{\bar{x}_{ij4}^w} \left(\frac{\bar{x}_{ij4}^w-x}{\bar{x}_{ij4}^w-\bar{x}_{ij3}^w} \right) .xdx}{\int_{\bar{x}_{ij1}^w}^{\bar{x}_{ij2}^w} \left(\frac{x-\bar{x}_{ij1}^w}{\bar{x}_{ij2}^w-\bar{x}_{ij1}^w} \right) dx + \int_{\bar{x}_{ij2}^w}^{\bar{x}_{ij3}^w} dx + \int_{\bar{x}_{ij3}^w}^{\bar{x}_{ij4}^w} \left(\frac{\bar{x}_{ij4}^w-x}{\bar{x}_{ij4}^w-\bar{x}_{ij3}^w} \right) dx} = \frac{-\bar{x}_{ij1}^w\bar{x}_{ij2}^w+\bar{x}_{ij3}^w\bar{x}_{ij4}^w+\frac{1}{3}(\bar{x}_{ij4}^w-\bar{x}_{ij3}^w)^2-\frac{1}{3}(\bar{x}_{ij2}^w-\bar{x}_{ij1}^w)^2}{-\bar{x}_{ij1}^w-\bar{x}_{ij2}^w+\bar{x}_{ij3}^w+\bar{x}_{ij4}^w}$$

The normalized aggregated decision matrix is created as follows:

$$Def(\bar{D}) = \begin{bmatrix} Def(\bar{x}_{11}^w) & \dots & Def(\bar{x}_{1j}^w) & \dots & Def(\bar{x}_{1n}^w) \\ \vdots & \dots & \vdots & \dots & \vdots \\ Def(\bar{x}_{i1}^w) & \dots & Def(\bar{x}_{ij}^w) & \dots & Def(\bar{x}_{in}^w) \\ \vdots & \dots & \vdots & \dots & \vdots \\ Def(\bar{x}_{m1}^w) & \dots & Def(\bar{x}_{mj}^w) & \dots & Def(\bar{x}_{mn}^w) \end{bmatrix}$$

Step-8: The defuzzification process is performed by applying the following procedure to the normalized aggregated decision matrix elements:

$$\overline{Def}(\bar{x}_{ij}^w) = \frac{Def(\bar{x}_{ij}^w)}{\sum_{s=1}^m Def(\bar{x}_{sj}^w)}, j = 1, 2, \dots, n$$

The defuzzified matrix is created as follows:

$$\overline{Def}(\bar{D}) = \begin{bmatrix} \overline{Def}(\bar{x}_{11}^w) & \dots & \overline{Def}(\bar{x}_{1j}^w) & \dots & \overline{Def}(\bar{x}_{1n}^w) \\ \vdots & \dots & \vdots & \dots & \vdots \\ \overline{Def}(\bar{x}_{i1}^w) & \dots & \overline{Def}(\bar{x}_{ij}^w) & \dots & \overline{Def}(\bar{x}_{in}^w) \\ \vdots & \dots & \vdots & \dots & \vdots \\ \overline{Def}(\bar{x}_{m1}^w) & \dots & \overline{Def}(\bar{x}_{mj}^w) & \dots & \overline{Def}(\bar{x}_{mn}^w) \end{bmatrix}$$

To calculate the degree of uncertainty of the criteria;

Step-9: The belief entropy ($E_a(C_j)$) of the C_j ($j = 1, 2, \dots, n$) criterion is calculated with the following formula (Kang & Deng, 2016):

$$E_a(C_j) = - \sum_{i=1}^m \overline{Def}(\bar{x}_{ij}) \log \frac{\overline{Def}(\bar{x}_{ij})}{2^{|A_i|-1}}$$

As a result of applying the following procedure to the calculated belief entropy, the uncertainty degree of the criterion is calculated:

$$U(C_j) = e^{E_a(C_j)} = e^{- \sum_{i=1}^m \overline{Def}(\bar{x}_{ij}) \log \frac{\overline{Def}(\bar{x}_{ij})}{2^{|A_i|-1}}}$$

Step-10: The degree of uncertainty of the C_j criterion is normalized with the help of the following formula:

$$\bar{U}(C_j) = \frac{U(C_j)}{\sum_{h=1}^n U_h}, j = 1, 2, \dots, n$$

Step-11: In terms of C_j criterion, the bpa value of A_i alternative is calculated with the help of the following formula (Sun, Li & Deng 2020):

$$m_{C_j}(\emptyset) = 0$$

$$m_{C_j}(A_i) = \overline{Def}(\bar{x}_{ij}^w) * (1 - \bar{U}_j)$$

$$m_{C_j}(\Theta) = 1 - \sum_{i=1}^m m_{C_j}(A_i), i = 1, 2, \dots, m; j = 1, 2, \dots, n$$

Step-12: Multiple proofs are combined with Dempster's rule of combination as follows:

$$m_C = ((m_{C_1} \oplus m_{C_2})_1 \oplus \dots \oplus m_{C_n})_{(n-1)}$$

Thus, it returns the belief (confidence) values of the $A_i (i = 1, 2, \dots, m)$ alternatives in terms of the C_j criterion:

$$Bel(A_i) = m_C(A_i)$$

Step-13: A_i alternatives are ranked according to their belief (confidence) values and thus the best alternative is decided:

$$\alpha = \underset{1 \leq i \leq m}{\operatorname{argmax}} \{Bel(A_i)\}$$

Conclusions

In this study, a new method has been described and a different perspective has been brought to multi-criteria decision making methods. The weights of the criteria were determined by the entropy method. The alternatives were listed by evaluating the criteria for each alternative by the decision makers. The values expressed verbally by the decision makers were converted into numerical values and the alternative ordering process was facilitated. This method, which was put forward to combat uncertainty, is preferred more than many multi-criteria decision-making methods because of its superior features.

References

- Beynon, M., Curry, B., & Morgan, P. (2000). The Dempster–Shafer theory of evidence: an alternative approach to multicriteria decision modelling. *Omega*, 28(1), 37-50. doi: [https://doi.org/10.1016/S0305-0483\(99\)00033-X](https://doi.org/10.1016/S0305-0483(99)00033-X).
- Büyükayıcı, M., & Sucu, M. (2009). Matematiksel kanıt kuramı'nda uzlaşma üretici yöntemler için bir çerçeve. *İstatistikçiler Dergisi: İstatistik ve Aktüerya*, 2(1), 19-27.
- Chatterjee, M., & Namin, A. S. (2021). A fuzzy Dempster–Shafer classifier for detecting Web spams. *Journal of Information Security and Applications*, 59, 102793. doi:10.1016/j.jisa.2021.102793.
- Çavdur, F. (2005) Arama Motorları Kullanıcı Oturumlarındaki Konu Değişikliklerinin Tespit ve Tahmin Yöntemleri. Master's Thesis. *Uludağ Üniversitesi Fen Bilimleri Enstitüsü*, Bursa.
- Çerçioğlu, H. (2004). Dempster Shafer Teorisi Kullanılarak Tedarikçi Seçimi Uzman sistemi Uygulaması. Master's Thesis. *İstanbul Teknik Üniversitesi Fen Bilimleri Enstitüsü*, İstanbul.
- Deng, X., Xiao, F., & Deng, Y. (2017). An improved distance-based total uncertainty measure in belief function theory. *Applied Intelligence*, 46(4), 898-915. doi: <https://doi.org/10.1007/s10489-016-0870-3>.
- Kalcı, K. (2008). Gemi Savunma Sistemlerinde Tehdit Değerlendirme ve Silah Atama Uygulamaları. Master's Thesis. *Ankara Üniversitesi Fen Bilimleri Enstitüsü*, Ankara.
- Kang, B., & Deng, Y. (2019). The maximum Deng entropy. *IEEE Access*, 7, 120758-120765. doi: 10.1109/ACCESS.2019.2937679.
- Seçkin, F. (2015). Sürdürülebilir Tedarik Zinciri Yönteminde Alıcı-Tedarikçi Regresyon Seviyelerinin Değerlendirme Kriterlerinin Formülasyonuna Yönelik Bir Model Geliştirilmesi. PhD Thesis. *Hava Harp Okulu Havacılık ve Uzay Teknolojileri Enstitüsü*, İstanbul.
- Shemshadi, A., Shirazi, H., Toreihi, M., & Tarokh, M. J. (2011). A fuzzy VIKOR method for supplier selection based on entropy measure for objective weighting. *Expert systems with applications*, 38(10), 12160-12167. doi: 10.1016/j.eswa.2011.03.027.
- Sun, C., Li, S., & Deng, Y. (2020). Determining weights in multi-criteria decision making based on negation of probability distribution under uncertain environment. *Mathematics*, 8(2), 191. doi: <https://doi.org/10.3390/math8020191>.
- Tong, Z., Xu, P., & Denoeux, T. (2021). An evidential classifier based on Dempster-Shafer theory and deep learning. *Neurocomputing*, 450, 275-293. doi: 10.1016/j.neucom.2021.03.066.
- Xiao, F. (2019). EFMCDM: Evidential fuzzy multicriteria decision making based on belief entropy. *IEEE Transactions on Fuzzy Systems*, 28(7), 1477-1491. doi: 10.1109/TFUZZ.2019.2936368.
- Xiong, L., Su, X., & Qian, H. (2021). Conflicting evidence combination from the perspective of networks. *Information Sciences*, 580, 408-418. doi: <https://doi.org/10.1016/j.ins.2021.08.088>.

Zhu, C., & Xiao, F. (2021). A belief Hellinger distance for D–S evidence theory and its application in pattern recognition. *Engineering Applications of Artificial Intelligence*, 106, 104452. doi: <https://doi.org/10.1016/j.engappai.2021.104452>.

Pandemics

Cihat Furkan Göv¹
Hulya Celik²

INTRODUCTION

The emergence and spread of infectious diseases with pandemic potential has occurred regularly throughout history. Many infectious diseases that lead to pandemics are caused by zoonotic pathogens transmitted to humans due to increased contacts with animals through breeding, hunting and global trade activities. Understanding the mechanisms of transmission of pathogens to humans allowed the creation of methods of preventing and controlling infections. For centuries, the implementation of public health measures such as isolation, quarantine and border control have helped control the spread of infectious diseases and maintain the community structure. Global friction programs of waterborne pathogens, vector-borne diseases and zoonotic spreads in the animal-human interface are of primary importance for rapidly detecting the emergence of infectious threats. In the event of a pandemic, new technologies are needed for rapid diagnostic tests, contact monitoring, reuse of drugs, biological markers of disease severity, and new platforms for the development and production of vaccines. In this research project, we review the major pandemics that have affected humanity throughout history, such as plague, cholera, influenza and coronavirus diseases, how they were contained in the past and how these diseases are managed today.

Virüs

The virus is a small agent that causes infection with only one of the deoxyribo nucleic acid or ribonucleic acids packaged in the protective sheath, which consists of a protein or complex structure. Viruses are not considered alive because they need host cells to grow and multiply. Since viruses do not independently have proliferation mechanisms and molecules, they depend on host cells for reproduction and are considered parasitic cells. Viruses often have a limited host range that they can infect, and viruses can only infect certain bacteria, plants or animals. Viruses depend on the metabolic molecules of the host cell. Viruses alter the host's normal metabolic reactions, allowing new virus particles to form. In order for viruses to survive, they must infect a cell and synthesize their own viral proteins and genetic material by capturing the mechanisms of the cell (Takz,2019).

¹ Ağrı Ibrahim Cecen University, Faculty of Pharmacy Basic Pharmaceutical Sciences Department / Fundamental Sciences of Pharmacy 03200 Agri/TURKEY

² Ağrı Ibrahim Cecen University, Faculty of Pharmacy Basic Pharmaceutical Sciences Department / Fundamental Sciences of Pharmacy 03200 Agri/TURKEY

Ways Viruses Are Transmitted

- Direct contact
- Injection of blood or contaminated liquids
- Tissue transplants
- Respiratory tract
- Fecal-oral pathway

Factors Affecting The Ways Viruses Are Transmitted

- Source of the virus
- Resilience of the virus
- Environmental conditions
- How the virus reaches the target tissues of the body (Basustaoglu,2010).

Proliferation of Viruses

When viruses encounter a host cell that can multiply by entering the body of the living creature, they activate their proliferation mechanisms. When the virus encounters a suitable host cell where it can multiply, it immediately clings to it. After viruses cling to the host cell, certain enzymes are used to break down the cell membrane and transfer genetic material into the cell. This genetic material can be a chain of ribonucleic acid or deoxyribonucleic acid, which contains information that provides the synthesis of proteins necessary to initiate the process of developing new viruses. The genetic material of the virus captures the mechanisms of the cell through enzymes belonging to the virus. The mechanisms of the cell are used to create new genetic material belonging to the virus and to create protein sheaths. New viruses in the cell usually come out when the cell breaks down. When the cell disintegrates, the cell dies. This cycle, which viruses use to multiply and cause the cell to die, is called a lytic (disruptive) cycle.

Viruses with membranes on protein bristles do not choose the way to break down the body in order to multiply. Unlike other viruses, such viruses pass through the cell membrane and enter the cell. These viruses, which enter the cell as a whole, multiply and then come out without breaking down the cell. Once the virus enters the cell, it stores its genetic material as part of the cell deoxyribonucleic acid. In this way, the virus continues to transfer genetic material to the baby cells every time the cell multiplies without revealing its presence to the cell. It can secretly transfer the genetic material of the virus from cell to cell without causing any signs of disease, and suddenly the virus starts the cycle of proliferation. This cycle is called the lysogenic cycle (Freudenric and Kiger 2020).

Pandemi

The word pandemic is derived from the ancient Greek words pan and demos, and 'pan' means 'demos' and people mean (Pandemic). Wikipedia, free encyclopedia,2022).

The effect is not a specific country or region; Infectious diseases that are effective all over the world are called pandemics. According to the World Health Organization, the pandemic is a rapidly spreading and unseasonal infectious disease in which the human population does not have immunological resistance (Qiu et al.2017).

General Characteristics of Pandemics

- Appearance in various geographical areas
- The emergence of many diseases that can be a precursor to infectious diseases
- Caused by mutated viruses
- Inadequate or no social immunity
- Formation of diseases resulting in death
- Causing changes and measures in the lifestyles of society
- Spreading without seasonal conditions (Özkoçak et al. 2020).

Major Pandemics in Human History

Amvâs Tâ:

The plague, which occurred in the Palestinian settlement of Amvâs during the reign of Omar, spread rapidly and was also seen in the territory of Syria and Iraq. Syria was the most common settlement of the epidemic.

The plague of cucumbers spreading in Amvâs is the most common of the plague species. It is defined by the Arabs as a blessing.

Since it appeared in Amvâs, the epidemic was called Amvâs tuânu.

There are three types of this plague, bubonic, septicaemia and pneumonic, caused by a bacterium called *Yersinia pestis*, which passes from one rodent infected with fleas to another. Tâun is a bubonic species also known as cucumber, which is one of the plague species.

The bacterium *pestis*, which enters the human body with the bite of fleas, causes the lymph node to become inflamed and stretched.

In the later stage of the disease, with the growth of lymph nodes, inflamed and severe pain-causing bulges appear in the body

Swelling is more common in the armpits, behind the ear, earlobe and groin areas where the skin is thin in the body

Swellings can be red, yellow, black in color. In the mildest type of the disease, the silus is red in color. With the increase in disease severity, the swellings turn yellow and then black.

In the Middle Ages, medical examiners did not know much about the treatment of taun disease. If the swellings in the bodies of those infected with Taun's disease spontaneously exploded

without intervention and the blood and pus in the boil emptied out, the patient had a chance of recovery. Otherwise, patients usually die within three days.

According to the imam shafi, he thought that the patient would be healthy by applying the ointment obtained by crushing the violet flower in the treatment of taun disease or by boiling the violet and containing it in the patient (Genghis,2020).

Black Plague

The disease was seen between 1347 and 1351. The disease is called black plague because of the appearance of black swelling in the body (Glitter, 2020).

Yersinia pestis is the cause of the plague epidemic that has killed many people in Europe (Jarus,2020).

Doctors who treated the plague also wore some special costumes. The protective costume consisted of a polished fabric coat, a beak-shaped mouthpiece usually filled with herbs, straw and spices, and a mask with a glass eye part. These doctors studied ways to treat blood draw, frog or leech (Byfield, 2010).

Cholera

Cholera is an infection whose factor is *Vibrio Cholerae*, which causes the body to lose high rates of water, showing signs of diarrhoea that starts suddenly and suddenly intensifies. When the bacteria, which is resistant to stomach acid, is taken into the body at high rates with liquid, the bacteria escapes stomach acid and reaches the intestines, causing infection (Undored and Altinbas 2020).

The outbreak was seen in Japan in 1817, Moscow in 1826, Berlin in 1831, Paris and London, Hamburg in 1892 and Canada. Many people have lost their lives in these outbreaks. Treatment for cholera, which has a high mortality rate, is quite simple.

Cholera patients recover in a short time with oral fluid treatment. Salt and glucose mixtures are given to eliminate the lack of electrolytes such as sodium, potassium, chlorine and bicarbonate lost in the treatment and to provide the necessary energy in patients with nutritional problems. In patients whose condition is too severe to meet the nutritional needs, the mixture is applied into the vein. In even more serious and urgent cases, tetracycline and tetracycline-like antibiotics are used (Aslan,2020).

Spanish Flu

The influenza epidemic, a subtype of H1N1 virus, was the cause of the H1N1 virus between 1918 and 1921. The surprising thing about the epidemic is that it affects more healthy young adults than the weak, the elderly and children. The reason the outbreak is called spanish flu is because Spain did not take part in World War I and there was no mention of the outbreak in other European states due to censorship, and the Spanish press brought up the outbreak for the first time (Aslan,2020).

Doctors used vaccines against the *hemophilus influenzae* and pneumococcal species to treat the outbreak. They gave oxygen to the patients. Although they resorted to ancient applications such as bleeding the patient, they could not find a definitive treatment in every intervention.

In order to reduce the spread of the epidemic, measures such as quarantine, isolation, mask use, closure of public areas were taken but were unsuccessful.

The vaccines and drugs used in the treatment were not effective. Although blood transfer from recovering patients to new patients was a silver lining, there was no definitive solution (Temel, 1918).

Hong Kong Flu

The disease was first seen in Hong Kong. It is the influenza epidemic that caused the deaths of nearly 1 million people between 1968 and 1969.

The disease-causing type A H3N2 virus is derived from the H2N2 virus with an antigenic deviation called the merger of many subtypes of the virus to produce different viruses than the original.

The new type of virus carries the genes of H2N2, one of the bird flu virus variants (Aslan, 2020).

Symptoms of Hong Kong flu include fever, muscle pain, weakness. These symptoms usually lasted 4-6 days. The mortality rates of children and elderly patients with Hong Kong flu are high. Although a vaccine for the virus was produced, it benefited after the outbreak affected people on a global scale (Hsieh et al.2006).

Smallpox

Variola virus is the cause of smallpox. Variola virus is in the Poxviridae family. When a case of smallpox is encountered, it is obligatory to be reported internationally. Smallpox falls into the group of infectious diseases among the types of diseases (Özer and Suna 2020).

The first vaccine produced in history is the smallpox vaccine (Badur,2020).

In 1966, as a result of the campaign led by the World Health Organization, the use of smallpox vaccines was mandatory worldwide. The World Health Organization has reported that the infection that causes smallpox worldwide has ceased permanently. The World Health Organization has recommended that the smallpox vaccine be removed from routine practice after the end of the disease. Smallpox is the only disease that has ever ended among human infectious diseases (Özer and Suna 2020).

Swine influenza

The cause of the disease is a virus in the family Orthomyxoviridae. The other name of the disease is "swine influenza virus", i.e. SIV.

Known swine flu types are usually Influenzavirus A, which is rarely type C influenza virus.

Swine flu is constantly changing its structure to spread among humans.

In 2009, an outbreak of swine flu was observed. The outbreak, which began in 2009, originated in Mexico and affected 191 countries worldwide. The outbreak that started in Mexico was caused by H1N1, a subspecies of influenza A virus.

The disease is transmitted to humans from those who come into contact with poultry and pigs closely and without protective clothing. When the meat of the sick animal is cooked under favorable conditions, the disease is not transmitted (Kara, 2010).

Symptoms of the disease are fever, cough without phlegm beats, unbearable pain throughout the body, fever, weakness, shortness of breath and sudden symptoms with a temperature of 38.30 °C. Sudden symptoms are high fever, pain, ache, diarrhea, which develop between 3-6 hours. Although these symptoms vary from person to person, they can usually vary between 4-7 days.

Oseltamivir or zanamivir drugs used to treat flu can be used in the treatment. These drugs should be used within the first 2 days after the onset of symptoms. Drugs should be administered under the supervision of a doctor and used in accordance with risk groups. Paracetamol should be used instead of aspirin as a painkiller. It is not recommended to consume medicines when going abroad for pandemic prevention purposes (Sanli,2010).

Bird Flu

Bird flu is a deadly disease transmitted from animals with the virus. Other names of the disease are Avian Influenza, Pestis Avium, Bird Flu, Avian Flu, Chicken Plague. The type of virus that is deadly to humans is H5N1 (Aslan,2020).

Bird flu is an infectious disease caused by influenza viruses found in birds. Disease-causing viruses are carried in the intestines of birds, are found in their feces and often do not show symptoms of the disease.

The virus that causes bird flu has been proven to be transmitted between pigs and humans, between chickens and humans, but there is no certainty about whether there is transmission between wild birds and humans (Goldrick and Goetz 2007).

Symptoms of the disease include fever, cough, sore throat, muscle aches and pain in the lung. Cases with pneumonia and respiratory distress are at risk of death. The disease is called blue death because the body begins to turn blue when not enough oxygen enters the cells.

There is no definitive treatment for the disease. Protection is provided by vaccination. Animals with disease factors need to be killed. Due to antigen changes in influenza virus, the activity of the virus should be monitored and the content of influenza vaccines should be updated every year (Aslan,2020).

Ongoing Pandemics

Hiv/Aids

The hiv virus is the cause of the disease. Hiv virus is known as the human immunodeficiency virus. Hiv virus affects the mechanisms of the immune system in humans, causing the system to collapse. The disease that hiv virus is a factor in is called AIDS. AIDS is known as acquired immunodeficiency syndrome. AIDS is an infectious disease in the zoonotic group (Undored and Altinbas 2020).

HIV virus, which is a factor in AIDS disease, is the virus that causes the collapse of the immune system by affecting cells involved in vital functions such as T cells, macrophages and dendritic cells, which are auxiliary cells in the human immune system (Özer and Suna 2020).

Ways hiv/aids are transmitted

HIV virus, which is a factor in AIDS disease, is found in the blood of people infected with the highest rates. Genital secretions, phlegm, breast milk, saliva, tears and cerebral spinal fluid may also be a disease factor. The most important factors that are effective in the transmission of the disease factor are blood, genital secretions and breast milk.

Stages and Cemptions of HIV Infection

Primary Infection

Hiv virus, which is a factor in AIDS disease, first acts on macrophage/dendritic cells in submucosal layers;

Approximately 87% of people infected with HIV 2-4 weeks after entering the body show flu-like symptoms. . People infected with this stage have high rates of HIV in their genital fluids and have a high amount of transmission (Lewthwaite and Wilkins 2009).

Serokonversiyon

This period, known as seroconversion, is the stage at which the body begins to produce antibodies to the virus (Card et al.2008).

Asymptomatic Infection

The stage of asymptomatic infection is known as the latent period. At this stage, the disease progresses quite insidiously. It does not show symptoms or symptoms. The duration of this period varies from person to person. The reason for the difference in duration is due to the difference in the health status and immune system functions of the person (Lever,2009).

Advanced HIV Infection/ Clinical AIDS

It is the stage where there is a significant reduction in immune system mechanisms, increased proliferation of HIV virus, cessation of antigen production and increased susceptibility to infections (Hazenberget al.2003).

HIV /AIDS Treatment

The aim of the treatment, known as antiretroviral, is to suppress HIV replication and increase immune functions by using drugs that control the proliferation of HIV virus, to keep the life expectancy of infected people at normal level and to normalize the quality of life. Effective viral suppression has a positive effect on the general health of the community by reducing the risk of disease transmission among individuals (Akgül et al. 2018).

Drugs Used to Treat HIV/ AIDS

Nükleozid Revers Transkriptaz İnhibitörleri (NRTİ)

Nucleoside Revers Transcriptase Inhibitors interact with the catalytic region of the revers transcriptase enzyme found in the HIV virus, a cause of AIDS disease (De Clercq,2007).

Nucleoside Revers Transcriptase Inhibitors have analogues 2',3'-dideoxynucleosine (ddN), and the effects of drugs in this group are similar. After nucleoside Revers Transcriptase Inhibitors enter the cell, they turn into 5'-monophosphate (ddNMP), 5'-diphosphate (ddNDP) and 5'-triphosphates (ddNTP), respectively. The transformation process occurs before ddNMP acts as a competitive inhibitor/alternative substrate of normal deoxynucleoside triphosphate (dNTP).

As a compelling inhibitor of the normal substrate, ddNTP inhibits the merging of the normal substrate with the DNA chain and participates in this chain as an alternative substrate in the form of ddNMP. Thus, it acts as a de-chain terminator (De Clercq,2009).

Non-Nükleozid Revers Transkriptaz Enzim İnhibitörleri (NNRTİ)

The first two classes of Non-Nucleoside Reversal Transcriptase Enzyme Inhibitors are known as 1-[(2hydroxytoxy)methyl]-6-(phenyltycyo)timin-structured compounds i.e. 4,5,000 with HEPT6.7-tetrahydro-5-methylimidazo[4,5,1-jk][1,4]benzodiazepin-2(1H)-on, i.e. TIBO derivatives (Pauwels et al. 1990).

Compounds of this nature primarily interact with the allosteric region of HIV-1 revers transcriptase. The drugs in this group are also called specific inhibitors of HIV-1 (De Clercq,2004).

Protease Inhibitors (PI)

Protease Inhibitors carry a hydroxyethylene skeleton opened by the HIV protease enzyme, which resembles a peptide bond but cannot be opened itself. The mechanism of action of drugs in this group prevents HIV protease from performing its normal function; thus, the proteolytic process of precursor viral proteins to mature viral proteins is prevented (Madruga et al.2007).

Fusion Inhibitors (FI)

Hiv virus, which is a factor of AIDS disease, creates fusion with normal cells thanks to gp41 in the membrane, transferring its viral RNA and viral enzymes to normal cells. Enfuvirtite, a physio inhibitory, was produced to prevent this fusion (Matthews et al. 2004).

The mechanism of action of drugs in this group is to prevent the virus molecule from fusing with the outer cell membrane (De Clercq,2009).

Co-receptor Inhibitors (CRI)

Co-receptor inhibitors must enter the target cells to show their effects, and the correlators used in M (macrophage)-tropical and T (lymphocyte)-tropical HIV lineages) should interact with CCR5 or CXCR4. The mechanism of action of drugs in this group is the interaction of the co-receptor and viral glycoprotein gp120, the interaction of gp120 with the CD4 receptor and the fusion of gp41 and the outer cell membrane (Westby and van der Ryst 2005)

The only CRI drug approved for use is maravirocytose (Perros, 2007), an antagonist ccr5.

Integrators (II)

The enzyme integral has attracted attention in the development of drugs against hiv virus. The first clinically approved integral inhibitor (II) is raltegravir. The effect of raltegarvirin is on thread transfer. This is the effect of elvitegravir. Elvitegravirin is effective in reducing viral loading in people infected with HIV (Sulukan et al. 2009).

Covid-19

Coronaviruses are single-chain, positive polarity, enveloped RNA viruses in the Coronavirinae subfamily of the Coronaviridae family in the Nidovirales class. The reason these viruses are called coronaviruses is due to the latin word "corona", which means "crown" due to the bar-shaped extensions found on the surface of the virus (Chen et al.2020).

The four structural proteins found in coronaviruses - the S (Spike) protein, the E (Envelope) protein, the M (Membrane) protein and the N (Nucleocapsid) protein -- are responsible for the formation of mature virus particles (virions) and the emergence of infection. The S protein is responsible for the formation of spikes on the surface of the coronavirus. The protrusions on the surface are responsible for the virus's adhesion to the host cell septators and its entry into the cell M protein, which allows the virus particle to form with three different transmembrane regions, to allow the virus to curve the cell membrane and bind to the nucleocap. Protein E is involved in the packaging and release of the virus and viral pathogenesis. The N protein contains regions connected to the viral genome in the RNA structure (Alpine and Unal 2020).

Ways Covid-19 Is Transmitted

The main way of transmission of coronavirus is the droplet path. The virus found in respiratory secretions can make the healthy individual sick by direct contact with the mucous membrane, while the infected individual coughs, sneezes or speaks through droplets. In finding a new host for the virus, the contact of another individual is effective with the droplets that the sick individual emits through coughing and sneezing (Gürsu,2020).

Stages and Cemptions of Covid-19 Infection

The severity of infection is divided into 5 groups: asymptomatic infection, mild form, moderate form, severe infection, critical infection.

Asymptomatic Infection

It is defined for cases that have tested positive for coronavirus and do not show clinical symptoms. Asymptomatic infection plays an important role in social transmission. This is due to the absence of clinical symptoms in those infected. Babies and children who do not show clinical symptoms play an important role in interpersonal transmission.

Mild Form Symptoms

Fever, fatigue, muscle pain, cough, sore throat, runny nose, sneezing, symptoms of acute upper respiratory tract

Symptoms of Medium Form

Pneumonia, usually fever and cough, wheezing in some cases

Symptoms of Severe Infection

Dyspnea, central cyanosis, decreased oxygen saturation, hypoxemia

Critical Signs of Infection

Acute respiratory distress syndrome, respiratory failure, multiple organ failure (Happy, 2020).

Covid-19 Treatment

The main goal in the treatment of coronavirus is supportive and symptomatic treatment. First of all, the infected persons should be removed from the community and quarantined. Cases with mild symptoms should be managed by home counseling without going to health centers. In treatment, the body's water and electrolyte level should be kept to a certain extent, nutrition should be taken care of, fever and cough should be checked. In cases where the body does not receive enough oxygen, the face mask, high-flow nasal cannula, oxygen should be provided through non-invasive ventilation. Mechanical ventilation and oxygen support may be required, and kidney replacement therapy may be required in some patients. Antibiotics and antifungal should be used in cases with two or more infections in the body at the same time (Jin et al. 2020).

Vaccines are the most effective way to prevent epidemics in the form of infections. This is because it takes both costly and a long time to develop drugs suitable for treatment. Vaccines are both a way to be used in the prevention of global epidemic diseases (DG et al. 2020).

Drugs Used to Treat Covid-19

Klorokin (CQ), Hidroksiklorokin (HCQ)

Although chloroquine has not been approved by the FDA in the treatment of coronavirus, it has allowed use if doctors deem it appropriate. The FDA has not approved any therapeutic agents or drugs for the treatment and prevention of coronavirus. Clinical efficacy and safety of chloroquine in the treatment of coronavirus is unclear. Since doctors are successful in the treatment of different diseases, they have approved the use of chloroquine.

Hydroxychloroquine is a chloroquine-derived drug. The mechanism of action of the drug inhibits the enzyme polymerase, preventing the merger by interfering with the glycosylation of the virus and cell receptors by increasing the pH of the place where the intracellular digestion of the substance formed and taken by the combination of phagosome and lysosome occurs.

Hydroxychloroquine is recommended in patients who will be monitored with outpatient treatment and treated by hospital in the coronavirus treatment guide of the Ministry of Health in our country.

Favipiravir

Favipiravir RNA viruses have an effect by inhibiting the enzyme RNA-dependent RNA polymerase. Favipiravir is an antiviral drug. Favipiravir forms favipiravir ribofuranosyl-5B-triphosphate, an active form of the body. For this activation process, favipiravir intraselectular phosphoribosylation occurs. Favipiravir ribofuranosyl-5B-triphosphate is a substrate of RNA-dependent RNA polymerase and inhibits RNA polymerase enzyme activity. Since the RNA-dependent RNA polymerase enzyme is found in many RNA viruses, favipiravir expands its spectrum by affecting this enzyme.

Remdesivir

Remdesivir is in the antiviral drug group. It is used in the treatment of Ebola and marburg virus infections. This drug is the precursor to nucleotide analogue, which is metabolized into the intracellular adenosine triphosphate analogue, which inhibits the enzyme viral RNA polymerase. Remdesivir is a wide-spectrum drug. It has a preventive and therapeutic effect in non-clinical studies against coronaviruses.

Lopinavir/ritonavir(LPV/R)

Lopinavir, a combination of ritonavir, is used to treat HIV infection. It is a protease inhibitor, one of the drugs used to treat AIDS. The enzyme protease plays a role in the processing of coronavirus polyprotein. Lopinavir and rheaavirin have contrasting effects against coronavirus separately and together.

Nitazoksanid

The drug nitazoksanid has strong in vitro activity against coronavirus. Apart from the coronavirus, this drug has broad-spectrum antiviral activity against influenza, respiratory syncytial virus, parainfluenza, rotavirus and norovirus. The mechanism of action of the drug is associated with the pathways regulated with the host during the proliferation of the virus.

Tosilizumab

The effect of the drug tosilizumab is caused by monoclonal antibodies due to membrane or inhibiting soluble interleukin-6 receptors (rIL-6). This drug has been approved for use in the treatment of rheumatoid arthritis patients.

İvermektin

Ivermectin is a broad-spectrum FDA-approved drug effective against parasites. It has had an effect on many viruses in studies on the drug. The mechanism of action of the drug ivermectin inhibits the nuclear intake of the host and viral proteins. Ivermectin both acts on some RNA virus infections and has an effect on some DNA viruses. In studies on the drug, the coronavirus has a reducing effect on its effectiveness (Mutlu et al. 2020).

Factors Affecting Viral Pandemics

Vaccines

Viral pandemics can be effectively prevented with inexpensive and effective vaccination strategies. Vaccines protect against pathogens by stimulating primary defense mechanisms.

Vaccination is the process of applying a small amount of an infectious agent, such as viruses or bacteria, to stimulate the immune system to recognize and respond to this agent. Vaccines are often used to prevent infectious diseases. Vaccines are administered by injection. Vaccines are often designed to stimulate the production of antibodies, proteins that neutralize foreign invaders in the body.

To improve the specific immunological system through vaccination, the human body can produce white blood cells (B and T cells) that can fight the pathogen (especially) in response to the immune system, allowing the adaptive immune system to grow.

Since the disease is mostly a new type of virus in virus-induced pandemics, it is impossible to produce a vaccine before the pandemic begins.

In the production of vaccines against pandemics, the disease factor is primarily stated. After the disease factor is determined, it is replicated in the cultural environment and the vaccine is produced. The spread of pandemics increases in the time spent in vaccine production. The vaccine produced is specific to the disease factor determined. Vaccines are effective on the black virus. The treatment of the infected person with the vaccine is limited (Şahin and Demir 2020).

Antiviral Drugs

Antiviral drugs are used in virus-induced infections. It is used in the prevention and treatment of virus-induced infections. In viral pandemics, the treatment of the disease is either through the application of vaccines or the use of antiviral drugs to prevent the disease before the disease occurs (Carrasco et al. 2011).

Virus-Related Protein Use

The protein associated with the virus contains anti-idiotypal antibodies, natural ligands of the receptor and anti-receptor antibodies. The mechanism of action prevents the virus from binding to host cell receptors and entering the cell before the viral infection begins.

Reverse Transcription Inhibitors/ Revers Transcription Inhibitors

Nucleotide or nucleoside analogues, similar to the building blocks of ribonucleic acid or Deoxyribo nucleic acid, are used as antiviral drugs. Since the mechanism of action is not 3'OH in analogues, viral Ribonucleic acid or Deoxyribo blocks enzymes that synthesize nucleic acid.

Antisense

When the virus genome becomes active in the host cell, it produces mRNA molecules that play a role in the synthesis of viral proteins. mRNA production begins by proteins. Antisense are

drugs made from short segments of DNA or RNA that can bind to their viral genomes as a complement and prevent transcription of the viral genome.

Ribozim

When the virus genome becomes active in the host cell, it produces mRNA molecules that play a role in the synthesis of viral proteins. mRNA production begins by proteins. Antisense drugs are drugs made from short segments of DNA or RNA that can bind to their viral genomes as a complement and prevent transcription of the viral genome.

Protease Inhibitors

Protease inhibitors developed for the treatment of HIV/ AIDS and hepatitis C are widely used in the treatment of these diseases. Some viruses break down viral protein chains after translation with the enzyme protease within the target cell, creating virions and spreading them in cells that are not infected with disease factors. Protease inhibitors take effect by inhibiting the enzyme viral protease.

İnterferonlar

Interferons suppress the disease-causing virus factor by strengthening the body's immune system instead of attacking the disease-causing virus factor. Interferon viruses prevent their proliferation. Interferons are signaling proteins produced due to the presence of several viruses in the body. Interferons are cytokines synthesized by cells in viral infection. It shows its effect by enabling communication between cells to strengthen the immune system against disease-causing factors. Interferons have opposite effects on the proliferation of viruses by protecting cells from virus infections.

Conventional Plasma Treatment

Conventional plasma therapy, which is used to treat and prevent epidemic diseases, is the treatment of the disease by taking blood from people who have suffered from the disease, separating antibodies and giving them to sick people (Şahin and Demir 2020).

3. RESULTS AND RECOMMENDATIONS

Pandemic epidemics that are effective worldwide. An epidemic pandemic not only is it widespread and the mortality rate is high, but it is also contagious must be high. Affecting human history pandemic. Although various methods have been applied in the treatment of related diseases for centuries, there is no definitive treatment method. For pandemic there is a unique way of treating the disease. These symptomatic and supportive treatment, lac treatment and vaccination of healthy people pandemic to reduce the effects. Pandemic investments in preventing factors increase, Ar-Thanks to the development of genetic studies, we may face in the future pandemic we strengthen our hand in their dangers.

Acknowledgement

This study was prepared from Cihat Furkan Göv's Research Project Thesis.

4. REFERENCES

- AKGÜL, Ö., ÇALŞKAN, R., & ÖNER, YA (2018). HIV/AIDS: Current Approaches. *Journal of Medical School Clinics* , 1 (1), 19-31.
- ALP, S., & ÜNAL, S. (2020). Pandemic caused by the new coronavirus (SARS-CoV-2): developments and current situation. *Flora Magazine*, 25.
- Aslan, R. (2020). From history to the present, epidemics, pandemics and Covid-19. *Journal of Detail*, 8(85), 35-41.
- Badur, S. (2010). H1N1 epidemiology and virus. *ANKEM Derg* , 24 , 190-5.
- Basustaoglu,A.C,2010.Medical Microbiology.Atlas Bookseller Tic.Ltd.Sti,947,Ankara
- Byfield T. (2010) . Renaissance: God in Man, A.D. 1300 to 1500: But Amid Its Splendors, Night Falls on Medieval Christianity, Christian History Project, p. 37.
- Card, J.J., Amarillas, A., Conner, A., Akers, D.D., Solomon, J., DiClemente, R.J. (2008). *The Complete HIV/AIDS Teaching Kit: With CD-ROM*, Springer Publishing Company, New York, 25-71.
- Carrasco, LR, Lee, VJ, Chen, MI, Matchar, DB, Thompson, JP and Cook, AR (2011). Antiviral stockpiling strategies for future influenza pandemics: a global epidemic-economic perspective. *Journal of the Royal Society Interface* , 8 (62), 1307-1313.
- Genoa, E. (2020). Amvas taunu and its effects that occurred during the Period of Omar. *Journal of Caucasus University Faculty of Theology*, 7(13), 129-150.
- Chen, Y., Liu, Q., & Guo, D. (2020). Emerging coronaviruses: genome structure, replication, and pathogenesis. *Journal of medical virology*, 92(4), 418-423.
- Craig Freudenrich, PhD & Patrick J. Kiger "How Viruses Work" 2020. <https://science.howstuffworks.com/life/cellular-microscopic/virus-human.htm>
- (Accessed:14 February 2022)
- De Clercq, E. (2004). Non-nucleoside reverse transcriptase inhibitors (NNRTIs): past, present, and future. *Chemistry & biodiversity*, 1(1), 44-64.
- De Clercq, E. (2007). "Anti-HIV drugs" *Verh. K. Acad. Healed. Belgian*, 69, 81-104.
- De Clercq, E. (2009). Anti-HIV drugs: 25 compounds approved within 25 years after the discovery of HIV. *International journal of antimicrobial agents*, 33(4), 307-320.
- DG, A., HJ, S., & MH, K. (2020). Lee S, Kim HS, Myoung J, et al. Current Status of Epidemiology, Diagnosis, Therapeutics, and Vaccines for Novel Coronavirus Disease 2019 (COVID-19). *J Microbiol Biotechnol [Internet]*, 30(3), 313-24.
- Goldrick, BA and Goetz, AM (2007). Pandemic flu: what infection control specialists need to know. *American journal of infection control* , 35 (1), 7-13.

GÜRSU, E. (2020). Coronavirus Pandemisi. https://www.researchgate.net/profile/ElifGuersu/publication/341599760_Koronavirus_Pandemisi_ve_SarsCoV2_Virusune_Genel_Bakis/links/5ec95c0392851c11a8820702/Koronavirues-Pandemisi-ve-Sars-CoV-2-Virusuene-Genel-Bakis.pdf

Hazenberg, MD, Otto, SA, van Benthem, BH, Roos, MT, Coutinho, RA, Lange, JM, ... & Miedema, F. (2003). Permanent immune activation in HIV-1 infection is associated with progression to AIDS. *Aid*, 17 (13), 1881-1888.

Hsieh, YC, Wu, TZ, Liu, DP, Shao, PL, Chang, LY, Lu, CY, ... & Huang, LM (2006). Flu outbreaks: past, present and future. *Journal of formosan Medical Association*, 105 (1), 1-6.

Jarus O. 20 of the worst epidemics and pandemics in history. Live Science, All About History March 20, 2020. <https://www.livescience.com/worst-epidemics-and-pandemics-in-history.html>

(Access 16.02.2022)

Jin, YH, Cai, L., Cheng, ZS, Cheng, H., Deng, T., Fan, YP, ... & Wang, XH (2020). A quick recommendation guide to the diagnosis and treatment of pneumonia (standard version) infected with the new coronavirus (2019-nCoV) in 2020. *Military Medical Research*, 7 (1), 1-23.

Kara, A. (2010). Swine Flu (Pandemic Influenza 2009, Influenza 2009 H1N1). *Journal of Child Health and Diseases*, 53(1).

Kutlu, R. (2020). What we have learned about the new coronavirus pandemic, current approaches to diagnosis and treatment and the situation in Turkey. *Turkish Journal of Family Medicine and Primary Care*, 14(2), 329-344.

Lever, AM (2009). HIV: virus. *Medicine*, 37 (7), 313-316.

Lewthwaite, P. and Wilkins, E. (2009). Natural history of HIV/AIDS. *Medicine*, 37 (7), 333-337.

Madruça, J. V., Cahn, P., Grinsztejn, B., Haubrich, R., Lalezari, J., Mills, A., ... & DUET-1 Study Group. (2007). Efficacy and safety of TMC125 (etravirine) in treatment-experienced HIV-1-infected patients in DUET-1: 24-week results from a randomised, double-blind, placebo-controlled trial. *The Lancet*, 370(9581), 29-38.

Matthews, T., Salgo, M., Greenberg, M., Chung, J., DeMasi, R., & Bolognesi, D. (2004). Enfuvirtide: the first therapy to inhibit the entry of HIV-1 into host CD4 lymphocytes. *Nature reviews Drug discovery*, 3(3), 215-225.

MUTLU, O., UYGUN, İ., & ERDEN, F. (2020). Drugs used to treat coronavirus disease (COVID-19). *Kocaeli University Journal of Health Sciences*, 6(3), 167-173.

Özer, M., & Suna, H. E. (2020). Covid-19 pandemic and education. Şeker, Özer, A. and C. Korkut (Der.), *Anatomy of the global epidemic: Within the future of man and society*, 171-192.

Özkoçak, V., Koç, F., & Gültekin, T. (2020). Anthropological View of Pandemics: Example of coronavirus (Covid-19). *Electronic Turkish Studies*, 15 (2).

Pandemic. Wikipedia, liberation. <https://tr.wikipedia.org/wiki/Pandemi>(Access:14.02.2020)

Glitter, H. (2020). Infectious disease outbreaks in history. *Tepecik Education and Research Hospital Journal*, 30, 19-26.

Pauwels, R., Andries, K., Desmyter, J., Schols, D., Kukla, M. J., Breslin, H. J., ... & Janssen, P. A. (1990). Potent and selective inhibition of HIV-1 replication in vitro by a novel series of TIBO derivatives. *Nature*, 343(6257), 470-474.

Perros, M. (2007). CCR5 antagonists for hiv infection and AIDS treatment. *Advances in Antiviral Drug Design* , 5 , 185-212.

Qiu, W., Rutherford, S., Mao, A., & Chu, C. (2017). Pandemic and its effects. *Health, culture and society* , 9 , 1-11.

SULUKAN, E. E., KÜÇÜKOĞLU, K., & GÜL, H. İ. (2009). AIDS and the drugs used to treat it. *Ankara Faculty of Pharmacy Journal*,38 (1) 47- 78.

Şahin, F., & Demir, S. (2020). Viruses, Factors and Consequences Affecting Viral Pandemics. Muzaffer Şeker, Ali Özer and Cem Korkut. *Turkish Academy of Sciences*, 55-76.

Sanlı, K. (2010). Influenza virus and swine flu. *Istanbul Legal Sultan Suleyman Medical Journal (IKSST)*, 2(1), 4-12.

Don't wear it, S. (2019). Review of Virus Subject in Secondary Education from the Point of View of Program, Teacher and Student. Master's Thesis, Hacettepe University Institute of Educational Sciences, Ankara.

UNMASKED, Ö. L., & ALTINBAS, SK (2020). Microorganisms existed long ago on the blue planet: the history of pandemics. *Turkish Journal of Women's Health and Neonatology* , 2 (2), 53-69.

Temel, M. K. (1918). Flu Pandemic. Istanbul University Institute of Health Sciences Master's Thesis, Istanbul.

Westby, M., & van der Ryst, E. (2005). CCR5 antagonists: host-targeted antivirals for the treatment of HIV infection. *Antiviral chemistry and chemotherapy*, 16(6), 339-354.

An Application of Distributed Order Differential Equations to a HIV Infection Model

Mehmet KOCABIYIK¹
Mevlüde YAKIT ONGUN²
İlkem TURHAN ÇETİNKAYA³

1. Introduction

In many fields of science and engineering, fractional differential equations are frequently encountered. Since fractional order differential equations are more realistic than ordinary differential equations, the researches give more attention to this subject, recently. The distributed order differential equations (DODEs) are also one of the important subjects in fracture analysis because of the density function included. Detailed information about distributed order fractional operators and their applications is given in (Ding et al., 2021). A numerical method for the DODEs in which the derivative is Caputo type is presented in (Diethelm & Ford, 2009). Some theorems are given for the convergence of the presented method. The study is supported by numerical examples. Dielectric induction and diffusion problems are modeled by DODEs in (Caputo, 2001). Katsikadelis presented a numerical method to linear and non-linear distributed order fractional differential equations in (Katsikadelis, 2014). Another efficient method for linear and non-linear distributed order fractional differential equations is presented in (Jibenja et al., 2018). This method is based on a hybrid of block-pulse functions and Taylor polynomials. The effectiveness of the method is presented by numerical examples. Najafi et.al. gives detailed theorems and definitions about distributed order fractional differential equations including non-negative density function in (Najafi et al., 2011). The proposed procedure is applied to a model of the solar-wind-driven magnetosphere-ionosphere to check the stability.

Many methods are available in literature to solve mathematical models. NSFD schemes developed by Mickens are very popular methods in solving differential equations leads from engineering and science (Mickens, 1989; Mickens, 1994; Mickens, 2002). The method is very popular since it is simple to construct and it gives opportunity to resolve the numerical instabilities. The basic procedure for determining denominator function and some applications is given in (Mickens, 2007). For detailed literature survey, one can check (Patidar, 2005; Patidar, 2016).

Recent studies show that NSFD schemes can be applied to the DODEs. A model of distributed order fractional multi strain Tuberculosis is considered in (Sweilam et al., 2020). The system of differential equation is discretized by NSFD scheme and midpoint quadrature. Numerical simulations are presented. A smoking model of distributed order is presented in (Kocabiyik & Ogun, 2021). NSFD shemes are used to discrete the model. Some theorems are given to analyze the stability of the model. Numerical simulations and phase portraits are presented. To present the

¹ Res. Asst., Burdur Mehmet Akif Ersoy University, Department of Mathematics, Orcid: 0000-0002- 7701-6946.

² Prof. Dr., Süleyman Demirel University, Department of Mathematics, Orcid: 0000-0003-2363-9395.

³ Asst. Prof. Dr., Kütahya Dumlupınar University, Department of Mathematics, Orcid: 0000-0002-5520-310X.

effect of the NSFD schemes, comparison with another two methods is done. A distributed order Malaria-Ross model is presented in (Kocabiyik, 2022). The model is discretized by NSFD schemes. In the view of the Jury conditions, the stability analysis is examined. As another example of DODE, SVIR model can be given (Kocabiyik et al., 2021). Numerical analysis and stability analysis is presented by using NSFD schemes. The numerical results for the different density functions are presented in graphical form.

In this study, it is aimed to give an application of DODEs on a biological model. So, the nonlinear system of ordinary differential equation given in (Perelson et al., 1993) and (Perelson & Nelson, 1999) is considered. The model presents the effect of the HIV infection on CD4⁺ T cells which has an important role on immune regulation. The same model is considered in (Ogun & Turhan, 2013) and it is approached by NSFD schemes developed by Mickens (Mickens, 1990) and (Mickens, 1993). They also present the stability analysis of the model. In this study, we rewrite the HIV model in distributed order form. The distributed order model is discretized by NFDS schemes. The equilibrium points are determined and stability analysis is performed. The detailed comparison is presented with the results obtained in (Ogun & Turhan, 2013).

2. Basic Definitions on Differential Equations of Fractional and Distributed Order

This section presents the basic definitions of fractional and DODEs. Some of them can be listed as below:

Definition 2.1. (Podlubny, 1999) Assume that $f(t)$ is a continuous in the range of $[a, t]$ and $(n+1)$ -th times differentiable function. Let n be an integer and a satisfy $n < a < n + 1$. Then Grünwald-Letnikov fractional derivatives of order α is defined by

$$\begin{aligned} {}_{GL}D_t^\alpha f(t) &= \lim_{h \rightarrow 0} b^{-\alpha} \sum_{i=0}^n (-1)^k \binom{\alpha}{i} f(t-ih) \\ &= \sum_{k=0}^n \frac{(t-a)^{-\alpha+k} f^{(k)}(a)}{\Gamma(-\alpha+k+1)} + \frac{1}{\Gamma(-\alpha+n+1)} \int_a^t (t-\tau)^{n-\alpha} f^{(n+1)}(\tau) d\tau. \end{aligned}$$

Definition 2.2. (Podlubny, 1999) Assume that $f(t)$ is an integrable function in the range of $[a, t]$ and $n-1 < \alpha \leq n, n \in \mathbb{N}^+$ Then, Riemann Liouville fractional derivative of order α is defined by

$${}_{RL}D_t^\alpha f(t) = \frac{1}{\Gamma(n-\alpha)} \frac{d^n}{dt^n} \int_a^t \frac{f^{(n)}(\tau)}{(t-\tau)^{\alpha-n+1}} d\tau.$$

Definition 2.3. (Podlubny, 1999) Assume that $f(t)$ is an integrable function in the range of $[a, t]$ and $n-1 < \alpha \leq n, n \in \mathbb{N}^+$. Then, Caputo fractional derivative of order α is defined by

$${}_CD_t^\alpha f(t) = \frac{1}{\Gamma(n-\alpha)} \int_a^t \frac{f^{(n)}(\tau)}{(t-\tau)^{\alpha-n+1}} d\tau.$$

Let us give the definition of approximate Grünwald-Letnikov formula since it will be used in this study:

Definition 2.4. (Meerschaert & Tadjeran) For DODEs, the approximate Grünwald-Letnikov formula is defined as

$${}_{GL}D_t^\alpha f(t) = \lim_{b \rightarrow 0} b^{-\alpha} \sum_{i=0}^n (-1)^i \binom{\alpha}{i} f(t-ib)$$

or

$${}_{GL}D_t^\alpha f(t) = \sum_{i=0}^n q_i^\alpha f(t_{n-i}), n = 1, 2, \dots, \frac{t-\alpha}{b},$$

where b is very small; and for $i = 0, 1, 2, \dots, n$, $q_i^\alpha = \left(1 - \frac{1+\alpha}{i}\right) q_{i-1}^\alpha$ and $q_0^\alpha = b^{-\alpha}$. (Dorciak, 1994).

3.An Application of DODEs

In this section, an epidemic model for the HIV infections of CD4⁺ T cells given in (Perelson et.al., 1993) and (Perelson & Nelson, 1999) is considered. The model is converted to the distributed order form. The model is discretized by using NSFD schemes. Equilibrium points and Jacobian matrix of the discrete model are determined. Applying Schur-Cohn criteria, the stability analysis is presented. Also, some numerical comparisons are given to present the effect of the NSFD schemes for different step sizes.

The reason of the prefer NSFD schemes which is first developed in 1989 by Mickens (Mickens, 1989) is to be a very useful method since it has a big role in dynamical consistency. Also, NSFD schemes lead to obtain the effective results with less effort.

Let us give short procedure about the application of the NSFD schemes to an ordinary differential equation. Taking into consideration of the first order ordinary differential equation given as

$$\frac{dx}{dt} = g(x, \lambda),$$

the discretization procedure can be expressed in the following form:

$$t \rightarrow t_n, x(t) \rightarrow x_n, g(t) \rightarrow g(t_n), \frac{dx}{dt} \rightarrow \frac{x_{n+1} - x_n}{\psi},$$

where λ is a parameter and ψ is the denominator function which can be determined as

$$\psi = \frac{1 - e^{-b\kappa}}{\kappa}.$$

One can see more details about constructing NSFD schemes, determining denominator functions and the extended applications of the method in (Mickens,1989; Mickens, 1994, Mickens; 2002; Mickens, 2005; Mickens 2007).

3.1.Discretization of Distributed Order Model

In this section, we rewrite the model of HIV infections of CD4⁺ T cells presented in (Perelson et.al., 1993) and (Perelson & Nelson, 1999) in the form of DODEs as

$$D_t^{d(\alpha)} T(t) = p - \alpha T(t) + rT(t) \left(1 - \frac{T(t)+I(t)}{T_{\max}}\right) - kV(t)T(t)$$

$$D_i^{d(\alpha)} I(t) = kV(t)T(t) - \beta I(t), \quad (1)$$

$$D_i^{d(\alpha)} V(t) = N\beta I(t) - \gamma V(t),$$

where, $T(t)$, $I(t)$ and $V(t)$ are the size of uninfected $CD4^+$ T cells, the size of infected $CD4^+$ T cells by the HIV viruses, and the size of HIV virus particles in the blood, respectively. The positive parameters k and N are the rate constant of infection and number of the produced virus particles by each infected $CD4^+$ T cells (Wang & Li, 2006). The maximum level of $CD4^+$ T cell population in the body and the rate of average specific T-cell growth are denoted by the parameters T_{max} and r (Perelson et.al. 1993). The positive constants p , α , β , and γ denotes the source of $CD4^+$ T cells within the body, the death rate of $CD4^+$ T cells, the death rate of the infected cells, and the rate of viral clearance, respectively (Naresh et.al., 2009), (Nowak & May, 1991) and (Yang & Xiao, 2010). $d(a)$ is the density function.

Applying NSFD schemes to the model (1) and considering approximate Grünwald-Letnikov derivative formula which is obtained by definition of DODE, the following discrete system is obtained:

$$\sum_{k=1}^m \frac{d(\alpha_k)}{m} \sum_{j=0}^{n+1} q_j^{\alpha_k} T_{n+1-i} = p + (r-a)T_{n+1} - r \frac{T_{n+1}}{T_{max}} (T_n + I_n) - kV_n T_{n+1},$$

$$\sum_{k=1}^m \frac{d(\alpha_k)}{m} \sum_{j=0}^{n+1} q_j^{\alpha_k} I_{n+1-i} = kV_n T_n + \beta I_n, \quad (2)$$

$$\sum_{k=1}^m \frac{d(\alpha_k)}{m} \sum_{j=0}^{n+1} q_j^{\alpha_k} V_{n+1-i} = N\beta I_n - \gamma V_n.$$

In this discrete system, for $i = 1, 2, 3$ and $0 < \alpha_k < 1$, it is obtained that $q_0^{\alpha_k} = (\theta_i(b))^{-\alpha_k}$ with approximate Grünwald-Letnikov derivation formula. The expressions $\theta_i(b)$ are the denominator functions obtained by NSFD schemes and for this system, the denominator functions are chosen as

$$\theta_1(b) = \frac{e^{(a-r)b} - 1}{a-r}, \quad \theta_2(b) = \frac{e^{\beta b} - 1}{\beta}, \quad \theta_3(b) = \frac{e^{\gamma b} - 1}{\gamma}.$$

To rearrange the discrete system (2), by expanding first term of the sum

$$\sum_{j=0}^{n+1} q_j^{\alpha_k} T_{n+1-i} = q_0^{\alpha_k} T_{n+1} + \sum_{j=1}^{n+1} q_j^{\alpha_k} T_{n+1-i}$$

and with the help of Grünwald-Letnikov formula, $(\theta_1(b))^{-\alpha_k}$ can be written instead of $q_0^{\alpha_k}$. So the first term of the discrete system is

$$\sum_{k=1}^m \frac{d(\alpha_k)}{m} \left((\theta_1(b))^{-\alpha_k} T_{n+1} + \sum_{j=1}^{n+1} q_j^{\alpha_k} T_{n+1-i} \right) = p + (r-a)T_{n+1} - r \frac{T_{n+1}}{T_{max}} (T_n + I_n) - kV_n T_{n+1}. \quad (3)$$

Substituting $\sum_{k=1}^m \frac{d(\alpha_k)}{m} = M$ into Eq. (3), T_{n+1} is obtained as

$$T_{n+1} = \frac{p - M \left(q_1^{\alpha_k} T_n + \sum_{j=2}^{n+1} q_j^{\alpha_k} T_{n+1-i} \right)}{M(\theta_1(b))^{-\alpha_k} + a - r + r \frac{T_n + I_n}{T_{\max}} + kV_n}.$$

Let us apply the same procedure to the second or third equations of Eq. (2) :

$$\sum_{j=0}^{n+1} q_j^{\alpha_k} I_{n+1-i} = q_0^{\alpha_k} I_{n+1} + \sum_{j=1}^{n+1} q_j^{\alpha_k} I_{n+1-i} = q_0^{\alpha_k} I_{n+1} + q_1^{\alpha_k} I_n + \sum_{j=2}^{n+1} q_j^{\alpha_k} I_{n+1-i}$$

$$\sum_{j=0}^{n+1} q_j^{\alpha_k} V_{n+1-i} = q_0^{\alpha_k} V_{n+1} + \sum_{j=1}^{n+1} q_j^{\alpha_k} V_{n+1-i} = q_0^{\alpha_k} V_{n+1} + q_1^{\alpha_k} V_n + \sum_{j=2}^{n+1} q_j^{\alpha_k} V_{n+1-i}$$

Inserting these expressions into the system, finally, the discrete system is obtained as

$$T_{n+1} = \frac{p - M \left(q_1^{\alpha_k} T_n + \sum_{j=2}^{n+1} q_j^{\alpha_k} T_{n+1-i} \right)}{M(\theta_1(b))^{-\alpha_k} + a - r + r \frac{T_n + I_n}{T_{\max}} + kV_n},$$

$$I_{n+1} = \frac{kV_n T_n - M \left(q_1^{\alpha_k} I_n + \sum_{j=2}^{n+1} q_j^{\alpha_k} I_{n+1-i} \right)}{M(\theta_2(b))^{-\alpha_k} + \beta},$$

(4)

$$V_{n+1} = \frac{N\beta I_n - M \left(q_1^{\alpha_k} V_n + \sum_{j=2}^{n+1} q_j^{\alpha_k} V_{n+1-i} \right)}{M(\theta_3(b))^{-\alpha_k} + \gamma}.$$

3.2. Equilibrium Points and the Jacobian Matrix of the Discrete System

In this section, the equilibrium points and the Jacobian matrix of Eq. (4) will be determined. The following equations should be solved to determine the equilibrium points of Eq. (4):

$$T_n = \frac{p - MQT_n}{M(\theta_1(b))^{-\alpha_k} + a - r + r \frac{T_n + I_n}{T_{\max}} + kV_n},$$

$$I_n = \frac{kV_n T_n - MQI_n}{M(\theta_2(b))^{-\alpha_k} + \beta},$$

(5)

$$V_n = \frac{N\beta I_n - MQV_n}{M(\theta_3(b))^{-\alpha_k} + \gamma}$$

where $\sum_{j=0}^{n+1} q_j^{\alpha_k} = Q$.

Firstly, choosing $I_n = V_n = 0$ and solving the first equation of Eq. (5) the equilibrium points E_1 and E_2 are obtained as

$$E_1 = \left(\frac{-T_{\max} (M\eta_1 + a - r) + \sqrt{(T_{\max} (M\eta_1 + a - r))^2 - 4rT_{\max}p}}{2r}, 0, 0 \right),$$

$$E_2 = \left(\frac{-T_{\max} (M\eta_1 + a - r) - \sqrt{(T_{\max} (M\eta_1 + a - r))^2 - 4rT_{\max}p}}{2r}, 0, 0 \right),$$

where

$$\eta_1 = Q + (\theta_1(b))^{-\alpha_k}.$$

Secondly, in the case of $I_n \neq V_n \neq 0$, the equilibrium point can be expressed as $E_3 = (e_{31}, e_{32}, e_{33})$, where

$$e_{31} = \frac{(M\eta_2 + \beta)(M\eta_3 + \gamma)}{N\beta k},$$

$$e_{32} = \frac{e_{32}^*}{N\beta k (\theta_2(b))^{\alpha_k} (\theta_3(b))^{\alpha_k} (\beta + M\eta_2)(Mr\eta_3 + kT_{\max}N\beta + r\gamma)},$$

$$e_{33} = \frac{e_{33}^*}{k (\theta_2(b))^{\alpha_k} (\theta_3(b))^{2\alpha_k} (\beta + M\eta_2)(M\eta_3 + \gamma) [r(M\eta_3 + \gamma) + kT_{\max}N\beta]},$$

$$e_{32}^* = (\theta_2(b))^{\alpha_k} (\theta_3(b))^{\alpha_k} \left\{ -r\eta_2^2\eta_3^2M^4 + \eta_2\eta_3(-T_{\max}N\beta k\eta_1 - 2r(\gamma\eta_2 + \beta\eta_3))M^3 - [T_{\max}N\beta k(\eta_1(\gamma\eta_2 + \beta\eta_3) + \eta_1\eta_3(a-r)) - r(\eta_1(\gamma\eta_2 + \beta\eta_3) + \eta_3(a-r))]M^2 - [T_{\max}N\beta k(a-r)(\gamma\eta_2 + \beta\eta_3) + \eta_1\gamma\beta + 2r\beta\gamma(\gamma\eta_2 + \beta\eta_3)]M + \beta^2 [T_{\max}Nk(Npk - \gamma(a-r)) - r\gamma^2] \right\},$$

$$e_{33}^* = (\theta_2(b))^{\alpha_k} (\theta_3(b))^{2\alpha_k} \left\{ -r\eta_3^2\eta_2^2M^4 - \eta_2\eta_3(T_{\max}N\beta k\eta_1 + 2r(\eta_2\gamma + \eta_3\beta))M^3 - [T_{\max}N\beta k(\eta_1(\eta_2\gamma + \eta_3\beta) + (a-r)\eta_2\eta_3) + r((\theta_3(b))^{-\alpha_k}\eta_2\gamma(4Q\beta + 4\beta + \gamma\eta_2^2) + \beta^2\eta_3^2)]M^2 - \beta [T_{\max}Nk((a-r)(\eta_2\gamma + \eta_3\beta) + \eta_1\beta\gamma) + 2\gamma r((a-r)(\eta_2\gamma + \eta_3\beta) + \eta_1\beta\gamma)]M + \beta^2 [T_{\max}Nk((r-a)\gamma + pNk) - r\gamma^2] \right\},$$

$$\eta_2 = Q + (\theta_2(b))^{-\alpha_k},$$

$$\eta_3 = Q + (\theta_3(b))^{-\alpha_k}.$$

Also, the Jacobian matrix which is necessary to analyze the equilibrium points of the discrete distributed order HIV model is obtained as

$$J(T, I, V) = \begin{pmatrix} j_{11} & j_{12} & j_{13} \\ j_{21} & j_{22} & j_{23} \\ 0 & j_{32} & j_{33} \end{pmatrix},$$

where

$$j_{11} = \frac{-Mq_1^{\alpha_k} \left(M(\theta_1(b))^{-\alpha_k} + a - r + r \frac{T_n + I_n}{T_{\max}} + kV_n \right) - \frac{r}{T_{\max}} \left(p - M \left(q_1^{\alpha_k} T_n + \sum_{j=2}^{n+1} q_j^{\alpha_k} T_{n+1-i} \right) \right)}{\left(M(\theta_1(b))^{-\alpha_k} + a - r + r \frac{T_n + I_n}{T_{\max}} + kV_n \right)^2},$$

$$j_{12} = -\frac{r}{T_{\max}} \frac{p - M \left(q_1^{\alpha_k} T_n + \sum_{j=2}^{n+1} q_j^{\alpha_k} T_{n+1-i} \right)}{\left(M(\theta_1(b))^{-\alpha_k} + a - r + r \frac{T_n + I_n}{T_{\max}} + kV_n \right)^2},$$

$$j_{13} = -k \frac{p - M \left(q_1^{\alpha_k} T_n + \sum_{j=2}^{n+1} q_j^{\alpha_k} T_{n+1-i} \right)}{\left(M(\theta_1(b))^{-\alpha_k} + a - r + r \frac{T_n + I_n}{T_{\max}} + kV_n \right)^2},$$

$$j_{21} = \frac{kV_n T_n}{M(\theta_2(b))^{-\alpha_k} + \beta},$$

$$j_{22} = \frac{-Mq_1^{\alpha_k}}{M(\theta_2(b))^{-\alpha_k} + \beta},$$

$$j_{23} = \frac{kT_n}{M(\theta_2(b))^{-\alpha_k} + \beta},$$

$$j_{32} = \frac{N\beta}{M(\theta_3(b))^{-\alpha_k} + \gamma},$$

$$j_{33} = \frac{-Mq_1^{\alpha_k}}{M(\theta_3(b))^{-\alpha_k} + \gamma}.$$

3.3. Stability Analysis of Equilibrium Points of HIV System

In this section, the stability of the model will be examined. The following Lemma and Theorem are one of the important lemmas and theorems for determining locally asymptotically stability of the equilibrium points. One can find some detailed definitions and theorems about locally asymptotically stability in (Jury, 1964), (Elaydi, 1999), (Gopal, 2009), (Richter, 2002), (Allen, 2007).

Theorem 3.1. (Richter, 2002) Let the equilibrium point of the difference equation $x_{n+1} = F(x_n)$ be \tilde{x} and assume that the function F is a continuously differentiable function defined on some open neighborhood of an equilibrium point \tilde{x} . The equilibrium point \tilde{x} is locally asymptotically stable, if absolute values of all the roots of the characteristic polynomial are less than one. Otherwise, the equilibrium point \tilde{x} is unstable.

Lemma 3.1 (Schur-Cohn criterion for n=3). (Elaydi, 1999) Let the characteristic polynomial be $p(\lambda) = \lambda^3 + c_1\lambda^2 + c_2\lambda + c_3$. The solutions $\lambda_i, i = 1, 2, 3$ of $p(\lambda) = 0$ lie inside the unit disk if the conditions below are satisfied:

i. $1 + c_1 + c_2 + c_3 > 0$.

ii. $1 - c_1 + c_2 - c_3 > 0$.

iii. $1 - c_3^2 > |c_2 - c_3c_1|$.

In the view of Theorem 3.1, the following theorem can be given.

Theorem 3.2. The equilibrium point E_1 of HIV system (1) is locally asymptotically stable if following conditions are satisfied.

i.

$$\left| 2(\theta_1(b))^{\alpha_k} \left[T_{\max} Q M^2 + (\theta_1(b))^{\alpha_k} Q T_{\max} (a-r) M + (\theta_1(b))^{\alpha_k} r p \right] \right| < \left| T_{\max} \left(1 + (\theta_1(b))^{2\alpha_k} Q^2 \right) M^2 + M(\theta_1(b))^{\alpha_k} \left(-2T_{\max} r - Q(\theta_1(b))^{\alpha_k} + \varpi \right) + \left((\theta_1(b))^{2\alpha_k} \right) \left((-r+a)\varpi + T_{\max} (-r+a)^2 - 2rp \right) \right|,$$

ii.

$$\left| M Q \left[M \left((\theta_3(b))^{-\alpha_k} + (\theta_2(b))^{-\alpha_k} \right) + \beta + \gamma \right] - \left\{ M^2 Q^2 \left(\beta - M \left((\theta_3(b))^{-\alpha_k} - (\theta_2(b))^{-\alpha_k} \right) - \gamma \right)^2 + M^2 (\theta_2(b))^{-\alpha_k} (\theta_3(b))^{-\alpha_k} \varsigma + M (\theta_2(b))^{-\alpha_k} \gamma \varsigma + \beta M (\theta_3(b))^{-\alpha_k} \varsigma + \beta \gamma \varsigma \right\}^{1/2} \right| < 2 \left| \left(M + \gamma (\theta_3(b))^{-\alpha_k} \right) \left(M + \beta (\theta_2(b))^{-\alpha_k} \right) \right|,$$

iii.

$$\left| M Q \left[M \left((\theta_3(b))^{-\alpha_k} + (\theta_2(b))^{-\alpha_k} \right) + \beta + \gamma \right] + \left\{ M^2 Q^2 \left(\beta - M \left((\theta_3(b))^{-\alpha_k} - (\theta_2(b))^{-\alpha_k} \right) - \gamma \right)^2 + M^2 (\theta_2(b))^{-\alpha_k} (\theta_3(b))^{-\alpha_k} \varsigma + M (\theta_2(b))^{-\alpha_k} \gamma \varsigma + \beta M (\theta_3(b))^{-\alpha_k} \varsigma + \beta \gamma \varsigma \right\}^{1/2} \right| < 2 \left| \left(M (\theta_3(b))^{-\alpha_k} + \gamma \right) \left(M (\theta_2(b))^{-\alpha_k} + \beta \right) \right|,$$

where,

$$\varpi = \sqrt{T_{\max} \left[T_{\max} \left(\left(Q + (\theta_1(b))^{-\alpha_k} \right) M + (-r+a) \right)^2 - 4rp \right]},$$

$$\zeta = \frac{2kN\beta \left(-T_{\max} \left(\left(Q + (\theta_1(b))^{-\alpha_k} \right) M + a - r \right) + \varpi \right)}{r}.$$

Remark 3.1. Since the equilibrium point E_3 of HIV system (1) leads to complicated process, the examination of stability of the equilibrium point E_3 is given in the numerical results section.

3.4. Numerical Results

In the view of Lemma 3.1 and Theorem 3.2, the stability of the model will be examined for the equilibrium points E_1 and E_3 which have biological meanings. So, the parameters given in (Wang & Li, 2010) and also used in (Ongun & Turhan, 2013) are considered to be able to compare the stability results. These parameters are given as

$$k = 0.0027, \beta = 0.3, T_{\max} = 1500, p = 0.1, a = 0.2, \gamma = 2.4, N = 10.$$

During the analysis the step size is chosen as $h = 0.01$. In addition, to show that DODEs are the general case of ordinary differential equations in some way, the density function is chosen as $d(\alpha) = 1$. To compare the results with (Ongun and Turhan, 2013) in which the system is ordinary differential equations the parameter of the average specific T-cell growth rate is chosen as $r = 0.05$. So, by substituting equilibrium point E_1 into Jacobian matrix, the characteristic equation is obtained as follows:

$$p(\lambda) = \lambda^3 - 0.012081\lambda^2 - 979898.33\lambda + 6517.47.$$

According to Schur-Cohn criteria, it can be seen that

1. $1 - 0.012081 - 979898.33 + 6517.47 = -973379.87 < 0.$
2. $1 + 0.012081 - 979898.33\lambda + 6517.47 = -986414.80 < 0.$
3. $(1 - 6517.47^2) - |-979898.33 - (-0.012081 \times 6517.47)| = -4345.10 < 0$

Since none of the condition of the Schur-Cohn criteria is satisfied, the equilibrium point E_1 is not stable as in (Ongun & Turhan, 2013). At the same time, the solution of characteristic equation is

$$\lambda_1 = 0.006651, \lambda_2 = 989.89, \lambda_3 = -989.89.$$

Since all of the absolute values of eigenvalues $\lambda_i, i = 1, 2, 3$ is not smaller than 1, it is approved that the equilibrium point is not stable.

For another comparison, by choosing $r = 0.8$, it is obtained that

$$p(\lambda) = \lambda^3 + c_1\lambda^2 + c_2\lambda + c_3$$

where

$$c_1 = 3495.7956, c_2 = -24.5591, c_3 = 19399.67520.$$

By using the values in the Schur-Cohn criteria,

1. $1 + c_1 + c_2 + c_3 = -15927.4386 < 0$

2. $1 - c_1 + c_2 - c_3 = 15880.3203 > 0$,
3. $1 - c_3^2 - |c_2 - c_3c_1| = -0.4441.10^9 < 0$

is obtained. So, similarly, the equilibrium point E_1 is not stable as in (Ongun & Turhan, 2013).

Now, let us choose the parameter as $r=0.001$. The characteristic equation for the equilibrium point E_1 is obtained as

$$p(\lambda) = \lambda^3 + 0.005382\lambda^2 - 0.002145\lambda - 0.000022.$$

The root of the characteristic equation is obtained as $\lambda_1 = -0.01093$, $\lambda_2 = 0.04851$, $\lambda_3 = -0.04296$. Since $|\lambda_i| < 1$, in this case, the equilibrium point is locally asymptotically stable as in (Ongun & Turhan, 2013). In addition, using Schur-Cohn criteria, it is satisfied that

1. $1 + c_1 + c_2 + c_3 = 1.00321 > 0$.
2. $1 - c_1 + c_2 - c_3 = 0.99249 > 0$.
3. $1 - c_3^2 - |c_2 - c_3c_1| = 0.99785 > 0$.

Now, let us compare the stability of the equilibrium point E_3 by choosing $r = 0.8$. The characteristic equation is obtained as

$$p(\lambda) = \lambda^3 - 0.00543\lambda^2 - 147344.33\lambda + 0.01474.$$

According to Schur-Cohn criteria

1. $1 + c_1 + c_2 + c_3 = -147343.3411 < 0$.
2. $1 - c_1 + c_2 - c_3 = -147343.3597 < 0$.
3. $1 - c_3^2 - |c_2 - c_3c_1| = -147343.3505 < 0$.

is obtained and it is seen that the equilibrium point E_3 is not stable.

On the other hand, as is known, discretization is depended to density function. So, under different circumstance, the density function can be chosen different. Due to this reason, unlike the other examples, let us choose the density function and the parameter r as $d(\alpha) = 3\alpha + 1$, $\alpha = 0.1$ and $r = 0.003$, respectively. For the equilibrium point E_1 , the characteristic equation is

$$p(\lambda) = \lambda^3 + c_1\lambda^2 + c_2\lambda + c_3,$$

where $c_1 = -0.15658$, $c_2 = -0.05652$ and $c_3 = 0.00842$. Considering Schur-Cohn criteria

1. $1 + c_1 + c_2 + c_3 = 0.79531 > 0$.
2. $1 - c_1 + c_2 - c_3 = 1.09163 > 0$.
3. $1 - c_3^2 - |c_2 - c_3c_1| = 0.94472 > 0$.

The equilibrium point E_1 is locally asymptotically stable because of satisfying all three conditions.

As another example by choosing $d(\alpha)=2\alpha-1$, $\alpha=0.005$ and $r=0.05$, the characteristic equation of the equilibrium point E_3 is found as

$$p(\lambda)=\lambda^3+0.0056\lambda^2-1.0093\lambda+0.0035.$$

Since the roots of the interested equation are $\lambda_1=0.00358$, $\lambda_2=1.00004$, $\lambda_3=-1.00922$, the equilibrium point E_3 is not stable.

As mentioned before, NSFD schemes are very effective methods. To show the effectiveness, finally we present the comparison of the convergency of the method in Table1 and Table 2. The compatibility of the results with (Ogun & Turhan, 2012) is seen.

Table 1. Stability of equilibrium point E_1 under application of different methods for different step-size h . ($r=0.001$, $d(\alpha)=1$)

h	Theta Method	Fourth-Order Runge-Kutta Method	Distributed Order NSFD schemes
0.0001	Conv.	Conv.	Conv.
0.001	Conv.	Conv.	Conv.
0.1	Conv.	Conv.	Conv.
0.8	Conv.	Conv.	Conv.
1	Div.	Conv.	Conv.
5	Div.	Div.	Conv.
10	Div.	Div.	Conv.

Table 2. Stability of equilibrium point E_3 under application of different methods for different step-size h . ($r=0.05$, $d(\alpha)=1$)

h	Theta Method	Fourth-Order Runge-Kutta Method	Distributed Order NSFD schemes
0.0001	Conv.	Conv.	Conv.
0.001	Conv.	Conv.	Conv.
0.1	Conv.	Conv.	Conv.
0.8	Div.	Conv.	Conv.
1	Div.	Div.	Div.
5	Div.	Div.	Div.

10	Div.	Div.	Div.
----	------	------	------

CONCLUSION

In this study, a model defines the HIV infection of $CD4^+$ T cells is rewritten in distributed order form. The advantage of rewriting HIV system by DODEs leads from the density function included in the derivative. By density function, DODEs can be regarded as the general case of the interested ordinary differential equation. So, under different circumstances, the behavior of the differential equation can be interpreted. In the discretization of the model, NSFD schemes are used. The stability analysis of the equilibrium points is presented. The stability results correspond to ordinary differential equation model is compared with the results in literature. Also, the efficiency of NSFD schemes for big step-size is presented in Table 1 and Table 2 by comparing with Theta method and Fourth-Order Runge-Kutta method. The effect and the importance of the NSFD schemes on convergency can be clearly seen from Table 1 and Table 2 for the big step size. By making detailed comparison of the stability results with the results given in literature, it is concluded that NSFD schemes can be applied to the system of DODEs.

REFERENCES

- Allen, L. J. S. (2007). *An introduction to mathematical biology*. Department of Mathematics and Statistics Texas Tech University, Pearson Education.
- Caputo, M. (2001). Distributed order differential equations modelling dielectric induction and diffusion. *Fractional Calculus and Applied Analysis*, 4(4), 421-442.
- Diethelm, K., & Ford, N. J. (2009). Numerical analysis for distributed-order differential equations. *Journal of Computational and Applied Mathematics*, 225(1), 96-104.
- Ding, W., Patnaik, S., Sidhardh, S., & Semperlotti, F. (2021). Applications of distributed-order fractional operators: A review. *Entropy*, 23(1), 110.
- Dorciak L. (1994). Numerical models for simulation the fractional-order control systems. *UEF-04-94, The Academy of Sciences, Institute of Experimental Physic, Kosice, Slovak Republic*.
- Elaydi, S. (1999). *An introduction to difference equations*. Springer, New York, NY, USA.
- Jury, E. I. (1964). *Theory and Application of the z-Transform Method*. Wiley.
- Gopal, M. (2009). *Digital Control and State Variable Methods, Conventional and Intelligent Control Systems*. New Delhi: Tata McGraw-Hill Publishing Company Limited.
- Jibenja, N., Yuttanan, B., & Razzaghi, M. (2018). An efficient method for numerical solutions of distributed-order fractional differential equations. *Journal of Computational and Nonlinear Dynamics*, 13(11).
- Katsikadelis, J. T. (2014). Numerical solution of distributed order fractional differential equations. *Journal of Computational Physics*, 259, 11-22.
- Kocabiyik, M. (2022). Nonstandard Discretization and Stability Analysis of a novel type Malaria-Ross Model. *Journal of the Institute of Science and Technology*, 12(2), 1023-1033
- Kocabiyik, M., & Yakıt Ogun, M. (2021). Construction a distributed order smoking model and its nonstandard finite difference discretization. *AIMS Mathematics*, 7(3), 4636-4654.
- Kocabiyik, M., Yakıt Ogun, M. & Turhan Çetinkaya, İ. (2021). Numerical analysis of distributed order SVIR model by nonstandard finite difference method . *Journal of Balikesir University Institute of Science and Technology*, 23 (2), 577-591 . (In Turkish)
- Meerschaert, M. M., & Tadjeran, C. (2004). Finite difference approximations for fractional advection-dispersion flow equations. *Journal of computational and applied mathematics*, 172(1), 65-77.
- Mickens, R. E. (1989). Exact solutions to a finite-difference model of a nonlinear reaction-advection equation: Implications for numerical analysis. *Numerical Methods for Partial Differential Equations*, 5(4), 313-325.
- Mickens, R. E. (1994). *Nonstandard finite difference models of differential equations*. World Scientific Publishing, Atlanta, Ga, USA.

Mickens, R. E. (2002). Nonstandard finite difference schemes for differential equations. *Journal of Difference Equations and Applications*, 8(9), 823-847.

Mickens, R. E. (2005). *Advances in the applications of nonstandard finite difference schemes*. World Scientific.

Mickens, R. E. (2007). Calculation of denominator functions for nonstandard finite difference schemes for differential equations satisfying a positivity condition. *Numerical Methods for Partial Differential Equations: An International Journal*, 23(3), 672-691.

Najafi, H. S., Sheikhan, A. R., & Ansari, A. 2011. Stability analysis of distributed order fractional differential equations. *Abstract and Applied Analysis* (Vol. 2011). Hindawi.

Naresh, R., Sharma, D., & Tripathi, A. (2009). Modelling the effect of tuberculosis on the spread of HIV infection in a population with density-dependent birth and death rate. *Mathematical and computer Modelling*, 50(7-8), 1154-1166

Nowak, M. A., & May, R. M. (1991). Mathematical biology of HIV infections: antigenic variation and diversity threshold. *Mathematical Biosciences*, 106(1), 1-21.

Patidar, K. C. (2005). On the use of nonstandard finite difference methods. *Journal of Difference Equations and Applications*, 11(8), 735-758.

Patidar, K. C. (2016). Nonstandard finite difference methods: recent trends and further developments. *Journal of Difference Equations and Applications*, 22(6), 817-849.

Podlubny, I., 1999. *Fractional Differential Equations*, Academic Press, New York.

Richter, H. (2002). The generalized Henon maps: Examples for higher-dimensional chaos. *International Journal of Bifurcation and Chaos*, 12(06), 1371-1384.

Sweilam, N., AL-Mekhlafi, S. M., & Albalawi, A. O. (2020). On the Distributed Order Fractional Multi-Strain Tuberculosis Model: A Numerical Study. *Statistics, Optimization & Information Computing*, 8(1), 175-186.

Wang, L., & Li, M. Y. (2006). Mathematical analysis of the global dynamics of a model for HIV infection of CD4+ T cells. *Mathematical Biosciences*, 200(1), 44-57.

Yakit Ogun, M., & Turhan, İ. (2013). A numerical comparison for a discrete HIV infection of CD4+ T-Cell model derived from nonstandard numerical scheme. *Journal of Applied Mathematics*, 2013.

Yang, Y., & Xiao, Y. (2010). Threshold dynamics for an HIV model in periodic environments. *Journal of Mathematical Analysis and Applications*, 361(1), 59-68.

Analysis of the Charge Transport Properties of Bis Chalcone Derivative from the Reorganization Energy, Band Gap under the Different Electric Fields and Results of Bond Length Alternation for Efficient Organic Field Effect Transistors

Gül YAKALI¹
Abdullah BİÇER
Günseli TURGUT ÇİN

Introduction

The π -conjugated organic molecules especially including polyaromatic systems have attracted considerable attention in the optoelectronic field due to having properties of stability, flexibility and delocalization of charges, etc (Siddiqui et al, 2012: 339, Cias et al, 2011:14519). These properties provide enhancing the charge transport rate therefore optoelectronic device performance by decreasing band gap (ΔE). Especially, π -conjugated containing thiophene backbone have considerably attention in semiconducting materials recently (Zhang et al., 2012: 879, Zhang et al., 2008: 5148).

Theoretical and experimental studies including Marcus Electron Transfer Theory and Density Functional Theory (DFT), single crystal x-ray crystallography (SCXRD) are very important methods to evaluate the charge transport properties of the molecules. Marcus Electron Transfer Theory is the powerful way for understanding the electron and hole transfer behavior of the organic semiconductor molecules in material science (Chai et al, 2011:3219). According to Marcus Electron Theory, the charge transfer rate strongly depends on the parameters of reorganization energy and charge transfer integral. The reorganization energy (λ) can be said that the change in the molecular geometry when an electron is added or removed from a molecule (inner reorganization) (Zhu et al, 2016:1078). For efficient electron or hole injection in the optoelectronic device form, it is desirable that reorganization energy is small (Qi et al, 2020:3677). Beside the reorganization energy, HOMO and LUMO orbitals, energy band gap value under the different electric fields play an important role to determine the mobility since electronic devices are operated under the electric field. Evaluation of theoretical results give the comprehensive information about the organic π -conjugated molecules for their device forms whether they can be used as an optoelectronic device or not.

The charge transfer integral of the conjugated molecules is highly desirable large that it is evaluated from the molecular arrangements of the molecules in solid phase obtained from SCXRD data. Solid film or the crystal phase of the molecules give the excellent information the device performance by considering their aggregation phase which created noncovalent interactions intra-intermolecular hydrogen bonding, intra-intermolecular $\pi \cdots \pi$ stacking interactions, short

¹ Assoc. Prof. Dr. Gül Yakalı, İzmir Katip Çelebi University, Engineering Sciences, Orcid: 0000-0002-0015-5948

interactions between the atoms and C–H \cdots π interactions in the crystal structure not only single molecule since molecules display aggregation in their solid phases through collective interactions between each other (Yao et al, 2018:9, Herman et al, 2016:3). High intermolecular overlaps and close intermolecular contacts in the crystal structure are beneficial for better performance of organic devices especially, organic semiconductors. According to reported results about the $\pi \cdots \pi$ stacking modes ,the antiparallel *H* type stacking which shows more overlap between the rings and *J* type stacking mode which shows less overlap or parallel displaced mode between the rings increases the optoelectronic device performance (Banerjee et al, 2019:2248, Li et al, 2020:970). Therefore, the high performance for n-type organic semiconductor with the small reorganization energy may be attributed to favourable $\pi \cdots \pi$ stacking mode with the close perpendicular distance (3.0Å- 4.0 Å) between the rings and structural rigidity with the perfect planar structure.

Ionization potential (IP), electron affinity (EA) are the important parameters to define electron and hole injection barriers. The IP value must be small for efficient hole injection into the HOMO of the molecule while EA value must be large to obtain efficient electron injection into LUMO of the molecule. The lower the IP of the hole transport layer (HTL), the easier will be the injection of holes from ITO (indium tin oxide) to HTL, the higher the EA of the electron-transport layer (ETL), and the easier the injection of electrons from the cathode to ETL (Lin et al, 2003:5241, Chai et al, 2017:697, Brückner et al, 2017:17603).

In present work, to analyze optical and electronic properties of the molecule, results of the theoretical calculations and SCXRD datas were interpreted and structure property relationship of the molecule was studied. Experimental and theoretical results demonstrated that this molecule can be used as an efficient electron transport material for OFET applications with the excellent properties in terms of small reorganization energy, high electron affinity value and desirable pi...pi stacking interactions mode in solid phase giving the information about charge transfer integral and modified to decrease reorganization energy and increase charge transfer integral.

Method

Density functional Theory Calculations including B3LYP functional and 6-311G basis set were performed to evaluate electronic and optical properties of the molecule for the use an organic semiconductors devices by using the cif file data obtained SCXRD experiment with the Gaussian software (Taydakov, 2016:32, Tsiper, 200:47).

According to Marcus Theory, the charge transfer rate is determined by the following equation.

$$W = \frac{V^2}{h} (\pi/\lambda k_B T)^{1/2} \exp(-\lambda/4k_B T)$$

Here, V and λ are the transfer integral and reorganization energy, respectively. The λ is divided into two parts as λ_{rel}^1 which represents to the geometry relaxation energy of one molecule from neutral to charged state and λ_{rel}^2 represents to the geometry relaxation energy from charged to neutral state.

$$\lambda = \lambda_{rel}^1 + \lambda_{rel}^2$$

$$\lambda_{anion} = \lambda_{rel}^1 + \lambda_{rel}^2 = [E^{(1)}(M) - E^{(0)}(M)] + [E^{(1)}(M^-) - E^{(0)}(M^-)]$$

$$\lambda_{cation} = \lambda_{rel}^1 + \lambda_{rel}^2 = [E^{(1)}(M) - E^{(0)}(M)] + [E^{(1)}(M^+) - E^{(0)}(M^+)]$$

Here $E^{(1)}(M)$ is the neutral energy the optimized charged geometry, $E^{(0)}(M)$ is the energy of the neutral geometry. $E^{(1)}(M^-) - E^{(1)}(M^+)$ are the energies of the charged state at the optimized neutral geometry and $E^{(0)}(M^-) - E^{(0)}(M^+)$ are the neutral energies of charged states. In the calculation of ionization energy, the adiabatic ionization potential (IPa) and vertical ionization potential (IPv) have been calculated as the following equation.

$$IPa = E^0(M)^+ - E^0(M) \text{ and } IPv = E^0(M)^+ - E^0(M)$$

The adiabatic/vertical electron affinity (EAa)/(EA_v) of all molecules have been calculated as following equation;

$$EAa = E^0(M) - E^0(M)^- \text{ and } EA_v = E^0(M)^- - E^1(M)^-$$

Results and Discussion

The optimized geometries of the compound in the neutral state created through the cif file of the single crystal x-ray diffraction data are demonstrated in the Figure 1. The moieties of the molecule have a slightly twisting and rigid molecular geometry in solid phase with the dihedral angle of 75° between the molecule plane and cyclohexane ring. The main aim of this study is to examine the molecular geometry and noncovalent interactions on its energy levels and charge transport properties. Therefore, HOMO and LUMO levels, ionization potential, reorganization energy, electron affinity were interpreted by taking into account the geometry and interactions of the molecule in solid phase. In addition, The electronic properties of the molecule under the different electric fields were investigated in the y direction which is the possible direction of charge transfer channels since the pi...pi stacking interactions are created along the y axis in its solid phase or crystal structure.

The molecule shows symmetrical structure with the central cyclohexane ring and thiophene rings at the ends of the molecule skeleton. Since the molecule is symmetrically twisted from the molecule plane it can be visualized as a propeller. The optimized geometric parameters of the molecule in neutral, anion and cation states are presented in Table 1.

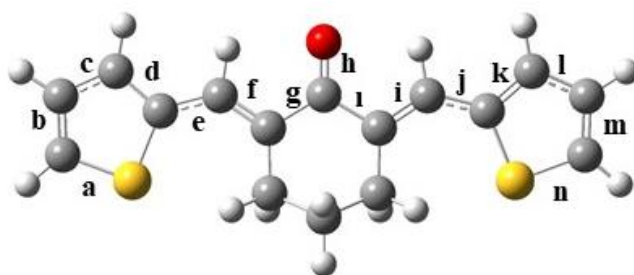


Figure 1. The optimized geometries of the studied compound.

Table 1. Bond Length Alternation Values of the compound

Index	Notr	Anion	Cation	$\Delta(C - N)$	$\Delta(A - N)$
a	1.72796	1.74615	1.71584	0.01212	0.01819
b	1.36811	1.36911	1.38465	0.01654	0.0010
c	1.41490	1.41311	1.39469	0.02021	0.00059
d	1.38305	1.39508	1.40679	0.02374	0.01203
e	1.43944	1.42518	1.41167	0.02777	0.01426
f	1.35429	1.37604	1.37920	0.02491	0.02175
g	1.50143	1.47283	1.49347	0.00796	0.0286
h	1.22652	1.25818	1.22335	0.00297	0.03166
ı	1.50144	1.47280	1.49355	0.00789	0.02864
i	1.35428	1.37605	1.37922	0.02494	0.02177
j	1.43943	1.42516	1.41166	0.02777	0.01427
k	1.38303	1.39507	1.40686	0.02383	0.01204
l	1.41491	1.41310	1.39467	0.02024	0.00181
m	1.36811	1.36910	1.38469	0.01658	0.00099
n	1.72797	1.74616	1.71586	0.01211	0.01819

The reorganization energy of the molecule can be predicted from the change in the molecular geometry optimized neutral, anion and cation states. When a molecule gains or loses charges, it will relax its molecular geometry for a new charge distribution. Due to the extended pi system, the change in the molecular parameters of the studied molecule are observed over the entire molecule. The bond length alternation (BLA) based on reduction and oxidation displayed small changes that BLA values upon reduction for the molecule are considerably larger than that of oxidation; this result verify the reorganization energy for electron is greater than those for hole of the molecule which support the results obtained from reorganization energy calculations (Table 2). In addition, the torsion angles about the cyclohexane ring in the molecule are 173.80, 174.46 and 158.86 for the neutral anionic and cationic states, respectively which supports the creation smaller geometrical changes in the anionic state than that of cationic state, also. According to following equation, the small reorganization energy (λ) which is supported by a smaller geometrical relaxation with respect to the neutral geometry is favorable to get high charge transport rate. Therefore, it can be predicted that studied molecule has electrons as a charge carriers and feature of the n-type molecule due to small electron reorganization energy value (0.20 eV).

$$W = \frac{V^2}{h} (\pi/\lambda k_B T)^{1/2} \exp(-\lambda/4k_B T)$$

Table 2. The value of the reorganization energies of the compound.

Compound	Boşluk reorganizasyon enerjisi (eV)	Elektron reorganizasyon enerjisi (eV)
Bis-chalcone	0.23	0.20

Table 3. The value of the ionization poteitael and electron affinity of the compound.

Strong stacking interactions of the compound				
Stacking parameters	Cg1 ... Cg1 (pathway 1)	Cg2...Cg2 (pathway 2)	Cg2...Cg2 (pathway 3)	Cg1 ... Cg1 (pathway 4)
Pitch angle (P: °)	26.7	21.3	18.6	24.1
Roll angle (R: °)	3.9(2)	5.3(2)	5.3(2)	3.9(2)
Pitch distance (d_p : Å)	1.95	1.55	1.30	1.78
Roll distance (d_r : Å)	0.26	0.36	0.36	0.26
Slipping angle (β : °)	24.1	18.6	21.3	26.7
Interplanar distance ($d_{\pi\pi}$: Å)	3.875	3.982	3.875	3.982

In device applications of organic π -conjugated systems beside the taking into account the reorganization energy, the molecular arrangement and assembly of molecules are considered to determine the charge transfer integral given in the equation 1 which is the parameter defined the molecular interaction between the adjacent fragments of the molecule through noncovalent interactions in solid phase. Molecular arrangements in solid phase created by π .. π (ring...ring) stacking interactions provide charge transport channels between the aggregated molecules. In this molecule, the antiparallel H type with helical stacking interactions in the solid phase of the molecule forms the charge transport channel for the molecule that this type stacking is a favourable to increase the charge transport rate, therefore transfer integral value since high transfer integral result in high charge mobility in the optoelectronic field (Figure 2). The π .. π stacking type of the studied molecule was decided by evaluating the stacking and interactions parameters given in the Table 4. In addition, the stacking interactions of the molecule are consolidated by the nonclassical hydrogen bonds.

Compound	IPa(eV)	IPv(eV)	EAA(eV)	EAV(eV)
Bis-chalcone	7.19	7.31	1.15	1.05

Table 4. Crystallographic stacking data of the compound.

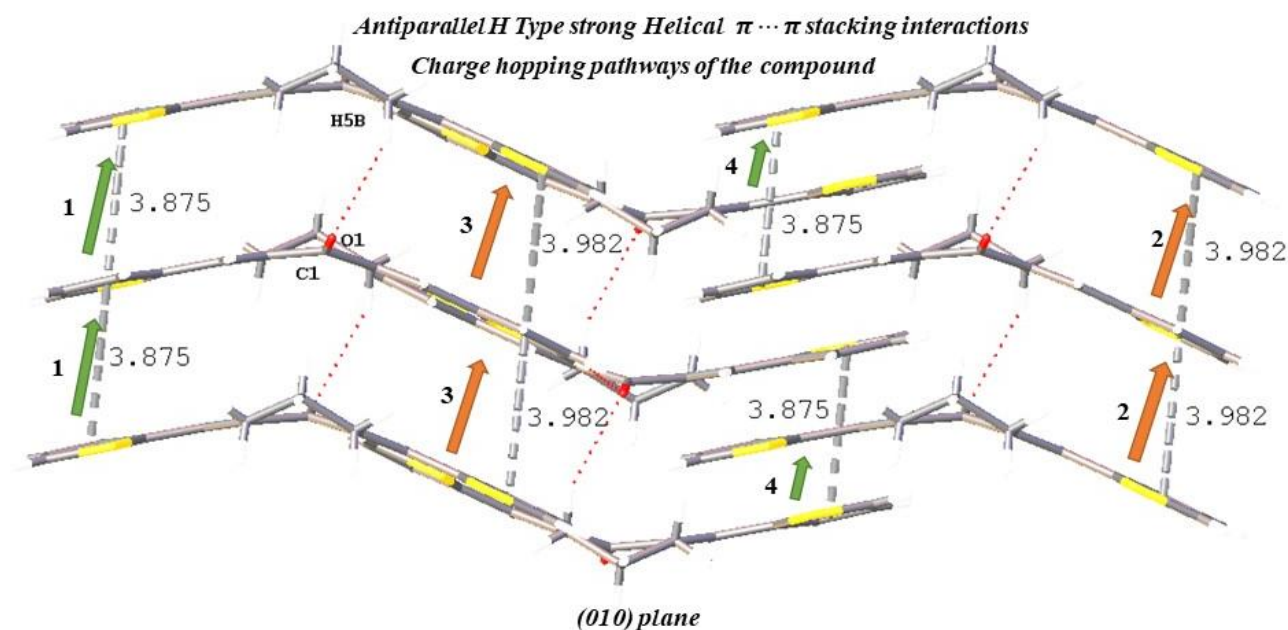


Figure 2. The favourable charge hopping pathways of the compound.

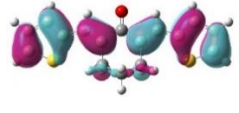
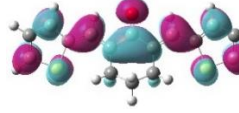

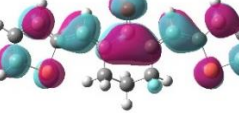


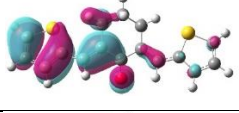
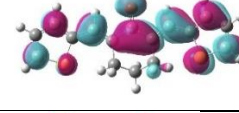
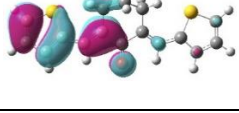

To further understanding the optoelectronic device performance of the molecule, injection of hole and electron into an organic molecule should be considered through evaluating IP and EA values. The IP value must be small for efficient hole injection into the HOMO of the molecule while EA value must be large to obtain efficient electron injection into LUMO of the molecule. The lower the IP result in easier the injection of holes, the higher the EA result in easier the injection of electrons. The calculated results of the IPs and EAs, HOMO-LUMO energy levels and band gaps are shown in Table 5 and 6. In our study, it is clear that IPv has higher value, whereas vertical electron affinity has a lower value when we compare the results with other studied similar molecules given in the literature (Wang et al, 2016:8405, Navamani et al, 2013:17948). The low electron affinity of molecule means large barrier for electron injection, which will result in a high threshold voltage. The LUMO level of the molecule should be lowered for easy electron injection. As a result our molecule are suitable for electron transport with the high EA value and hole transport material with the small IP value. It could be good candidate material to obtain efficient ambipolar (n type and p type) type charge transport material in optoelectronic field.

The distribution of the HOMO and LUMO of the molecule at different electric fields from 0.0 eV to 0.40 eV were calculated in the y direction which is the possible direction of charge transfer since the pi...pi stacking interactions are created along the y axis in its solid phase or crystal structure. (Figure 2). Since HOMO and LUMO orbitals are delocalized over the entire molecule, it has good conducting channel for the electron transfer. The total dipole moment of the molecule has been found as small 2.078 debye when there is no electric field. It means that the molecule has high polarizability. Its dipol moment value decreased as the electric field applied that the electron transport property of the molecule is strengthened as electric field increased. The change in the electric field has the effect on the HOMO and LUMO energy levels and band gap value (Table 5 and Table 6). It has also been observed that the increase in electric field leads to the decrease in band gap and the HOMO and LUMO start localizing at the opposite side of the molecule showing that the molecule under electric field is a better electron transport material.

Table 5. HOMO, LUMO, band gap and Total dipol momens of the molecule under the different electric fields.

Electric Fields (eV)	HOMO (eV)	LUMO (eV)	Band Gap (eV)	Dipole Moment (debye)
0.00	-5.9749	-2.4136	-3.5613	2.078274
0.10	-6.4974	-3.0764	-3.4210	2.629898
0.20	-6.9722	-3.6557	-3.3165	3.509276
0.30	-7.4506	-4.2846	-3.1660	4.756478
0.40	-7.9023	-4.8432	-2.1798	5.922111

Table 6. Spatial distribution of HOMO and LUMO under the various electric fields.

Electric Fields ($V/\text{\AA}$)	HOMO	LUMO
0.00		
0.10		
0.20		
0.30		
0.40		

Conclusions

In conclusion, the electronic and charge transport properties of the bischalcone derivative have been studied by considering the Marcus Electron Theory and DFT calculations from the crystallographic data. The electron reorganization energy of the molecule was defined smaller than that of hole that the molecule displays feature of n type organic molecule due to having the electrons as a charge carrier. In addition, electron injection barrier of the molecule was predicted as a small since it has high EA value when we compared it with similar molecules given in the literature. The small IP value makes the molecule durable for optoelectronic devices. Beside the reorganization energy to verify the charge transfer integral of the molecule which is shown in the mobility formula, the molecular arrangements of the molecule in solid phase was considered. According the crystallographic stacking data and stacking view of the molecule , it displayed antiparallel stacking type with the helical formation in solid phase which is a favourable type to create efficient optoelectronic device. The HOMO-LUMO behavior of the molecule was observed in the different electric fields via calculation of DFT because the organic semiconductors are

conducted under the electric field. As the electric field increased from 0.0 eV to 0.40 eV band gap value decreases and situation of the orbitals changes that they are located opposite sides of the molecule. Also, its dipol moment value decreased as the electric field applied that the electron transport property of the molecule is strengthened as electric field increased. Experimental and theoretical results demonstrated that this molecule can be used as an efficient electron transport material for OFET applications and modified to decrease reorganization energy and increase charge transfer integral.

Acknowledge

This work was supported at Dokuz Eylül University and Akdeniz University. The authors would like to thank Akdeniz University for the synthesis of the molecule and Dokuz Eylül University for the use of the Agilent Xcalibur Eos diffractometer and Assoc. Prof. Dr. Muhittin Aygün for the use of Gaussian Software.

References

Banerjee, A.; Saha, A.; Saha, B. K. *Crystal Growth and Design* **2019**. Understanding the Behavior of π - π Interactions in Crystal Structures in Light of Geometry Corrected Statistical Analysis: Similarities and Differences with the Theoretical Models, 19(4), 2245–2252. <https://doi.org/10.1021/acs.cgd.8b01857>.

Brückner, C.; Walter, C.; Stolte, M.; Braïda, B.; Würthner, F.; Engels, B.; Brückner, C.; Walter, C.; Stolte, M.; Braïda, B.; Meerholz, K.; Bru, C.; Walter, C.; Stolte, M.; Meerholz, K. *Journal of Physical Chemistry C*, **2017**. Structure – Property Relationships for Exciton and Charge Reorganization Energies of Dipolar Organic Semiconductors: A Combined Valence Bond Self-Consistent Field and Time-Dependent Hartree-Fock and DFT Study of Merocyanine Dyes, 119, 31, 17602–17611, <https://doi.org/10.1021/acs.jpcc.5b06206>.

Chai, S.; Wen, S. H.; Huang, J. D.; Han, K. L. *Journal of Computational Chemistry* **2011** Density Functional Theory Study on Electron and Hole Transport Properties of Organic Pentacene

Derivatives with Electron-Withdrawing Substituent, 32 (15), 3218–3225. <https://doi.org/10.1002/jcc.21904>.

Chai, S.; Chen, D.; Huang, J. *Research Papers*. **2017**, Charge-transport properties of 4-(1,2,2-triphenyl-vinyl)aniline salicylaldehyde hydrazone: tight-packing induced molecular ‘hardening’ 695–699. <https://doi.org/10.1107/S2052252517010685>.

Cias, P.; Slugovc, C.; Gescheidt, G. Hole Transport in Triphenylamine Based OLED Devices: From Theoretical Modeling to Properties Prediction. *Journal of Physical Chemistry A* 2011, 115 (50), 14519–14525. <https://doi.org/10.1021/jp207585j>.

Hermann, J.; Alfè, D.; Tkatchenko, A. *Nature Communications* **2017**, Nanoscale π - π Stacked Molecules Are Bound by Collective Charge Fluctuations. 8 (14052), 1-8. <https://doi.org/10.1038/ncomms14052>.

Li, Q.; Li, Z. *Accounts of Chemical Research*, **2020**. Molecular Packing: Another Key Point for the Performance of Organic and Polymeric Optoelectronic Materials., 53 (4), 962–973. <https://doi.org/10.1021/acs.accounts.0c00060>.

Lin, B. C.; Cheng, C. P.; Ping, Z.; Lao, M. *Journal of Physical Chemistry A*, **2003**. Reorganization Energies in the Transports of Holes and Electrons in Organic Amines in Organic Electroluminescence Studied by Density Functional Theory, 5241–5251. <https://doi.org/10.1021/jp0304529>

Navamani, K.; Saranya, G.; Kolandaivel, P.; Senthilkumar, K. *Chemical Physics* **2013**. Effect of Structural Fluctuations on Charge Carrier Mobility in Thiophene, Thiazole and

Thiazolothiazole Based Oligomers. *Physical Chemistry* 15 (41), 17947–17961. <https://doi.org/10.1039/c3cp53099j>.

Qi, Y.; Chen, C.; Zheng, C.; Tang, Y.; Wan, Y.; Jiang, H.; Chen, T.; Tao, Y.; Chen, R. *Physical Chemistry Chemical Physics* **2020**. Heteroatom-Bridged Heterofluorenes: A Theoretical Study on

Molecular Structures and Optoelectronic Properties, 22(6), 3675–3682. <https://doi.org/10.1039/c9cp06458c>.

Siddiqui, S. A.; Al-Hajry, A.; Al-Assiri, M. S. *International Journal of Quantum Chemistry* **2016**. Ab Initio Investigation of 2,2'-Bis(4-Trifluoromethylphenyl)-5,5'-Bithiazole for the Design of Efficient Organic Field-Effect Transistors, 116 (5), 339–345. <https://doi.org/10.1002/qua.25034>.

Taydakov, I. V.; Akkuzina, A. A.; Avetisov, R. I.; Khomyakov, A. V.; Saifutyarov, R. R.;

Avetisov, I. C. *Journal of Luminescence* **2016**. Effective Electroluminescent Materials for OLED Applications Based on Lanthanide 1,3-Diketonates Bearing Pyrazole Moiety. 177, 31–39. <https://doi.org/10.1016/j.jlumin.2016.04.017>.

Tsiper, E. V.; Soos, Z. G.; Gao, W.; Kahn, A. *Chemical Physics Letters* **2002**. Electronic Polarization at Surfaces and Thin Films of Organic Molecular Crystals: PTCDA. 360 (1–2), 47–52. [https://doi.org/10.1016/S0009-2614\(02\)00774-1](https://doi.org/10.1016/S0009-2614(02)00774-1).

Yao, Z. F.; Wang, J. Y.; Pei, J. *Crystal Growth and Design* **2018**. Control of π - π Stacking via Crystal Engineering in Organic Conjugated Small Molecule Crystals. 18 (1), 7–15. <https://doi.org/10.1021/acs.cgd.7b01385>.

Wang, L.; Li, T.; Shen, Y.; Song, Y. A. *Physical Chemistry Chemical Physics* **2016**. Theoretical Study of the Electronic Structure and Charge Transport Properties of Thieno[2,3-b]Benzothiophene Based Derivatives, 18 (12), 8401–8411. <https://doi.org/10.1039/c5cp07879b>.

Zhang, M.; Zhao, G. Ming-Xing Zhang and Guang-Jiu Zhao. *ChemSusChem* 2012. Modification of n-Type Organic Semiconductor Performance of Perylene Diimides by Substitution in Different Positions: Two-Dimensional π -Stacking and Hydrogen Bonding, *ChemSusChem* 2012, 5, 879 – 887. <https://doi.org/10.1002/qua.25034>

Zhang, Y.; Cai, X.; Bian, Y.; Li, X.; Jiang, J. *Journal of Physical Chemistry C* 2008. Heteroatom Substitution of Oligothiophenes: From Good p-Type Semiconductors to Good Ambipolar Semiconductors for Organic Field-Effect Transistors. 112 (13), 5148–5159. <https://doi.org/10.1021/jp710123r>.

Zhu, R.; Duan, Y. A.; Geng, Y.; Wei, C. Y.; Chen, X. Y.; Liao, Y. *Computational and Theoretical Chemistry* **2016**. Theoretical Evaluation on the Reorganization Energy of Five-Ring-Fused Benzothiophene Derivatives. 1078, 16–22. <https://doi.org/10.1016/j.comptc.2015.12.017>.

Assembly Line Balancing using Lean Techniques and Mathematical Modeling: A Case Study

Betül KAYIŞOĞLU¹
İsmet SÖYLEMEZ²
Özgül DEMİREL³
Gamzenur ARIKAN³
Kübra KURTOĞLU³

Introduction

The competitiveness of companies is determined as a result of the efficient and effective use of resources. The efficient and effective use of resources in the production sector is possible as a result of the balanced distribution of workloads to workstations on assembly lines. The assembly line balancing problem in institutions with assembly lines is to arrange the workstations during the assembly process, taking into account the priority relations between the works.

Assembly lines can be defined as systems in which small modular transport systems called conveyor belts are added one after the other and the product is transported either automatically or manually (Soylemez, 2020). Each product becomes the final product after the successive processes called "tasks" are completed. In the technical relations of the tasks with each other, that is, in the priority relations, other tasks cannot be started before some tasks are completed. In the assembly line balancing problem, 3 different objectives take these constraints into account. Type-1 is to find the minimum number of stations in the given cycle time, Type-2 is to find the cycle time in the given number of stations, and Type-E is to maximize line efficiency that considers not the only number of stations but also cycle time. In this study, the type-2 assembly line balancing problem is handled. The amount of time it takes to complete a product from start to finish is defined as cycle time. A new product is processed in each cycle. The final product is obtained by completing the processes at all stations.

Lean manufacturing was born in the Toyota Factory. The lean manufacturing system is also called Toyota Production System. The general definition of Lean according to the Lean Institute that "Lean is a way of thinking about creating needed value with fewer resources and less waste. And lean is a practice consisting of continuous experimentation to achieve perfect value with zero waste." (<https://www.lean.org/explore-lean/what-is-lean/>). There are generally 7 wastes in the production systems. These are Inventory, Waiting, Quality Defects, Overproduction, Over-processing, Motion, and Transportation. Experts are also talking about an 8th waste these days. This is about Unused Talent or Skills. Lean manufacturing techniques are used to eliminate these

¹ Dr, Abdullah Gül Üniversitesi, Endüstri Mühendisliği, 0000-0001-9979-5269

^{2,*} Dr, Abdullah Gül Üniversitesi, Endüstri Mühendisliği, 0000-0002-8253-9389, Corresponding Author

³ Abdullah Gül Üniversitesi, Endüstri Mühendisliği

wastes. 5S and Kaizen are the two lean manufacturing techniques that are applied to eliminate wastes.

In this study, the simple assembly line balancing problem (ALB) is discussed. The system, which was simplified by using lean techniques first, was then balanced using a mathematical model. A case study is conducted in a company producing ovens. With lean techniques, wastes are eliminated and the process time of the tasks is achieved. With the precedence relation of the tasks, a mathematical model is run to achieve a balanced assembly line. Different computational experiments are conducted with different numbers of workstations. According to the results of the mathematical model, cycle time and the number of workstations both decreased.

The rest of the study is organized as follows: The literature about assembly line balancing is discussed in Section 2. Section 3 gives the current system and first solution approach which is lean techniques discussed. The mathematical model is presented in Section 4. Section 5 gives the mathematical modeling results. Section 6 concludes the study.

Literature Review

Some literature review studies about the ALB problem that have been carried out are as follows: Baybars (1986); Becker and Scholl (2006); Boysen, Fliedner, and Scholl (2007); Battaia and Dolgui (2013); Sivanankaran and Shahabudeen (2014); Hazır, Delorme, and Dolgui (2014); Eghtesadifarda, Khalifehb, and Khorrama (2020).

Ertürk et al. (2014) performed the "Ranked Positional Weight Assembly Line Balancing Method" which is one of the heuristic methods for the ALB problem. Sahin et al. (2018) handled multi-manned assembly line balancing problem which also handled the number of required resources. The authors applied a simulated annealing algorithm for the solution methodology. Delice et al. (2018) handled two-sided U-type assembly lines with sequence-dependent set-up times. In this article, the ant colony optimization method was applied.

Sahin and Kellegoz (2019) handled multi-manned assembly lines with walking workers. In this article, they developed mathematical modeling and used Electromagnetic Field Optimization Algorithm as a solution methodology.

Yıldız et al. (2020) discussed the line balancing problem with a two-stage approach. In the first stage, the determination of whether the workers can perform the work elements and the necessary equipment determination was completed, and then the line balancing problem was solved in the existing system with mathematical modeling (using LINGO). In the second stage, a simulation model was designed in ARENA to determine whether the balanced assembly line in the new system complies with the real conditions, thanks to the data obtained in the first stage.

In the study by Campana et al. (2022), different from simple assembly line balancing, assignments were made by considering hierarchical worker assignments. In the article, mathematical models and heuristic methods are used and heuristic methods are compared.

The study by Qattawi Madathil (2019) consists of two phases; the first phase is applying lean manufacturing principles to reduce waste and improve the overall assembly-line efficiency. In this phase, Heijunka (production leveling), Muda elimination, and supermarket are applied. The second is line balancing using optimization modeling. After the second phase, the number of stations decreases from 27 to 21, and the total number of workers decreases from 27 to 23.

Case Study

A case study is conducted in an oven company. This company produces different types of gas and electrical cooking ranges. Firstly, lean manufacturing studies were carried out in the production area, and the studies related to the optimization mentioned in section 4 were developed.

Company has an assembly line that is used for the assemble process for the ovens. There are 28 workstations in the assembly line. Figure 1 shows the operation times in each station after wastes are eliminated. The longest operation time in the workstations gives us the cycle time that is 70 in the current system. It can be easily observed that the workers in the workstations do not do the same amount of work, some do less work, while others work longer than average. Figure 1 shows us how unbalanced the assembly line is in the current system.

One of the most basic assumptions of the assembly line balancing problem is that task times are standard. That is, there is a standard time for the time spent in producing each product. Assembly line balancing in the current production system does not mean achieving very good results. Because current task times need to be analyzed in detail. Thanks to detailed video analysis; value-added, non-value-added, and waste times are revealed in detail. With small touches, shorter standard times can be reached thanks to productivity increases in the processes. For this reason, processes with lean manufacturing techniques were analyzed first. Standard times are reached in a shorter time. Then, it is aimed to reach the optimum assembly line with the help of a mathematical model. The studies on lean manufacturing are given, firstly.

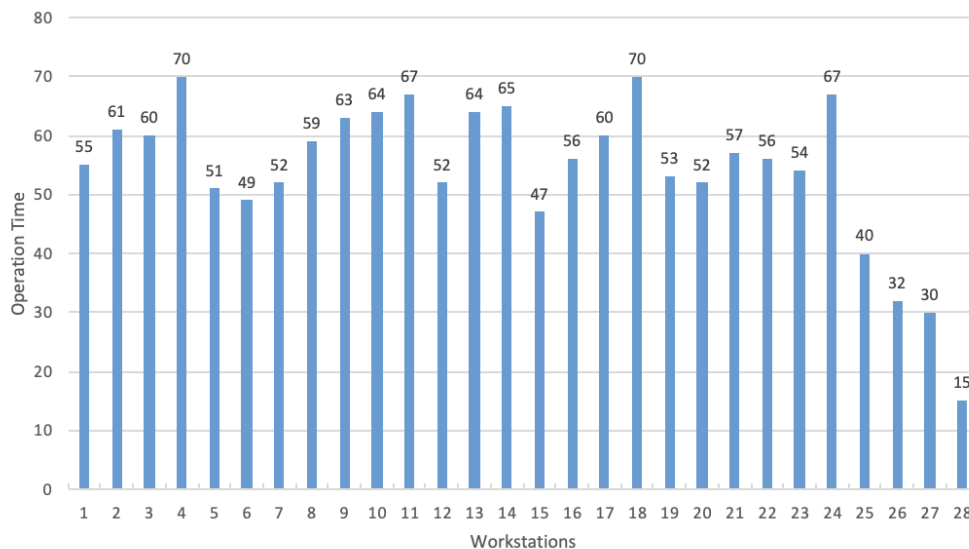


Figure 1. Operation time in each workstation in the current system

Lean Manufacturing

Before starting the analysis, it is necessary to choose which product family to work with first. The product group with the highest demand was selected according to the previous year's demand. Secondly, the determination of job elements by microanalysis was done.

While using the video analysis method, the business processes of the selected product family were determined. Then, videos of the processes were taken. Each video is examined in detail and

detailed with the microanalysis method. As a result of the video analysis, each process was divided into 3 basic parts. These are value-added, non-value-added, and waste activities. “Cutting, bending, screwing, welding, painting” will be given as value-added activities (VA). “Turn on, close, fix, check, control” are the non-value added activities (NVA). Waste activities (W) will be “walking, repairing or looking for” etc. Figure 2 shows different types of process times. Task i takes 62 seconds. However, NVA and W activities must be completely or partially eliminated. Firstly, waste time should be completely eliminated. When the first stage is completed, it is aimed to shorten the times that NVA in lean manufacturing. Even in VA activity, the time can be shortened with kaizens.

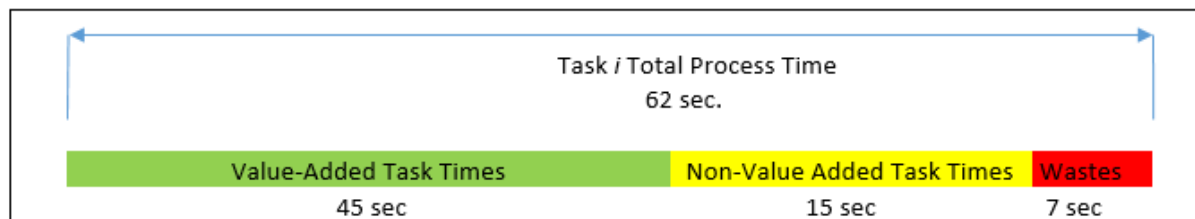


Figure 2. Types of task process times

With small touches, wastes are eliminated. And also small kaizens were carried out to remove some non-value adding activities. After eliminating unnecessary activities, it will be possible to move on to the mathematical modeling part for assembly line balancing.

An example of improving processes with the microanalysis method is as follows:

Hitting the bottom and side hairs of the oven with a hammer is one activity and takes 35 seconds. Turning and holding the hammer takes 2 seconds in the current system. Instead of the operator turning around and picking up the hammer every cycle, placing the hammer on the side of the assembly line table or with a top-hanging system can be achieved more easily. In this way, a gain of 2 seconds will be provided for each product/cycle. Another waste minimization example is "placing the oven in the packing carton". In the current situation, it takes about 40 seconds. When this preparation time is eliminated, the processing time is halved which is about 20 seconds waste time. Elimination of this process for the assembly line is an important gain for assembly line balance.

Two detailed video analysis gains are mentioned above. There are 48 work items in the selected product group. Video microanalysis was performed for all items. The total processing time has been reduced from 1341 to 1072. In this way, about 20% efficiency increase was achieved before the line balance was made.

After these analyses, new processing times are obtained for 48 tasks. After this stage, a better line balance was achieved with the help of mathematical modeling. In the following part, the mathematical modeling approach is presented.

Methodology

After the necessary improvements were completed with lean techniques, the optimization phase was started. There are three main constraints for the assembly line balancing problem. these constraints; assignment of all tasks to stations, ensuring priority relations, and not exceeding the number of stations given. It is aimed to reach the best cycle time by satisfying these constraints.

Mathematical Modeling

In this study, the type-2 assembly line balancing problem is studied in which the cycle time is minimized with the given number of stations. Let N denote the set of tasks where $i, j \in N$, and S denote the set of workstations where $k \in S$. P_j is the set of immediate predecessors of task j in the precedence network where $P_j \subset N$. t_i is the operation time of task i . The last parameter c is the cycle time. x_{ik} is defined as a binary variable that takes the value 1 if task i is assigned to Workstation k , 0 otherwise.

With these definitions, the type-2 assembly line balancing model (T2ALBM), is given below:

Model T2ALBM:

$$Z^* = \text{Min } c \quad (1)$$

s.t.

$$\sum_{k \in S} x_{ik} = 1 \quad \forall i \in N \quad (2)$$

$$\sum_{i \in N} t_i x_{ik} \leq c \quad \forall k \in S \quad (3)$$

$$\sum_{k \in S} k x_{ik} - \sum_{k \in S} k x_{jk} \leq 0 \quad \forall j \in N, \forall i \in P_j \quad (4)$$

$$x_{ik} \in \{0,1\} \quad \forall i \in N, \forall k \in S \quad (5)$$

The objective function defined in Equation (1) minimizes the cycle time. Constraints (2) ensure that every task is assigned to a workstation. Constraints (3) guarantee that the total time in a station does not exceed the cycle time. Constraints (4) satisfy the precedence relations between tasks. Constraints (5) define decision variables.

Results

There are 48 different tasks done on the assembly line of the company in which we conduct our case study. Process time of these tasks and the precedence relation between them are defined. We run the model (T2ALBM) type-2 assembly line balancing model for this problem. We consider the different number of workstations from 17 to 30. We run with CPLEX and obtain the optimal solution for each instance in seconds. Figure 3 gives the cycle times achieved with the mathematical model for the different numbers of stations.

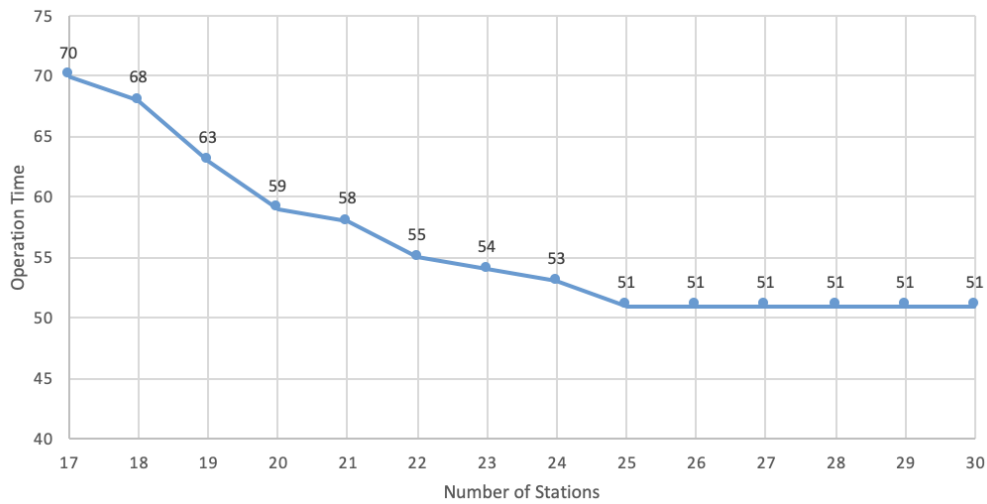


Figure 3. Cycle times achieved with T2ALBM for different numbers of stations

When Figure 3 is examined, it is seen that cycle time decreases as the number of stations increases as expected. However, when the number of stations is 25, there is no improvement in the cycle time even if we increase it more. The operation time of one of the tasks is 51 seconds. For that reason, we do not get any improvement as much as we increase the number of workstations. In the current system, the number of workstations is 28 with cycle time 70 seconds. When we check the mathematical model solution with 28 workstations, the cycle time is 51 seconds which is 27% lower than the current cycle time. Moreover, with the mathematical model, we are able to achieve the same cycle time with the lower number of workstations. Decreasing the number of stations from 28 to 25 is possible with cycle time 51. This means that we also have an improvement in the number of employees. It can be easily seen from Figure 4 that there is a more balanced assembly line with the solution achieved with T2ALBM.

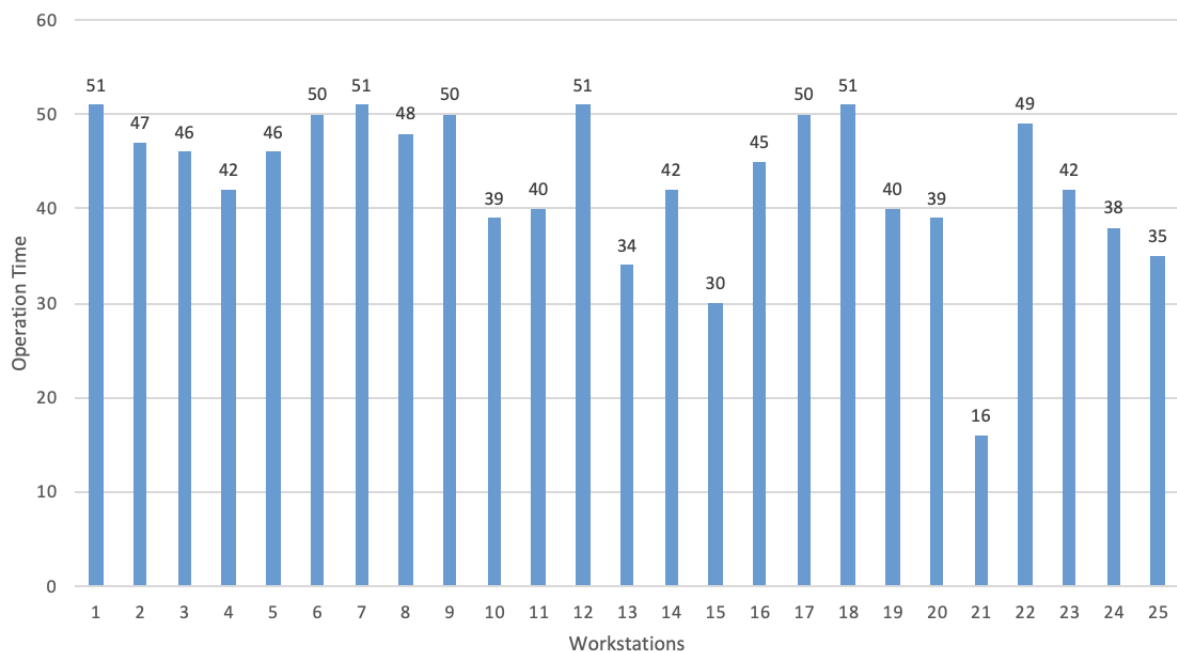


Figure 4. Operation time in each workstation in the solution achieved with T2ALBM for the number of workstations 25.

If the company does not need to decrease the cycle time in the current system. In other words, if the cycle time 70 is appropriate for their current production system, then we can check the number of workstations needed for this cycle time from the solutions of the mathematical model. In this case, 17 workstations are enough instead of 28 workstations which imply 39% improvement in the workforce.

Conclusion

In this study, a simple assembly line balancing problem is studied. A case study is conducted in a company producing ovens. The product group with the highest demand is chosen to study. All the tasks conducted to produce this product group are listed. Non-value added and waste activities are determined and eliminated with small kaizens. The operation time of each task and precedence relations of these tasks are obtained. In the current system, the assembly line is examined. The operation times in each workstation are observed and it is seen that the assembly line is not balanced effectively. Cycle time is directly related to the task assignments to workstations. For that reason, it is crucial to be able to obtain balanced assembly lines.

To be able to solve ALB problem, the mathematical model is given. The mathematical model is solved for the different number of workstations. The cycle time achieved by the mathematical model with the same number of workstations in the current system is 27% lower than the current cycle time. Moreover, when we analyze the results of the mathematical model, we see that the number of workstations required to achieve the same cycle time in the current system is 39% lower than the number of workstations in the current system. To sum up, with the mathematical model, the cycle time or/and the number of workstations in a system can be improved significantly.

References

- Battaia, O. and Dolgui, A. (2013). A taxonomy of line balancing problems and their solution approaches. *International Journal of Production Economics*, 142(2), 259-277.
- Baybars, I., (1986). A survey of exact algorithms for the simple assembly line balancing problem. *Management Sciences*, 32, 909–932.
- Becker, C. and Scholl, A. (2006). A survey on problems and methods in generalized assembly line balancing. *European Journal of Operational Research*, 168(3), 694- 715.
- Boysen, N., Fliedner, M., and Scholl, A. (2007). A classification of assembly line balancing problems, *European Journal of Operational Research*, 183, 674-693.
- Campana, N. P., Iori, M., & Moreira, M. C. O. (2022). Mathematical models and heuristic methods for the assembly line balancing problem with hierarchical worker assignment. *International Journal of Production Research*, 60(7), 2193-2211
- Delice, Y., Aydoğan, E. K., Söylemez, İ., & Özcan, U. (2018). An ant colony optimisation algorithm for balancing two-sided U-type assembly lines with sequence-dependent set-up times. *Sādhanā*, 43(12), 1-15.
- Eghtesadifard, M., Khalifeh, M., and Khorram, M. (2020). A systematic review of research themes and hot topics in assembly line balancing through the web of science within 1990–2017. *Computers and Industrial Engineering*, 139, 106-182.
- Eryürük, S. H., Kalaoğlu, F., & Baskak, M. (2011). Assembly line balancing by using statistical method in clothing production. *Textile and Apparel*, 21(1), 65-71.
- Hazır, Ö., Delorme, X., and Dolgui, A. (2014). A survey on cost and profit oriented assembly line balancing. *International Federation of Automatic Control Proceedings*, 47 (3), 6159-6167.
- Qattawi, A., & Chalil Madathil, S. (2019). Assembly line design using a hybrid approach of lean manufacturing and balancing models. *Production & Manufacturing Research*, 7(1), 125-142.
- Sahin, M., Kellegoz, T., & Soylemez, I (2018). Çok işçili montaj hatlarında istasyon ve kaynak yatırımı maliyetinin enküçüklenmesine yönelik tavlama benzetimi ve tam sayılı doğrusal programlamaya dayalı yeni bir algoritma. *Dicle Üniversitesi Mühendislik Fakültesi Mühendislik Dergisi*, 9(2), 727-739.
- Sahin, M., & Kellegoz, T. (2019). Balancing multi-manned assembly lines with walking workers: problem definition, mathematical formulation, and an electromagnetic field optimization algorithm. *International Journal of Production Research*, 57(20), 6487-6505.
- Sivasankaran, P. and Shahabudeen, P. (2014). Literature review of assembly line balancing problems. *The International Journal of Advanced Manufacturing Technology*, 73, 9- 12, 1665-1694.
- Soylemez, I (2020). Kaynak Paylaşımli Kaynak Kısıtlı Montaj Hattı Dengeleme Problemi için Bir Çözüm Yaklaşımı, Gazi University, PHD dissertation.

Topalođlu Yıldız, Ő., & Yıldız, G., & Cin, E. (2020). A mathematical programming and simulation modeling based solution approach to the worker-assigned assembly line balancing problem in an electronics company. Kocatepe İİBF Journal, June 2020, 22(1), 57-73.

Access time: 29.11.2022, <https://www.lean.org/explore-lean/what-is-lean/>.

Nonlinear Deformation Capacities of RC Frames Under Seismic Loads and Pushover Analysis.

Mehmet Fatih Yılmaz¹

1.Introduction

The most important part of the building in Turkey are composed of Reinforced Concrete structures. Considering the seismic event in the region, it is require to determine the seismic behavior of the RC structures with a more proper and correct methods. For these purposes many linear and nonlinear analysis approach are investigated. With the new specification about seismic design of building the design approach changes from strength base design to displacement base design. Displacement based design approach allow engineer to consider the nonlinear deformation capacities of the structures and economically design structure under seismic loads. The equal displacement rule are the critical acceptance of these approach. It accept that the elastic models and nonlinear model of building have equal displacement demand under seismic loads. There for if the structure design to reach the demand displacement of the seismic load without crashing, it can safely carry the seismic loads.

For these purpose determining nonlinear response of the RC structure become critical and many affords are focuses on this. Rasheed and Dinno [1] develop a new method for reinforced concrete structural elements, taking into account the nonlinear behavior capacities, and with the help of these approaches, more economical designs can be made. Rasheed and Dinno [1] conduct a study, in order to determine the nonlinear behavior of reinforced concrete structures, analytical models were created with the help of the Sap 2000 program by using the experimental data in the literature and testing the compatibility of these models with experimental studies. Most literature research presumes that the frame systems' flexibility is simply the bending of the columns and beams. Although the bending of columns and beams is modeled with the generally used plastic hinge, it is impossible to predict the joint's flexibility. For this reason, there is a need for advanced models that will take into account the joint's flexibility and better represent the structure's lateral deformations and earthquake responses [2]. Rajasankar, Iyer, and Prasad [3] developed formulations of lumped plastic behavior and nonlinear behavior to calculate reinforced concrete sections. The effect of shear force on the collapse in reinforced concrete elements is generally neglected in nonlinear analysis approaches. However, shear force and axial loads have significant effects on bending failure.

Shayanfar and Akbarzadeh Bengar [4] conduct a study presenting a spring model describing the bending behavior and the effects arising from the shear effect was proposed, and the reality of the proposed model was examined with parametric studies. Habibi and Moharrami [5] conduct a study to determine the nonlinear sensitivity analysis of reinforced concrete moment frame structure. Nonlinear pushover analysis with both material and geometric nonlinearity was considered. The improved computer technology makes more advanced structure analysis available, and the specification requirements are changed from static analysis to nonlinear analysis. Moreover,

¹ Mehmet Fatih Yılmaz, Assit Prof Dr, Ondokuz Mayıs University, Civil Engineering Department

the probabilistic uncertainties should be determined in the structure's design. For these purposes, some efforts are presented in the literature to determine the reliability analysis of structure with the first-order reliability methods and nonlinear analysis [6].

One of the important factor effecting the nonlinear behavior of the RC structure is the reinforcing details. The proper detailing of the reinforcement include both longitudinal and transverse reinforcing. For this purpose a detailed study conducted to determine the reinforcing configuration and minimum and maximum reinforcing requirement of the RC structure. This study discusses a reinforced concrete frame beam system, which has been experimentally studied in the literature. Firstly, pushover analyzes of the RC frame system were performed with the help of Sap 2000 and Seismo-struct programs, and its compatibility with the experimental data was observed. Thus, it has been shown that the mathematical model is compatible with the actual model. Then, real earthquake records were applied to the frame system, and the base shear force and peak displacement values of the frame beam were obtained under the near-fault and far-fault earthquake records. Earthquake records were scaled so that elastic earthquake forces exceeded the beam base shear capacity, and analyzes were performed for new records. In addition, pushover analyzes were carried out by forming different transverse reinforcement details, and the effects of the change in transverse reinforcement details on the frame deformation capacity and ductility were examined.

2.FE model of the frame structure

2.1.Description of the frame structure

A reinforced concrete frame system, which can make large deformations under the effect of bending, has been examined in this study. Studies on both analytical and mathematical models were carried out by the examined system [7], and a system with details in the literature was selected. The purpose of choosing this system is to compare the results obtained from the model created in the computer environment with the results obtained from the experimental study and to determine the compatibility of the model created with the real model, taking into account the assumptions to be made during modeling.

The studied system consists of a two-story frame. This system has a foundation section with a width of 800 (mm) and a height of 400 (mm) at the bottom. In the experimental studies, the foundation section was attached to the strong floor in the laboratory with the help of pre-stressed bolts. Thus moment-transmitting fixed support was obtained. The height of the first floor is 2200 (mm) between the beam axis and the column foundation connection points, and the height of the second floor is 2000 (mm) between the beam axes. The horizontal distance between the column axes is taken as 3500 (mm).

A 40 cm height and 30 cm width section was used as the column-reinforced concrete section. Column longitudinal reinforcements were formed with the help of 8 Q20 reinforcements. Moreover, Q10 reinforcement was used as transverse reinforcement, and it was formed with 125 (mm) intervals. The clearance distance from the center of the longitudinal reinforcements to the outer surface of the column is taken as 40 (mm). Also, the beam element with 40 cm height and 30 cm width was selected. As transverse reinforcement, Q10 reinforcement was formed at 125 (mm) intervals. In both elements, transverse reinforcement is formed with two stirrup arms in both directions, which are formed from a single stirrup. The depth of concrete cover in the beams is taken as 50 (mm). Concrete material strength was determined as C30 in the tests performed by Güner and the concrete elasticity module was obtained as 23674 MPa [7]. The material properties

of the reinforcement were determined as 418 MPa and 454 MPa, respectively, for the yield strengths for Q20 and Q 10 reinforcements [7].

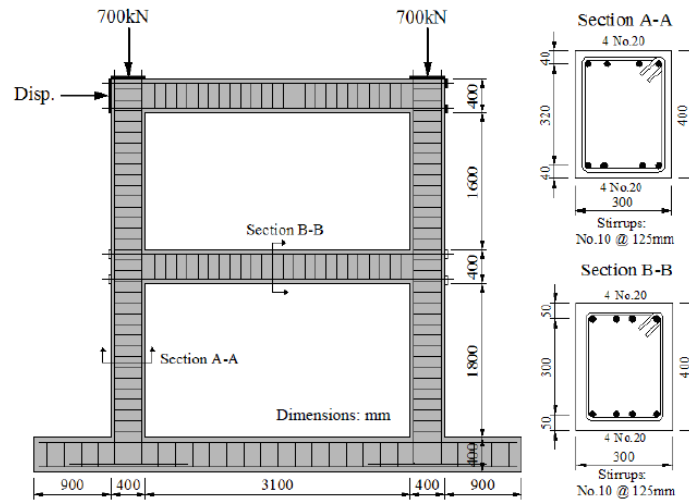


Figure 1 Details of Vecchio and Emara Frame [7]

2.2.FE model of the frame structure.

The finite element model of the structure was created with the help of both Sap 2000 and Seismo Struct programs. Since both programs are widely and effectively used in nonlinear structural analysis applications, they were preferred within the scope of this study. The SeismoStruct program allows users to define a more advanced material and plastic joint description in creating nonlinear models. However, the interface used in modeling large structures brings some difficulties. The Sap 2000 program, on the other hand, has significant advantages and conveniences in terms of the interface used and provides little opportunity for the assumptions made for the mathematical model and the modification of the parameters used.

Güner [7] in their study, the behavior of the frame system under the effect of experimental lateral thrust was investigated in the laboratory environment, and obtained the shear force and top peak displacement of the frame system. In addition, the mathematical model of the framework was obtained with the help of two different programs. Experimental data and mathematical models were compared. The mathematical model produced within the scope of this study was verified with experimental data. Figure 2 contains a comparison of experimental data and mathematical models. Although it is seen that experimental data and mathematical models have specific separations, they have acceptable differences from each other.

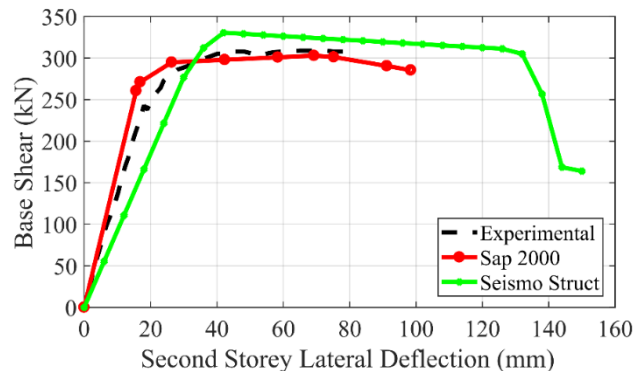


Figure 2 Comparison of Load Deflection Response of Vecchio and Emara Frame.

2.3. Plastic hinge formation and moment-curvature relation.

It is seen that the first plastic hinge for the analyzed frame system occurs in the first-floor beams. Then the second plastic hinges are formed at the column foundation connection points. Following hinge formation occurs at the endpoints of the first-floor beam and the endpoints of the second-floor column, respectively. It has been determined that the system has six plastic hinges in the pre-failure condition as shown in the Figure 3.

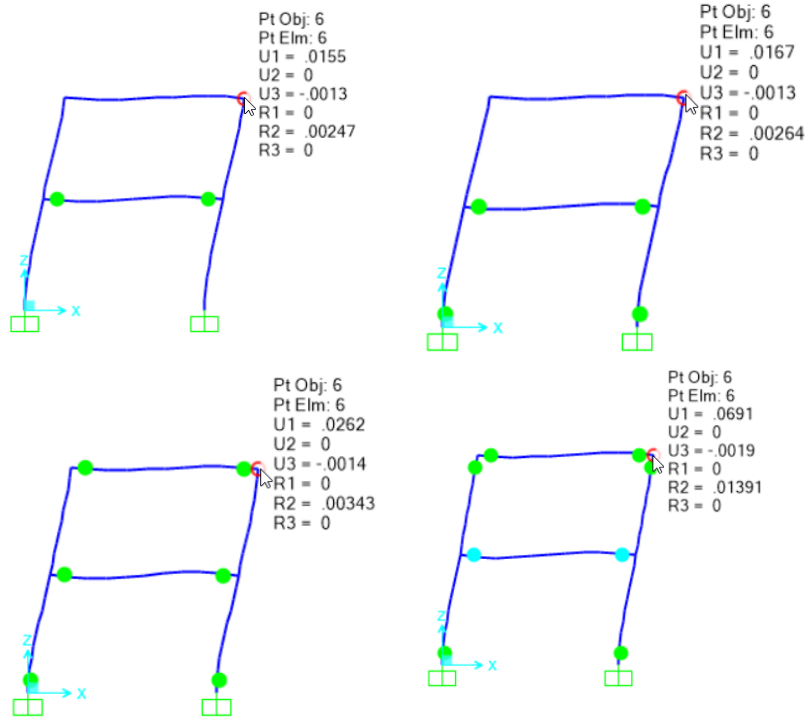


Figure 3 Propagation of the plastic hinge on the frame structure

The stress-strain capacities of the reinforcement of the frame system sections were obtained with the help of the Mander approach. It is seen that with the increase of the confinement reinforcement in this model, the concrete reaches a large deformation capacity and can carry large stresses. Suppose the moment-curvature relationship of the section is calculated considering the behavior of the confined concrete and its strain capacity. In that case, it can be seen that there will be significant decreases in the moment capacity of the section after the reinforcement starts to yield, as can be seen in Figure 4. However, the section can undergo large deformations until collapse occurs in the section.

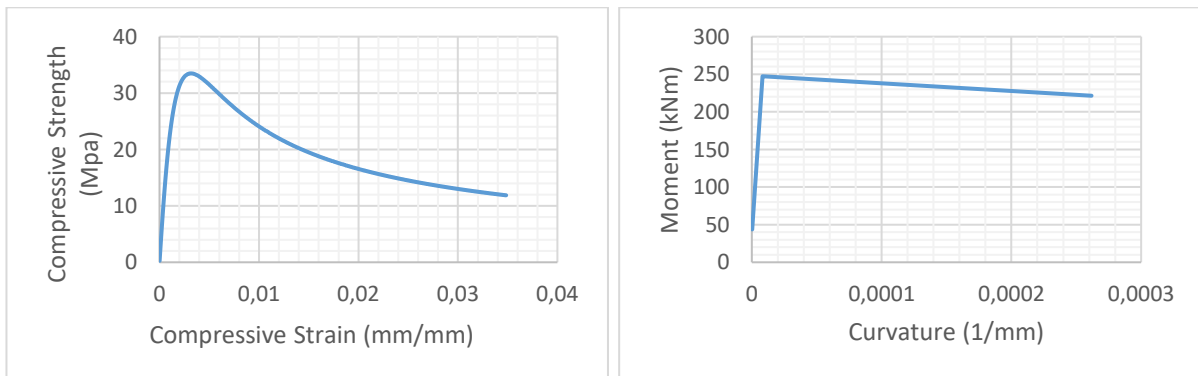


Figure 4 Moment curvature relation of the Beam section

Selection of the Earthquake records.

3.1. 3.1.Selection of the earthquake records.

Within the scope of this study, a total of 10 real earthquake records, five near faults and five far faults, were selected to determine the behavior of the reinforced concrete frame system under the earthquake loads. If the distance of the measurement station to the earthquake center is 15 km or less, it is considered a near fault, and if it is above, it is considered a far fault. Earthquake records with Mw 6 and above were selected in order to ensure that the earthquake intensity is at a level that can cause damage to the structure. Selected near earthquake records are given in Table 1, and far fault earthquake records are given in

Table 2.

Table 1 Near-fault ground motion records.

No	Earthquake	Year	Station	Mw	Dist. (km)	VS30 (m/s)
1	Loma Prieta	1989	Corralitos	6.93	3.85	462.2
2	Imperial Valley-02	1940	El Centro Array #9	6.95	6.09	213.4
3	Cape Mendocino	1992	Petrolia	7.01	8.18	422.2
4	Morgan Hill	1984	Gilroy Array #6	6.19	9.87	663.3
5	Kobe, Japan	1995	KJMA	6.90	0.96	312.0

Table 2 Far-field ground motion records.

No	Earthquake	Year	Station	Mw	Dist. (km)	VS30 (m/s)
1	Landers	1992	Amboy	7.28	69.21	382.9
2	N. Palm Springs	1986	Anza Fire Station	6.06	42.36	360.5
3	Loma Prieta	1989	Monterey City Hall	6.93	44.35	638.6
4	Northridge	1994	Castaic-Old Ridge Route	6.69	20.72	450.3
5	El Mayor-Cucapah, Mexico	2010	Salton City	7.20	72.63	324.5

3.2.Frequency content of the records.

The spectral acceleration graphs obtained by taking the FFTs of the selected earthquake records are shown in Figure 4. It is seen that extreme acceleration values are observed in the 0-1.5 sec frequency range in the near fault earthquake records. In the far fault earthquake records, it is seen that extreme acceleration values are observed in the frequency range of 0-0.5 seconds, except for the Kobe earthquake. The frequency contents and acceleration values of earthquake records show that near-fault earthquake records are expected to be more devastating for low and medium-rise buildings.

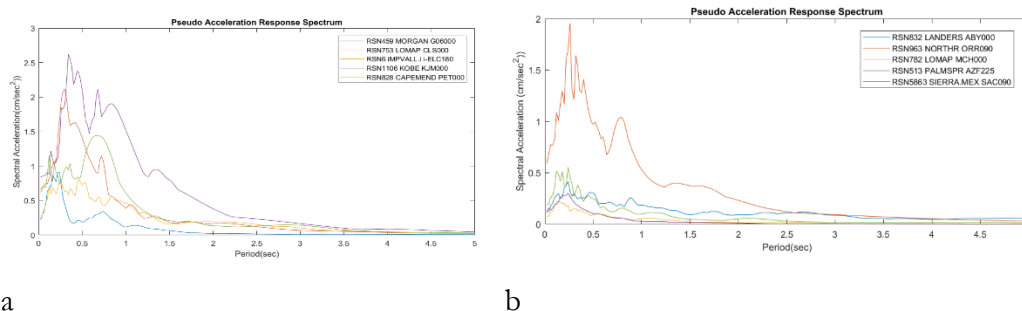


Figure 5 Spectral Acceleration graph of the a) Near field and b) Far field earthquake records.

4. Time history analysis of the Frame

4.1. 4.1. Nonlinear deformation capacities of the frames.

By using the obtained mathematical model and selected earthquake records, the behavior of the frame system under the near and far fault earthquake records was simulated. While performing the time history analysis, the structure's elastic base shear forces and elastic top lateral displacement values were determined using the linear time history. Then, nonlinear analyzes of the structure were performed in the time domain by using both material and geometry nonlinearity.

Elastic base shear force V_E obtained from these analyses, base shear force V_{max} obtained from nonlinear time history analyses, and elastic peak displacement δ_e and peak displacement δ_{max} obtained from nonlinear time history analyses are presented in Table 3, Table 4, Table 5, and Table 6 separately.

Table 3 Near Field Records

Record Name	V_E (kN)	V_{max} (kN)	δ_e (cm)	δ_{max} (cm)
MORGAN G06000	110.953	68.147	0.4929	0.3119
LOMAP CLS000	17.635	18.393	0.0772	0.0772
iMPVALL.i_i ELC180	49.452	54.572	0.207	0.207
KOBE KJM000	37.475	41.5	0.1572	0.1572
CAPEMEND PET000	19.024	19.582	0.0843	0.0843

Table 4 Far Field Records

Record Name	V_E (kN)	V_{max} (kN)	δ_e (cm)	δ_{max} (cm)
Landers_ABY_000	13.911	51.817	0.0624	0.0239
Northridge_Orr_090	24.833	25.984	0.1082	0.1082
Palms_AZF_225	12.59	13.004	0.0557	0.0557
LOMA_MCH_000	8.974	9.06	0.0402	0.0402
Sierra_mex_Sac_000	12.513	13.094	0.0548	0.0548

As a result of the analyses, it was determined that the system exhibited elastic behavior in some earthquake records. , the earthquake records were scaled with the coefficients determined to have an elastic base shear force of 400 kN to examine the frame system's nonlinear behavior. The analysis results for the scaled earthquake records are shown in Table 5 Increased Near Field Records Table 5 and Table 6.

Table 5 Increased Near Field Records

Record Name	V_E (kN)	V_{max} (kN)	δ_e (cm)	δ_{max} (cm)
MORGAN G06000	400	242.107	0.4929	0.3119
LOMAP CLS000	400	258.761	0.0772	0.0772
iMPVALL.i_i ELC180	400.001	298.544	0.207	0.207

KOBE KJM000	400.002	382.57	0.1572	0.1572
CAPEMEND PET000	400.002	294.371	0.0843	0.0843

Table 6 Increased Far Field Records

Record Name	V_E (kN)	V_{max} (kN)	δ_e (cm)	δ_{max} (cm)
Landers_ABY_000	400	180.243	1.7952	0.6875
Northridge_Orr_090	399.999	360.297	1.743	1.4233
Palms_AZF_225	400.014	325.198	1.7695	1.3416
LOMA_MCH_000	399.985	251.754	1.7935	1.0229
Sierra_mex_Sac_000	400.002	347.627	1.7515	1.6785

4.2. Calculating the ductility of the frame with different confinement reinforcements.

As seen from the analyzes performed in the time domain, the elastic base shear force gives higher values than the nonlinear base shear force. According to the equal displacement rule, the displacement value obtained in elastic behavior is expected to be equal to the displacement value in the nonlinear ideal model. It has been determined that the equal displacement rule is met in the frame system examined under the effect of the near-fault, but this rule is not fully satisfied in the far fault.

The equal displacement rule allows structural engineers to economically dimension their buildings by using base shear values much smaller than the elastic base shear force. For this, the structure is expected to not collapse during an earthquake, and it must be able to deform sufficiently to meet the peak displacement demand of the earthquake safely. In reinforced concrete structures, crushing concrete under pressure is the most critical factor limiting this deformation capacity. For this reason, it should be ensured that the deformation capacity of the concrete is increased by using reinforcement detail and that the building can safely carry the loads under the demanded top displacement.

In order to better understand the effect of the confinement reinforcement, static pushover analyzes were carried out considering different confinement reinforcement configurations, and the ductility values of the frame system for each confinement reinforcement were calculated as in

Table 7. Figure 6 shows the pushover analysis results obtained for the respective confinement reinforcements.

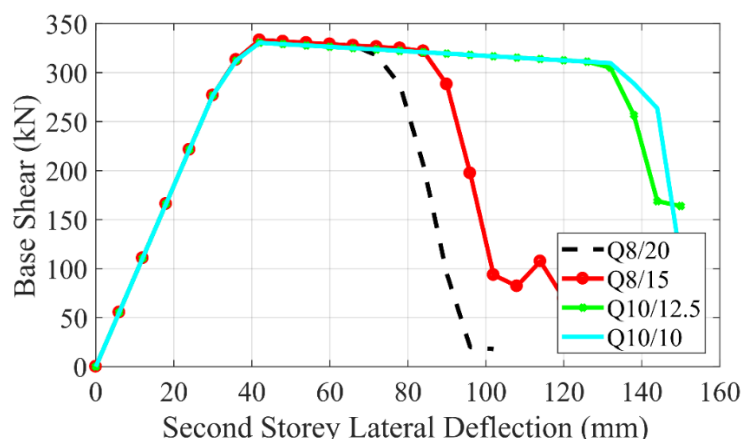


Figure 6 Push-over analysis of different confinement reinforcement configuration of frame sections.

Table 7 Effect of confinement reinforcement in to the ductility of the concrete section

Confinement Reinforcement	δ_y (mm)	δ_{max} (mm)	μ
Φ8/20	36	84	2.3
Φ8/15	36	90	2.5
Φ10/12.5	36	132	3.7
Φ10/10	36	132	3.7

5. Conclusion.

Within the scope of this study, a reinforced concrete frame system, which has been experimentally analyzed in the literature, is discussed, and the pushover analyzes of this system were carried out with the help of Sap2000 and Seismo-Struct programs. The mathematical model and the experimental model of the selected structure were compared, and the accuracy of the mathematical model was determined. Then, time history analyzes were performed under the selected near and far fault earthquake records, and elastic and nonlinear base shear forces and peak displacements formed in the structure were examined. In addition, different confinement reinforcement details were examined to determine the ductile demand of the frame system with the help of static pushover analyses.

When the confinement reinforcement decreases, the maximum deformation rate that the RC frame can achieve without crushing decreases, so the ductility of the frame system decreases significantly. The ductility value of the frame system is determined as $\mu = 2.3$ and $\mu = 3.7$ for the Φ8/20cm and Φ10/12.5cm confinement reinforcement respectively. After this value, stirrups were placed at Φ10 10 cm intervals, but no change was observed in the ductile response capacity of the frame system. In this case, it has been observed that the deformation capacity of the section is no longer limited by the crushing of the concrete, but by the yielding and rupture of the reinforcement, so that large deformations can occur in the section.

References

- [1] Rasheed HAS, Dinno KS. An improved nonlinear analysis of reinforced concrete frames. *Comput Struct* 1994;53:625–36. doi:10.1016/0045-7949(94)90106-6.
- [2] Birely AC, Lowes LN, Lehman DE. A model for the practical nonlinear analysis of reinforced-concrete frames including joint flexibility. *Eng Struct* 2012;34:455–65. doi:10.1016/j.engstruct.2011.09.003.
- [3] Rajasankar J, Iyer NR, Prasad AP. Modelling inelastic hinges using CDM for nonlinear analysis of reinforced concrete frame structures. *Comput Concr* 2009;6:319–41. doi:10.12989/cac.2009.6.4.319.
- [4] Shayanfar J, Akbarzadeh Bengar H. Nonlinear analysis of RC frames considering shear behaviour of members under varying axial load. *Bull Earthq Eng* 2017;15:2055–78. doi:10.1007/s10518-016-0060-z.
- [5] Habibi AR, Moharrami H. Nonlinear sensitivity analysis of reinforced concrete frames. *Finite Elem Anal Des* 2010;46:571–84. doi:10.1016/j.finel.2010.02.005.
- [6] Dimitri V, Bljucer F, Yankelevsky D. Reliability evaluation in nonlinear analysis of reinforced concrete structures. *Struct Saf* 1997;19:203–17. doi:10.1016/s0167-4730(96)00025-2.
- [7] Guner S. Performance Assessment of Shear-Critical. University of Toronto, 2008.

Impacts of Remote Working on Productivity of Civil Engineers during the COVID-19 Pandemic

Ayşegül TEPE¹
Bengi AYKAÇ²
Murat AYHAN³

Introduction

The first cases of COVID-19 disease, caused by the novel coronavirus, were reported in December 2019 in Wuhan, China. Due to the spreading speed and severity of the disease, the World Health Organization (WHO) declared that COVID-19 is qualified as a pandemic (WHO, 2020). Unfortunately, this highly contagious disease has spread to more than 200 countries and has caused more than 600 million confirmed cases, with more than 6.5 million deaths worldwide as of 21 November 2022 (WHO, 2022). Besides the adverse effects of the pandemic on the public health, commercial establishments, including the construction industry, were also affected severely (Ogunnusi et al., 2020: 120). Due to the contagious nature of the disease, social distancing was needed to slow the spread of COVID-19 and therefore all business activities were initially suspended or limited, except in essential sectors such as the medical and supply sectors (Gamil and Alhagar, 2020: 122-123). For this reason, commercial organizations have resorted to alternative forms of work and many companies had to switch to remote work, which can also be called Work-From-Home (WFH). Several on-site activities in the construction industry were stopped or postponed and employees were encouraged to work remotely to fulfill their ongoing tasks (Esa et al., 2020: 977). Besides on-site activities that cannot be performed remotely (i.e., concrete casting), there is no other option but to switch to remote work in order to carry out activities such as design and management in the construction industry.

Aim of the Study

Considering that remote working has a significant impact on employee performance due to various factors (Mardianah and Hidayat, 2020: 1043-1044), investigating the productivity during remote working period has become an issue that needs to be taken into consideration. In the construction industry, which makes a significant contribution to the country's economy and Gross Domestic Product, the effects of the COVID-19 on productivity should be examined in order to prevent performance loss and to continue business activities as before. In this study, it is thought that working remotely or WFH will have direct effects on the productivity of civil engineers. The study has two major objectives. First, it is aimed to provide empirical evidence showing whether there is an increase or a decrease in the productivity of civil engineers during the remote working period using the data collected from the construction industry. Secondly, is it aimed to identify the

¹ Student, Gazi University, Civil Engineering Department, Orcid: 0000-0002-5220-0309

² Assoc. Prof., Gazi University, Civil Engineering Department, Orcid: 0000-0002-6285-5667

³ Asst. Prof., Gazi University, Civil Engineering Department, Orcid: 0000-0002-2011-4190

factors affecting the engineering productivity in the construction industry during the remote working period and to reveal improvement opportunities for the sector.

Research Background

The impact of remote working on employee productivity has been discussed in the literature for more than a decade (Mustajab et al., 2020: 14). Recent studies on this subject have revealed two opposing findings. It was stated that the COVID-19 pandemic caused disruptions in the performance of employees in various activities (Mardianah and Hidayat, 2020: 1043-1044). In a study that examines the effects of the COVID-19 on companies from the Ghana construction industry, Agyekum et al. (2021: 231) stated that there were delays in project deliveries due to COVID-19. Kutluay Tutar et al. (2021: 705-706) stated that the works in the construction industry were disrupted during the COVID-19 period. In another study, the results of a questionnaire conducted with 71 civil engineers, the positive and negative experiences of the participants in the process of WFH were revealed (Ogunnusi et al., 2020: 126-127). It is also claimed that the virtual working environment provided during the pandemic period can be considered as a new normal. Shibani et al. (2020: 57), investigated the effects of the pandemic on the construction industry in the United Kingdom and observed an increment in the office productivity during the remote working period. There are other researchers claiming that remote work can increase employee productivity (Akça and Tepe Küçüköglü, 2020: 79-80; Angelici and Profeta, 2020: 23-24; Galanti et al., 2021: 430-431).

Previous Studies on Productivity in the Construction Industry

Productivity includes all factors that can affect the progress, development, and production outputs of construction processes (King et al., 2021: 5). Considering the competitive nature of the construction industry, it is clear that achieving higher productivity is critically important and performance improvements are a constant requirement for construction companies to remain competitive and profitable (Zhang et al., 2018: 1). In a broad perspective, productivity is the ratio of output produced to all or some of the input resources expended in the production process, or vice versa (Hughes and Thorpe, 2014: 211; Poirier et al., 2015: 75; Ayele and Fayek, 2019: 195-198). In the literature, the productivity measurement levels in the construction industry are classified as (1) Activity level (i.e., the productivity of steel elements' assembly activity), (2) Project level (i.e., the productivity of the construction of a new building), and (3) Industry level (i.e., the productivity of a country's construction industry as a whole). Regardless of the measurement level, the productivity of the construction industry can be divided into three: (1) Single factor productivity, (2) Partial factor productivity, and (3) Multi-factor productivity. If productivity corresponds to the ratio of output to a single particular input (i.e., labor force only), then this measurement is considered as a single factor productivity measure. On the other hand, the ratio of output to all relevant inputs is considered as a multi-factor productivity measure (Huang et al., 2009: 2139). Partial factor productivity is the ratio of output to some of the expended inputs spent (i.e., labor and capital resources). The tendency in the literature is to focus on single-factor productivity measures and on the labor productivity in particular (Ellis Jr and Lee, 2006: 317; Poirier et al., 2015: 74-84; Vereen et al., 2016: 2). Labor productivity; corresponds to the ratio of output to the working hours required to install a unit of that output (as cited in Hughes and Thorpe, 2014: 211). Labor productivity is an adequate way of monitoring the performance of an activity; however, activity-based labor productivity may not represent the true state of productivity at project or industry levels (Bernstein, 2003: 47-50). In other words, the overall performance to produce an output can be affected by various factors that need to be considered and it may not reveal the whole picture based solely on the performance of certain activities (AlChaer and Issa,

2020: 1). Therefore, in the case of performance monitoring on labor productivity, measurements at the project level are more appropriate than measurements at the activity level.

Based on the findings of the literature review, a single factor productivity approach over labor productivity is adopted in this study. Labor productivity will be measured at the project level.

Previous Studies on Engineering Productivity in the Construction Industry

Engineering productivity is the ratio of output to input; however, output has intangible aspects, unlike tangible products in the construction process (Sacks and Barak, 2008: 440). Rather than dealing with intangible inputs and outputs, previous studies have used simplified approaches for quantifications and measurements. In one of the earliest studies on design and engineering productivity by Thomas et al., (1999: 1), the amount of design sheets produced was used as the output and the hours required to create these sheets were used as the amount of input, and the productivity was measured in hours per design sheet. Song and AbouRizk (2005: 362) mentioned that working hours are the primary inputs in design work, since working hours are measurable, easily traceable, and most engineering companies keep records of working hours.

$$\text{Engineering Productivity} = \left(\frac{\text{Output}}{\text{Input}} \right) = \left(\frac{\text{Construction Quantity}}{\sum \text{Direct Engineering Work Hours}} \right) \quad (1)$$

In this study, engineering productivity will be compared using a project-level measurement approach, considering that the selected cases should have similar project scopes. In the study, (1) the engineering productivity before remote working will be compared with the engineering productivity during the remote working period, and (2) the productivity of similar projects undertaken by the same team before and during the pandemic will be compared, instead of comparing the project-level productivity values of different projects between companies or industries. The study's dataset will compare similar with similar, which removes output heterogeneity. Therefore, the sample cases in the dataset were selected based on similar project scope constraints.

Methodology

In the study, the Impacts of WFH/Remote Working Process on Civil Engineering Productivity during the COVID-19 Pandemic Period are quantitatively determined and evaluated. The basis of the study is primarily the determination of the factors affecting the productivity of an employee. A questionnaire was designed to categorize the factors affecting employee productivity for data collection and statistical analysis. Productivity was measured by conducting a questionnaire with the construction industry employees who produced similar works before and during the COVID-19 Pandemic in Ankara and comparing the works produced by the individuals in unit time. The questionnaire was sent to the participants online and then confirmed by phone. 102 people were reached, but 12 people were not included in the study because they filled the questionnaire incompletely. The study was completed with a total of 90 participants. In the first part of the questionnaire, there are questions to collect demographic information. In other sections, questions are categorized related to sub-factors which are affecting productivity.

Research Findings

While evaluating the data obtained in the study, SPSS (Statistical Package for Social Sciences for Windows) 22.0 program was used for the statistical analysis. Shapiro Wilk-W test and Kolmogorov Smirnov test were used to show the normality distribution of the data. In addition,

skewness and kurtosis values were used to understand the shape of the distribution. Descriptive statistics were expressed as mean and standard deviation for continuous variables and were given as frequency and percentage for categorical data. Chi-square test was used for comparisons of categorical data. In the comparison of quantitative data, Independent Samples T-Test and One-Way Analysis of Variance (ANOVA) test were used for variables that met the assumption of normal distribution. When significance was detected in the ANOVA test, the significance was evaluated with Tukey measure as a post-hoc test. Statistical significance was accepted as $p < 0.05$. For those who did not meet the normal distribution assumption, the Mann-Whitney U test, which is the non-parametric equivalent of the Independent Samples T-Test, and the Kruskal-Wallis H test, which is the non-parametric equivalent of the One-Way ANOVA, were used.

The questionnaire was based on a 5-point Likert-scale. The Cronbach Alpha (α) coefficient was used in the reliability and internal consistency analysis of the factors. Cronbach Alpha (α) coefficient, which takes a value in the range of 0 to 1, provides acceptable reliability for any value greater than 0,7 (Kılıç, 2016: 47). The Cronbach Alpha (α) values calculated for all the sub-factors were either very close to the threshold of 0,7 or higher. This indicates that the sub-factors are adequately reliable.

Table 1 shows the percentages and frequency distributions of the socio-demographic variables from the first part of the questionnaire .

Table 1 - Distribution of Participants' Socio-Demographic Characteristics

Variables and Corresponding Categories	n (%)	
Gender	Male	47 (%52,22)
	Female	43 (%47,78)
Marital Status	Single	55 (%61,11)
	Married	35 (%38,89)
Position	Project Engineer	41 (%45,56)
	Center Office Engineer	13 (%14,44)
	Architect	17 (%18,89)
	Project Director	6 (%6,67)
	Draftsman	9 (%10,00)
	Other	4 (%4,44)
Professional Experience	0-2 Years	21 (%23,33)
	2-4 Years	20 (%22,22)
	5-9 Years	26 (%28,89)
	10 Years and Over	23 (%25,56)
Designated-Separate Room as a Workstation	No	14 (%15,56)
	Yes	76 (%84,44)
Support of Government	No	28 (%31,11)
	Yes	28 (%31,11)
	No idea	34 (%37,78)
Changes in Work Duration	Decreased	22 (%24,44)
	Not Changed	35 (%38,89)
	Increased	33 (%36,67)
Use of Building Information Modeling Tools	No	41 (%45,56)
	Yes	49 (%54,44)

The mean and standard deviation values for the continuous variables and factor scores are given in Table 2.

Table 2 - Mean, Standard Deviation, and Median Scores of Sub-Factors

	Mean & Standard Deviation	Median (minimum-maximum)
Employee	2,911±0,934	2,93 (1-4,43)
Manager	2,929±0,767	3 (1,33-5)
Equipment	3,27±1,32	3 (1-5)
Financial	2,86±1,27	3 (1-5)
Project	2,64±1,25	2,5 (1-5)
Environment	3,14±0,95	3,2 (1,2-5)
Productivity Change Percentage	0,626±6,018	0 (-13,01-16)

The distribution of the responses of participants for each variable is given in Table 3.

Table 3 - The Distribution of the Responses

Sub-Factor	Question	Strongly Disagree	Disagree	Neither agree nor disagree	Agree	Strongly Agree
		n (%)	n (%)	n (%)	n (%)	n (%)
Employee	Job Discipline	23 (%25,56)	14 (%15,56)	21 (%23,33)	19 (%21,11)	13 (%14,44)
	Changes in the Methods of Communication	20 (%22,22)	21 (%23,33)	19 (%21,11)	16 (%17,78)	14 (%15,56)
	Remote Control of CAD Files	22 (%24,44)	13 (%14,44)	20 (%22,22)	11 (%12,22)	24 (%26,67)
	Same Workplace and Living Space	17 (%19,1)	25 (%28,09)	10 (%11,24)	22 (%24,72)	15 (%16,85)
	External Stimuli in the House	16 (%17,78)	23 (%25,56)	12 (%13,33)	22 (%24,44)	17 (%18,89)
	The Disappearance of Control Pressure	30 (%33,33)	12 (%13,33)	11 (%12,22)	11 (%12,22)	26 (%28,89)
	Changes in Work Duration	23 (%25,56)	17 (%18,89)	15 (%16,67)	19 (%21,11)	16 (%17,78)
Manager	Not Familiar with the WFH Process	13 (%14,44)	20 (%22,22)	21 (%23,33)	11 (%12,22)	25 (%27,78)
	Motivation Enhancing Flexibility	14 (%15,56)	11 (%12,22)	34 (%37,78)	21 (%23,33)	10 (%11,11)
	Online Meeting Productivity	4 (%6,56)	8 (%13,11)	10 (%16,39)	29 (%47,54)	10 (%16,39)
	Status of Hiring a New Person	35 (%42,17)	16 (%19,28)	22 (%26,51)	4 (%4,82)	6 (%7,23)
Equipment	Lack of Infrastructure and Materials	15 (%16,67)	21 (%23,33)	10 (%11,11)	13 (%14,44)	31 (%34,44)
	Need for Technical Support	5 (%8,06)	18 (%29,03)	13 (%20,97)	13 (%20,97)	13 (%20,97)
Financial	Payment Problems	5 (%10,2)	9 (%18,37)	13 (%26,53)	5 (%10,2)	17 (%34,69)
	No Overtime Pay	25 (%40,98)	13 (%21,31)	6 (%9,84)	7 (%11,48)	10 (%16,39)
	Not Receiving the Expected Raises	12 (%23,53)	8 (%15,69)	10 (%19,61)	7 (%13,73)	14 (%27,45)
Project	Repetition of Work	23 (%26,14)	12 (%13,64)	20 (%22,73)	14 (%15,91)	19 (%21,59)
	Unforeseen Changes in the Project	33 (%36,67)	20 (%22,22)	17 (%18,89)	11 (%12,22)	9 (%10)
Environment	Decreased Health Concern	2 (%2,22)	17 (%18,89)	10 (%11,11)	22 (%24,44)	39 (%43,33)
	Lack of Coordination	13 (%14,44)	19 (%21,11)	14 (%15,56)	28 (%31,11)	16 (%17,78)
	Home Office Performance Drop	20 (%22,22)	17 (%18,89)	9 (%10)	32 (%35,56)	12 (%13,33)
	Work-Life Balance	17 (%18,89)	22 (%24,44)	12 (%13,33)	28 (%31,11)	11 (%12,22)
	Chores	27 (%30)	14 (%15,56)	16 (%17,78)	21 (%23,33)	12 (%13,33)

Hypotheses of the Research

The hypothesis of the study is listed below. The statistical analysis with respect to these hypotheses can be seen in Table 4.

H₁: Socio-demographic characteristics have a direct effect on productivity sub-factors.

H₁: Gender has a direct effect on the environment-related sub-factors related to productivity.

H₁: Presence of a designated-separate room as a workstation directly affects the changes in the productivity.

H₁: Changes in the work duration has a direct effect on the changes in the productivity.

Table 4: Statistical evaluation of H₁, H₂ and H₃ hypotheses

		Mean & Standard Deviation	Median (minimum-maximum)	t\F	p
Gender	Male	3,40±0,90	3,60 (1,40-5,00)	t=2,796	0,006
	Female	2,86±0,93	2,80 (1,20-4,20)		
Designated-Separate Room as a Workstation	No	-2,49±5,46	-1,45 (-13,01-9,00)	t=-2,150	0,034
	Yes	1,19±5,97	0,00 (-11,56-16,00)		
Changes in Work Duration	Decreased	4,73±5,05	4,78 (-3,67-16,00)	F=23,193	<0,001 p ^{ac} <0,001 p ^{bc} <0,001
	Not Changed	2,30±4,76	0,00 (-6,44-12,05)		
	Increased	-3,89±4,92	-3,50 (-13,01-7,40)		

A statistically significant difference was identified between male (3.40±0.90) and female (2.86±0.93) participants related to the environmental sub-factor scores with respect to gender (t=2.796; p=0.006). In terms of environment-related variables, the productivity of males was affected more severely than the productivity of females.

A statistically significant difference was identified between those who have a designated-separate room as a workstation at home (1.199±5.971) and those who do not (-2,489±5.464) with respect to the change percentage in the productivity (t=-2,150; p=0,034). The productivity of those who do not have a designated-separate room as a workstation in their home is lower than those who have.

A statistically significant difference was identified between the change percentage in the productivity and the change in work duration (F=23,193; p<0,001). Tukey's test was performed as a post-hoc analysis to determine which groups originated the difference. There is a difference between those whose working hours have decreased (4.733±5.046) and those whose working hours have increased (-3.892±4.922). There is also a difference between those whose working hours did not change (2.304±4.758) and those whose working hours increased (-3.892±4.922) (p^{ac}<0,001; p^{bc}<0,001). The productivity of those whose working hours increased was lower than the productivity of those whose working hours decreased or did not change.

In the light of these explanations, hypothesis H₁, H₂ and H₃ were accepted.

Discussion of Findings

This study aims to determine how the transition to remote working, which is a new way of doing business, has affected employees' productivity in the construction industry during the COVID-19 pandemic. In addition, it is aimed to determine the factors affecting engineering productivity during the remote working period and to make improvement suggestions for the industry. Limitations of the study include the dataset being collected from a specific region only and the questionnaire being applied to people who produced similar projects before and during the COVID-19 pandemic. In other words, the dataset was collected from participants that produced similar projects before and during the pandemic period in Ankara.

Impact of Gender on Productivity

Transitions to remote work with the COVID-19 pandemic reduced health concerns as well as limiting people's social interactions. This exposed people at high levels of loneliness. In

particular, remote workers may suffer more from the process of staying at home because they do not have the opportunity to socialize with their colleagues. This situation reflects negatively on their work performance (Larson et al., 2020: 3; Toscano and Zappalà, 2020: 14; Wang et al., 2021:27). While people, who work in a regular office environment but had to switch to remote working due to the pandemic, may have a negative impact on their desire to work and their productivity may decrease. In addition, the same working and living space makes it difficult to determine the boundaries and balance between home responsibilities and work duties (Awada et al., 2021:1173). Work-related stress, role ambiguity arising from responsibilities between home and work, family-work conflict, disagreements with other people living at home are reflected in the performance of employees and affect their work productivity and work commitment (Galanti et al., 2021:427; Tong et al., 2021: 1). In a study that acknowledges work-family conflicts as gender-related, it is stated that such conflict attributes to women due to women being primary responsible of housework and childcare. The same study argued that men are affected by family-work conflict as much as women in the transition to WFH with the COVID-19 pandemic (Galanti et al., 2021: 427). Today, although men contribute more to housework, the traditional gender roles of society, which places childcare and housework responsibilities on women (Cerrato and Cifre, 2018: 9; Baert et al., 2020: 9). Therefore, WFH facilitates the balance of women's responsibilities between family-work-home and meeting the demands of other household members at home (Awada et al., 2021: 1183; Farooq and Sultana, 2021: 309). In another study, it was stated that while WFH, women were able to balance their work-home-child care responsibilities better than when they worked at the office and this was contributing to their productivity (Colley and Williamson, 2020: 23). It has been observed that women are more willing to work remotely than men and have higher productivity during the remote working period (Awada et al., 2021: 1185; Pérez et al., 2002: 273).

Impact of Having a Designated-Separate Room as a Workstation on Productivity

WFH during the COVID-19 pandemic has also highlighted the need for physical space in home-office environments. The point to be noted is that not all individuals working from home have a designated area for work. In this case, it may be necessary to use other areas in the house, such as the dining table or areas such as the kitchen counter and the coffee table. The lack of a special work area can affect the person both physically and mentally and reduce her/his performance at work (Xiao et al., 2021: 182-189). Working in a designated room for work ensures that the employee is isolated from distractions and gets the work done without interruption. Employees need to leave the living space and distractions to focus on their own work (Mello, 2007: 258). Huls et al., (2022: 84) found that participants, who have a designated-separate room at home and work there all day, had a higher productivity than those without a designated-separate room at home, or only use a designated-separate room for part of the day.

Impact of Changes in Work Duration on Productivity

Labor productivity depends on long working hours (Maqsoom et al, 2018: 16). Continuing overtime period throughout the project causes a decrease in labor productivity (Acikara, 2016: 43). Employees who work overtime feel stress and fatigue that do not only decrease their productivities but also it causes them to make mistakes and get sick (Pencavel, 2015: 2073). Considering a certain hourly working time per week, overtime hours longer than 3 or 4 weeks cause fatigue and lead to productivity losses (Thomas and Raynar, 1997: 184-187). Moreover, the long working hours and the fact that individuals have to work outside of working hours negatively affect the work-life balance (Suvacı and Şimşek, 2021: 186). Work-life balance is the balancing of expectations at the work and private life of employees (Bekmezci et al., 2021: 3-4). Failure to establish a work-life balance causes an elevated level of stress in employees and accordingly negatively affects

motivation, performance, and productivity (Yılmaz and Sağlam, 2021: 522). Some of the employees believe that working fewer hours will reduce distraction and increase productivity as it will establish a better work-life balance (Colley and Williamson, 2020: 10).

Conclusion

In the fight against the COVID-19 pandemic, it has become a significant issue to continue the normal flow of life and work without interruption. Therefore, examining the changes in the productivity of employees during the transition to remote work has become a necessity for both managers and employees. This study aims to reveal how remote work, which is a new way of doing business after the COVID-19 pandemic, affects the productivity of employees in the construction industry. At the same time, it is aimed to determine the factors affecting productivity and to make suggestions for the improvements. Limitations of the study include the dataset being collected from a specific region only and the questionnaire being applied to people who produced similar projects before and during the COVID-19 pandemic.

If the productivity of the employees is increased and they are required to work with maximum efficiency, the first thing to do is to determine the factors affecting employee productivity. Therefore, within the scope of this study, the factors affecting the productivity of an employee, mostly a construction industry employee, were examined. With the results obtained from the literature review, the factors affecting the engineering productivity were categorized and a questionnaire was designed. The results of the questionnaire were analyzed statistically, and the acceptance-rejection status of the hypotheses was determined.

It was concluded that gender has a direct effect on the environment-related sub-factors of productivity. In other words, it was concluded that women are more productive than men during the remote working period. This shows that the remote working provides an advantage for women to establish a more comfortable home-work-life balance. In this regard, although the fact that men stay at home more and become more involved in the routines at home during the pandemic, this interrupts them although it is not an insurmountable situation.

Another hypothesis is that having a designated-separate room at home affects productivity. Having a designated-separate room as a workstation increases productivity. However, a designated-separate room as a workstation may not be in everyone's home. In this case, great sacrifice falls on the employee and the household members who lives with them. Employees, who do not have a designated-separate room, can use any room in the house as a workstation. Appropriate work duties may be assigned to employees, who do not have a designated-separate room, by managers. For example, they may attend only mandatory meetings and not included in every meeting.

The last hypothesis is the changes in working duration having an effect on productivity. It has been concluded that employees whose working durations decrease or do not change are more productive than those that increase. Working overtime does not always mean the work is perfect. After a while, working overtime gets tiring and wears out the employee. It also makes them more prone to mistakes. Although remote working provides flexibility, managers observing a decrease in the performance of their employees should intervene in this situation and certain time schedule for work should be arranged similar to the normal office environment.

References

- Acıkara, T. (2016). Türk inşaat sektöründe verimlilik faktörleri uygulamalarının değerlendirilmesi: en iyi verimlilik uygulamaları endeksi, Master's Thesis, Antalya: Akdeniz University.
- Agyekum, K., Kukah, A. S., and Amudjie, J. (2021). The impact of COVID-19 on the construction industry in Ghana: the case of some selected firms. *Journal of Engineering, Design and Technology*, 20(1), p. 222-244. <http://dx.doi.org/10.1108/JEDT-11-2020-0476>,
- Akça, M., and Tepe Küçüköğlü, M. (2020). COVID-19 ve iş yaşamına etkileri: evden çalışma. *Journal of International Management Educational and Economics Perspectives*, 8(1), p. 71-81.
- AlChaer, E., and Issa, C. A. (2020). Engineering productivity measurement: a novel approach. *Journal of Construction Engineering and Management*, 146(8), 04020087, p. 1-11, [https://doi.org/10.1061/\(ASCE\)CO.1943-7862.0001875](https://doi.org/10.1061/(ASCE)CO.1943-7862.0001875).
- Angelici, M., and Profeta, P. (2020). Smart-Working: work flexibility without constraints. CESifo Working Paper, No. 8165, Center for Economic Studies and info Institute (CESifo), p. 1-116.
- Awada, M., Lucas, G., Becerik-Gerber, B., and Roll, S. (2021). Working from home during the COVID-19 pandemic: Impact on office worker productivity and work experience. *Work*, (Preprint), p. 1-19, doi: 10.3233/WOR-210301
- Ayele, S., and Fayek, A. R. (2019). A framework for total productivity measurement of industrial construction projects. *Canadian Journal of Civil Engineering*, 46(3), p. 195-206. <http://dx.doi.org/10.1139/cjce-2018-0020>.
- Baert, S., Lippens, L., Moens, E., Sterkens, P., and Weytjens, J. (2020). The COVID-19 crisis and telework: a research survey on experiences, Expectations and Hopes. *IZA Discussion Papers*, p. 1-37, Bonn: Institute of Labor Economics (IZA).
- Bekmezci, M., Mert, İ. S., and Abubakar, M. (2021). İş-yaşam dengesinin yaşam tatminini yordamasında çalışılan sektörün düzenleyici etkisi. *Anadolu Üniversitesi Sosyal Bilimler Dergisi*, 21(1), p. 1-22, <https://doi.org/10.18037/ausbd.902535>.
- Bernstein, H. M. (2003). Measuring productivity: An industry challenge. *Civil Engineering (N.Y.)*, 73(12), p. 46-53.
- Cerrato, J., and Cifre, E. (2018). Gender inequality in household chores and work-family conflict. *Frontiers in psychology* 9,1330, p. 1-11. <https://doi.org/10.3389/fpsyg.2018.01330>.
- Colley, L., and Williamson, S. (2020). Working during the pandemic: From resistance to revolution? Canberra, Australia: UNSW Canberra.
- Ellis Jr, R. D., and Lee, S.-h. (2006). Measuring project level productivity on transportation projects. *Journal of construction engineering and management*, 132(3), p. 314-320. [https://doi.org/10.1061/\(ASCE\)0733-9364\(2006\)132:3\(314\)](https://doi.org/10.1061/(ASCE)0733-9364(2006)132:3(314)).

Esa, M. B., Ibrahim, F. S., and Kamal, E. B. (2020). Covid-19 pandemic lockdown: The consequences towards project success in Malaysian construction industry. *Advances in Science, Technology and Engineering Systems Journal* Vol. 5(5), p. 973-983. <https://dx.doi.org/10.25046/aj0505119>.

Farooq, R., and Sultana, A. (2021). The potential impact of the COVID-19 pandemic on work from home and employee productivity. *Measuring Business Excellence*, p. 308-325. <http://dx.doi.org/10.1108/MBE-12-2020-0173>.

Galanti, T., Guidetti, G., Mazzei, E., Zappalà, S., and Toscano, F. (2021). Work from home during the COVID-19 outbreak: The impact on employees' remote work productivity, Engagement, and Stress. *Journal of occupational and environmental medicine*, 63(7), p. 426-432. <https://doi.org/10.1097/jom.0000000000002236>.

Gamil, Y., and Alhagar, A. (2020). The impact of pandemic crisis on the survival of construction industry: A case of COVID-19. *Mediterranean Journal of Social Sciences*, 11(4), p. 122-128. <https://doi.org/10.36941/mjss-2020-0047>.

Huang, A. L., Chapman, R. E., and Butry, D. T. (2009). *Metrics and Tools for Measuring Construction Productivity: Technical and Empirical Considerations*. Gaithersburg, MD: Special Publication (NIST SP) National Institute of Standards and Technology.

Hughes, R., and Thorpe, D. (2014). A review of enabling factors in construction industry productivity in an Australian environment. *Construction Innovation*, Vol. 14 (2), p. 210-228. <https://doi.org/10.1108/CI-03-2013-0016>.

Huls, S. P., Sajjad, A., Kanters, T. A., Hakkaart-van Roijen, L., Brouwer, W. B., and van Exel, J. (2022). Productivity of working at home and time allocation between paid work, unpaid work and leisure activities during a pandemic. *Pharmacoeconomics*, 40(1), p. 77-90. <https://doi.org/10.1007/s40273-021-01078-7>.

Kılıç, S. (2016). Cronbach's alpha reliability coefficient. *Psychiatry and Behavioral Sciences*, 6(1), p. 47-48.

King, S. S., Rahman, R. A., Fauzi, M. A., and Haron, A. T. (2021). Mechanisms for addressing the impact of COVID-19 on infrastructure projects. *4th National Conference on Wind and Earthquake Engineering In IOP Conference Series: Earth and Environmental Science*, Vol. 682 (1), p. 1-9, <http://dx.doi.org/10.1088/1755-1315/682/1/012047>.

Kutluay Tutar, F., Ekici, M., Balkaya, D., and Tutar, N. F. (2021). Öğrenen ekonomi bağlamında kendisi küçük ama tahribatı büyük. *International Academic Social Resources Journal*, (e-ISSN: 2636-7637), 6 (24), p. 699-712, doi: 10.31569.

Larson, B. Z., Vroman, S. R., and Makarius, E. E. (2020). A guide to managing your (newly) remote workers. *Harvard Business Review*, p. 1-6.

Maqsoom, A., Mughees, A., Khan, A. K., and Arif, M. I. (2018). Labor productivity in construction industry: investigating the influence of internal psychosocial stressors. In *ICCREM (International Conference on Construction and Real Estate Management) 2018: Analysis of Real Estate and the Construction Industry*, p. 10-17. Reston, VA: American Society of Civil Engineers.

Mardianah, L., and Hidayat, S. (2020). Empirical study of the impact of work from home (WFH) policy and top management support on employee performance. *Journal of Research in Business, Economics, and Education*, 2(5), p. 1039-1045.

Mello, J. A. (2007). Managing telework programs effectively. *Employee responsibilities and rights journal*, 19(4), p. 247-261. <https://doi.org/10.1007/s10672-007-9051-1>.

Mustajab, D., Bauw, A., Rasyid, A., Irawan, A., Akbar, M. A., and Hamid, M. A. (2020). Working from home phenomenon as an effort to prevent COVID-19 attacks and its impacts on work productivity. *TIJAB (The International Journal of Applied Business)*, 4(1) , p. 13-21.

Ogunnusi, M., Hama-Adama, M., Salman, H., and Kouider, T. (2020). COVID-19 pandemic: the effects and prospects in the construction industry. *International journal of real estate studies*, 14(Special Issue 2), p. 120-128.

Pencavel, J. (2015). The productivity of working hours. *The Economic Journal*, 125(589), p. 2052-2076. <https://doi.org/10.1111/eoj.12166>.

Pérez, M. P., Carnicer, M. P., and Sánchez, A. M. (2002). Differential effects of gender on perceptions of teleworking by human resources managers. *Women in Management Review*, p. 262-275.

Poirier, E. A., Staub-French, S., and Forgues, D. (2015). Measuring the impact of BIM on labor productivity in a small specialty contracting enterprise through action-research. *Automation in construction*, 58, p. 78-84. <http://dx.doi.org/10.1016/j.autcon.2015.07.002>.

Sacks, R., and Barak, R. (2008). Impact of three-dimensional parametric modeling of buildings on productivity in structural engineering practice. *Automation in Construction*, 17(4), p. 439-449. <http://dx.doi.org/10.1016/j.autcon.2007.08.003>.

Shibani, A., Hassan, D., and Shakir, N. (2020). The effects of pandemic on construction industry in the UK. *Mediterranean Journal of Social Sciences*, 11(6), p. 48-60. <https://doi.org/10.36941/mjss-2020-0063>.

Song, L., and AbouRizk, S. M. (2005). Quantifying engineering project scope for productivity modeling. *Journal of construction engineering and management*, 131(3), p. 360-367. [https://doi.org/10.1061/\(ASCE\)0733-9364\(2005\)131:3\(360\)](https://doi.org/10.1061/(ASCE)0733-9364(2005)131:3(360)).

Suvacı, B., and Şimşek, M. C. (2021). İş-Yaşam dengesi, örgütsel bağlılık ve çalışanların işten ayrılma niyetleri arasındaki ilişkinin belirlenmesi. *Social Sciences Research Journal*, 10(1), p. 185-194.

Thomas, H. R., and Raynar, K. A. (1997). Scheduled overtime and labor productivity: Quantitative analysis. *Journal of construction engineering and management*, 123(2), p. 181-188.

Thomas, H. R., Korte, Q. C., Sanvido, V. E., and Parfitt, M. K. (1999). Conceptual model for measuring productivity of design and engineering. *Journal of architectural engineering*, 5(1), p. 1-7.

Tong, R., Wang, L., Cao, L., Zhang, B., and Yang, X. (2021). Psychosocial factors for safety performance of construction workers: taking stock and looking forward. *Engineering*,

Construction and Architectural Management, p. 1-19. <https://doi.org/10.1108/ECAM-09-2021-0786>.

Toscano, F., and Zappalà, S. (2020). Social isolation and stress as predictors of productivity perception and remote work satisfaction during the COVID-19 pandemic: The role of concern about the virus in a moderated double mediation. *Sustainability*, 12(23), 9804, p. 1-14. <https://doi.org/10.3390/su12239804>.

Vereen, S. C., Rasdorf, W., and Hummer, J. E. (2016). Development and comparative analysis of construction industry labor productivity metrics. *Journal of Construction Engineering and Management*, 142(7), 04016020, p. 1-9. [http://dx.doi.org/10.1061/\(ASCE\)CO.1943-7862.0001112](http://dx.doi.org/10.1061/(ASCE)CO.1943-7862.0001112).

Wang, B., Liu, Y., Qian, J., and Parker, S. K. (2021). Achieving effective remote working during the COVID-19 pandemic: A work design perspective. *Applied psychology*, 70(1), p. 16-59. <https://doi.org/10.1111/apps.12290>.

WHO. (2020). World Health Organization, Retrieved from (<https://covid19.who.int/>), on (November 21, 2022).

WHO. (2022). World Health Organization, Retrieved from (<https://covid19.who.int/>), on (November 21, 2022).

Xiao, Y., Becerik-Gerber, B., Lucas, G., and Roll, S. C. (2021). Impacts of working from home during COVID-19 pandemic on physical and mental well-being of office workstation users. *Journal of Occupational and Environmental Medicine*, 63(3), p. 181-190. <https://doi.org/10.1097/jom.0000000000002097>.

Yılmaz, B., and Sağlam, M. (2021). COVID-19 algılanan stres ve tehdidinin, çalışanların iş yaşam dengesi ve motivasyonu üzerindeki etkisi. *Akademik Araştırmalar ve Çalışmalar Dergisi (AKAD)*, 13(25), p. 518-538. <https://doi.org/10.20990/kilisiibfakademik.977745>.

Zhang, L., Wen, M., and Ashuri, B. (2018). BIM log mining: Measuring design productivity. *Journal of Computing in Civil Engineering*, 32(1), 04017071, p. 1-13. [https://doi.org/10.1061/\(ASCE\)CP.1943-5487.0000721](https://doi.org/10.1061/(ASCE)CP.1943-5487.0000721).

Investigation of Energy Management Studies in Specified Microgrid Applications

Fatma Yaprakdal¹

Introduction

The great increase in the world population in the last twenties and the rapidly developing technology cause a great increase in the global electrical energy demand. Fossil fuels such as natural gas, oil and coal, which are among the sources that meet a large part of the global energy demand, have many environmental side effects, especially greenhouse gas emissions [1]. In addition, the existing coal reserves in the world are expected to expire in approximately one hundred and twenty years, and oil reserves in approximately fifty years [2]. The importance of using renewable energy sources instead of fossil fuels which is leading to rapidly declining reserves and significantly large environmental problems is gradually increasing. In order to increase awareness on this issue and to achieve a cleaner world, clean and sustainable energy generation is encouraged in many countries with the help of the World Bank and local leading companies of the countries [3]. In this context, with the increase in the integration of distributed renewable energy sources into the grid, traditional grids have started to become inadequate. As an alternative solution to this situation, a great increase is observed in the use of more reliable, highly efficient and energy-saving MGs [4]. Apart from these advantages of MGs, the fact that they are systems that can control the electricity supply to a significant extent is among the most striking features. Thanks to these features, MGs have the ability to meet its own energy and sell surplus energy production back to the main grid, making the system economically very profitable. In addition, MGs can ensure the continuity of the system by using this energy stored for a certain period in case of sudden interruptions in electrical energy [5]. However, the high cost of renewable energy sources and the fact that they have some disadvantages such as providing intermittent energy due to climatic conditions can negatively affect the MGs in which these resources are integrated [6].

MGs can operate in grid-tied or islanded mode. In case of any problem in the main grid, the usage of islanded mode in MGs is more preferred since the MGs can continue to operate safely by switching to islanded mode. MGs increase the efficiency of the main grid by exchanging the energy with other MGs connected to the grid in the mode of grid-tied operation mode [7]. However, MGs must have the same phase and voltage with other networks that switch to island mode in case of any failure, and then with this network when reconnecting to the main grid [8]. In the MG applications examined here, MGs operated in island mode are more common. In order to use distributed energy resources in MGs at an optimal scale with smart, safe, reliable and accurate coordination, energy management is required. In addition, energy management studies in MGs are carried out especially to minimize financial cost and electrical power losses. These energy management studies in MGs vary according to the power system application area. In this chapter, a research study is conducted on energy management studies for specific MG applications. MGs have mainly been considered in two segments as on-grid and off-grid as first stage. Then, on-grid

¹ Fatma Yaprakdal, Assistant Prof., Kırklareli University, Electrical and Electronics Engineering

MGs are divided into community-level and residential-level categories. MGs in the the area of regional-rural, industrial-commercial, hospital, university campus and military are included in the community-level MG category while private residential customers that can be found in a particular residential area, as well as individual homes, buildings and structures like farms are included in the residential-level MG category. In off-grid MG applications, all remote MG varieties have been examined. The main reason for categorizing MGs in this way is that energy management studies vary considerably depending on the location of MGs, internal dynamics such as user profiles, and whether they are connected to the grid or not.

The rest of the paper is organised as follows. General characteristics of MGs are mentioned in Section 1 while energy management system definition, mission and aims are emphasized in Section 2. After these general definitions, detailed information on energy management and control architecture in MGs are given in Section 3. In the 4th Section, MG applications are categorized in on-grid and off-grid and the some studies regarding energy management of these applications are mentioned. Conclusions are given in Section 5.

1. Microgrid Structure

According to the IEEE 2030.7 standard, an MG is defined as 'a group of interconnected loads and distributed energy resources with clearly defined electrical boundaries that act as a single controllable entity with respect to the grid and can be connected to and disconnected from the grid to operate in both grid-tied mode and islanded-mode'. Based on this definition, the basic units that form the MGs are distributed conventional energy generation units (micro turbines and diesel generators), distributed renewable energy resources, energy storage systems, electric vehicle charging stations, intelligent devices such as circuit breakers (CBs) and intelligent switches, and energy end-users.

Distributed energy resources in MGs are composed of micro turbines, internal combustion engines, fuel cells and combined cycle gas turbines and renewable energy generation units such as solar panels and wind turbines [11]. Renewable energy sources are increasingly preferred in distributed power generation to compensate for the disadvantages of centralized power generation such as high cost, transmission line losses and environmental impacts. However, problems such as weakening of the reliability index of the power system occur when integrating it into the main grid due to the intermittent nature of the RE sources. Problems that may arise due to such reasons in the power system can be overcome by using a correct protection scheme and isolation systems and a redundant generation system diversified with traditional DERs.

Distributed power generation units operate at low voltage (1V-1kV) and medium voltage (1kV-35kV) levels. Their installed power values vary between 1W and 100MW and in this respect; they are examined in four groups as micro scale (1W-5kW), small scale (5kW-5MW), medium scale (5MW-50MW) and large scale (50MW-100MW). Micro turbines and solar cells are in the micro-scale power group, while wind systems are in the small-scale power group [11], [12].

Main battery technologies used in large-scale applications are lead-acid batteries, lithium-ion batteries, sodium-sulfur batteries and flow batteries. Lithium-ion batteries and sodium-sulfur batteries have high power, energy densities and high efficiency while lead-acid batteries low power density and capital cost. Although flow batteries show high energy density, independent power and energy ratings, they have low storage capacity. The main use of ESSs in MG applications is to minimize the discontinuity in energy supply caused by the intermittent nature of renewable energy sources, that is, to ensure system reliability.

Electric vehicle charging stations also support a more eco-friendly system by integrating to the MGs, enabling the electrical energy required for the vehicle to be produced with renewable and clean energy [13]. In MGs integrated with electric vehicles, the direction of power flow is from vehicle to grid or from grid to vehicle. The power flow from the vehicle to the grid occurs during periods of high demand or high electricity pricing hours, and while this system is not suitable for every electric vehicle, battery and fuel cell electric vehicles are the most suitable vehicle types for such use [14].

Energy end-users are group of interconnected loads belong to factories, campuses, hospitals or residences who meet their energy needs such as cooling, heating and lighting in the MG. While traditional power grids have a communication network from the generation units to the consumers, an MG has a bi-directional communication network in addition to that network. With this two-way network, energy production units such as fuel cells, solar panels, wind turbines and energy storage systems can instantly provides feedback about their energy generation and filling rates to the end-users (responsive loads) [9].

MG-wide control and coordinated operation is performed by the MG central controller and local controllers. Control, coordination and efficient management of DERs in MG increases system performance and supports continuity in development. The MG's connection to main grid is provided by a point of common coupling (PCC). The DERs are connected to the system via power electronic interface (PEI) in grid-tied or islanded modes for control, measurement and protection purposes thanks to their plug-and-play features. While an MG connected to the grid enjoys the advantage of energy exchange with the main grid under normal operating conditions, it switches to islanded mode in case of failure in the main grid, thus maintain the system stability. In this mode, DERs perform efficient integrated operation with demand response and load shedding, providing uninterrupted power to critical loads.

MGs are located in remote areas, in areas belonging to certain consumer groups and divers sectors, in line with their aim, taking into account the load types, geographical and climatic conditions. Except for operating mode, MGs can be grouped according to the type of electrical power type, supply phases, integrated renewable energy sources variety, application area and supervisory control system type.

2. Energy Management System (EMS)

Regarding EMS application program interface in power systems management, an EMS is described as “a computer system comprising a software platform providing basic support services and a set of applications providing the functionality needed for the effective operation of electrical generation and transmission facilities so as to assure adequate security of energy supply at minimum cost” in the standard IEC 61970 by the International Electrotechnical Commission.

Energy management supports the power system in terms of supply-demand security, increasing the integration of renewable energy sources into the system, minimizing power losses and producing quality electrical energy [21]. In this context, energy management includes many different optimization types such as cost optimization, carbon dioxide emission minimization and energy generation-consumption optimization. One of the most important distinguishing features for these optimization applications is the time period that will be taken as a basis in the work to be done. The time period in which the energy management will be implemented is an important criterion. Setting very short-term periyods (seconds-30mins) for dynamic control of renewable energy sources, short-term periyods (30min-6hrs) for the relationship between source and storage systems, medium-term periyods (6hr-24hrs) for market pricing and long term periods (1 day – 1

week) should be set for load dispatch and maintenance scheduling [22]. For the studies in these time periods, various data types such as camera, meteorological data, power system data are used. It is the duty of the energy management system to process such data and make the necessary optimizations regarding these types of datas [23].

The mathematical methodologies used within the scope of the energy management system can be examined under three basic categories: classical methods, meta-heuristic methods and intelligent methods. Classic methods do not have branch, bound, and integer constraints. As an optimization method, these methods can use linear and non-linear optimization techniques. These techniques, on the other hand, are used to solve two basic optimization problems under certainty and uncertainty. Linear programming, mixed integer programming and nonlinear programming are used in optimization problems under certainty while dynamic programming and stochastic programming are used in optimization problems under uncertainty [25].

Meta-heuristic methods are heuristics that can work with missing or redundant data, with or without constraints. These methods are unlikely and iterative; the desired value is obtained by taking the average of the studies performed many times. Particle swarm optimization, rule-based bat optimization, genetic algorithm, gray wolf optimization, artificial bee colony, crow search algorithm, teaching-learning-based-optimization, adaptive differential evaluation, gravity search algorithm (GSA), modified firefly algorithm, social spider algorithm and whale optimization algorithm (WOA) are types of meta-heuristic algorithms [26].

The last mathematical methodology used within the scope of the energy management system is artificial intelligence (AI) based methods. AI based methods include problem-based classification, fuzzy control and neural networks, multi-agent based on model prediction, game theory and deep learning and they are the most advanced and comprehensive mathematical methods. All numerical methods are given in Figure 1.

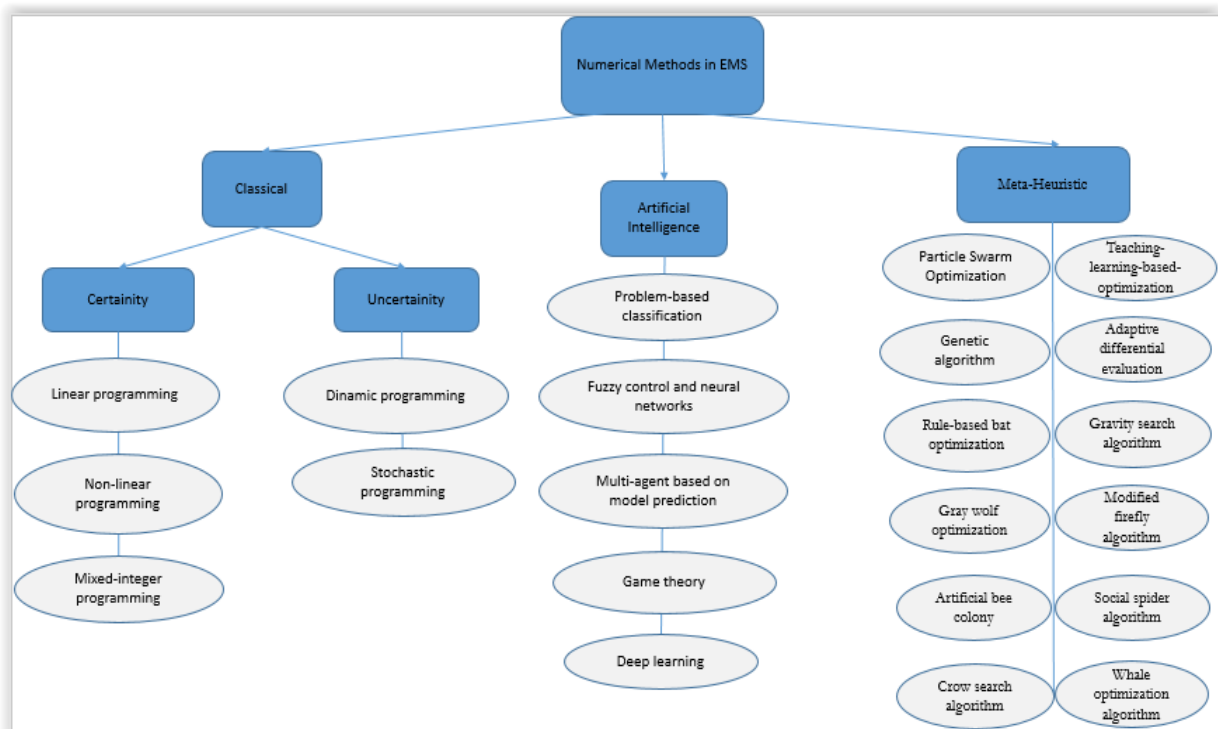


Fig. 1 Numerical methods used for energy management studies

3.MG Control and EMS

The MG-EMS or control system has been defined as follows by the reputable major institutions. IEEE standard 2030.7 defines a MG control system as ‘A system that includes the control functions that define the MG as a system that can manage itself, operate autonomously, and connect to and disconnect from the main distribution grid for the exchange of power and the supply of ancillary services; it includes the functions of the MG-EMS; it is the MG controller if implemented in the form of a centralized system’ [6]. An MG-EMS is defined as ‘System operating and controlling energy resources and loads of the MG’ in IEC-TS 62898-1 [11]. In order to provide certain functional needs and necessary benefits in microgrids, an EMS, which is an advanced real-time control and optimization system, must be implemented to operate at the grid-tied and the islanded mode. An EMS mainly preserves grid efficiency and economy based on DERs' power generation, devices on the grid, electrical and climatic forecast data, and electricity-energy market in MGs.

A MG control system includes software and hardware systems and could be physically centralized or distributed. MGs have their own control systems, defined as hierarchical control, and each MG has an MG central control that collects and processes data, operates according to control procedures, and regularly checks the system. If there is one of this control system in the established MG system, it is called a central control system, if each unit in the system is designed to be connected to a different control system, it is called a decentralized control system [16]. These systems are flexible systems that can be expanded in parallel with the increase in the number of consumers. Control levels in MG are divided into three main groups as primary, secondary and tertiary control levels according to their important characteristics such as response, communication and operation [17].

The primary control level can be called field control and is based on system changes and local measurements. The main purpose of this system is to increase reliability, improve performance and realize power distribution. As a standard power dispatch method it provides voltage tracking, active and reactive power mode control, frequency and voltage tracking, but it cannot prevent voltage and frequency fluctuations [18]. The secondary control level improves the parts where the primary control level falls short. At this control level, voltage and frequency fluctuations are damped. It has the characteristics of improving the quality of the power system, taking into account the cost. The system can change the target according to the geographical environment, the preferences of the users and manufacturers, and the equipment costs [19]. The last and top level control, the tertiary control level, is the most advanced control level. This level particularly interested in cost between MG and main grid, electricity market operations and optimal power dispatch. This control level adjusts the cost based on meteorological forecasts. It strengthens the prediction model by incorporating many algorithms such as the K-nearest neighbor algorithm [20], machine learning, long short-term memory, k-nearestneighbors, generalized regression neural network, neural network community and deep recurrent neural networks.

4.EMS in Specified MG Applications

MG applications have different optimization purposes within the scope of energy management, such as maximizing the renewable energy generation, minimizing operating costs, maximizing the life of the system used, and minimizing environmental costs [15]. These purposes vary depending on the campus designed as an MG. In this study, MG applications containing the EMSs have been examined in two basic categories as on-grid (grid-tied) and off-grid (islanded) according to their connection to the main grid. On-grid MG applications are grouped under 2 main subgroups; including community-level and building (individual) level MG applications in this scope

of work. The aim here is to examine regional MG-EMS application studies according to campus types and the relevant needs specific to these campuses. Since there are not many off-grid MG application studies, these studies are examined in a single category.

4.1.EMS in On-Grid MG Applications

An EMS in on-grid MG applications uses the information it receives from the energy generation sources, energy end-consumers and also the energy market to program the generation of its DERs and the net energy it will import from or export to the upstream electricity grid at an optimal level since it has to achieve many objectives like minimizing net power importation from the upstream electricity grid, energy cost and emissions maximizing renewable energy generation and thereby maximizing profits on energy exports to the upstream electricity grid at the same time.

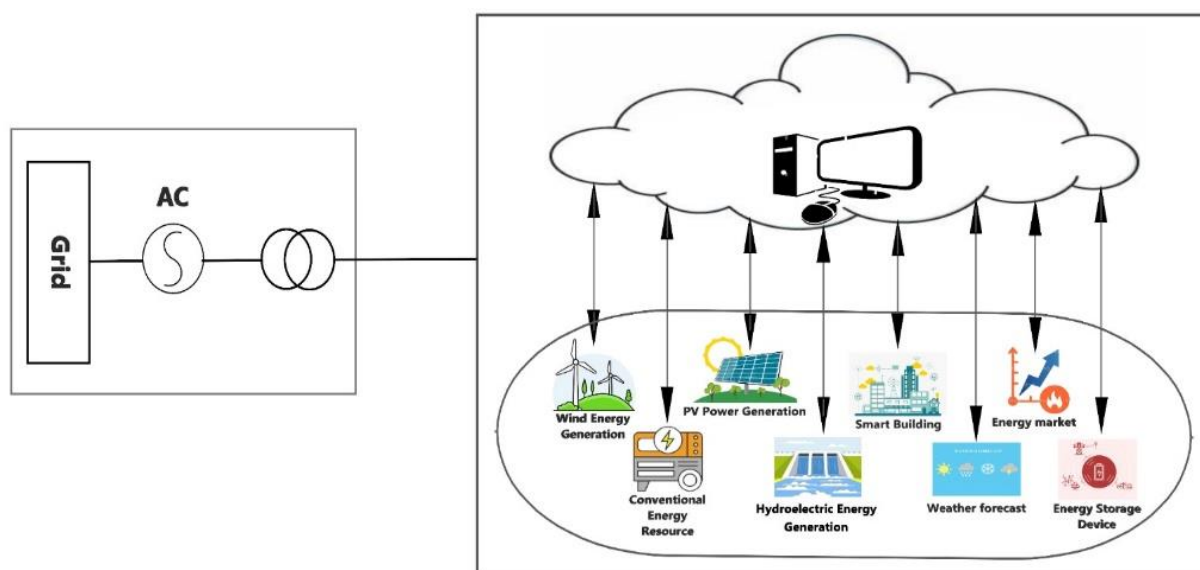


Fig. 2 On-grid MG components and connection

4.1.1.Community – Level MG Applications

Community-level MG application areas consist of regional and rural, industrial and commercial, hospital, university campus and military, and they are connected to the upstream power grid at single point of common coupling (PCC) to ensure system reliability and economy. The most important basic elements that should be in a community microgrid; being self-sufficient in energy production, reliability and sustainability in the supply of energy, and being able to produce low- cost energy. In ordinary operating circumstances, each MG community supports separate MGs to decrease power losses and improve system stability by sharing resources internally [6]. In case of extraordinary conditions, each MG community is able to operate independently of the main grid to ensure its own unity and reliability.

4.1.1.1.Regional - Rural MGs

As of 2021, the number of people without access to electricity is 768 million. The regions with these communities are mostly rural areas and distributed villages far from the main power

grid. It is very expensive to extend the power grid up to these regions and many technical problems may occur in these regions, such as voltage drop more than acceptable voltage drop values. Therefore, establishing independent systems such as renewable energy-based MG in these regions will be very beneficial in terms of technical, economic, social and environmental aspects. Wind-photovoltaic power generation systems are a convenient preference to meet the electrical energy needs of rural areas away from the main grid.

On the other hand, cities and especially capitals are among the most preferred campuses in terms of MG studies. The biggest reason for this is that such important metropolises should not be interrupted during power cuts. Then, there are reasons such as improved resilience, being advantageous in cost and independence in energy. In this context, some developed countries have initiated pilot regional MG programs. For example, in October 2020 the Australian Government announced that it would support regional MG pilot programs with an investment of \$50 million. Another example can be given from Sweden; here, too, the first trial steps for the transition to local energy systems (LESSs) are being carried out in the Swedish town of Simris with a LES composed of local wind turbine, the PV farm, and the containers hosting the battery energy storage system (BESS) and the backup generator and EMS. While Europe is currently facing an energy crisis, the race to catch up with the deadlines of the Paris Agreement continues in the energy sector. Therefore, energy utilities everywhere are striving to make the best strategic plan to accelerate energy transitions. Transition steps to (LESSs) are gaining importance in this sense. In [41], instead of using the secondary control level, particle swarm optimization has been performed to reduce frequency and voltage fluctuations in MG. The renewable energy sources of this system, which is established for Beijing, are created with a wind turbine of 2500kW and 3 PV panels of 200kW. It has been announced that the use of preferred sources prevents frequency and voltage fluctuations. Azaza and Wallin designed the MSC with a wind turbine and a PV panel. The load profiles that may occur if the obtained MSs are used for different cities in Sweden for 6 months were analyzed by particle swarm optimization [43]. Minimizing the cost through the linear programming method is studied in [31] for a small region in Colombia, used PV panels as a renewable energy source. Cases such as different battery sizes and installation of PV panels have been examined and it is explained that the cost increases in proportion to the battery size. MG study is carried out in [32] for the Kallar Kahar region in Pakistan. Mixed integer linear programming is used as an optimization algorithm. A 500kW wind turbine and a 2000kW PV panel have been used to energize the region, which has a power of 73.6MW. With the help of the HOMER program, the microgrid size and total cost have been minimized and electrical load peak shaving is realized. In [34], an MG operating in three modes called continuous operation mode, power sharing mode and on/off mode is designed. The system, which includes a 200kW PV panel and 2x 100kW solid oxide fuel cells, has determined a mixed-mode energy management strategy and optimum battery size to ensure minimum operating cost. As a result of the study, it is announced that PV panel powers reduce the operating cost and the low charge level causes an increase in the energy cost in the MG.

4.1.1.2. Industrial-commercial MGs

Interest in MGs is also increasing rapidly by large commercial companies and industrial enterprises such as mining company, independent power producer, oil&gas company, datacenter, hotels&resorts and food&beverage company. The primary purpose of commercial and industrial segments is to increase reliability against potential energy interruptions and then to minimize corporate energy costs. Therefore, the commercial and industrial MG sector is a rapidly growing and developing segment among other MG segments. In commercial and industrial (C&I) microgrids, optimization studies can be applied in order to meet their own energy needs, which are their priority targets according to energy market pricing in general in the context of energy management. In fact, the general tendency for the last few years has been to sell energy to the main

grid operator in case of surplus power generation or during peak energy pricing times, and to buy energy from the main grid during periods of low energy prices.

Industrial plants use large step changes under normal and sensitive loading. To protect the system from failures caused by lack of power supply, DERs must be sized satisfactorily and have adequate EMS that provides the system the essential robustness and resilience.

4.1.1.3. Hospital MGs

The devices used in hospitals are of vital importance. In this respect, hospital loads are critical electrical loads and also the electrical energy demand in hospitals is at a very high level in line with the size of hospitals. Hospitals connected to the conventional grid use backup diesel generators and UPS to meet their energy needs in case of power outages just for a limited period. However, besides the depletion of fossil fuel reserves in the near future, there is also an unforeseen fluctuation in diesel prices. Moreover, these generators have risk of error to start up. Therefore, in hospitals where both heat and electrical energy demand is quite high, cogeneration systems that can efficiently produce both electricity and heat energy, especially in which renewable energy sources such as solar power, biomass and wind energy plants are integrated, are quite necessary systems. If a hospital is regulated as MG, its ESSs will store the electrical energy produced by DERs integrated cogeneration system primarily for use in critical situations. While this system supports resilience of power supply for the hospital power demand, it also provides financial benefits to the hospital.

The issues such as capacity planning and solar system efficiency of a general hospital located in New Jersey, with a 3,642kW photovoltaic (PV) panel and energy storage system have been worked in [27]. As a result of this study; It has been determined that as the efficiency of PV panels rises above 16%, the payback period increases, the payback of PV panels operating with 16% efficiency will take 50 months. Besides, the energy cost of the PV panels used decreases by 30%.

In [29], an MG system is designed in a hospital with PV panels, Li-ion energy storage units and diesel generators. Optimization of the dimensions of the structures in the MG system has been carried out by using REopt® software, taking into account the economic benefit of the system and the endurance capacity of the system elements. With the MG hospital application designed in this way, approximately \$ 440,191 savings have been obtained from the power losses prevented during power outages and from the energy provided by the main-grid.

4.1.1.4. University Campus MGs

University campus MGs are parts of the utility grid consisting of a group of DERs and energy consumers. The multiple uncertainties in an MG, such as limited solar generation, fluctuations in market prices, and controlling different loads, are challenging points in managing campus energy with an MG system, and therefore this type of application study is very open to research and development. MGs established in a campus can be successfully operated with the robust energy management system to overcome these challenges by offering a variety of solutions to minimize greenhouse gas emissions, maintenance costs and peak load demands of the microgrid infrastructure. Therefore, today, universities generally provide their basic requirements in order to transform their energy supply systems into campus MGs. University campus MGs have been pioneered the service as a testing ground for observing the economic, technical and environmental benefits of using an MG system in the electrical grid. The operational management of electrical consumption and generation units of each building within the campus is monitored by a central controller.

An energy management system (EMS) parametric optimization application for the efficient and traceable coordination of distributed energy resources consisting of wind turbine and solar panels has been implemented in [30] at a residential level MG in Lambton College, Canada. In this MG, which has an energy storage unit as well as distributed energy sources, the energy management study is presented as a two-level parametric-mixed integer linear programming problem to provide significant improvement in uncertainty management with the aim of net cost minimization. It is concluded that the proposed system can make smart decisions in the face of current uncertainties without violating operational constraints, and it is emphasized that this proposed approach can be easily applied in real-time applications.

In [2], a three-phase AC microgrid system including a solar panel that can generate a maximum total of 100 kW of energy for 24 hours of operation and an energy storage unit with the capacity of 175 kWh or 300 kWh to examine different operating scenarios, at Eskişehir Osmangazi University. In order to reduce the total amount of electricity consumption for the phasor mode, which is a new application model that allows the analysis of the 24-hour time interval of the modeling in the Matlab / Simulink environment, the cost optimization study was carried out by utilizing the multi-time tariff. Instead of meeting most of MG's energy needs from the electricity grid, different scenarios have been studied on to provide support from the PV energy generation unit and energy storage unit, and a remarkable cost minimization is achieved.

In [44], a real-time MG study with both a wind turbine and a PV panel connected to a 380kW load is presented. It is envisaged that this system, which is carried out at Aalborg University MG Research Laboratory in Denmark, will be put into island mode or switch to normal mode at a specified time in order to keep the balance between the amount of energy production and consumption stable.

4.1.1.5. Military MGs

Some MGs may be operated by organizations serving or elements of the armed forces. This is usually the smallest of the various MG markets. However, it is a market that is often of prime importance to national security, as individual bases may rely on these MGs for energy independence for enhanced resilience (often up to 2 weeks or more) and to improve cybersecurity in an age where military equipment is rapidly becoming highly technical. National Defence Departments own many local installations from sensitive scientific search facilities like microelectronics and biological laboratories to major industrial facilities like dockyards and aviation warehouses and those facilities are connected to the national power grid. Prolonged power outages in the national power grid will adversely affect National Defence Departments' operational mission, while creating significant financial losses. Therefore, MGs integrated with a proper and cyber secure EMS are a good opportunity for military applications.

Some military MGs are mobile, which means they can be deployed quickly and easily on a battlefield, in turn reducing the need for fuel to be transported over long distances to remote locations. These types of military MG applications will be mentioned within the scope of off-grid MG applications segment.

4.1.2. Residential-Level MG Applications

Under this MG segment, private residential customers that can be found in a particular residential area, as well as individual homes, buildings and structures like farms, are considered. These MGs are connected to the main grid and they may include centralized or distributed power generation and distribution systems, energy storage devices and electrical vehicles charge units.

They can sell the excess of the energy they generate and participate in the energy market as 'prosumers'. In an MG system where there is more than one individual residence, it may take longer to take decisions regarding operation and development of the system due to the large number of people involved in the system and, accordingly, the high number of decision makers. In these MG systems, since each home has its own internal energy dynamics, the main difficulty in terms of energy management is that neither renewable generation nor the electrical consumption can be controlled.

In [35], a usable, 3-tier hierarchical MG system is implemented in Australia. An EMS device is placed in each of the houses connected to the MG and it is followed by this system. As a result of the study, the continuity of the system is ensured by giving electricity to the houses with electricity production, more than electricity consumption, to neighbors in need of electricity, and then to the system. The design of an MS according to the residential profile is carried out in [36], using a DC-PV panel and an AC-wind turbine. It is aimed that to increase the life of the system used by using genetic algorithm. In addition, optimization study has been expanded to reduce radiation and CO₂ emissions. In [37], an MG study is carried out for a house powered by a PV panel. In the Matlab environment, the energy management system is implemented using real user data. The reason for giving importance to real user data is to show that the MG system is actually usable. A new graphical method is proposed to show the change of energy flow. In [38], a control study is carried out for MG, which has an electric vehicle charging station that can be used as commercial and residential. In this system, where PV panels are located, the importance of the batteries to be used has emphasized that the electricity production is insufficient from time to time. It has been proven that electric vehicles provide a significant increase in energy needs. The biggest reason for this is the inability to provide a power flow from the vehicle to the grid. Zhuo suggested using MC for an Australian farm with PV panels and a wind turbine. The purpose of existence of MG is to meet the energy needs while minimizing the cost. For this study, he made the system close to reality with the constantly changing electrical peaks and weather conditions in the system. As a result of the study, it is announced that the system has been optimized in terms of financial and electrical load [39].

4.2.EMS in Off-Grid MG Applications

These microgrids will be similar to community microgrids with the main difference being that they will not usually be connected to a utility national grid. They will instead operate as an "island" microgrid system, usually because of economic issues or their geographical location – they may be located some distance away from national transmission lines. Examples of remote microgrids are for communities in remote regions like Alaska, Western Australia or islanded nations around the world. Their main function will be reliability and resilience. Due to their remoteness, system maintenance and access to parts can be challenging and needs to be considered when designing such a system. This means that they will often be designed to operate autonomously and are even more likely than other MGs to draw on distributed and diverse generation technologies. This needs to be balanced with the MG needs and levelized cost of electricity (LCOE).

Moreover remote military applications are in off-grid MG segment and they are installed in an ad-hoc way. Security of forward operating bases are in the most important point in the framework of MG setup. This security issue, which is of priority and importance, determines the installation location of the MG, energy requirements, generator and building layouts. Bases have the potential to evolve in an ad-hoc manner, which can double or even halve overnight due to modifications in mission and force needs. Therefore, these systems are powerful but not well organized. They meet their energy needs by means of diesel generators and these generators are usually over-sized for their energy needs. This decreases performance and leads to wet stacking,

which damages the generator motor. Load planning is not possible in advance, as these MGs are systems that are built in an ad-hoc way.

5. CONCLUSION

Smart grids consisting of MGs are expected to replace traditional power systems in the near future. Energy crisis and increasing greenhouse gas emission are key issues accelerating this situation. Due to the increasing importance of MGs in this respect, there have been many relevant research studies and on-going studies. In this chapter, the studies carried out in the field of energy management in MGs are examined by grouping them according to their locational feature. Therefore, this study will be a guide for researchers and practitioners who will carry out an MG study or installation in any of the categories described, in terms of energy management studies and also in terms of giving an idea for the relevant MG installation. In the relevant literature, these studies are handled one by one according to the campuses where MG is applied, while energy management studies for all campus types are discussed here. In the examined studies, it has been determined that the researchers who implement and plan the MG project have goals and preferences in line with their specific needs. These are briefly as follows;

- An MG design with integrated charging station for EV technology that remains popular,
- Cost optimization is one of the priorities in the implemented systems. In this context, in order to keep the cost in the desired balance, issues such as fuel cost optimization and battery size optimization should be handled as a priority,
- Even though the optimization goals are the same in the studies, the methods and software programs used differ.
- System life and maintenance costs are important. In order to reduce these expenses, the choice of quality and appropriate equipment, taking into account cost optimization,
- Solar panels and wind turbines are preferred because they have reliable, sustainable, widespread technology and have less investment costs compared to other energy sources,
- Providing an appropriate system design for this situation as the voltage/frequency stability of the system is of critical importance especially when the MG transitions from island mode to grid-tied mode and vice versa.

REFERENCES

- [1] Hu, N. Xie, D. Fang, and X. Zhang. (2018). The role of renewable energy consumption and commercial services trade in carbon dioxide reduction: Evidence from 25 developing countries, *Applied Energy*, 211, 1229-1244.
- [2] G. Tarihi, İ. Çetinbaş, B. Tamyürek, M. Demirtaş. (2018). Eskişehir Osmangazi Üniversitesi Kampüsünde Elektrik Tüketim Maliyetinin Azaltılmasına Yönelik FV Üretim ve Enerji Depolama Biriminden Oluşan bir Mikro Şebekenin Optimal Tasarımı G. Üniversitesi, Teknoloji Fakültesi 1. Ulusal Elektrik Enerjisi Dönüşümü Kongresi Bilimsel Makalesi. 8, 41-49.
- [3] Y. Zahraoui, M. R. Basir Khan, I. Alhamrouni, S. Mekhilef, and M. Ahmed.(2021). Current status, scenario, and prospective of renewable energy in algeria: A review. *Energies*, 14,907-916
- [4] Güven D. (2019). Verimliliği düşmüş bataryaların hizmet sektöründe Kullanımı: Akıllı tesis uygulaması, Yüksek Lisans Tezi, İstanbul Teknik Üniversitesi, Enerji Enstitüsü, İstanbul,
- [5] K. Normandeau,(2020) Microgrids for Hospitals and Healthcare Microgrids in Hospitals. *Microgrid Knowledge*
- [6] K. Shivarama Krishna and K. Sathish Kumar, (2015).A review on hybrid renewable energy systems, *Renewable and Sustainable Energy Reviews*. 52,907–916.
- [7] M. F. Zia, E. Elbouchikhi, and M. Benbouzid,(2018). Microgrids energy management systems: A critical review on methods, solutions, and prospects. *Applied Energy*, 222, 1033–1055.
- [8] İ.Anabilim,(2021). ENERJİ DEPOLAMA ÜNİTELİ TRİJENERASYON MİKRO ŞEBEKE SİSTEMİNDE ÇİZELGELEME OPTİMİZASYONU: HASTANE, Yüksek Lisans Tezi, İstanbul Teknik Üniversitesi, Lisansüstü Eğitim Enstitüsü, İstanbul
- [9] Burhan.B,(2017). YENİLENEBİLİR ENERJİ KAYNAKLARINI İÇEREN MİKRO-ŞEBEKE SİSTEMLERİN AKILLIYÖNETİMİ, Doktora Tezi, İnönü Üniversite, Fen Bilimleri Enstitüsü, Malatya
- [10] B. Kocaman, (2014). Mikro Şebekeler için Örnek Bir Enerji Yönetimi Uygulaması, *Bitlis Eren Üniversitesi Fen Bilimleri Dergisi*. 3, (35-52)
- [11] A. Basa Arsoy, F. M. Nuroğlu. (2009) Dağıtılmış Üretim Kaynağı İçeren Dağıtım Sistemlerinde Sürekli Durum ve Kısa Devre Analizi. 3, (104)
- [12] T. S. Ustun, C. Ozansoy, and A. Zayegh, (2011).Recent developments in microgrids and example cases around the world - A review, *Renewable and Sustainable Energy Reviews*, 15, (4030–4041).
- [13] D. A. Savio, V. A. Juliet, B. Chokkalingam, S. Padmanaban, J. B. Holm-Nielsen, and F. Blaabjerg,(2019) .Photovoltaic integrated hybrid microgrid structured electric vehicle charging station and its energy management approach. *Energies (Basel)*. 12, (168-186)

- [14] C. B. Robledo, V. Oldenbroek, F. Abbruzzese, and A. J. M. van Wijk, (2018). Integrating a hydrogen fuel cell electric vehicle with vehicle-to-grid technology, photovoltaic power and a residential building. *Applied Energy*, 215, (615–629).
- [15] Y. E. G. Vera, R. Dufo-López, and J. L. Bernal-Agustín, (2019). Energy management in microgrids with renewable energy sources: A literature review, *Applied Sciences (Switzerland)*, 9, (384-412).
- [16] L. Meng et al, (2017). Review on Control of DC Microgrids and Multiple Microgrid Clusters, *IEEE Journal of Emerging and Selected Topics in Power Electronics*, 5, (928–948).
- [17] M. F. Zia, M. Benbouzid, E. Elbouchikhi, S. M. Muyeen, K. Techato, and J. M. Guerrero, (2020). Microgrid transactive energy: Review, architectures, distributed ledger technologies, and market analysis, *IEEE Access*, 8, (19410–194329).
- [18] P. Borazjani, N. Izzri, A. W. Hashim, B. H. Azura. (2014). A Review on Microgrid Control Techniques. 2014 IEEE Innovative Smart Grid Technologies - Asia (ISGT Asia) Conference, 8, (749-753)
- [19] S. K. Sahoo, A. K. Sinha, and N. K. Kishore, (2018). Control Techniques in AC, DC, and Hybrid AC-DC Microgrid: A Review, *IEEE Journal of Emerging and Selected Topics in Power Electronics*, 6, (738–759).
- [20] D. Y. Yamashita, I. Vechiu, and J. P. Gaubert, (2020). A review of hierarchical control for building microgrids,” *Renewable and Sustainable Energy Reviews*, 118.
- [21] B. Kocaman, (2014). Mikro Şebekeler için Örnek Bir Enerji Yönetimi Uygulaması, *Bitlis Eren Üniversitesi Fen Bilimleri Dergisi*, 3, (35-52)
- [22] J. Ma and X. Ma, (2018) A review of forecasting algorithms and energy management strategies for microgrids,” *Systems Science and Control Engineering*, 6, (237–248).
- [23] L. Liu, Y. Wang, L. Liu, and Z. Wang, (2018). Intelligent Control of Micro Grid: A Big Data-Based Control Center, *IOP Conference Series: Earth and Environmental Science*, 108.
- [24] O. Kahouli, H. Alsaif, Y. Bouteraa, N. ben Ali, and M. Chaabene, (2021). Power system reconfiguration in distribution network for improving reliability using genetic algorithm and particle swarm optimization, *Applied Sciences (Switzerland)*, 11, (3092-3107)
- [25] H. Karimi and S. Jadid, (2020). Optimal energy management for multi-microgrid considering demand response programs: A stochastic multi-objective framework, *Energy*, 195, (1-13).
- [26] S. Leonori, M. Paschero, F. M. Frattale Mascioli, and A. Rizzi, (2020). Optimization strategies for Microgrid energy management systems by Genetic Algorithms, *Applied Soft Computing Journal*, 86, (19-56)
- [27] K. Chau, K. Mahani, M. A. Jafari, and S. Haghani, (2018) Solar-Powered Microgrid Capacity Planning for a General Hospital. *IEEE Green Energy and Smart Systems Conference (IGESSC)*, 18(1-6)

- [28] K. Sirviö, K. Kauhaniemi, A. A. Memon, H. Laaksonen, and L. Kumpulainen, (2020) Functional analysis of the microgrid concept applied to case studies of the sundom smart grid, *Energies (Basel)*, 13, (4223-4234)
- [29] A. Lagrange, M. de Simón-Martín, A. González-Martínez, S. Bracco, and E. Rosales-Asensio, (2020). Sustainable microgrids with energy storage as a means to increase power resilience in critical facilities: An application to a hospital, *International Journal of Electrical Power and Energy Systems*, 119, (1-12).
- [30] E. C. Umeozor and M. Trifkovic, (2016), Energy management of a microgrid via parametric programming,” in *IFAC-PapersOnLine*, 7, (272–277).
- [31] C. A. Correa, G. Marulanda, and A. Garces, (2016) Optimal Microgrid Management in the Colombian Energy Market with Demand Response and Energy Storage.1944.
- [32] J. Ahmad *et al.*, (2018). Techno economic analysis of a wind-photovoltaic-biomass hybrid renewable energy system for rural electrification: A case study of Kallar Kahar, *Energy*, 148, (208–234).
- [33] V. N. Coelho, M. Weiss Cohen, I. M. Coelho, N. Liu, and F. G. Guimarães, (2017). Multi-agent systems applied for energy systems integration: State-of-the-art applications and trends in microgrids, *Applied Energy*, 187, (820–832).
- [34] S. Sukumar, H. Mokhlis, S. Mekhilef, K. Naidu, and M. Karimi, (2017). Mix-mode energy management strategy and battery sizing for economic operation of grid-tied microgrid, *Energy*, 118, (1322–1333).
- [35] M. N. Akter, A. Mahmud, Amanullah M. T. (2016) A Hierarchical Transactive Energy Management System for Microgrid IEEE Power & Energy Society. General Meeting (2016 : Boston and Institute of Electrical and Electronics Engineers. 8
- [36] A. S. O. Ogunjuyigbe, T. R. Ayodele, and O. A. Akinola, (2016). Optimal allocation and sizing of PV/Wind/Split-diesel/Battery hybrid energy system for minimizing life cycle cost, carbon emission and dump energy of remote residential building, 171, (153–171)
- [37] S. Leonori, A. Martino, F. M. Frattale Mascioli, and A. Rizzi, (2020). Microgrid Energy Management Systems Design by Computational Intelligence Techniques, *Applied Energy*, 277.
- [38] J. L. Torres-Moreno, A. Gimenez-Fernandez, M. Perez-Garcia, and F. Rodriguez, (2018). Energy management strategy for micro-grids with PV-battery systems and electric vehicles, *Energies (Basel)*, vol. 11, (552-565).
- [39] W. Zhuo, (2018). Microgrid energy management strategy with battery energy storage system and approximate dynamic programming. Proceedings of the 37th Chinese Control Conference.1 (7581-7587)
- [40] Mohamed S. Taha, Yasser A.-R. I. Mohamed, (2016) Robust MPC-Based Energy Management System of a Hybrid Energy Source for Remote Communities .IEEE Power Electronics Society, IEEE Power & Energy Society, and Institute of Electrical and Electronics Engineers, 1, (1-6)

- [41] H. Li, A. T. Eseye, J. Zhang, and D. Zheng, (2017). Optimal energy management for industrial microgrids with high-penetration renewables,. *Protection and Control of Modern Power Systems*, 2,(2-12)
- [42] M. S. Behzadi and M. Niasati, (2015). Comparative performance analysis of a hybrid PV/FC/battery stand-alone system using different power management strategies and sizing approaches, *International Journal of Hydrogen Energy*, 40, (538–548)
- [43] M. Azaza and F. Wallin, (2017). Multi objective particle swarm optimization of hybrid micro-grid system: A case study in Sweden, *Energy*, 123, (108–118).
- [44] A. C. Luna, L. Meng, N. L. Diaz, M. Graells, J. C. Vasquez, and J. M. Guerrero, (2018). Online Energy Management Systems for Microgrids: Experimental Validation and Assessment Framework, *IEEE Transactions on Power Electronics*, 33, (2201–2215).
- [45] R. R. Nivedha, J. Govind Singh, and W. Ongsakul,(2018) PSO based Economic Dispatch of a Hybrid Microgrid System. *IEEE*, 5,(18-23).
- [46] B. Papari, C.S. Edrington, T. V. Vu, F. Diaz-Franco,(2017). A Heuristic Method for Optimal Energy Management of DC Microgrid, *2017 IEEE Second International Conference on DC Microgrids* 17, (337-343).
- [47] X.-F. Lin, X. Yan-Zhao, C.-N. Song, S.-J. Song, and L. Bin,(2016)An Experiment And Research Platform For DC Micro-grid. *Proceedings of the 35th Chinese Control Conference*. 1, (8588-8595)
- [48] J. Jimeno, J. Anduaga, J. Oyarzabal, and A. G. de Muro, (2011).Architecture of a microgrid energy management system, *European Transactions on Electrical Power*,21, (1142–1158)

The effect of the use of different materials and design optimization in the connecting rod on fatigue analysis

Berkay KARAÇOR¹
Ali Kemal DUMAN²
Mustafa ÖZCANLI³

1. INTRODUCTION

The connecting rod in internal combustion engines plays a noteworthy role in transferring the vertical force it receives from the piston as a result of combustion events to the rotational force of the crankshafts (Joakim, 2020: 1). The connecting rod is exposed to multidirectional amplitude bending loads, gas and mass forces, inertia forces and buckling loads, axial tension and compression loads during operation. From the moment the engine starts to move, the connecting rod is subjected to repetitive loads millions of times. For this reason, it is important for the life of the connecting rod to be strong enough to withstand the high stresses that will occur while moving in the engine (Acar, 2016: 1-2). This situation can be applied with design optimizations as a result of using new generation materials and performing detailed stress-strain analysis on engine components in the optimization to be carried out in the connecting rod, efforts to increase the strength, decrease in weight, and reduce the production cost come to the fore (Ismail *et al.*, 2021: 8728). Long connecting rod life and low deformation critically depend on material selection and material quality. Among these material choices, titanium materials have become particularly interesting in the automotive industry in areas where hardness and toughness are required. (Ajayi *et al.*, 2020: 4390). Modern connecting rods are also manufactured from alloying elements of magnesium, aluminum, and polymeric connecting rods, especially titanium. In the automotive field, connecting rods are traditionally produced by forging from powder metal or forged steel, as well as being produced as a casting type (Kaliappan S *et al.*, 2018: 14599). Many elements such as poorly made design, fatigue, application of excessive load to critical stress areas, excessive bending, as well as material selection can cause failure in connecting rod parts (Gök and Cihan, 2021: 222-223). In this case, the researchers simulate real fatigue tests in the finite element analysis of connecting rod designs. For this, firstly, a three-dimensional design model is created, then the material is defined to the design, and after the limitations and loads are defined, the necessary analysis data for the results are obtained from the process (Zhang *et al.*, 2019: 1). In the literature, there are many studies on the optimization of the connecting rod design, the use of different materials, and the comparison of static and fatigue analysis. In a study of these, Vijayvergiya *et al.* analyzed the connecting rod design using the finite element method, using three different sections in the connecting rod. They observed that the I-type section design gave the best results in terms of deformation, equivalent stress, equivalent elastic strain, and factor of safety (Vijayvergiya *et al.*, 2008: 239-243). Sathish and Muthulakshmanan examined how to improve the design in terms of strength,

¹ Research Assistant, Cukurova University, Department of Automotive Engineering, Orcid: 0000-0001-5208-366X

² Bachelor's degree, Cukurova University, Department of Automotive Engineering, Orcid: 0000-0002-3722-2868

³ Prof. Dr., Cukurova University, Department of Automotive Engineering, Orcid:0000-0001-6088-2912

weight, and safety with numerical analysis by using Aluminum alloys and AISI 4340 steel instead of traditional materials in connecting rod design (Sathish and Muthulakshmanan, 2018: 1123-1125). In their study, Basavaraj et al. simulated connecting rod fatigue analysis in ANSYS using four different materials. It has been determined that 42CrMo4 steel gives 1.01 times better results in terms of safety factor and 10 times better in terms of the number of cycles, while the deformation and equivalent stress values are the same compared to the second-best material after itself (Basavaraj, *et al.*, 2021: 2812-2814). In another connecting rod numerical analysis study, they aimed to find the optimum material both dynamically and cost-effectively by changing the connecting rod material (Ali H. and Haneef. 2016: 1273-1275). Seralathan et al. performed static analysis on an I-type connecting rod they designed. In their comparison of equivalent stress, total deformation, and equivalent elastic strain, they discovered that the best results were obtained with A356-5%SiC-10% Flyash stir cum squeeze casting material. It was found that this material gave better results in terms of equivalent stress, total deformation, and equivalent strain results by 0.11%, 62.6%, and 61.32%, respectively, compared to the base material (Seralathan, *et al.*, 2020: 3724-3728). While testing the connecting rods both experimentally and numerically, Gao et al. tried to come up with a design that did not compromise safety while reducing the weight of the connecting rod. They concluded that verifying the real tests they conducted with simulated tests would provide an opportunity to provide an economic advantage with longer cycle numbers while reducing the weight of the connecting rod and increasing the strength (Gao *et al.*, 2022: 3–23). In this study, C45 Carbon Steel, AISI 4340 Steel, and Titanium alloys, which are not used together in the literature, were defined as connecting rod materials. The connecting rod design has been optimized depending on the effects of the 3 different materials applied on the static and fatigue analysis effect. A study was carried out to increase the efficiency of connecting rods to be used in vehicles by researching the most suitable material and design combination.

2. MATERIAL

In this study, C45 steel and AISI 4340 steel and Titanium alloy materials were preferred as connecting rod materials. The mechanical characteristics of the materials defined in the ANSYS software program are indicated in Table 1 (Ajayi *et al.*, 2020: 4393; Hagos, 2018: 23).

Table 1. Material Characteristics

	Density (kg/m ³)	Tensile Ultimate Strength (MPa)	Young's Modulus (GPa)	Tensile Yield Strength (MPa)	Poisson Ratio
C45 Steel	7850	565	200	310	0.3
AISI 4340 Steel	7850	745	200	470	0.3
Titanium Alloy	4620	1070	96	930	0.36

3. METHOD

Finite element methods were used to find mechanical properties in connecting rod analysis. The finite element method helps the designer to simulate real analysis. Errors and deficiencies in the model can be determined in advance in this way and necessary precautions can be taken in the actual design and analysis (Godara *et al.*, 2022: 1896). The calculation tools that customize the

outlines of the design, taking into account certain design limits, are Finite Element Analysis. With this method, very small elements are needed in the analysis while solving the most fundamentally complex components within certain limits (Muhammad and Shanono, 2019:25-26). FEM is a practical method used for fatigue analysis and evaluation of part life, which has many pros compared to other processes used in many diverse analyses. By means of this method, critical points can be determined and the stress/strain distribution in the whole part can be found, as well as providing great benefits to the designer in case the loading conditions are complex or the part does not have a regular geometric shape (Mirehei *et al.*, 2008: 22) . In this study, ANSYS 2020 R2 Static Structural module was used for static and fatigue analysis, and connecting rod designs were designed in CATIA V5 R20. The distance between the inner diameter of the small end and inner diameter of the big end is 146 mm. While the inner diameter of the small end is 18 mm, the outer diameter of the small end is 24 mm. In parallel, the inner diameter of the big end is 17 mm, the outer diameter of the big end is 21 mm. The width of the section design is 60 mm. Also, the thickness of the design is 10 mm. The visuals of the connecting rod design are given in Figure 1. According to the results of the design analysis, optimization was achieved by reducing the connecting rod width by 1.3 times and increasing the thickness by 1.1-1.2 times.

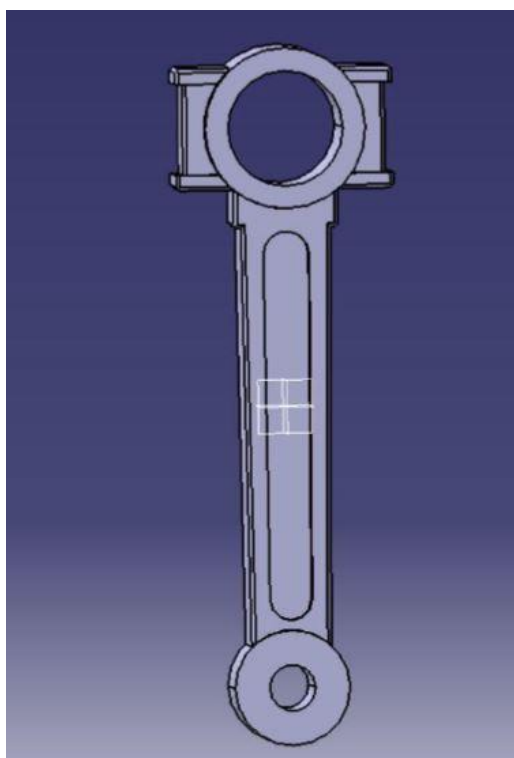


Figure 1. 3D model of connecting rod design

Figure 2 and Figure 3 indicate the cylindrical support region and applied force region for analysis. The assumptions applied in the analysis are: The connecting rod head was fixed with the fixed support command. According to ideal gas calculations and gas force calculations, the force on the connecting rods is accepted as 25000 N in the -Z direction (Basavaraj, *et al.*, 2021: 2809-2810). The module is meshed with the lowest possible element size to find the best mesh quality. The mesh should be thinner only in certain areas and key areas such as re-entered corners, holes, and areas where stress concentration is expected.



Figure 2. Fixed support region for design

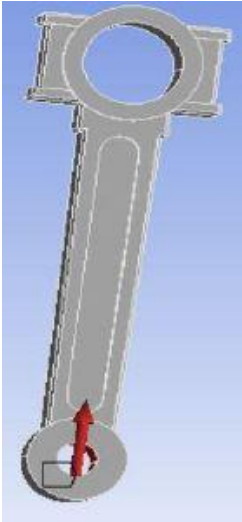


Figure 3. Applied force region for design

Figure 4 indicates mesh images of the connecting rod design. In design mesh statistics, the connecting rod design has 425726 nodes and 284306 elements.



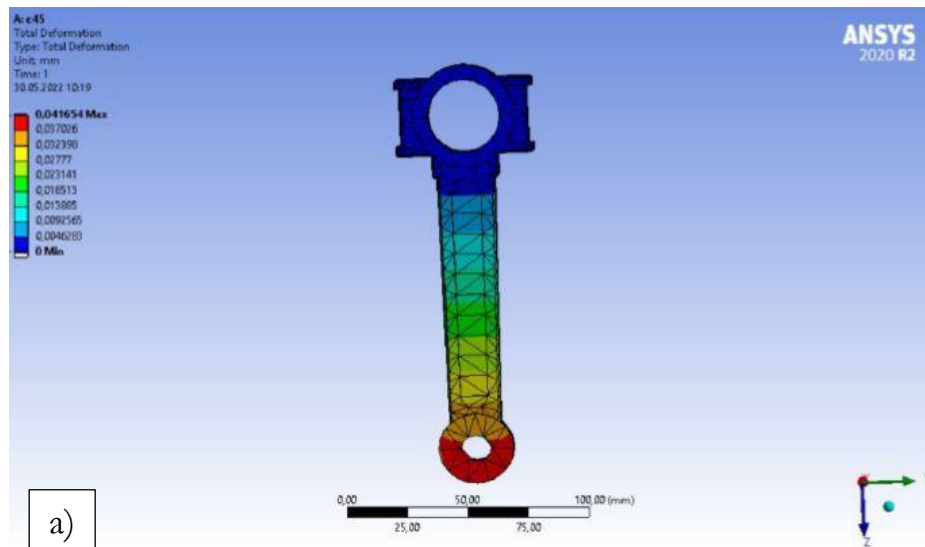
Figure 4. Mesh view of connecting rod design

4. RESULT AND DISCUSSIONS

The total deformation, equivalent stress, equivalent elastic strain, safety factor, lifetime, and damage values obtained as a result of the analysis are given in Table 2. In the comparison of total deformation values, the lowest value was obtained in C45 steel with 0.042 mm. In the results of equivalent stress values, the lowest value was found with a value of 81.836 MPa when titanium alloy material was used. When the safety factor results are examined, it is seen that the highest number is reached in the titanium alloy material design. Equivalent elastic strain results also indicate that the lowest value was reached with C45 steel material, as in total deformation. This value is 0.5 times the highest equivalent elastic strain value obtained with Titanium alloy. The highest value in damage values was determined in Titanium alloy and the lowest value in AISI4340 steel. The damage value of C45 steel is 1.2 times higher than that of AISI 4340 steel. Figure 5, Figure 6, and Figure 7 indicate the total deformation, Von-Mises stress, and safety factor distribution, respectively, of the three materials, used.

Table 2. Results of Analysis

	C45 Steel	AISI 4340 Steel	Titanium Alloy
Total Deformation(mm)	0.042	0.048	0.086
Equivalent Von-Mises Stress (MPa)	82.096	113.94	81.836
Equivalent Elastic Strain(mm/mm)	0.0004	0.0006	0.0008
Safety Factor	3.776	4.125	11.364
Life (Cycle)	100×10^5	100×10^5	100×10^4
Damage	120.58	100	100×10^{30}



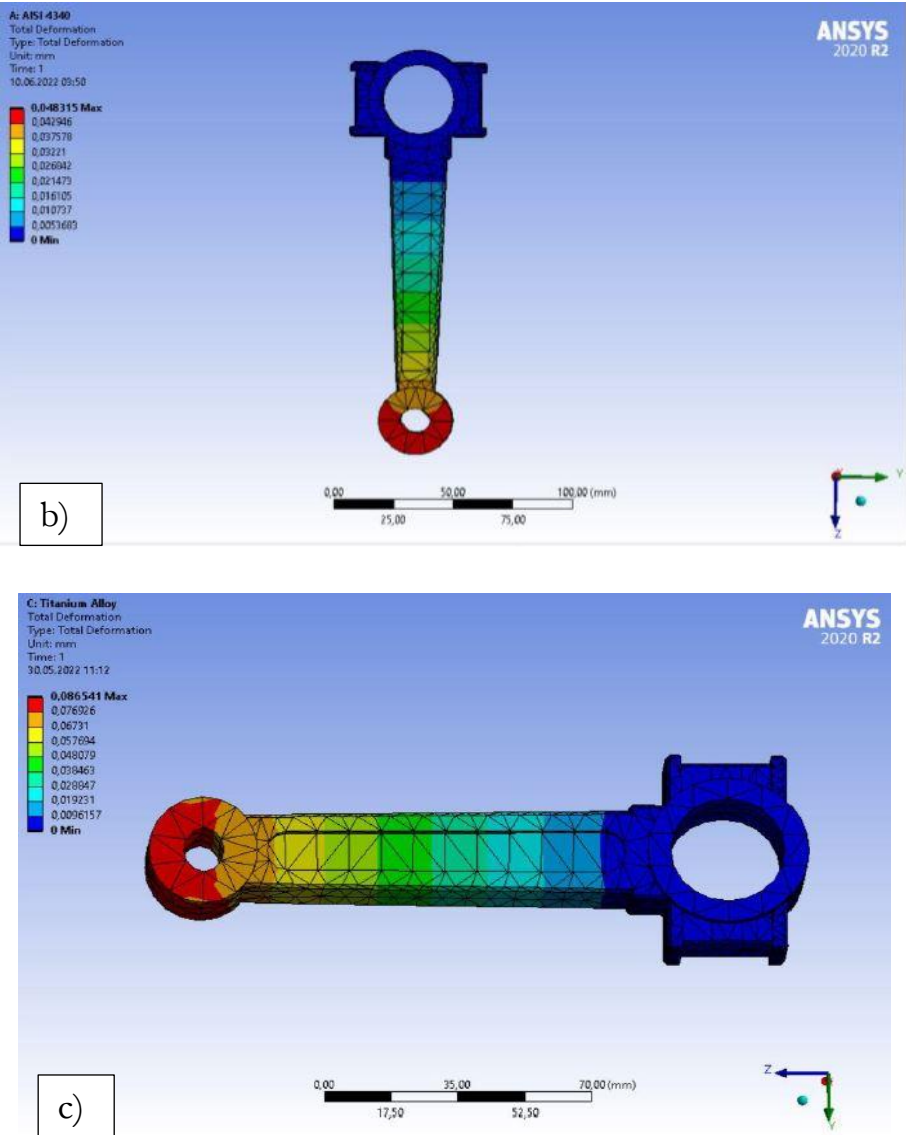


Figure 5. Total deformation in connecting rod design of (a) C45 steel (b) AISI 4340 steel c) Titanium alloy

As indicated in Figure 5a, Figure 5b, and Figure 5c, the C45 steel design has the lowest deformation value, this value is 0.49 times lower than the Titanium alloy design, which reaches the highest value. AISI 4340 steel design has 1.14 times higher deformation value than C45 steel design.

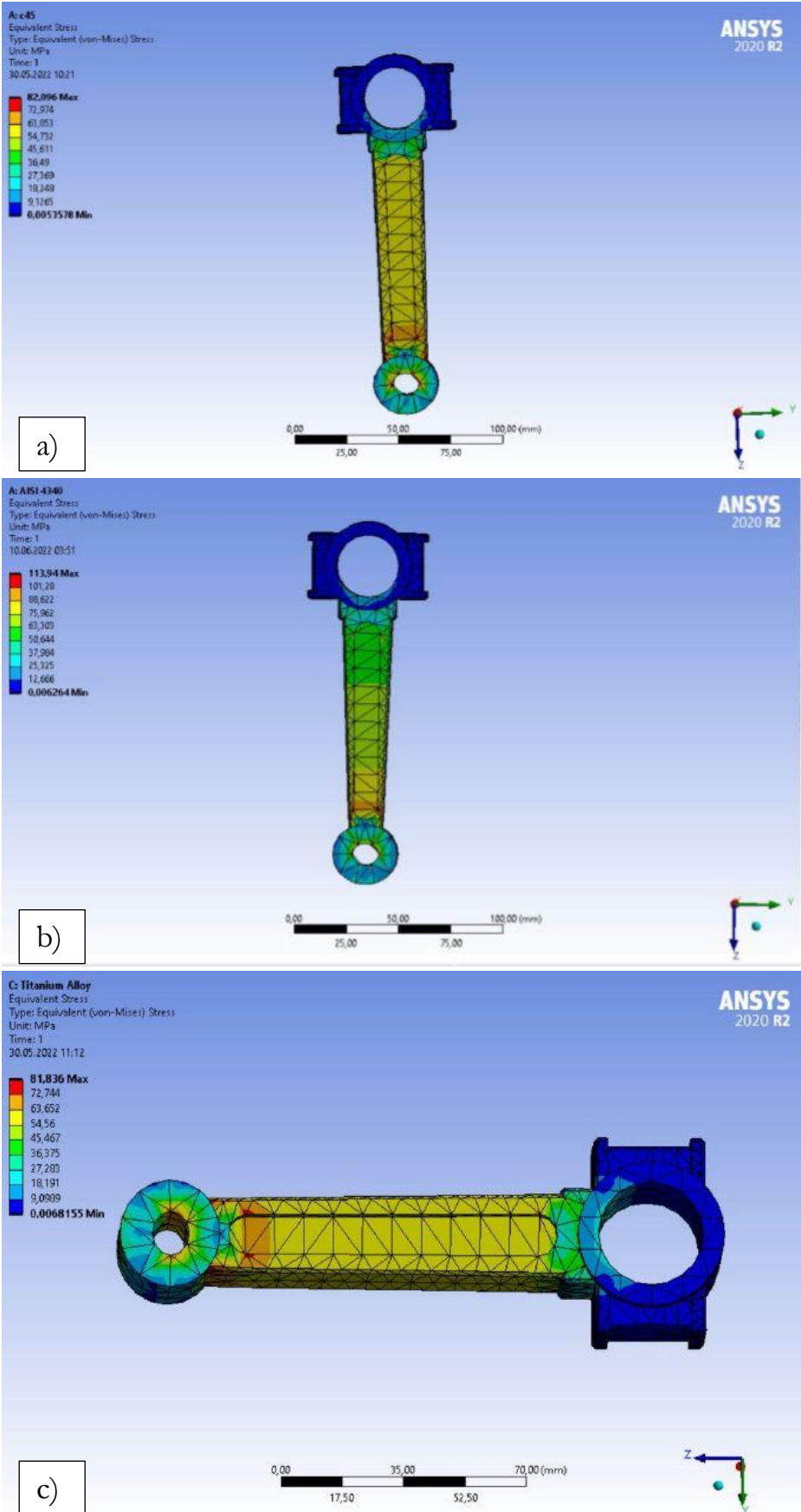


Figure 6. Equivalent stress in connecting rod design of (a) C45 steel (b) AISI 4340 steel (c) Titanium alloy

Equivalent stress distribution values are given in Figure 6a, Figure 6b, and Figure 6c. While the lowest value is reached with the titanium alloy design, this value is 0.72 times lower than the AISI 4340 steel design, which has the highest value. The C45 steel design has an equivalent stress value of 0.72 times lower than the AISI 4340 steel design.

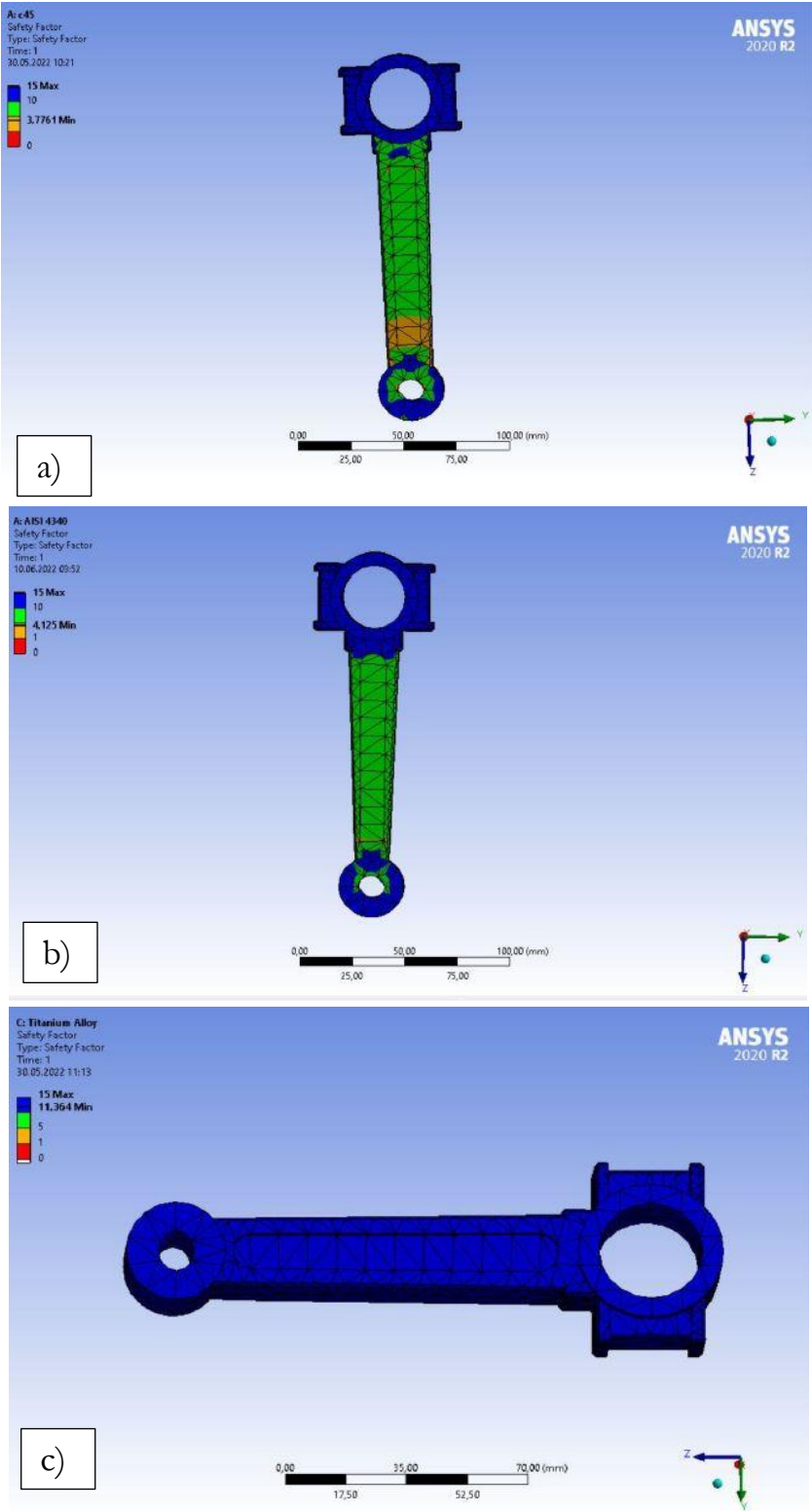


Figure 7. Safety factor in connecting rod design of (a) C45 steel (b) AISI 4340 steel (c) Titanium alloy

In Figure 7a, Figure 7b, and Figure 7c, the safety factor values of the three materials are presented. Titanium alloy design has the highest factor of safety value, which is 3 times higher than the lowest factor of safety value obtained with C45 steel. The titanium alloy design showed a factor of safety 2.75 times higher than the AISI 4340 steel design.

Table 3 presents the data obtained from the fatigue graphs of the three materials. It is seen that AISI 4340 and C45 steel have 1.8 times and 2.7 times more cycles at final loading conditions, respectively than titanium alloy. In the design of C45 steel, the first ruptures occur at loading between 0.75 times and 1 time, while in the design of AISI 4340 steel, the first ruptures are observed at loading between 1 layer and 1.25 times. It has been determined that there is no change in the number of lifetimes up to 1.5 times loading in the titanium alloy design.

Table 3. Fatigue Sensitivity Results

	Material	Loading History				
		0.5	0.75	1.0	1.25	1.5
Life Cycle Values	C45 Steel	100×10^5	100×10^5	75×10^5 - 87.5×10^5	37.5×10^5	18.39×10^5
	AISI 4340 Steel	100×10^5	100×10^5	100×10^5	50×10^5 - 60×10^5	27.04×10^5
	Titanium Alloy	100×10^4	100×10^4	100×10^4	100×10^4	100×10^4

5. CONCLUSION

Considering the repeated loads that the connecting rod is exposed to in internal combustion engines, it is very critical to know the performance of the engine throughout its life. In this study, three different materials such as C45 steel, AISI 4340 steel, and titanium alloy were used and the results of the static and fatigue analyzes of these materials in the connecting rod were compared. It is understood from the analysis results that C45 steel material can also be used instead of titanium alloy, which is generally preferred in the design of the connecting rod. The following numerical results during the study also support this indicator:

1. The total deformation value is 51.16% less deformation value in C45 steel design compared to the Titanium alloy design.
2. In the comparison made in terms of equivalent elastic strain, the C45 steel design showed 50% less equivalent elastic strain than the Titanium alloy design.
3. Both the C45 material design and the AISI 4340 material design have 10 times more cycles than Titanium alloy.

Numerical analyzes have shown that C45 material can also be used in connecting rod design in light of all analysis results. However, these analyzes should be verified with real tests and the parts to be optimized in the design should be revealed with real tests.

REFERENCES

- Acar, H. (2016). *Biyel kolu analizi, optimizasyonu ve yorulma davranışının incelenmesi*. Master Science Thesis. Bursa Technical University, Bursa.
- Ajayi, O. K. Malomo, B. O. Paul, S. D. Adeleye, A. A. Babalola, S. A. (2021). Failure modeling for titanium alloy used in special purpose connecting rods. *Materials Today: Proceedings*, 45(January),4390–4397.
- Ali, H. M. M. Haneef, M. (2015). Analysis of fatigue stresses on connecting rod subjected to concentrated loads at the big end. *Materials Today: Proceedings*, 2(4–5),2094–2103.
- Basavaraj, Y. Joshi, R. Setty, G. R. Samiullah, M. Museb, M. Tayab, M. Banu, H. (2021). FEA of nx-11 unigraphics modeled connecting rod using different materials. *Materials Today: Proceedings*, 46(October),2807–2813.
- Gao, W. Wang, G. Zhu, J. Fan, Z. Li, X. Wu, W. (2022). Structural optimization design and strength test research of connecting rod assembly of high-power low-speed diesel engine. *Machines*, 10(9),815.
- Godara, S. S. Brenia, V. Soni, A. K. Singh Shekhawat, R. Saxena, K. K. (2022). Design and analysis of connecting rod using ANSYS software. *Materials Today: Proceedings*, 56,1896–1903.
- Gök, M. G. Cihan, Ö. (2021). Investigation of failure mechanism of a DCI engine connecting rod. *European Journal of Technic*, 11(2),222-228.
- Hagos, T. (2018). *Static structural and life prediction analysis of feeder table head shaft for wonji-shoa sugar factory using Ansys*. Addis Ababa University, Addis Ababa.
- Ismail, I. Abdelrazek, S. M. Ismail, M. Emara, A. (2021). Enhancing the durability of connecting rod of a heavy-duty diesel engine. *International Journal of Automotive and Mechanical Engineering*, 18(2), 8728–8737.
- Joakim, A. (2020) *Design optimization of a connecting rod for internal combustion engine*. California State University, California.
- Kaliappan, S. Revanth Raam, A. B, C. Asswin, S. Mohammed Ibrahim, Dr. T. Mothilal, M.D. Rajkamal (2018). Modal and kinematic analysis of a connecting rod for different modal and kinematic analysis of a connecting rod. *International Journal of Pure and Applied Mathematics*, 119(12),14599–14608.
- Mirehei, A. Hedayati Zadeh, M. Jafari, A. and Omid, M. (2008). Fatigue analysis of connecting rod of universal tractor through finite element method (ANSYS). *Journal of Agricultural Technology*, 4(2),21–27.
- Muhammad, A. Shanono, I. H. (2019). Static analysis and optimization of a connecting rod. *International Journal of Engineering & Technology Sciences*, 6(June),24–40.
- Sathish, T. Muthulakshmanan, A. (2018). Design and simulation of connecting rods with several test cases using al alloys and high tensile steel. *International Journal of Mechanical and Production Engineering Research and Development*, 8(1),1119–1126.

Seralathan, S. Mitnala, S. V. Sahith Kumar Reddy, R. V. Venkat, I. G. Reddy, D. R. T. Hariram, V. Micha Premkumar, T. (2020). Stress analysis of the connecting rod of compression ignition engine. *Materials Today: Proceedings*, 33, 3722–3728.

Vijayvergiya, A. Kumari, E. Lal, S. (2021). Design and shape optimization of connecting rod end bearing through ANSYS. *International Research Journal on Advanced Science Hub*, 3(11),235–242.

Zhang, M. Zhao, C. Yan, Z. Yao, L. Yang, Z. Hassa, M. (2019). The structure, stress and modal analysis of 1.6-liter gasoline engine connecting rod based on finite element analysis. *IOP Conference Series: Materials Science and Engineering*, 677(3), 032094.

Ballistic evaluation of armor plates at different angles

Umut KUMLU¹
Mustafa Atakan AKAR²
Dođukan BAŐER³
Ömer HÜKÜMDAR⁴
Berkay KARAÇOR⁵

1. INTRODUCTION

Human has been in need of protection throughout their history. As a result of this need, they have been in constant work to discover the better, both in their daily life and in war situations. For this, they developed weapons that started with the use of stones and sticks (Demir, 2008: 1). The proliferation of armaments has created the need for protection against the threat of weapons. In line with these needs, human beings have had to use personal protective shields and armors (Robinson, 1967: 45-50). It has been through wars throughout history and has used new weapons and armor equipment that it has produced with developing technology (Yavas, 2009: 3-5). Taking precautions against threats and attacks of ammunition and weapons is always among the top priorities in the defense industry, which is the sector in which technology is developing the fastest (Agrawal, 2011: 1-4). From the past to the present, the ballistic performance of various materials has been the subject of constant research. Along with the development of weapons and ammunition, armors that can show ballistic performance against the threats they may pose have also been developed (Murray *et al.*, 2008: 1-23). On the other hand, according to the place where the armor in question will be used, a suitable armor material should be selected or an appropriate armor design should be made. For example, in some armor applications, the weldability of the armor is very important. Therefore, it is not possible to use a material with weak welding ability, no matter how much ballistic protection it provides and no matter how light it is (Ashby *et al.*, 1998: 3-161-219-263). In some applications; continuity of the armor is desired. In other words, a similar protection should be provided each time against successive threats. In such cases, ceramics, etc., which often provide one-time protection due to their fragile structure. The materials are not suitable for use (Carlucci and Jacobson, 2008: 3). In short, in order to select the most suitable material to meet the need, there is always a need for ballistic examination of many different materials or a system formed by these materials. While the ballistic performance definition of armors can be realized through FEM (Finite Element Method), it helps in determining critical design parts and material performance during the design phase (Kartikeya, *et al.*, 2019:514-520). The effect of the order of plates against bullet impact were studied by several authors. Teng *et al.* (Teng, *et al.*, 2008: 870-884) performed the ballistic tests through the analysis program in order to

¹ Research Assistant, Cukurova University, Department of Automotive Engineering, Orcid: 0000-0001-7624-6240

² Assoc. Prof. Dr., Cukurova University, Department of Automotive Engineering, Orcid: 0000-0002-0192-0605

³ Bachelor degree, Cukurova University, Department of Automotive Engineering, Orcid: 0000-0002-1530-3595

⁴ Bachelor degree, Cukurova University, Department of Automotive Engineering, Orcid: 0000-0002-0806-3562

⁵ Research Assistant, Cukurova University, Department of Automotive Engineering, Orcid: 0000-0001-5208-366X

find the strong and weak configurations in the double-plate armors. It created ideal properties for the strongest configuration in the low strength and high ductility front layer and the high strength and low ductility back sheet. Babaei et al. (Babaei, *et al.* 2011: 208-217) tried the ballistic test application to examine which material should be placed in the front and rear positions on the plates made of steel and aluminum plates. They found that the aluminum-steel sequence did not perform well in providing ballistic protection compared to the steel-aluminum sequence. Yunfei et al. (Yunfei, *et al.*, 2014: 38-49) examined the effect of plate order on ballistic performance in double-layer steel plates by real ballistic test. With the presence of high strength and low ductility material in the first layer, it gives better ballistic results than the presence of low strength and high ductility material in the first layer. In a study by Iqbal et al. (Iqbal *et al.*, 2010: 185–195) it was aimed to see the effect of 1100-H12 aluminum alloy plates and Weldox steel plates on ballistic tests. They discovered that not only the change in curvature but also the thickness of the material affects the ballistic limit of the formed plates. When the literature is examined, it is seen that there is no study showing the change of directional deformation in armor plates at varying angles. For this reason, in this study, three different angles (0°, 30°, 60°) were used for the target multi-material hybrid plates, and the directional deformation of the plates was determined by explicit dynamic analysis. As a result, the results of this study will be developed and will provide important findings in terms of ballistic performance evaluation that can be used in the defense industry.

2. MATERIAL

In this study, Ramor 500 and Armox 500T were used as plate material and lead material was used for 7.62 x 51 NATO bullet design. The mechanical properties of the materials defined in the ANSYS software program are presented in Table 1 (Ssab,2022: 5; Ssab,2022: 4).

Table 1. Material Characteristics

	Density (kg/m ³)	Tensile Ultimate Strength (MPa)	Young's Modulus (GPa)	Tensile Yield Strength (MPa)	Poisson Ratio
Ramor 500	7850	1700	-	1450	1.
Armox 500T	7760	1650	209	1300	0.3

Johnson-Cook material models are commonly used in ballistic impact simulations. While the material properties are given in Table 1, a simplified Johnson Cook model is used for plate materials in these models. The following equation describes the flow voltage as:

$$\sigma_y = (A + B\varepsilon^n)(1 + C \ln \dot{\varepsilon}^*) \quad (1)$$

A, B, C and n are the constants in the equation; σ_y represents the effective stress, ε the effective plastic strain, $\dot{\varepsilon}^*$ the normalized effective plastic strain rate, and n the work hardening exponent (Dietenberger *et al.*, 2005: 1-10). Model factors for Ramor 500 and Armox 500T are listed in Table 2 and Table 3.

Table 2. Model parameters for Armox 500T

	A_A(MPa)	B_A (MPa)	n	C
Armox 500T	1372.48	835.021	0.2467	0.0617

where A_A , B_A , n and c are Johnson-Cook parameters for Armox 500T. A_A is the yield stress, B_A is the hardening stress, n is the strain hardening, and c is the strain-rate hardening (Iqbal *et al.*, 2016: 146-164).

Table 3. Model parameters for Ramor 500

	A_R(MPa)	B_R (MPa)	n	C
Ramor 500	1021	965	0.057	0.001

where A_R , B_R , n and c are Johnson-Cook parameters for Ramor 500. A_R is the yield stress, B_R is the hardening stress, n is the strain hardening, and c is the strain-rate hardening (Scazzosi *et al.*, 2021: 14).

3. METHOD

The FEM is a numerical analysis process frequently used in engineering and mathematical models (Seshu, 2019: 1-15). The finite element method consists of three main stages. The first stage is the preprocessing stage, where a finite element mesh is improved and material characteristics and boundary conditions are used to subdivide the subject geometry for mathematical analysis. The second stage is the stage that includes the solution stage of the program by deriving the basic matrix equations from the main example and solving the basic quantities. The post-processing and third stage include examining the base quantity values, such as stresses and displacements, for which the solution is verified, and the derivation and investigation of additional quantities, such as error index and particular stresses. The created geometric models are transferred in order to execute Finite Element Analysis. In the program interface, element type selection on the mathematical model, creation of the mesh form, determination of the contact areas, boundary conditions, environmental and material properties and analysis type were performed (Hutton, 2014) In this study, ANSYS 18.0 Explicit Dynamics module was used for dynamic collision analysis, while bullet and plate designs were designed in CATIA V5 R20. The target plate is 100x200 mm in size and 14.5 mm thick, designed in CATIA V5 R20 and then transferred to ANSYS 18.0 Workbench for analysis. Images of the projectile and plate design are given in Figure 1 and Figure 2. The 7.62×51 mm bullet is a specially designed bullet with a diameter of 7.62 mm, a sleeve length of 51.2 mm.

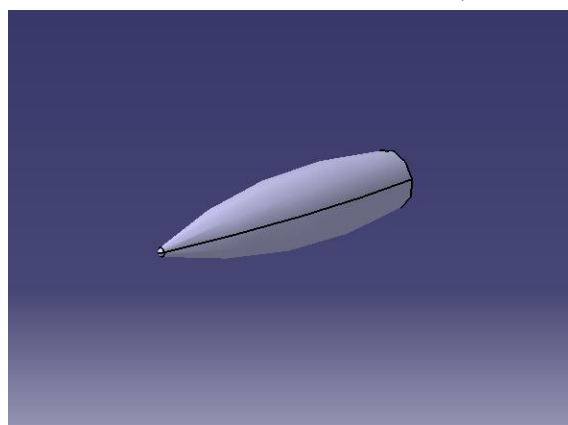


Figure 1. CATIA view of 7.62x51 mm bullet

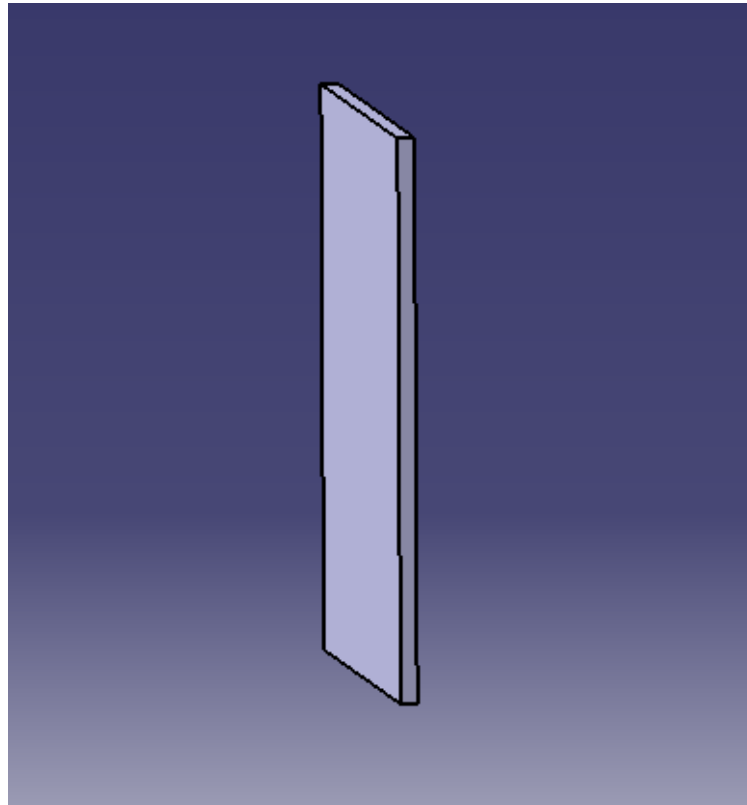


Figure 2. CATIA view of the designed plate

The most important step in finite element analysis is the meshing phase. The selecting and implementation the appropriate- mesh enables easy analysis for users (Uçtu, *et al.*, 2017: 37-43). Figure 3 shows mesh images of the steel plate and bullet. In plate and bullet mesh statistics, the target plate is 2162846 elements, the bullet core is 9036 elements, and the bullet jacket is 6888 elements.

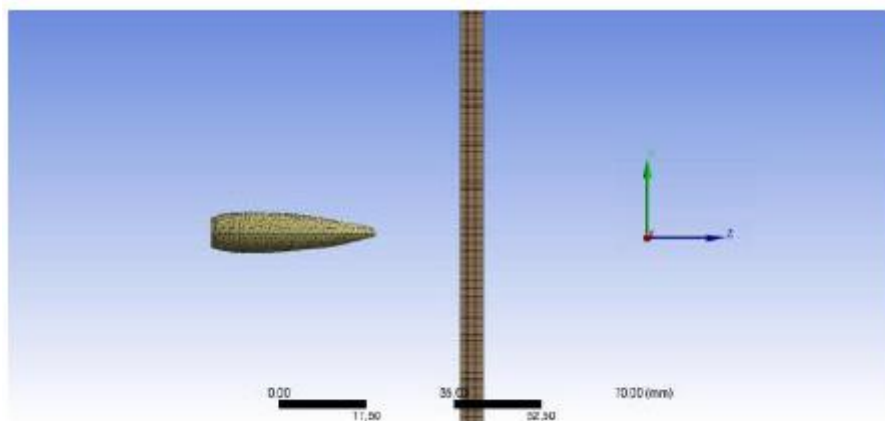


Figure 3. Mesh view of 7.62x51mm bullet and plate

In Figure 4, ANSYS images of the boundary conditions given to the target layer are given. The analysis was applied according to the following assumptions:

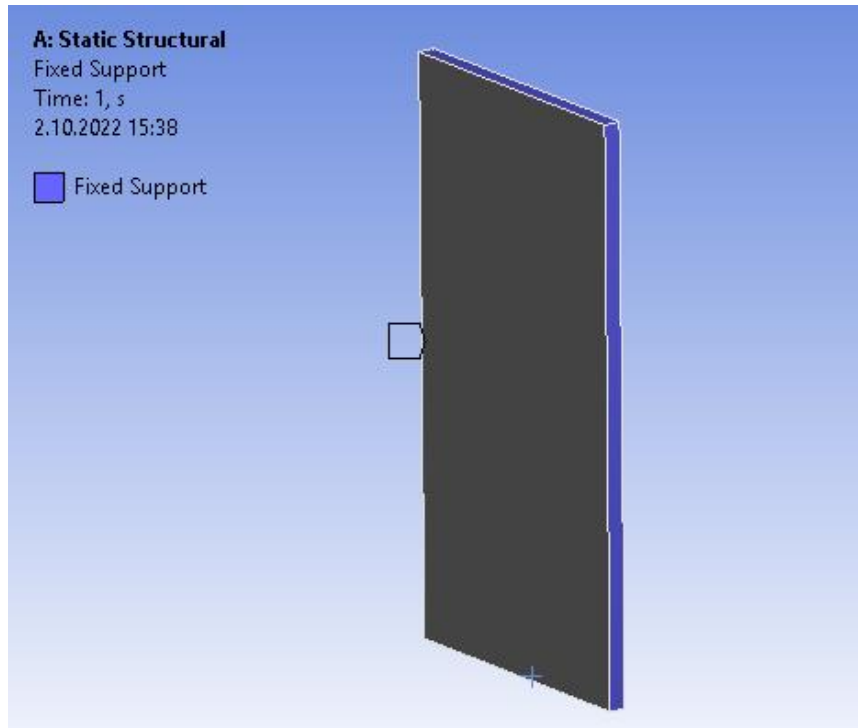


Figure 4. Boundary conditions for plate

In the mesh phase, the bullet models were updated on ANSYS and mesh was applied, and then the plate was supported from 4 side surfaces. In this explicit dynamic analysis, the lead was first applied to hit ArmoX 500T and then Ramor 500. The rate of fire of the bullet varies according to the type and caliber of the bullet, the diameter of the barrel and the groove sets in the gun. In order to achieve the most ideal result, 850 m/s average velocity is accepted for 7.62x51 mm bullet.

4. RESULT AND DISCUSSIONS

Explicit dynamic analysis through finite element analysis showed that the lowest directional deformation value occurs in the layer combination with 60°. In the numerical analysis of the layer combination with 0°, the highest directional deformation value was obtained. The results of the analysis are shown in Table 4. Figures 5 to 7 show the distribution of directional deformation values of the plate. When the plate angle increased from 0° to 30°, a decrease of 20.68% was observed in the amount of directional deformation, while a significant decrease of 197.25% was observed in the angle increasing from 30° to 60°. For the plate angle of 60°, the minimum deformation value is obtained, the deformation value is 3.385 mm, while for the plate angle of 0°, the angle with the maximum deformation value is obtained, the deformation value of 12.143 mm. It is seen that the minimum deformation value is 3.59 times less than the maximum deformation value.

Table 4. Results of Analysis

Angle	Directional Deformation (mm)
0°	12.143
30°	10.062
60°	3.385

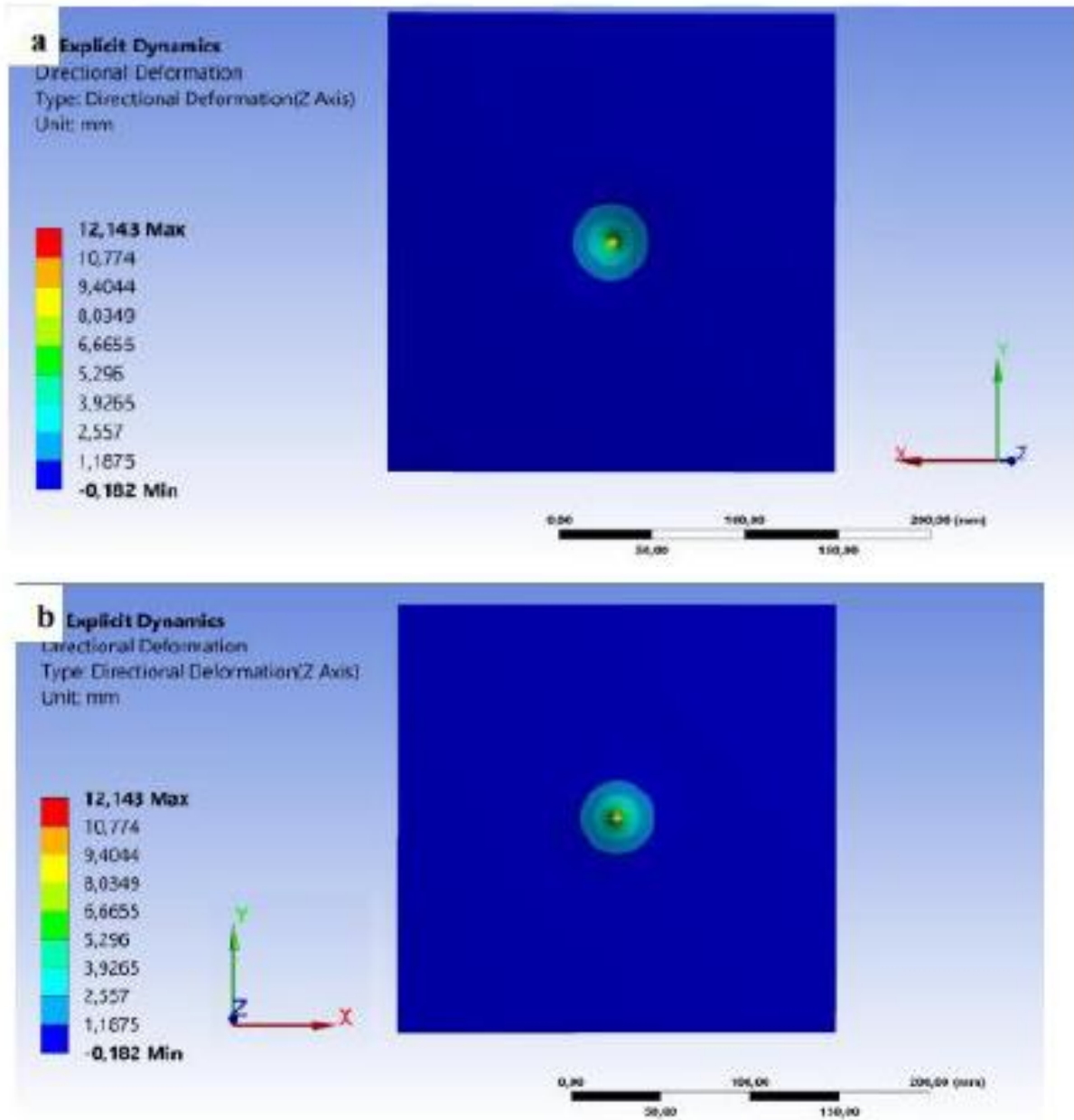


Figure 5. Directional deformation on the front (a) back (b) surfaces in the Z direction at 0° angle on the plate

As seen in Figure 5a and Figure 5b, the directional deformation value was found to be 12.143 mm in the explicit dynamic analysis made at 0° angle and the plate was pierced by the bullet as in the test. In this case, it has the maximum directional deformation value in the explicit dynamic analysis made with 0° angle.

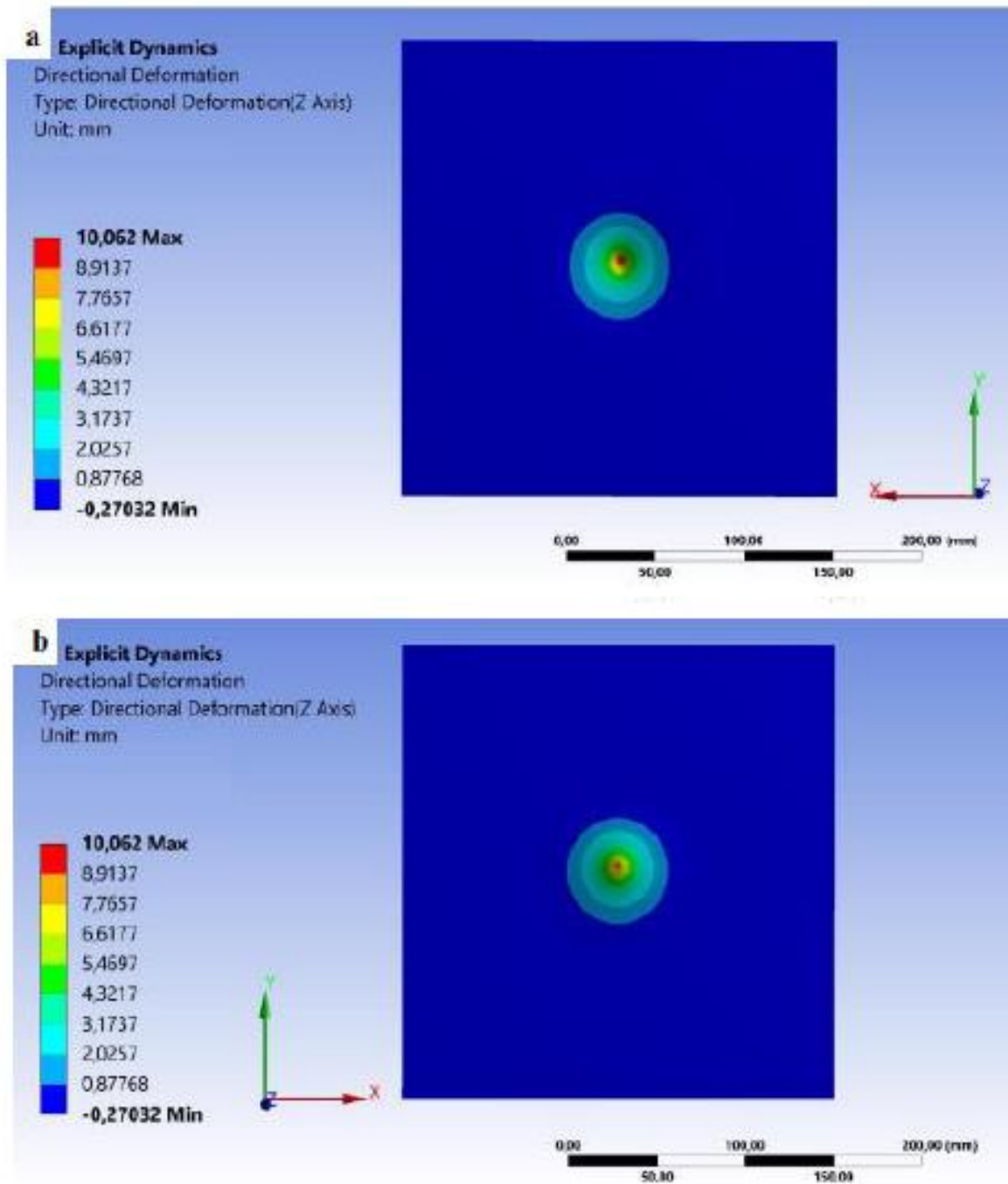


Figure 6. Directional deformation on the front (a) back (b) surfaces in the Z direction at 30° angle on the plate

As seen in Figure 6a and Figure 6b, the directional deformation value was found to be 10.062 mm in the explicit dynamic analysis made with an angle of 30° and the plate was not pierced by a bullet as in the test.

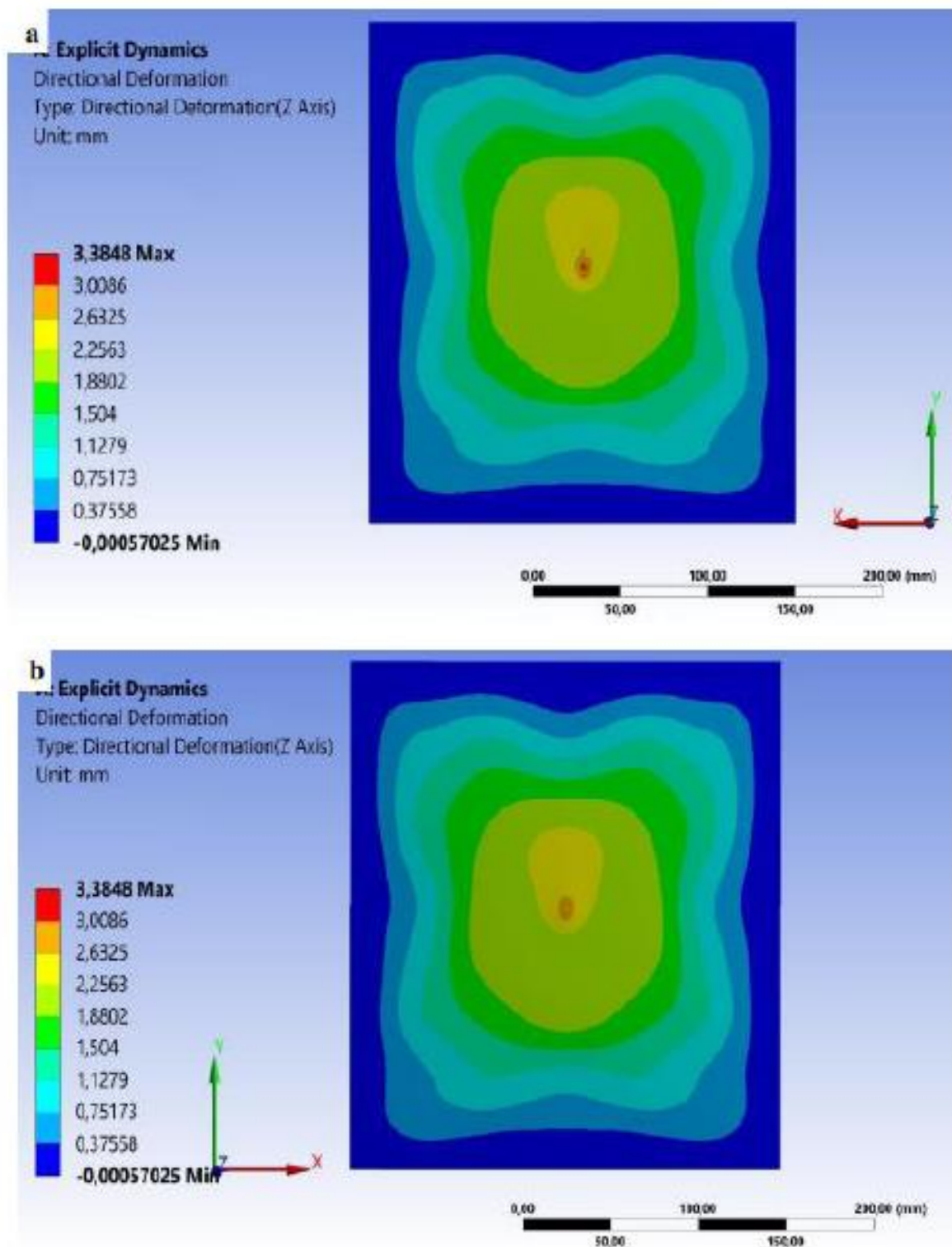


Figure 7. Directional deformation on the front (a) back (b) surfaces in the Z direction at 60° angle on the plate

As seen in Figure 7a and Figure 7b, the directional deformation value was found to be 3.3848 mm in the explicit dynamic analysis made with an angle of 60°, and the plate could not be pierced by the bullet and bounced, as in the test. In this case, it has a minimum directional deformation value in the explicit dynamic analysis made with an angle of 60°.

5. CONCLUSION

It is very important to know the ballistic performance of engineering materials in order to choose armor materials that provide full ballistic protection in civil and military applications. Ballistic protection is an increasingly developing situation in the defense industry. In this study, the effects on finite element analysis were shown by performing explicit dynamic analysis at three different angles (0° , 30° , 60°) for the hybrid plate obtained by using Armor 500T and Ramor 500 materials. It was found in the analysis results that the directional deformation results decreased as the angle increased. The following results were obtained during the study:

1. In the analyses made at 0° collision angle, the result of 12.143 mm directional deformation was reached. At this angle, the plate was pierced with 7.62x51mm bullets and the failure mode was observed. The maximum deformation value at this angle is 258.73% higher than the minimum deformation value.
2. In the analyses made at 30° collision angle, the result of 10.062 mm directional deformation was reached. At this angle, the plate was not pierced by 7.62x51mm bullets and a significant bulge was observed on the back of the target.
3. In the analyses made at 60° collision angle, the result of directional deformation of 3.3848 mm was reached. At this angle, the plate was not pierced by 7.62x51mm bullets and no obvious protrusion was observed on the back of the target. With this, the least deformation value occurred.

REFERENCES

- Agrawal, B. J. (2011). High performance textiles for ballistic protection, *Defense Science Research Conference and Expo (DSR)*, Singapore, 1-4.
- Ashby, M. F., Jones, D. R. H. (1998). *Engineering materials 2*, 2nd ed., Butterworth-Heinemann, Oxford.
- Babaei, B. Shokrieh, M.M. Daneshjou, K. (2011). The ballistic resistance of multilayered targets impacted by rigid projectiles, *Mater. Sci. Eng. A*, 530 208–217.
- Carlucci, D. E., Jacobson, S. S., (2008). *Ballistics; theory and design of guns and ammunition*, Taylor and Francis Group, New York.
- Demir, T. (2008). *Metal ve katmanlı zırh malzemelerinin 7,62 mm lik zırh delici mermiler karşısında balistik başarımlarının incelenmesi*, Master's Thesis, TOBB Ekonomi ve Teknoloji Üniversitesi, Ankara.
- Dietenberger, M., Büyük, M. Kan, C.D. (2005). Development of a high strain-rate dependent vehicle model. *LS-Dyna Anwenderforum*, 1, 1–10.
- Hutton, D.V. (2004). *Fundamental of finite element analysis*, Mc Graw Hill, New York.
- Iqbal, M.A., Senthil K., Sharma P., Gupta N.K. (2016). An investigation of the constitutive behavior of Armox 500T steel and armor piercing incendiary projectile material. *Int. J. Impact Eng.*, 146–164.
- Iqbal, M.A. Chakrabarti, A. Beniwal, S. Gupta, N.K. (2010). 3D numerical simulations of sharp-nosed projectile impact on ductile targets. *Int. J. Impact Eng.*, 185–195.
- Kartikeya, Prasad, S. Bhatnagar, N. (2019). Finite element simulation of armor steel used for blast protection. *Procedia Struct. Integrity*, 14 (2018), 514–520.
- Murray, G. White, C. V. Weise, W. (2008). *Introduction to engineering materials*, 2nd ed., CRC Press, New York.
- Robinson, H.R. (1967). *Oriental armour*, Walker, New York.
- Scazzosi, R. Giglio, M. Manes, A. (2021). Experimental and Numerical Investigation on the Perforation Resistance of Double-Layered Metal Shield under High-Velocity Impact of Armor-Piercing Projectiles, *Materials*, 14, 626.
- Seshu, P. (2009). *Textbook of finite element analysis*, PHI Learning Pvt. Ltd.
- Ssab, (2022). *Armox 500T*. [Access available:28.09.2022]: <https://www.ssab.com/tr-tr/products/brands/armox/armox-500t>.
- Ssab, (2022). *Ramor500*. [Access available:28.09.2022]: <https://www.ssab.com/en/brands-and-products/armox/product-offer/ramor-500>.
- Teng, X. Wierzbicki, T. Huang, M. (2008). Ballistic resistance of double-layered armor plates, *Int. J. Impact Eng.*, 870–884.

Uçtu, Ö. Sevim, İ. Karatař, B. řahin, B. (2017). Determination of optimum mesh size to measure tooth root stress of spur gear using finite element analysis”, *Turkish Journal of Engineering (TUJE)*, 1 (1), 37-43.

Yavař, M. O. (2009). *Hafif silablara karşı bireysel savunma amaçlı kompozit malzeme tasarımı ve balistik dayanımı*, Master’s Thesis, Selçuk Üniversitesi, Konya.

Yunfei, D. Wei, Z. Yonggang, Y. Lizhong, S. (2014). Experimental investigation on the ballistic performance of double-layered plates subjected to impact by projectile of high strength, *Int. J. Impact Eng.*, 38–49.

Does Hardun Change Colors?: A Preliminary Study on Ventral Color Alterations of Anatolian Harduns

Melodi YENMIŞ¹
Yusuf BAYRAKCI²

Introduction

Reptilian integument is specialized for terrestrial life. It consists of two main layers as epidermis and dermis. Epidermis is a hard cover of the body with its keratinized and cornified structure. Dermis, on the other hand, is thicker than the epidermis and consists of chromatophores and cells that supports epidermis. Chromatophores are the cells that give the skin it's color and they vary according to their structures and pigments they carry (Ligon and McCartney, 2016).

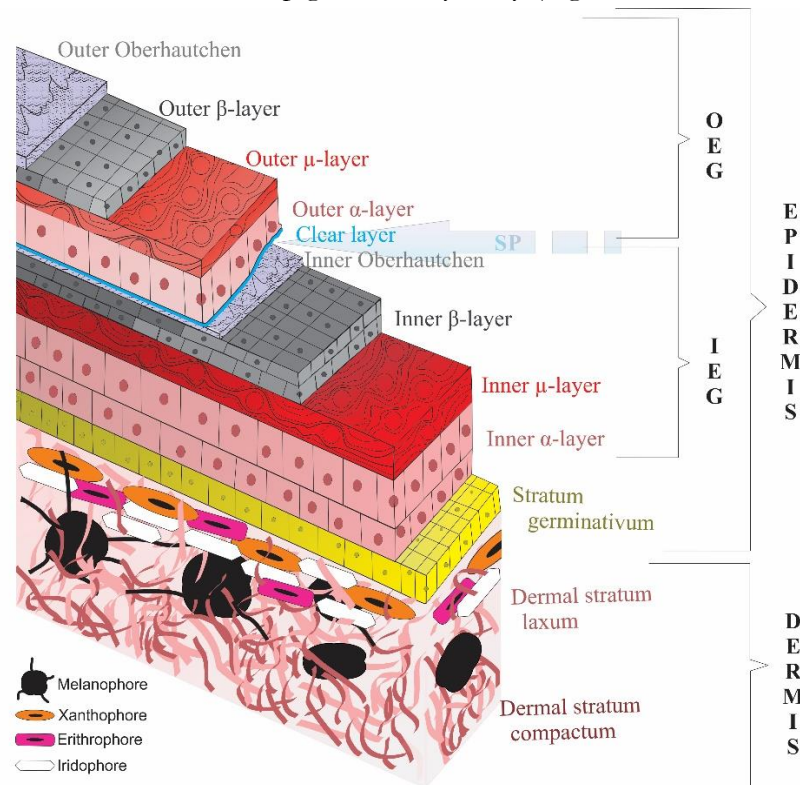


Figure 1 - Illustration of the layers, shedding pane (SP) and the chromatophores of reptile skin.
OEG: Outer epidermal generation, IEG: Inner epidermal generation.

¹ Melodi Yenmiş, Dr., Ege University, Science Faculty, Biology Dept., 0000-0003-2627-6008

² Yusuf Bayrakçı, Dr., Ege University, Science Faculty, Biology Dept., 0000-0001-5992-0643

There are four types of chromatophores in the dermis (Figure 1). Xanthophores which are the closest ones to epidermis comprise pteridine pigments. They are responsible for yellow-orange colors of the skin. Erythrophores comprise carotenoid pigments which produce red and orange colors. When xanthophores and erythrophores are close and covering each other, they produce various color combinations. Iridophores (guanophores, granulophores) are different from the previous chromatophores in terms of structure and function. They have reflective properties due to the crystal guanine pigments they contain. The density and the deployment of the crystals designate the way of diffraction of light (iridescence). The primer color they produce is blue, due to the reflection of blue wavelengths. Green coloration is produced by the combination of this blue reflection of the iridophores and orange color of the carotenoids (Bagnara et al., 1979; Kuriyama et al., 2006; Scharlt et al., 2015; De Mello et al., 2021).

Melanophores lie deeper in the dermis, beneath the former chromatophores. The pigments of melanophores are called melanin and they are responsible for brown and black coloration. Melanophores have dendrites which are facing toward the epidermis, and they can be dispersed or aggregated along with their melanin bearing melanosomes. Aggregation of the dendrites makes the skin area look lighter while dispersion makes it look darker (Ligon and McCartney, 2016) (Figure 2).

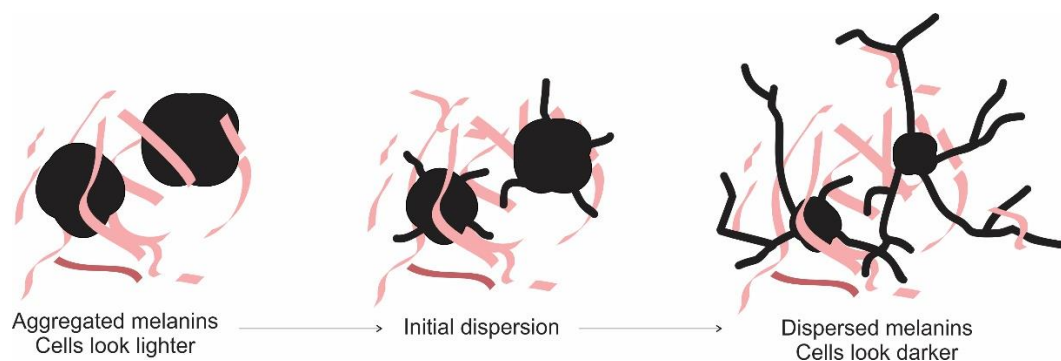


Figure 2 - Movement of the melanophores' dendrites showing lighter look with aggregation and darker look with dispersion.

Color changing abilities are vital for many reptiles since it helps to avoid predators and provide disguise for preys as in aposematism, crypsis and mimicry. It is also a signaling instrument among conspecifics as in mating and territorial behaviors. It is more distinct in males since they change into eye-ful colors during mating seasons both for attracting females and intimidating other male counterparts. Although rare, females are also observed to change color. For example, some gravid female members of Agamidae and Chamaeleonidae families reflect distinctive colors to avoid disturbance from their conspecifics (Olsson et al., 2013; Assis et al., 2020). Some members of Testudines and crocodiles are also known to have the ability to change color. Snakes are the only extant reptiles which are unable to alter their coloration (Merchant et al., 2018).

Hardun, Starred agama or *Laudakia stellio* is the most abundant Agamid in Turkey. Their total length can be up to 40 cm. The scales in the ventral body region are rectangular. Scales of the dorsal body and the head are carinated (spiny). Tails consisting of two rows of scales arranged in rings. The head is a triangular form expanding towards the body. They are one of the rock agamas of Euroasia and even though some relatively close species were shown to have color changing abilities (Panov and Zykova, 1997), there are very limited information about the color change of the Hardun (Brammah et al., 2010; Baig et al., 2012). Here we show that Anatolian Harduns change their ventral color during morphological observations.

Material and Methods

We have recorded 5 individuals from four different localities (Figure 3). The studies were made with the permission of Ege University Animal Experiments Local Ethics Committee (Permission no: EGE HADYEK 2017-065) and Ministry of Forestry and Water Affairs, General Directorate of Nature Conservation and National Parks (Permission no: 72784983-488.04). All the individuals were immediately released to their habitats after taking photos and videos. The details of the localities and the individuals are given in Table 1.



Figure 3 - Localities of the individuals studied (Made via Google Earth Pro)

The individuals were recorded during ventral color change. Canon EOS 6D (WG) camera, Canon Zoom Lens (24-105 mm) and Canon Macro Lens EF (100 mm) were used for photography and video shooting.

Table 1 - Localities (east to west), GPS data and the individual numbers and sexes studied.

Locality	GPS	Individuals
Hatay	36°28'55.2"N 36°29'20.6"E	1 ♂, 1 ♀
Konya	37°42'48.5"N 33°34'47.0"E	1 ♂
Manisa	38°29'17.5"N 28°02'25.4"E	1 ♂
İzmir	38°28'34.6"N 27°11'11.4"E	1 ♂

Results

Some males and females were ventrally spotless to begin with. And some were spotted with randomly distributed darker scales (Figure 4). Among the spotted individuals which are the main subject of the present study, it was noted that the spots on the ventral body disappeared in an average of 7 minutes.

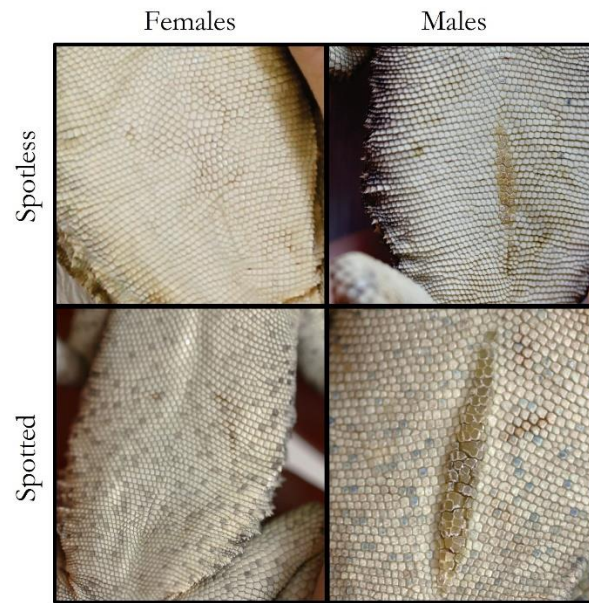


Figure 4 - Examples of male and female individuals that are spotless and spotted at the ventral body.

During the study period, individuals stood in the hands of the researcher. Spotted scales, which appeared randomly scattered among the rectangular ventral scales, gradually changed color during this time, turning into the general ventral color which is milky white or gray (Figure 5). No variations in the process were observed between male and female individuals.

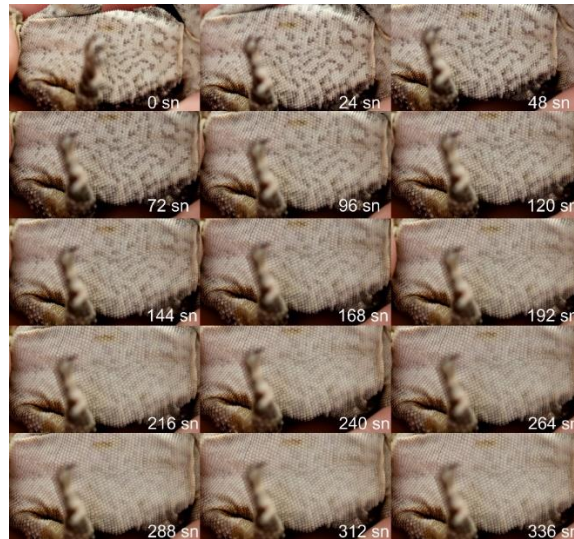


Figure 5 - Frames taken every 24 seconds from the ventral body of a female individual showing the disappearance of the spots in approximately 6 minutes.

Discussion

The ventral body patterning in *L. stellio* is completely spotless with milky white or gray background color in the vast majority of individuals. Only some has spots at the ventral body. The frequency of the spots and the darkness of their colors differ between individuals.

Previous studies have mentioned the color change of the rock agamas of Eurasia. In addition to the signaling context of this change, they said it was a response to changes in physiological state and the air temperature (Panov and Zykova, 1997). However, there are limited information on the color change of *L. stellio*: Brammah et al., (2010) stated that *L. stellio* changes color rapidly depending on the temperature and said that it takes lighter colors in hot and darker colors in cold. Baig et al. (2012) stated that different color variations are seen in one of the subspecies, *L. stellio stellio*, depending on the physiological color change, but further studies are needed. Yet no previous study reported visual proof for this change in *L. stellio* and no such change has been reported for the Anatolian populations.

Here we showed ventral color change in *L. stellio* from Anatolia. In the five ventrally spotted individuals studied, we found that the spots disappeared in an average of 7 minutes. That is, individuals changed the color of the ventral body during the examination period. And in about 7 minutes, the body has taken on a completely spotless, milky white appearance. Since it is a change of brown-black coloration, it can be stated that the melanophores are responsible for these spots and these results indicate that the melanophores beneath these scales aggregate under certain conditions (Ligon and McCartney, 2016).

The contribution of melanophores to physiological color change in reptiles is very important due to their dynamic nature. The dynamism in terms of dispersion/aggregation of melanosomes is controlled by hormones (e.g., α -MSH) and neurotransmitters (e.g., EPI), (Summers and Greenberg, 1994; Ligon and McCartney, 2016). Therefore, further detailed studies are needed to understand the conditions that effect such controllers for a ventral color change in Hardun.

We should state that this study is preliminary and was conducted under noncontrollable field conditions, and no tissue samples were taken from the individuals. Therefore, along with the above-mentioned hormonal studies, live animal experiments under different temperature and light and genetic research (especially for MC1R and Agouti genes that influence adaptive coloration) (Hoekstra, 2006; Hubbard et al., 2010) are needed as well as histological studies to understand the status of melanophores during this change. Having said that, it is important to note this phenomenon, because ventral coloration has been used as a taxonomical character for years for *L. stellio* (e.g., Göçmen et al., 2003; Almog et al., 2005; Ilgaz et al., 2005; Gül and Tosunoğlu, 2011).

Ventral patterning of Hardun should not be considered a permanent morphology and should not be included in intra- or inter-population studies. Further research of this phenomenon will provide new insights into the physiology of color change in Harduns and under what conditions it occurs.

Acknowledgements

This study was partially financially supported by Ege University Office of Scientific Research Projects (EGEBAP) (Grant number: FGA-2021-22483 and 18FEN-016). The data examined in this study was partially obtained from PhD thesis of the first author.

Conflict of interest

There are no competing interests to declare.

References

- Almog, A., Bonen, H., Herman, K., & Werner, Y. L. (2005). Subspeciation or none? The hardun in the Aegean (Reptilia: Sauria: Agamidae: *Laudakia stellio*). *Journal of Natural History*, 39(7), 567-586. doi: 10.1080/00222930400001293
- Assis, B.A., Jarrett, B.J., Koscky, G., Langkilde, T. and Avery, J.D. (2020). Plastic sexual ornaments: Assessing temperature effects on color metrics in a color-changing reptile. *PLoS one*, 15(5):p.e0233221.
- Bagnara, J.T.; Matsumoto, J.; Ferris, W.; Frost, S.K.; Turner, W.A.; Tchen, T.T.; Taylor, J.D. (1979). Common Origin of Pigment Cells. *Science*, 203, 410–415.
- Baig, K.J., Wagner, P., Böhme, W. and Ananjeva, N. B. (2012) A morphologybased taxonomic revision of *Laudakia* Gray, 1845 (Squamata: Agamidae), *Vertebrate Zoology*, 62(2): 213-260.
- Brammah, M., Hoffman, J. I., Amos, W. (2010). Genetic divergence between and within two subspecies of *Laudakia stellio* on islands in the Greek Cyclades. *The Herpetological Journal*, 20(2), 91-98.
- De Mello, P.L.H.; Hime, P.M.; Glor, R.E. (2021). Transcriptomic Analysis of Skin Color in Anole Lizards. *Genome Biology and Evolution*, 13, doi:10.1093/gbe/evab110
- Göçmen, B., Tosunoglu, M., Taskavak, E. (2003). A taxonomic comparison of the Hardun, *Laudakia stellio* (Reptilia, Agamidae), populations of southern Turkey. *Zoology in the Middle East*, 28, 25-32.
- Gül, Ç., Tosunoğlu, M. (2011). External morphological and osteological features of Turkish populations of *Laudakia stellio* (Linnaeus, 1758). *Herpetozoa*, 24, 73-88.
- Hoekstra, H. E. (2006). Genetics, development and evolution of adaptive pigmentation in vertebrates. *Heredity*, 97(3), 222–234. <https://doi.org/10.1038/sj.hdy.6800861>
- Hubbard, J. K., Uy, J. A. C., Hauber, M. E., Hoekstra, H. E., Safran, R. J. (2010). Vertebrate pigmentation: From underlying genes to adaptive function. *Trends in Genetics*, 26(5), 231–239. <https://doi.org/10.1016/j.tig.2010.02.002>
- Ilgaz, Ç., Baran, İ., Avcı, A., Olgun, K., Kumlutaş, Y. (2005). On *Laudakia caucasia* (Eichwald, 1831)(Sauria: Agamidae: *Laudakia*) specimens collected from northeastern Anatolia. *Russian Journal of Herpetology*, 12(3), 184-187.
- Kuriyama, T.; Miyaji, K.; Sugimoto, M.; Hasegawa, M. (2006). Ultrastructure of the Dermal Chromatophores in a Lizard (Scincidae: *Plestiodon latiscutatus*) with Conspicuous Body and Tail Coloration. *Zoological Science*, 23, 793–799. <https://doi.org/10.2108/zsj.23.793>
- Ligon, R. A., McCartney, K. L. (2016). Biochemical regulation of pigment motility in vertebrate chromatophores: a review of physiological color change mechanisms. *Current Zoology*, 62(3):237-252. <https://doi.org/10.1093/cz/zow051>

Merchant, M., Hale, A., Brueggen, J., Harbsmeier, C., Adams, C. (2018). Crocodiles alter skin color in response to environmental color conditions. *Scientific Reports*, 8(1), 1–10. <https://doi.org/10.1038/s41598-018-24579-6>

Olsson, M., Stuart-Fox, D., Ballen, C. (2013). Genetics and evolution of colour patterns in reptiles. *Seminars in cell & Developmental Biology*, 24(7): 529-541. <https://doi.org/10.1016/j.semcdb.2013.04.001>.

Panov, E.N., Zykova, L.Y. (1997). Differentiation and interrelations of two representatives of *Laudakia stellio* complex (Reptilia: Agamidae) in Israel. *Russian Journal of Herpetology*, 4(2):102-114.

Schartl, M.; LaRue, L.; Goda, M.; Bosenberg, M.W.; Hashimoto, H.; Kelsh, R. (2015). What is a vertebrate pigment cell? *Pigment Cell Melanoma Research*, 29, 8–14. <https://doi.org/10.1111/pcmr.12409>

Summers, C. H., & Greenberg, N. (1994). Somatic correlates of adrenergic activity during aggression in the lizard *Anolis carolinensis*. *Hormones and Behavior*, 28(1), 29–40.

Software-Defined Network Application With AI Techniques

Fatih Şahin

1.Introduction

Data centers are getting bigger and bigger with the developing technology. In growing data centers, large volumes of complex and irregular information begin to take place. This information in big data needs to be processed in order to be meaningful and valuable. Big data cannot be processed, managed and stored with traditional methods. In other words, the traditional network management approach is insufficient at this stage. With a better network approach, new methods and a wider bandwidth, this data becomes processable. Software Defined Network (SDN) emerges as a method that meets these needs. SDN provides ease of management, hardware independence, dynamic, flexible and scalable network architecture. Therefore, it offers an effective solution to large and complex network management.

Installing and managing networks requires skilled specialists in configuring multiple network elements. A systems-based approach is needed where communication between network elements (switches, routers, etc.) is complex. This is difficult to achieve with the current programming interfaces in most of today's networking equipment. In order to achieve this, a new network model was needed and the concept of LTA emerged in the meantime (Sezer et al., 2013). The Open Networking Foundation is a non-profit organization dedicated to the development, standardization and commercialization of SDN. The Foundation gives the definition that best explains SDN as follows: SDN is a new network architecture where network control is separated from transmission and can be directly programmed (Xia et al., 2015).

SDN architecture consists of three layers, namely application, control and data layers, and two interfaces between application-control and control-data layers. The control layer is basically where the sending of packets takes place. In the data layer, the traffic flow that occurs during the transmission of packets is regulated.

In traditional network traffic, routers and switches determine the destination of the packet. These, in turn, are located on the same hardware, integrated with each other in the control and data layers. SDN is mainly focused on separating these two layers. In SDN, the control plane is moved to a high-performance server and network management is performed by a central controller software. The data layer ensures that routers and switches are only responsible for stream routing. The control layer is known as the network operating system. In this layer, communication between network applications and data layer takes place. The communication between the control layer and the data layer is provided by the open source network protocol OpenFlow (Niyaz et al., 2015). SDN architecture not only enables the network to be programmed directly, but also creates the necessary infrastructure for network services and applications.

The main purpose of the communication network is to transfer information packets from one point to another. Since transmission occurs to more than one node in the network, this causes a heavy traffic flow. In the meantime, effective and efficient traffic flow can be ensured thanks to the controller using SDN. Thus, a simpler and easier management approach is offered by avoiding the confusion caused by the traffic that causes density and diversity.

In this study, it is aimed to realize the traffic flow in the networks depending on the SDN controller and to optimize the data obtained here by using artificial intelligence optimization techniques. In the light of the obtained data, it is aimed to develop an application on prediction by using artificial neural networks (ANNs). The content of the study continues as follows: General information about the tools and methods used in the 2nd chapter, the application steps of the proposed method in the 3rd chapter, the results obtained from the application in the 4th chapter, and finally the conclusion and discussion about the subject in the 5th chapter.

1.1. Software Defined Networking

Work on advancing computer networks can be divided into three phases in terms of programmability:

- Active networks: (mid 1990s to early 2000s) leads to the addition of programmable functions in the network. Where switching devices can perform operations to process packets.
- Control and data plane separation (2001 to 2007) leading to new capabilities such as predicting or controlling routing behavior.
- OpenFlow API (2007 to 2010) which is the first common southbound interface to handle L2-L4 network flows between control and data plane. However, to handle L5-L7 flows to give the ability to support Network Virtualization Function (NVF), OpenFlow protocol needs to be extended. Each flow chart consists of (i) header fields, (ii) counters, and (iii) movements. If there is no packet match, a PACKET-IN message is sent to the controller over a secure channel, which is encrypted using Transport Layer Security (TLS) to notify the controller about this packet, as shown in Figure 1.

The first OpenFlow version, OF 1.0, was released in March 2008 with support for a single flow table. Later versions of OpenFlow, such as OF 1.1, support more advanced features such as various flow tables, which involve using the "goto" command as a pointer to another flow table. OF 1.2 includes IPv6, which is extensible mapping using the TLV structure, giving switches the ability to communicate with multiple controllers simultaneously. Added OF 1.3m tables for QoS support. Later OF 1.4 TLV structures were used more to support optical ports on switches and were optimized to save time spent communicating between switch and controller if the flow table was full.

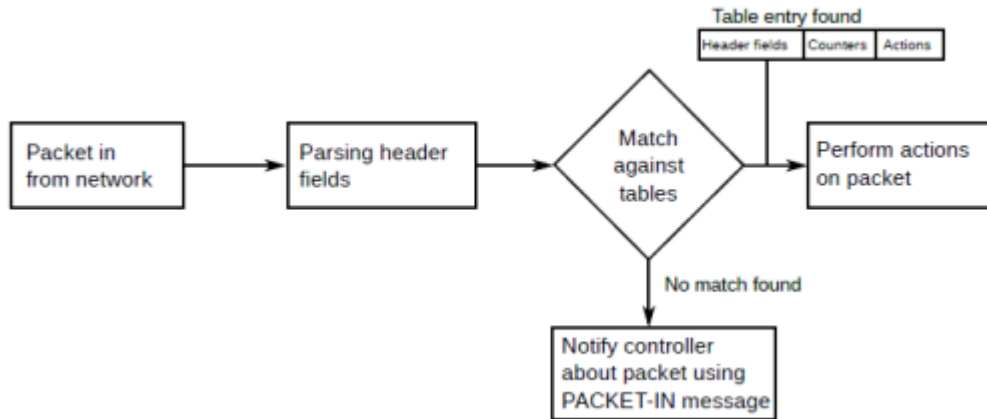


Figure 1. Open vSwitch basic packet routing

Decomposition of the network system provides the ability to manage it through a high level of abstraction. SDN, the latest paradigm of programmable networks, facilitates network operations such as routing or adding rules to routing devices with a single central controller. This means that the routing units will implement the decisions made by this controller. A comparison between the SDN architecture shown in Figure 2 and the traditional network architecture. The main abstraction concepts defined by SDN are: 1. Routing, 2. Distribution, and 3. Specification. The routing abstraction allows any routing action to be performed by the controller while hiding low-level processing with switching devices. Distribution abstraction involves replacing the traditional distributed control plane with a logically centralized plane. Routing abstraction hides low-level use with switching devices during which any forwarding action is performed by the controller. Specification abstraction allows developers to write network applications by defining desired flow actions and configurations without dealing with low-level or physical configurations.

The logically centralized control plane shown in Figure 2 provides a global view of the network, which opens the door for more optimized control of the guiding elements. It can be achieved with a single or distributed controller(s). In addition, FlowVisor, a proxy controller, provides a logical localization for network virtualization purposes. A brief comparison of the controller platforms shown in Table 1.

Common SDN simulators and emulators such as Mininet, NS-3 and Estinet are described and compared in Table 2

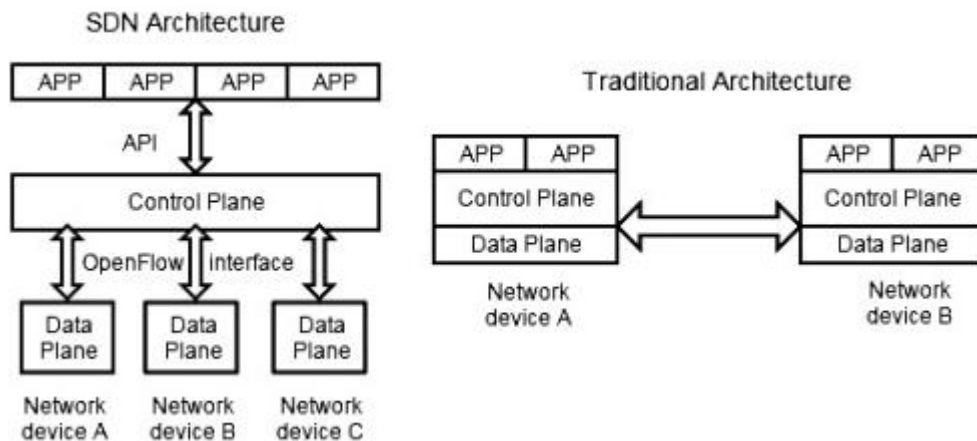


Figure 2. Comparison of traditional network architecture with SDN.

Table 1. A comparison of controller platforms

Controller	Language	Created by	OpenFlow version
NOX ¹⁷	Python, C++	Nicira	1.0, 1.3
POX ¹⁸	Python (2.7)	Nicira	1.0
Beacon ¹⁹	Java	Stanford university	1.0.1
Maestro ²⁰	Java	Rice university	1.0
Floodlight ²¹	Java	Big Switch Networks	1.0
Floodlight-plus ²²	Java	Big Switch Networks	1.3
Ryu ²³	Python	NTT Labs	1.0 to 1.4
(ODL)OpenDaylight ²⁴	Java	Linux Foundation	1.0, 1.3

Table 2. Comparison of SDN simulators and emulators

Simulator/emulator	Open source	Language	Platform	OpenFlow version
Mininet (Emulator)	Yes	Python	BSD open source	OF 1.3 of the reference user switch and NOX from CPqD and Ericsson
NS-3 (Simulator)	Yes	C++, Python	GNU GPLv2	Pre OF 1.0 and version of OF-SID that support MPLS
EstiNet (emulator/simulator)	No	-	-	OF 1.3 and 1.0

The ability of SDN to program the routing plane by the SDN controller can reduce the cost required to add custom networking devices such as firewalls, load balancers, and Intrusion Detection Systems (IDS). Also, the SDN approach provides more dynamic and less expensive solutions for technologies used in WANs such as path computing technology, extending these solutions as an SDN application allows network operators to program the Path Computing Element (PCE) directly. As a result, the controller is a virtual machine manager in different environments, for example a private cloud.

1.2. Artificial Intelligence on SDN

Recently, soft computing and artificial intelligence methods have started to play an important role in most modern systems such as intelligent transportation. This gives us a chance to improve the performance of existing computer networks. Integration between the concept of abstraction in the SDN paradigm and AI techniques can lead to more adaptive behavior of network elements. It will also introduce new mechanisms to deal with both traditional networking issues and new SDN related issues. This section will discuss recent efforts in this regard.

1.2.1. Load Balance and Flow Routing

The load balance function is a requirement to minimize latency and maximize throughput in computer networks that support multiple routing approaches. Load balancing is also considered a defense technique against some network attacks such as DDoS attack. In the SDN approach, abstraction provides a significant advantage for the global view and discovery of the topology of the network. In Back Propagation Neural Network (BPNN), which is used to provide real-time dynamic load balance and delay, it is reduced by 19.3% compared to DLB and static Round Robin methods. The input vector for the neural network contains the following path information: 1. Bandwidth utilization rate 2. Packet loss rate 3. Transmission delay and 4. Transmission hops. The authors also proposed a BPNN-based approach for load balancing in data centers. BPNN is implemented internally within Open vSwitch, which reduces the time it takes to send the routing decision from the controller to Open vSwitch. The input vector consists of: 1. Available bandwidth and 2. Packet loss. And from that, it proposes a genetic algorithm in SDN-based client-server architecture. The fitness function defined by formula (1):

$$\text{Min} \frac{\sqrt{\frac{(\sum_{j=1}^k X[j]^2) - \left(\frac{\sum_{j=1}^k X[j]}{K}\right)^2}{K}}}{\frac{\sum_{j=1}^k X[j]}{K}} \quad (1)$$

K stands for servers and each has X workload sets. Performance comparison was made with random and cyclic trial methods and showed better performance. In addition, a genetic algorithm for SDN-based voice stream routing optimization over IP network is introduced. Network defined as a connected graph. The problem is to show that the graph satisfies the demand with the bandwidth and latency requirements of the source and destination. The fitness function given by the formula shown in equation (2).

$$\text{Max} \frac{\sum \text{embedded demands}}{\sum \text{demands}} \quad (2)$$

Due to time consumption issues, the authors did not apply the crossover operation. Population size and non-allocation probability were the most important parameters for the algorithm. Also, since the genetic algorithm was implemented in python, the time efficiency was 10 times less than the mixed integer linear programming algorithm implemented in C++. The advantage of using the genetic algorithm approach is to obtain a partial solution of the problem during the solution phase, while this is not possible in a linear program; this partial solution helps to evaluate other algorithms. In another context, an Ant Colony Optimization (ACO) approach for QoE-sensitive flow routing. ACO is a swarm intelligence method that uses metaheuristic optimization. Quality of Experience (QoE) in computer networks specifies requirements for customers to measure the value of the service provided from the customer's perspective. In SDN applications, it passes user session parameters to the controller, which runs the ACO algorithm on a weighted graph; where the weights between the peaks are the latency and loss rate for each network device. The fitness function depends on the type of stream and the estimated value of the corresponding QoE model (ie: audio, video or data). ACO achieved a 24.1% increase for the maximum QoE achieved with the shortest path routing approach.

1.2.2. Network security

The SDN approach introduces a number of new security issues and seems to be one of the biggest problems with SDNs. Possible threats include targeting the controller by programming vulnerabilities in the secure channel, error configurations, and DDo attacks, as shown in Figure 3. In addition, SDN has advantages over traditional networks in terms of security as shown in Table 3. Artificial intelligence and data mining techniques, which were previously used in conventional network architectures to solve routing problems and optimize the performance of packet filters, are playing an important role in SDN-based networks after adding programming ability as authors to a proposed information security management. It is a system based on the combination of fuzzy inference system and both TRW-CB and Rate Limiting algorithms in SDN environment.

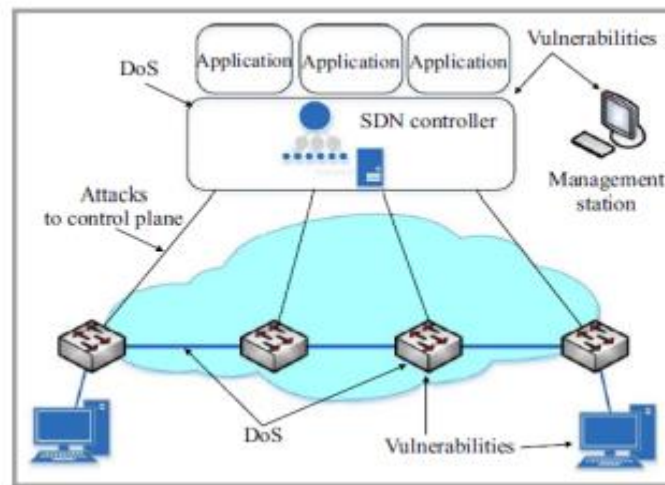


Figure 3. Potential attack vector in SDN.

Table 3. SDN security benefits.

SDN Characteristic	Security Use
Global Network View	<ul style="list-style-type: none"> - Network-Wide Intrusion Detection - Detection of Switch's Malicious Behavior. - Network Forensics.
Self-Healing Mechanisms	<ul style="list-style-type: none"> - Reactive Packet Dropping. - Reactive Packet Redirection.
Increased Control Capabilities	<ul style="list-style-type: none"> - Access Control.

TRW-CB algorithm that detects SYN Flooding caused by a host based on the idea that a benign host will achieve a higher probability of successful connection than a malicious host. The degree of attack obtained as input and output for the fuzzy logic module obtained by the specified algorithms. The decision making system is implemented as SDN controller application with short-term learning module as shown in Figure 4. The proposed system showed better results compared to a non-fuzzy logic approach.

It is a BPNN-based collaborative intrusion prevention system, taking advantage of the global view in the SDN paradigm. Each Open vSwitch is responsible for collecting data to perform input for several ANNs. The system is offline trained by MATLAB. Open vSwitches need to

communicate with each other as it is a collaborative system. Unfortunately in the SDN paradigm Open vSwitchs cannot talk to each other. Therefore, a neural routing table has been implemented in each Open Vswitch and the controller can assist in the creation of these tables. Figure 5 shows the pattern of a neural message, and the experimental results show that as the network grows, the detection rate of DDoS attack increases and the false positive rate decreases.

Whereas, Self-Organizing Maps (SOM) approach has been proposed to detect DDOS attack. SOM is a kind of artificial neural networks based on unsupervised learning. SOM can be used as a classification mechanism when processing with unlabeled input vector. The training in SOM is based on a set of features required from streaming inputs of Open vSwitches. The detection cycle consists of three phases: 1. Stream collection, which requests stream inputs from all Open vSwitches. 2. It is feature extraction that takes the output of the stream collection module and extracts the most important features that constitute a possible DDoS attack. These features include: Average of Packets per Stream (APf), Average Bytes per Stream (ABf), Average Time per Stream (ADf), Even Percentage Streams (PPf), Odd Streams Growth (GSf), and Differential Ports Growth (GDP), and (iii) the SOM classification used as the classification method. These stages are implemented as application level modules in the SDN controller. Compared to different methods run on the well-known KDD-99 dataset, the proposed approach showed a lower overhead.

1.2.3.Smart Network Applications

Integration between SDN and AI space opens the door to building smarter network applications. As the authors suggest, it is a reinforcement learning approach for adaptive video streaming in the SDN paradigm. The controller represents a periodic decision maker that determines when to choose a new path and when the server should change the quality of the video. The decision Markov process used to model decision-making actions. It is a Q-learning technique used in case of unknown rewards for moving between the current and next state. The percentage of packet losses and the number of quality changes represent the most important parameters for defining the reward. The Q values are updated by the function shown in Equation (3) and stored in the Q-table, where γ and η represent the discount factor and the learning factor, respectively.

$$\begin{aligned} \tilde{Q}(s_t, a_t) &= \tilde{Q}(s_t, a_t) + \eta(r_{t+1} + \gamma \\ \max_{a_{t+1}} \tilde{Q}(s_{t+1}, a_{t+1}) - Q(s_t, a_t)) \end{aligned} \quad (3)$$

And the softmax function shown in Equation (4) represents the probability of choosing an action at state t at time s.

$$P(a|s) = \frac{\exp\left[\frac{Q(s, a)}{T}\right]}{\sum_{b \in A} \exp\left[\frac{Q(s, b)}{T}\right]} \quad (4)$$

Here T represents a random motion currently used in the simulated annealing method to escape the local optimum problem. The controller can modify the existing path and/or adaptively remove/add selected layers based on available bandwidth to increase the QoE of the video

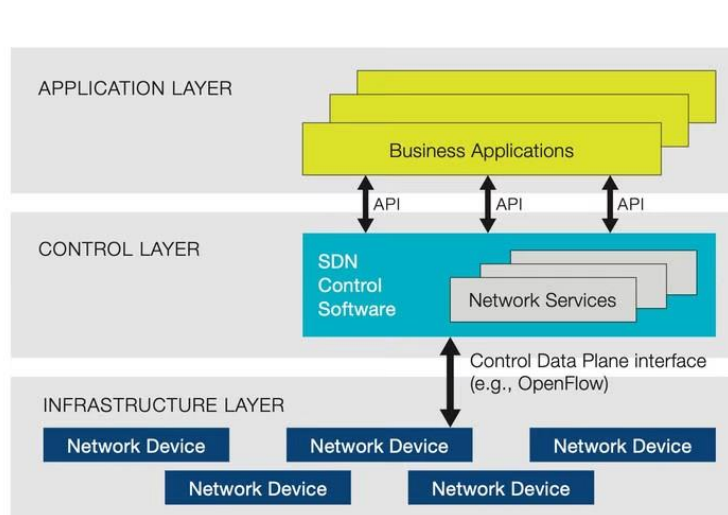
streaming service. The aforementioned approach showed a reduction in frame loss rate of 89% and 70%, respectively, compared to the shortest path forwarding and greedy-based approaches.

2.General Information

In the subheadings of this section, basic explanations about the concept of the controller from which the data required for the application part is obtained and its functioning in the network environment, the preferred ANN method for using the collected network data, the Tabu Search Algorithm and the Annealing Simulation Algorithm, which are among the artificial intelligence optimization techniques used to determine the regions where the flow is the most intense on the network, are given respectively.

In SDN architecture, control and management operations are performed by a central controller. This controller has full control of the network topology and address information. When a switch sends a packet send request to the controller for a packet that is not in the flow table, the controller receives those requests. The controller then takes actions and listens for traffic and defines packet forwarding routes on demand. OpenFlow controllers are programmed by network operators with a control interface. MILLER and YILTAŞ KAPLAN 10.21923/jesd.676110 1001 As shown in Figure 1, large networks are being built to include more SDN controllers, that is, SDN application layers. This application layer is responsible for network virtualization, traffic engineering, routing, monitoring and quality of service services.

Communication between the application layer and the SDN controllers is handled by a set of application programming interfaces (APIs) called the Northern Interface. Similarly, the interface between the SDN controller and OpenFlow network devices is called the Southern Interface (Kutay and Ercan, 2016). SDN architecture provides ease of transmission, control and management over complex networks. In addition, thanks to the interactions between the network layers, it has an important place in today's technology as a powerful control platform in terms of traffic flow.



The application, control, and infrastructure layers are kept separate in SDN and communicate through APIs. Source: Open Networking Foundation

2.1. Artificial Neural Networks (Artificial Neural Networks)

Artificial intelligence is divided into various sub-titles according to the solutions it brings to different types of problems. The most common types of artificial intelligence are knowledge-based expert systems, fuzzy logic approach and ANNs. The preferred method used in this study is ANNs.

When the neurological structure of the human brain was examined, it was understood that it had a completely different working mechanism than digital computers, and the concept of ANN emerged. The information processing system of the human brain is quite complex. The nerve cell in the brain, called a neuron, performs certain calculations even faster than the computer, which is considered the fastest by humans today. A neural network is a massively parallel distributed processor composed of simple processing units, which has a natural disposition that experiential information is made available for storage and use (Haykin, 2009). ANNs, on the other hand, are systems where artificial neurons come together in the same way as neurons in the human brain, collect information about the problem and solve the problem. In short, ANN is a network system structure formed by connecting artificial neurons using different geometrical paths (Staub et al., 2015). ANN is similar to the human brain in two fundamental ways. The first is the acquisition of knowledge by the network through a learning process from the environment. The second is the use of internal neuron connection strengths, also known as synaptic weights, to store acquired information. While the ANN structure allows learning nonlinear relationships, it also adapts to changing environments. Among the most preferred features of ANNs is the ability to handle missing parameter values. Thanks to this feature, an ANN based on a limited number of training sets can be a good classifier (Mourrain et al., 2006). ANNs have the ability to make decisions using what they have learned when faced with a problem. In ANNs, information is acquired by the network and this information is stored using the connections between neurons. In ANNs, the network can be defined as a processor that stores information and makes this information functional (Taşhan, 2017).

In a study designed with the help of ANNs related to a different problem area, there is a general representation of the ANN example as input layer, hidden layer and output layer (Abu Salam and Keskin, 2018). It is also emphasized here that there are different ANN models such as back propagation.

2.2. Artificial Intelligence Optimization Techniques

Effective results are obtained by using artificial intelligence optimization techniques, also known as meta-heuristics, for the solution of optimization problems. A heuristic algorithm tries to find a particular example of a solution that maximizes profit by recursively calling a heuristic function. The example solution that maximizes profit will be the optimal solution for the optimization problem. Heuristic techniques are methods that perform different solution modifications to reach a solution that is either superior or superior (Oommen & Rueda, 2005). Artificial intelligence optimization techniques are a promising technique for solving optimization problems. Because it can imitate the operations of the brain and use parallel processing to save computation time (Shih et al., 2004). These techniques, which consist of computer algorithms, aim to find the one that will give the best result from the various moves available to reach the best solution. Since many of the problems do not have a final solution and the time required to solve these problems is very large, the researchers tried to find the fastest algorithm that gives a result close to the final solution. As a result, artificial intelligence optimization techniques have emerged. These techniques are also important because they create an upper or lower limit for exact solution methods. They also aim to find the best possible solution, although they do not reach a definitive solution.

2.2.1. Taboo Search Algorithm

Tabu search algorithm, which was put forward by Fred Glover in 1986, was created to overcome the shortcomings of local search methods. Some complex problems could not be best solved by local search methods. Taboo search aims to bring the most effective heuristic solution to this type of problem. Tabu search is an intelligent search procedure that starts from an initial possible point and tries to reach an optimal solution by constructing a finite sequence. Neighboring subsets of the initially selected possible solution point are created and the next point is determined as the best solution. Tabu movements are listed under the name of the tabu list in order to prevent a return to some previous points, as tabu search allows ascending movements. Due to the exit movement, the procedure avoids traps in the local optimum (Kovačević-Vujčić et al., 1999). To summarize briefly, the working principle of tabu search is to continue tracking through local search by allowing this non-optimal solution when the local optimum is encountered (Gendreau and Potvin, 2010). The tabu search algorithm uses some restrictions when searching. For this reason, the algorithm is called "taboo", that is, "forbidden search". Constraints are created by making use of memory structures (Aladağ, 2009). Thanks to these constraints, normally acceptable difficult situations are bypassed and the best result is achieved. An adaptive memory and sensitive research are required for problem solving in taboo search to qualify as intelligent. Tabu search algorithm, which gains the ability to produce problem-specific solutions with these features, is accepted as a meta-heuristic search algorithm (Michalska et al., 2016).

2.2.2. Simulated Annealing Algorithm

The annealing simulation algorithm, which is a probability-based heuristic algorithm, was created by Kirkpatrick, Gelatt, and Vecchi. The annealing simulation algorithm is a technique created to find a good solution of the optimization problem by using a random variation around the existing solution (Zhao et al., 2013). This algorithm, which is based on the physical annealing process of solid objects, is used in solving complex optimization problems. After heating the solid body to its melting point, the process of gradually cooling the body until it crystallizes is called annealing. The energy of the system decreases to the minimum level while the atoms of the objects with high energy levels at high temperatures pass into a regular crystal. The temperature is also reduced to reduce the energy of the system. If this cooling process is acted too quickly, the crystallized structure of the object will deteriorate and an irregularity will occur in the structure of the object (Kalknı, 2003).

The annealing simulation algorithm, which is designed to find the largest or smallest values of the function in multivariate functions, finds the best solution in the shortest time. For this reason, it is preferred in the optimization of problems that cannot be expressed with a mathematical model. In the annealing simulation algorithm, the objective function value tends to decrease (Çakır, 2006). However, in some cases, this function can be accepted at high values in order not to be stuck with the local minimum. In this way, a better global solution can be sought without being stuck with the local minimum (Kılıçaslan, 2019).

3. Application of the Proposed Method

Within the scope of this study, Floodlight VM, Eclipse, MATLAB and nntool tools were used while developing an application for monitoring the flow traffic depending on the SDN controller. Floodlight, which has become widespread worldwide as a constantly developing project among SDN controller software, is open source and an application that supports the Java programming language (Floodlight, 2020). On the official website of the Floodlight project, all necessary steps and installations for software developers are presented in detail. Eclipse

environment, which is open source code and especially Java-based software is designed, is used for the program stages of the proposed method. Eclipse comes integrated with the Floodlight VM during installation. In fact, there are Floodlight v1.0, Eclipse, Mininet v2.2.0, Open vSwitch v3.2.1, Wireshark w/openflow software in the Floodlight VM installed during this study. The topologies created in the application are created with the Python programming language on Mininet. Another alternative example that can be preferred as a Java platform for mutual transactions with Floodlight is IntelliJ IDEA. Instead of all these application environments, different tools can be used for different controller software. For example, the POX controller is designed with the Python programming language (Author, 2013). Likewise, the Ryu controller requires basic knowledge of Python. After deciding on the most suitable controller and programming environments in the proposed study, MATLAB and nntool, which are more efficient and easier to use, were preferred for operations based on artificial intelligence techniques.

The data required to spy on the traffic in the application are the key, port number, the amount of packets received and transmitted, bandwidth, drops, collisions and the time in seconds (sec) that they occur. This data is accessed through the Floodlight project in the Floodlight VM. In order to increase the accuracy, statistical data were obtained over various topologies. For this, five different topologies consisting of different numbers of switches and machines (hosts) were created in the Mininet environment. Five different data sets were obtained by running each of the created topologies for 27 seconds. By selecting the duration of 27 seconds, thousands of rows of data were obtained, which was considered sufficient during the processing of the data. Since it was observed that an excessive increase in the amount of data occurred with increasing the time, and this would pose a problem during the processing of the data, the 27-second period was preferred. Key, port, received and transmitted packet amount and time columns of the data transferred on matrix structures in MATLAB were selected and other columns were ignored. A separate point to be noted here is that data transmission in LTAs is in the form of flows. Since a stream has many packet contents, conceptual confusion may arise in studies related to classical network structures. Therefore, within the scope of this study, the term "packet amount", which is the concept in classical computer networks, has been preferred to express the amount of data obtained through Floodlight. Thus, the main focus is on the obtained data sets and the application processes on them. The factors that will make the difference for the application part of the study are the algorithms used and the approach in the analysis of the results.

The application part of the study is based on artificial intelligence. The aim here is to try to estimate how many packets are received and forwarded from a given switch and port at a given moment. This estimation part was carried out with ANN, which is one of the artificial intelligence methods. With nntool, which is a MATLAB tool, data is processed on ANN. With the help of MATLAB matrix operations, 80% of the data sets are reserved for training and 20% for testing. The key, port and time columns of the data sets are set as input data, and the received packet and transmitted packet columns are set as output data. Networks were created by selecting the necessary parts on nntool. The first created network is a network with three inputs and two outputs. However, since the prediction success is low, the networks are designed to be three-input and one-output. Thus, separate networks were created for each topology according to received packets and transmitted packets. A two-layer ANN with ten neurons was sufficient because there were no very complex data sets. The accuracy of the predictions of the ANNs created for five different topologies at certain moments was compared. Accuracies were calculated using MAPE (Mean Absolute Percentage Error) and R2 (R-squared) functions.

The last part of the application consists of optimization. The problem to be optimized, that is, the value desired to be obtained as the optimum result, is which route in the topology has the highest density. For this purpose, optimization was carried out with four different methods and

their results were compared. The first of these is the traditional search method linear search, the second tabu search, the third modified tabu search, and the fourth is a mixture of annealing simulation and tabu search algorithms (hereinafter, it will be called the mixing algorithm). The last two methods are the methods revealed for the first time within the framework of this study. As a result of these four different optimization methods, the route with the highest packet traffic was determined. The important criteria for the choice of the algorithms used at this stage are that they can be functionally adapted to the network problem, that is, they can compare the density in the regions on the network with each other and be fast. The process created by the optimization step in this study is to prioritize the shortest time to go to the correct solution of the problem. For this purpose, it was tried to find the most suitable methods. In a previous different network study (Yılmaz, 2007), genetic algorithm, which is among the evolutionary algorithms, was used. Genetic algorithm is a particularly suitable method for routing, assignment or placement based optimization problems, and there are other examples in the literature such as the solutions of Ünsal and Yiğit (2018) and Yiğit and Aydemir (2018). However, the steps such as generation, crossover, mutation in the genetic algorithm are incompatible with the determination of dense network regions in a short time, which is the main purpose of this study. By considering the tabu search and annealing simulation algorithms, which are seen to be able to perform appropriate and fast operations through the programs created in this study, two additional models (modified tabu algorithm and mixing algorithm) are proposed, and it is planned to compare them with the linear search algorithm. The modified tabu search algorithm was obtained by subtracting the tabu list from the tabu search algorithm. When the tabu search algorithm is examined, it is observed that the tabu list is unnecessary for this problem and slows down the optimization. An increase in performance was observed when the list was removed from the algorithm. From here, it has been observed that although artificial intelligence optimization techniques are convenient, they are not always successful because they are problem-specific. In another problem, for example the traveling salesman problem, this algorithm, which is very convenient, causes poor performance in the current study problem.

The first part of the mixing algorithm, which is the last method, comes from the tabu search algorithm. Instead of the randomly chosen initial solution in the annealing simulation algorithm, the case of assigning the first value in the tabu search algorithm as the initial solution is preferred. Taboo search is not included in the following sections. In the remaining part, neighboring solutions were created and the change in the objective function, that is, in the total packet value, was observed. In addition, a change has been made in this section. Normally, if there is a decrease in the objective function, while the solution is the current solution, the opposite is taken into account in this algorithm. In other words, if there is an increase in the objective function, the solution becomes the current solution. Because the basis of the problem is the region densities in the network, that is, the excess of the packet flow is observed.

The connection of the processing elements in the application part with each other is briefly seen in Figure 2.

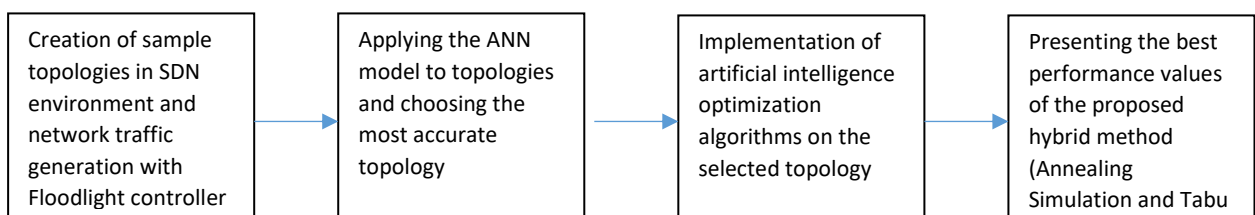


Figure 2: Application Operations

References

- Abu Salam, Z. K. A., Keskin, M. E., 2018. Level Estimation of Dibis Dam with Artificial Neural Networks. *Journal of Engineering Sciences and Design*, 6(4), 564-569.
- Aladag, C. H., 2009. Tabu Search Algorithm for Architecture Selection of Artificial Neural Networks. Doctoral Thesis. Hacettepe University, Institute of Science and Technology, Department of Statistics, Ankara, Turkey.
- Çakır, B., 2006. Annealing Simulation Algorithm for Assembly Line Balancing with Stochastic Process Time. Master Thesis, Industrial Engineering, Gazi University, Institute of Science, Ankara.
- Değirmenci, Ş., 2018. Packet Surveillance Application and Optimization Connected to Software Defined Network Controller. Master Thesis. Istanbul University, Institute of Science and Technology, Department of Computer Engineering, Istanbul, Turkey
- Floodlight. Project Floodlight-Floodlight Controller-Installation Guide, [Online]. Available: <https://floodlight.atlassian.net/wiki/spaces/floodlightcontroller/pages/1343544/Installation+Guide#InstallationGuideLinux>.
- Gendreau, M., Potvin, J.-Y., 2010. *Handbook of Metaheuristics*, 2nd ed. Springer Science+Business Media.
- Haykin, S., 2009. *Neural Networks and Learning Machines*, Third ed. New Jersey, USA: Pearson Education, Inc., [Online]. Available: <http://dai.fmph.uniba.sk/courses/NN/haykin.neural-networks.3ed.2009.pdf>
- Kalınlı, A., 2003. Training of Elman Network Using Simulated Annealing Algorithm. *Erciyes University Journal of Science Institute*, 19(1), 28-37.
- Kılıçaslan, K. Heat Treatment Algorithm (Simulated Annealing), [Online]. Available: <Ders.kilicaslan.nom.tr/doc/19/52/Isil%20Operation%20Algorithm.docx>
- Kovačević-Vujčić, V. V., Čangalović, M. M., Ašić, M. D., Ivanović, L., Dražić, M., 1999. Taboo Search Methodology in Global Optimization. *Computers & Mathematics with Applications*, 37, 125-133
- Kutay, M., Ercan, T., 2016. An Overview of Software Defined Campus Networks. *Selcuk University Journal of Engineering, Science and Technology*, 4(2), 155-164.
- Michalska, M., Zufferey, N., Mattevelli, M., 2016. Taboo Search For Partitioning Dynamic Dataflow Programs. *The International Conference on Computational Science, Procedia Computer Science*, 80, 1577-1588.
- Mourrain, B., Pavlidis, N. G., Tasoulis, D. K., Vrahatis, M. N., 2006. Determining the Number of Real Roots of Polynomials Through Neural Networks. *Computers & Mathematics with Applications*, 51(3-4), 527-536.
- Niyaz, Q., Sun, W., Alam, M., 2015. Impact on SDN Powered Network Services Under Adversarial Attacks. *The 2015 International Conference on Soft Computing and Software Engineering (SCSE 2015), Procedia Computer Science*, 62, 228 – 235.

Oommen, B. J., Rueda, L. G., 2005. A Formal Analysis of Why Heuristic Functions Work. *Artificial Intelligence*, 164, 1-22.

Sezer, S., Scott-Hayward, S., Chouhan, P. K., Fraser, B., Lake, D., Finnegan, J., Viljoen, N., Miller, M., Rao, N., 2013. Are We Ready for SDN? Implementation Challenges for Software-Defined Networks. *IEEE Communications Magazine*, 51(7), 36-43.

Shih, H. S., Wen, U. P., Lee, E. S., Lan, K. M., Hsiao, H. C., 2004. A Neural Network Approach to Multiobjective and Multilevel Programming Problems. *Computers & Mathematics with Applications*, 48, 95-108.

Staub, S., Karaman, E., Kaya, S., Karapınar, H., Güven, E., 2015. Artificial Neural Network and Agility. *World Conference on Technology, Innovation and Entrepreneurship, Procedia - Social and Behavioral Sciences*, 195, 1477 – 1485.

Taşhan, B., 2017. Road Lane Detection System With Convolutional Neural Network. Master's Thesis. Bahçeşehir University, Graduate School of Natural and Applied Sciences, Computer Engineering, İstanbul, Turkey.

Ünsal, Ö., Yiğit, T., 2018. Optimization of School Bus Routing Problem by Using a Method with Artificial Intelligence and Clustering Techniques, *Journal of Engineering Sciences and Design*, 6(1), 7-20.

Xia, W., Wen, Y., Foh, C. H., Niyato, D., Xie, H., 2015. A Survey on Software-Defined Networking. *IEEE Communication Surveys & Tutorials*, 17(1), 27-51.

Author, S., 2013. Using OpenFlow Protocol and Pox Controller in Network Switches. Master Thesis. University of Trakya. Graduate School of Natural and Applied Sciences, Department of Computer Engineering, Edirne, Turkey.

Yıltaş, D., 2007. Design of a New Routing Algorithm in Low-Orbit Satellite Systems. Doctoral Thesis. Istanbul University. Graduate School of Natural and Applied Sciences, Department of Computer Engineering, Istanbul, Turkey.

Yiğit, T., Aydemir, M., 2018. Container Loading Problem Optimization By Using Genetic Algorithm Without Rotating The Package, *Journal of Engineering Sciences and Design*, 6(1), 21-28.

Zhao, X., Lin, W., Yu, C., Chen, J., Wang, S., 2013. A New Hybrid Differential Evolution with Simulated Annealing and Self-Adaptive Immune Operation.

Open Networking Foundation. Software-defined networking: The new norm for networks. Available from: <https://www.opennetworking.org/images/stories/downloads/sdnresources/white-papers/wp-sdn-newnorm.pdf>

Astuto BN, Mendonca M, Nguyen XN, Obraczka K, Turletti T. A survey of software-defined networking: past, present, and future of programmable networks. *IEEE Communications Surveys and Tutorials*. 2014; 16(3):1617–34

Bakshi K. Considerations for Software Defined Networking (SDN): Approaches and use cases. *IEEE Aerospace Conference, Big Sky; MT*. 2013 Mar. p. 1–9.

Shinde MB, Tamhankar SG. Review: software defined networking and OpenFlow. International Journal of Scientific Research in Network Security and Communication. 2013Jun; 1(2):18–20.

Feamster N, Zegura E, Rexford J. The road to SDN: An intellectual history of programmable networks. ACM SIGCOMM Computer Communication Review archive. 2014; 44(2):87–98.

Kreutz D, Ramos FMV, Verissimo P, Rothenberg CE, Azodolmolky S, Uhlig S. Software-defined networking: A comprehensive survey. Proceedings of the IEEE. 2015; 103(1):14–76.

Basta A, Kellerer W, Hoffmann M, Hoffmann K, Schmidt E-D. A virtual SDN-enabled LTE EPC architecture: A case study for S-/P-gateways functions. Future Networks and Services (SDN4FNS); Trento. 2013 Nov. p. 1–7.

Jammal M, Singh T, Shami A, Asal R, Li Y. Software defined networking: State of the art and research challenges. Computer Networks. 2014; 72:74–98.

Rowshanrad S, Namvarasl S, Abdi V, Hajizadeh M, Keshtgary M. A survey on SDN, the future of networking. Journal of Advanced Computer Science and Technology. 2014; 3(2): 232–48.

Braun W, Menth M. Software-defined networking using OpenFlow: Protocols, applications and architectural design choices. Future Internet. 2014; 6(2):302–36.

OpenFlow	Switch	Specification	Version	1.0.0.	Available	from:
https://www.opennetworking.org/images/stories/specifications/openflow/					downloads/sdn-resources/onf-	
specifications/openflow/					openflow-spec-v1.0.0.pdf	

OpenFlow	Switch	Specification	Version	1.1.0.	Available	from:
http://archive.openflow.org/documents/openflowspec-v1.1.0.pdf						

OpenFlow	Switch	Specification	Version	1.2.0.	Available	from:
https://www.opennetworking.org/images/stories/specifications/openflow/					downloads/sdn-resources/onf-	
specifications/openflow/					openflow-spec-v1.2.pdf	

OpenFlow	Switch	Specification	Version	1.3.0.	Available	from:
https://www.opennetworking.org/images/stories/specifications/openflow/					downloads/sdn-resources/onf-	
specifications/openflow/					openflow-spec-v1.3.0.pdf	

OpenFlow	Switch	Specification	Version	1.4.0.	Available	from:
https://www.opennetworking.org/images/stories/specifications/openflow/					downloads/sdn-resources/onf-	
specifications/openflow/					openflow-spec-v1.4.0.pdf	

FlowVisor.	Available	from:	https://github.com/OPENNET
WORKINGLAB/flowvisor/wiki			

NOX.	Available	from:	http://archive.openflow.org/
downloads/Workshop2009/OpenFlowWorkshopMartinCasado.pdf			

POX. Available from: <https://en.wikipedia.org/wiki/Pox>

Beacon. Available from: <https://openflow.stanford.edu/display/Beacon/Home>

Ng TSE, Cai Z, Cox AL. Maestro: A system for scalable OpenFlow control. Available from: <http://www.cs.rice.edu/~eugeneng/papers/TR10-11.pdf>

Floodlight OpenFlow Controller- Project Floodlight. Available from: <http://www.projectfloodlight.org/floodlight/>

Announcing release of Floodlight with OF 1.3 support. Available from: <http://sdnhub.org/releases/floodlight-plusopenflow13-support/>

Ryu 3.9 documentation. Available from: http://ryu.readthedocs.org/en/latest/getting_started.html#what-s-ryu

Open day light. Available from: <http://www.opendaylight.org/>

Gorsansson P, Black C. Software defined networks- A comprehensive approach.1st ed. Morgan Kaufmann, an imprint of Elsevier; 2014.

Eadala SY, Nagarajan V. A review on deployment architectures of path computation element using software defined networking paradigm. Indian Journal of Science and Technology. 2016 Feb; 9(10). DOI: 10.17485/ijst/2016/ v9i10/84944.

Mandekar AV, Chandramouli K. Centralization of network using openflow protocol. Indian Journal of Science and Technology. 2015 Jan; 8(S2). DOI: 10.17485/ijst/2015/ v8iS2/61217.

Mittal P, Singh Y. Development of intelligent transportation system for improving average moving and waiting time with artificial intelligence. Indian Journal of Science and Technology. 2016 Jan; 9(3). DOI: 10.17485/ijst/2016/ v9i3/84156.

Davis B. Leveraging the load balancer to fight DDoS. Available from: <http://www.sans.org/reading-room/whitepapers/firewalls/leveraging-load-balancer-fightddos-33408>

Califano A, Dincelli E, Goel S. Using features of cloud computing to defend smart grid against DDoS attacks. 10th Annual symposium on information assurance (Asia 15), ALBANY; 2015Jun. p. 44–50.

Chen-Xiao C, Ya-Bin X. Research on load balance method in SDN. International Journal of Grid and Distributed Computing. 2016; 9(1):25–36.

Ruelas AMR, Rothenberg CE. Implementation of neural switch using OpenFlow as load balancing method in data center. Campinas, Brasil: University of Campinas; 2015.

Chou L-D, Yang Y-T, Hong Y-M, Hu J-K, Jean B. A genetic-based load balancing algorithm in openflow network. Advanced Technologies, Embedded and Multimedia for Human-centric Computing. 2013; 260:411–7.

Balaguer R. Flow embedding algorithms for software defined audio networks [Master thesis]. Zurich, Switzerland: Swiss Federal Institute of Technology. Available from: <http://ftp.tik.ee.ethz.ch/pub/.../MA-2014-14.pdf>

Dobrijevic O, Santl M, Matijasevic M. Ant colony optimization for QoE-centric flow routing in software-defined networks. 2015 11th International Conference on Network and Service Management (CNSM); Barcelona. 2015 Nov. p. 274–8

Latah M. Solving multiple TSP problem by K-means and crossover based modified ACO algorithm. *IJERT*. 2016 Feb; 5(2):430–4.

Akhunzada A, Ahmed E, Gani A, Khan MK, Imran M, Guizani S. Securing the software defined networks: taxonomy, requirements, and open issues. *IEEE Communications Magazine*. 2015Apr; 53(4):36–44

Jankowski D, Amanowicz M. Intrusion detection in software defined networks with self-organized maps. *Journal of Telecommunications and Information Technology*. 2015; 4:3–9.

Dabbagh M, Hamdaoui B, Guizaniy M, Rayes A. Softwaredefined networking security: Pros and cons. *IEEE Communications Magazine*. 2015; 53(6):73–9.

Bai H. A survey on artificial intelligence for network routing problems. NM,USA: University of New Mexico; 2007

Mustafa U, Masud MM, Trabelsi Z, Wood T, Al Harthi Z. Firewall performance optimization using data mining techniques. 2013 9th International Wireless Communications and Mobile Computing Conference (IWCMC); Sardinia. 2013 Jul. p. 934–40.

Mukherjee D, Acharyya S. Ant colony optimization technique applied in network routing problem. *International Journal of Computer Applications*. 2010; 1(15):66–73.

Dotcenko S, Vladyko A, Letenko I. A fuzzy logic-based information security management for software-defined networks. 16th International Conference on Advanced Communication Technology (ICACT); Pyeongchang. 2014 Feb. p. 167–71.

Mikians J, Barlet-Ros P, Sanjuas-Cuxart J, Solé-Pareta J. A practical approach to portscan detection in very highspeed links. *PAM'11 Proceedings of the 12th International Conference on Passive and Active Measurement*; Atlanta. 2011Mar. p. 112–21.

Williamson MM. Throttling viruses: Restricting propagation to defeat malicious mobile code. *Proceedings 18th Annual Computer Security Applications Conference*; Las Vegas. 2002 Dec. p. 61–8

Mehdi SA, Khalid J, Khayam SA. Revisiting traffic anomaly detection using software defined networking. *RAID'11 Proceedings of the 14th International Conference on Recent Advances in Intrusion Detection*; California. 2011Sep. p. 161–80.

Chen X-F, Yu S-Z. CIPA: A collaborative intrusion prevention architecture for programmable network and SDN. *Computers and Security*. 2016; 58:1–19.

Braga R, Mota E, Passito A. Lightweight DDoS flooding attack detection using NOX/OpenFlow. 2010 IEEE 35th Conference on Local Computer Networks (LCN); Denver, CO. 2010 Oct. p. 408–15.

Deepa SN, Devi BA. A survey on artificial intelligence approaches for medical image classification. *Indian Journal of Science and Technology*. 2011 Nov; 4(11). DOI: 10.17485/ijst/2011/v4i11/30291.

Yan Q, Yu FR, Gong Q, Li J. Software-Defined Networking (SDN) and Distributed Denial of Service (DDoS) attacks in cloud computing environments: a survey, some research issues, and challenges. *IEEE Communications Surveys and Tutorials*. 2016; 18(1):602–22.

Uzakgider T, Cetinkaya C, Sayit M. Learning-based approach for layered adaptive video streaming over SDN. *Computer Networks*. 2015; 92(P2):357–68.

https://www.researchgate.net/publication/284696928_Software-Defined_Networking_Using_OpenFlow_Protocols_Applications_and_Architectural_Design_Choices/figures?lo=1

Machine Learning Applications on COVID-19 Pandemic: A Systematic Literature Review

Kübra KÖKSAL¹
Buket DOĞAN²
Zehra Aysun ALTIKARDEŞ³

Introduction

Sars-Cov-2 (Covid-19) virus, which comes from the coronavirus family such as Mers-Cov and Sars-Cov, is an enveloped RNA virus that causes respiratory failure (Alwaeli and Ibrahim, 2020: 1). The Covid-19 disease first appeared in December 2019 in Wuhan, China. This virus, which was detected to be transmitted from person to person on January 7, 2020, spread rapidly across the world. It was named as Covid-19 virus by the World Health Organization (WHO) on February 11, 2020 (Albahri et al., 2020: 2). It was declared a pandemic by WHO on 11 March 2020.

Common symptoms include fever, fatigue, loss of taste, cough, and shortness of breath. Polymerase chain reaction (PCR) is one of the common methods used for detection. In addition to this method, computed tomography (CT) images are also used as a reliable and increasingly common diagnostic method for detecting the virus.

The World Health Organization announced that by January 2021, more than 84 million people were detected as positive, approximately one million 800 thousand people died, and coronavirus cases were detected in 192 countries/territories and 26 cruise/naval ships countries. Since the disease first emerged, many studies have been conducted in the field of vaccines. A few types of vaccines used in January 2021:

1. Pfizer / BioNTech vaccine produced by Germany based BioNTech-Pfizer and the US Food and Drug Administration (FDA)
2. MRNA-1273 produced by Moderna
3. China based Sinovac vaccine
4. Russia based Sputnik V

In addition to vaccine studies, many researchers have carried out various studies in order to better analyze the characteristics of Covid-19 to apply new detection methods. Computer based

¹ Master Student, Marmara Univ., Department of Computer Engineering, 0000-0002-4252-7295

² Assoc. Prof., Marmara Univ., Department of Computer Engineering, 0000-0003-1062-2439

³ Asst. Prof., Marmara Univ., Hypertension and Arteriosclerosis Center, 0000-0003-3875-1793

systems played a very important role in the fight against Covid-19 in areas such as diagnosis, detection, predicting the spreading of the virus and the number of cases in this period and aimed to alleviate the burden of health sector employees. Deep learning, machine learning and artificial intelligence methods are among the frequently used analysis methods with computer aided systems.

In this study, a systematic literature review was conducted on articles using machine learning methods for detection, diagnosis or prediction purposes and the results were evaluated. The purpose of this study is to evaluate the machine learning algorithms, datasets and the results obtained with Covid-19 and to examine how the studies conducted in this field so far have dealt with machine learning methods.

This paper is structured as follows: Section 2 explains the research method used in the systematic literature review; Section 3 presents the analysis results obtained as a result of the literature review; and Section 4 provides a conclusion.

Method

The systematic literature review method applied in the study of Albahri AS, et al. was followed to determine the machine learning methods used to combat the Covid-19 virus and to perform performance analysis. The review style recommended by the Preferred Reporting Items (PRISMA) for Systematic Reviews and Meta Analyses was used (Albahri et al., 2020: 2).

Two different digital databases, IEEE and ScienceDirect, were used. IEEE Explore is a database of research articles on computer technologies, computer science, data science and medical practice. Science Direct is a platform with many publications that benefit researchers in scientific and medical issues. The steps constituting the scope of the research are as follows: determining the research protocol, determining the research questions, determining the search queries, determining the inclusion and exclusion criteria, determining the relevant literature by conducting a comprehensive research, selection of the studies, interpretation of the results. These steps will be explained in detail later in this section. Çalışmanızın yöntem bölümünü buraya yazın.

Search Strategy

English publications published between 2019-2021 using two different digital databases were examined within the scope of this study. In order to comprehensively examine the studies using the machine learning method in the fields of Covid-19 detection, diagnosis or prediction, four different search strategies consisting of selected keywords were used. Four different search queries and results used within the scope of this study are shown in Table 1 Search operations in Science Direct and IEEE digital databases were carried out using AND and OR queries. For example "sars-cov-2 AND machine learning AND (diagnosis OR prediction OR classification)

The main purpose of the review is to answer the following questions:

1. Which machine learning algorithms were used in computer science to combat Covid-19?
2. For what purpose were the machine learning methods used?
3. What are the performance contributions of machine learning methods to combat Covid-19?

Table 1 – Search Queries and Results

Search Query	Result Of Databases	Total Result
Covid-19 AND machine learning AND diagnosis	Science Direct: 26 IEEE: 33	59
Covid-19 AND machine learning AND prediction	Science Direct: 55 IEEE: 29	84
Covid-19 AND machine learning AND classification	Science Direct: 25 IEEE: 46	71
Covid-19 AND machine learning	Science Direct: 131 IEEE: 136	267
Sars-Cov-2 AND machine learning	Science Direct: 38 IEEE: 13	51

Criteria For Inclusion and Exclusion

The following criteria were used to select among the studies to be examined for a systematic literature search.

1. Studies should provide experimental data on machine learning algorithms used in the Covid-19 field.
2. Research studies should have been published between 2019-2021.
3. Studies must be in English
4. Machine learning methods should be related to Covid-19 detection, diagnosis or prediction areas.

Criteria that was not included:

1. Studies are beyond the scope of machine learning algorithms and the performance impact it provides.
2. Studies that have not provided empirical data.
3. Studies examining the relationship of the virus with areas such as weather conditions, stress rate, education and other than Covid-19 detection or diagnosis are excluded.

Selection of Studies

Studies published between 2019-2021 were filtered using the specified search queries, and a total of 532 studies were obtained. A two-stage elimination process was carried out on the studies to be examined. In the first step, after the repetitive publications were removed, the abstracts and titles of the remaining studies were examined and the publications covering the determined criteria were selected. After the first step was completed, 71 out of the 532 publications remained.

In the second step, the remaining publications went through a complete reading process. At this stage, the articles suitable for the purpose of the study were selected and the title, year of publication, methods used and the results obtained were recorded in an Excel file. As a result of this process, a total of 49 articles were selected for use within the scope of the study. Figure 1 represents the steps of the applied research process.

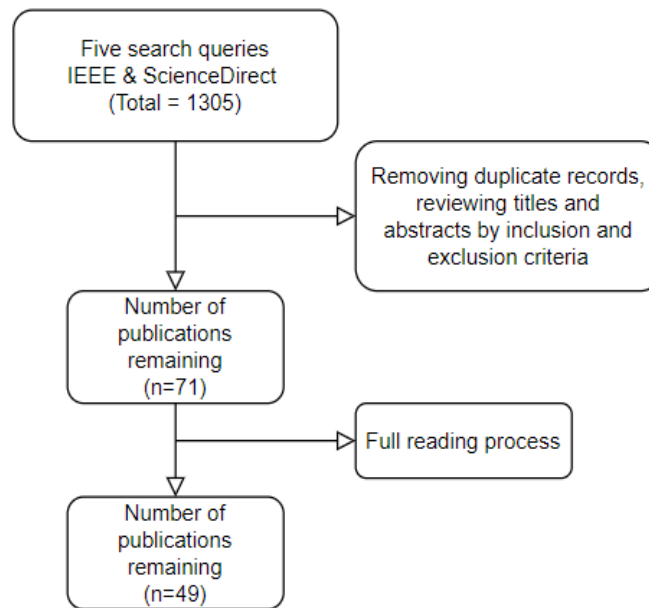


Fig. 1. Steps of the applied research process

Results

Within the scope of the research, 49 articles were examined in detail and the results obtained were analyzed under this title. Using 49 studies examined, author, country, problem type, dataset type, machine learning algorithm and obtained result information were recorded for each study. Table 4 shows this information from 49 publications. First, the distribution chart of the published articles by country was drawn. Figure 2 shows the number of scientific publications using machine learning algorithms in the Covid-19 field by geographic region. According to the chart, India ranks first with 11 publications then comes the USA with nine publications and China with seven publications.

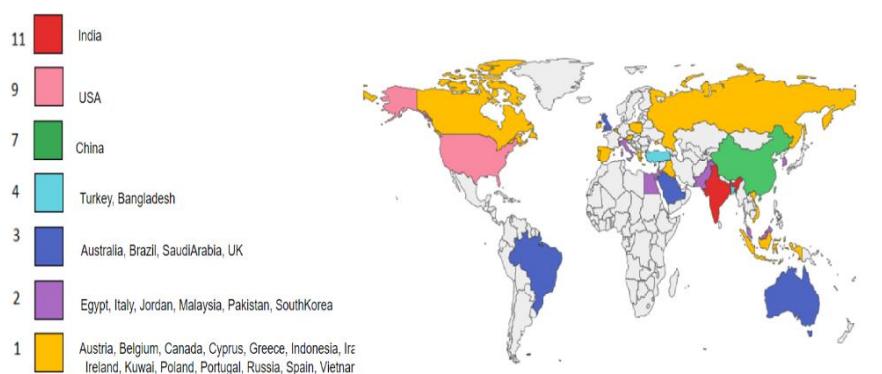


Fig. 2. Number of publications according to geographical regions.

Datasets and Resources

One of the analyzes made over the articles is to determine the types of data used. In this context, three different data types were determined. These are time series, text dataset and image dataset.

Time Series Data. Information such as the number of Covid-19 cases associated with geographic locations, the number of deaths, the number of Covid-19 tests performed or the number of people recovered are time series data. These data help researchers to predict many important information such as the growth, distribution, end time and peak time of the pandemic in the articles reviewed. In this context, many countries collect such time series information and share it publicly. Of the reviewed studies, 22 perform analysis on time series type data sets (Amar, Taha, and Mohamed, 2020: 4; Andreas et al., 2020: 1; Ballı, 2021: 2; Chakraborti et al., 2021: 3; Gambhir et al., 2020: 2; Istaiteh et al., 2020: 2; Khan, Abbas, and Truong, 2020: 4; Kuo and Fu, 2021: 2; Kurniawan et al., 2020: 2; Mandayam et al., 2020: 2; Mojjada et al., 2020: 2; Mondal et al., 2020: 1; Nikil, Dalmia, and Kumar, 2020: 2; Peng and Nagata, 2020: 1; Prakash et al., 2020: 3; Ribeiro et al., 2020: 3; Rustam et al., 2020: 2; Singh et al., 2020: 2; Wadhwa et al., 2021: 3; Wang et al., 2020: 2; Yadav, Perumal, and Srinivas, 2020: 2; Yeşilkanat, 2020: 3).

Clinical or Text Dataset. Clinical data are the main sources used in most medical research. These sources are frequently used in the diagnosis and prediction of any disease. They have also been used in the diagnosis of the Covid-19. Within the scope of the studies examined, vital values, laboratory and demographic data, comorbidities, laboratory tests, blood gas measurements, blood tests values were used as clinical data. 14 of the studied studies (Ahamad et al., 2020: 2; AlJame et al., 2020: 4; Althnian et al., 2020: 4; Arvind et al., 2021: 2; Banerjee et al., 2020: 2; Burdick et al., 2020: 2; Di Castelnuovo et al., 2020: 4; Kavadi et al., 2020: 4; Kramarenko, 2020: 3; Li et al., 2021: 2; Mondal et al., 2020: 1; Otoom et al., 2020: 3; Soltan et al., 2021: 3; Yadaw et al., 2020: 3) used machine learning algorithms on clinical data. Five studies reviewed (Althnian et al., 2020: 1; Arvind et al., 2021: 1; Burdick et al., 2020: 4; Di Castelnuovo et al., 2020: 1; Yadaw et al., 2020: 1) were used for mortality, respiratory decompensation and susceptibility estimation process, 3 studies (Kavadi et al., 2020: 1; Kramarenko, 2020: 4; Mondal et al., 2020: 11) for curve fitting procedures and the remaining 6 studies were used for diagnostic process. Table 2 shows which features are used in studies using clinical datasets.

Image Dataset. Image-based clinical data are also frequently used methods in the diagnosis of the disease. There are two types of image datasets that are frequently used in the Covid-19 diagnosis. The first of these is chest CT scans. Studies have revealed that Chest CT scans, which

have a lower false positive value than X-ray and ultrasound scans, can diagnose Covid-19. The second is X-ray scans. Although such data are less sensitive than CT scans, they have a lower dose of ionizing radiation and are more portable.

Table 2 – Features used in clinical data sets according to publication.

Ref.	Clinical features
(Arvind et al., 2021: 3)	Partial pressure of arterial CO ₂ (PACO ₂), oxygen saturation (O ₂ SAT), Temperature, Creatinine, Platelet count, white blood cell (WBC), systolic blood pressure (SBP), Partial pressure of arterial oxygen (PAO ₂), respiratory rate, Pulse and Diastolic blood pressure (DBP)
(Burdick et al., 2020: 2)	DBP, WBC, SBP, blood urea nitrogen (BUN), creatinine, platelet count, lactate, temperature, heart rate (HR), oxygen respiratory rate (RR), saturation (SpO ₂) and bilirubin.
(Kramarenko, 2020: 3)	Countries' population, area, urbanization rate, numbers of doctors, nurses, public funding, COVID tests, percentage of the elderly, percentage of smokers and Google's people mobility data
(Yadaw et al., 2020: 4)	Age, gender and ethnicity, comorbidities such as asthma and diabetes, smoking status of the patients, oxygen saturation level and body temperature.
(AlJame et al., 2020: 4)	100 laboratory tests including urine tests, blood tests, rt-PCR test and Sars-Cov-2 test
(Soltan et al., 2021: 3)	Point-of-care blood gas results, Blood tests, blood test results from baseline, vital signs and baseline comorbidity data (Charlson comorbidity index)
(Ahamad et al., 2020: 2)	Gender, Age, Cough, Fever, Pneumonia, Lung Infection, Muscle Soreness, Diarrhea, Runny Nose, and Isolation Travel History
(Li et al., 2021: 3)	Population density, percentage of population aged <10 years life expectancy, sex ratio, prevalence of tuberculosis, prevalence of diabetes, percentage of urban population, two immunization coverages among children ages 12–23 months, percentage of population using unimproved water sources, prevalence of HIV, smoking rate, average age of childbirth, geographic location and temperature.
(Otoom et al., 2020: 4)	Symptoms, contact history with potentially infected people, and travel history.
(Althnian et al., 2020: 4)	Demographic values, result and test date, screening and confirmatory result.
(Banerjee et al., 2020: 2)	Age, full blood count and and rtPCR Sars-Cov-2 test, hematocrit, haemoglobin, eosinophils, mean corpuscular volume (MCV), leukocytes, basophils, platelets, neutrophils, mean corpuscular haemoglobin (MCH), mean platelet volume (MPV), lymphocytes, red blood cells (RBC), monocytes and red blood cell distribution, mean corpuscular haemoglobin concentration (MCHC).
(Mondal et al., 2020: 11)	RT-PCR and additional laboratory test
(Di Castelnuovo et al., 2020: 6)	Gender, age, chronic kidney disease, chronic pulmonary disease, diabetes, CRP, heart failure, hypertension, history of myocardial infarction, obesity and smoking habit.
(Kavadi et al., 2020: 4)	AgeGroupDetails, Covid_19_india, IndividualDetails, HospitalBedsIndia, StatewiseTestingDetails, ICMRTestintDetails, ICMRTestingLabs, Population.

14 of the studied studies (Brunese et al., 2020: 4; El-Kenawy et al., 2020: 1; Haritha, Praneeth, and Pranathi, 2020: 3; Hussain et al., 2021: 3; Javor et al., 2020: 1; Kang et al., 2020: 1; King et al., 2020: 1; Lai et al., 2020: 2; Mohammed et al., 2020: 8; Saha, Sadi, and Islam, 2021: 2; Sun et al., 2020: 1; Toğaçar, Ergen, and Cömert, 2020: 2; Tuncer, Dogan, and Ozyurt, 2020: 3; Ohata et al., 2021: 3) aimed to diagnose Covid-19 using machine learning algorithms on image data.

Machine Learning Applications

In this section, it has been investigated for which problem types machine learning algorithms are used in publications and the results obtained are presented.

Diagnosis of Covid-19. One of the most frequently used methods in the diagnosis of Covid-19 is RT-PCR test, as well as CT scans and X-ray scans. However, the rapid increase in the number of patients and the number of cases worldwide makes it difficult to apply these methods. For this reason, various studies have been carried out to develop computer aided solution systems. Most of the studies carried out aim to accelerate the diagnosis step by reaching accurate values close to reality. 21 of the studied studies (Ahamad et al., 2020: 1; AlJame et al., 2020: 1; Banerjee et al., 2020: 1; Brunese et al., 2020: 2; El-Kenawy et al., 2020: 5; Haritha, Praneeth, and Pranathi, 2020: 3; Hussain et al., 2021: 10; Javor et al., 2020: 1; Kang et al., 2020: 1; King et al., 2020: 1; Lai et al., 2020: 1; Li et al., 2021: 2; Mohammed et al., 2020: 5; Mondal et al., 2020: 11; Ootom et al., 2020: 3; Saha, Sadi, and Islam, 2021: 1; Soltan et al., 2021: 5; Sun et al., 2020: 3; Toğaçar, Ergen, and Cömert, 2020: 2; Tuncer, Dogan, and Ozyurt, 2020: 3; Ohata et al., 2021: 1) used the machine learning method for Covid-19 diagnosis. 14 of these studies (Brunese et al., 2020: 4; El-Kenawy et al., 2020: 1; Haritha, Praneeth, and Pranathi, 2020: 3; Hussain et al., 2021: 3; Javor et al., 2020: 1; Kang et al., 2020: 1; King et al., 2020: 1; Lai et al., 2020: 2; Mohammed et al., 2020: 8; Saha, Sadi, and Islam, 2021: 2; Sun et al., 2020: 1; Toğaçar, Ergen, and Cömert, 2020: 2; Tuncer, Dogan, and Ozyurt, 2020: 3; Ohata et al., 2021: 3) performed the diagnosis on image data sets and the remaining seven (Ahamad et al., 2020: 2; AlJame et al., 2020: 4; Banerjee et al., 2020: 2; Li et al., 2021: 2; Mondal et al., 2020: 1; Ootom et al., 2020: 3; Soltan et al., 2021: 3) studies performed the Covid-19 diagnostic procedure on non image clinical data sets.

Curve Fitting. Another important information about the Covid-19 pandemic can be obtained using time series data. By using curve fitting techniques on these data, information about the spread of the pandemic can be obtained. Using information such as the number of cases, number of deaths, the number of tests performed, the number of patients, it can be predicted when the number of cases will reach a peak, when it will end, or how it will show at certain times. This information enables countries to have information about which measures to take, when it will be better to maintain the shutdown, or how the pandemic will progress. Twenty of the studies examined in this scope (Amar, Taha, and Mohamed, 2020: 1; Andreas et al., 2020: 4; Balli, 2021: 1; Chakraborti et al., 2021: 1; Gambhir et al., 2020: 1; Kavadi et al., 2020: 2; Kramarenko, 2020: 2-3; Kuo and Fu, 2021: 2; Mandayam et al., 2020: 1; Mojjada et al., 2020: 5; Mondal et al., 2020: 1; Peng and Nagata, 2020: 5; Prakash et al., 2020: 7; Ribeiro et al., 2020: 2-3; Rustam et al., 2020: 4; Singh et al., 2020: 2; Wadhwa et al., 2021: 3; Wang et al., 2020: 3; Yadav, Perumal, and Srinivas, 2020: 3; Yeşilkanat, 2020: 1) used machine learning algorithms for curve fitting purposes.

Prediction. In addition to Covid-19 diagnosis and prediction techniques made with curve fitting, estimation processes such as estimating the mortality rate, estimating the need for intubation can be performed and more accurate decisions can be made in the treatment process. Eight of the studied studies (Althnian et al., 2020: 1; Arvind et al., 2021: 2; Burdick et al., 2020: 3; Di Castelnuovo et al., 2020: 3; Istaiteh et al., 2020: 7; Khan, Abbas, and Truong, 2020: 1; Nikil, Dalmia, and Kumar,

2020: 2; Yadaw et al., 2020: 1) used machine learning methods for prediction. The process of estimating intubation rate in the study of Varun Arvind, et al. (Arvind et al., 2021: 4) achieves 0.83 AUC and 0.32 AUPRC value, respiratory decompensation in the study of Burdick, H. et al. (Burdick et al., 2020: 5) achieves sensitivity with a value of 0.90, mortality rate in the study of Yadaw AS (Yadaw et al., 2020: 7) achieves 0.91-0.94 AUC value and estimation of sensitivity in the study of Althnion et al. (Althnion et al., 2020: 6) achieves 85.6% accuracy and 0.76 AUC for decision tree algorithm.

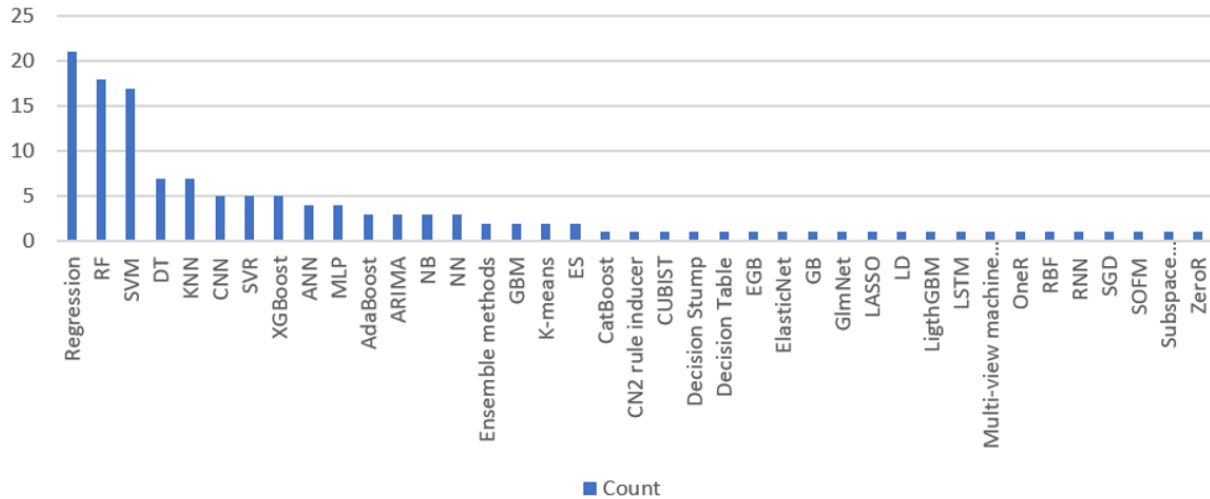


Fig. 3. Used machine learning methods and their counts.

Many different machine learning techniques have been used in the reviewed studies. Figure 3 shows the machine learning techniques used and the number of times they were used. As can be seen from the graph, regression techniques are the most commonly used machine learning method in curve fitting problems. Next comes the RF algorithm with 18 numbers and the SVM algorithm with 17 numbers. (ES: Exponential smoothing, LD: Linear discriminant) Within the scope of this study, three different use cases were determined and the examined publications were divided into at least one of these three articles. The list of machine learning algorithms used in these types determined in Table 3 is given.

Table 3 – Features used in clinical data sets according to publication.

Application type	Methods
Diagnosis	Ensemble, RF, KNN, NB, RF, MLP, SVM, CNN, NN, RBF, KNN, SGD, Regression, DT, AdaBoost, CN2 rule inducer, Multi-view machine learning technique, SOFM, XgBoost, GBM, EGB, Decision Table, Decision Stump, OneR, ZeroR, Linear discriminant (LD), subspace discriminant (SD) , Glnet
Prediction	RF, XgBoost, K-means, ARIMA, ANN, LSTM, CNN, Regression, SVM, MLP, DT, FBM
Curve Fitting	Regression, SVM, ANN, RF, SVR, ARIMA, Elasticnet (EN), LASSO, RNN, MLP, KNN, PCR, GBM, LightGBM, DT, Ensemble, Catboost, regression tree (RT), AdaBoost, Exponential Smoothing, GB, XGBoost

Conclusions

After the removal of duplicates from 532 studies obtained as a result of the systematic literature review and the elimination process, taking into account the inclusion and exclusion criteria, 71 publications were obtained. As a second step, after the detailed examination of the publications, a total of 49 studies were determined to be examined within the scope of this study. In the analysis of these 49 studies, three data types that are frequently used were determined. These are clinical data, time series and image data. Three different categories, namely curve fitting, prediction and diagnosis, were determined as the usage situation, and all the articles examined were assigned to at least one type. While most of the data types used for the curve fitting process consisted of series, clinical data and image data were used for the diagnostic process. Studies conducted in the diagnosis category aim to accelerate this process by reaching high accuracy values and to alleviate the burden of healthcare professionals. The three most used machine learning methods in the analysis results were determined as Regression, RF and SVM. Although regression techniques are used in all three categories, it has been found to be a popular technique used for curve fitting. This study is a literature search created for future studies. It is aimed to be a guiding study for those who will work in this field by analyzing which data types are used for what purposes with which methods in the field of Covid-19 and machine learning.

In line with the results obtained, it was concluded that the most used of the 3 data types was the time series and the Covid-19 diagnosis was the most studied problem type among the 3 uses. In addition, while the most used machine learning method is Regression, it has been observed that RF and SVM methods are frequently used in the diagnosis of Covid-19. In addition to supervised learning techniques, unsupervised clustering techniques such as K-Means were also used. It has been observed that the studies examined have reached an accuracy close to manual determinations for purposes such as Covid-19 diagnosis, prediction and curve fitting.

References

- Ahamad M. M., Aktar S., Rashed-Al-Mahfuz M., Uddin S., Liò P., Xu H., . . . Moni M. A. (2020). A machine learning model to identify early stage symptoms of SARS-Cov-2 infected patients. *Expert Systems with Applications*, 160, 113661. doi:https://doi.org/10.1016/j.eswa.2020.113661
- Albahri A. S., Hamid R. A., Alwan J. K., Al-Qays Z. T., Zaidan A. A., Zaidan B. B., . . . Madhloom H. T. (2020). Role of biological data mining and machine learning techniques in detecting and diagnosing the novel coronavirus (COVID-19): A systematic review. *J Med Syst*, 44, 122. doi:10.1007/s10916-020-01582-x
- Aljame M., Ahmad I., Imtiaz A., and Mohammed A. (2020). Ensemble learning model for diagnosing COVID-19 from routine blood tests. *Informatics in Medicine Unlocked*, 21, 100449. doi:https://doi.org/10.1016/j.imu.2020.100449
- Althnian A., Elwafa A. A., Aloboud N., Alrasheed H., and Kurdi H. (2020). Prediction of COVID-19 individual susceptibility using demographic data: A case study on Saudi Arabia. *Procedia Computer Science*, 177, 379-86. doi:https://doi.org/10.1016/j.procs.2020.10.051
- Alwaeli Z. A. A., and Ibrahim A. A. (2020). Predicting Covid-19 trajectory using machine learning. *2020 4th International Symposium on Multidisciplinary Studies and Innovative Technologies (ISMSIT)*, 1-4. doi:10.1109/ISMSIT50672.2020.9255149
- Amar L. A., Taha A. A., and Mohamed M. Y. (2020). Prediction of the final size for COVID-19 epidemic using machine learning: A case study of Egypt. *Infectious Disease Modelling*, 5, 622-34. doi:https://doi.org/10.1016/j.idm.2020.08.008
- Andreas A., Mavromoustakis C. X., Mastorakis G., Mumtaz S., Batalla J. M., and Pallis E. (2020). Modified machine learning technique for curve fitting on regression models for COVID-19 projections. *2020 IEEE 25th International Workshop on Computer Aided Modeling and Design of Communication Links and Networks (CAMAD)*, 1-6. doi:10.1109/CAMAD50429.2020.9209264
- Arvind V., Kim J. S., Cho B. H., Geng E., and Cho S. K. (2021). Development of a machine learning algorithm to predict intubation among hospitalized patients with COVID-19. *J Crit Care*, 62, 25-30. doi:10.1016/j.jcrc.2020.10.033
- Balli S. (2021). Data analysis of Covid-19 pandemic and short-term cumulative case forecasting using machine learning time series methods. *Chaos, Solitons & Fractals*, 142, 110512. doi:https://doi.org/10.1016/j.chaos.2020.110512
- Banerjee A., Ray S., Vorselaars B., Kitson J., Mamalakis M., Weeks S., . . . Mackenzie L. S. (2020). Use of machine learning and artificial intelligence to predict SARS-CoV-2 infection from full blood counts in a population. *International Immunopharmacology*, 86, 106705. doi:https://doi.org/10.1016/j.intimp.2020.106705
- Brunese L., Martinelli F., Mercaldo F., and Santone A. (2020). Machine learning for coronavirus covid-19 detection from chest x-rays. *Procedia Computer Science*, 176, 2212-21. doi:https://doi.org/10.1016/j.procs.2020.09.258

Burdick H., Lam C., Mataraso S., Siefkas A., Braden G., Dellinger R. P., . . . Das R. (2020). Prediction of respiratory decompensation in Covid-19 patients using machine learning: The READY trial. *Computers in Biology and Medicine*, 124, 103949. doi:<https://doi.org/10.1016/j.combiomed.2020.103949>

Chakraborti S., Maiti A., Pramanik S., Sannigrahi S., Pilla F., Banerjee A., and Das D. N. (2021). Evaluating the plausible application of advanced machine learnings in exploring determinant factors of present pandemic: A case for continent specific COVID-19 analysis. *Science of The Total Environment*, 765, 142723. doi:<https://doi.org/10.1016/j.scitotenv.2020.142723>

Di Castelnuovo A., Bonaccio M., Costanzo S., Gialluisi A., Antinori A., Berselli N., . . . Iacoviello L. (2020). Common cardiovascular risk factors and in-hospital mortality in 3,894 patients with COVID-19: survival analysis and machine learning-based findings from the multicentre Italian CORIST Study. *Nutrition, Metabolism and Cardiovascular Diseases*, 30, 1899-913. doi:<https://doi.org/10.1016/j.numecd.2020.07.031>

El-Kenawy E. S. M., Ibrahim A., Mirjalili S., Eid M. M., and Hussein S. E. (2020). Novel feature selection and voting classifier algorithms for COVID-19 classification in CT Images. *IEEE Access*, 8, 179317-35. doi:[10.1109/ACCESS.2020.3028012](https://doi.org/10.1109/ACCESS.2020.3028012)

Gambhir E., Jain R., Gupta A., and Tomer U. (2020). Regression analysis of COVID-19 using machine learning algorithms. *2020 International Conference on Smart Electronics and Communication (ICOSEC)*, 65-71. doi:[10.1109/ICOSEC49089.2020.9215356](https://doi.org/10.1109/ICOSEC49089.2020.9215356)

Haritha D., Praneeth C., and Pranathi M. K. (2020). Covid prediction from X-ray Images. *2020 5th International Conference on Computing, Communication and Security (ICCCS)*, 1-5. doi:[10.1109/ICCCS49678.2020.9276795](https://doi.org/10.1109/ICCCS49678.2020.9276795)

Hussain E., Hasan M., Rahman M. A., Lee I., Tamanna T., and Parvez M. Z. (2021). CoroDet: A deep learning based classification for COVID-19 detection using chest X-ray images. *Chaos, Solitons & Fractals*, 142, 110495. doi:<https://doi.org/10.1016/j.chaos.2020.110495>

Istaitieh O., Owais T., Al-Madi N., and Abu-Soud S. (2020). Machine learning approaches for COVID-19 forecasting. *2020 International Conference on Intelligent Data Science Technologies and Applications (IDSTA)*, 50-57. doi:[10.1109/IDSTA50958.2020.9264101](https://doi.org/10.1109/IDSTA50958.2020.9264101)

Javor D., Kaplan H., Kaplan A., Puchner S. B., Krestan C., and Baltzer P. (2020). Deep learning analysis provides accurate COVID-19 diagnosis on chest computed tomography. *European Journal of Radiology*, 133, 109402. doi:<https://doi.org/10.1016/j.ejrad.2020.109402>

Kang H., Xia L., Yan F., Wan Z., Shi F., Yuan H., . . . Shen D. (2020). Diagnosis of coronavirus disease 2019 (COVID-19) with structured latent multi-view representation learning. *IEEE Transactions on Medical Imaging*, 39, 2606-14. doi:[10.1109/TMI.2020.2992546](https://doi.org/10.1109/TMI.2020.2992546)

Kavadi D. P., Patan R., Ramachandran M., and Gandomi A. H. (2020). Partial derivative nonlinear global pandemic machine learning prediction of COVID 19. *Chaos, Solitons & Fractals*, 139, 110056. doi:<https://doi.org/10.1016/j.chaos.2020.110056>

Khan Y. A., Abbas S. Z., and Truong B.-C. (2020). Machine learning-based mortality rate prediction using optimized hyper-parameter. *Computer Methods and Programs in Biomedicine*, 197, 105704. doi:<https://doi.org/10.1016/j.cmpb.2020.105704>

King B., Barve S., Ford A., and Jha R. (2020). Unsupervised clustering of COVID-19 chest X-Ray images with a self-organizing feature map. *2020 IEEE 63rd International Midwest Symposium on Circuits and Systems (MWSCAS)*, 395-98. doi:10.1109/MWSCAS48704.2020.9184493

Kramarenko E. R. (2020). Testing the applicability of IT Instrumentation to projecting the spread of viral epidemics. *2020 International Multi-Conference on Industrial Engineering and Modern Technologies (FarEastCon)*, 1-5. doi:10.1109/FarEastCon50210.2020.9271094

Kuo C.-P., and Fu J. S. (2021). Evaluating the impact of mobility on COVID-19 pandemic with machine learning hybrid predictions. *Science of The Total Environment*, 758, 144151. doi:https://doi.org/10.1016/j.scitotenv.2020.144151

Kurniawan R., Abdullah S. N. H. S., Lestari F., Nazri M. Z. A., Mujahidin A., and Adnan N. (2020). Clustering and correlation methods for predicting coronavirus COVID-19 risk analysis in pandemic countries. *2020 8th International Conference on Cyber and IT Service Management (CITSM)*, 1-5. doi:10.1109/CITSM50537.2020.9268920

Lai Y., Li G., Wu D., Lian W., Li C., Tian J., . . . Jiang G. (2020). 2019 Novel coronavirus infected pneumonia on CT: A feasibility study of few shot learning for computerized diagnosis of emergency diseases. *IEEE Access*, 8, 194158-65. doi:10.1109/ACCESS.2020.3033069

Li M., Zhang Z., Cao W., Liu Y., Du B., Chen C., . . . Wang X. (2021). Identifying novel factors associated with COVID-19 transmission and fatality using the machine learning approach. *Science of The Total Environment*, 764, 142810. doi:https://doi.org/10.1016/j.scitotenv.2020.142810

Mandayam A. U., R A. C., Siddesha S., and Niranjana S. K. (2020). Prediction of Covid-19 pandemic based on Regression. *2020 Fifth International Conference on Research in Computational Intelligence and Communication Networks (ICRCICN)*, 1-5. doi:10.1109/ICRCICN50933.2020.9296175

Mohammed M. A., Abdulkareem K. H., Al-Waisy A. S., Mostafa S. A., Al-Fahdawi S., Dinar A. M., . . . Díez I. D. L. T. D. L. T. (2020). Benchmarking methodology for selection of optimal COVID-19 diagnostic model based on entropy and TOPSIS methods. *IEEE Access*, 8, 99115-31. doi:10.1109/ACCESS.2020.2995597

Mojjada R. K., Yadav A., Prabhu A. V., and Natarajan Y. (2020). Machine learning models for covid-19 future forecasting. *Materials Today: Proceedings*. doi:https://doi.org/10.1016/j.matpr.2020.10.962

Mondal M. R. H., Bharati S., Podder P., and Podder P. (2020). Data analytics for novel coronavirus disease. *Informatics in Medicine Unlocked*, 20, 100374. doi:https://doi.org/10.1016/j.imu.2020.100374

Nikil C. V. S. S., Dalmia H., and Kumar G. J. R. P. (2020). Covid-19 outbreak analysis. *2020 International Conference on Smart Technologies in Computing, Electrical and Electronics (ICSTCEE)*, 347-50. doi:10.1109/ICSTCEE49637.2020.9276790

Ohata E. F., Bezerra G. M., Chagas J. V. S. d., Neto A. V. L., Albuquerque A. B., Albuquerque V. H. C. d., and Filho P. P. R. (2021). Automatic detection of COVID-19 infection using chest X-ray images through transfer learning. *IEEE/CAA Journal of Automatica Sinica*, 8, 239-48. doi:10.1109/JAS.2020.1003393

Otoom M., Otoum N., Alzubaidi M. A., Etoom Y., and Banihani R. (2020). An IoT-based framework for early identification and monitoring of COVID-19 cases. *Biomedical Signal Processing and Control*, 62, 102149. doi:<https://doi.org/10.1016/j.bspc.2020.102149>

Peng Y., and Nagata M. H. (2020). An empirical overview of nonlinearity and overfitting in machine learning using COVID-19 data. *Chaos, Solitons & Fractals*, 139, 110055. doi:<https://doi.org/10.1016/j.chaos.2020.110055>

Prakash A., Sharma P., Sinha I. K., and Singh U. P. (2020). Spread & Peak prediction of Covid-19 using ANN and regression (Workshop Paper). *2020 IEEE Sixth International Conference on Multimedia Big Data (BigMM)*, 356-65. doi:10.1109/BigMM50055.2020.00062

Ribeiro M. H. D. M., da Silva R. G., Mariani V. C., and Coelho L. d. S. (2020). Short-term forecasting COVID-19 cumulative confirmed cases: Perspectives for Brazil. *Chaos, Solitons & Fractals*, 135, 109853. doi:<https://doi.org/10.1016/j.chaos.2020.109853>

Rustam F., Reshi A. A., Mehmood A., Ullah S., On B. W., Aslam W., and Choi G. S. (2020). COVID-19 future forecasting using supervised machine learning models. *IEEE Access*, 8, 101489-99. doi:10.1109/ACCESS.2020.2997311

Saha P., Sadi M. S., and Islam M. M. (2021). EMCNet: Automated COVID-19 diagnosis from X-ray images using convolutional neural network and ensemble of machine learning classifiers. *Inform Med Unlocked*, 22, 100505. doi:10.1016/j.imu.2020.100505

Singh S., Parmar K. S., Makkhan S. J. S., Kaur J., Peshoria S., and Kumar J. (2020). Study of ARIMA and least square support vector machine (LS-SVM) models for the prediction of SARS-CoV-2 confirmed cases in the most affected countries. *Chaos, Solitons & Fractals*, 139, 110086. doi:<https://doi.org/10.1016/j.chaos.2020.110086>

Soltan A. A. S., Kouchaki S., Zhu T., Kiyasseh D., Taylor T., Hussain Z. B., . . . Clifton D. A. (2021). Rapid triage for COVID-19 using routine clinical data for patients attending hospital: development and prospective validation of an artificial intelligence screening test. *The Lancet Digital Health*, 3, e78-e87. doi:[https://doi.org/10.1016/S2589-7500\(20\)30274-0](https://doi.org/10.1016/S2589-7500(20)30274-0)

Sun L., Mo Z., Yan F., Xia L., Shan F., Ding Z., . . . Shen D. (2020). Adaptive feature selection guided deep forest for COVID-19 classification with chest CT. *IEEE Journal of Biomedical and Health Informatics*, 24, 2798-805. doi:10.1109/JBHI.2020.3019505

Toğaçar M., Ergen B., and Cömert Z. (2020). COVID-19 detection using deep learning models to exploit social mimic optimization and structured chest X-ray images using fuzzy color and stacking approaches. *Computers in Biology and Medicine*, 121, 103805. doi:<https://doi.org/10.1016/j.compbiomed.2020.103805>

Tuncer T., Dogan S., and Ozyurt F. (2020). An automated residual exemplar local binary pattern and iterative relief based COVID-19 detection method using chest X-ray image. *Chemometrics and Intelligent Laboratory Systems*, 203, 104054. doi:<https://doi.org/10.1016/j.chemolab.2020.104054>

Wadhwa P., Aishwarya, Tripathi A., Singh P., Diwakar M., and Kumar N. (2021). Predicting the time period of extension of lockdown due to increase in rate of COVID-19 cases in India using

machine learning. *Materials Today: Proceedings*, 37, 2617-22. doi:https://doi.org/10.1016/j.matpr.2020.08.509

Wang P., Zheng X., Li J., and Zhu B. (2020). Prediction of epidemic trends in COVID-19 with logistic model and machine learning technics. *Chaos, Solitons & Fractals*, 139, 110058. doi:https://doi.org/10.1016/j.chaos.2020.110058

Yadav M., Perumal M., and Srinivas M. (2020). Analysis on novel coronavirus (COVID-19) using machine learning methods. *Chaos, Solitons & Fractals*, 139, 110050. doi:https://doi.org/10.1016/j.chaos.2020.110050

Yadaw A. S., Li Y.-c., Bose S., Iyengar R., Bunyavanich S., and Pandey G. (2020). Clinical features of COVID-19 mortality: development and validation of a clinical prediction model. *The Lancet Digital Health*, 2, e516-e25. doi:https://doi.org/10.1016/S2589-7500(20)30217-X

Yeşilkanat C. M. (2020). Spatio-temporal estimation of the daily cases of COVID-19 in worldwide using random forest machine learning algorithm. *Chaos, Solitons & Fractals*, 140, 110210. doi:https://doi.org/10.1016/j.chaos.2020.110210

Table 4 – Overview of Primary Studies.

	Country	Problem Category	Dataset type	Technology	Result
(Arvind et al., 2021: 4)	USA	Prediction intubation	Clinical data-vital values, laboratory and demographic data	RF	The machine learning algorithm used has 0.83 AUC and 0.32 AUPRC, which performs significantly better than the ROX index in terms of intubation risk.
(Saha, Sadi, and Islam, 2021: 8-10)	Bangladesh	Diagnosis of Covid-19	Image dataset - X-ray images	CNN based feature extraction, ensemble of ML classifiers (RF, SVM, DT, AdaBoost)	The proposed deep learning and machine learning based detection system achieved a better performance than other deep learning systems with 98.91% accuracy, 100% precision, 97.82% recall, 98.89% F1 score and 0.9894 ROC.
(Burdick et al., 2020: 3)	USA, Belgium	Prediction respiratory decompensation	Clinical data - vital values, laboratory	XGBoost	The proposed algorithm has a higher diagnostic likelihood ratio in the Modified Early Warning Score (MEWS), a higher sensitivity with a value of 0.90 than MEWS, which has a sensitivity value of 0.78.
(Sun et al., 2020: 5)	China	Diagnosis of Covid-19	Image dataset - CT images, gender, age	RF based Adaptive Feature Selection guided Deep Forest (AFS-DF)	The obtained accuracy, sensitivity, specificity, AUC, sensitivity and F1 score were 91.79%, 93.05%, 89.95%, 96.35%, 93.10% and 93.07%, respectively. The proposed method performed better than the Four commonly used machine learning models in CAP (community acquired pneumonia) classification. When compared with Lasso and ElasticNet feature selection methods, a better result was obtained with the proposed AFS-DF structure.
(Ohata et al., 2021: 5-8)	Brazil	Diagnosis of Covid-19	Image dataset - Chest X-ray images	CNN based feature extraction, KNN, NB,	SVM algorithm used with MobileNet feature extractor achieved 98.5% accuracy and F1 score value, MLP algorithm used with DenseNet201 reached an accuracy of 95.6% and F1 score value.

Kahraman, Zafer & Hacı, Murat & Soyhan, Hakan Serhad; Using Various Renewable Energy Sources In Commercial Kitchens And Ensuring Energy Efficiency

				RF, MLP, SVM	
(Lai et al., 2020: 5-6)	China	Diagnosis of Covid-19	Image dataset - Chest CT images	Deep convolutional neural network (DCNN), MaskR-CNN-SVM	The proposed algorithm (NCIP-Net) for the detection of normal and NCIP (novel coronavirus-infected pneumonia) reached 0.91 AUC value, 0.95 AUC value for NCIP and lung nodule detection, and 0.83 AUC value for NCIP and other pneumonia detection. It also appears to perform better than the Mask-R-CNN trained for comparison.
(Andreas et al., 2020: 3)	Cyprus, Greece, Poland, Portugal	Curve Fitting	Time series dataset	Linear, Exponential, 6th degree Polynomial Regression	Linear Regression 0.8609, Exponential Regression 0.922 and 6th degree Polynomial 0.999336 R2 values were achieved. When the results were examined, it was concluded that the 6th order polynomial regression was more suitable for the dataset. The 10th degree polynomial developed for curve fitting corresponding to cumulative infectious cases in Italy reached the value of 0.999934933 R2.
(Haritha, Praneeth, and Pranathi, 2020: 4)	India	Diagnosis of Covid-19	Image dataset - X-ray images	Transfer learning CNN with VGG	The proposed method reached 99.49% accuracy with 1.0000 sensitivity and 1.0000 specificity values for 5-class multi-class. For Covid and normal class classification, 1.0000 sensitivity, 0.9890 and specificity reached 98% accuracy.
(Mohammed et al., 2020: 1)	Iraq, Malaysia, Saudi Arabia, Spain	Diagnosis of Covid-19	Image dataset - Chest X-ray images	NN, SVM, NB, RBF, KNN, SGD, Linear R, AdaBoost, RF, DT, CN2 rule inducer, SVM(Polynomial)	By using Entropy and TOPSIS integration, the problem of selecting and comparing diagnostic models was solved effectively. SVM (linear) was chosen as the best diagnostic model for COVID19 with a proximity coefficient value of 0.9899.
(Kurniawan et al., 2020: 1)	Indonesia, Malaysia,	Predicting COVID-19 Risk Analysis	Time series dataset	K-means clustering, correlation	When the number of clusters is 5, the best cluster number performance is reached. With the cluster [Iran, France], [Spain, Germany], [United States and Italy], [Indonesia, Malaysia, Philippines] an performance about 97% has been achieved. At the same time, a suitable relation of 0.85 was predicted between total deaths and characteristics of critically infected patients.
(El-Kenawy et al., 2020: 14-16)	Egypt, Australia, South Korea	Diagnosis of Covid-19	Image dataset - CT images	SVM, NN, KNN, DT	It has been found that the highest classification accuracy can be achieved when AlexNet is used in the feature extraction stage. The used SFS Guided WOA feature selection algorithm performs better than the compared algorithms including the original WOA algorithm, and LSH-SMOTE preprocessing and the proposed PSO-Guided WOA voting classifier with the binary prediction result of 0.995 and 2.49569E- 05 It has been observed that it achieves an AUC with MSE, which outperforms other state of the art community learning.
(Istaiteh et al., 2020: 7)	Jordan	COVID-19 Forecasting, Prediction	Time series dataset	ARIMA, ANN, LSTM, CNN	Deep learning models performed better than ARIMA model in terms of three error measures (MAPE, RMSLE, MSLE). However, one dimensional CNN performed slightly better than the other two deep learning models, followed by

Kahraman, Zafer & Hacı, Murat & Soyhan, Hakan Serhad; Using Various Renewable Energy Sources In Commercial Kitchens And Ensuring Energy Efficiency

					ANN and LSTM models. CNN reached 3.13 MAPE, 0.13 RMSLE, 0.02 MSLE values.
(Kang et al., 2020: 8)	China	Diagnosis of Covid-19	Image dataset - Chest CT images	Multi-view machine learning technique	The multiple view representation learning technique used in the study reached 95.5% accuracy, 96.6% sensitivity and 93.2% specificity.
(Mandayam et al., 2020: 3-4)	India	Curve Fitting	Time series dataset	Linear R., SVR	It was observed that the LR model reached 99% R2 in predicting cases and the Linear Regression algorithm performed better when compared with SVR. Because the dataset is linear.
(Rustam et al., 2020: 1,10)	Pakistan, Saudi Arabia, South Korea	Curve Fitting	Time series dataset	Linear R., LASSO, SVM, ES	Three types of estimates are made, such as the number of newly infected cases, deaths and recovery over the next 10 days. While ES performed the best among all models, LASSO and LR cases performed best after ES in predicting mortality and recovery rate. It has been observed that SVM performs poorly in all forecast scenarios.
(Prakash et al., 2020: 4-10)	India	Curve Fitting	Time series dataset	Linear R., PR, ANN	Linear regression captures the data distribution, but appears to be slightly different from the actual numbers for Spain, Italy and the USA. It has been observed that linear regression catches the curve better compared to fourth order polynomial regression. However, the estimates made by the polynomial regression were far from the actual number of cases in the Spanish and Italian data. It has been seen that the predictions made with the ANN model are quite accurate; especially for the top five most affected states of India. While there was some deviation for the Top five States least affected, the Top five States moderately affected showed average modeling performance.
(King et al., 2020: 3-4)	USA	Diagnosis of Covid-19	Image dataset - Chest X-ray images	Self-Organizing Feature Maps (SOFM)	It has been shown that with the SOFM unsupervised learning technique, it can effectively extract features from Covid-19 chest x-ray images and classify the image correctly. The biggest advantage of this model is that there is no need for a labeled data requirement for training.
(Gambhir et al., 2020: 6)	India	Curve Fitting	Time series dataset	SVM, PR	With this study, the current situation of Covid-19 transmission has been successfully analyzed. The Polynomial Regression algorithm predicted a 60-day incidence increase with an accuracy of 93% compared to the SVM.
(Kramarenko, 2020: 3)	Russia	Curve Fitting	Clinical data	ANN, RNN, RF, GB, AdaBoost, Catboost, LightGBM	Gradient boosting over decision trees was chosen as the most efficient model.
(Yadaw et al., 2020: 8-9)	USA	Prediction mortality	Clinical data - comorbidities and demographic data	RF, Linear R., SVM, XGBoost	Prediction models used in the study obtained 0.91 - 0.94 AUC values in two independent verification data sets. The model obtained using only three features was as successful as the model using all features. Minimum oxygen saturation and age were chosen as the most determining features and the XGBoost produced the most accurate predictive value.

Kahraman, Zafer & Hacı, Murat & Soyhan, Hakan Serhad; Using Various Renewable Energy Sources In Commercial Kitchens And Ensuring Energy Efficiency

(AlJame et al., 2020: 1)	Kuwait	Diagnosis of Covid-19	Clinical data - laboratory (blood tests)	Ensemble Learning (extra trees, RF, Logistic R., XGBoost)	The proposed assembly model reached 99.88% accuracy, 99.38% AUC, 98.72% sensitivity and 99.99% specificity.
(Soltan et al., 2021: 1,6)	UK	Diagnosis of Covid-19	Clinical data - laboratory tests, blood gas measurements, and vital signs	Logistic R., RF, XGBoost	Compared to other classifiers, the XGBoost algorithm has shown the highest performance. The developed ED (emergency services) model reached 0.939 AUROC, 77.4% sensitivity, 95.7% specificity, while the acceptance model reached 0.940 AUROC, 77.4% sensitivity, 94.8% specificity. Eosinophils, basophils and CRP were chosen as the highest determinant features for the ED model.
(Mojjada et al., 2020: 5)	India	Curve Fitting	Time series dataset	Linear R., LASSO R., SVM, Exponential Smoothing	ES showed the best predictive performance depending on the size of the dataset. LR and LASSO have been successful to some extent in predicting the number of deaths. SVM showed the worst prediction performance in this study.
(Wadhwa et al., 2021: 5-6)	India	Curve Fitting	Time series dataset	Linear Regression	A machine learning model has been developed to predict the number of cases, deaths and recovery in India. Using this model, the lockdown time is estimated. It has been learned that if all measures are properly implemented, the cases will begin to decrease and the lockdown will disappear on 9 September 2020.
(Ballı, 2021: 6)	Turkey	Curve Fitting	Time series dataset	Linear regression, MLP, RF, SVM	Machine learning has been used to predict the trend of the epidemic. According to the obtained results, SVM achieved the best predictive performance. SVM and linear regression have close RMSE and MAPE values. MLP ranks third in performance and RF has the worst performance. According to the information obtained, it is estimated that the epidemic will reach its peak in January 2021 and 80 million people will be infected cumulatively.
(Yeşilkanat, 2020: 1,7)	Turkey	Curve Fitting	Time series dataset	RF	Case numbers were estimated for 190 countries using RF and compared with the actual number of confirmed cases. At the end of the study, the RF algorithm obtained 0.843 and 0.995 (avg R2 = 0.959), 141.76 and 526.18 (mean RMSE = 259.38) for the test dataset. This shows that the RF algorithm is a suitable algorithm for near future case prediction.
(Ahamad et al., 2020: 1,5)	Bangladesh, USA, UK, China, Australia	Diagnosis of Covid-19, prediction symptoms	Clinical data - Demographic and symptom data	DT, RF, GBM, EGB, SVM	A machine learning model has been developed that provides features that provide high determination in the diagnosis of Covid-19 disease. The XGBoost achieved the highest accuracy (> 85%) to select features in all age groups compared to other models. The analysis showed that the most significant symptoms were cough (30.3%), fever (41.1%), runny nose (8.43%) and lung infection (13.1%).
(Hussain et al., 2021: 11)	Bangladesh, Australia	Diagnosis of Covid-19	Image dataset - Chest X-ray images	CNN	The proposed model has reached 99.1% accuracy for two (COVID and Normal) class classification, 94.2% for three (Normal, COVID and non-COVID) class classification and 91.2% for four (COVID, non-COVID viral pneumonia, Normal,

					and non-COVID bacterial pneumonia) class classification.
(Peng and Nagata, 2020: 1)	Brazil	Curve Fitting	Time series dataset	SVR	Case estimation was performed for 12 countries using the SVR algorithm and different kernel functions were tested. The Gaussian Kernel had the best within sample performance and the worst out of sample performance. The Linear Kernel function performed poorly within the sample, but achieved a good out of instance performance
(Javor et al., 2020: 3)	Austria	Diagnosis of Covid-19	Image dataset - CT images	CNN	The proposed CNN-based machine learning model classifier reached 94.5% accuracy and 0.956 AUC. The proposed algorithm has achieved superior predictive performance than two radiologists with more than 15 years of experience.
(Wang et al., 2020: 4-5)	China	Curve Fitting	Time series dataset	Logistic R., Prophet	The fastest growth point among five countries, the size of the epidemic and the time of peak was predicted. The outbreak size for the global is estimated to peak on June 21 with 3,603,111 active infections. It is learned that it will be 14.117.911 at the end of October and the fastest growth point is on May 16.
(Li et al., 2021: 3)	China, USA	Diagnosis of Covid-19, prediction symptoms	Clinical data	logistic regression	Factors associated with mortality and case rates were identified for 154 countries and 50 US states. 27 variables were selected using LASSO, and AUC values of 0.80, 0.83, and 0.81 were reached in estimates of case, death, and case fatality rates in the test set.
(Otoom et al., 2020: 7)	Jordan, Canada	Diagnosis of Covid-19	Clinical data-symptom data	SVM, NN, NB, KNN, Decision Table, Decision Stump, OneR, and ZeroR	The results showed that five algorithms achieved over 90% success. SVM achieved an accuracy of 92.95%, NN 92.89%, NB, 90.58%, KNN 92.89%.
(Althnian et al., 2020: 6-7)	Saudi Arabia, US	Prediction susceptibility	Clinical data - demographic data	MLP, SVM, DT, RF	Susceptibility describes the likelihood of an individual becoming infected. As a result of the study, DT achieved 85.6% RF 85.3%, MLP 77.2%, and SVM 74.2% accuracy. DT 0.76 and RD 0.77 performed slightly better than MLP 0.71 and SVM with AUC value of 0.77.
(Singh et al., 2020: 7-8)	India	Curve Fitting	Time series dataset	LS-SVM, ARIMA	According to the error information measured at the end of the article (MAE, MSE and RMSE), LS-SVM performed better than the ARIMA model and showed a sharp increase for one month later cases within five countries.
(Toğaçar, Ergen, and Cömert, 2020: 11)	Turkey	Diagnosis of Covid-19	Image dataset - X-ray images	SVM	In the article, a classification process in three classes (coronavirus, pneumonia, normal) was carried out. The success rate was 99.34% in Covid-19 data, 98.47% in Pneumonia data and 98.68% in normal images. The overall classification rate is 99.27%, which shows that the SMO algorithm contributes to the classification success.
(Tuncer, Dogan, and Ozyurt, 2020: 9)	Turkey	Diagnosis of Covid-19	Image dataset - X-ray images	DT, linear discriminant (LD),SVM, kkNN, subspace	SVM was chosen as the best classifier with 100.0% classification accuracy and 99% overall success rate. DT was the worst performing result.

				discriminant (SD)	
(Khan, Abbas, and Truong, 2020: 4-8)	China, Vietnam, Pakistan	Prediction mortality	Time series dataset	Gaussian Process Regression, Polynomial R.	Turkey, Spain, Sweden, France and five different models were generated using the number of deaths and cases according to the number of cases in Pakistan. According to the results, the RMSE value of GPR is lower among five countries. The Pakistan model created using GPR has an RMSE value of 1.796739, while the Swedish model has an RMSE value of 2.370486. Therefore, the Swedish model is the most suitable model for predicting Pakistan's mortality rate.
(Ribeiro et al., 2020: 7)	Brazil	Curve Fitting	Time series dataset	ARIMA, RF, SVR, cubic regression (CUBIST), ridge regression (RIDGE), stacking-ensemble learning	The article aims to estimate the daily number of cases in Brazil 1, 3 and 6 days ahead. In most scenarios, SVR and stacking-ensemble learning has achieved better performance than other algorithms. Order of algorithms by success values SVR, stacking ensemble learning, RIDGE, CUBIST, ARIMA and RF.
(Banerjee et al., 2020: 5-7)	UK	Diagnosis of Covid-19	Clinical data - laboratory (blood tests)	Logistic regression, RF, ANN, Glnet	In the diagnostic procedure using the full blood count, ANN achieved 95%, RF 94% and glmnet 94% AUC. ANN 82%, RF 86% and glmnet 84% AUC values were obtained in the diagnosis process for patients not admitted to the hospital.
(Mondal et al., 2020: 11-12)	Bangladesh	Curve Fitting, Diagnosis of Covid-19	Clinical data - laboratory, time series	SVM, kNN, XGBoost, MLP, logistic R., DT, RF, ensemble methods, Linear R, Polynomial R.	The number of cases worldwide is modeled using regression, and classification algorithms are used to diagnose COVID-19. Among the regression models used for the number of cases, polynomial regression of degree Two cases were predicted with 98.60% accuracy and performed better than linear regression. MLP, Logistic regression and XGBoost were chosen as the best classification models with 91% accuracy. In addition, "Serum Glucose" was determined as the first best feature, Respiratory Syncytial Virus "second" Influenza A "was the third best feature.
(Nikil, Dalmia, and Kumar, 2020: 3)	India	Prediction	Time series dataset	K-means	The chart created using Tests vs. Cases contains two sets, while the Cases and Deaths chart contains three sets. In this study, it was found that different conditions and precautions should be taken for different people by cluster analysis. At this stage, regional precautions are one of the good ways to be followed, and the elderly and those with respiratory problems are more risky than other groups.
(Kuo and Fu, 2021: 5-6)	USA	Curve Fitting	Time series dataset	Elasticnet (EN), PCR, partial least squares regression (PLSR) model, KNN, regression tree (RT),	In the article, a case prediction model based on demographic, mobility and environmental data was developed at district level. All classifiers reached a value of $R^2 > 0.81$ for the number of cases per day, and a value of $R^2 > 0.92$ for the estimation of the cumulative number of cases. In addition, RF, GBM and ANN models have achieved good results in estimating the number of daily cases, while EN and GBM have obtained good results in estimating the cumulative number of cases due to low RMSE and MAE values.

				RF, GBM, ANN	
(Di Castelnuovo et al., 2020: 7-13)	Italy, USA	Prediction	Clinical data - vital values, laboratory and demographic data	RF and COX	In this study, the most determining factors were analyzed by predicting the susceptibility to death for Covid-19 patients. The RF model achieved a strong prediction success with 95.2% sensitivity, 30.8% specificity, 83.4% classification accuracy, and 90.4% F1 value. He also found that the most defining characteristics were eGFR, CRP and age. These results have been validated using Cox survival analysis.
(Yadav, Perumal, and Srinivas, 2020: 9)	India	Curve Fitting	Time series dataset	Linear R., Polinomial R.,SVR	In the study, five different analyzes such as the date the epidemic will end, the transmission rate and the growth rate were carried out. The results showed that the SVR model obtained efficient and effective results compared to other models in the estimations made for five countries.
(Amar, Taha, and Mohamed, 2020: 12)	Egypt	Curve Fitting, Prediction	Time series dataset	7 regression model	In the study, it was estimated when the epidemic would end with the number of patients to be infected. Exponential fourth-order, fifth-order, and sixth-order polynomial regression models have reached the best results for predictions over a one-month period. In addition, as a result of the logit growth regression model, it is predicted that the peak of the epidemic will be on 22 June 2020 and the end time will be on 8-September 2020.
(Brunese et al., 2020: 9)	Italy	Diagnosis of Covid-19	Image dataset - Chest X-ray images	k-NN	The method suggested in the article reached 0.965 average sensitivity and an average recall values. Compared to other categories, a precision of 0.968 and a recall value of 0.964 show that the machine learning method can distinguish between Covid-19 and other categories with good performance.
(Chakraborti et al., 2021: 3)	India, Ireland	Curve Fitting, Prediction	Time series dataset	RF, GBM	Machine learning methods were used in this study to determine the characteristics associated with the Covid-19 case and death numbers. A total of 11 variables were determined for Covid-19 cases and a total of 15 variables for their deaths. Among the variables considered, the explanatory variables discussed in this study were air pollution, demographic, migration, and economy data as the most determining factors.
(Kavadi et al., 2020: 6-7)	India	Curve Fitting	Clinical data	Partial derivative regression and nonlinear machine learning (PDR-NML)	The proposed model reduces the prediction time by 7% compared to the linear regression and 9% compared to the AI-based model, and it also increases the prediction accuracy by 2% compared to the linear regression and 3% compared to the AI-based model. This shows that the proposed method achieves better results than existing methods.

Using Various Renewable Energy Sources In Commercial Kitchens And Ensuring Energy Efficiency

Zafer KAHRAMAN³⁷

Murat HACI³⁸

Hakan Serhad SOYHAN³⁹

Introduction

Commercial kitchen products (oven, cooker, grill, dishwasher, refrigerator, etc.) are widely used in places where there is mass food consumption (restaurants, hotels, dormitories, shopping centers, etc.). These products generally work with electricity or gas (natural gas, LPG, etc.) depending on the place of use. In addition to the increase in the population worldwide, the demands for energy are also increasing with the technological developments. Especially in fossil fuels (petroleum, natural gas, coal, etc.), the limited resources as well as the difficulties in supplying energy, fluctuations in prices and the polluting emissions of these resources in terms of the environment have emerged as important problems in recent years (Ang & et al., 2022; Ilechukwu & Lahiri, 2022; Shrestha & et al., 2022; Yang & et al., 2022; Yang, Zheng & Chang, 2022). For this reason, interest and investments in renewable energy sources (green energy) are increasing hydrogen, biogas, solar, wind, etc., which are within the scope of environmentally friendly resources. Research and development studies are also carried out intensively to expand the usage areas of energy resources (Hailemariam, Ivanovski & Dzhumashev, 2022).

Within the scope of this study, evaluations were made regarding the use of renewable energy (hydrogen, biogas, solar energy, wind energy, etc.) for various products in commercial kitchens and various studies to be carried out in the future. Innovative prototypes with original designs have been developed with activities based on R&D systematics, especially for commercial kitchen cooking products that use hydrogen and biogas from renewable energy sources. With the data in the test and evaluation stages, it has been achieved to use renewable energy sources effectively and efficiently in innovative prototypes.

Literature Review

Summaries of various literature studies on the characteristics and use of different renewable energy sources are given below.

It was emphasized that continuous improvements should be made in the research methods used in cooking studies in order to benefit the ecological environment and human health. It was stated that the literature should be systematically reviewed in order to facilitate rational design and improvements to be made in relation to cooking activities in line with sustainable development goals. While designing

³⁷ Zafer Kahraman, Dr., Öztiryakiler Madeni Eşya San. ve Tic. A.Ş, ORCID: 0000-0002-2008-0533

³⁸ Murat Hacı, Eng., Öztiryakiler Madeni Eşya San. Ve Tic. A.Ş, ORCID: 0000-0001-9172-8096

³⁹ Hakan Serhad Soyhan, Prof.Dr., Sakarya University, ORCID: 0000-0003-3723-9640

models to be simulated in commercial and residential kitchens, large-scale measurements and taking various precautions were emphasized (Li, 2021).

Due to the long-term negative effects of petrochemical use and economic crises, wind energy has emerged as a cost-effective energy source. It has been emphasized that it is emission-free, green and at the same time has the advantages of government subsidies and credits for taxes. It has various positive effects such as (i) environmental (ii) social (iii) economic and (iv) cultural effects. The potential impacts of emerging renewable technology are given in Figure 1 (Nazir & et al., 2020).

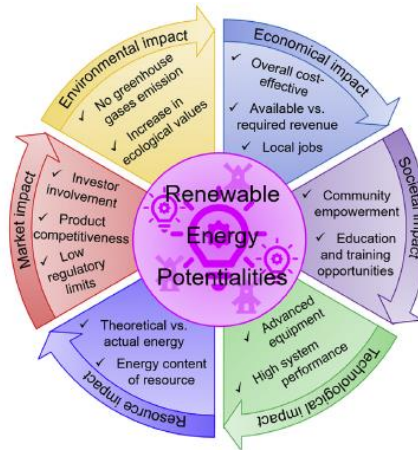


Figure 1. A view of the potential impacts of emerging renewable technology (Nazir & et al., 2020).

Renewable energies are defined as energy sources that do not run out as they are used. Renewable energy sources can be evaluated under five main headings, such as biomass obtained from plants and other wastes, wind energy, solar energy, hydroelectric energy obtained from running water and geothermal energy. Renewable energy can also be defined as clean energy as it does not produce additional pollution or waste like fossil fuel energies. Renewable energy sources have a low carbon footprint and produce less greenhouse gases. Clean energy has grown in popularity in recent years as various countries and economies are concerned to minimize their high dependence on fossil fuels. Renewable and sustainable clean energy conversions and applications are shown in Figure 2 (Jaiswal & et al., 2022).

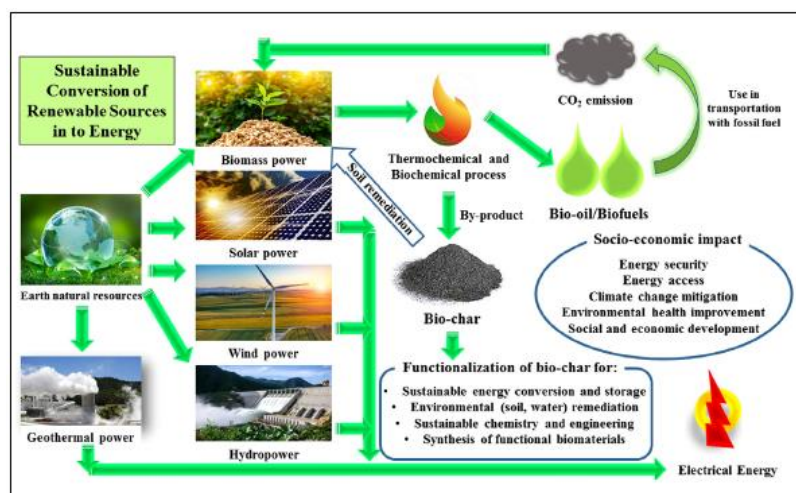


Figure 2. Renewable and sustainable clean energy conversion and applications (Jaiswal & et al., 2022).

Biomass includes bioenergy producing plant and animal materials such as bio-oil, cellulosic ethanol, renewable hydrocarbon fuels and biodiesel. Biomass includes agricultural waste, food waste, animal waste (fish, chicken waste, etc.), wood waste, food processing waste, organic waste, organic household waste and municipal waste. Various biomass feedstock sources for renewable bioenergy and biofuels are given in Table 1 (Jaiswal & et al., 2022).

Table 1. Different biomass feedstock sources for renewable bioenergy and biofuels (Jaiswal & et al., 2022).

Sources of biomass	Feedstocks	Bioenergy and biofuels	Applications
Wood by-Products	Firewood, wood chips, wood pellets, lumber, bark, furniture mill sawdust, wood processing residues	Heat energy, light energy, combined heat and power, cellulosic ethanol, electricity production, compost	Domestic use for cooking/heating, natural fertilizers, soil conditioners, agriculture mulches
Agricultural by-products	Corn cobs, fruit pits, straw, leaves, grass trimmings, lumber, bark, branches, agricultural crop residues, algae, forestry residues	Heat energy, light energy, combined heat and power, cellulosic ethanol, electricity production, compost	Domestic use for cooking/heating, natural fertilizers, soil conditioners, agriculture mulches
Solid waste	Residential and commercial garbage, paper/cardboard, vegetable/fruit peels, leftover/waste food	Heat energy, light energy, electricity production, compost	Domestic use for cooking/heating, natural fertilizers, soil conditioners, agriculture mulches
Non-crop foods plants, corn, sugarcane, agricultural residues	Cellulosic components	Bio-alcohol fuels, cellulosic ethanol, methanol, ethanol-blended petrol	Transportation vehicle usage
Landfills, leachate, manure, municipal wastewater, industrial wastewater	Biogas	Methane, liquid fuel, electricity generation, methanol production	Transportation and domestic fuel for cooking

Clean energy solutions include protecting the environment and ensuring energy security. A 3S concept including resource, system and service is being implemented. The resource specified in this concept constitutes the identification and selection of clean resources that are naturally available and whose use is technologically valid. They stated that the choice of resource depends on the natural and infrastructural situation in a particular region. The system specified in the concept includes the identification and selection of methods and systems that use environmentally friendly raw materials for clean energy production. forms. Hydrogen application of the 3S concept to obtain clean and sustainable products is given in Figure 3 (Razi & Dincer, 2022).

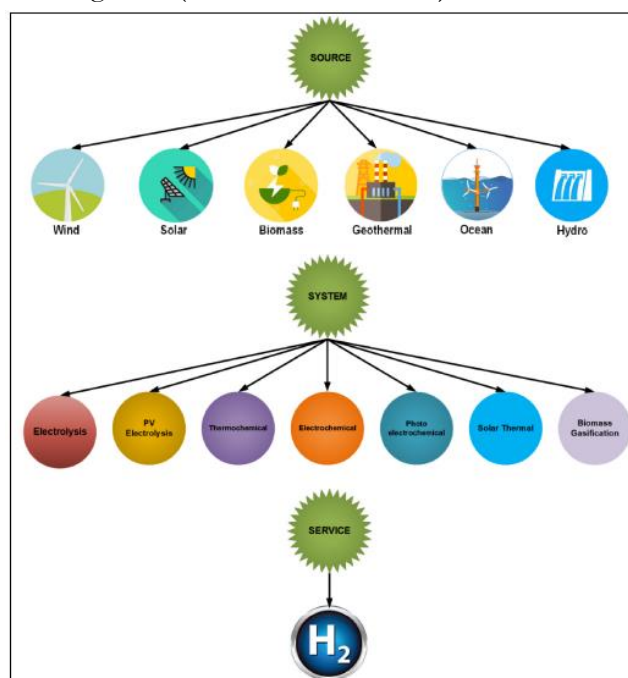


Figure 3. 3S (Source, System, Service) conceptual illustration for clean hydrogen production (Razi & Dincer, 2022).

Olabi and Abdelkareem reported that there are different obstacles to the spread of renewable energy sources as a reliable power source. The main barriers to renewable energy sources are shown in Figure 4 (Olabi & Abdelkareem, 2022).

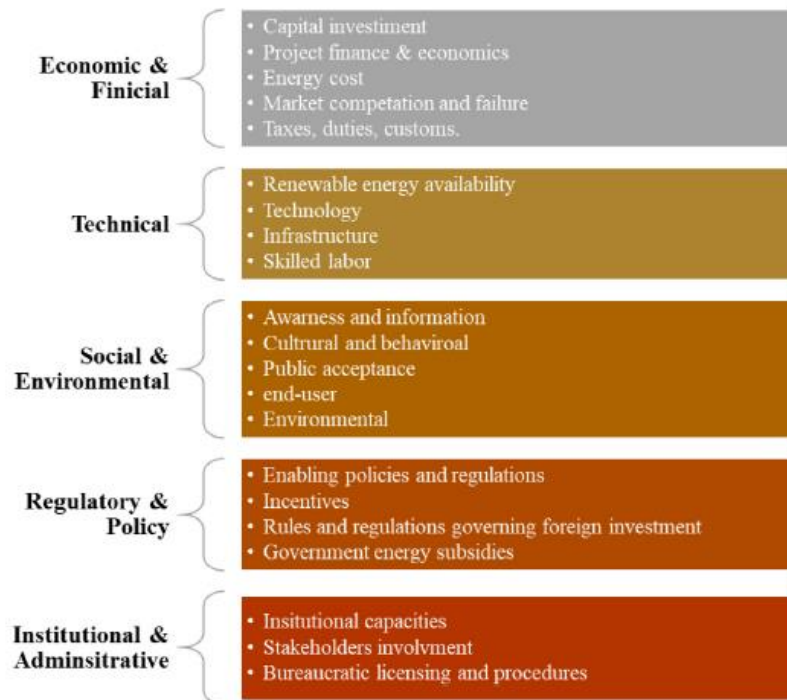


Figure 4. The main obstacles to renewable energy sources (Olabi & Abdelkareem, 2022).

While fossil fuels dominate in hydrogen production, a low amount of renewable energy sources are used. The classification of various methods used in hydrogen production is given in Figure 5 (Amin & et al., 2022).

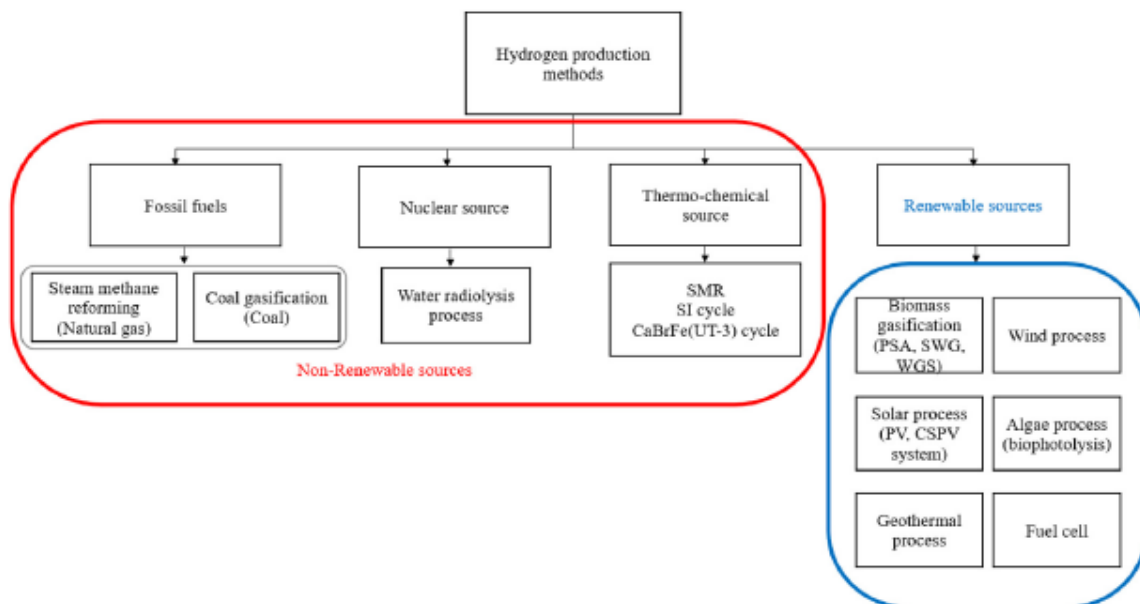


Figure 5. The classification of various methods used in hydrogen production (Amin & et al., 2022).

It was emphasized that the use of water electrolysis technology to produce hydrogen is a clean and efficient development. They emphasized that in addition to the high costs of water electrolysis technologies, the unit electric energy price also stands out as the main factor in the cost of hydrogen production by water electrolysis. The trend estimate for the main hydrogen sources is given in Figure 6 (Wang & et al., 2022).

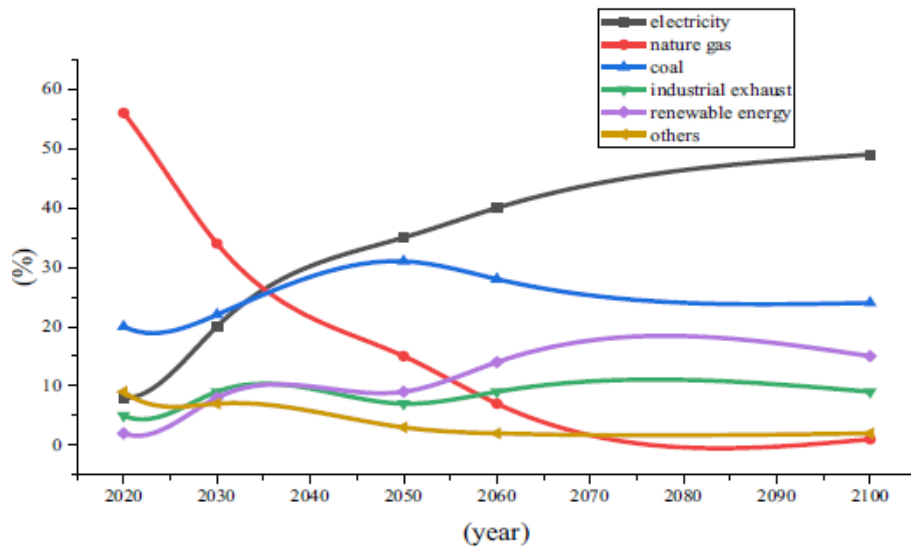


Figure 6. Trend forecast for the main hydrogen sources (Wang & et al., 2022).

The hydrogen energy industrial chain is basically divided into 3 main groups. These groups cover upstream hydrogen production, midstream hydrogen storage and distribution, and downstream integrated applications. In addition, various technologies such as material innovation, equipment production, assembly procedures and project techniques are also included in the industrial chain. Illustration of hydrogen energy industry chain is given Figure7 (Pingkue & Xue, 2022).

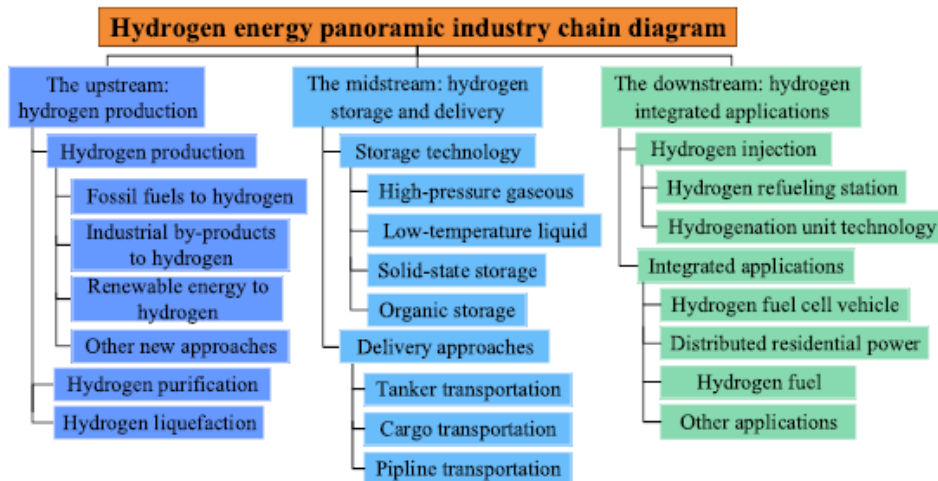


Figure 7. Illustration of hydrogen energy industry chain (Pingkue & Xue, 2022).

Arenas evaluated the design of a small-volume, folding parabolic solar reflector and the kitchen for cooking using portable solar energy, prototype production and tests. With the developed prototype, it has been reported that an average power value of 175 W and an energy efficiency of 26.6% have been achieved by using solar energy. It has been reported that a portable, inexpensive, environmentally friendly heating system has been developed for cooking, which can improve the quality of life of people in need and reduce traditional energy consumption. The environmental

changes (ambient temperature and water) in the kitchen using solar energy are given in Figure 8 (Arenas, 2007).

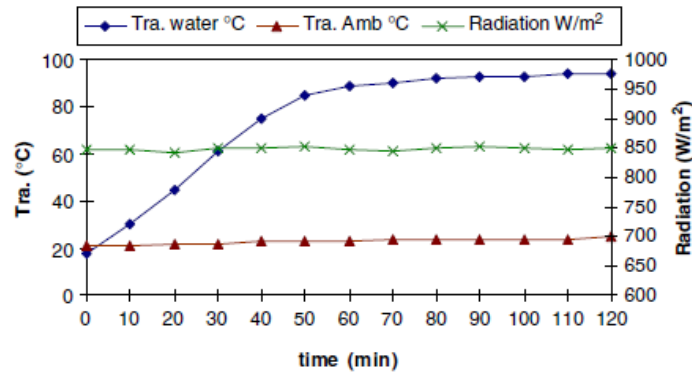


Figure 8. Variation of ambient temperature and water in the kitchen using solar energy (Arenas, 2007).

Methods

Two different innovative prototypes using hydrogen and biogas as clean energy sources for commercial kitchens have been developed with R&D systematics. Original designs were made for two different prototypes. In line with the standards for the long-term use of commercial kitchen products, the main bodies of the prototypes are made of stainless steel materials.

Original designs of various equipment (burner, injector, burner head, etc.) constituting the combustion unit of the hydrogen using commercial cooker developed specifically for the design were made. During the design verification phase, simulation studies were carried out according to various parameters, and a unique burner structure was obtained according to various hole diameters and numbers, especially on the burner head in the use of hydrogen. The commercial kitchen cooker using hydrogen is shown in Figure 9.



Figure 9. The image of the prototype of the commercial kitchen cooker using hydrogen (a) front view, (b) top view.

The photograph of the commercial cooker prototype using biogas is given in Figure 10. Food waste has been evaluated for the operation of the environmentally friendly system.

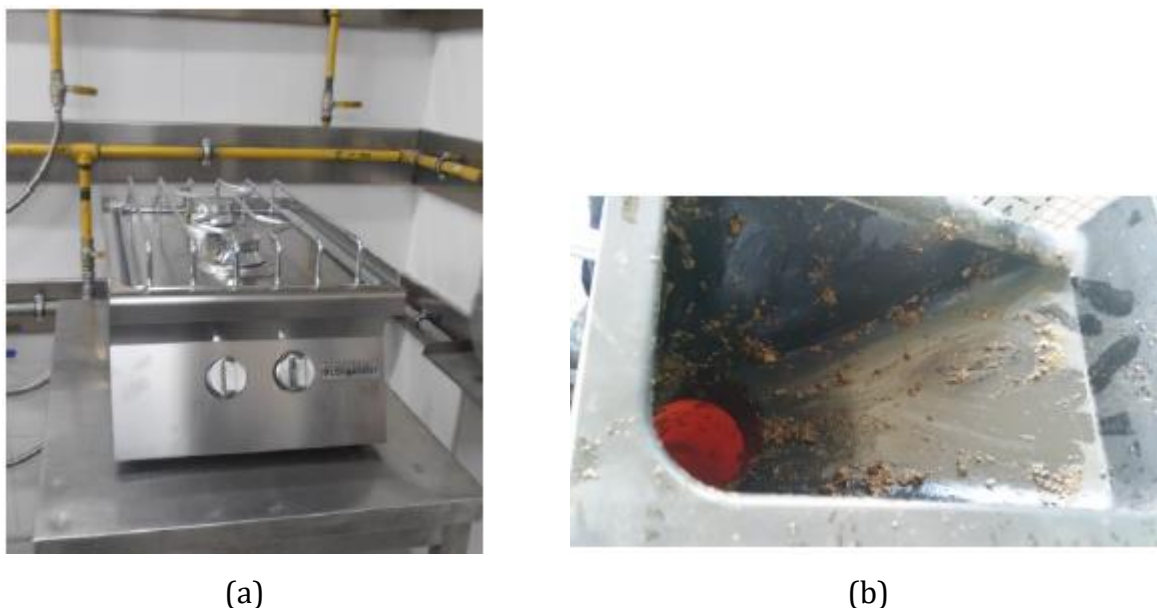


Figure 10. Photograph of the commercial cooking cooker prototype using biogas (a) front view, (b) input of food waste into the system.

After the test and evaluation stages, it has been achieved to obtain innovative prototypes (hydrogen and biogas) using two different green energy in the commercial kitchen area.

Conclusion

In this study, evaluations were made regarding the use of renewable energy (hydrogen, biogas, solar energy, wind energy, etc.) for various products in commercial kitchens and various studies to be carried out in the future. Innovative prototypes with original designs have been developed with activities based on R&D systematics, especially for commercial kitchen cooking products that use hydrogen and biogas from renewable energy sources. With the data in the test and evaluation stages, it has been achieved to use renewable energy sources effectively and efficiently in innovative prototypes. It has been provided with scientific data on innovative prototypes that can be used as alternative energy of green energy sources for commercial kitchens. In addition to the reduction of unit cooking times of hydrogen energy, significant gains have been achieved in terms of energy efficiency.

In the commercial kitchen sector, within the scope of the development of the green kitchen concept against fossil fuels, the production of innovative products using clean energy (hydrogen, biogas) has been achieved through activities based on the R&D system.

Acknowledgement

This study was prepared from the project studies numbered 3120882 and 3160502 within the scope of TÜBİTAK-TEYDEB 1501 coded Industry Research Technology Development and Innovation Projects Support Program. We would like to thank TÜBİTAK-TEYDEB Transport, Defense, Energy and Textile Technologies Group (USETEG) for their contribution to the project.

References

- Amin, M., Shah, H.H., Fareed, A.G., Khan, W.U., Chung, E., Zia, A., Farooqi, Z.U.R., Lee, C. (2022). Hydrogen production through renewable and nonrenewable energy processes and their impact on climate change. *International journal of hydrogen energy*, (47), 33112-33134.
- Ang, T-Z., Salem, M., Kamarol, M., Das, H.S., Nazari, M.A., Prabakaran, N.A. (2022). A comprehensive study of renewable energy sources: Classifications, challenges and suggestions. *Energy Strategy Reviews*, (43), 100939.
- Arenas, J.M. (2007). Design, development and testing of a portable parabolic solar kitchen. *Renewable Energy*, (32), 257–266.
- Hailemariam, A., Ivanovski, K., Dzhumashev, R. (2022). Does R&D investment in renewable energy technologies reduce greenhouse gas emissions?. *Applied Energy*, (327), 120056.
- Ilechukwu, N. & Lahiri, S. (2022). Renewable-energy consumption and international trade. *Renewable Energy*, (8), 10624–10629.
- Jaiswal, K.K., Chowdhury, C. R., Yadav, D., Verma, R., Dutta, S., Jaiswal, K.S., SangmeshB, Karuppasamy, K.S.K. (2022). Renewable and sustainable clean energy development and impact on social, economic, and environmental health. *Energy Nexus*, (7), 100118.
- Li, J. (2021). Insights into cooking sources in the context of sustainable development goals. *Sustainable Production and Consumption*, (26), 517–531.
- Nazir, M.S., Bilal, M., Sohail, H.M., Liu, B., Chen, W., Iqbal, H.M.N. (2020). Impacts of renewable energy atlas: Reaping the benefits of renewables and biodiversity threats. *International journal of hydrogen energy*, (45), 22113-22124.
- Olabi, A.G., Abdelkareem, M.A. (2022). Renewable energy and climate change. *Renewable and Sustainable Energy Reviews*, (158), 112111.
- Overland, I., Juraev, J., Vakulchuk, R. (2022). Are renewable energy sources more evenly distributed than fossil fuels?. *Renewable Energy*, (200), 379-386.
- Pingkuo, L., Xue, H. (2022). Comparative analysis on similarities and differences of hydrogen energy development in the World's top 4 largest economies: A novel framework. *International journal of hydrogen energy*, (47), 9485-9503.
- Razi, F. & Dincer, I. (2022). Renewable energy development and hydrogen economy in MENA region: A review. *Renewable and Sustainable Energy Reviews*, (168), 112763.
- Shrestha, A., Mustafa, A.A., Htike, M.M., You, V., Kakinaka, M. (2022). Evolution of energy mix in emerging countries: Modern renewable energy, traditional renewable energy, and non-renewable energy. *Renewable Energy*, (199), 419–432.
- Wang, H., Zhao, X., Zhang, K., Wang, W. (2022), Economic assessment of a renewable energy-electricity-hydrogen system considering environmental benefits. *Sustainable Production and Consumption*, (33), 903–920.

Yang, Q-C., Zheng, M., Chang, C-P. (2022). Energy policy and green innovation: A quantile investigation into renewable energy. *Renewable Energy*, (189), 1166-1175.

Yang, Z., Zhang, M., Liu, L., Zhou, D. (2022). Can renewable energy investment reduce carbon dioxide emissions? Evidence from scale and structure. *Energy Economics*, (112), 106181.

References

- Amin, M., Shah, H.H., Fareed, A.G., Khan, W.U., Chung, E., Zia, A., Farooqi, Z.U.R., Lee, C. (2022). Hydrogen production through renewable and nonrenewable energy processes and their impact on climate change. *International journal of hydrogen energy*, (47), 33112-33134.
- Ang, T-Z., Salem, M., Kamarol, M., Das, H.S., Nazari, M.A., Prabakaran, N.A. (2022). A comprehensive study of renewable energy sources: Classifications, challenges and suggestions. *Energy Strategy Reviews*, (43), 100939.
- Arenas, J.M. (2007). Design, development and testing of a portable parabolic solar kitchen. *Renewable Energy*, (32), 257–266.
- Hailemariam, A., Ivanovski, K., Dzhumashev, R. (2022). Does R&D investment in renewable energy technologies reduce greenhouse gas emissions?. *Applied Energy*, (327), 120056.
- Ilechukwu, N. & Lahiri, S. (2022). Renewable-energy consumption and international trade. *Renewable Energy*, (8), 10624–10629.
- Jaiswal, K.K., Chowdhury, C. R., Yadav, D., Verma, R., Dutta, S., Jaiswal, K.S., SangmeshB, Karuppasamy, K.S.K. (2022). Renewable and sustainable clean energy development and impact on social, economic, and environmental health. *Energy Nexus*, (7), 100118.
- Li, J. (2021). Insights into cooking sources in the context of sustainable development goals. *Sustainable Production and Consumption*, (26), 517–531.
- Nazir, M.S., Bilal, M., Sohail, H.M., Liu, B., Chen, W., Iqbal, H.M.N. (2020). Impacts of renewable energy atlas: Reaping the benefits of renewables and biodiversity threats. *International journal of hydrogen energy*, (45), 22113-22124.
- Olabi, A.G., Abdelkareem, M.A. (2022). Renewable energy and climate change. *Renewable and Sustainable Energy Reviews*, (158), 112111.
- Overland, I., Juraev, J., Vakulchuk, R. (2022). Are renewable energy sources more evenly distributed than fossil fuels?. *Renewable Energy*, (200), 379-386.
- Pingkuo, L., Xue, H. (2022). Comparative analysis on similarities and differences of hydrogen energy development in the World's top 4 largest economies: A novel framework. *International journal of hydrogen energy*, (47), 9485-9503.
- Razi, F. & Dincer, I. (2022). Renewable energy development and hydrogen economy in MENA region: A review. *Renewable and Sustainable Energy Reviews*, (168), 112763.
- Shrestha, A., Mustafa, A.A., Htike, M.M., You, V., Kakinaka, M. (2022). Evolution of energy mix in emerging countries: Modern renewable energy, traditional renewable energy, and non-renewable energy. *Renewable Energy*, (199), 419–432.
- Wang, H., Zhao, X., Zhang, K., Wang, W. (2022), Economic assessment of a renewable energy-electricity-hydrogen system considering environmental benefits. *Sustainable Production and Consumption*, (33), 903–920.

Yang, Q-C., Zheng, M., Chang, C-P. (2022). Energy policy and green innovation: A quantile investigation into renewable energy. *Renewable Energy*, (189), 1166-1175.

Yang, Z., Zhang, M., Liu, L., Zhou, D. (2022). Can renewable energy investment reduce carbon dioxide emissions? Evidence from scale and structure. *Energy Economics*, (112), 106181.

Evaluation of Grapefruit Peel Extract for Control of *Meloidogyne Incognita* on Tomato

Fatma Gül GÖZE ÖZDEMİR¹

INTRODUCTION

Plants in the genus produce Citrus fruits, including important crops such as oranges, mandarins, lemons, grapefruits, pomelos, and limes. Citrus are a group of fruits that are widely produced and consumed around the world. Around 98 million tons of citrus fruits were produced in the world in 2021, 7 million tons of which was grapefruit production (USDA, 2021). Citrus fruits can be consumed fresh or processed and used as additives in fruit juices, jams, carbonated beverages and food products. Its consumption has also increased in recent years due to its potential benefits associated with antioxidant, anticancer and anti-inflammatory properties (Benavente-García ve Castillo 2008; Dosoky ve Setzer, 2018). These properties make citrus essential oils and compounds a potential and valuable alternative for the pharmaceutical and food industries. Large-scale consumption and processing of citrus fruits results in the production of large volumes of citrus peel, which is often disposed of as agro-industrial waste. Fruit peels can be used positively for oil production. However, industrial processing increases the value of citrus fruits by producing various seconder products (pectin, pulp and flavonoids etc.) (Ahmed vd., 2019). Citrus essential oils contain compounds rich in monoterpene and sesquiterpene hydrocarbons as well as their oxygenated derivatives (González-Mas vd., 2019). It has been reported that some compounds in the monoterpenoid group cause significant inhibition of acetylcholinesterase activity, thus affecting the nervous system of nematodes (Saad vd., 2018). In addition, different researchers have determined the nematicidal effects of citrus extracts on plant parasitic nematodes (Oyedunmade vd., 2001; Oyedunmade, 2004; Abolusoro vd., 2010). Limonene, linalool, citronellal and citral compounds found in most Citrus plants are among the monoterpenes (Liu vd., 2022).

The most common root-knot nematode species in vegetable growing areas in the world and in Türkiye are *Meloidogyne incognita* (Kofoid ve White, 1919) Chitwood, 1949 (Tylenchida: Meloidogyidae), *Meloidogyne javanica* (Treub, 1885) Chitwood, 1949, *Meloidogyne arenaria* (Neal, 1889) Chitwood, 1949, and *Meloidogyne hapla* Chitwood, 1949 (Adam vd., 2007; Uysal vd., 2017; Gürkan vd., 2019; Ghaderi ve Karsen, 2020; Maleita vd., 2021). *Meloidogyne incognita* is the most common species among root knot nematodes, it can infect almost all plants and causes significant economic damage in all subtropical-tropical regions (Hallmann ve Kiewnick, 2018; Eder vd., 2021). Root-knot nematodes feed on roots and vascular tissues, disrupt water and nutrient flow, and show symptoms such as stunning, slow growth, yellowing of leaves, wilting and early plant death in infected plants (Asaturova vd., 2022). It is seen that mostly nematicide-effective chemicals are used in the control of root-knot nematodes (Hajihassani vd., 2022). Although nematicides can effectively

¹ Dr. Öğr. Üyesi, Isparta Uygulamalı Bilimler Üniversitesi, Ziraat Fakültesi, Bitki Koruma Bölümü, Orcid: 0000-0003-1969-4041

suppress nematodes, their use is limited due to their short-term effects. In addition, high costs, adverse health and environmental hazards, residue, negative effects on soil fauna and beneficial microflora, and phytotoxic effects on plants are other factors limiting the use of nematicides (Haydock vd., 2013; da Silva vd., 2019). This situation has made it necessary to search for alternative control methods for the control of plant parasitic nematodes. Plant extracts are inexpensive and readily available compared to conventional nematicides and are considered environmentally safe (Abolusoro vd., 2010). Natural plant products are currently the focus of research efforts due to their ability to produce chemicals that are less harmful to the environment and more effective (Javed vd., 2006). Many plants have nematicidal properties in their roots, shoots, leaves, flowers, seeds and extracts, essential oils, oilseed cake and derivatives (Regaieg vd., 2017).

Grapefruit (*Citrus paradisi*) contains various phytochemicals such as flavonoids (naringin), carotenoids, limonoids, organic acids, pectin and folate, and it is known that grapefruit has health-protecting properties thanks to these phytochemicals (Girenavar vd., 2008; Vikram vd., 2010; Uckoo vd., 2011). The single and combined treatments of aqueous extracts of the peels of lemon, orange, grapefruit and pomegranate fruits were investigated on the mortality effect on *M. incognita* second stage juveniles (J2s) and the nematostatic effects on hatching (Göze Özdemir, 2022). The mortality effect of only the aqueous extracts of grapefruit peel on J2s was found to be 63.7% after 24 hours, and 99.0% after 48 hours *in vitro*. In addition, the percentage of suppression of the hatching of *M. incognita* 7 days after the application of the aqueous extract of grapefruit peel was reported as 54.2%. It was determined that the nematicidal effect increased in combinations of grapefruit with other fruit peels (Göze Özdemir, 2022). It is seen that studies on the use of fruit wastes or fruit peels against plant parasitic nematodes are quite scarce (Ashraf ve Khan, 2008; Tsai, 2008, Ismail, 2015; Akhtar vd., 2019). In the control of root-knot nematodes, direct mixing of fruit peels into the soil or using their extracts can provide multi-faceted benefits with both waste management and reduction of pesticide use. In present study, the effect of direct mixing of grapefruit peels into the soil and application of aqueous extract on *M. incognita* gall and egg masses was investigated.

MATERIALS AND METHODS

Fruit Peel Extraction

Five kg of grapefruit s were peeled and the peels were cut into small pieces of about 0.25 cm². It was sun-dried on paper for 3 days and powdered in an herbal spice grinder. It has been used in application to be mixed directly into the soil. To prepare the aqueous extract, 100 g of powdered fruit peel was weighed and 400 ml of sterilized distilled water was added to it. This mixture was then stirred at room temperature for 24 hours using a magnetic stirrer. Twenty-four hours later, it was filtered through Whatman No.41 filter paper and the extracts were pooled and concentrated under vacuum at 40 °C. This filtrate was used as 100% concentration and diluted with distilled water to obtain other concentrations (10%, 25% and 50%). It was then covered and stored in the bottles in a refrigerator at +4 °C until the experiment was set up (Regaieg vd., 2017).

Nematode Inoculum

In the study, *M. incognita* isolate, which is kept in Tuezta F1 tomato cultivars and renewed every 2-3 months, was used in the climate room conditions (24±1 °C, 60%±5% RH) of ISUBU Faculty of Agriculture, Department of Plant Protection (Göze Özdemir vd., 2022).

In order to obtain *M. incognita* J2s, 2 of the galled tomato roots were selected and sterilization was carried out containing 0.5% sodium hypochlorite for 3 minutes and washed 3 times with sterile water. The egg masses were removed from these roots with the help of forceps and scalpel under a stereomicroscope and incubated for 5 days at 28°C in a 9 cm petri dish containing distilled water (Misiha vd., 2013). At the end of the five days, the hatched J2s were settling for 6 hours after taking a tape measure. Then, by counting under the light microscope, the inoculums were prepared in eppendorf tubes with 1000 J2 per pot and stored at 4°C in the refrigerator until the experiment was established.

Effect of Application of Grapefruit Peel Extracts to Tomato Roots on The Development of *Meloidogyne incognita*

Varied concentrations of dry powder (3.0, 6.0 and 9.0 g/1 kg soil) and aqueous extracts (undiluted, diluted concentration 10%, 25% and 50%) from grapefruit peels as a soil amendment were investigated on *M. incognita* in Tuezta F1 tomato cv. Four-week-old tomato seedlings of tomato were transplanted into 15-cm-diameter pots containing 1 kg of sterile soil mixture (% 68 sand, % 21 silt and %11 clay). Only plants treated with nematodes were used as a control. Five replicated pots per treatment were used. The 1000 J2s were used in the nematode inoculum. Two days after nematode inoculation, different rates of powdery extracts were incorporated into the soil by sprinkling it over the soil around the plant. Fifty millilitre of aqueous extract was measured and applied to each of the pots using the various concentrations obtained. After six weeks, plants were carefully removed and the roots were excised from the shoot and washed under tap water. Then, galls and egg masses in roots were counted under the binocular stereo microscope. Evaluation was made according to the 0-5 root gall index where 0 = no galls, 1 = slight infection, 2 = moderate infection, 3 = moderately severe, 4 = severe, 5 = very severe (Regaieg, 2011).

SPSS (version 20.0) program was used for statistical analysis of the data obtained as a result of the experiment, and analysis of variance (ANOVA) was performed to test the differences between the means. Means were compared with the Tukey HSD test at $P \leq 0.05$.

RESULT and DISCUSSION

The highest number of galls (74.8) and egg masses (72.8) were found in the control. It was determined that powder and aqueous extract treatments of grapefruit decreased galls and egg masses significantly when compared to the control. While the number of galls in the treatments varied between 13.0 and 74.8, the number of egg masses varied between 12.4-72.8. In powder treatments, the number of gall and egg mass decreased as the amount added to the soil increased. The highest number of galls and egg masses was found in 3 g/kg soil powder treatment, while the lowest was found in 9 g/kg soil. In the treatment of aqueous extract, it was observed that the suppressive effect on the gall and egg mass decreased as the dilution increased. There was no statistically significant difference between the mean of galls and egg masses of undiluted concentration (100%) and 10% diluted concentration treatments. The effects of 25% and 50% diluted aqueous extract treatments on gall and egg masses were found to be similar. The lowest number of gall and egg masses was determined in of 9 g/kg soil powder treatment, undiluted and 10% diluted aqueous extract treatments (Table 1).

The gall index of the treatments varied between 2.8 and 4.0. The highest gall index were determined in 25% and 50% concentration aqueous extract and control treatments and there was no statistical difference between them. The gall index of undiluted and 10% diluted concentration treatments was found to be lower than 25% and 50% treatments. There is no statistical difference

between the gall index of the powder application doses and undiluted and 10% diluted aqueous extract treatments (Table 1).

Table 1. The effects of grapefruit peel powder and aqueous extract treatments on the development of *Meloidogyne incognita* on tomato

Treatments		The number of galls	The number of egg masses	Gall index*
		Mean±Standard error**		
Powder	3 g/ kg soil	27,0±2,4 bc	26,4±2,1 bc	3,2±0,2 b
	6 g/ kg soil	17,4±1,5 cd	16,2±1,3 cd	3,0±0,0 b
	9 g/ kg soil	14,0±1,7 d	13,0±1,4 d	2,8±0,2 b
Aqueous extract	%100	13,0±1,2 d	12,4±1,3 d	2,8±0,2 b
	%10	15,4±2,2 d	15,0±2,0 d	2,8±0,2 b
	%25	30,0±2,2 b	28,8±2,2 b	3,4±0,2 ab
	%50	38,0±3,1 b	37,2±3,0 b	4,0±0,0 a
	Control	74,8±4,0 a	72,8±4,0 a	4,0±0,0 a

*Gall index (0-5) index (Regaieg 2011); where 0 = no galls, 1 = slight infection, 2 = moderate infection, 3 = moderately severe, 4 = severe, 5 = very severe.

**Lowercase letters shown in the same column indicate statistical differences between treatments ($P \leq 0.05$)

Treatment of powder or undiluted aqueous extract of grapefruit peels was found to suppress galls and egg masses on tomato compared to control. It appears to be promising in root knot nematode control. The decrease in nematode infections is due to the toxicity of secondary products caused by the degradation of plant extracts in the soil and changes in the physical and chemical properties of the soil (Kayani vd., 2012). In some studies conducted with the essential oil of citrus peels, the main components were found to be limonene, neral, geranial, geranyl acetate and geraniol (Chutia vd., 2009; Goyal vd., 2021). Nematicidal and nematotoxic monoterpenes are reported as anethole, citral, carvacrol, cymene, cineole, eugeneol, geraniol, limonene, pinene, terpineol and thymol (Liu vd., 2022). Regieg vd. (2017) reported that pomegranate powder extract was more toxic than aqueous extract. However, when the gall indexes are evaluated in this study, there is no difference between powder and aqueous extract treatments of grapefruit peel. This may be due to the difference in nematicidal compounds in pomegranate and grapefruit. Viuda-Martos vd. (2010) stated that the variety, cultivar, age, growing conditions and storage method of the plants may change the amount and efficacy of active compounds. Tsai (2008) reported that pulpified peels of lemon, orange, and grapefruit kept in the refrigerator for one week showed strong nematicidal activity as compared to extracts of fresh peels. There were significant differences in physicochemical, antioxidant properties and volatile profiles of extracted juice and oil extracted from eight grapefruit cultivars (Ahmed vd., 2019).

It was observed that the efficiency increased as the dose increased in powder treatments, while the dilution of more than 10% decreased the efficiency in the aqueous extract treatment in the study. Manju ve Sankari Meena (2015) found that the efficacy of botanicals increased with increasing doses, and generally higher dose was more effective in improving plant growth characteristics, reducing root-knot index and final soil nematode population. Ismail (2015) found

that nematode parameters showed a greater percentage reduction when higher rates of pomegranete peels were used.

This study shows that powder and aqueous extract of grapefruit can be applied to suppress root-knot nematode *Meloidogyne incognita* populations. When using only the aqueous extract, care should be taken not to dilute more than 25%. However, it is necessary to verify the nematicidal activity in field conditions as well.

The use of agro-industrial wastes for nematode control is important not only to provide an alternative to chemical nematicides, but also to assist in the disposal of agro-industrial wastes. In organic and sustainable agriculture, mixing organic wastes with soil has an important in suppressive soil formation. In this way, positive effects are obtained on beneficial soil microorganisms. For this reason, it is thought that it can also take part in the integrated control. Combining different methods in the integrated control is necessary in order to increase the success of nematode control.

REFERENCE

- Abolusoro, S. A., Oyedunmade, E. A., Olabiyi, T. I. (2010). Evaluation of sweet orange peel aqueous extract (*Citrus sinensis*) as root-knot nematode suppressant. *Agro Science*, 9(3):170-175.
- Adam, M. A. M., Phillips, M. S., Blok, V. C. (2007). Molecular diagnostic key for identification of single juveniles of seven common and economically important species of root-knot nematode (*Meloidogyne* spp.). *Plant Pathology*, 56: 190-197.
- Ahmed, S., Rattanpal, H. S., Gul, K., Dar, R. A., Sharma, A. (2019). Chemical composition, antioxidant activity and GC-MS analysis of juice and peel oil of grapefruit varieties cultivated in India. *Journal of Integrative Agriculture*, 18(7), 1634-1642.
- Akhtar, W., Abbasi, M.W., Rauf, A., Jahan, I, Anis, M., Javed Zaki M. (2019). Nematicidal activity of fruit pericarps against root knot nematode, *Meloidogyne javanica*. *International Biology Research*, 7(1): 57-65.
- Asaturova, A. M., Bugaeva, L. N., Homyak, A. I., Slobodyanyuk, G. A., Kashutina, E. V., Yasyuk, L. V., Garkovenko, A. V. (2022). *Bacillus velezensis* Strains for protecting cucumber plants from root-knot nematode *Meloidogyne incognita* in a greenhouse. *Plants*, 11(3): 275.
- Ashraf, M.S., Khan, T.A. (2008). Bio-management of reniform nematode, *Rotylenchulus reniformis* by fruit wastes and *Paecilomyces lilacinus* on chickpea. *World Journal of Agriculture Sciences*, 4(4): 492-494.
- Benavente-Garcia, O., Castillo, J. (2008). Update on uses and properties of citrus flavonoids: new findings in anticancer, cardiovascular, and anti-inflammatory activity. *Journal of agricultural and food chemistry*, 56(15): 6185-6205.
- Chutia, M., Bhuyan, D.P., Pathak, M.G., Sarma, T.C., Boruah. P. (2009). Antifungal activity and chemical composition of *Citrus reticulata* Blanco essential oil against phytopathogens from North East India. *Food Science Technology*, 42(3):777-780.
- da Silva, M. N., Pintado, M. E., Sarmiento, B., Stamford, N. P., Vasconcelos, M. W. (2019). A biofertilizer with diazotrophic bacteria and a filamentous fungus increases *Pinus pinaster* tolerance to the pinewood nematode (*Bursaphelenchus xylophilus*). *Biological Control*, 132: 72-80.
- Dosoky, N. S., Setzer, W. N. (2018). Biological activities and safety of *Citrus* spp. essential oils. *International journal of molecular sciences*, 19(7): 1966.
- Eder, R., Consoli, E., Krauss J., Dahlin, P. (2021). Polysulfides applied as formulated garlic extract to protect tomato plants against the root-knot nematode *Meloidogyne incognita*. *Plants*, 10 (2): 394-494.
- Ghaderi, R., Karssen, G. (2020). An updated checklist of *Meloidogyne* Göldi, 1887 species, with a diagnostic compendium for second-stage juveniles and males. *Journal of Crop Protection*, 9(2): 183-193.
- Girenavar, B., Cepeda, M. L., Soni, K. A., Vikram, A., Jesudhasan, P., Jayaprakasha, G. K., Patil, B. S. (2008). Grapefruit juice and its furocoumarins inhibits autoinducer signaling and biofilm formation in bacteria. *International journal of food microbiology*, 125(2): 204-208.

González-Mas, M. C., Rambla, J. L., López-Gresa, M. P., Blázquez, M. A., Granell, A. (2019). Volatile compounds in citrus essential oils: A comprehensive review. *Frontiers in Plant Science*, 10: 12.

Goyal, L., Kaushal, S., Dhillon, N. K., Heena. (2021). Nematicidal potential of *Citrus reticulata* peel essential oil, isolated major compound and its derivatives against *Meloidogyne incognita*. *Archives of Phytopathology and Plant Protection*, 54(9-10): 449-467.

Göze Özdemir, F. G. (2022). Use of Lemon, Orange, Grapefruit and Pomegranate Fruit Peels Against *Meloidogyne incognita* (Kofoid and White, 1919) Chitwood, 1949. *The Journal of Graduate School of Natural and Applied Sciences of Mehmet Akif Ersoy University*, 13(2): 221-228.

Göze Özdemir, F. G., Tosun, B., Şanlı, A., Karadoğan, T. (2022). Nematotoxic activity of some Apiaceae essential oils against *Meloidogyne incognita* (Kofoid & White, 1919) Chitwood, 1949 (Nematoda: Meloidogynidae). *Journal of Agricultural Faculty of Ege University*, 59(3): 529-539.

Hajihassani, A., Marquez, J., Woldemeskel, M., Hamidi, N. (2022). Identification of Four Populations of *Meloidogyne incognita* in Georgia, United States, Capable of Parasitizing Tomato-Bearing Mi-1.2 Gene. *Plant Disease*, 106(1): 137-143.

Hallmann, J., Kiewnick, S. (2018). Virulence of *Meloidogyne incognita* populations and *Meloidogyne enterolobii* on resistant cucurbitaceous and solanaceous plant genotypes. *Journal of Plant Diseases and Protection*, 125 (4): 415-424.

Haydock, P. P. J., Woods, S. R., Grove, I. G., Hare, M. C. (2013). Chemical control of nematodes. In: *Plant nematology*. R. N. Perry and M. Moens, (eds.), Wallingford, CABI Publishing, 459-479.

Ismail, A.E. (2015). Management of root knot nematode *Meloidogyne javanica* on tomato by dry crushed pomegranate *Punica granatum* L. peels as a bio-fumigant in Egypt. *Archives of Phytopathology and Plant Protection*, 48: 253-258.

Javed, N., Gowen, S.R., Inam-ul-Haq, M., Abdullah, K., Shahina, F. (2006). Systemic and persistent effect of neem (*Azadirachta indica*) formulations against root-knot nematodes, *Meloidogyne javanica* and their storage life. *Crop Protection*, 26: 911–916.

Kayani, M. Z., Mukhtar, T., & Hussain, M. A. (2012). Evaluation of nematicidal effects of *Cannabis sativa* L. and *Zanthoxylum alatum* Roxb. against root-knot nematodes, *Meloidogyne incognita*. *Crop Protection*, 39, 52-56.

Liu, Z., Li, Q. X., Song, B. (2022). Pesticidal Activity and Mode of Action of Monoterpenes. *Journal of Agricultural and Food Chemistry*, 70(15): 4556-4571.

Maleita, C., Cardoso, J. M., Rusinque, L., Esteves, I., Abrantes, I. (2021). Species-specific molecular detection of the root knot nematode *Meloidogyne luci*. *Biology*, 10(8): 775. <https://doi.org/10.3390/biology10080775>

Manju P, Sankari Meena K. 2015. Antinemic properties of the botanicals. *International Journal of Security and Networks*, 6(2):125–134.

Misiha, P.K., Aly, A.Z., Mahrous, M.E., Tohamy, M.R.A. (2013). Effect of culture filterates of three *Trichoderma* species, *Fusarium solani* and *Rhizoctonia solani* on egg hatching and juvenile mortality of *Meloidogyne incognita* in vitro. *Zagazig Journal of Agricultural Research*, 40 (3): 1-9.

Oyedunmade, E.E.A (2004). Laboratory and field toxicities of the African marigold (*Tagetes erecta*) to root-knot nematodes. *The Plant Scientist*, 4 (4): 115-121.

Oyedunmade, E.E.A, Ayooke, O.F, Olabiyi, T.I (2001). Comparative efficacies of soil amendment and a synthetic nematicide on growth, yield and food components of a root-knot infected soyabean (*Glycine max.L. Merril*). *Nigerian Society of Experimental Biology*, 1: 367-371.

Regaieg H. (2011). Contribution à l'étude des champignons filamenteux associés au *Meloidogyne* spp. Sur culture de tomate en Tunisie et évaluation de leur potentiel en tant qu'agents de lutte biologique [Contribution to the study of filamentous fungi associated with *Meloidogyne* spp. on tomato crop in Tunisia and evaluation of their biocontrol potential. higher agronomic institut]. Thèse de doctorat en science agronomiques. Sousse: Institut Supérieur Agronomique de Chott Mariem; p.163.

Regaieg, H., Bouajila, M., Hajji, L., Larayadh, A., Chiheni, N., Guessmi-Mzoughi, I., Horrigne-Raouani, N. (2017). Evaluation of pomegranate (*Punica granatum* L. var. Gabsi) peel extract for control of root-knot nematode *Meloidogyne javanica* on tomato. *Archives of Phytopathology and Plant Protection*, 50(17-18): 839-849.

Saad, M. M. G., Abou-Taleb, H. K., Abdelgaleil, S. A. M. (2018). Insecticidal activities of monoterpenes and phenylpropenes against *Sitophilus oryzae* and their inhibitory effects on acetylcholinesterase and adenosine triphosphatases. *Applied Entomology and Zoology*, 53(2): 173–181.

Tsai, B.Y. (2008). Effects of peels of lemon, orange and grapefruit against *Meloidogyne incognita*. *Plant Pathology Bulletin*, 17: 195-201.

Uckoo, R. M., Patil, B. S., Jayaprakasha, G. K. (2011, September). Separation of Furocoumarins and Polymethoxyflavones from Grapefruit Byproduct Using Flash Chromatography. In *Hortscience* (Vol. 46, No. 9, pp. S318-S319).

USDA, 2021, The United States Department of Agriculture, (<http://www.usda.gov>).

Uysal, G., Söğüt, M.A., Elekçioğlu, İ.H. (2017). Identification and distribution of root-knot nematode species (*Meloidogyne* spp.) in vegetable growing areas of Lakes Region in Turkey. *Turkish Journal of Entomology*, 41 (1): 105-122.

Vikram, A., Jesudhasan, P. R., Jayaprakasha, G. K., Pillai, B. S., Patil, B. S. (2010). Grapefruit bioactive limonoids modulate *E. coli* O157: H7 TTSS and biofilm. *International journal of food microbiology*, 140(2-3), 109-116.

Viuda-Martos, M., Fernández-López, J., Pérez-Álvarez, J. A. (2010). Pomegranate and its many functional components as related to human health: a review. *Comprehensive reviews in food science and food safety*, 9(6), 635-654.

Convergence by Modified Post-Widder Operators Preserving e^{2ax} ; $a > 0$

Gülten TORUN¹

Introduction

Approximation theory is one of the main subjects in mathematics that is used by researchers. For years, many publications related to the approximation theory has made and has still being studied, too. This theory deals with the problem of approximation of continuous functions on a finite closed interval with the sequences of the linear positive operators. Linear positive operators take an important place in approximation theory, since they are monotonous operators. This property allows to proving inequalities for positive operators (Hacısalıhoğlu & Hacıyev, 1995).

Widder (1941) examined the Post-Widder operators for $f \in C(0, \infty)$ is defined by

$$P_n(f; x) = \frac{1}{n!} \left(\frac{n}{x}\right)^{n+1} \int_0^\infty t^n e^{-\frac{nt}{x}} f(t) dt, \quad (1)$$

where $n \in \mathbb{N} = \{1, 2, \dots\}$, $x \in (0, \infty)$, and these operators protect only fixed functions.

Rathore & Sing (1980) defined in the following way

$$P_n^p(f; x) := \frac{1}{(n+p)!} \left(\frac{n}{x}\right)^{n+p+1} \int_0^\infty t^{n+p} e^{-\frac{nt}{x}} f(t) dt, \quad (2)$$

where p be a fixed integer. In the case of $p = 0$, the operators (2) reduce to the operators (1). In addition, for the $p = -1$ case, the operators (2) was handled by May (1976).

Rempulska & Skorupka (2009) introduced the Post-Widder and Stancu operators preserving the function x^2 in polynomial weighted space and showed that these operators had better approximation properties than classical Post-Widder and Stancu operators.

In recent years, the Post-Widder operators preserving test functions x^r for $r \in \mathbb{N}$ have been appropriately modified to get a better approximation. The approximation properties of the modified form of the Post-Widder operators have been studied by Gupta & Agrawal (2019) and Gupta & Tachev (2022).

In addition, the several linear operators preserving the functions constantly and e^{2ax} for fixed $a > 0$ were studied by Acar, Aral & Gonska (2017), Gürel-Yılmaz, Gupta & Aral (2017), Gürel-Yılmaz, Bodur & Aral (2018), Bodur, Gürel-Yılmaz & Aral (2018), Aral, Inoan & Raşa (2019), Sofyaloğlu & Kanat (2019), Gupta & Maheshwari (2019), Sofyaloğlu & Kanat (2020), Kanat & Sofyaloğlu (2021).

¹ Dr. , Kastamonu University, Faculty of Education, Mathematics and Science Education

Sofyalioğlu & Kanat (2020) has been handled the case $p = -1$ of Post-Widder operators (2) preserving the functions constant and e^{2ax} for fixed $a > 0$. For $f \in C(0, \infty)$, they constructed the modified form of Post-Widder operators as follows

$$P_{n,\theta}^*(f; x) = \frac{1}{(n-1)!} \left(\frac{n}{\theta_n(x)} \right)^n \int_0^\infty t^{n-1} e^{-\frac{nt}{\theta_n(x)}} f(t) dt, \quad n \geq 1$$

where the function $\theta_n(x)$ is defined by

$$\theta_n(x) = \frac{n}{2a} \left(1 - e^{-\frac{2ax}{n}} \right),$$

and investigated the approximation properties of these operators.

These study is organized as follows. Firstly, Stancu type Post-Widder operators are introduced, which are a modification of the Post-Widder operators that preserve the functions constant and e^{2ax} for fixed $a > 0$. Then, uniform convergence of these modified operators for the function f on $[0, \infty)$ is examined and the convergence rate is investigated with the help of the continuity module. In addition, the Voronovskaja type asymptotic formula is obtained to examine the asymptotic behavior of these operators. Several studies were conducted on Voronovskaja type approximation for some operators by Dinlemez Kantar & Ergelen (2019), Cai, Dinlemez Kantar & Çekim (2020), Cai, Torun & Dinlemez Kantar (2021), Dinlemez Kantar & Yüksel (2022), Torun, Boyraz & Dinlemez Kantar. (2022). Finally, numerical examples and graphs are given to show the convergence of Stancu type Post- Widder operators and compared with Post Widder operators.

For $f \in C[0, \infty)$, let be defined the Stancu type Post-Widder operators as

$$G_{n,\Psi}^{\alpha,\beta}(f; x) := \frac{1}{n!} \left(\frac{n}{\Psi_n(x)} \right)^{n+1} \int_0^\infty t^n e^{-\frac{nt}{\Psi_n(x)}} f\left(\frac{nt+\alpha}{n+\beta}\right) dt, \quad (3)$$

where $n \in \mathbb{N}$, $x \in [0, \infty)$, α and β positive real numbers satisfying $0 \leq \alpha \leq \beta$. For $a > 0$, assume that operators (3) preserve the function e^{2ax} . It can be easily seen that the conditions

$$G_{n,\Psi}^{\alpha,\beta}(e^{2at}; x) = e^{2ax}$$

are satisfied. In this case, since

$$\begin{aligned} G_{n,\Psi}^{\alpha,\beta}(e^{2at}; x) = e^{2ax} &= \frac{1}{n!} \left(\frac{n}{\Psi_n(x)} \right)^{n+1} \int_0^\infty t^n e^{-\frac{nt}{\Psi_n(x)}} e^{2a\frac{nt+\alpha}{n+\beta}} dt, \quad \frac{n+\beta}{\Psi_n(x)} > 2a \\ &= \frac{e^{\frac{2a\alpha}{n+\beta}}}{n!} \left(\frac{n}{\Psi_n(x)} \right)^{n+1} \int_0^\infty t^n e^{-\frac{(n+\beta)-2a\Psi_n(x)}{(n+\beta)\Psi_n(x)} nt} dt \\ &= e^{\frac{2a\alpha}{n+\beta}} \left(\frac{n+\beta}{n+\beta-2a\Psi_n(x)} \right)^{n+1}, \end{aligned}$$

the function $\Psi_n(x)$ is obtained as follows

$$\Psi_n(x) = \frac{n+\beta}{2a} \left(1 - \left(e^{\frac{2a(x(n+\beta)-\alpha)}{n+\beta}} \right)^{\frac{-1}{n+1}} \right). \quad (4)$$

And it can be shown that $\lim_{n \rightarrow \infty} \Psi_n(x) = x$. If the function $\Psi_n(x)$ given in (4) is replaced in (3), the Stancu type Post-Widder operators take the form

$$G_n^{\alpha, \beta}(f; x) := G_{n, \Psi}^{\alpha, \beta}(f; x) = \frac{1}{n!} \left(\frac{2an}{(n+\beta) \left(1 - e^{-\frac{-2a(x(n+\beta)-\alpha)}{(n+\beta)(n+1)}} \right)} \right)^{n+1} \int_0^\infty t^n e^{-\frac{-2ant}{(n+\beta) \left(1 - e^{-\frac{-2a(x(n+\beta)-\alpha)}{(n+\beta)(n+1)}} \right)}} f\left(\frac{nt+\alpha}{n+\beta}\right) dt. \quad (5)$$

Some preliminary results

In this section, several lemmas and their results are given to prove the main theorem.

Lemma 1 Let $\Psi_n(x)$ be function given in (4). The operators (3) give the following equation

$$G_{n, \Psi}^{\alpha, \beta}(e^{\eta t}; x) = e^{\frac{\eta \alpha}{n+\beta}} \left(1 - \frac{\eta \Psi_n(x)}{n+\beta} \right)^{-(n+1)}, \quad \eta \in \mathbb{R}. \quad (6)$$

Proof: Let $f(t) = e^{\eta t}$, $\eta \in \mathbb{R}$. From the operators (3), the following equation is given by

$$\begin{aligned} G_{n, \Psi}^{\alpha, \beta}(e^{\eta t}; x) &= \frac{1}{n!} \left(\frac{n}{\Psi_n(x)} \right)^{n+1} \int_0^\infty t^n e^{-\frac{nt}{\Psi_n(x)}} e^{\eta \frac{nt+\alpha}{n+\beta}} dt \\ &= \frac{1}{n!} \left(\frac{n}{\Psi_n(x)} \right)^{n+1} e^{\frac{\eta \alpha}{n+\beta}} \int_0^\infty t^n e^{-\left(\frac{1}{\Psi_n(x)} - \frac{\eta}{n+\beta}\right) nt} dt. \end{aligned}$$

By substituting the variable $\left(\frac{1}{\Psi_n(x)} - \frac{\eta}{n+\beta}\right) nt = u$ in the integral on the right-hand side of the above equation and then using the gamma function, the proof is completed.

Lemma 2 For the test function $e_j(t) = t^j$, $j = 0, 1, 2, 3, 4$, one has the equalities as

- (i) $G_{n, \Psi}^{\alpha, \beta}(e_0(t); x) = 1,$
- (ii) $G_{n, \Psi}^{\alpha, \beta}(e_1(t); x) = \frac{n+1}{n+\beta} \Psi_n(x) + \frac{\alpha}{n+\beta},$
- (iii) $G_{n, \Psi}^{\alpha, \beta}(e_2(t); x) = \frac{(n+2)(n+1)}{(n+\beta)^2} \Psi_n^2(x) + \frac{2\alpha(n+1)}{(n+\beta)^2} \Psi_n(x) + \frac{\alpha^2}{(n+\beta)^2},$
- (iv) $G_{n, \Psi}^{\alpha, \beta}(e_3(t); x) = \frac{(n+3)(n+2)(n+1)}{(n+\beta)^3} \Psi_n^3(x) + \frac{3\alpha(n+2)(n+1)}{(n+\beta)^3} \Psi_n^2(x) + \frac{3\alpha^2(n+1)}{(n+\beta)^3} \Psi_n(x) + \frac{\alpha^3}{(n+\beta)^3},$
- (v) $G_{n, \Psi}^{\alpha, \beta}(e_4(t); x) = \frac{(n+4)(n+3)(n+2)(n+1)}{(n+\beta)^4} \Psi_n^4(x) + \frac{4\alpha(n+3)(n+2)(n+1)}{(n+\beta)^4} \Psi_n^3(x) + \frac{6\alpha^2(n+2)(n+1)}{(n+\beta)^4} \Psi_n^2(x) + \frac{4\alpha^3(n+1)}{(n+\beta)^4} \Psi_n(x) + \frac{\alpha^4}{(n+\beta)^4}.$

Proof: (i) Taking $e_j(t) = t^j$, $j = 0$ in operators $G_{n,\Psi}^{\alpha,\beta}(e_j(t); x)$, the following equation can be obtained by

$$G_{n,\Psi}^{\alpha,\beta}(e_0(t); x) = \frac{1}{n!} \left(\frac{n}{\Psi_n(x)} \right)^{n+1} \int_0^\infty t^n e^{-\frac{nt}{\Psi_n(x)}} dt.$$

If the variable $\frac{n}{\Psi_n(x)} t = u$ is changed in integral on the right side of the above equation and then gamma function is used, the following equation is obtained

$$G_{n,\Psi}^{\alpha,\beta}(e_0(t); x) = \frac{1}{n!} \left(\frac{n}{\Psi_n(x)} \right)^{n+1} \left(\frac{\Psi_n(x)}{n} \right)^{n+1} \int_0^\infty u^n e^{-u} du = \frac{1}{n!} \Gamma(n+1) = 1$$

(ii) The operators $G_{n,\Psi}^{\alpha,\beta}(e_j(t); x)$ for $j = 1$ are yielded as follows

$$\begin{aligned} G_{n,\Psi}^{\alpha,\beta}(e_1(t); x) &= \frac{1}{n!} \left(\frac{n}{\Psi_n(x)} \right)^{n+1} \int_0^\infty t^n e^{-\frac{nt}{\Psi_n(x)}} \left(\frac{nt+\alpha}{n+\beta} \right) dt \\ &= \left(\frac{n}{\Psi_n(x)} \right)^{n+1} \int_0^\infty t^{n+1} e^{-\frac{nt}{\Psi_n(x)}} dt + \frac{\alpha}{n!(n+\beta)} \left(\frac{n}{\Psi_n(x)} \right)^{n+1} \int_0^\infty t^n e^{-\frac{nt}{\Psi_n(x)}} dt. \end{aligned}$$

From (i), the value of the second sum on the right hand side of the above equation is $\frac{\alpha}{n+\beta}$. In the first integral in the above equation, by taking the variable $\frac{n}{\Psi_n(x)} t = u$ and then using the gamma function, the following equation is obtained

$$G_{n,\Psi}^{\alpha,\beta}(e_1(t); x) = \frac{n+1}{n+\beta} \Psi_n(x) + \frac{\alpha}{n+\beta}.$$

(iii) For $j = 2$, the operators $G_{n,\Psi}^{\alpha,\beta}(e_j(t); x)$ are written as follows

$$\begin{aligned} G_{n,\Psi}^{\alpha,\beta}(e_2(t); x) &= \frac{1}{n!} \left(\frac{n}{\Psi_n(x)} \right)^{n+1} \int_0^\infty t^n e^{-\frac{nt}{\Psi_n(x)}} \left(\frac{nt+\alpha}{n+\beta} \right)^2 dt \\ &= \frac{n^2}{n!(n+\beta)^2} \left(\frac{n}{\Psi_n(x)} \right)^{n+1} \int_0^\infty t^{n+2} e^{-\frac{nt}{\Psi_n(x)}} dt \\ &\quad + \frac{2n\alpha}{n!(n+\beta)^2} \left(\frac{n}{\Psi_n(x)} \right)^{n+1} \int_0^\infty t^{n+1} e^{-\frac{nt}{\Psi_n(x)}} dt \\ &\quad + \frac{\alpha^2}{n!(n+\beta)^2} \left(\frac{n}{\Psi_n(x)} \right)^{n+1} \int_0^\infty t^n e^{-\frac{nt}{\Psi_n(x)}} dt. \end{aligned}$$

In the first integral on the right side of the above equation, the variable $\frac{n}{\Psi_n(x)} t = u$ is changed and then the gamma function is used. From (i) and (ii), the following equation is found

$$G_{n,\Psi}^{\alpha,\beta}(e_2(t); x) = \frac{(n+2)(n+1)}{(n+\beta)^2} \Psi_n^2(x) + \frac{2\alpha(n+1)}{(n+\beta)^2} \Psi_n(x) + \frac{\alpha^2}{(n+\beta)^2}.$$

Similarly, the equations (iv) and (v) are proved.

Corollary 3 Let $\varphi_x^j(t) = (t-x)^j$, $j = 0, 1, 2, 4$. The central moments of the operators (3) are given below

$$G_{n,\Psi}^{\alpha,\beta}(\varphi_x^0(t); x) = 1,$$

$$G_{n,\Psi}^{\alpha,\beta}(\varphi_x^1(t); x) = \frac{(n+1)\Psi_n(x)+\alpha}{n+\beta} - x,$$

$$G_{n,\Psi}^{\alpha,\beta}(\varphi_x^2(t); x) = \frac{(n+2)(n+1)\Psi_n^2(x)+2\alpha(n+1)\Psi_n(x)+\alpha^2}{(n+\beta)^2} - 2x \frac{(n+1)\Psi_n(x)+\alpha}{n+\beta} + x^2,$$

$$G_{n,\Psi}^{\alpha,\beta}(\varphi_x^4(t); x) = \frac{(n+4)(n+3)(n+2)(n+1)\Psi_n^4(x)+4\alpha(n+3)(n+2)(n+1)\Psi_n^3(x)}{(n+\beta)^4}$$

$$+ \frac{6\alpha^2(n+2)(n+1)\Psi_n^2(x)+4\alpha^3(n+1)\Psi_n(x)+\alpha^4}{(n+\beta)^4}$$

$$- 4x \left(\frac{(n+3)(n+2)(n+1)\Psi_n^3(x)+3\alpha(n+2)(n+1)\Psi_n^2(x)+3\alpha^2(n+1)\Psi_n(x)+\alpha^3}{(n+\beta)^3} \right)$$

$$+ 6x^2 \left(\frac{(n+2)(n+1)\Psi_n^2(x)+2\alpha(n+1)\Psi_n(x)+\alpha^2}{(n+\beta)^2} \right) - 4x^3 \left(\frac{(n+1)\Psi_n(x)+\alpha}{n+\beta} \right) + x^4.$$

In addition, the following limits are obtained

$$(i) \quad \lim_{n \rightarrow \infty} nG_{n,\Psi}^{\alpha,\beta}(t - x; x) = -ax^2 \tag{7}$$

$$(ii) \quad \lim_{n \rightarrow \infty} nG_{n,\Psi}^{\alpha,\beta}((t - x)^2; x) = x^2 \tag{8}$$

$$(iii) \quad \lim_{n \rightarrow \infty} n^2G_{n,\Psi}^{\alpha,\beta}((t - x)^4; x) = 3x^4 \tag{9}$$

The uniform convergence of the operators $G_{n,\Psi}^{\alpha,\beta}$

The uniform convergence of a sequence of linear positive operators was demonstrated by Boyanov & Veselinov (1970). In the following theorem, the uniform convergence of the operators (3) for the function f on $[0, \infty)$ is investigated.

Let $C^*[0, \infty)$ denote the subspace of all continuous and real-valued functions on $[0, \infty)$ with the property that $\lim_{x \rightarrow \infty} f(x)$ exists and finite, equipped with the uniform norm.

Theorem 4 If the sequence $\{G_{n,\Psi}^{\alpha,\beta}f\}$ of the operators (3) satisfy

$$\lim_{n \rightarrow \infty} G_{n,\Psi}^{\alpha,\beta}(e^{-\nu t}; x) = e^{-\nu x}, \quad \nu = 0,1,2 \tag{10}$$

uniformly in $[0, \infty)$, then for each $f \in C^*[0, \infty)$

$$\lim_{n \rightarrow \infty} G_{n,\Psi}^{\alpha,\beta}(f; x) = f(x) \tag{11}$$

uniformly in $[0, \infty)$.

Proof: For $\nu = 0$, it becomes that $\lim_{n \rightarrow \infty} G_{n,\Psi}^{\alpha,\beta}(1; x) = 1$ from (i) of Lemma 2. Now the equation (6), and the function $\Psi_n(x)$ will be used to prove the images of $f(t) = e^{-\nu t}$ for $\nu = 1,2$ respectively,

$$G_{n,\Psi}^{\alpha,\beta}(e^{-t}; x) = e^{-\frac{\alpha}{n+\beta}} \left(1 + \frac{1}{2a} \left(1 - e^{\frac{-2a(x(n+\beta)-\alpha)}{(n+\beta)(n+1)}} \right) \right)^{-(n+1)}, \tag{12}$$

$$G_{n,\Psi}^{\alpha,\beta}(e^{-2t}; x) = e^{-\frac{2\alpha}{n+\beta}} \left(1 + \frac{1}{a} \left(1 - e^{\frac{-2a(x(n+\beta)-\alpha)}{(n+\beta)(n+1)}} \right) \right)^{-(n+1)}. \tag{13}$$

Using the Maple software to calculate the right-hand sides of the equalities (12) and (13), the following equations are obtained, respectively,

$$G_{n,\Psi}^{\alpha,\beta}(e^{-t}; x) = e^{-x} + \frac{(2a+1)e^{-x}x^2}{2n} + \frac{(2a+1)(3(2a+1)e^{-x}x^4 - 8(a+1)e^{-x}x^3 - 12e^{-x}x^2 - 24ae^{-x}x)}{24n^2} + O\left(\frac{1}{n^3}\right), \tag{14}$$

$$G_{n,\Psi}^{\alpha,\beta}(e^{-2t}; x) = e^{-2x} + \frac{2(a+1)e^{-2x}x^2}{n} + \frac{(a+1)(6(a+1)e^{-2x}x^4 - 4(a+2)e^{-2x}x^3 - 6e^{-2x}x^2 - 12ae^{-2x}x)}{3n^2} + O\left(\frac{1}{n^3}\right). \tag{15}$$

Thus, $\lim_{n \rightarrow \infty} G_{n,\Psi}^{\alpha,\beta}(e^{-vt}; x) = e^{-vx}$, $v = 0, 1, 2$ in the interval $[0; \infty)$. That, $\lim_{n \rightarrow \infty} G_{n,\Psi}^{\alpha,\beta}(f; x) = f$ for any $f \in C^*[0; \infty)$. That is, the sequence $\{G_{n,\Psi}^{\alpha,\beta}f\}$ uniformly converges in the interval $[0, \infty)$ for any $f \in C^*[0, \infty)$.

After Boyanov & Veslinov, the uniform convergence of a sequence of linear positive operators was studied by Holhoş (2010). In his work, he obtained the following theorem for a sequence of positive and linear operators.

Theorem 5 If $\{P_n\}$ is a sequence of linear positive operators from $C^*[0, \infty)$ to $C^*[0, \infty)$, then for each $f \in C^*[0, \infty)$, the following inequality is satisfied

$$\|P_n(f; x) - f(x)\|_{[0,\infty)} \leq \|f\|_{[0,\infty)} a_n + (2 + a_n)\omega^*(f, \sqrt{a_n + 2b_n + c_n}),$$

where a_n, b_n and c_n are defined as follows

$$\|P_n(1; x) - 1\|_{[0,\infty)} = a_n,$$

$$\|P_n(e^{-t}; x) - e^{-x}\|_{[0,\infty)} = b_n,$$

$$\|P_n(e^{-2t}; x) - e^{-2x}\|_{[0,\infty)} = c_n$$

and they tend to zero as n goes to infinity. The modulus of continuity ω^* is expressed by

$$\omega^*(f, \gamma) = \sup_{|e^{-t} - e^{-x}| \leq \gamma; x, t \geq 0} |f(t) - f(x)| \tag{16}$$

and this modulus has to property:

$$|f(t) - f(x)| \leq \left(1 + \frac{1}{\gamma^2} (e^{-t} - e^{-x})^2\right) \omega^*(f, \gamma), \quad \gamma > 0 \tag{17}$$

According to Theorem 5, the uniform convergence of a sequence of linear positive operators with the help of the continuity module is given with the following theorem.

Theorem 6 Let $\{G_{n,\Psi}^{\alpha,\beta} f\}$ be a sequence of linear positive operators $G_{n,\Psi}^{\alpha,\beta}: C^*[0, \infty) \rightarrow C^*[0, \infty)$. For every function $f \in C^*[0; \infty)$, the following inequality is satisfied

$$\left\| G_{n,\Psi}^{\alpha,\beta}(f; x) - f(x) \right\|_{[0,\infty)} \leq 2\omega^*(f, \sqrt{2\sigma_n + \mu_n}), \tag{18}$$

where the modulus of continuity which is defined in (16) and

$$\left\| G_{n,\Psi}^{\alpha,\beta}(e^{-t}; x) - e^{-x} \right\|_{[0,\infty)} = \sigma_n,$$

$$\left\| G_{n,\Psi}^{\alpha,\beta}(e^{-2t}; x) - e^{-2x} \right\|_{[0,\infty)} = \mu_n,$$

Here σ_n and μ_n tend to zero as n goes to infinity and the sequence $\{G_{n,\Psi}^{\alpha,\beta} f\}$ uniformly converges to f .

Proof: From (i) of Lemma 2, $\rho_n = \left\| G_{n,\Psi}^{\alpha,\beta}(1; x) - 1 \right\|_{[0,\infty)} = 0$ is obtained. To calculate σ_n and μ_n , the equalities (14) and (15) are taken, respectively,

$$\begin{aligned} \sigma_n &= \left\| G_{n,\Psi}^{\alpha,\beta}(e^{-t}; x) - e^{-x} \right\|_{[0,\infty)} = \sup_{x \in [0,\infty)} \left| G_{n,\Psi}^{\alpha,\beta}(e^{-t}; x) - e^{-x} \right| \\ &= \sup_{x \in [0,\infty)} \left| \frac{(2a+1)x^2}{2ne^x} + \frac{(2a+1)(3(2a+1)e^{-x}x^4 - 8(a+1)e^{-x}x^3 - 12e^{-x}x^2 - 24ae^{-x}x)}{24n^2} + O\left(\frac{1}{n^3}\right) \right| \\ &\leq \frac{2(2a+1)}{ne^2} + \frac{2a+1}{n^2} \left(\frac{32(2a+1)}{e^4} - \frac{9(a+1)}{e^3} - \frac{2}{e^2} - \frac{\alpha}{e} \right) + O\left(\frac{1}{n^3}\right), \\ \mu_n &= \left\| G_{n,\Psi}^{\alpha,\beta}(e^{-2t}; x) - e^{-2x} \right\|_{[0,\infty)} = \sup_{x \in [0,\infty)} \left| G_{n,\Psi}^{\alpha,\beta}(e^{-2t}; x) - e^{-2x} \right| \\ &= \sup_{x \in [0,\infty)} \left| \frac{2(a+1)x^2}{ne^{2x}} + \frac{(a+1)(6(a+1)e^{-2x}x^4 - 4(a+2)e^{-2x}x^3 - 6e^{-2x}x^2 - 12ae^{-2x}x)}{3n^2} + O\left(\frac{1}{n^3}\right) \right| \\ &\leq \frac{2(a+1)}{ne^2} + \frac{a+1}{n^2} \left(\frac{32(a+1)}{e^4} - \frac{9(a+2)}{e^3} - \frac{2}{e^2} - \frac{2\alpha}{e} \right) + O\left(\frac{1}{n^3}\right). \end{aligned}$$

As a consequence, σ_n and μ_n tend to zero as n goes to infinity. Thus, the proof of the theorem is completed.

Approximation properties of the operators $G_{n,\Psi}^{\alpha,\beta}$

In this section, firstly, the convergence rate is examined with the help of the continuity module.

Let $C_B[0, \infty)$ be the space of all bounded and uniform continuous functions f on $[0, \infty)$ endowed with the norm $\|f\|_{C_B} = \sup_{x \in [0,\infty)} |f(x)|$. For $\varepsilon > 0$, the Peetre K-functional is defined by

$$K_2(f, \varepsilon) = \inf_{g \in C_B^2[0,\infty)} [\|f - g\| + \varepsilon \|g''\|],$$

where $C_B^2[0, \infty) = \{g \in C_B[0, \infty): g', g'' \in C_B[0, \infty)\}$.

In Theorem 2.4 (De Vore & Lorentz, 1993 : 177) , there exists an absolute constant $C > 0$ such that

$$K_2(f, \varepsilon) \leq C \omega_2(f, \sqrt{\varepsilon}), \quad \varepsilon > 0 \tag{19}$$

where the function ω_2 is the second-order modulus of continuity of $f \in C_B[0, \infty)$ is given by

$$\omega_2(f, \sqrt{\varepsilon}) = \sup_{0 < h \leq \sqrt{\varepsilon}} \sup_{x, x+h, x+2h \in [0, \infty)} |f(x+2h) - 2f(x+h) + f(x)|.$$

In addition, the first-order modulus of continuity of $f \in C_B[0, \infty)$ is defined as follows

$$\omega(f, \varepsilon) = \sup_{0 < h \leq \varepsilon} \sup_{x, x+h \in [0, \infty)} |f(x+h) - f(x)|.$$

Lemma 7 For $f \in C_B[0, \infty)$, the following inequality is obtained

$$|G_{n, \Psi}^{\alpha, \beta}(f; x)| \leq \|f\|. \tag{20}$$

Proof: Taking the operators (5) and using the equation (i) of Lemma 2, it is found that

$$\begin{aligned} |G_{n, \Psi}^{\alpha, \beta}(f; x)| &= |G_n^{\alpha, \beta}(f; x)| \\ &\leq \frac{1}{n!} \left(\frac{2an}{(n+\beta) \left(1 - e^{-\frac{-2a(x(n+\beta)-\alpha)}{(n+\beta)(n+1)}}\right)} \right)^{n+1} \int_0^\infty t^n e^{-\frac{-2ant}{(n+\beta) \left(1 - e^{-\frac{-2a(x(n+\beta)-\alpha)}{(n+\beta)(n+1)}}\right)}} \left| f\left(\frac{nt+\alpha}{n+\beta}\right) \right| dt. \\ &\leq \|f\| G_{n, \Psi}^{\alpha, \beta}(1; x) = \|f\|. \end{aligned}$$

Theorem 8 For $f \in C_B[0, \infty)$, there exists a positive constant L such that

$$\left| G_{n, \Psi}^{\alpha, \beta}(f; x) - f(x) \right| \leq L \omega_2\left(f, \sqrt{\frac{\xi_{n, \Psi}^{\alpha, \beta}}{8}}\right) + \omega\left(f, \left| \frac{n+1}{2a} \left(1 - e^{-\frac{-2a(x(n+\beta)-\alpha)}{(n+\beta)(n+1)}}\right) + \frac{\alpha}{n+\beta} - x \right| \right),$$

where

$$\xi_{n, \Psi}^{\alpha, \beta} = \frac{(n+1)(2n+3)}{(n+\beta)^2} \Psi_n^2(x) + 4 \left(\frac{\alpha(n+1)}{(n+\beta)^2} - \frac{x(n+1)}{n+\beta} \right) \Psi_n(x) + \frac{2\alpha^2}{(n+\beta)^2} - \frac{4x\alpha}{n+\beta} + 2x^2.$$

Proof: Let the auxiliary operators $\tilde{G}_{n, \Psi}^{\alpha, \beta}$ from $C_B[0, \infty)$ to $C_B[0, \infty)$ be defined as

$$\tilde{G}_{n, \Psi}^{\alpha, \beta}(g; x) = G_{n, \Psi}^{\alpha, \beta}(g; x) + g(x) - g\left(\frac{n+1}{2a} \left(1 - e^{-\frac{-2a(x(n+\beta)-\alpha)}{(n+\beta)(n+1)}}\right) + \frac{\alpha}{n+\beta}\right). \tag{21}$$

From the equalities (i) and (ii) of Lemma 2 and the linearity of the operators $\tilde{G}_{n, \Psi}^{\alpha, \beta}(g; x)$,

$$\tilde{G}_{n, \Psi}^{\alpha, \beta}(t - x; x) = 0 \tag{22}$$

is obtained. Using Taylor’s expansion formula for $g \in C_B^2[0, \infty)$, it can be written as

$$g(t) = g(x) + g'(x)(t - x) + \int_x^t (t - u)g''(u)du. \tag{23}$$

Applying the auxiliary operators (21) to both sides of equation (23) and using (22), it is obtained

$$\begin{aligned} \tilde{G}_{n,\Psi}^{\alpha,\beta}(g; x) &= g(x) + \tilde{G}_{n,\Psi}^{\alpha,\beta} \left(\int_x^t (t-u)g''(u)du; x \right). \\ \left| \tilde{G}_{n,\Psi}^{\alpha,\beta}(g; x) - g(x) \right| &\leq \left| G_{n,\Psi}^{\alpha,\beta} \left(\int_x^t (t-u)g''(u)du; x \right) \right| \\ &\quad + \left| \int_x^{G_{n,\Psi}^{\alpha,\beta}(e_1; x)} (G_{n,\Psi}^{\alpha,\beta}(e_1; x) - u)g''(u)du \right| \\ &\leq \frac{\|g''\|}{2} G_{n,\Psi}^{\alpha,\beta}((t-x)^2; x) + \frac{\|g''\|}{2} \left(\frac{n+1}{2a} \left(1 - e^{-\frac{-2a(x(n+\beta)-\alpha)}{(n+\beta)(n+1)}} \right) + \frac{\alpha}{n+\beta} - x \right)^2 \\ &\leq \frac{\|g''\|}{2} \left(\left(G_{n,\Psi}^{\alpha,\beta}((t-x)^2; x) \right) + \left(G_{n,\Psi}^{\alpha,\beta}(t-x; x) \right)^2 \right) = \frac{\|g''\|}{2} \xi_{n,\Psi}^{\alpha,\beta}, \quad (24) \end{aligned}$$

where

$$\xi_{n,\Psi}^{\alpha,\beta} = \frac{(n+1)(2n+3)}{(n+\beta)^2} \Psi_n^2(x) + 4 \left(\frac{\alpha(n+1)}{(n+\beta)^2} - \frac{x(n+1)}{n+\beta} \right) \Psi_n(x) + \frac{2\alpha^2}{(n+\beta)^2} - \frac{4x\alpha}{n+\beta} + 2x^2.$$

Taking the norm of the auxiliary operators (21) and using Lemma 7, the following inequality is obtained

$$\left\| \tilde{G}_{n,\Psi}^{\alpha,\beta}(f; x) \right\| \leq 3 \|f\|, \quad f \in C_B[0, \infty). \quad (25)$$

Using the operators (21) and the inequalities (24) and (25), for every $g \in C_B^2[0, \infty)$, it can be written as

$$\begin{aligned} \left| G_{n,\Psi}^{\alpha,\beta}(f; x) - f(x) \right| &\leq \left| \tilde{G}_{n,\Psi}^{\alpha,\beta}(f-g; x) - (f-g)(x) \right| \\ &\quad + \left| f \left(\frac{n+1}{2a} \left(1 - e^{-\frac{-2a(x(n+\beta)-\alpha)}{(n+\beta)(n+1)}} \right) + \frac{\alpha}{n+\beta} \right) - f(x) \right| + \left| \tilde{G}_{n,\Psi}^{\alpha,\beta}(g; x) - g(x) \right| \\ &\leq 4 \|f-g\| + \frac{\|g''\|}{2} \xi_{n,\Psi}^{\alpha,\beta} + \left| f \left(\frac{n+1}{2a} \left(1 - e^{-\frac{-2a(x(n+\beta)-\alpha)}{(n+\beta)(n+1)}} \right) + \frac{\alpha}{n+\beta} \right) - f(x) \right|. \quad (26) \end{aligned}$$

If the infimum on the right-hand side of (26) over all the function $g \in C_B^2[0, \infty)$ is taken, then

$$\begin{aligned} \left| G_{n,\Psi}^{\alpha,\beta}(f; x) - f(x) \right| &\leq 4K_2 \left(f, \frac{\xi_{n,\Psi}^{\alpha,\beta}}{8} \right) + \omega \left(f, \left| \frac{n+1}{2a} \left(1 - e^{-\frac{-2a(x(n+\beta)-\alpha)}{(n+\beta)(n+1)}} \right) + \frac{\alpha}{n+\beta} - x \right| \right) \\ &\leq L\omega_2 \left(f, \sqrt{\frac{\xi_{n,\Psi}^{\alpha,\beta}}{8}} \right) + \omega \left(f, \left| \frac{n+1}{2a} \left(1 - e^{-\frac{-2a(x(n+\beta)-\alpha)}{(n+\beta)(n+1)}} \right) + \frac{\alpha}{n+\beta} - x \right| \right), \end{aligned}$$

where L is a positive constant. Thus, Theorem is proved.

Remark 9 Since $\lim_{n \rightarrow \infty} \xi_{n,\Psi}^{\alpha,\beta} = 0$ and $\lim_{n \rightarrow \infty} \left(\frac{n+1}{2a} \left(1 - e^{-\frac{-2a(x(n+\beta)-\alpha)}{(n+\beta)(n+1)}} \right) + \frac{\alpha}{n+\beta} - x \right) = 0$, these limits guarantees a rate of pointwise convergence of the operators $G_{n,\Psi}^{\alpha,\beta}(f; x)$ to $f(x)$.

Finally, the Voronovskaja type asymptotic formula is given to examine the asymptotic behavior of the operators (3).

Theorem 10 For each $f \in C^*[0, \infty)$ and $x \in [0, \infty)$, the following inequality is found

$$\begin{aligned} & \left| n \left(G_{n,\Psi}^{\alpha,\beta}(f; x) - f(x) \right) + ax^2 f'(x) - \frac{x^2}{2} f''(x) \right| \\ & \leq |u_n(x)| |f'(x)| + \frac{1}{2} |v_n(x)| |f''(x)| + 2(v_n(x) + x^2 + w_n(x)) \omega^* \left(f'', n^{-\frac{1}{2}} \right), \end{aligned}$$

where f', f'' exists in $C^*[0, \infty)$, and

$$u_n(x) = nG_{n,\Psi}^{\alpha,\beta}(t - x; x) + ax^2,$$

$$v_n(x) = nG_{n,\Psi}^{\alpha,\beta}((t - x)^2; x) - x^2,$$

$$w_n(x) = \left(n^2 G_{n,\Psi}^{\alpha,\beta}((e^{-t} - e^{-x})^4; x) \right)^{\frac{1}{2}} \left(n^2 G_{n,\Psi}^{\alpha,\beta}((t - x)^4; x) \right)^{\frac{1}{2}}.$$

Proof: By Taylor's formula for a function f , the following equation can be written

$$f(t) = f(x) + f'(x)(t - x) + \frac{f''(x)}{2}(t - x)^2 + r(t, x)(t - x)^2, \tag{27}$$

where the remainder $r(t, x)$ is defined by

$$r(t, x) := \frac{f''(\tau) - f''(x)}{2}, \quad x < \tau < t.$$

By applying the operators $G_{n,\Psi}^{\alpha,\beta}(f; x)$ on both sides of the equation in (27), the equality

$$\begin{aligned} G_{n,\Psi}^{\alpha,\beta}(f; x) - f(x) &= f'(x)G_{n,\Psi}^{\alpha,\beta}(t - x; x) + \frac{f''(x)}{2}G_{n,\Psi}^{\alpha,\beta}((t - x)^2; x) \\ &\quad + G_{n,\Psi}^{\alpha,\beta}(r(t, x)(t - x)^2; x) \end{aligned}$$

is obtained. Considering the Corollary 3, the following inequality can be written

$$\begin{aligned} & \left| n \left(G_{n,\Psi}^{\alpha,\beta}(f; x) - f(x) \right) + ax^2 f'(x) - \frac{x^2}{2} f''(x) \right| \\ & \leq \left| nG_{n,\Psi}^{\alpha,\beta}(t - x; x) + ax^2 \right| |f'(x)| + \frac{1}{2} \left| nG_{n,\Psi}^{\alpha,\beta}((t - x)^2; x) - x^2 \right| |f''(x)| \\ & \quad + \left| nG_{n,\Psi}^{\alpha,\beta}(r(t, x)(t - x)^2; x) \right|. \end{aligned}$$

Let $u_n(x) = nG_{n,\Psi}^{\alpha,\beta}(t - x; x) + ax^2$, and $v_n(x) = nG_{n,\Psi}^{\alpha,\beta}((t - x)^2; x) - x^2$. Then

$$\begin{aligned} & \left| n \left(G_{n,\Psi}^{\alpha,\beta}(f; x) - f(x) \right) + ax^2 f'(x) - \frac{x^2}{2} f''(x) \right| \\ & \leq |u_n(x)| |f'(x)| + \frac{1}{2} |v_n(x)| |f''(x)| + nG_{n,\Psi}^{\alpha,\beta}(|r(t, x)|(t - x)^2; x). \tag{28} \end{aligned}$$

From the equalities (7) and (8), $u_n(x)$ and $v_n(x)$ approach zero, as n goes to infinity at any point $x \in [0, \infty)$. To calculate the term $|r(t, x)|$ in the equality (28), from inequality (17),

$$|r(t, x)| \leq \left(1 + \frac{(e^{-t} - e^{-x})^2}{\gamma^2} \right) \omega^*(f'', \gamma), \quad \gamma > 0$$

can be written and here the modulus of continuity $\omega^*(f, \gamma)$ is defined in (16). Since

$$|r(t, x)| \leq \begin{cases} 2\omega^*(f'', \gamma) & , \quad |e^{-t} - e^{-x}| \leq \gamma \\ 2 \frac{(e^{-t} - e^{-x})^2}{\gamma^2} \omega^*(f'', \gamma), & |e^{-t} - e^{-x}| > \gamma \end{cases} ,$$

the inequality $|r(t, x)| \leq 2 \left(1 + \frac{(e^{-t} - e^{-x})^2}{\gamma^2} \right) \omega^*(f'', \gamma)$ is obtained.

If the Cauchy Schwarz inequality is applied to the last term in the sum on the right-hand side of (28) and $\gamma^2 = n^{-1}$ is selected, then

$$\begin{aligned} nG_{n,\Psi}^{\alpha,\beta}(|r(t, x)|(t-x)^2; x) & \leq 2n\omega^*(f'', n^{-\frac{1}{2}}) \left(G_{n,\Psi}^{\alpha,\beta}((t-x)^2; x) + nG_{n,\Psi}^{\alpha,\beta}((e^{-t} - e^{-x})^2(t-x)^2; x) \right) \\ & \leq 2\omega^*(f'', n^{-\frac{1}{2}}) \left(nG_{n,\Psi}^{\alpha,\beta}((t-x)^2; x) \right. \\ & \quad \left. + \left(n^2 G_{n,\Psi}^{\alpha,\beta}((e^{-t} - e^{-x})^4; x) \right)^{\frac{1}{2}} \left(n^2 G_{n,\Psi}^{\alpha,\beta}((t-x)^4; x) \right)^{\frac{1}{2}} \right) \\ & \leq 2(v_n(x) + x^2 + w_n(x))\omega^*(f'', n^{-\frac{1}{2}}), \end{aligned}$$

where $w_n(x) = \left(n^2 G_{n,\Psi}^{\alpha,\beta}((e^{-t} - e^{-x})^4; x) \right)^{\frac{1}{2}} \left(n^2 G_{n,\Psi}^{\alpha,\beta}((t-x)^4; x) \right)^{\frac{1}{2}}$.

Thus, the Voronovskaja type asymptotic formula is obtained.

Remark 11 Using the Maple software, the following equation is obtained

$$\lim_{n \rightarrow \infty} n^2 G_{n,\Psi}^{\alpha,\beta}((e^{-t} - e^{-x})^4; x) = 3e^{-4x}x^4.$$

In (9), it was also given that $\lim_{n \rightarrow \infty} n^2 G_{n,\Psi}^{\alpha,\beta}((t-x)^4; x) = 3x^4$.

Thus, taking into account the Remark 11, a result of Theorem 10 can be given as follows :

Corollary 12 Let $f, f', f'' \in C^*[0, \infty)$. Thus

$$\lim_{n \rightarrow \infty} n \left(G_{n,\Psi}^{\alpha,\beta}(f; x) - f(x) \right) = -ax^2 f'(x) + \frac{x^2}{2} f''(x)$$

holds for any $x \in [0, \infty)$.

Some graphical analysis

In this section, firstly, the convergence of the Stancu type Post-Widder operators $G_{n,\Psi}^{\alpha,\beta}(f; x)$ to the function $f(x) = x^3 e^{-3x}$ for different values of n, a, α and β is shown in Figure 1. It is observed that the operators $G_{n,\Psi}^{\alpha,\beta}(f; x)$ tend to the function $f(x)$ as n increases.

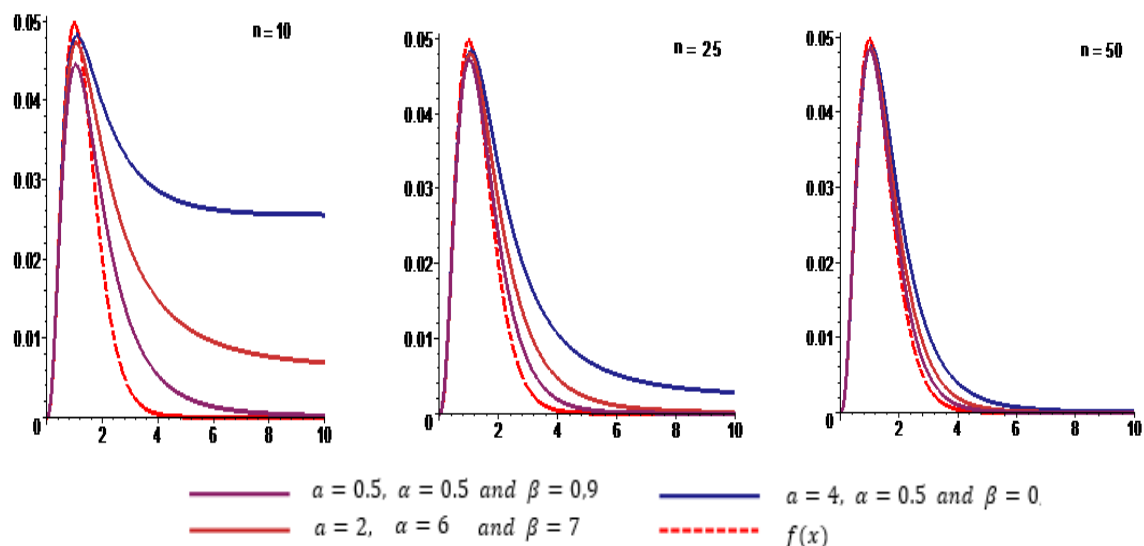


Figure 7. Convergence of $G_{n,\psi}^{\alpha,\beta}(f; x)$ for different values of n , a , α and β

Secondly, the convergence of the Post-Widder Operators $P_{n,\theta}^*(f; x)$ and the Stancu type Post-Widder Operators $G_{n,\psi}^{\alpha,\beta}(f; x)$ to the function $f(x) = x^3 e^{-3x}$ for $n = 50$, $a = 4$ and different values of α and β is shown in Figure 2.

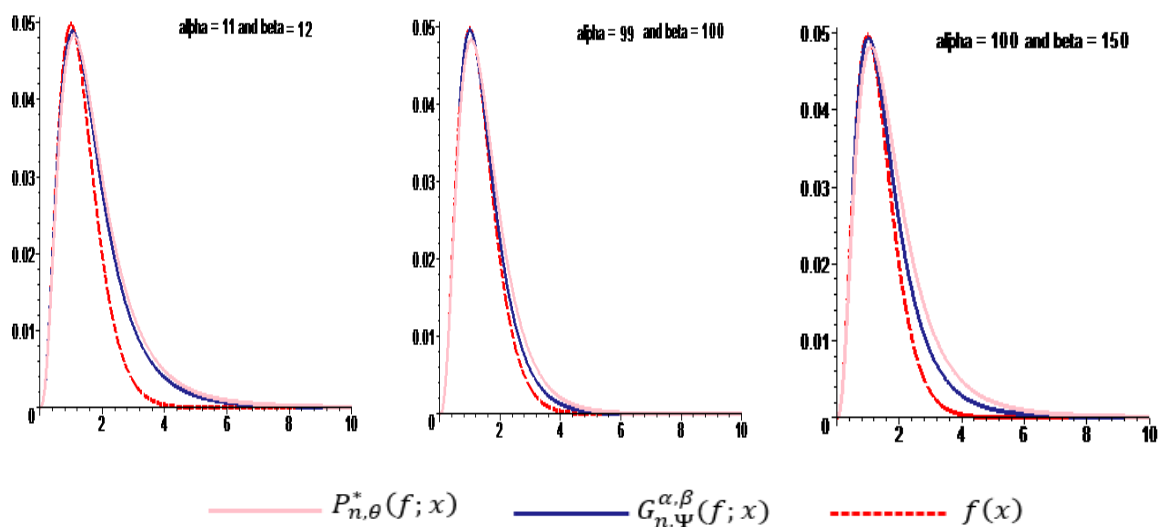


Figure 2. Convergence of $P_{n,\theta}^*(f; x)$ and $G_{n,\psi}^{\alpha,\beta}(f; x)$ to $f(x)$ for $n = 50$ and $a = 4$

References

- Acar, T., Aral, A. & Gonska, H. (2017). On Szász-Mirakyan operators preserving e^{2ax} , $a > 0$. *Mediterranean J Math*, 14(6), 1-14. Doi: 10.1007/s00009-016- 0804-7
- Aral, A., Inoan, D. & Raşa, I. (2019). Approximation properties of Szász-Mirakyan operators preserving exponential functions. *Positivity*, 23, 233-246. Doi: 10.1007/s11117-018- 0604-3
- Bodur, M., Gürel-Yılmaz, Ö. & Aral, A. (2018). Approximation by Baskakov-Szász-Stancu operators preserving exponential functions. *Constructive Mathematical Analysis*, 1(1), 1-8. Doi: 10.33205/cma.450708
- Boyanov, B.D. & Veselinov, V.M. (1970). A note on the approximation of functions in an infinite interval by linear positive operators. *Bull Math Soc Sci Math Roum*, 14(62), 9-13.
- Cai, Q.B., Dinlemez Kantar, Ü. & Çekim, B. (2020). Approximation properties for the genuine modified Bernstein-Durrmeyer-Stancu operators. *Applied Mathematics-A Journal of Chinese Universities* 35 (4), 468-478. Doi: 10.1007/s11766-020-3918-y.
- Cai, Q.B., Torun, G. & Dinlemez Kantar, Ü. (2021). Approximation properties of generalized λ -Bernstein–Stancu-type operators. *Journal of Mathematics*, Article ID 5590439, 1-17. Doi: 10.1155/2021/5590439
- DeVore, R.A. & Lorentz, G.G. (1993). *Constructive Approximation*. (177). Berlin: Springer
- Dinlemez Kantar, Ü. & Ergelen, G. (2019). A voronovskaja-type theorem for a kind of Durrmeyer-Bernstein-Stancu operators. *Gazi University Journal of Science.*, 32 (4), 1228-1236. Doi: 10.35378/gujs.513478
- Dinlemez Kantar, Ü. & Yüksel, İ. (2022). Investigating (p, q) -hybrid Durrmeyer-type operators in terms of their approximation properties. *Gazi University J. Sci. Part A: Engineering and Innovation*, 1-11. Doi: 10.54287/gujsa.1029633
- Gupta, V. & Agrawal, D. (2019). Convergence by modified Post-Widder operators. *RACSAM*, 113(2), 1475-1486. Doi: 10.1007/s13398-018- 0562-4
- Gupta, V. & Maheshwari, P. (2019). Approximation with certain Post-Widder operators. *Publications de L'Institut Mathématique*, 105(119), 131--136. Doi: 10.2298/PIM1919131G
- Gupta, V. & Tachev, G. (2022). Some results on Post-Widder operators preserving test function x^r . *Kragujevac J Math.*, 46(1), 149-165. Doi: 10.46793/KgJMat2201.149G
- Gürel-Yılmaz, Ö., Bodur, M. & Aral, A. (2018). On approximation properties of Baskakov-Schurer-Szász operators preserving exponential functions. *Filomat*, 32(15), 5433-5440. Doi: 10.2298/FIL1815433Y
- Gürel-Yılmaz, Ö., Gupta, V. and Aral, A. (2017). On Baskakov operators preserving the exponential function. *J Numer Anal Approx Theory*, 46(2), 150-161
- Hacısalıhoğlu, H. & Hacıyev, A. (1995). *Lineer Pozitif Operatör Dizilerinin Yakınsaklığı*. (31). Ankara: A.Ü.F.F. Yayınları
- Holhoş, A. (2010). The rate of approximation of functions in an infinite interval by positive linear operators. *Stud Univ Babeş-Bolyai Math.*, 55(2), 133-142.

- Kanat, K. & Sofyaloğlu, M. (2021). On Stancu type Szász-Mirakyan-Durrmeyer operators preserving e^{2ax} , $a > 0$. *Gazi University Journal of Science*, 34 (1), 196-209. Doi: 10.35378/gujs.691419
- May, C.P. (1976). Saturation and inverse theorems for combinations of a class of exponential-type operators. *Canad. J. Math*, 28(6), 1224-1250. Doi: 10.4153/CJM-1976-123-8
- Rathore, R.K.S. & Singh, O.P. (1980). On convergence of derivatives of Post-Widder operators. *Indian J. Pure Appl. Math*, 11(5), 547-561.
- Rempulska, L., & Skorupka, M. (2009). On approximation by Post-Widder and Stancu operators preserving x^2 . *Kyungpook Math J*, 49(1), 57-65. Doi: 10.5666/KMJ.2009.49.1.057
- Sofyaloğlu, M. & Kanat, K. (2019). Approximation properties of generalized Baskakov–Schurer–Szász–Stancu operators preserving e^{2ax} , $a > 0$. *Journal of Inequalities and Applications*, Article number: 112(2019). Doi: 10.1186/s13660-019-2062-2
- Sofyaloğlu, M., & Kanat, K. (2020). Approximation properties of the Post-Widder operators preserving e^{2ax} , $a > 0$. *Math Meth Appl Sci*, 43:4272-4285. Doi: 10.1002/mma.6192
- Torun, G., Boyraz, MM. & Dinlemez Kantar, Ü. (2022). Investigation of the Asymptotic Behavior of Generalized Baskakov-Durrmeyer-Stancu Type Operators. *Cumhuriyet Sci J*, 43 (1), 98-104. Doi: 10.17776/csj.1030637
- Widder, D.V. (1941). *The Laplace Transform*. Princeton Mathematical Series, New Jersey: Princeton University Press.

Experimental research of hybrid thermoset composites mechanical properties

Yunus Hüseyin Erkendirci¹
Selim Hartomacıoğlu¹
Metin Yüksek²

Introduction

In hybrid composites, it is aimed to make better the composites mechanical properties by adding more than one fiber type as a reinforcement component into the matrix phase [1-2-3-4-5]. In general, fiber-reinforced hybrid composites show higher strength and hardness and higher strength to fatigue damage and corrosion compared to metal alloys [6-7]. In hybrid composites, the matrix material can be fiber-reinforced or particle-reinforced [8-9-10-11]. They are used to produce the components that complement each other's weaknesses [12-13]. Carbon fiber has low density, tensile strength and abrasion resistance [14]. Glass fiber has high tensile strength resistance to chemicals and does not retain moisture [15] and also kevlar has low density, non-flammability and chemical resistance [16-17]. The type of fiber used as a reinforcing element in a hybrid composite is one of the important factors affecting to mechanical behavior. There are many experimental studies comparing the tension strength of hybrid and other composites, in which different fibers like carbon, glass, flax and kevlar are used as the reinforcement phase and the matrix phase is epoxy. In an experimental study conducted with hybrid and non-hybrid composites. Poyyathappan [18] concluded that fiber reinforcement materials can be listed as carbon, glass-carbon hybrid and glass, from high to low tensile strength, in accordance with the rule of mixture (ROM). Experimental study by Vinay [19] showed that carbon-kevlar hybrid composite materials have higher strength than glass-carbon hybrid composite materials. When the tension strengths of carbon, glass & glass-carbon EHC materials produced by vacuum infusion method were compared under different temperature values, it was determined better than that the tensile strength were carbon reinforced, hybrid and glass reinforced composites, respectively [20].

As can be seen from the literature review, studies on carbon fabric-glass fabric and non-woven polypropylene composites rarely used for hybridization. In this study, two different types as 5 layers (5L) and 9 layers (9L) were produced by vacuum infusion method (VARTM). As reinforcement material; In the first material (type 1) plain woven (PW), glass fabric (GF), polypropylene mat (GN) and plain woven (PW), glass fabric (CF) and thermoset epoxy resin matrix were used. The other (type 2) 2x2 twill woven (TW) carbon fabric (CF) were used like with the other fibers and also matrix being the same. Our aim is to compare how the stacking sequence and

¹ Yunus Hüseyin Erkendirci, Master Student, Marmara University, Mechanical Engineering Department Orcid: 0000-0002-7776-088X

¹ Selim Hartomacıoğlu Associate Professor, Marmara University Mechanical Engineering Department

² Professor, Marmara University Textile Engineering Department

increasing the layer numbers & hence the material thickness affect the epoxy hybrid composites mechanical properties.

In this research, as mentioned above, they were subjected to tension and other test two different types of materials mechanical properties and damage behaviour to investigate and compare. Graphs were plotted for two types of materials and tables were created from the data obtained from the experiments. Afterwards, the results were compared with each other and the effects of twill and PW carbon fabric on mechanical properties and damage behaviour were examined. The results were supported and reported with photographs and microscope images.

Materials and Experiments

Two different types of EHC laminets of 5 and 9 layers had been produced by vacuum assisted resin transfer molding method (VARTM). Carbon, nonwoven polypropilen and E-glass fibers were supplied from Metyx (Telateks) company in Turkey. Also, epoxy resin was arranged with mixing (Resin: HEXION EPIKOTE, Curing agent: MGS RIMR 135 and HEXION EPIKURE™, Hardener: MGS BPH 137 GF, (resin/ hardener ratio is %30)) supplied from the company, Metyx Turkey. The stacking sequences of Type 1 and Type 2 EHC layers was shown in Table 1.

Types Number	Material	Carbon Glass Polypropilen Nonwoven Mat
	Number of Layer	Stacking Sequence
1	5	[G/C/NW/C/G]
1	9	[G/C/G/NW/C/G/CG]
2	5	[G/CTw/NW/CTw/G]
2	9	[G/CTw/G/CTw/NW/CTw/G/CTw/G]

Table 1. EHC laminates stacking sequences.

Carbon-Glass-Polypropilen Non Woven Glass/epoxy "HEXION EPIKOTE Resin MGS RIMR 135" EHC materials (Type 1) were produced using with PW carbon, glass fabric and non woven glass (245 gr/m², 210 gr/m² and 250 gr/m²) and then were cut into (600x600 mm) sheets. Also, Carbon-Glass-Nonwoven Polypropilen, (275 gr/m², 210 gr/m² and 250 gr/m²) then they were cut into (600x600 mm) sheets as shown Fig.1. The all various panel layers types are produced with (Resin: HEXION EPIKOTE, MGS RIMR 135" (%70 mixing rate)) epoxy resin and curing Agent (HEXION EPIKURE MGS BPH 137 GF (30% mixing rate)) hardeners with vacuum assisted transfer molding process (VARTM). All EHC materials were cured at room temperature (23 °C) under 900 mBar vacuum pressure for 12 hours.

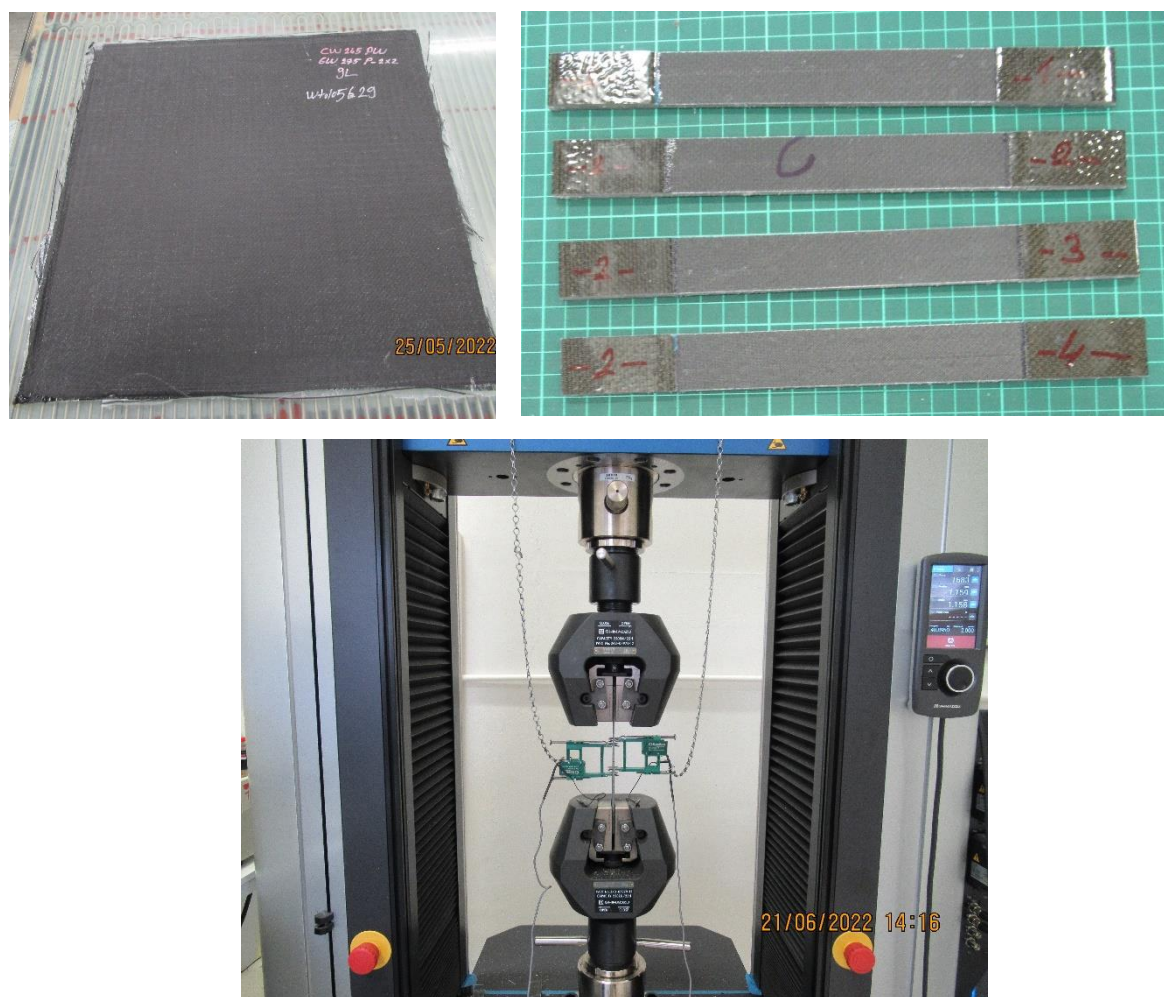


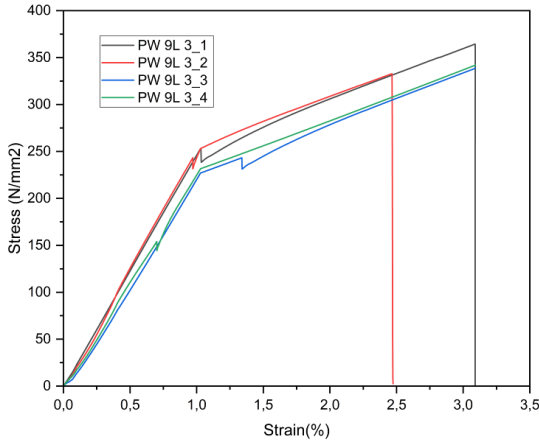
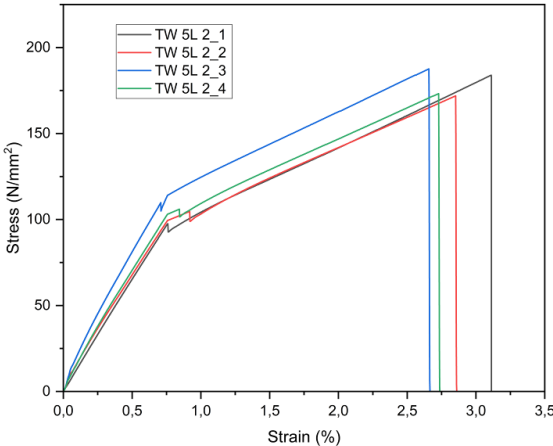
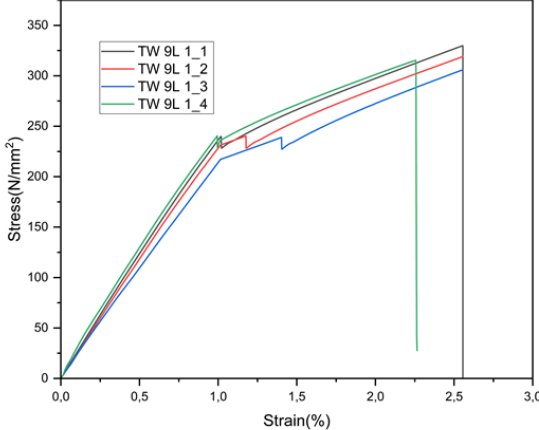
Figure 1. Photographs of sample EHC plate, test specimens & Shimadzu tensile test machine

Tension Test

The static tensile test were performed two types of EHC materials for each of them (5L and 9L) and different thickness regarding ASTM D 3039 standart. Tensile test specimens (250x250 mm) are prepared presented in Fig.1b, tensile tests were made by the Shimadzu tensile test machine (Capacity: 250 KN) (see Fig.1c). The tensile load velocity at room temperature (RT) is 0.5 mm/min. The static tensile test results are captured & recorded with a digital camera. Throughout the recording of videos, the displacement or extension and load amounts captured with Epsilon extensometer. During the test, the displacement or extension and load amounts captured are saved and uploaded in Shimadzu tensile testing machine's data acquisition computer. Figure 2 presents Stress-Strain plots of all of EHC material types (PW & TW) and all layers (5L & 9L). Figure 3 are graphed to compare layers and materials. The dimensions, thickness & mass are used to compute the areal density (AD) & density of EHC materials. Fiber volume fractions (V_f) & density (ρ) of the EHC laminates were evaluated by ASTM D2584 standart. The EHC panels areal densities are computed from the measured thickness & density of the EHC materials,

$$(AD = \rho_c H_c)$$

where, is H_c is the average thickness & ρ_c the average density of EHC material panels. EHC materials geometric and mass properties of Type 1 and Type 2 for all layers (5L and 9L) sequentially are shown at Table 2.



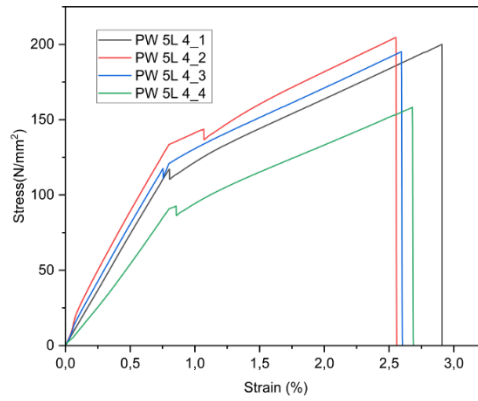


Figure 2. Tension Stress-Strain graphs EHC materials for all types and layers

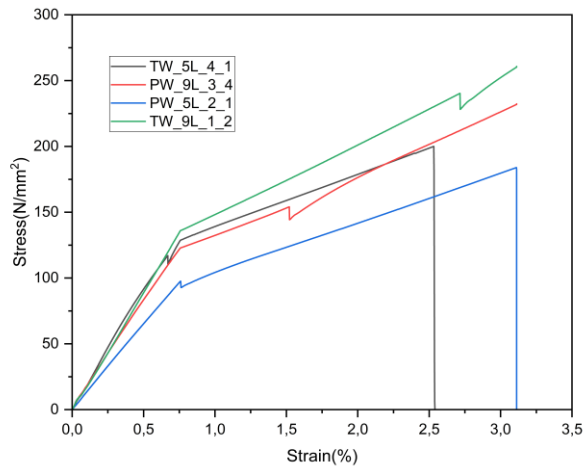


Figure 3: Stress Strain Compression graphs all types EHC materials

Table 2. All types EHC materials mechanical, mass and geometric properties

Hybrid Composite Materials Mechanical, Mass and Geometric Properties								
	σ_{max} (MPa)	ϵ %	E (MPa)	ρ_c (g/cm ³)	A_D (g/cm ²)	v_f %	H_c (mm)	B-Ratio (mm/mm)
Type1 9L	329,84	2,56	24919,22	1,29	0,41	32,23	3,17	0.0132
Type1 5L	187,58	2,94	13874,8	1,19	0,36	18,22	3,10	0,0121

Type2 9L	364,44	3,09	27421,59	1,19	0,40	33,87	3,28	0,051
Type2 5L	204,65	2,53	14336,415	1,24	0,39	18,40	3,18	0,021668

Damage Mechanism

Subsequently, the tension test, damaged specimens were investigated for understanding of damage mechanism. As a result in all types of EHC material systems brittle matrix cracks & brittle fiber fracture have been observed. Throughout the tension tests, dozens test samples were examined. For there are 96 samples, just one of them is presented in this paper as a specimen. Fiber pull out, brittle matrix cracks & brittle fiber fracture, have been occurred on all types of EHC material panels. After the tension test, the fractured or damaged digital sample photographs was presented in Fig.4.



Fig. 4 The damaged digital sample photographs after the tension tests

Discussion and conclusion

In this experimental research, two types EHC materials (Type 1) plain woven (PW), glass fabric (GF), polypropilen (non-woven) fabric (GN) and plain woven (PW), glass fabric (GF) and epoxy resin as matrix were used for Type 1 of two types of EHC materials. For the other type (Type 2), twill woven (TwW) carbon fabric (CF) were used with the other fibers and matrix being the same and different layers (5L and 9L) of EHC materials laminates were researched to figure out the effect of the woven type on EHC material mechanical properties with varous thickness (i.e HC = 3.10-3.18 mm).

For EHC material (Type 1) panels were utilized as the main material & for the other types EHC material (Type 2) panels were checked with that one. Geometric properties, mechanical properties & mass of EHC materials were presented on the Table 2 to check them. Tension test were carried out to measure EHC materials elastic modulus, stress & strain for all types.

It has been determined that the stress-strain behavior of Type 2 EHC materials is different from the main Type 1 (5L and 9L), and the stress-strain graphs of EHC materials (5L and 9L) for all types and are shown in detail in the tables.

The results of this article are as follows:

1. The maximum stress of Type 1 and Type 2 EHC materials was formed in the order of Type 2 (9L), Type 1 (9L), Type 2 (5L) and Type 1 (5L). Thus, TwW Carbon fabric has been affected by the situation and its mechanical properties have increased. Elongation load capacity and stress of EHC laminates for Type 2 (5L and 9L) as shown in Table 2, Figure 2 and Figure 3.
2. Elastic modulus was determined to be thought very close to each other for all types (Type 1, 5L and Type 2, 5L& Type 1, 9L and Type 2, 9L) of EHC material panels. This presents that results are steady & the quality of production EHC materials is so good.
3. All EHC material panels densities were very close to each other.
4. The increased load capacity ratio for all EHC material panels was found to be linear with respect to EHC laminate thickness.
5. TwW carbon fabric affected EHC material panels mechanical properties of between 5% and 12%
6. Brittle matrix cracks & brittle fiber fracture have been observed in all EHC material types as expected.

References:

- [1] Sun G, Zun G, Yu H, Li, et al. "Energy absorption of metal composite and metal/composite hybrid structures under oblique crushing loading". *Int J mech Sci*, 2018, vol 135:458-83
- [2] Gopinath A, Kumar S, Elayaperumal, "Experimental investigations of mechanical properties of jute fiber reinforced composites with polyester and epoxy resin matrices", *Procedia Engineering*, 2014, 97:2052-2065
- [3] Gökmen U, "Fabrication and Characterization of Hot Extruded Hybrid Composites AI 2024 Reinforced with B4C/AI203", *J. of Polytechnic*, 2016, 19(4) 420-480
- [4] Gökmeşe H, Karadağ H B, "IC-B4C Kompozit Hibrit Malzemelerinin Mikroyapı & Mekanik Özelliklerinin İncelenmesi", *Gazi Üniversitesi, F. B. Dergisi, Part C: Tasarım ve Teknoloji*, 2018, 6 (2): 350-435
- [5] Sun G, Wang Z, Hong J, et al., 'Experimental investigation of the quasi-static axial crushing behavior of filament-wound CFRP and aluminum/CFRP hybrid tubes'. *Compos Struc*, 2018, 190-220-35-15
- [6] Davoodi MM, Ahmad D, Sapuan SM, Ali A, Khalina A, Jonobi M, 'Mechanical properties of hybrid kenaf/glass reinforced epoxy composites for passenger car bumper beam'. *Mater Des*, 2010, 20:5000-22
- [7] N Hashim, D. I. Amajid, E. S. Mahdi, R. Zahari, N. Yidris, 'Effect of fiber loading directions on the low cycle fatigue of intraply carbon Kevlar reinforced epoxy hybrid composite'. *Composite Structures*, 2019, V.212 450-490
- [8] Campbell FC, *Structural composite materials*. ASM Int US 2010:60
- [9] Swolfs Y, Gorbatiikh L, Verpoest I 'Fibre hybridisation in polymer composite: a review'. *Compos Part A App Sci Manuf* 2014;67:181-200
- [10] Muhammad F. Ismail, Mohammed T. H. Sultan, Ahmad Hamdan, Ain UM Shah, Mohammad Jawaid, 'Low Velocity Impact Behaviour And Post-Impact Characteristics of Kenaf/Glass Hybrid Composites With Various Ratios'. *Journal of Materials Research and Technology*, 2019, 8(3):2500:2750
- [11] Shah AUM, Sultan MTH, Jawaid M, Cardona F, Talib ARA, 'A review on the tensile properties of bamboo fibre reinforced polymer composites'. *BioRes*, 2016;11:10654-76, <http://dx.doi.org/10.15376/biores.11.4.Shah>.
- [12] Davoodi MM, Sapuan SM, Ahmad D, Ali A, Khalina A, Jonobi M, 'Mechanical properties of hybrid kenaf/glass reinforced epoxy composite for passenger car bumper beam'. *Mater Des*, 2010;31:4927-32.
- [13] Sanjay M.R., Arpitha G.R., Yogesha B., 'Study on Mechanical Properties of Natural - Glass Fibre Reinforced Polymer Hybrid Composites: A Review', *Materials Today: Proceedings*, 2015, Volume 2, Issues 4-5, Pages 2959-2967

[14] D. Gay, SV Hoa, SW Tsai, Composite Materials Design and Applications. Boca raton FL. CRC Press LLC, 2003.

[15] S.S. Chee, M. Jawaid, M.T.H. Sultan, BioResources, 2003, 12 (2017) 7118–7132 ?

[16] J. Gustin, A. Joneson, M. Mahinfalah, J. Stone, Compos. Struct., 69 (2005) 396– 406

[17] Vinay, H.B, Experimental Study on Mechanical Properties of Polymer Based Hybrid Composite, 2016

[18] Poyyathappan, K,. Experimental Analysis and Comparative Mechanical testing on Glass- Carbon Hybrid Composites, 2019.

[19] S. Choong Woo, T. Won Kim., High Strain-Rate Failure İn Carbon/Kevlar Hybrid Woven Composites Via A Novel SHPB-AE Coupled Test. Composites Part B: Engineering, 2016, Volume 97, Pages 317-328

[20] Aklilu, G., Tensile behaviour of hybrid and non-hybrid polymer composite specimens at elevated temperatures, 2019.

Flexible Photovoltaic Applications for Non-Planar Surfaces Geometry

İbrahim GÜNEŞ¹

Introduction

Conventional modeling takes advantage of the homogenous nature of flat surface for harvest predictions. The characteristics of a planar module yields identical performance because all cells on the module are operating under the exact same conditions. The issue arises when this homogeneity is no longer the case, producing a non- uniform gradient of incoming solar energy. The effect of this gradient remains unaddressed in the current photovoltaic modeling research.

This research takes a scale-invariant meshing approach to model the gradient of factors introduced by non-planar photovoltaic. This research develops a standardized foundation for future research in this area while investigating potential complications, detailing practical design considerations, and providing insight into nonplanar photovoltaic generation optimization.

A PV cell converts sunlight into electricity using a physical process called the photoelectric effect. Sunlight is the radiated energy from the sun. This energy can be reflected, absorbed, or just pass through a PV cell. The energy absorbed by the PV cell is then transferred to the electrons of the material. The added energy from the sunlight forces the electrons from a static position in the semiconductor material and induces a built-in electric field.

Non Planar PV Systems

The ideal single diode model is illustrated in Figure 1, considering the photocurrent and the diode current. Figure 2 is the graphical representation of which details Kirchhoff's current law at the top node of the ideal diode model. Understanding this basic principle of PV operation provides the fundamental framework vital to developing accurate models for practical applications.

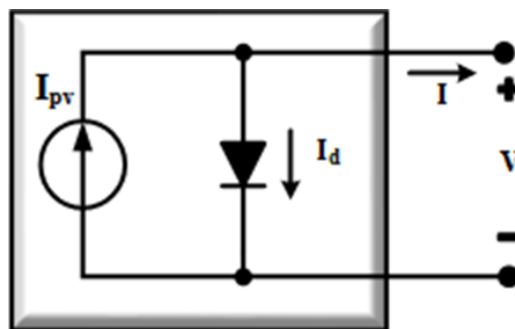


Figure 1. Ideal single diode model using the Shockley diode

¹ Assoc. Prof. Dr. , Istanbul University Cerrahpasa Engineering Faculty Electrical Engineering Department Avcılar 34320 Istanbul Turkey, gunesi@iuc.edu.tr

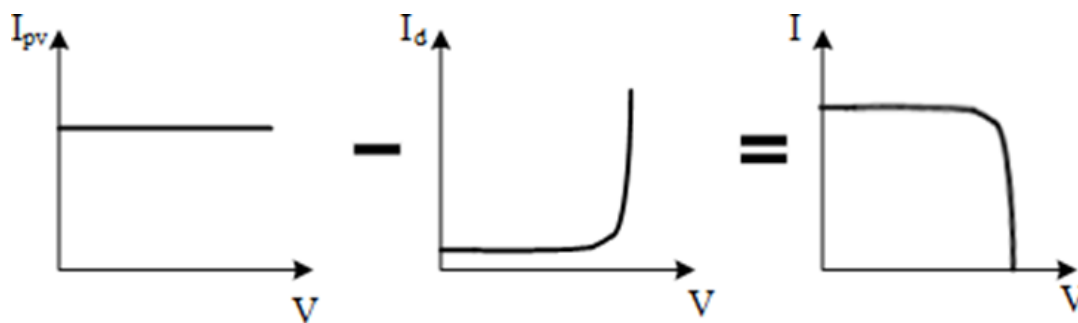


Figure 2. Fundamental concept that defines the I-V characteristics of a PV cell.

A simplified single diode model approach has been proposed that omits the parallel resistance. The reasoning is that when the parallel resistance is much greater than the series component, the current diverted through this element is reduced to a negligible value. This can be verified by referring to the shunt or parallel current term (I_p) for a PV cell. As parallel resistance increases, the impact of this current term approaches zero. On the other hand, the series resistance continues to correlate with the diode saturation current directly.

The result of this model provides the I-V characteristic curve expected by the PV cell, as presented in Figure 3. There are several essential characteristics on the curve that are used to evaluate the material operation. The short circuit current is the operating condition at which a difference of 0V occurs across the two PV terminals and depicts the maximum current generation ability of the PV cell at the specified insolation. Oppositely, the open circuit voltage condition describes a no-load system, corresponding to the maximum voltage at the specified insolation. These two points provide a boundary for the PV operation. The maximum power point (MPP) is the optimal operating point that delivers the most output power.

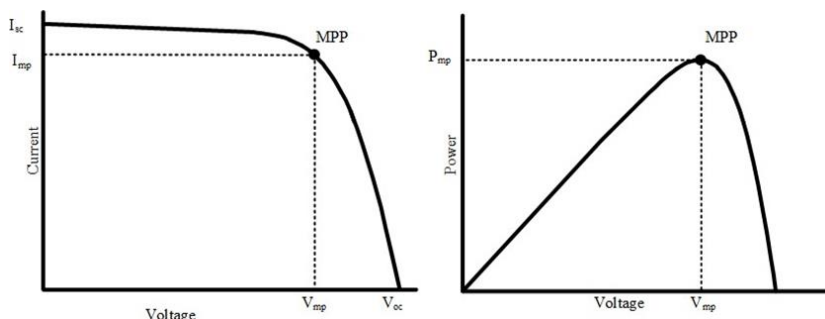


Figure 3. I-V and P-V curve with important descriptive points.

The only remaining parameter of the single diode model equation that does not need extraction is the operating voltage. This is because the voltage operating range is known, such that the open circuit voltage is a specified parameter in the datasheet provided by the manufacturer. To fully describe the I-V characteristics of a PV cell, the model must be computed incrementally throughout the voltage range.

Non-planar photovoltaics present three novel issues in practical applications. The most fundamental issue is the view factor gradient apparent on a curved collector. Conventional PV relies on homogeneity, so any gradient in view factor results in reduced performance. The concept of view factor will be discussed in the next section. Incoming radiation is also known as insolation and is described by W/m^2 .

The concept of view factor has been used predominantly in the study of heat transfer. Since heat results from increased energy, they also provide a useful tool to translate the available solar energy into expected incident radiation on a PV collector.

Figure 4 illustrates the normal vectors of differing surface form factors. This resembles a discrete Gauss map, yielding a unit vector normal for each facet on the surface. For the flat plate, all normal vectors are homogeneous, which is ideal for achieving optimal performance. On the other hand, the semi-cylinder surface curvature yields a gradient of normal vector directions, dependent on the surface geometry.

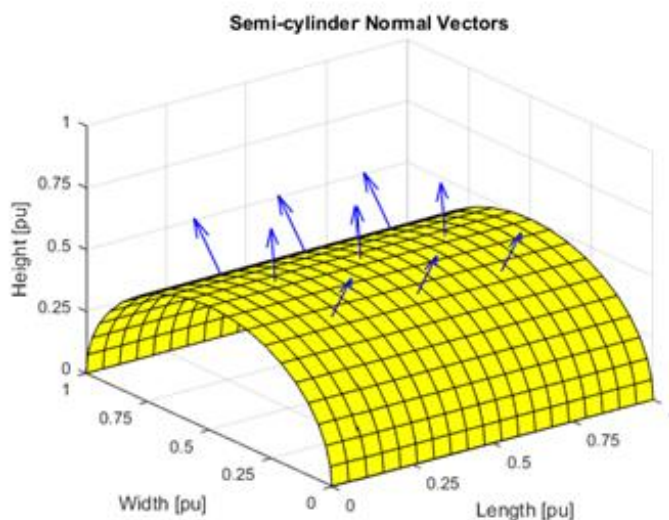


Figure 4. Gauss map for non-planar collectors.

The flat plate results correspond to an apparent symmetry of incoming insolation at solar noon. The top cell of the semi-cylinder is homogeneous to the planar module, and it evident in the energy profiles. While the top of the semi-cylinder is the same as the plane, the non-horizontal positions yield shifted curves.

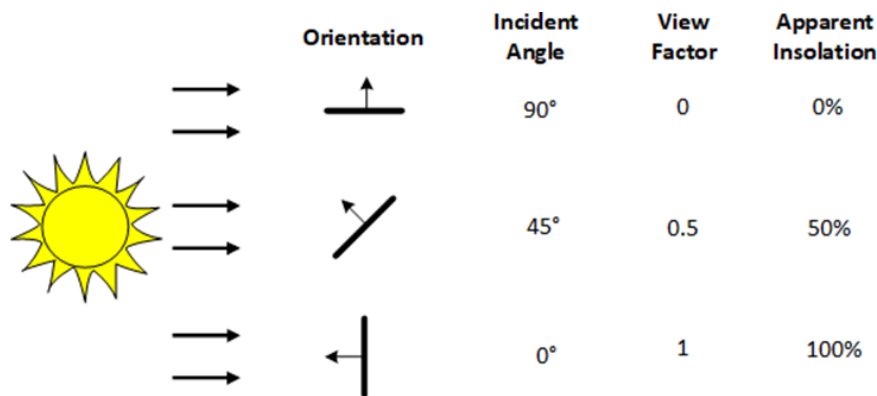


Figure 5. Diagram of normal vector, incident angle, view factor, and apparent insolation.

The most common deviation from homogeneity is shading. The two leading causes of a mismatch in the current generation of conventional planar solar arrays are inconsistent material degradation and shading. Since material physics lies outside the scope of this work, the focus will remain on the impact of shading. Shading of a single cell in a series connected array can drastically drop the generated output current, as illustrated in figure 6. When wholly shaded, the short circuit current, the photocurrent of the PV cell, drops to zero. The current from other series-connected cells must find an alternate circuit path. Instead, the current must travel through the parallel resistance, which results in power loss.

Since the parallel resistance value is assumed to be multiple orders of magnitude greater than the series resistance, this power loss can be substantial and results in localized heating of the cell. With enough upstream potential current density built up by the unshaded cells, the internal diode can be reverse biased due to the induced shunt voltage. This occurrence is highly detrimental to the performance of PV applications. Damage to the module is much more likely because it is now dissipating a significant amount of power. The shaded cell forces the upstream current produced through the internal resistances, causing hot spots.

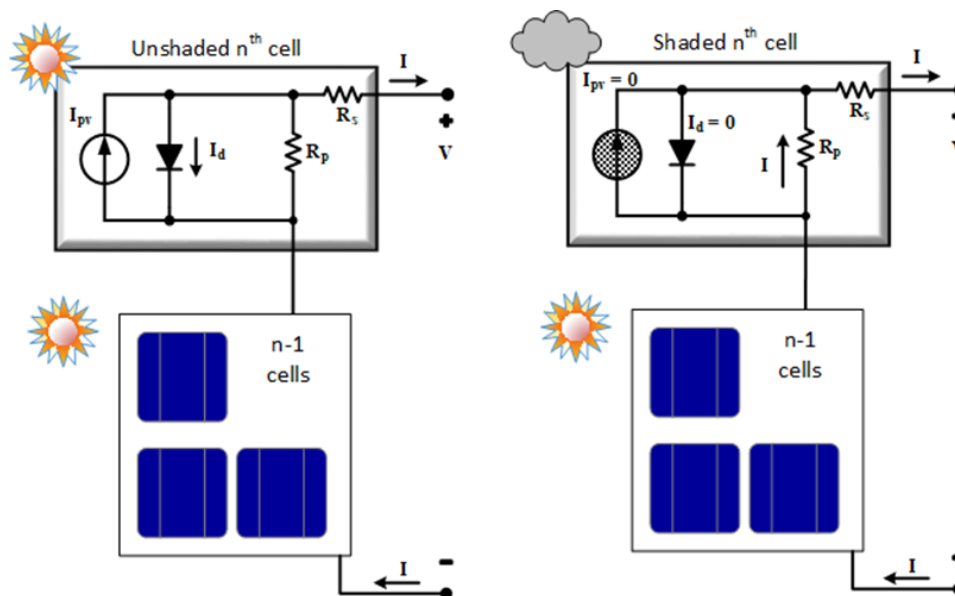


Figure 6. Current path with and without partial shading.

For planar PV installations, the leading cause of a mismatch current in a PV string is meteorological, like clouds or variations in the atmospheric conditions, which are stochastic. Although weather patterns can be modeled at a large scale with some confidence, the certainty of local conditions or patterns is often low. So, accurately predicting a passing cloud or non-uniform insolation for a specific PV application area is improbable.

NP-PV introduces another major cause of mismatch in the form of self-shading. Even though the unpredictable weather patterns will always be a concern for any PV applications, curved surfaces' geometric characteristics are definable. Therefore, analyzing the consistent pattern is possible. An investigation of how the curvature impacts the electrical aspects of PV must be done. Only then can the design optimization considerations be made.

The performance of PV is susceptible to high operating temperatures. Even in the most fundamental representation of the circuit equation, the relationship to temperature is evident in the diode saturation current equation in the ideal model. Temperature plays a more significant role as natural and dynamic characteristics are introduced for improved estimation.

The temperature has a significant effect on operation for every PV system, which can be seen throughout all of the modeling equations, so a thermal model is needed. In addition to defining the isolated models for electrical production and the thermal balance, it is necessary to develop an approach that couples both electrical and thermal operating models for a more accurate portrayal of realistic operational performance.

In addition to adjusting MPPT algorithms, the power electronics must also be improved for the practical use of NP-PV. A curved PV application-specific differential power processor was proposed with a flexible transformer [43]. The proposed converter design resulted in the elimination of local MPP and a slight improvement in the extracted MPP.

Geometric Design of Nonplanar PV Systems

To further improve NP-PV performance, an optimization method for the electrical design and layout of NP-PV is presented capable of modeling performance under shading and curvature. Cell dimension, interconnection, and bypass diode integration influence on module performance were investigated. The approach was applied to a double curved roof for validation. In a more general design approach, the k-means algorithm was implemented to optimize module interconnection strategies for improved electrical production on curved PV.

The analyzed surfaces are defined with a collector azimuth of 0° from the south and a tilt of 0° . This keeps the surface level on the local horizontal plane, as illustrated in Figure 7. In all plots displayed, the x-axis is oriented such that the value increases toward the south. The y-axis is oriented such that the value increases toward the east. This standardized orientation is consistent for all surfaces to narrow the scope of investigation. Because of the effect that the geometry and cell orientation have on the radiative transfer of solar energy, the morphology was presented first. The morphology techniques were conducted such that the implementation of electrical characteristics can be made on a cell level. Once electrical parameters are extracted, and the I-V curves are defined, pixelization techniques can be explored to best coordinate with the MPPT.

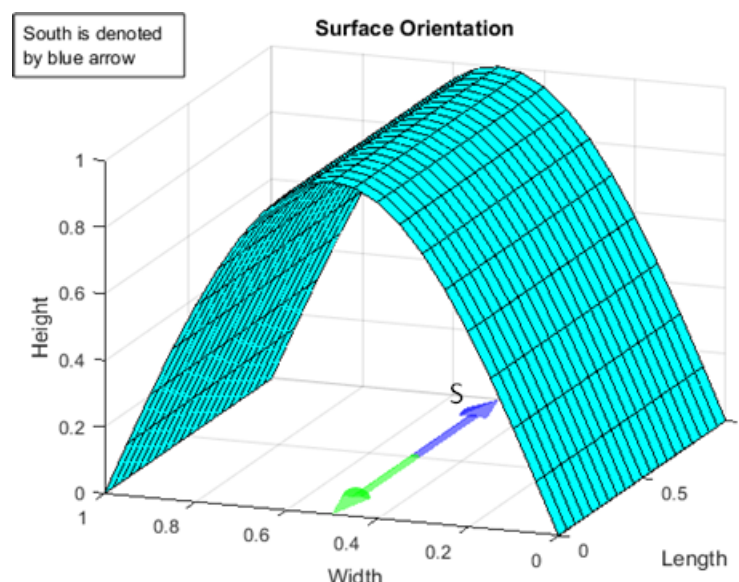


Figure 7. Orientation of defined collector geometries

Performance of Non Planar PV Systems Models

The potential performance of NP-PV is defined using three physics models. First, it is necessary to determine how much insolation the surface receives from the sun. This gives a theoretical maximum amount of energy that will strike the surface. Although perfect efficiency is not possible, comparing the insolation values with a flat surface yields valuable insight on NP-PV energy capacity, and validates further investigations. Introducing real-world efficiencies and power losses will give a more reasonable estimation of the electrical performance of the system.

The simulation conditions used in the following section are provided in Table 1. The collector orientations were selected to align the curvature of the surface with the diurnal solar. The latitude corresponds to the Tropic of Cancer, which is the northernmost latitude that experiences the sun directly overhead at solar noon.

Table 1: Parameters of Non Planar Surface

Collector Azimuth	0°
Collector Tilt	0°
Latitude	23.45°N
Day # of year	173

The flat plate serves as a control for the comparison of collection for the non-planar surfaces. The developed approach suggests that a unique power profile is produced, depending on the geometry of the curvature. The sinusoid curvature provides insight into the previously unutilized potential in that it provided three local peaks during a single day. The cells near the base of the sinusoid show little change in the rate of curvature, beginning with a tilt of about 45 degrees with respect to the planar footprint. The orientation of these cells produces the local peak in both the morning and afternoon.

The expected benefit of curved PV is that the end-user would have the ability to adjust the harvest profile as desired. If the system demands specific power curves, the surface can be designed to satisfy a practical need. The flexibility in design allows for more application-specific uses of curved photovoltaics, increasing peak available power, or a more stable harvesting profile. The evidence suggests that the geometry of the curvature is correlated to performance. Introducing an electrical model to this work provides insight into how these technologies can be optimized for applications.

Since our tuning of reflectance was based on minimizing overall error for each row, it is clear that the reflectance is not a static variable in a diurnal cycle. This introduces another factor for NP-PV applications to consider.

This analysis cannot rule out meteorological or experimental abnormalities. Therefore, the goal of this section was to establish an error bound for the model to account for significant observed impacts confidently. These results imply that this approach to thermal modeling of NP-PV provides a model capable of accurately depicting the module temperature of this surface with a margin of error expected to be within 10°C. This does not consider any variations with respect to partial shading due to meteorological events like clouds or planes.

The single diode model provides an ideal version of the operation of real cell fabrication. The double diode model would provide improved prediction accuracy of the photodiode exponential. In past work the double diode model structure has proven more precisely represent the nonlinearity of the I-V characteristics.

The short circuit current and open circuit voltage appear to be reasonably accurate. The location of the local maximum power points differs. The reason behind this deviation was determined to be due to the active diode voltage drop across the bypass diodes. The diode voltage would shift the figures to the left, depending on the diode specifications. This correction would relocate each local maximum power point to a more accurate representation of the measurements.

Some insight can be gleaned from this evaluation. Initially, it was assumed that the larger the angle difference between modules would produce equally different points of operation. This was found not to be the case. The variations of the modules with 15° angle differences were found to exceed that of the modules with a 30° change between horizontal and adjacent modules. It can be inferred that the variations in the angle from row to row have more impact with higher values of tilt. Tilt from 45°-0° experienced diminished variations on a row to row basis. This suggests the

closer to horizontal the modules are, the less deviation in production within that range. This new understanding promotes the capabilities of NP-PV applications without using bypass diodes in a design of this nature.

The traditional approach to validation is qualitative, meaning it is based on a deterministic form of analysis. Qualitative methods use graphical representations of the data to determine the significance of error, although uncertainty is not acknowledged in either the predicated or measured data. Visual interpretations may vary from person to person. Although the insight from this method of validation is flawed, the ability to visually compare data provides the ability to recognize otherwise unseen patterns. The quantitative form of analysis provides a stochastic approach to validation, considering various sources of uncertainties from the model and experiment. Both forms of validation are used within this work, each of which is intended to satisfy specific objectives.

The main objective of this study was to develop a model capable of predicting the potential generation of NP-PV applications constrained by a single axis of rotation. Insight into the theoretical energy harvest benefits regarding the traditional flat photovoltaic installations was determined using a structured quadrilateral meshing method.

In the results and conclusions made should only be associated with the specified geometry, material, location, orientation, environment, and meteorological conditions. This work is not meant to be conclusive for all NP-PV. As was established at the beginning of this research, there are many parameter combinations, so a comprehensive analysis for all cases is not feasible for one investigation. Any change in the parameters could have been investigated and probably would have exhibited different characteristics.

For a nonplanar surface, the view factor changes relative to the position of the sun and the orientation of the collector. An analysis is necessary for each cell to approximate the surface potential. A nonlinear surface would produce a nonlinear progression of average view factors instead of the linear change of a planar system. Figure 10 compares incident angles and view factors of a flat plate and semi-cylinder from Figure 8, where the length label denotes the eastward direction. The flat plate results correspond to an apparent symmetry of incoming insolation at solar noon. The top cell of the semi-cylinder is homogeneous to the planar module, and it evident in the energy profiles. While the top of the semi-cylinder is the same as the plane, the non-horizontal positions yield shifted curves.

This work has suggested many potential avenues such as water tanks, tower structural buildings, sphere, semi-sphere, cone and circle shape area to investigate in depth. Evaluating energy harvest profiles, estimating thermal impacts, predicting realistic generation, and optimizing the connection topology are all proposed within this research, suggesting potential design considerations along the way. This standardized approach promotes the use of nonplanar photovoltaic on any scale.

REFERENCES

- Solar Impulse Foundation "Historic Flight Overview." <https://aroundtheworld.solarimpulse.com/> (accessed Aug. 19, 2019).
- H. Zhang and R. S. Balog, "Experimental verification of energy harvest from non-planar photovoltaic surfaces," in IEEE Energy Conversion Congress and Exposition, Sept. 15-19, 2013, pp. 4481-4487, doi: 10.1109/ECCE.2013.6647300.
- M. Shibasaki and T. Yachi, "A power generation estimate of cylindrically-shaped flexible PV cell systems for off-grid use," in 2014 IEEE 40th Photovoltaic Specialist Conference (PVSC), June 8-13, pp. 2759-2764, doi: 10.1109/PVSC.2014.6925500.
- R. Ramchurn, "Energy Forum on Solar Building Skins," Architects' Journal, Oct. 2012, Accessed: June 3, 2018. [Online]. Available: <https://www.architectsjournal.co.uk/specification/energy-forum-on-solar-building-skins>
- J.-P. Pelissier. "Solar France." Reuters. <https://www.reuters.com/news/picture/solar-france-idUSRTR4VM6Z> (accessed Nov. 11, 2020).
- A. Khaligh and O. C. Onar, Energy Harvesting: Solar, Wind, and Ocean Energy Conversion Systems (Energy, Power Electronics, and Machines). Boca Raton: Taylor & Francis, 2010.
- W. Shockley, "The Theory of p-n Junctions in Semiconductors and p-n Junction Transistors," The Bell System Technical Journal, vol. 28, no. 3, pp. 435-489, 1949, doi: 10.1002/j.1538-7305.1949.tb03645.x.
- S. Shi and Z. Zhou, "Applied Technology in Simulation of Photovoltaic Cell Model Based on MATLAB/Simulink," Applied Mechanics and Materials, Article no. 662, pp. 209-213, 2014, doi: 10.4028/www.scientific.net/AMM.662.209.
- L. Reis, J. Camacho, and D. Novacki, "The Newton Raphson Method in the Extraction of Parameters of PV Modules," Renewable Energy and Power Quality Journal, vol. 1, pp. 634-639, 2017, doi: 10.24084/repqj15.416.
- B. Tuncel, B. G. Akinoglu, T. Ozden, and R. S. Balog, "Thermal Modeling and Verification of PV Module Temperature and Energy Yield Using Outdoor Measurements for Ankara, Turkey," in 2018 International Conference on
- P. Hoang, V. Bourdin, Q. Liu, G. Caruso, and V. Archambault, "Coupling Optical and Thermal Models to Accurately Predict PV Panel Electricity Production," Solar Energy Materials and Solar Cells, vol. 125, pp. 325-338, 2014, doi: 10.1016/j.solmat.2013.11.032.
- O. Dupré, R. Vaillon, and M. A. Green, "A full thermal model for photovoltaic devices," Solar Energy, vol. 140, pp. 73-82, 2016, doi: 10.1016/j.solener.2016.10.033.
- R. S. Balog, Y. Kuai, and G. Uhrhan, "A photovoltaic module thermal model using observed insolation and meteorological data to support a long life, highly reliable module-integrated inverter design by predicting expected operating temperature," in 2009 IEEE Energy Conversion Congress and Exposition, San Jose, CA, USA, Sept. 20-24, pp. 3343-3349, doi: 10.1109/ECCE.2009.5316107.

A. Arias-Rosales and P. R. LeDuc, "Comparing View Factor modeling frameworks for the estimation of incident solar energy," *Applied Energy*, vol. 277, 2020, doi: 10.1016/j.apenergy.2020.115510.

A. F. Mills, *Heat Transfer*, 2nd ed. Upper Saddle River, NJ, USA: Prentice Hall, 1999.

J. Appelbaum, "The role of view factors in solar photovoltaic fields," *Renewable and Sustainable Energy Reviews*, vol. 81, pp. 161-171, 2018, doi: 10.1016/j.rser.2017.07.026.

T. Maor and J. Appelbaum, "View factors of photovoltaic collector systems," *Solar Energy*, Article vol. 86, pp. 1701-1708, 2012, doi: 10.1016/j.solener.2012.03.017.

A. Pressley, "Curvature of surfaces," in *Elementary Differential Geometry*, 2nd ed. (Springer Undergraduate Mathematics Series). London: Springer, 2010, ch. 7, pp. 159-177.

G. M. Masters, *Renewable and Efficient Electric Power Systems*, 2nd ed. Somerset, NJ, USA: John Wiley & Sons, 2013. [Online]. Available: <http://site.ebrary.com/lib/tamu/docDetail.action?docID=10716205>.

N. D. Kaushika and A. K. Rai, "An investigation of mismatch losses in solar photovoltaic cell networks," *Energy*, vol. 32, no. 5, pp. 755-759, 2007, doi: 10.1016/j.energy.2006.06.017.

A. McEvoy, T. Markvart, and L. Castañer, *Practical Handbook of Photovoltaics*, 2nd ed. (Fundamentals and Applications). Elsevier, 2012.

D. Picault, B. Raison, S. Bacha, J. de la Casa, and J. Aguilera, "Forecasting photovoltaic array power production subject to mismatch losses," *Solar Energy*, vol. 84, no. 7, pp. 1301-1309, 2010, doi: 10.1016/j.solener.2010.04.009.

H. Tian, F. Mancilla-David, K. Ellis, E. Muljadi, and P. Jenkins, "A cell-to-module-to-array detailed model for photovoltaic panels," *Solar Energy*, vol. 86, no. 9, pp. 2695-2706, 2012, doi: 10.1016/j.solener.2012.06.004.

I. Banu and M. Istrate, "Modeling and simulation of photovoltaic arrays," presented at the World Energy System Conference (WESC2012), Suceava, Romania, June 28-30, 2012.

J. A. Gow and C. D. Manning, "Development of a photovoltaic array model for use in power-electronics simulation studies," *IEE Proceedings - Electric Power Applications*, vol. 146, no. 2, pp. 193-200, 1999, doi: 10.1049/ip-epa:19990116.

M. Izu et al., "Lightweight flexible rooftop PV module," in *1994 IEEE 1st World Conference on Photovoltaic Energy Conversion (WCPEC)*, Dec. 5-9, vol. 1, pp. 990-993, doi: 10.1109/WCPEC.1994.520127.

Artificial Intelligence Based Sleep Apnea Detection with Ecg

Erdem TUNCER¹

Çiğdem TUNCER²

Introduction

Sleep is one of the most important needs among our daily activities. On average, people spend about a third of their lifetime sleeping. Getting enough sleep indicates that blood pressure is regulated, heart rate is restored, and tissues are relaxed. Obstructive Sleep Apnea (OSA) is a sleep-related breathing disorder. It is characterized by repeated upper airway obstructions during sleep and subsequent waking periods (Remmers & et al. 1978). It is among the very common respiratory sleep disorders. In addition to reducing the quality of daily life of the person, OSA can also cause the development of many cardiovascular diseases. Therefore, it is important to diagnose OSA. The diagnosis of OSA plays a key role in choosing the appropriate treatment. No clinical data alone are sufficient to determine OSA. Therefore, objective tests are needed (Faal & et al. 2021, Yang & et al. 2022). The main objective test used in the diagnosis of the disease is Polysomnography (PSG). Many physiological signals are collected simultaneously with PSG all night long (Uçar 2017). These recorded signals; electroencephalography (EEG), Electrooculography (EOG) and electromyography (EMG), electrocardiography (ECG) and airflow and oximetry that provide understanding of respiratory events (Ünlü & et al. 2014, Lakadamyalı & et al. 2013).

In this study, the classification of sleep apnea data scored over ECG data was performed. The ECG signal has been preprocessed (Normalization). Then, classification was made from the windowed ECG data. At the feature extraction stage, 5 features were obtained, and ECG data were classified with Artificial Neural Network (ANN) and Support Vector Machine (SVM) classifier algorithms. As a result of the classification made between apnea and normal ECG data, a maximum success rate of 91,5% was achieved.

Materials and Method

In this study, PhysioNet-Apnea ECG database was used. Data from Phillips University, Dr. Provided by Thomas Penzel. The data set consists of a total of 70 records, divided into 35-record learning set (a01-a20, b01-b05 and c01-c10) and 35-record test set (x01-x35). Each recording contains a digitized ECG signal, expert-generated apnea note, and machine-generated QRS note. The lengths of the ECG signals vary according to the recording. Several files are associated with each record. Rnn files contain digitized ECG signals. Hea files are header files that specify the names and formats of the signal files. Apn are annotation files that contain a description for each minute of each recording indicating whether there is apnea or not. The sampling frequency of the data is 100 Hz. Amplitude values were recorded in mV. (Penzel & et al. 2000). Figure 1(a) shows an example of 10-second normalized ECG data scored normally by experts. Figure 1(b) shows an

¹ Dr. Erdem TUNCER, Republic of Türkiye Ministry of National Education, erdemtuncerr@gmail.com

² Çiğdem TUNCER, Republic of Türkiye Ministry of National Education, cigdemmtuncer@gmail.com

example of 10-second normalized ECG data scored as apnea. Data from 4 patients (a01, a02, a03, a04) were used in this study. For the sake of diversity, 166,66 minutes of each patient from the first data recording were included in the study. Data are organized into 10-second windows. The number of windows and data set information obtained from the data are given in Table 1.

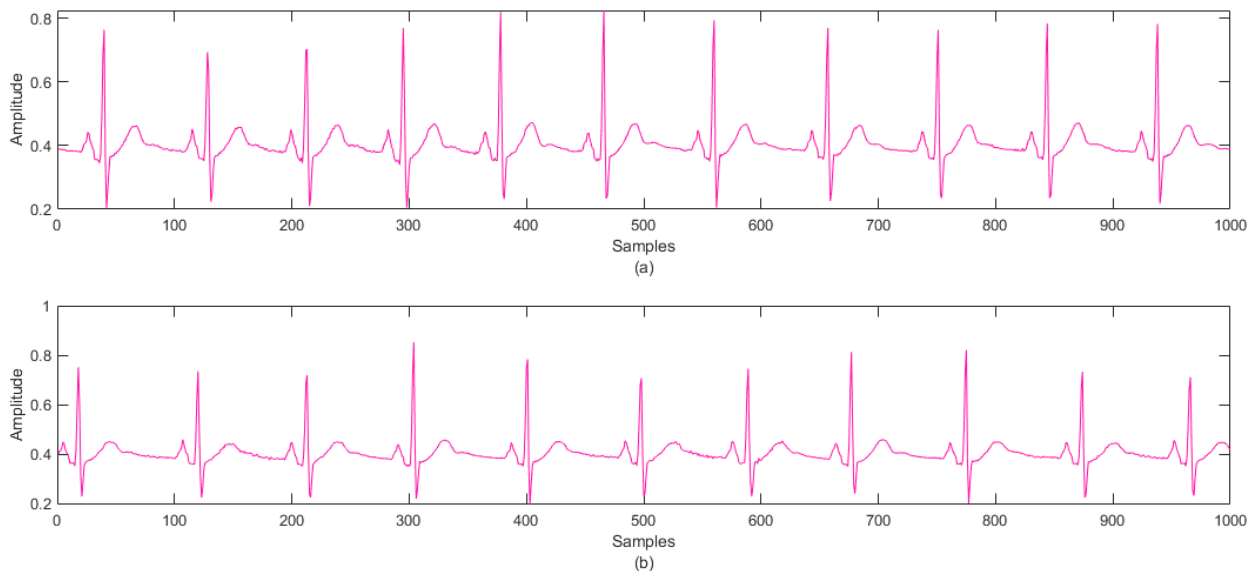


Fig 1. Typical ECG patterns of Normal (a), Apnea (b) with 1000 samples.

Table 1. ECG Dataset information

Data type	Number of epochs	Total time (Minutes)
Normal	2900	483,3
Apnea	1100	183,3
Total	4000	666,6

Mean absolute deviation, mean strength of the signal, kurtosis, skewness and variance features were obtained for each window data. The feature matrix obtained from 5 features is given as input to the classifier algorithms. Data were validated by 5-folds cross validation. ANN and SVM algorithms were used as classifier algorithms.

Artificial neural networks are information processing systems that mimic the working principles of the human brain or central nervous system in general. The generalization ability of the neural network is related to the correct selection of the network topology. The optimal architecture for the network should be large enough to learn about the problem and small enough to generalize. Therefore, the selected parameters must be carefully selected by the user. ANNs are generally divided into two as single-layer perceptrons and multi-layer perceptrons (Öztürk & et al. 2018, Mehdi & et al. 2013).

SVM is based on statistical learning theory. SVM is mainly used to distinguish the two data classes in the best possible way. For this purpose, decision boundaries or hyperplanes that can be separated linearly are determined. The algorithm determines where to draw these planes. In a

nonlinear dataset, SVMs cannot plot a linear hyperplane. It therefore uses a set of mathematical functions defined as kernels. Kernel functions greatly improve performance on nonlinear data. Different SVM algorithms use different kinds of kernel functions. These functions can be of different types such as linear, nonlinear, polynomial, radial basis kernel function. In this study, the radial basis kernel function, whose mathematical form is given in Equation (1), was used (Tuncer & et al. 2022, Melgani & et al. 2008).

$$X = (x_1, x_2), Y = (y_1, y_2) \text{ and } K(x, y) = \exp(-\gamma (x - y)^2) \quad (1)$$

One of the adjustable parameters given in Equation (1) γ , shows the gamma value.

Results and Discussion

In this study, the results of the two classifier algorithms were compared in order to diagnose apnea data from ECG data correctly and it was suggested to use the algorithm with high accuracy. In this study using the PhysioNet ECG dataset, normal-apnea data were classified.

ECG data is divided into windows and classified by calculating 5 features. The success rates of ANN and SVM classifier algorithms were compared. Certain network parameters are used as the basis for the ANN algorithm. In this study; The number of neurons in the input layer is 5, the number of neurons in the hidden layer is 8, the number of neurons in the output layer is 2, the learning rate is 0,03, the momentum is 0,2, and the batch size is 50. Radial basis kernel function, regularization parameter (C)=0.5, batch size=50 for the SVM algorithm. As a result of the study, a success rate of 91,5% with the ANN algorithm and 84,75% with the SVM algorithm was achieved in the correct classification of apnea diagnosis.

The diagnosis of Obstructive Sleep Apnea disease is carried out using the PSG device. In this study, an artificial intelligence-based algorithm that can diagnose from ECG signal, which will be an alternative to apnea diagnosis using PSG device, is proposed. The success rates of the two classifier algorithms were compared, and the ANN algorithm with a high success rate was proposed. Using single-channel ECG recordings with the proposed model, OSA detection in the patient will be more economical and practical. A high success rate (91,5%) was achieved with the classification made using 5 features (with the ANN algorithm).

The obtained features and the proposed classifier algorithm can be applied to larger datasets and the study can be improved by optimizing. In future studies, it is considered to carry out economic and practical solution-oriented studies with higher accuracy.

REFERENCES

- Faal, M. & Almasganj, F. (2021) Obstructive sleep apnea screening from unprocessed ECG signals using statistical modelling. *Biomedical Signal Processing and Control*, 68, 102685.
- Lakadamyalı, H. (2013) Polysomnographic findings in sleep disordered breathing. *Turkish Respiratory Society*, 15(2), 68-74.
- Mehdi, B. & Khan, T. & Ali, Z. A. (2013) Artificial neural network based electrocardiography analyzer. *3rd IEEE International Conference on Computer, Control and Communication*, 1-7, DOI: 10.1109/IC4.2013.6653767.
- Melgani, F. & Bazi, Y. (2008) Classification of electrocardiogram signals with support vector machines and particle swarm optimization. *in IEEE Transactions on Information Technology in Biomedicine*, 12(5), 667-677. DOI: 10.1109/TITB.2008.923147.
- Öztürk, K. & Şahin, M. E. (2018) A General view of artificial neural networks and artificial intelligence. *Takvim-i Vekayi*, 6(2), 25-36.
- Penzel, T. & Moody, G. B. & Mark, R. G. & Goldberger, A. L. & Peter, J. H. (2000) The Apnea-ECG database. *Computers in Cardiology*, 27, 255-258.
- Remmers, J. E. & Sauerland, E. K. & Anch, A. M. (1978) Pathogenesis of upper airway occlusion during sleep. *Journal of applied physiology*, 44(6), 931-938.
- Tuncer, E. & Bolat, E. D. (2022) Epileptic seizure classification from eeg signals with support vector machines. *Journal of polytechnic*, 25(1), 239-249. DOI: 10.2339/politeknik.672077.
- Uçar, M. K. (2017) Suggestions for alternative system designs for polysomnography device. *Clinical medical sciences*, 5(3), 1-12.
- Ünlü, M. & İriz, A. & Doğan, B. A. & Dinç, A. S. K. & Dursun, E. & Eryılmaz, A. & Acar, A. (2014) Relationship between obesity with symptoms and findings of obstructive sleep apnea syndrome. *Journal of Medical Updates*, 2014, 4(1), 11-15.
- Yang, Q. & Zou, L. & Wei, K. & Liu, G. (2022) Obstructive sleep apnea detection from single-lead electrocardiogram signals using one-dimensional squeeze-and-excitation residual group network. *Computers in Biology and Medicine*, 140, 105124.

Investigation of the Effects of Third Generation Biofuel/Alcohol Mixtures on Emission and Combustion Behaviors

Erdal ÇILGIN¹

Introduction

The world automotive industry is one of the industries that ensures the steady growth of developed and developing countries, supports technological advances and helps many other sectors to grow. With a total size of approximately 4 trillion dollars, it constitutes approximately 5% of the world economy. In addition, the automotive industry directly and indirectly provides employment to 80 million people in the world. Global vehicle demand, which has accelerated in recent years, increased by 1.1% in 2015 compared to the previous year and reached 90.8 million units. However, the rapidly growing automotive sector, which is the 4th largest sector in the world, has a great impact on global warming, climate change and other air emissions due to fossil fuel consumption (Nowak,2019). As an example, according to data from the International Energy Agency, 99 million tons of CO₂, or 4.7% of total emissions, was generated by China's transport sector in 1990, compared to 889 million tons and 9.6% in 2018, respectively (Peterson,2020). With the growing demand, oil-derived fuel consumption is increasing and energy diversity becomes essential. Fuel property plays an important role in emission formation in the combustion process. For this reason, the concept of fuel design and diversity and the use of biofuels and biomass have come to the fore (Alam & Rahman.,2013). Biomass is non-fossil organic matter of biological origin. All natural substances of plant and animal origin are biomass energy sources, and the energy obtained from these sources is biomass energy. Biomass energy is transformed into biogas, bioethanol, biomethanol, biooil and biodiesel in modern applications. Among them, the most common use is biodiesel. Biodiesel is the mono alkyl ester of the fatty acid chain obtained from animal or vegetable oils. Biodiesel sources are classified as first generation, second generation and third generation (Ong et al., 2014). Food and edible oils such as sunflower, palm and canola are first generation biodiesel sources (Samani et al, 2021). It is stated that first generation sources reduce the amount of global food and increase its prices (Bhuiya et al., 2020). Raw materials such as domestic and commercial waste oils and inedible oils are second generation biodiesel sources. Second generation sources have reduced the dependence on edible food crops for biodiesel production. These resources are more environmentally friendly and more efficient than first generation resources (Pinzi et al., 2009). However, large fertile lands are needed to cultivate second generation resources. This creates competition as fertile lands are generally used to produce food resources. As an alternative to first and second generation biodiesel sources, third generation sources have come to the fore. Third generation sources are microalgae based sources. Microalgae describe microscopic algae (Molina et al., 2019). First of all, microalgae can be grown in fresh and salt water environments that are not suitable for first and second generation sources. They are 100 times more efficient than terrestrial-based resources. They can complete biomass formation in less than 24 hours. Microalgae do not pose a threat to terrestrial plants or to food and forage crops (Chung et al.2017). In addition, they are an effective source of biodiesel since their chemical compositions are similar to other lipid compositions. Another source of fuel diversity is alcohols. Alcohols have been seen as a suitable

¹ Doç. Dr, Dicle Üniversitesi

diesel fuel additive due to their liquidity and high oxygen content (Kumar et al,2013). Although there are many types of alcohol, short-chain alcohols have been tested by many researchers in internal combustion engines (Jamrozik et al,2019). Short-chain alcohols are alcohols containing three or fewer carbon atoms. The most important advantages of these alcohols are that they have advanced production technologies and reduce the emission levels of engines (Xingcai et al,2004). However, the use of methanol and ethanol, which are short chain alcohols, in diesel engines is difficult due to their low calorific values, miscibility problems and low cetane numbers. Ethanol causes phase formation below 10 °C when mixed with diesel or biodiesel for use in diesel engines. In addition, it cannot be mixed with diesel fuel with high mixing ratios because it causes ignition delay (ID), low calorific value and poor lubricity due to its low cetane number. As the number of carbons in alcohols increases, they can be mixed more easily with diesel and biodiesel. With the increase of carbons in alcohols, while the mass percentage of oxygen decreases, the cetane number, density and caloric value increase. In contrast to Ethanol (C₂H₅OH) and Methanol (CH₃OH), propanol (C₃H₇-OH) has a higher cetane number, calorific value and viscosity. In addition, it can be easily mixed with diesel and biodiesel due to its better solvent properties. In similar studies with propanol, it is stated that there is an improvement in diesel engine emissions, but worsening in HC emissions (Laza & Bereczky,2009) Atmanli (2016) In his study, by adding 20% propanol to the waste cooking oil biodiesel/diesel fuel mixture, he reported that the fuel with propanol added increased the specific fuel consumption by 5.28%, the CO emissions increased by 39.95% and the NO_x emissions decreased by 15.05%. There are many studies in the literature investigating the performance and emission characteristics of various alcohol/diesel blend fuels. However, studies on the combustion behavior of propanol alcohol blended fuels are quite limited. Therefore, it was necessary to analyze the effects of propanol alcohol and microalgae biodiesel mixtures on combustion characteristics and exhaust emissions. The aim of the study is to examine the combustion and emission behavior of propanol alcohol blended with microalgae biodiesel and to discuss the results in the light of current literature. In this direction, biodiesel produced from microalgae was blended with 20% alcohol by volume and P-20 fuel was formed. Then, biodiesel (B-100) was blended with the reference DF fuel at a rate of 20% by volume and B-20 fuel was obtained. These fuels have been tested in a generator diesel engine at constant speed and different loads.

Experiments And Methodology

Fuel Production

Fuel production is in the form of the chemical reaction of oils, in the presence of alcohol and catalyst, to form fatty acid methyl esters and glycerine as the main product. This process is necessary for the use of vegetable oils as fuel. Because the thermal efficiency, viscosity and density of vegetable oil should be similar to diesel fuel. The most common process used for this is the transesterification reaction (Alptekin & Çanakçı,2006)

Transesterification reaction

Alcohol type, oil/alcohol molar ratio, catalyst type and amount, reaction temperature and time are important in the reaction (Azcan & Yilmaz,2011). While the use of different alcohols may slightly affect the fatty acid ester conversion rate, significant differences may occur in terms of processing costs. Methanol has been preferred because of its low cost, more polar and small molecules, easy dissolution and easy reaction. The stoichiometric ratio for alcohol: oil molar ratio is 3:1. However, since the 6:1 ratio is widely accepted as optimum, the alcohol: oil molar ratio is

6:1 in this study. The catalyst affects the efficiency and duration of the process. The catalytic activity of homogeneous alkaline catalysts is higher than that of acidic catalysts, and the reaction can be completed in an hour. Homogeneous alkaline catalyst (KOH) was used in the reaction. The reaction temperature shortens the time and increases the conversion. It was noted that the conversion took place 80% in the first 30 minutes of the reaction, and there was no remarkable increase after 60 minutes (Boz et al,2008). In this reaction, the temperature was maintained at 60°C for 60 minutes and left to stand for 24 hours. The resulting biodiesel and glycerin were separated from gravity differences by centrifugation and excess alcohol was removed by flash evaporation. It was washed with warm water to remove residual catalyst and soaps. After the reaction of approximately 1000 g of oil with methanol, 1004.9 grams of biodiesel and 105.3 grams of glycerin were obtained. Fuel production images are given in Figure 1, and the properties of fuels are given in Table 1.



Figure 1. Fuel production visuals

Table 1. Fuel properties.

Feature	DF	1-Propanol	Biodiesel
Density (kg / m ³) 15 °C	839	803	869
Viscosity (mm / s ²) 40 °C	2.88	1.77	4.58
Lower Heat Value (Mj / kg)	42.44	30.65	38.62
Evaporation Heat (kj / kg)	377	727.81	-
Flash point (°C)	> 55	11.6	126

Experimental setup and test installations

The engine used: It is a four-stroke diesel generator engine with a volume of 2400 cm³ and a compression ratio of 17/1. Each of the fuels was tested at 1500 constant speed and loading of 3.6 kW, 7.2 kW and 10.8 kW. CAPELEC CAP 3200 gas device was used for emission measurements. The accuracy and uncertainty of their measurements are shown in Table 2. The schematic image of the experimental setup is given in Figure 2.

Table 2. Accuracy and uncertainty of their measurements

Engine Parameter	Measurement range	Accuracy
NO _x	0-5000ppm	±1 ppm
CO	0–15%	±0.001%
HC	0–200000 ppm	±1 ppm
Sensor of cylinder gas pressure	0–200 bar	≤ ±0.5%
Engine speed	0–12000 rpm	±0.1% [o]

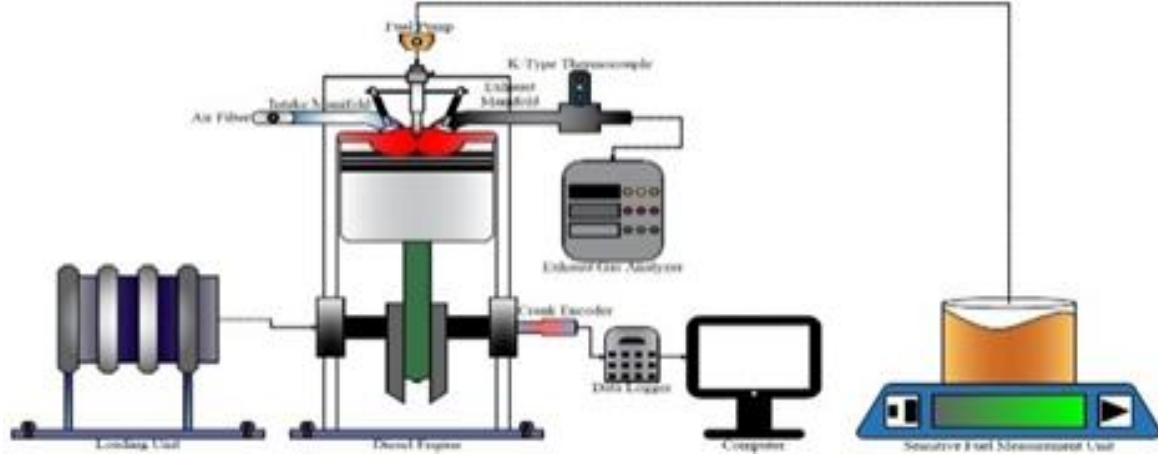


Fig. 2. Schematic image of the experimental setup

Research Findings

Specific Fuel Consumption (BSFC)

The load-dependent changes of the BSFC curves obtained by dividing the instantaneously consumed fuel volume by the power at the engine output are plotted in Figure 3. When the changes were examined, it was seen that B-20, P-20 fuels produced 2.84% and 5.13% higher g/kWh BSFC, respectively, compared to DF fuel. It is known that the energy released by the breakdown of oxygen bonds is lower than the bonds formed by hydrogen and carbon. The oxygen content of alcohols is higher than that of diesel fuel. Therefore, its thermal energy is lower (Topgül,2006). Therefore, the reason why P-20 fuel produces a high BSFC value is its high oxygen content. Fig.4 variation of the calorific value of fuels with the amount of oxygen.

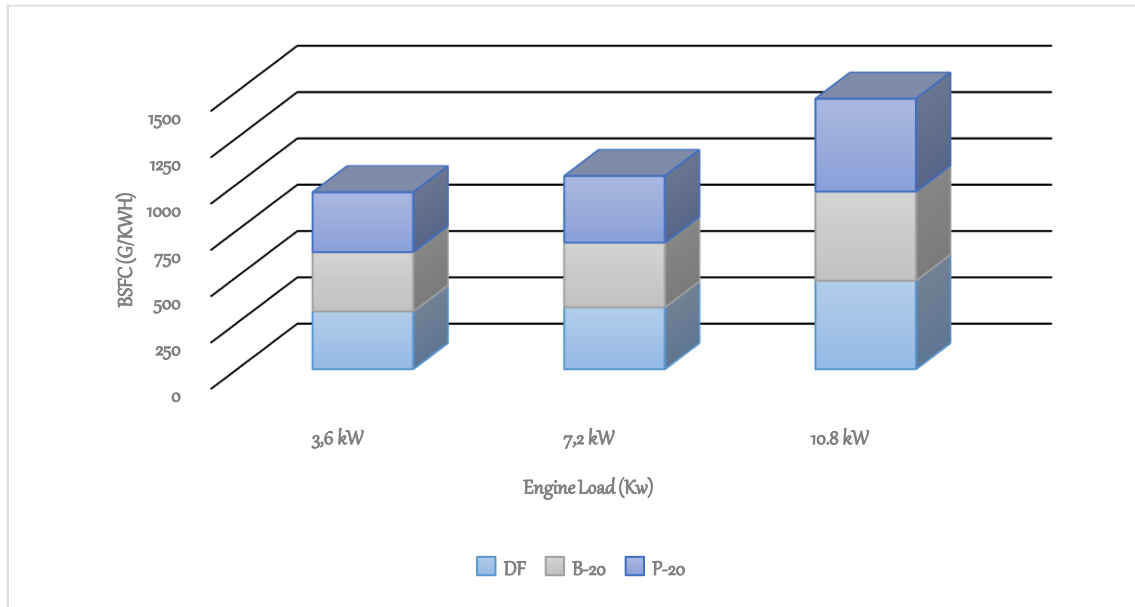


Fig 3. BSFC variation depending on load

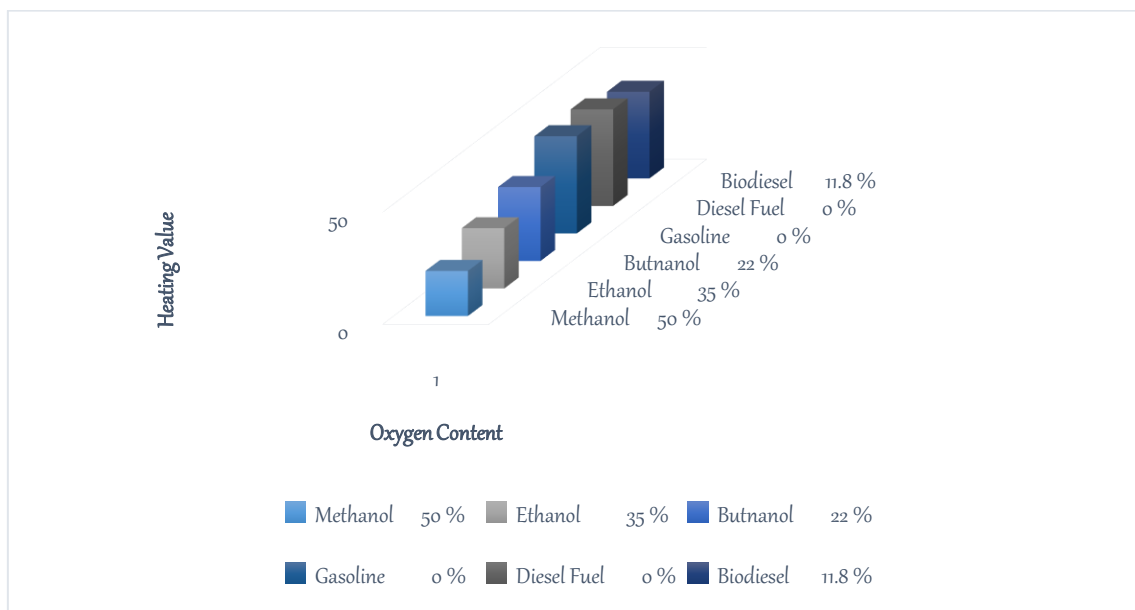


Fig.4 Oxygen content, calorific value amount

Exhaust Emissions

At the end of the expansion period in a 4th-stroke internal combustion engine, the exhaust valve opens and the exhaust gases pressurized in the cylinder are thrown out. CO_2 , N_2 , O_2 and large amounts of CO , HC , NO_x and soot are exhaust gas components in diesel engines. The composition and temperature of the exhaust gases are greatly affected by the amount of load on the diesel engine. In diesel engines, the amount of load is balanced with the amount of fuel. Therefore, the oxygen concentration in the exhaust gas differs significantly at various levels. Generally, diesel engines carry 5% oxygen in the exhaust gas at full load and 20% oxygen at idle. With increasing engine load, the amount of oxygen in the exhaust decreases, because as excess fuel

is sent, oxygen joins the combustion and more CO₂ is produced. The specific heat of exhaust gases increases (Zheng ,2004).

Carbon Monoxide Emission

Among the pollutants originating from motor vehicles, CO takes the first place with a rate of 66%. The CO changes of the experimental fuels are given in figure 5. It was observed that the CO values of B-20 fuel decreased by 7,14% on average compared to DF fuel, while the P-20 fuel decreased by 15.38%. Labeckas and Slavinskas (Labeckas et al,2016). stated in their study that the decrease in CO emissions was due to the low C atoms in the structure of biodiesel and alcohol, and the high O₂ atoms. Engines with added alcohol work with a lower air-fuel ratio due to the oxygen content, minimizing CO emissions.

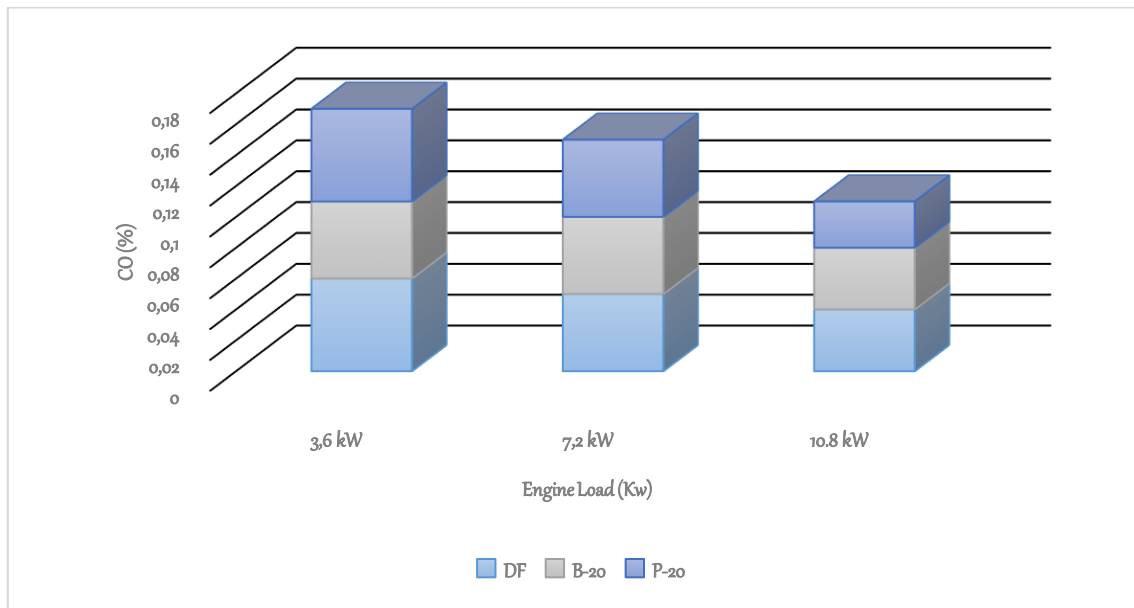


Figure 5. CO changes depending on engine load

Nitrogen Oxide Emission

High temperatures and residence times at elevated temperatures are the main causes of NO_x formation (Boruff et al,1982). NO_x is formed when nitrogen reacts with oxygen at high temperatures. It is known that in-cylinder temperatures greatly affect NO_x formation, and NO_x emissions increase as the temperature increases. When the NO_x changes in Figure 6 are examined, DF fuel produced 4.28% more NO_x than B-20 fuel. This high NO_x has been interpreted as being closer to complete combustion with the use of DF (İlkılıç et al,2009). It is seen that there is a 3.17% decrease in NO_x value with the use of P-20. It is thought that the high enthalpy of evaporation of propanol added to biodiesel reduces the combustion end temperatures, thus reducing NO_x emissions from high temperatures (İlkılıç et al.2015). Table 5 shows the evaporation enthalpies of the fuels

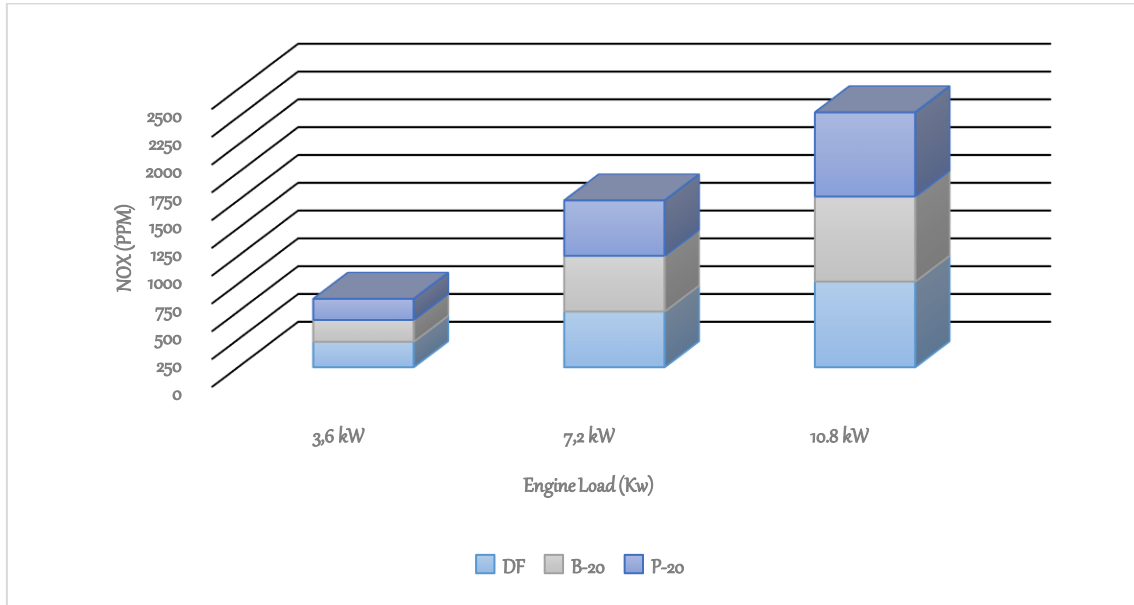


Figure 6. NO_x changes depending on engine load

Table 5. Ignition temperatures of fuels [°C]

Fuels	Ignition Temperature [oC]
Methyl / Ethyl Alcohol	400-470
Methane	600-650
Propane	520-590
Butane	530-600
Diesel	270-350

Hydrocarbon Emission

If the Air / Fuel (A/F) ratio increases too much in internal combustion engines, the mixture becomes very weak, especially in certain areas in the combustion chamber (Adams et al,1987).Therefore, if the mixing ratio exceeds the ignition and combustion limit, HC emissions increase. Figure 7. When the HC changes were examined, it was seen that the B-20 fuel was 5.73% lower than the DF. This decrease is due to the increased oxidation of the extra oxygen in the biodiesel content (Hazar & Uyar ,2015). It is seen that there is an increase of 4.83% in P-20 fuel compared to DF fuel. The increase is due to the high latent heat of evaporation of propanol alcohol lowering the ambient temperature and the lowering temperature causing the flame to extinguish, especially near the cylinder walls (Xue et al, 2011)

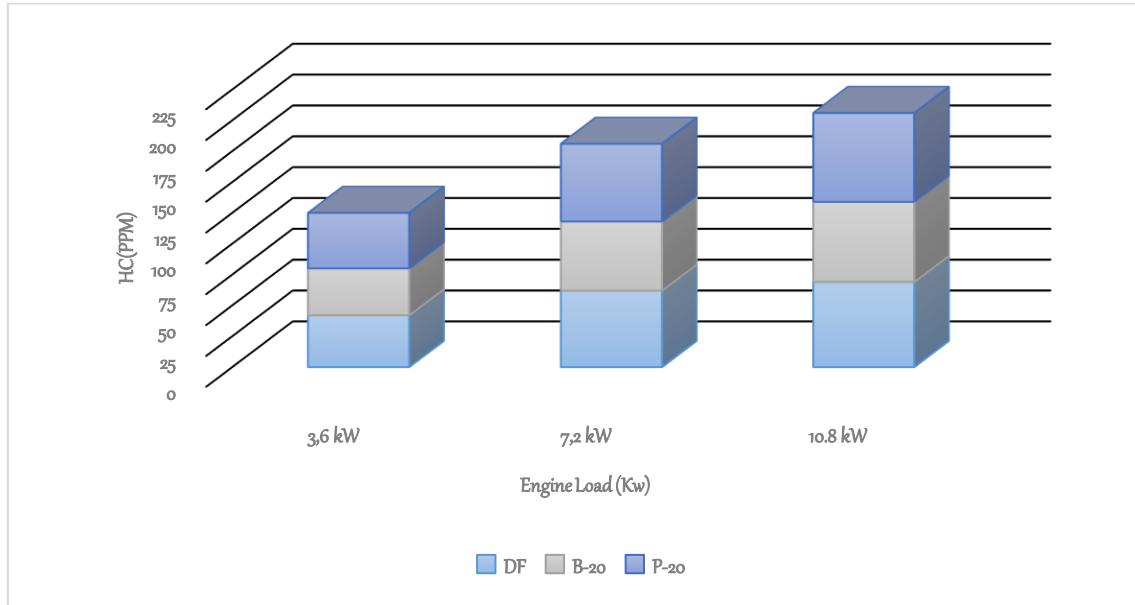


Fig.7 HC changes depending on the load

Patch Data and Burn Mechanism

The combustion process is a dynamic, physical and chemical interaction. While energy and mass transfer are associated with physical phenomena (Safgönül et al,1999). molecular interactions between fuel and oxygen are chemical reactions. During combustion, there are several parameters that affect all these relationships (Raşidova,2003). The phase, which begins with the evaporation of the injected fuel, ends with combustion and job creation (Polat, 2012). Fuel is disintegrated as a result of friction with air while being injected (Challen, 1999). Fragmentation rate is higher due to excessive friction around the fuel package (Heywood,1988). With the spraying, reactions start in the combustion chamber (Borat et al,1992). Fragmented fuel evaporates and diffusion flame is formed with ignition delay (Safgönül et al, 2008). In diesel engines, combustion is in the form of diffusion and it is local combustion zone conditions that affect combustion (Ceviz, 2005). In addition to these, air movements that occur together with heat and mass transfer in the combustion chamber are other factors affecting combustion

Combustion Analysis

In Combustion Analysis, the entire combustion cycle (720° KMA) can be examined, as well as a measurement range. Conditions in experimental purple from which combustion data were obtained: Specific Gas Const (kJ/kgK): 1.00, Air Density (kg/m³): 1.17, Adiabatic Index: 1.41, Polytrophic Index: 1.22, Number Of Cycles: 100, Cylinder Pressure Reference: 4, Smoothing 2, TDC Reference: 0.

Investigation of Cylinder Pressure (CP) and Heat Release Changes (NHR)

Pressure and heat release changes were generated by averaging over 100 cycles. (Figure 8.a, b, c) CP values of fuels increased with loading. Maximum values for all fuels occurred after top dead center. It was observed that B-20 fuel produced lower CP compared to DF. The decrease is thought to be due to possible consequences of the chemical and physical properties of the B-20 fuel. Because high density, viscosity and surface tension reduce the spray pressure (Ramkumar & Kirubakaran, 2016). Low spray pressure enlarges the droplet diameter (Taştan, 2018). Although

the droplet diameters are large, low penetration depths due to low pressure adversely affect the CP values (Topgöl et al, 2006). In addition, the lowest cylinder pressures occurred with P-20 fuel. The high oxygen content of propanol added to the fuel content decreased the thermal efficiency of the mixed fuel and thus the cylinder pressure values. When the heat release changes were examined, it was determined that P-20 and B-20 fuels produced lower emissions than DF. The lowest heat release among fuels occurred with P-20 fuel. This decrease is due to the low thermal energy due to the fact that the energy released by the disintegration of the O₂ bond in the alcohols is less than the bonds made by H and C (Enweremadu et al, 2011).

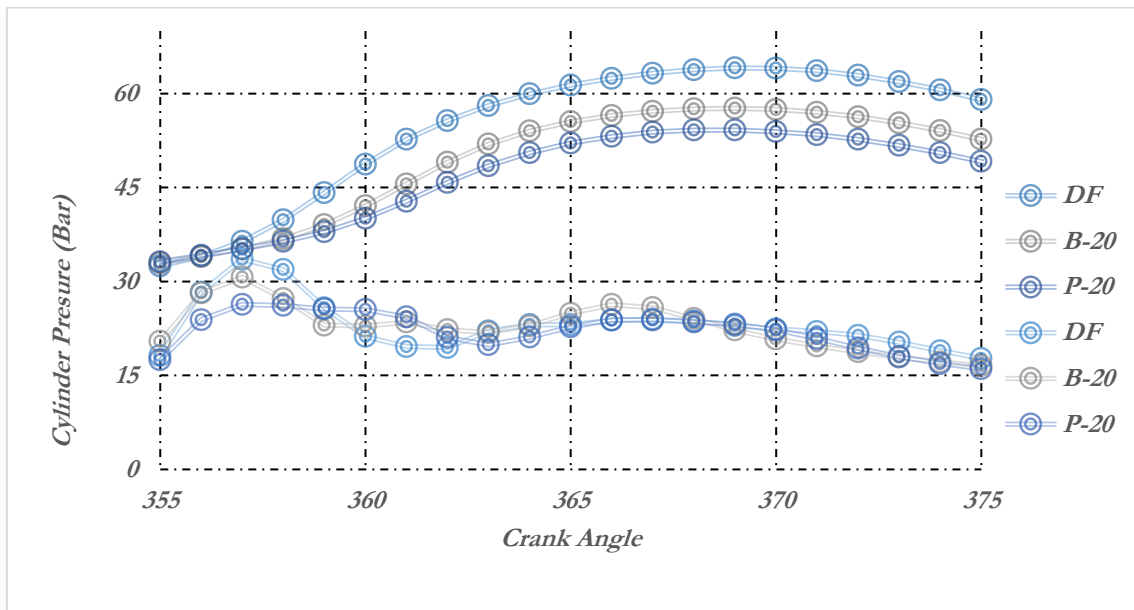


Figure 8. a Change of cylinder pressure and heat discharge rates [3.6 kw]

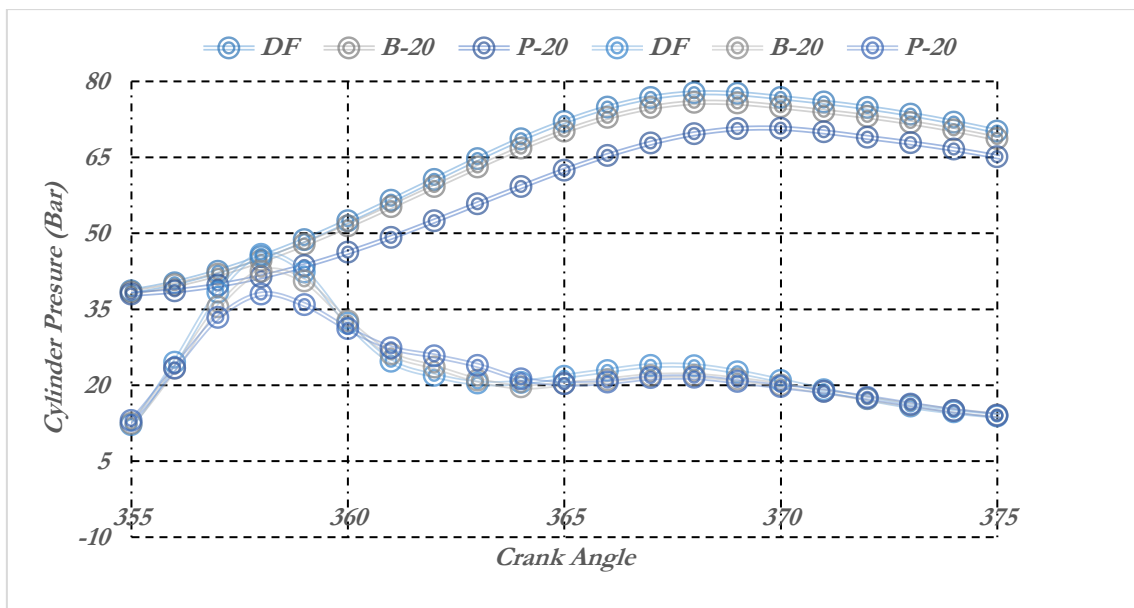


Figure 8. b Change of cylinder pressure and heat discharge rates [7.2 kW]

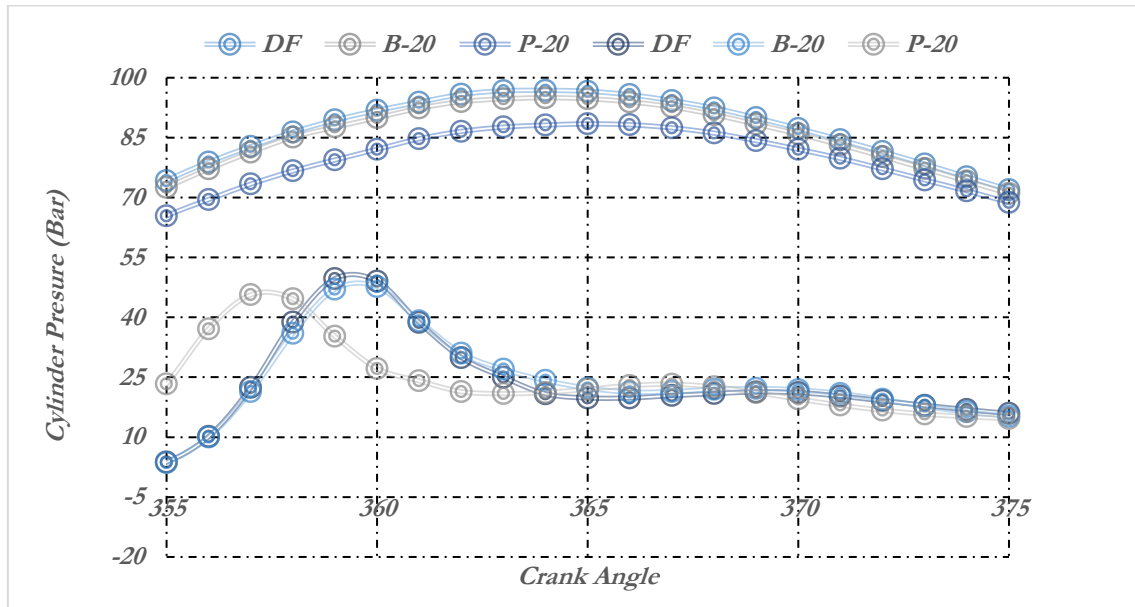


Figure 8.c Change of cylinder pressure and heat discharge rates [10.8kW]

Change of Cumulative Heat Release (CHR) and Pressure Rise Rate (RPR) Data

CHR, which is defined as the sum of instantaneous heat release rates, occurs in the form of S. It is slow in the beginning and increases rapidly until it reaches its peak value. The evaporation of the accumulated fuel during the ignition delay (ID) causes a negative value at the beginning of the curve. With its ignition, the heat emission values become positive. B-20 / P-20 fuels are fuels with low thermal values compared to DF. It is also seen in figure 9(a,b,c) that DF produces the highest CHR. Because fuels with low heat value create low CHR curves at equal injection amounts. In addition, fuels with high CHR curves are expected to have high NO_x emissions (Aydın, 2020). DF fuel NO_x emissions were higher than P-20 and B-20 fuels. The pressure rise rate defines the load applied to the cylinder head and other combustion chamber components during the combustion process (Graboski & McCormick ,1998). In an internal combustion engine, the rate of pressure rise depends on the rate of combustion in the initial stages, which is affected by the amount of fuel involved in uncontrolled combustion. When the diagram prepared with the averages of 100 cycles was examined, it was seen that all test fuel values increased with the loading. Because the average in-cylinder gas temperatures have increased. It was observed that the maximum values progressed before the top dead center with loading. This indicates that mass and mass flow rate shorten the ignition delay. Also, these data, which seem to increase with loading, are a basic measure for monitoring the knocking of the combustion process. These higher levels that occur indicate higher NO_x emissions. When the fuels were examined, it was determined that DF fuel had a higher pressure increase compared to B-20 and P-20 fuels, despite a shorter ID time.

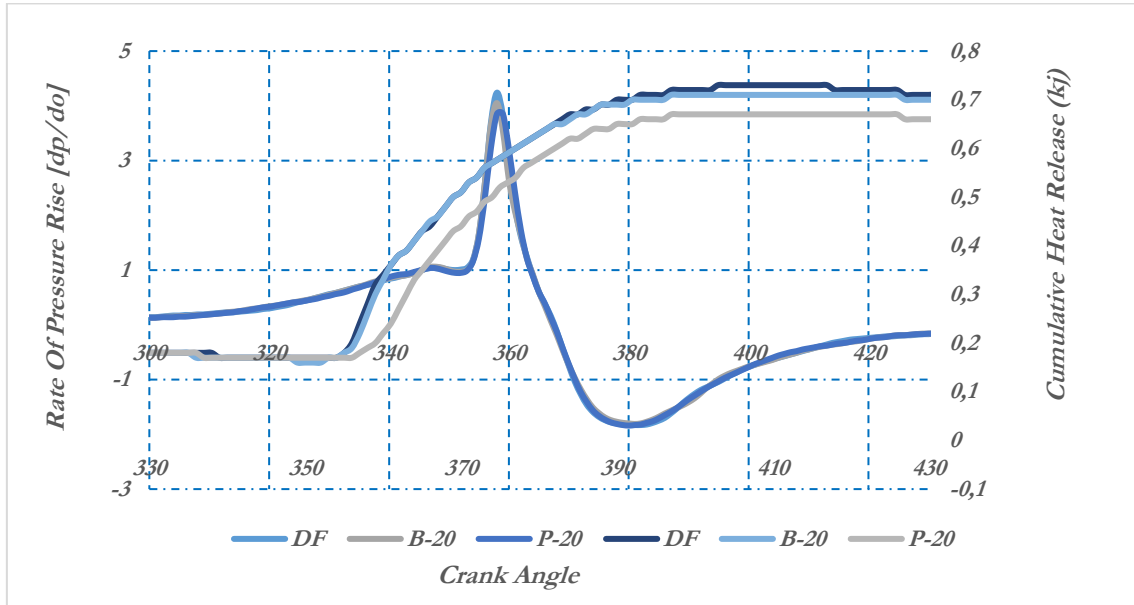


Figure 9.a. Variation of pressure mean velocity and cumulative heat release according to crank angle. [3.6kW]

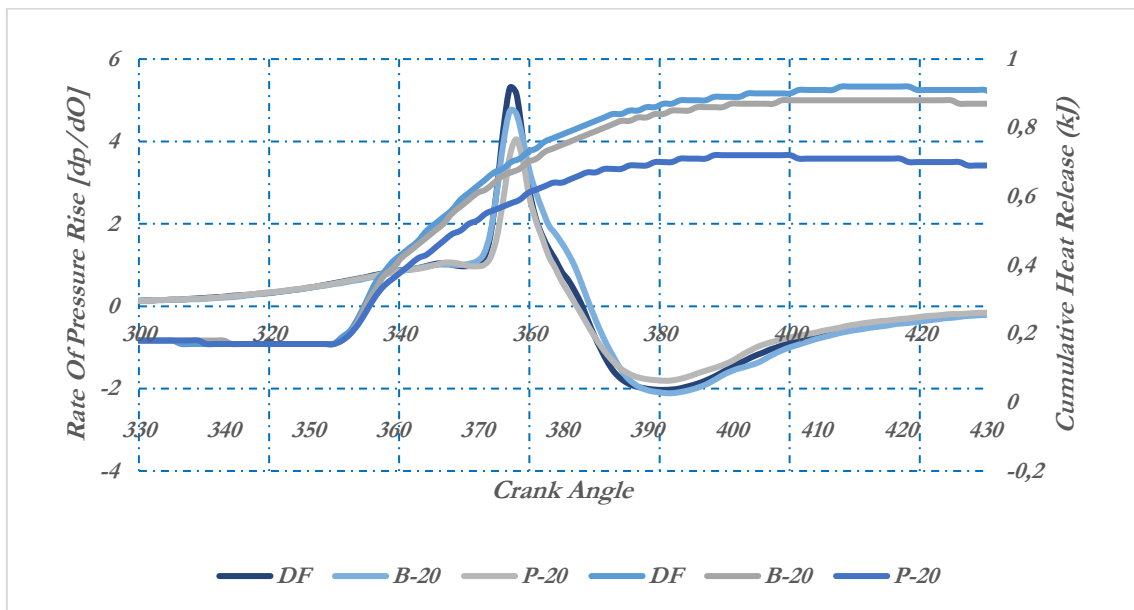


Figure 9.b. Variation of pressure mean velocity and cumulative heat release according to crank angle [7.2kW]

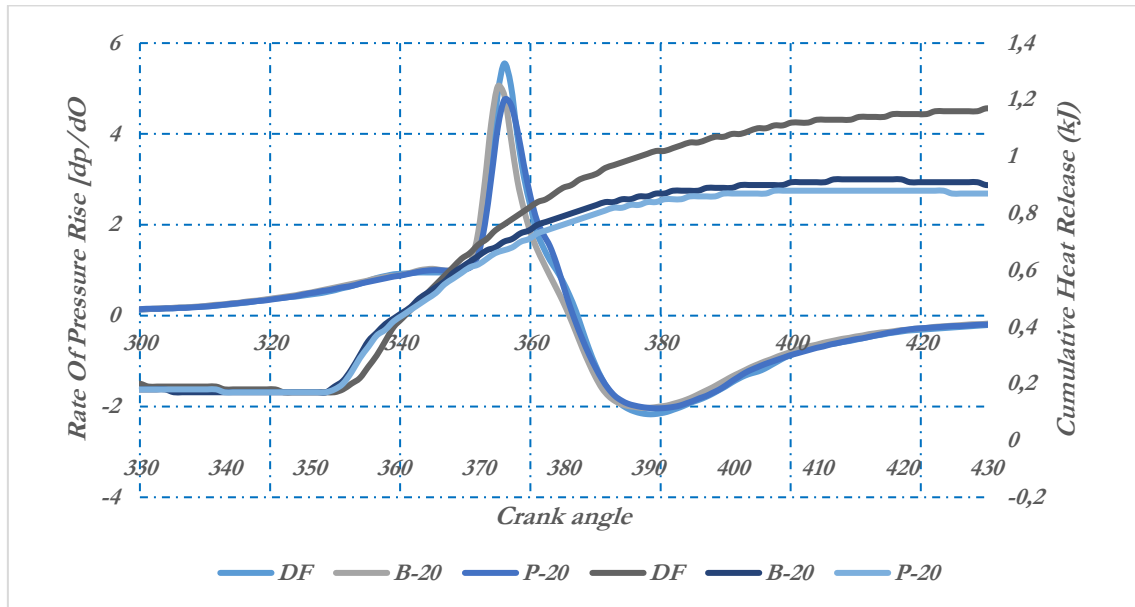


Figure 9.c. Variation of pressure mean velocity and cumulative heat release according to crank angle [10.8kW]

Average Gas Temperature (AGT)

When the figures 10a, 10b, 10c, where AGT values are given, are examined, it is seen that AGT values of all test fuels increase with loading. The maximum values occurred at a load of 10.8 kW. These were measured as 1810.84 in DF: 381CA, 1714.11 in B-20: 380CA, and 1613.45 OC in 378 CA for P-20. Combustion process in internal combustion engines is improved by the presence of oxygen (Challen ,1999). The alcohol-doped P-20 fuel mixture consisted of biodiesel and propanol. There is 20-22% oxygen in propanol alcohol and 10-12% oxygen in biodiesel. Despite these oxygen values, the lowest AGT values occurred in P-20 fuel. The reason for this was interpreted as the high molar enthalpy of vaporization and low cetane number of alcohols reduce the combustion temperature of P-20 fuel (Kuti et al,2010). Combustion data are presented in detail in table 7 and table 8.

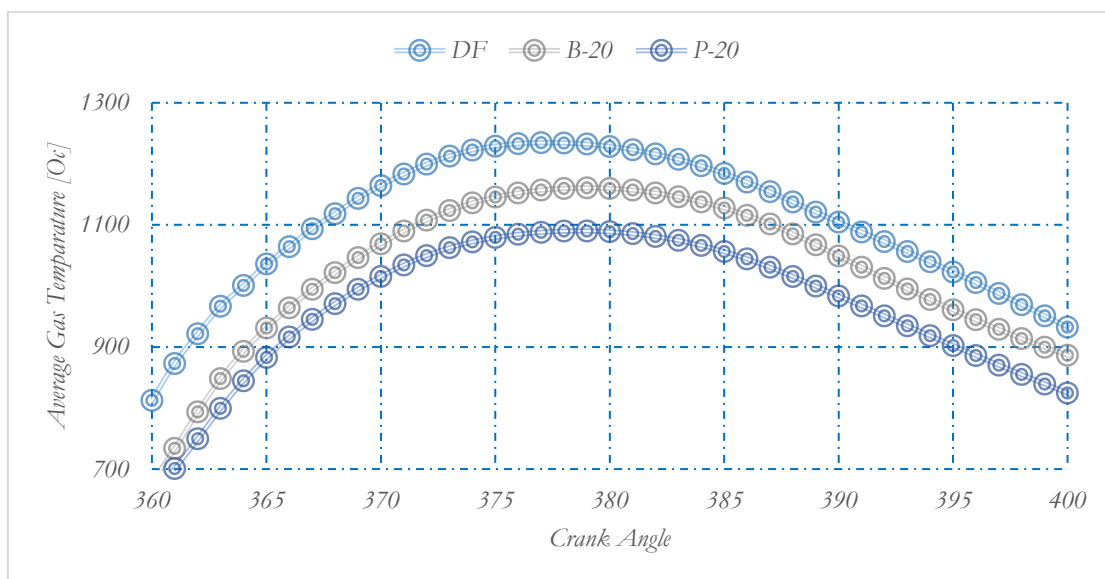


Figure 10.a Average gas temperature [3.6 kw load]

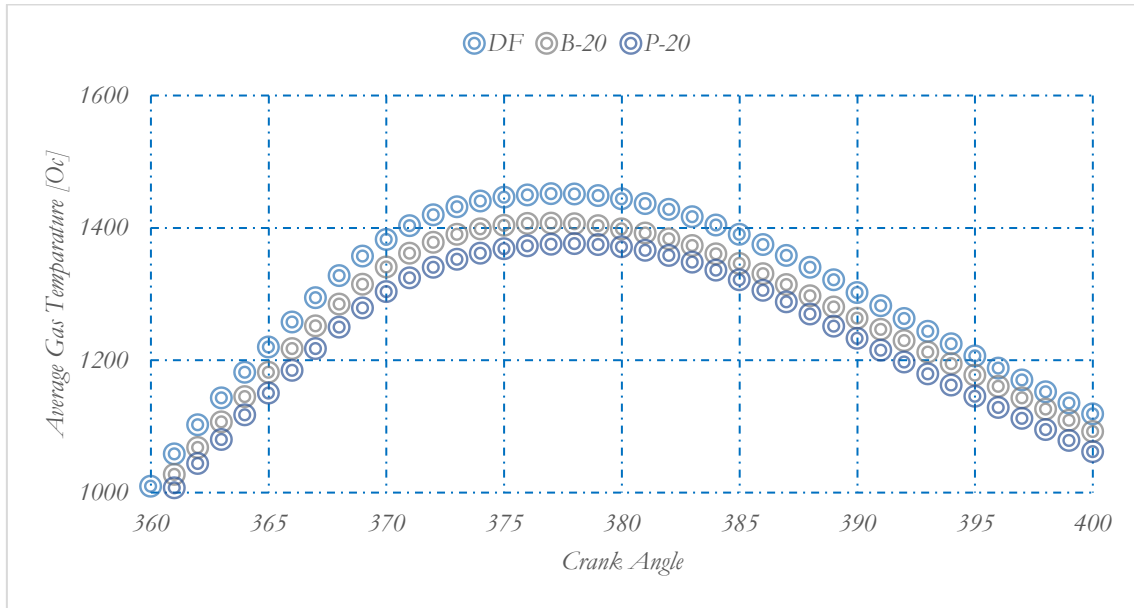


Figure 10.b Average gas temperature [7.2kW Load]

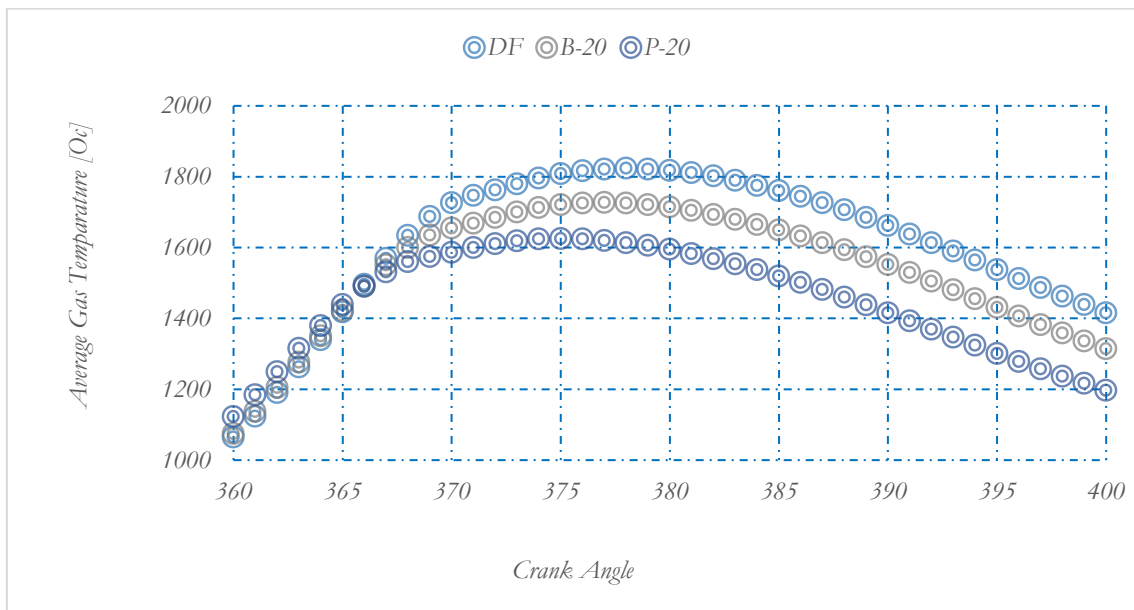


Figure 10.c Average gas temperature [10.8 kW Load]

Conclusion

The prominent results of the study conducted to see the effects of adding alcohol to microalgae on combustion and emission behaviors; First of all, the addition of alcohol decreases the cetane number, density, viscosity and calorific value of the blended fuels, while increasing the heat of evaporation. Especially the decrease in the heating value caused 5.13% g/kWh more fuel consumption in BSFC values with the use of P-20 fuel. The physical and chemical properties of the mixture fuel formed by the addition of alcohol caused a slight decrease in the combustion data.

When the effects of alcohol addition on emissions were examined, there was an increase of 4.83% in HC emissions, effective reductions of 3.17% in NO_x values and 15.38% in CO values. The addition of alcohol to biodiesel indicates that it is a renewable fuel that can be used in diesel engines without modification. However, more studies are needed to determine the ideal mixing ratios.

References

- Adams WH, Hinrichs HG, Adamis P. (1987). Analysis of The Combustion Process of A Spark Ignition Engine with A Variable Compression Ratio,” SAE Transactions. vol.89, no.4,pp. 749-757
- Atmanli A. (2016). Comparative analyses of diesel–waste oil biodiesel and propanol, n-butanol or 1-pentanol blends in a diesel engine. *Fuel*, 176:209-215.
- Alam MM, Rahman KA. (2013) “Biodiesel from mustard oil: a sustainable engine fuel substitute for Bangladesh,” *Int. J. Renewable Energy Dev.* Vol. 2, no.3, pp. 1-19, 2013.
- Alptekin E, Çanakçı M (2006).“Biyodizel ve Türkiye’deki Durumu” *Mühendis ve Makina*, 47:561, 57-64.
- Aydın S(2020). Detailed evaluation of combustion, performance and emissions of ethyl proxitol and methyl proxitol-safflower biodiesel blends in a power generator diesel engine.” *Fuel*, vol.270, no.4, pp.117492.
- Azcan N, Yılmaz Ö. (2011). “Yemeklik Atık Yağın Mikrodalga Destekli Transesterifikasyonu ile Biyodizel Eldesi ve Moleküler Distilasyonla Saflaştırılması” Tübitak Proje No: 110M011.
- Boz N, İlgen, O, Yıldız M, Kibar ME, Kar, M, Sunal O.(2008). Atık Yemeklik Yağların ve Bitkisel Yağların Transesterifikasyon Reaksiyonu için Uygun Katalizör Tasarımı ve Kinetik Çalışmalar” Tübitak Proje No:106M04.
- Bayındır H, Işık MZ, Argunhan Z, Aydın H. (2017). Combustion, performance and emissions of a diesel power generator fueled with biodiesel-kerosene and biodiesel-kerosene-diesel blends. *Energy*, 123, pp. 241-251
- Brunt M.F.J, Rai H, Emtage AL. (1998). The calculation of heat release energy from cylinder pressure data SAE Paper No. 981052.
- Bencheikh K, Atabani AE, Shobana S, Mohammed MN, Uguz G, Arpa O, Kumar G, Ayanoglu A, Bokhari A. (2019). Fuels properties, characterizations and engine and emission performance analyses of ternary waste cooking oil biodiesel–diesel–propanol blends. *Sustainable Energy Technol Assess*; 35:321–34.
- Bhuiya M.M. K, Bhuiya M. Rasul M, Khan N, Ashwath M.(2020). Mofijur.Comparison of oil extraction between screw press and solvent (n-hexane) extraction technique from beauty leaf (*Calophyllum inophyllum* L.) feedstock *Ind. Crop. Prod.*, 144, p. 112024
- Borat O, Balcı M, Sürmen A (1992). İçten Yanmalı Motorlar,” Gazi Üniversitesi Teknik Eğitim Fakültesi Matbaası, Ankara, pp. 85- 197.
- Boruff A.W, Schwab C.E, Goering E.H. (1982). “Evaluation of Diesel Fuel - Ethanol Micro-Emulsions”, *Transactions of the ASAE*, vol.25, no. 9, pp: 47-53.
- Challen B, Baranescu R. (1999). *Diesel Engine Reference Book 2nd ed.*”, ButterworthHeinemann, Oxford, pp.22-24.
- Ceviz MA, Yüksel F (2005). Effects of ethanol–unleaded gasoline blends on cyclic variability and emissions in an SI engine.” *Applied Thermal Engineering* vol.25, pp. 917–925, 2005.

- Chung J.-W, Lee C, (2017). Molecular challenges in microalgae towards cost-effective production of quality biodiesel. *Renew Sustain Energy Rev*, 74, pp. 139-144
- Checkel J. (1986). Dale Computerized Knock Detection from Engine Pressure Records SAE Technical Paper, 860028, 10.4271/860028
- Dhanasekaran R, Ganesan S, Rajesh Kumar B, Saravanan S. (2019). Utilization of waste cooking oil in a light-duty DI diesel engine for cleaner emissions using bio-derived propanol. *Fuel* 2019; 235:832–7.
- Enweremadu CC, Rutto HL, Oladeji JT. (2011). Investigation of the Relationship Between Some Basic Flow Properties of Shea Butter Biodiesel and their Blends with Diesel Fuel, “*International Journal of the Physical Sciences*, vol. 6, no.4, pp. 758-767.
- Graboski MS, McCormick RL. (1998). Combustion of fat and vegetable oil derived fuels in diesel engines”. *Prog. Energy Combust. Sci*, Vol.24, pp.125-164.
- Hohenberg GH, (1997). Advanced approaches for heat transfer calculations SAE Paper No. 790825
- Hazar H, Uyar M. (2015). Experimental Investigation of Isopropyl Alcohol (IPA)/Diesel Blends in a Diesel Engine for Improved Exhaust Emissions”, *International Journal of Automotive Engineering and Technologies*, vol. 4, no.1, pp.1-6.
- Heywood JB. (1988). *Internal Combustion Engine Fundamentals*”, McGraw-Hill, London, pp. 486-494, 1988.
- İlkılıç C, Behçet R, Aydın S, Aydın H. (2009). “Nox Formation in diesel engines and control methods.” 5. Uluslararası İleri Teknolojiler Sempozyumu, Karabük, Türkiye. 13–15 Mayıs.
- İlkılıç C, Çılğın R, Aydın H. (2015). “Terebinth oil for biodiesel production and its diesel engine application. ” *Journal of the Energy Institute*. Vol. 88, no. 3, pp. 292-303.
- Jamrozik, A, Tutak W, Gnatowska R, Nowak . (2019). Comparative analysis of the combustion stability of diesel-methanol and diesel-ethanol in a dual fuel engine. *Energies*, 12(6):971.
- Kuti OA, Xiangang WG, Zhang W, Nishida K, Huang ZH. (2010). “Characteristics of the ignition and combustion of biodiesel fuel spray injected by a common rail injection system for a direct–injection diesel engine,” *Proceedings of the Institution of Mechanical Engineers, Part D: Journal of Automobile Engineering*, vol.224, pp.1581-1596.
- Kumar S, Cho J. H, Park J, Moon I. (2013). Advances in diesel–alcohol blends and their effects on the performance and emissions of diesel engines. *Renewable and Sustainable Energy Reviews*, 22:46-72.
- Laza, T, Bereczky Á. (2009). “Influence of Higher Alcohols on the Combustion Pressure of Diesel Engine Operated with Rape Seed Oil”, *Acta Mechanica Slovaca*, 13(3): 54-61.
- Labeckas S. (2006). “The Effect of Rapeseed Oil Methyl Ester on Direct Injection Diesel Engine Performance and Exhaust Emissions”, *Energy Conversion and Management*, vol.47, no.14, pp.1954–1967.
- Molina D, Molina J.C, Carvalho A.I, Magalhães Jr C, Faulds E, Bertrand C.R. (2019). Soccol. Biological contamination and its chemical control in microalgal mass cultures *Appl. Microbiol. Biotechnol.*, 103 (23–24), pp. 9345-9358, 10.1007/s00253-019-10193-7

- Nowak, D. J. (2019) The atmospheric system: air quality and greenhouse gases” Hall. M, Balogh. S, (Eds.), Understanding Urban Ecology, Springer, Cham 2019.
- Samani BH, Behruzian M, Najafi G, Fayyazi E, Ghobadian B, Behruzian A, Mofijur M, Mazlan M, Yue I.(2021). The rotor-stator type hydrodynamic cavitation reactor approach for enhanced biodiesel fuel production. Fuel, 283, p. 118821
- Safgönül B, Ergeneman M, Arslan HE, Soruşbay C. (1999). İçten Yanmalı Motorlar,” İstanbul Teknik Üniversitesi, Makine Fakültesi, Otomotiv Anabilim Dalı,”Birsen Yayınevi”, İstanbul..
- Safgönül B, Ergeneman M, Arslan HE, Soruşbay C. (2008). İçten Yanmalı Motorlar”, Birsen Yayınevi, istanbul, pp. 38-41, 196-205, 2008.
- Taştan M. (2018). İçten Yanmalı Bir Motorda Hidrojenle Zenginleştirilmiş Metanol-Benzin Karışımlarının Performans Ve Emisyona Etkisinin Deneysel İncelenmesi” Doktora Tezi. Ocak Kayseri.
- Topgül T, Yücesu HS, Çınar C, Koca A. (2006). The Effects of Ethanol-Unleaded Gasoline Blends and Ignition Timing on Performance and Exhaust Emissions,” Renewable Energy, vol.31, no. 15, pp. 2534-2542, 2006.
- Topgül T. (2006). “Buji ile ateşlemeli motorlarda etil alkol-benzin karışımı kullanımında optimum çalışma parametrelerinin araştırılması, ” Doktora Tezi. Gazi Üniversitesi, Fen Bilimleri Enstitüsü, Türkiye
- Ong H.H, Masjuki, T.M.I. Mahlia, A.S. Silitonga, W.T. Chong, K.Y.(2014). Leong.Optimization of biodiesel production and engine performance from high free fatty acid Calophyllum inophyllum oil in CI diesel engine. Energy Convers. Manag., 81 (2014), pp. 30-40
- Polat S. (2013). Bir Dizel Motorunun Bilgisayar Yardımı Đle Termodinamik ve Performans Analizi.” Gazi Üniversitesi Fen Bilimleri Dergisi Part: C, Tasarım Ve Teknoloji GU J Sci Part: C vol.1, no. 3, pp.139-151.
- Peterson, B. (2013) “Car Ownership Statistics” (2020). Date of access: 06.10.2020. <https://www.valuepenguin.com/auto-insurance/car-ownership-statistics>.
- Pinzi F.J, Lopez-Gimenez M.D, Luque de Castro G, Dorado M.P. (2009) Dorado The ideal vegetable oil-based biodiesel composition: a review of social, economic and technical implications. Energy Fuels, 23 (5).
- Raşidova A. (2013). Vibe Fonksiyonu Kullanılarak Dizel Motorlarında Yanma Hızının Gürültü Emisyonuna Etkisinin İncelenmesi.” Yüksek Lisans Tezi. İstanbul Teknik Üniversitesi.
- Ramkumar S, Kirubakaran V. (2016). Biodiesel from vegetable oil as alternate fuel for C.I engine and feasibility study of thermal cracking: a critical review,” Energy Conversion and Management, vol.118, pp.155-169.
- Yılmaz N, Atmanlı A, Vigil FM. (2018). Quaternary blends of diesel, biodiesel, higher alcohols and vegetable oil in a compression ignition engine. Fuel 2018; 212:462–9.
- Zheng M, Reader GT, Hawley J.(2004). “Diesel engine exhaust gas recirculation- a review on advanced and novel concepts.” Energy Conversion and Management, Energy Conversion and Management vol.45, no. 6, pp. 883- 900.
- Xue J, Grift TE, Hansen AC. (2011). Effect of Biodiesel on Engine Performances and Emissions”, Renewable and Sustainable Energy Reviews, vol.15, no.2, pp.1098-1116.

Xingcai, L, Zhen H, Wugao Z, Degang L (2004). The influence of ethanol additives on the performance and combustion characteristics of diesel engines. *Combustion Science and Technology*, 176(8):1309-1329.

Application of the Rescheduling Approach in Manufacturing Systems

Ediz ATMACA

1. Introduction

A production schedule is predetermined before the execution of the manufacturing processes in the manufacturing systems. However, the unscheduled disruptions such as the delays of manufacturing processes or the addition of jobs often occur in the manufacturing systems, and an initial production schedule may not satisfy the constraints due to the disruptions. A dynamic scheduling method is therefore required to cope with the unscheduled disruptions. The reactive scheduling method is one of the dynamic scheduling methods that satisfy this requirement (Sakaguchi et al., 2008).

The changeable nature of manufacturing environments complicates the application of the very first tables and causes a decrease in table performance. To improve the performance of tables, new quests are plunged. Reactive scheduling emerges from these quests. In case of an unforeseeable incident during manufacturing, tables can be updated and new tables can be established. Every product needs different raw material and different semi-manufactured good which can be provided from various suppliers in manufacturing atmosphere. A completely reproduced table may not cover the time needed for procurement of raw material and semi-manufactured product. Sudden changes in tables raise the transportation distance, time and cost. Tables can be needed to be rescheduled in some workbenches. To avoid the deviation during application stage, alterations should be minimized in tables. Consequently, it is a healthier approach to improve tables than to start all over again (Suh et al., 1998).

Reactive scheduling is defined as the process of amending table put into practice in case of unpredictable situations in application area. Also, it is stated as the healing of table arranged before application during manufacturing operation or as the adaptation of it to process.

In other words, it is an update operation of tables while they are in process. The algorithm of reactive scheduling repairing is presented in Figure 1 (Rabeja and Subramaniam, 2002).

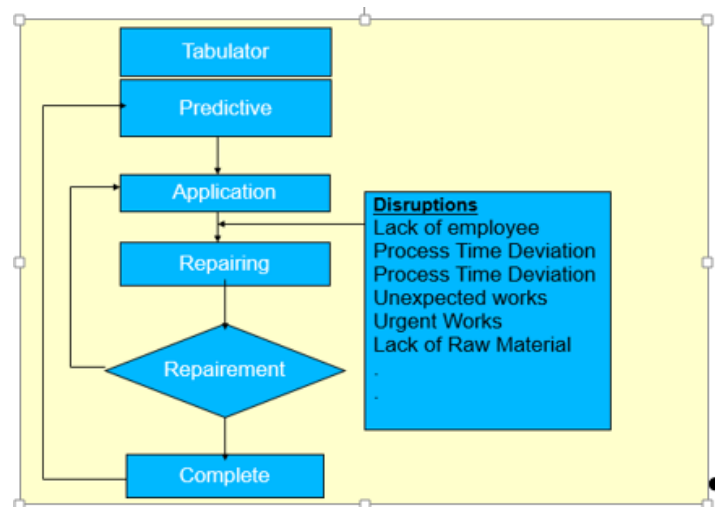


Figure 1. Reactive Scheduling Repairing.

2.Reactive Scheduling

Since reactive scheduling problems are very complicated, conventional operational research approach is not appropriate for the solution. To get healthy results, artificial intelligence and sophisticated method routine are used. Some of the operational research approaches are listed below (Rabeja and Subramaniam, 2002).

- Right Shift Rescheduling – RSS
- is the simplest approach to reactive rescheduling. The process is formed shifting whole schedule forward and expanding them to the right to adopt the breakdowns.
- Affected Operation Rescheduling
- However, it is easy to apply; more qualified schedules appear with RSS approach. Within this algorithm, only disturbed schedules are to be rescheduled.
- A heuristic - based approaches are applicable and response to changes in an effective way but they do not assure the best result.
- Multi–Agents system in Distributed Artificial Intelligent Approaches
- These systems are for solving independent agents’ problems and arranging them while they are working in this common purpose. Intelligent agents have information for scheduling and also work to improve schedule.

Knowledge-based Scheduling and Artificial Intelligent Approaches

❖ *Incident based thinking*

The aim of incident based thinking is to determine the best answer for breakdowns considering past events so the solutions of past events can be used for new problems.

❖ *Constraint based scheduling*

It is a good approach in which interactions and audit are better. Since it is based on knowledge-based and incident based module, it operates effectively than incident based scheduling.

❖ *Fuzzy logic*

After all corrections for constraint violation, there is a complete checking and schedule is optimized globally during correction period. Since the same modules are used for scheduling and adjustment, there is a quick reaction but the algorithm is not developed.

❖ *Neural networks*

The predictions are made according to past experiences and they are assuring. The reaction time is very fast to educate neural network. For correct estimation, very carefully trained sets are needed.

❖ *Genetic algorithm*

This algorithm considers genes’ natural selection process for rescheduling. To reduce deviations on the original schedule, it needs transverse and mutation applications. Genetic algorithms are active and produce fairly good schedules however it requires high calculation effort. Demands of reactive scheduling systems can be examined in there heading given below (Vieira, 2003).

Robust: Robust approximation schedule can be valid against various corruptions. Robustness is a requested feature. It reduces decisions to approve schedule during reactive scheduling. Robustness can be improved by purifying from unnecessary reactions to failure and

underestimation. Good performance can be gained by producing small corrections and robust schedules.

Nervousness: Schedule react corruption by being restored or rescheduling. To schedule from all over again seems to be applicable but this kind of solutions may not be very successful. Reactive scheduling should be adapted to existing situations instead of high-cost and dynamic updates. In brief, Nervousness means certain changes, is opposite of stagnation. One of the goals of reactive scheduling systems must be to reduce nervousness.

Stability: It should react system failure and abide the first schedule.

Insignificant changes affect whole schedule performance. Efforts in scheduling area are constructed in scheduling and its predictive nature. In recent years, generation and control of reactive schedules not to loose its effectiveness and protection of validity are concentrated.

The procedure of schedule application, controlling, and restoring has become an important matter lately. The first studies were held in late 70s about rescheduling concept but reactive scheduling concept has appeared in early 90s with cooperation of NIST and US industry. At first they tried to solve problems about rescheduling with analytical approach. With the aid of computer technology and its progress, analytical approaches gave place to artificial intelligence techniques and knowledge-based systems. Reactive scheduling gains importance together with knowledge-based systems. Rescheduling and reactive scheduling solutions can be listed according to solution approach or corruption accruing (unpredictable incident) or can be classified. The study focused on one corruption but more than one corruption can be focused on.

Because of the nature of production area, corruptions can not be separated from each other [5].

3.Application Study

In this case study, an effort of reactive scheduling is made in a defense company’s composite division for a specific job. The company has a very wide production capabilities and advanced technology. Since the manufacturing is intense and there is no scheduling because of workload, some difficulties are faced during scheduling. Because of the dynamic structure, reactive scheduling is applied. Flow-process diagram of composite division is shown in Figure 2.

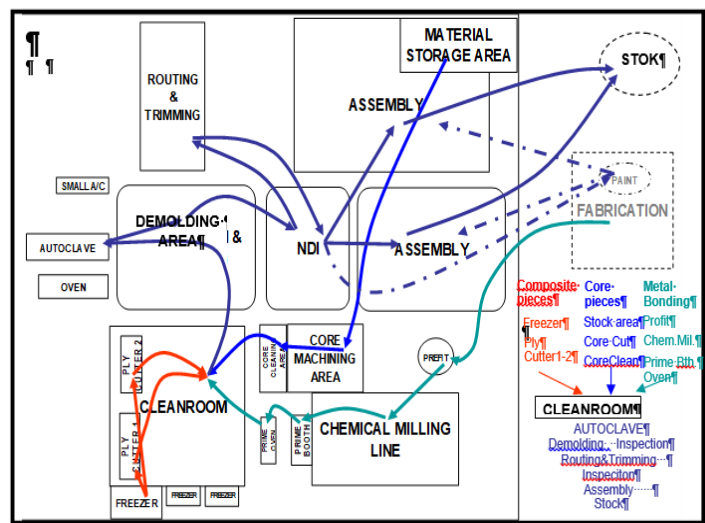


Figure 2. General Composite Flow-Process

At Cleanroom, changes in the system disturb existing schedule. Since there is no certain solution, engineers use their senses, judgments and experiences to take action. The aim of scheduling in this study is to determine the process time for composite products manufactured in Cleanroom, delivery date of products according to entrance and exit time of Autoclave and to minimize process time. The products which are impossible to repair are scraped and to they are listed in schedule in regard to delivery date to be manufactured again. For example, if the product is the last part of manufacturing it should be the first, if not it is scheduled with pieces in line with other part family going Autoclave.

Because of these inconveniences, some problem come out such as not properly using production sources, late response to clients, not corresponding delivery time, increasing in semi finished products and obeying are not used properly, overtime working.

The reason of using reactive scheduling as solution technique is that it act as coordinated effective system in spite of changes during manufacturing. In this case study, it is aimed that the main schedule is updated in Composite division, which is the main part in the factory, without letting any delay in delivery time and other troubles.

Aims of reactive scheduling are summarized as follow;

1. to establish a first schedule which can be adapted in a variety materials and products in Cleanroom.
2. to track workshop circumstances during manufacturing
3. to use workshops existing condition to activate schedule
4. to react changes around workshop while developing advanced schedule in existing workshop environment.
5. to deliver in time
6. to provide Cleanroom-autoclave coordination
7. to use sources (machine, area, personnel) effectively
8. to make long-term plan and to anticipate
9. to calculate time of needs in the basis of piece, to plan material effectively
10. to eliminate scrap materials.

In Cleanroom, end products are delivered to Autoclave. By using Visual Basic at Microsoft Excel, Macro database is developed in order to maximize labor, to minimize product stock (product size x waiting time) for updating of the schedule with troubles determined which covers machine breakdowns, urgent processes, early delivery time and late delivery time. In Figure 3, the time schedule of Cleanroom is shown. Kit No and Item No also known as item families which are determined by work planning department are registered in database. Item's registration information, footprint, personnel need and material used are indicated as constraint in software. The software operates with AC Entrance Date and Hour. The software calculates AC Exit Date and Hour, MAX and MIN Cleanroom Entrance and Exit Date and Hour by using data given and Autoclave schedule. Also the software determines Cleanroom Entrance and Exit Date and Hour which minimizes program aim function

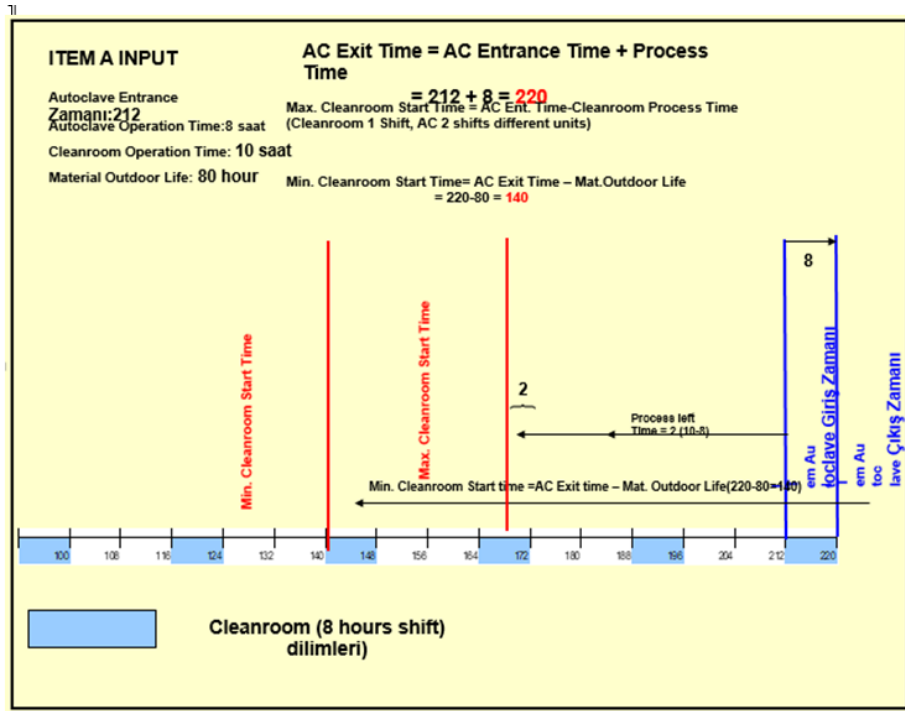


Figure 3. Autoclave - Cleanroom Schedule

The algorithm of data base stated in Figure 3 is given as following;

- ❖ The Cleanroom's process time of Pieces scheduled on Autoclave, number of workers and area occupied are determined.
- ❖ Material life is subtracted from Autoclave exit time and the result is *Minimum Cleanroom Start Time*. Process time is subtracted from Autoclave entrance time and the result gives *Maximum Cleanroom Start Time*. Scheduling must start in between these times.
- ❖ Items are scheduled backward starting from Maximum Cleanroom Start Time.
- ❖ Items' footprint, personnel and tool number are controlled instantaneously for every scheduling process.
- ❖ If space and personnel constraints are overcome or more tool is scheduled in both Cleanroom and Autoclave, rescheduling starts from the previous time interval and is controlled
- ❖ Time interval never exceeds *Minimum Cleanroom Start Time*. For this reason, if some parts are not scheduled because of time interval, personnel and tool number, new schedule is created in regard to overtime.

Some assumptions in algorithm:

- ❖ It is assumed that there is 1 shift per week between 08:00 and 17:00
- ❖ Item's life is limited by the life of material having the shortest "outdoor life time".

After algorithm Cleanroom Schedule is obtained in terms of Soir/Item date and hour. In database it is assumed that the Autoclave process time is 8 hours and Cleanroom process time is estimated in the basis of Autoclave entrance time before item life expires. Cleanroom process time is subtracted from Autoclave entrance date and Cleanroom process start time is calculated.

Rough drafts of relations for program and data flow diagram are illustrated in Figure 4. In Figure 5, 0-Degree Data Flow Diagram is shown.

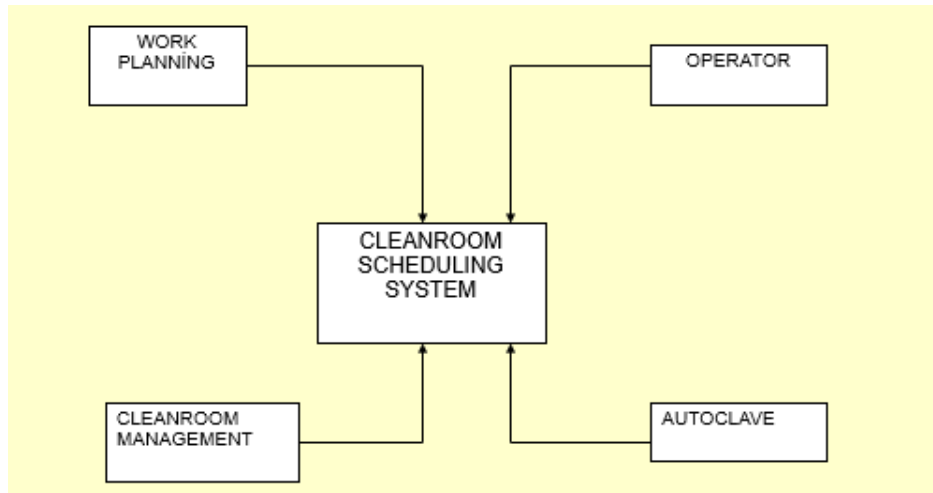


Figure 4. Rough Relation Diagram

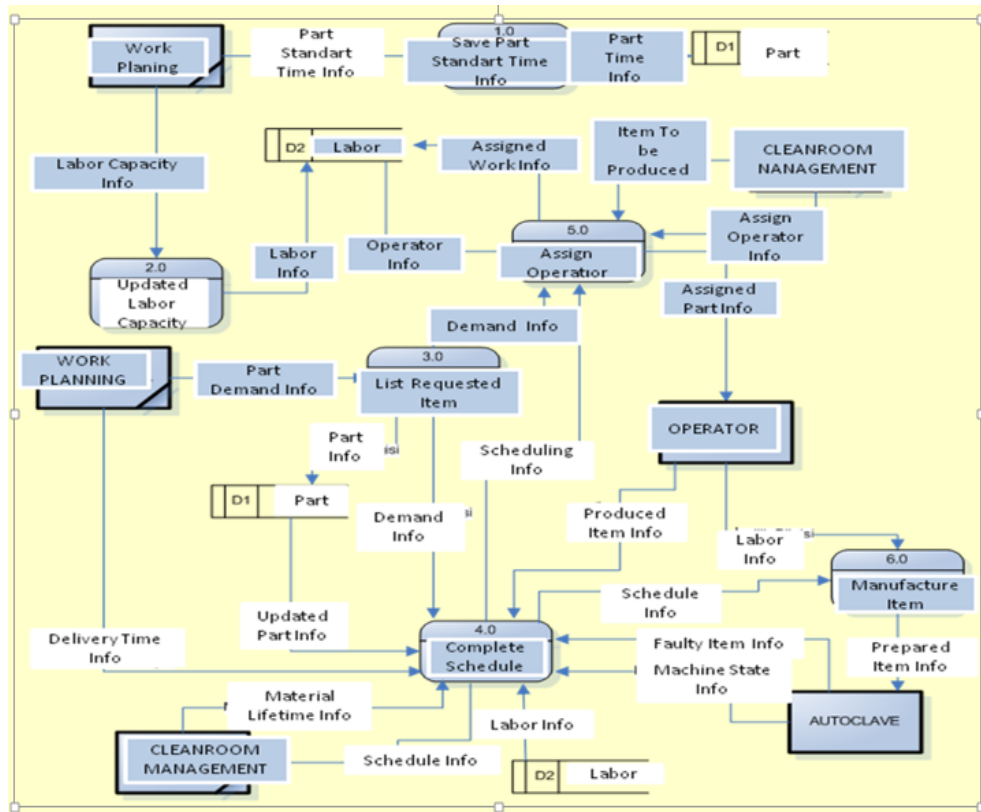


Figure 5. 0-Degree Data Flow Diagram.

As shown in Figure 4 and Figure 5, item standard time information, workload capacity, item request information and delivery date information are gained from Work Planning Department. Item standard time information is saved and sent to item data storing area. Workload capacity is updated and then sent to data storing area. Items demanded by item request information are listed and outputs are sent to data storing area. Delivery time information from Work Planning Department, material life time information from Cleanroom management, information from workload and item data storing area, machine situation and faulty product information from Autoclave and item information requested are used to produce a schedule. The schedule is used to manufacture items and assign operator to process and outputs are reported to Cleanroom Management.

To assign operators to processes some information are supplied by Cleanroom Management such as data of item to be manufactured, operators, item to be requested, and operators are assigned in the basis of workload data storing area. Assigned item information is sent to operator and assigned work is sent to workload data .Item is produced with labor information given by operator and manufactured item information is sent to Autoclave.

Conclusion

In case of unexpected events during application of schedules, update in real time is the basis of reactive scheduling. In this study, according to company's demand, a division was observed and some problems were faced on workshop scheduling. Since the problem had a dynamic structure, it was decided to apply reactive scheduling method.

In Microsoft Excel with Visual Basic, a Macro database was constituted and item scheduling was prepared. To illustrate reactive scheduling process, machine breakdown, urgent works, and early delivery time which led to a repayment on schedule were examined. Only affected items were updated without affecting the general frame of schedule. Software's interfaces were improved by MS Access for engineers to use.

References

Min Soo Suh, Albert Lee, Yung Jae Lee and Young Kwan Ko. (1998). Evaluation of ordering strategies for constraint satisfaction reactive scheduling. *Decision Support Systems*, 2(2), 187-197.

Rabeja, A.S. and Subramaniam, V. (2002). Reactive Recovery of Job Shop Schedules-A Review. *Int. J. Manuf.Tech.*, 19, 756-763

Sakaguchi, T., Kamimura, T., Shirase, K. and Tanimuzu, Y.(2008). GABased Reactive Scheduling For Aggregate Production Scheduling. *The 41stCIRP Conference On Manufacturing Systems, May 26-28 2008, Tokyo*, 257-278.

Vieira,G.E., Herrmann, J.W. and Lin, E.(2003). Rescheduling manufacturing systems: a framework of strategies, policies, and methods. *Journal of scheduling*, 6, 39-62.

Irrigation and Salt Relations in Citrus

Uğur KEKEÇ
Burçak KAPUR

In irrigated agricultural lands, when there is no drainage system to remove excess water from the plant root zone after irrigation, when the constantly rising ground water evaporates from the soil surface, the dissolved salts remain in the soil and soil salinity occurs. Since irrigation is a continuous process, the salt concentration in the soil will increase in conditions where there is very little salt in the water and there is no drainage system in the land. As a result, plants will not be able to grow on the soils in these areas.

In lands that have not been irrigated before, farmers often think that overwatering will result in higher yield increases in areas that will be used for agriculture. They ignore the amount of salt added to the soil with the irrigation water and do not find it necessary to build drainage systems.

As a result, the ground water level increases and rises capillary up to a point very close to the soil surface, and the soil salinity increases (Jorenoosh & Sepaskhah, 2003). Increasing salinity of irrigation water with increasing salinization of agricultural soils hinders agricultural productivity in many semi-arid and arid regions of the world. Citrus fruits are salt sensitive plants. (Maas and Hofmann, 1977) Table 1 shows the relative resistance to salt of some fruit species by classifying them as;

1. Salt-resistant,
2. Moderately salt-resistant,
3. Salt-sensitive (Sönmez and Balaban, 1968).

Citrus varieties are among the “salt sensitive” fruits. According to the sensitivities of citrus fruits among themselves:

- a- Lemon,
- b- Grapefruit
- c- Orange.

Table 1 Relative Salt Resistance Degrees of Some Fruit Species (Sönmez and Balaban, 1968).

FRUIT TREES		
Salt Resistant	Salt Medium Salt Resistant	Salt Sensitive
Ec= 12 ds/m Date	Ec= 10 ds/m Pomegranate Fig Olives Grape Melon Ece= 4 ds/m	Ec= 4 ds/m Pear Apple Orange Grapefruit Plum (for drying) Almond Apricot Peach Strawberry Lemon Avocado Ece= 2 ds/m

Precautions to be Taken Against the Risk of Soil Salinity in Citrus

Citrus fruits are salt sensitive plants. In many parts of the world, salinity significantly limits citrus production. Salty irrigation water reduces the yield in citrus fruits. Every 1.0 dS m⁻¹ increase in soil extract electrical conductivity (EC_e) causes about 13% yield reductions in citrus fruits (Hepaksoy., S 2000). The precautions to be taken against possible soil salinity before the citrus orchards are established are listed below (Maas, 1993; Walker et al., 1983; Zekri & Parsons, 1989).

- 1) Drainage conditions
- 2) Land leveling
- 3) Infiltration rate of soil
- 4) Applying mulch
- 5) Irrigation methods and water management
- 6) Irrigation schedule

Basic Principles to be Considered in Citrus Orchards in Terms of Irrigation, Drainage and Salinity

The necessary procedures before planting citrus orchard saplings are listed below (Çevik, 2002).

- (1) The land should be cleared of weeds and bushes
- (2) The soil should be loosened to a depth of at least 120 cm or more with special digging machines.
- (3) Soil should be analyzed in terms of salinity and plant nutrients content.

- (4) Irrigation water must be analyzed to determine its quality.
- (5) The area should be leveled according to the determined irrigation methods.
- (6) Large areas should be divided into sections suitable for irrigation.
- (7) An irrigation plan should be prepared to ensure uniform distribution of irrigation water to all sides.
- (8) Drainage system is absolutely necessary for loamy and clayey textured soils except sandy soils.
- (9) In sloping areas, “prevention-turning drains” should be opened against surface flows.
- (10) Protection against erosion should be provided by contour ploughing, planting and irrigation up to 15% slope on slope lands, and “terracing” on slopes higher than 15%.
- (11) Establishing citrus orchards on shallow, fine-textured (heavy, dense clay) soils and lands with high ground water should be avoided.

The Quality and Classification of the Most Suitable Irrigation Water for Citrus Fruits

Irrigation waters, whether they are obtained from surface or ground water sources, contain some chemicals that they dissolve from the soil and rocks on which they flow. Concentration and natural properties of these dissolved substances determine the quality of water in terms of irrigation. The type of salt in the irrigation water is more important than the amount. For example, a small amount of boron harms or even kills the plant. If the amount of sodium in the irrigation water is high, the soil becomes unproductive over time. On the other hand, waters contain mainly plant nutrients or some useful salts that help keep the soil productive. When necessary precautions are taken in terms of irrigation and soil and drainage facilities are provided, water of poor quality can be used for irrigation without damaging the soil and plant. Careful and meticulous analysis of irrigation water shows the important salts in the water and their concentrations. Based on these analyzes, it may be possible to classify waters in terms of their suitability for irrigation and to determine the effects of water on plants and soil with confidence (Sönmez & Balaban, 1968).

Detailed water analyzes are time consuming and expensive. Therefore, it should be noted that water samples must accurately represent the water source from which they were taken. Stream samples should be taken from very distant parts of the branches and junctions of the water flowing. Well samples should be taken from wells that have been used for some time. The water samples taken should be placed in clean bottles with cork or rubber stoppers and taken to the laboratory without waiting (Sönmez & Balaban, 1968).

When determining the quality of irrigation water: It is necessary to pay attention to the total concentration of soluble salts, the relative ratio of sodium to other cations, the concentration of boron or other toxic elements.

Electrical Conductivity: The total concentration of soluble salts in irrigation waters can be expressed as electrical conductivity values for diagnostic and classification purposes. Electrical conductivity is very useful because it can be determined easily and precisely. The symbol for electrical conductivity is $EC \times 10^6$. In general, the classification of irrigation waters is made according to the electrical conductivity (micromhos/cm) values as follows (Zhang, 2017):

Waters with an $EC \times 10^6$ value of 0-250 (1st Class)

Waters with an $EC \times 10^6$ of 250-750 (Class 2)

Waters with an $EC \times 10^6$ value of 750-2250 (Class 3)

Waters with an $EC \times 10^6$ value greater than 2250 (Class 4) are waters.

Sodium Adsorption Rate: Since the sodium adsorption rate of the soil solution is related to the adsorption of sodium by the soil, there are obvious benefits in using this rate as an index of sodium or alkali damage of water.

Concentration of Boron or Other Potentially Toxic Elements: Boron; It is a characteristic element of compounds known as boric acid or borax. It is found in almost all natural waters. The concentration of this element ranges from trace amounts to a few ppm. Although it is one of the essential elements for plant development, it has a toxic effect on the plant when the limits to which the plants can tolerate are exceeded. According to the researches, while most of the plants develop normally in the amount of boron between 0.03-0.04 ppm, they are damaged if the amount of boron is 1 ppm.

Classification and use of irrigation water in terms of salinity.

In the classification of irrigation water, the water; It is assumed that it is used under normal conditions in terms of soil texture, infiltration rate, drainage, amount of water used, climate and salt resistance of the plant. As can be seen in the diagram used in the classification of irrigation waters; In this classification, sodium adsorption rate (SAR) is taken as an index of sodium damage and electrical conductivity ($E_c \times 106$) values are taken as an index of salinity damage. Irrigation water classification diagram is shown in Figure 1 (Sonmez & Balaban, 1968).

As stated before, irrigation waters are divided into 4 classes according to their electrical conductivity values. The water classes in terms of salinity are given as follows on the diagram used in the classification of irrigation waters (Sönmez & Balaban, 1968).

Low Salt Water (C1): Generally, it can be used safely for irrigation of many plants in all soils. Some leaching is required, but this occurs spontaneously under normal irrigation conditions, except in soils with extremely low permeability.

Medium Salt Water (C2): It can be used in cases where there is moderate washing. Plants that are moderately resistant to salt can be grown without applying special methods of salinity control.

High Salinity Waters (C3): Special management and selection of salt-tolerant plants are needed to control salinity in soils with limited drainage.

Very High Salinity (C4): Not suitable for irrigation under normal conditions. It can sometimes be used in very rare cases. If it is used, the soils should be permeable, adequate drainage should be provided, plenty of irrigation water should be given to ensure excessive washing and plants should be selected that are very resistant to salt.

Among the water classes mentioned above, suitable areas for citrus fruits should be 1st and 2nd class waters.

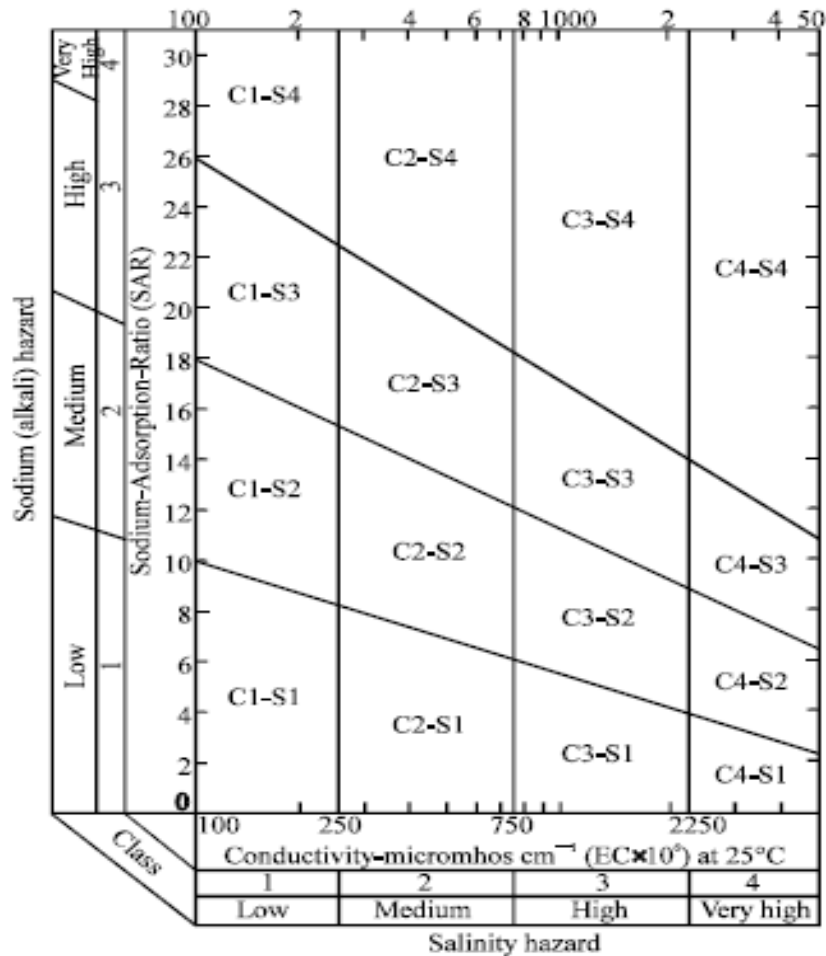


Figure 1. Water classification Scheme by USDA (1954).

Sodium Damage and Classification of Irrigation Waters According to Sodium Content.

Classification of waters according to their quality in terms of sodium damage is more complex than the classification made according to salinity damage. This problem can be addressed to some extent by reducing the degree to which soil absorbs sodium from the water and the absorption that would occur if water was introduced into the soil. The SAR (Sodium Adsorption Rate) value is used as an index of sodium damage.

Classification of irrigation waters in terms of SAR is made in terms of the effect of changeable sodium on the physical properties of the soil (Zaman, Shahid & Heng, 2018).

Water with Low Sodium (S1): It can be used as irrigation water in almost all soils with little risk of damage due to exchangeable sodium. However, plants sensitive to sodium, such as stone fruit trees, can accumulate sodium, which may be harmful to them.

Medium Sodium Waters (S2): In cases where there is no gypsum in the soil and especially under unfavorable washing conditions, it causes excessive sodium damage in fine textured soils with high cation exchange capacity. These waters can be used in coarse textured soils or organic soils with high permeability.

High Sodium Waters (S3): It often leads to the emergence of exchangeable sodium at harmful levels in soils. It requires some special soil management, such as good drainage, excess leaching and the addition of organic matter. Harmful levels of such water exchangeable sodium do not occur in gypsum soils. May require chemical amendments to remove exchangeable sodium, except where amendments cannot be applied in very high saline waters.

Very High Sodium Waters (S4): They are generally not suitable for irrigation except in low and medium salinity conditions. These waters can only be used for irrigation if there is open calcium in the soil or if improvement materials such as gypsum are used. The classification diagram of irrigation water according to sodium content is shown in Figure 2.

When irrigation water is given to calcareous soils, it dissolves excess calcium and this greatly reduces sodium damage. This should be taken into account when using C1-S3 and C1-S4 waters. For calcareous or non-calcareous soils with high pH, the sodium status of water in classes C1-S3, C1-S4 and C2-S4 can be improved by adding gypsum to the water. In case of using C2-S3 and C3-S2 waters like this, it is beneficial to periodically add gypsum to the soil.

As a result, the most suitable irrigation water for citrus fruits is first class water in the C1S1 class. However, it may not be possible to find water of this quality constantly and everywhere. For example, the quality of the water collected in the Seyhan Dam and used for irrigation is in the C2S1 class. It should be noted that when irrigation waters with higher salinity and sodium content must be used, the precautions described above are required. However, it should not be ignored that high salinity and sodium amounts for citrus fruits will be inconvenient, even if precautions are taken.

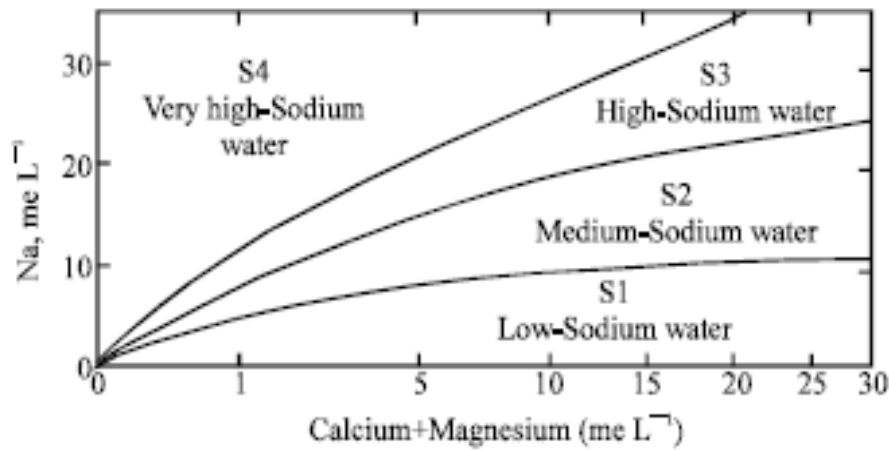


Figure 2. Sodium diagram according to Wilcox (1948)

REFERENCES

- Çevik,B. (2002). "Sulama ve Drenaj." Ç.Ü. Ziraat Fakültesi, Genel Yayın No: 243, Ders Kitapları Yayın No: A-77, Adana.
- Hepaksoy,S. (2000). "Effect Of Salinity On Citrus" *Anadolu, J. Of Aarı* 10 (1) 2000, 52 - 72
- Jorenush,M.H., & Sepaskhah, A.R.(2003). Modelling capillary rise and soil salinity for shallow saline water table under irrigated and non-irrigated conditions. *Agricultural Water Management*. Volume 61, Issue 2, 30 June 2003, Pages 125-141
- Maas, E. V., & Hoffman,G.J.(1977).Crop salt tolerance current assessment. *J. Irr. And Drainage Division, ASCE* 103 (IR2): 115-134.
- Maas, E.V. (1993). Salinity and citriculture. *Tree Physiol.* 12:195–216, DOI: 10.1093/treephys/12.2.195
- Sönmez, N.,&Balaban, A. (1968). "Kültürteknik", Cilt II. Ankara Üniversitesi Yayınları 317, Ders Kitabı 112, Ankara,
- US Salinity Lab. Staff, 1954. *Diagnosis and Improvement of Saline and Alkali Soils*. USDA, Washington, DC., USA
- Walker, R.R., Torokfalvy,E., Grieve, A.M., & Prior,L.D.(1983). Water relations and ion concentrations of leaves on salt stressed citrus plants. *Austral. J. Plant Physiol.* 10:265–277.
- Wilcox, L.V. (1948). *The quality of water for irrigation use*. US Department of Agriculture. Tech. Bulletin 962, pp: 40.
- Zaman, M., Shahid, S.A.,&Heng, L. (2018). *Irrigation Water Quality*. In: *Guideline for Salinity Assessment, Mitigation and Adaptation Using Nuclear and Related Techniques* . Springer, Cham. https://doi.org/10.1007/978-3-319-96190-3_5
- Zekri, M., & Parsons, L.R.. (1989). Growth and root hydraulic conductivity of several citrus rootstocks under salt and polyethylene glycol stresses. *Physiol. Plant.* 77:99–106.
- Zhang H. (2017). *Classification of Irrigation Water Quality*. Extension Oklahoma State University.<https://extension.okstate.edu/fact-sheets/classification-of-irrigation-water-quality.html> , accessed 05.11.2022.

Author Identification with Artificial Neural Networks and Fuzzy Neural Networks in English Documents

Rasim CEKİK¹
Abdullah TURAN²

Introduction

The rapid development of Internet technologies has brought both difficulties and convenience. The massive amount of dirty data that occurs in the Internet environment is at the root of these difficulties. However, text documents make up a large portion of this data. One of the most recent issues being researched is the extraction of meaningful information from this data. The text mining process extracts meaningful and useful information from large amounts of dirty text data. Text mining is performed on written texts to achieve various goals such as natural language processing, sentiment analysis, classification, and clustering. The most commonly used of these purposes is classification. Text classification, known as document classification and verification processes, is a sub-topic in text mining. Author identification is a document classification and verification process. Author identification can be briefly defined as the process of automatically finding which author an article belongs to, through a trained system or model. It is primarily selected features that determine success in author identification. These features should be intended to determine the author's style. Important studies in this field emerged in the 1970s as automatic indexing of documents. Some of these studies are Burrows frequency of words in the document (Burrows, 1992), Brinegar number of words and letters (Brinegar, 1963), Morton lengths of sentences (Morton, 1965), average value of Brainerd syllable numbers (Brainerd, 1974), Holmes number of words in the document and length of the document (Holmes, 1994), used as author features. In this study, the approach of Solorio et al., which accepts every word in all documents as a feature, was used. In the study, the articles of 15 authors with more than 50 articles written in English from the PAN-2011 database were discussed.

When a person comes across an article by an author he regularly reads and follows, even if he does not see the author's name, he can tell that it belongs to the author based on characteristics such as the author's style and writing style. Can this human characteristic be transferred to a system? With the rapid development of technology and the increase in success in adapting the events in nature and the biological structure of living things to technological systems, an answer to this question can be given. The most successful learner of this is Artificial Neural Networks (ANNs) (Abiodun & ark., 2019) which imitate the neural structure of the human brain. Artificial Neural Networks, inspired by the information processing method in the brain, form a network with layers and neurons within these layers. With the numerical values assigned to the neurons and the transfer functions at the outputs of the layers, the calculation is made within the system and the result is obtained from the output layer. ANN analysis was used for author identification in the study. In addition to ANN, adaptive fuzzy neural networks are also used in this study. Fuzzy neural networks

¹ Asisstant Proffesor, Department of Computer Engineering, Sirnak University, Sirnak, TÜRKİYE,

² Asisstant Proffesor, Department of Mechanical and Metal Technologies, Sirnak University, Sirnak, TÜRKİYE,

can be thought of as a combination of fuzzy logic and neural networks. Mamdani-type ANFIS is used as a fuzzy neural network in the study. In experimental studies, it has been observed that ANFIS provides more successful results than ANN for author identification.

Text Mining and Processes

Text Data Mining and Knowledge Discovery from Textual Databases are other names for text mining. Text mining is a subtopic of data mining, but it is not the same as data mining. It is the extraction of patterns from natural language texts rather than event-based databases in Text Mining. It does, however, provide knowledge discovery in stages similar to data mining. In conclusion, text mining is the process of focusing structured data on unstructured text data. The process of extracting meaningful and useful information from large amounts of text documents in electronic environments is known as text mining, also known as text analytics. The goal of text mining is to extract confidential information from data by processing customer comments about products, social media messages, XML documents, and website content such as news, sports, and magazines (Mecca, Raunich & Pappalardo, 2007). The data processing steps in text mining is shown in Figure-1.

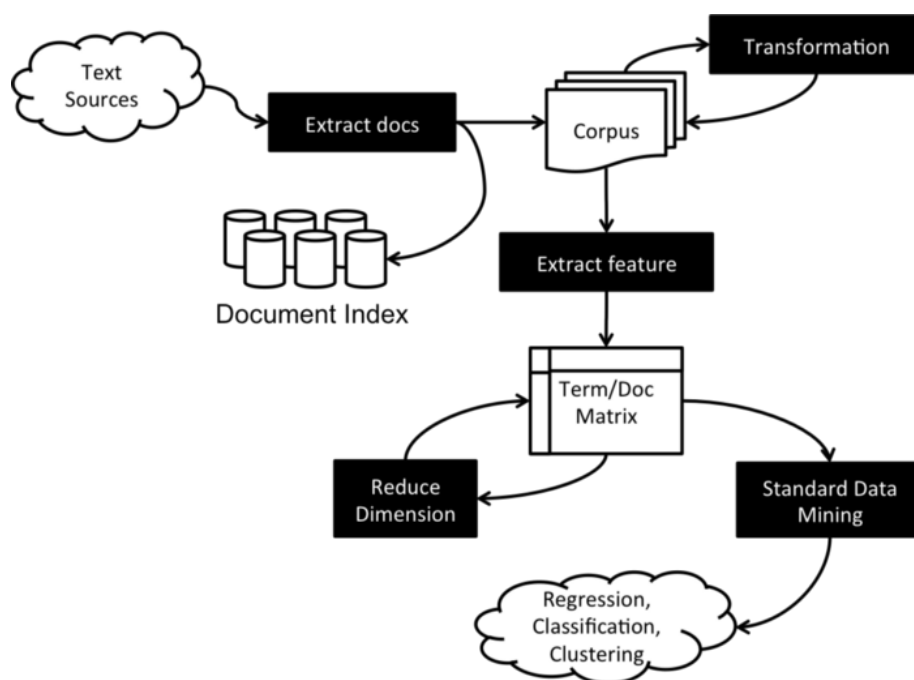


Figure 1. Basic Text Mining Flow

One of the primary tasks of text mining is text classification, which is the process of determining the category of unlabeled documents using labeled text documents. At the end of text preprocessing, feature extraction, feature selection, and weighting, this process is carried out with the help of classifiers, one of the machine learning approaches.

Extraction Author Features

In comparison to other methods, the bag of words (BoW) method, also known as N-gram, is the most widely used and simplest. The frequency and order of a word in the document are irrelevant in this approach. The only thing that matters is whether or not it is included in the document. As an attribute, the method uses the name as many words as possible. For example, if each word is considered a feature, 1-gram (unigram), if two words are considered, 2-grams (bigram),

if three words are considered, 3-grams (trigram), and so on for N-grams. In this study, Unigram was used.

The general framework of the author identification process is given in Figure 2.

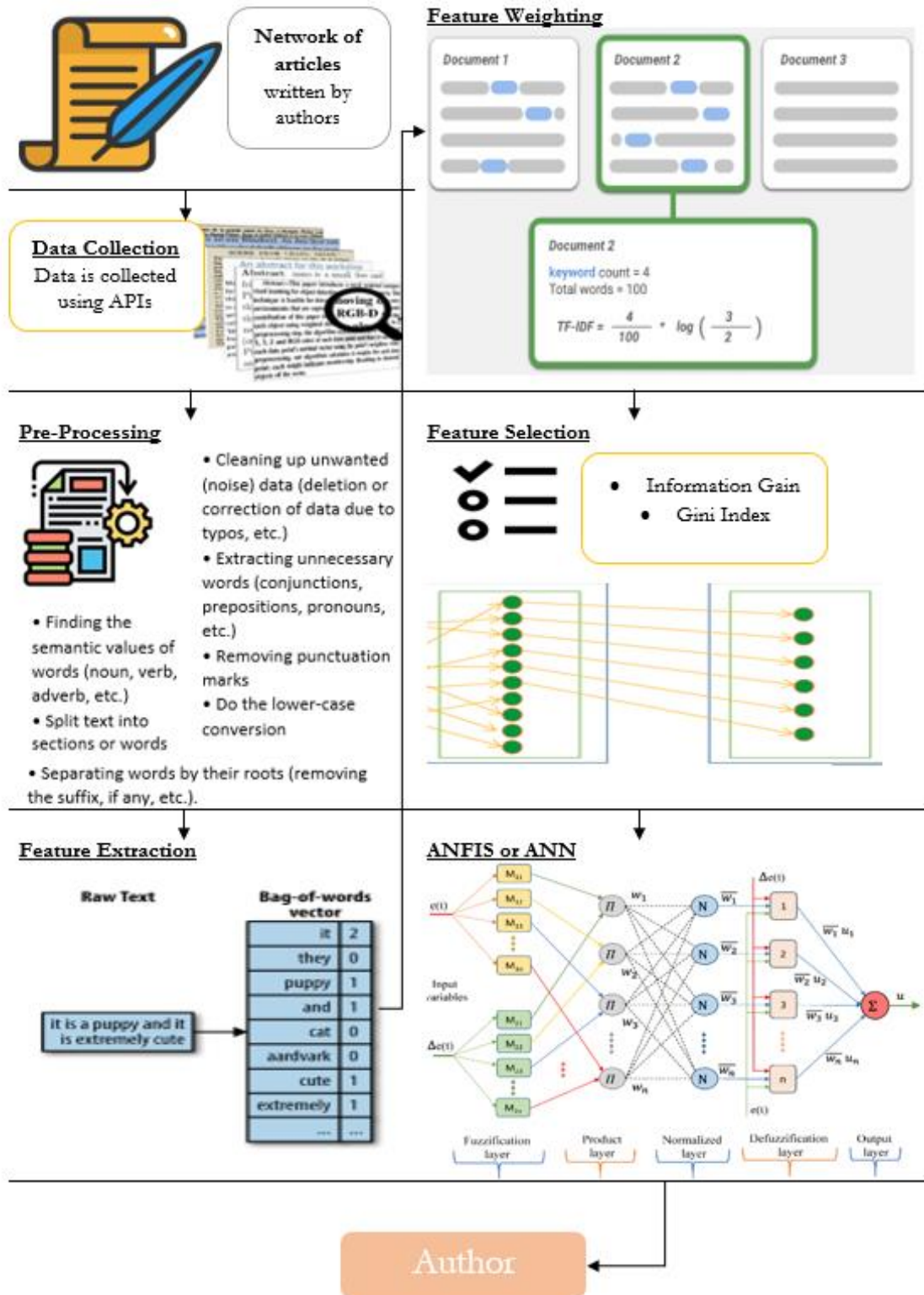


Figure 2. The general structure of the author identification system

Pre-Processing

Because each word in the documents is treated as a feature, some preprocessing is required before performing this operation. In this study, all punctuation in the documents was removed, uppercase letters were converted to lowercase letters, and unnecessary spaces were removed. Following completion of these processes, all remaining words and words or letters are assigned a feature.

Determining Value Sets of Features (Feature Weighting)

Each feature must have a set of values known as the feature space. After the features are determined, the action to be taken is to determine the value set of the features. Various value set determination methods are available for the document classification process. The most well-known of these are term frequency and inverse document frequency. These two terms are often used as term frequency - reverse text frequency (TF-IDF) (Dogan & Uysal, 2020). TF-IDF is the product of TF and IDF. This method is used more. Because it reduces the importance of the words in all documents. This method is also used in the study. This method is calculated by dividing the frequency of occurrence of terms in the document by the frequency of occurrence of terms in the entire dataset. Thus, the terms found in each document are penalized.

Let t_k show the weight of the word for the d_j document. In this case, $TF - IDF$ is expressed mathematically as Equation 1.

$$TFIDF(t_k, d_j) = TF(t_k, d_j) * \log \frac{|Tr|}{|Tr(t_k)|} \quad (1)$$

Where, $TF(t_k, d_j)$ shows frequency of t_k in d_j . $|Tr|$ and $|Tr(t_k)|$ indicate total number of documents, number of documents containing t_k , respectively.

Feature Selection

The main issues in text classification are the large feature dimension space and the highly empty associated information system. This situation reduces the performance of the classifiers while increasing the computational cost. The best way to solve high dimensionality is to choose the best subset from the entire feature set. This process uses feature selection approaches. Feature selection approaches fall into three types: filter, wrapper, and embedded. After each word is determined as a feature, what needs to be done is the process of selecting the determinant features from these features. Various methods are available in the literature for this process (Cekik & Uysal, 2020; Cekik & Uysal, 2022; Parlak & Uysal, 2021a; Cekik & Uysal, 2021b). Information Gain (IG) and Gini Index (GI) are the most widely used feature selection methods in text mining (Raileanu, Laura & Kilian, 2004). Both methods are used in the study. Below are the GI and IG equations, respectively.

c : author,
 m : number of authors,
 t : indicates a feature;

$$IG(t) = - \sum_{i=1}^m p(c_i) \log p(c_i/t) + p(t) \sum_{i=1}^m p(c_i) \log p(c_i/t) + p(\neg t) \sum_{i=1}^m p(c_i/\neg t) \log p(c_i/\neg t) \quad (2)$$

$$GI(t) = \sum_{i=1}^m p(t/c_i)^2 p(c_i/t)^2 \quad (3)$$

Methods Used in The Study

In the study, two different methods were used for author recognition analysis. In other words, Multilayer Artificial Neural Networks (MLANN) and Fuzzy Artificial Neural Networks (ANFIS) were used as analysis methods that determine which article belongs to which author and classify it.

Multilayer Artificial Neural Networks (MLANN)

MLANN are densely parallel systems consisting of many processing elements connected to each other with different weights. Figure 3 shows the general structure of a three-layer MLANN. Where, i is the input layer, j is the hidden layer and k is the output layer, and W_{ij} and W_{jk} are the connection

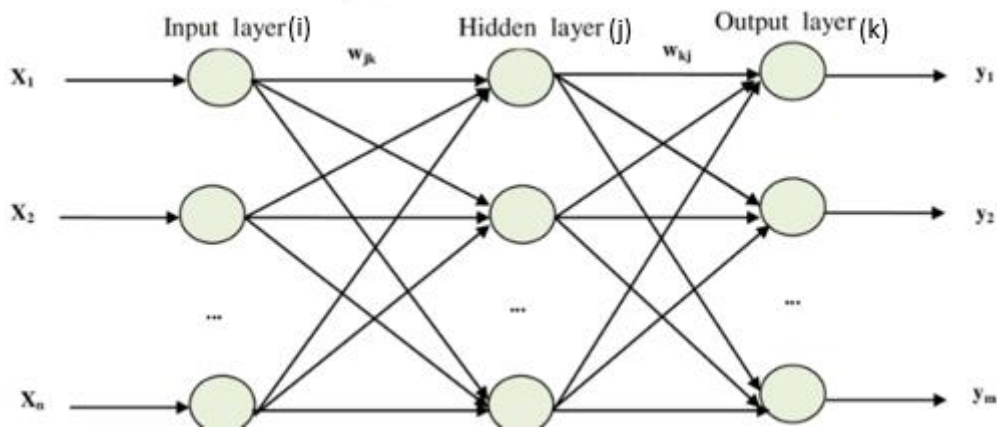


Figure 3. The general structure of a three-layer MLANN

weights between the cell layers. Initially randomly assigned weights are constantly changed during the training process by comparing the estimated outputs with the actual output values, and the errors propagate backwards (right to left in Figure 3) until the link weights that minimize the errors are adjusted. The method used to adjust the weights here is the Levenberg-Marquardt method (Marquardt, 1963). In Figure 3, each cell in layers j and k takes as input the NET-weighted aggregate outputs from the previous layer. NET value is calculated by Equation 4.

$$NET_{pj} = \sum_{i=1}^D W_{ij} C_{pi} + Q_j \quad (4)$$

D is the size of the input vector, Q_j is the bias constant, W_{ij} is the set of weights between layers i and j , and C_{pi} is the output set of layer i for the p sample. Each cell in layers j and k produces the output $f(NET)$ by passing the NET value through a nonlinear description function. This commonly used depiction function is:

$$f(NET) = \frac{1}{1 - e^{-NET}} \quad (5)$$

In the training phase, the total error H_p for the sample p is calculated by Equation 6 based on the difference of squares between the predicted and actual outputs.

$$H_p = \sum_{k=1}^N (G_{pk} - C_{pk})^2 \quad (6)$$

N is the number of iterations, G_{pk} and C_{pk} are the actual and predicted output values for the p sample, respectively. Each link weight A_{ij} is replaced by Equation 7.

$$W_{ij}^{new} = W_{ij}^{old} - [J^T J + \mu I]^{-1} J^T H_p \quad (7)$$

where J is the Jacobian matrix containing the derivatives of the errors according to the weights; J^T transposes the Jacobian matrix; I is the unit matrix and μ is a parameter that affects the convergence rate. When the value of μ increases, the equation turns into a slope reduction algorithm, and when it gets smaller, the equation turns into a Gauss-Newton algorithm.

Fuzzy Artificial Neural Networks (ANFIS)

Adaptive fuzzy neural networks can be thought of as a combination of fuzzy logic and neural networks.

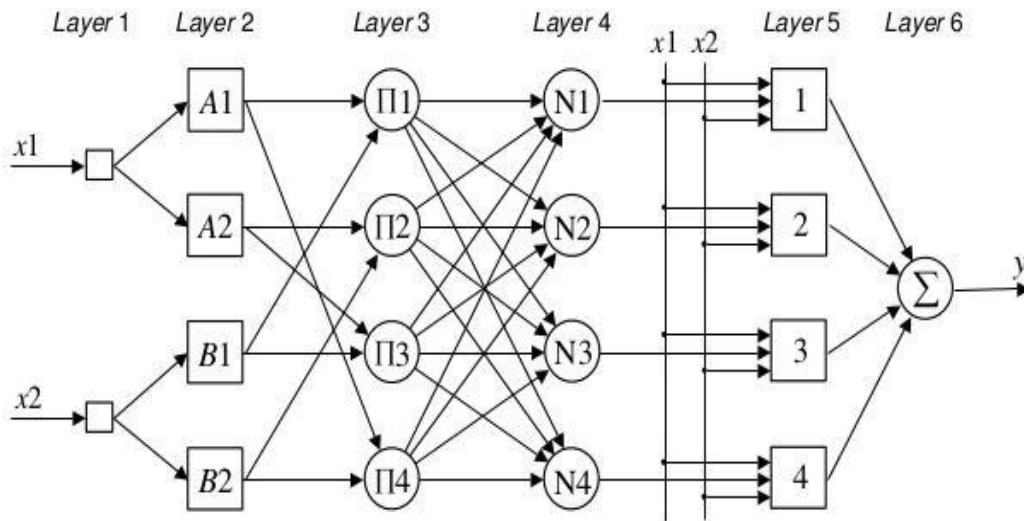


Figure 4. The general structure of a ANFIS

There are two generally known types of ANFIS. These are the Mamdani and Sugenu ANFIS. Mamdani type ANFIS was used in this study. In Mamdani type fuzzy systems, the input, that is, the information and outputs in the database, consists of fuzzy values. The most important drawback of such a fuzzy system is that the digital database cannot enter the general fuzzy system and cannot be used directly in engineering designs because the outputs are not numerical (Sen, 1999). As seen in Figure 4, there are certain layers in ANFIS. We can briefly describe these layers as follows:

- LAYER 1: It is known as the input layer.
- LAYER 2: It is the blur layer. In this layer, the membership function is determined as the activation functions of the neurons to make the blurring.
- LAYER 3: It is the layer where the fuzzy rules are determined.
- LAYER 4: It is the normalization layer. Normalized operations i th for the node:

$$\bar{W}_i = \frac{W_i}{W_1 + W_2 \dots W_n} \quad (8)$$

- LAYER 5: It is the defocusing layer. The weighted result values of a given rule are calculated at each node in the sharpening layer. The parameters in this layer are called result parameters. For each i node in this layer, the normalized neurons and x_1, x_2 inputs are interconnected.
- LAYER 6: In this layer, all neurons are collected with a single sum.

Experimental Works

Experiments for this study, including feature extraction, value and vector set determination, and feature selection, are carried out in JAVA using the ECLIPSE program. In other words, the information system for the analysis systems, specifically the classifiers (ANFIS and MLAAN), is written in JAVA and employs the appropriate methods to perform the author identification process. Analysis systems, on the other hand, are carried out using the appropriate MATLAB tools. MLAAN is represented by NFTOOL, and ANFSED T is represented by ANFSED T. The number of hidden neurons in NFTOOL is 15, and this value is been chosen after experimenting with different neuron numbers (eg 20 25 30). Below are the general structures of the selected analysis systems in Figure 5 and Figure 6.

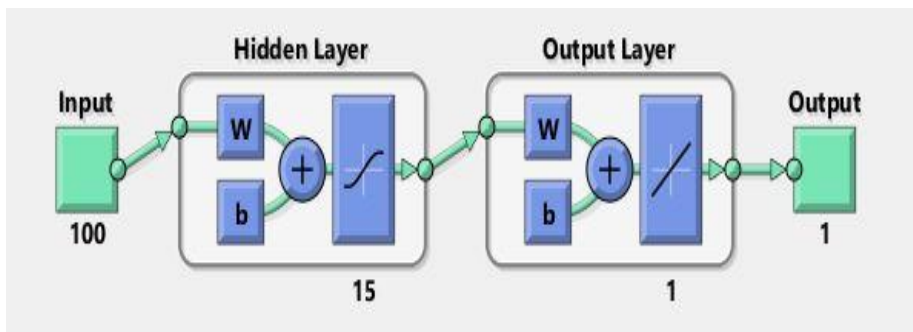


Figure 5. The general structure of the selected MLAAN (This figure was taken with 100 features selected.)

If we move on to the learning algorithm of ANFIS, the hybrid algorithm, which is a combination of the least squares method and the gradient descent method, can be used. However, ANFIS also includes a back propagation algorithm. If the hybrid algorithm is selected, some operations are performed on the least squares estimator.

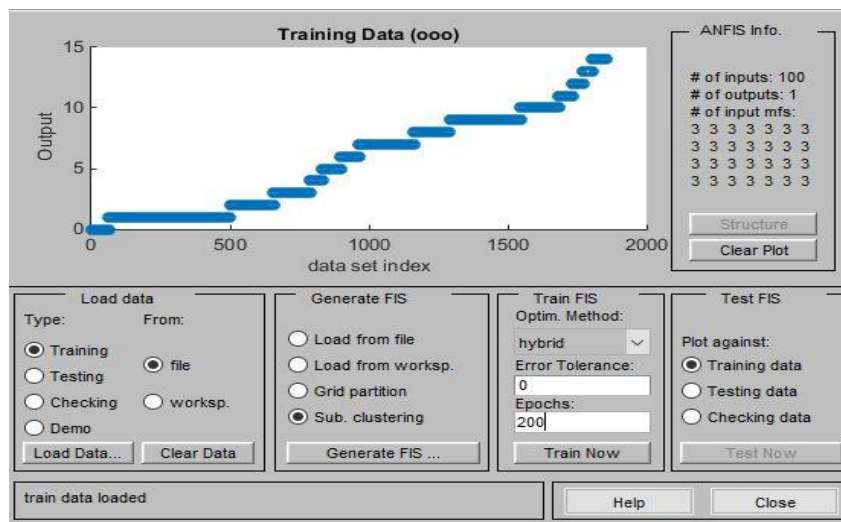


Figure 6. The general structure of the selected ANFIS (This figure was taken with 100 features selected.)

In the study, a total of 6 data sets are used according to the feature selection methods and the number of features, and their results are evaluated. Information Gain and Gini Index from the feature selection algorithms and the performance of each selection algorithm with 100, 150, and 200 features, respectively, are evaluated by analysis systems.

Accuracy Analysis

F-score and Root mean squared error (RMSE) are used as criteria for evaluating the results. The MLAAN and ANFIS performances for Information Gain are given in Table 1 and in Tables (A), (B) and (C) for each selected feature number. Likewise, this situation is expressed in Table 2 for the Gini Index.

Table 1. Information Gain results for 100, 150, and 200 feature sizes

(100)				
	Training Performance		Test Performance	
	f-score	RMSE	f-score	RMSE
MLAAN	0.6782	2.7822	0.3720	3.6126
ANFIS	0.8202	0.8907	0.4806	2.0062

(150)				
	Training Performance		Test Performance	
	f-score	RMSE	f-score	RMSE
MLAAN	0.6782	2.9353	0.2997	3.4674
ANFIS	0.8615	0.7138	0.5285	0.9823

(200)				
	Training Performance		Test Performance	
	f-score	RMSE	f-score	RMSE
MLAAN	0.6782	2.8730	0.2984	3.7515
ANFIS	0.7026	1.0199	0.4108	1.7555

Table 2. Gini Index results for 100, 150, and 200 feature sizes

(100)				
	Training Performance		Test Performance	
	f-score	RMSE	f-score	RMSE
MLAAN	0.6847	3.0688	0.3136	3.7039
ANFIS	0.7956	1.2130	0.4012	1.7750

(150)				
	Training Performance		Test Performance	
	f-score	RMSE	f-score	RMSE
MLAAN	0.6800	2.3569	0.3009	3.4758
ANFIS	0.8012	1.5138	0.5016*	1.5010

(200)				
	Training Performance		Test Performance	
	f-score	RMSE	f-score	RMSE
MLAAN	0.6716	2.9868	0.3055	3.7007
ANFIS	0.8529*	0.6138*	0.4884	1.0158*

When Table 1 and Table 2 are examined, it is seen that the best result is obtained when 150 attributes are selected with information gain and analyzed with ANFIS. In addition, the best results for both selection algorithms are indicated in bold, and the best results for a selection algorithm in

itself are indicated with a bold * sign. For example, when 150 features are selected with gini index, it can be said that the best result for the test is obtained with ANFIS based on f-score. It is also worth noting that when the f-score was calculated for ANFIS, the results were subjected to a masking process and then the relevant calculations were made.

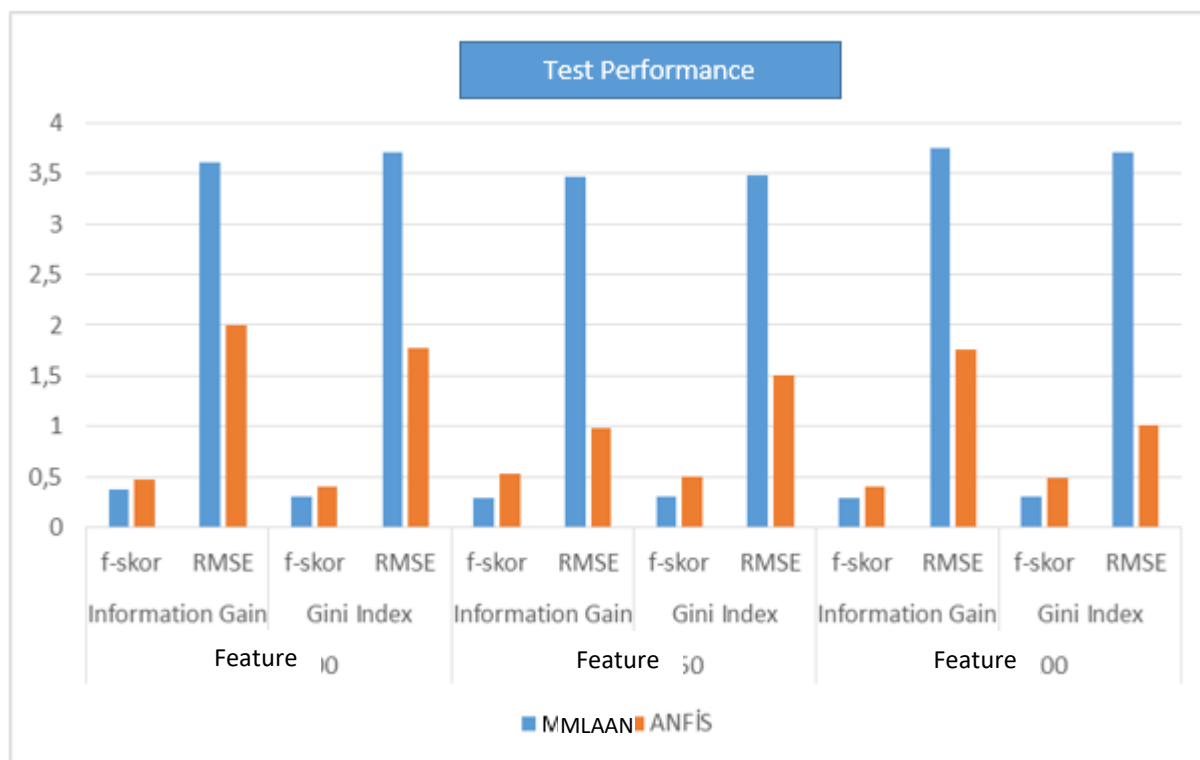


Figure 7. The general structure of a ANFIS

As a result, ANFIS gave more successful results than MLAAN for author identification. In this case, it is more convenient and understandable to see the performance of analysis systems for test data on Figure 7. Finally, it would be useful to underline that the performance may be low for analysis systems in such studies in the literature, especially in author identification processes in text mining.

Conclusion

In this study, the articles written by different authors belong to which author, using machine learning approaches ANFIS and MLAAN. After applying the Information Gain and Gini Index approaches for feature selection to the authors' documents, ANFIS and MLAAN approaches were used in the analysis part. F-score and AAA error value were used for performance evaluation. In the experimental studies, it has been seen that it gives better results with ANFISIN Information.

REFERENCES

- Abiodun, O. I., Jantan, A., Omolara, A. E., Dada, K. V., Umar, A. M., Linus, O. U., ... & Kiru, M. U. (2019). Comprehensive review of artificial neural network applications to pattern recognition. *IEEE Access*, 7, 158820-158846.
- Brainerd, B. (1974). *Weighting Evidence in Language and Literature: A Statistical Approach*. University of Toronto Press.
- Brinegar, C.S. (1963). Mark Twain and the Quintus Curtius Snodgrass Letters: A Statistical Test of Authorship. *Journal of the American Statistical Association*, 58, 85-96.
- Burrows, J.F. (1992). Not unless you ask nicely: the interpretative nexus between analysis and information. *Literary Linguist Comput.* 7, 91-109.
- Cekik, R. & Uysal, A. K. (2020). A novel filter feature selection method using rough set for short text data. *Expert Systems with Applications*, 160, 113691.
- Cekik, R. & Uysal, A. K. (2022). A new metric for feature selection on short text datasets. *Concurrency and Computation: Practice and Experience*. e6909.
- Dogan, T. & Uysal, A. K. (2020). A novel term weighting scheme for text classification: TF-MONO. *Journal of Informetrics*, 14(4), 101076.
- Holmes, D.I. (1994). Authorship Attribution. *Comput Humanities*, 28, 87-106.
- Marquardt, D. (1963). An algorithm for least squares estimation of non-linear parameters. *J.Soc.Ind. Appl.Math.*, 431-441.
- Morton, A.Q. (1965). The Authorship of Greek Prose. *Journal of the Royal Statistical Society, Series A*, 128, 169-233.
- Mecca, G., Raunich, S. & Pappalardo, A. (2007). A new algorithm for clustering search results. *Data & Knowledge Engineering*, 62(3), 504-522.
- Parlak, B. & Uysal, A. K. (2021a). A novel filter feature selection method for text classification: Extensive Feature Selector. *Journal of Information Science*, 0165551521991037.
- Parlak, B., & Uysal, A. K. (2021b). The effects of globalisation techniques on feature selection for text classification. *Journal of Information Science*, 47(6), 727-739.
- Raileanu, R., Laura E. & Kilian S. (2004). Theoretical comparison between the gini index and information gain criteria. *Annals of Mathematics and Artificial Intelligence*, 41(1), 77-93.
- Sen, Z. (1999). *Modelleme İlkeleri*, İTÜ, İnşaat Fak, İnşaat Müh.Böl., Hidrolik A.B.D., İstanbul.

Certain Curvature Tensor Fields on α -Kenmotsu Pseudo Metric Manifolds

Hakan ÖZTÜRK¹
Sermin ÖZTÜRK²

Introduction

A systematic study of contact structures satisfying associated pseudo Riemann metric were introduced by Calvaruso and Perrone (Calvaruso & Perrone, 2010). This structure was first undertaken by Takahashi in Sasakian structures (Takashi, 1969). Contact pseudo metric structures (η, g) where η is a contact 1-form and g a pseudo Riemann metric associated to it. These structures are inherently generalization of contact metric structures.

The class of almost contact metric manifolds which are called Kenmotsu manifolds were firstly introduced by Kenmotsu (Kenmotsu, 1972). It is well known that Kenmotsu manifolds can be characterized through their Levi-Civita connection. Kenmotsu defined a structure closely related to the warped product which was characterized by tensor equations.

In recent times, a systematic study of almost Kenmotsu pseudo metric manifolds has yet to be undertaken. Wang and Liu introduced the geometry of almost Kenmotsu pseudo metric manifolds (Wang & Liu, 2016). The authors emphasized the analogies and differences in connection with the Riemannian metric tensor and obtained certain classification results related to local symmetry and nullity condition.

Locally symmetry is a strong restriction for Kenmotsu manifolds. Furthermore, if Kenmotsu structure holds the Nomizu's condition (Nomizu, 1968), i.e., $R \cdot R = 0$, then it has negative constant curvature and if Kenmotsu manifold is conformally flat, then the manifold is a space of constant negative curvature -1 for dimension greater than 3. The notion of semi-symmetric manifold is defined by

$$R(X, Y) \cdot R = 0 \quad (1)$$

for all vector fields X, Y on M , where $R(X, Y)$ acts as a derivation on R (Nomizu, 1968). Such a space is called "semi-symmetric space" since the curvature tensor of (M, g) at a point $p \in M, R_p$; is the same as the curvature tensor of a symmetric space (that can change with the point of p). Thus locally symmetric spaces are obviously semi-symmetric, but the converse is not true (Calvaruso & Perrone, 2002). Ogawa obtained that if a compact Kaehler manifold is semi-symmetric, then it is locally symmetric (Ogawa, 1977). These spaces were studied in the sense of a complete intrinsic classification by Szabó (Szabó, 1982).

The study is organized as follows: In introduction section, we shall give the short literature information of the study title. In preliminaries section, we shall present the concepts of the

¹ Assoc. Prof., Afyon Kocatepe University, Afyon Vocational School,

² Assoc. Prof., Afyon Kocatepe University, Faculty of Science and Literature, Department of Math.,

manifold theory and the next section is devoted to describe the basic formulas and some propositions of α -Kenmotsu pseudo metric manifolds. The last section contains the main results of the study. We shall give some results and an illustrative example of α -Kenmotsu pseudo metric manifolds satisfying certain curvature tensor conditions. Here, α is taken as a smooth function such that $d\alpha \wedge \eta = 0$ in all calculations on such manifolds.

Preliminaries

Let M be a $(2n + 1)$ -dimensional smooth manifold endowed with a triple (φ, ξ, η) , where φ is a type of $(1,1)$ tensor field, ξ is a vector field, η is a 1-form on M such that

$$\eta(\xi) = 1, \varphi^2 = -I + \eta \otimes \xi, \varphi(\xi) = 0, \eta \circ \varphi = 0, \text{rank}(\varphi) = 2n \quad (2)$$

If M admits a Riemannian metric g , defined by

$$g(\varphi X, \varphi Y) = g(X, Y) - \eta(X)\eta(Y), \eta(X) = g(X, \xi) \quad (3)$$

then M is called almost contact structure (φ, ξ, η, g) . Also, the fundamental 2-form Φ of M is defined by

$$\Phi(X, Y) = g(X, \varphi Y) \quad (4)$$

(Yano & Kon, 1984). If the Nijenhuis tensor vanishes, defined by

$$N_\varphi(X, Y) = [\varphi X, \varphi Y] - \varphi[\varphi X, Y] - \varphi[X, \varphi Y] + \varphi^2[X, Y] + 2d\eta(X, Y)\xi \quad (5)$$

then (M, φ, ξ, η) is said to be normal (Blair, 1976). It is obvious that a normal almost Kenmotsu manifold is said to be Kenmotsu manifold.

Let (M, g) be an n -dimensional Riemannian manifold. We denote by ∇ the covariant differentiation with respect to the Riemann metric g . Then we have

$$R(X, Y)Z = \nabla_X \nabla_Y Z - \nabla_Y \nabla_X Z - \nabla_{[X, Y]} Z, \quad (6)$$

The Ricci tensor of M is defined as

$$S(X, Y) = \sum_{i=1}^n R(X, e_i, Y, e_i) \quad (7)$$

where $\{e_1, e_2, \dots, e_n\}$ is a local orthonormal basis. Also, the Ricci operator Q is a tensor field of type $(1,1)$ on M defined by

$$g(QX, Y) = S(X, Y) \quad (8)$$

for any vector fields (Blair, 1976).

Almost contact metric manifolds such that η and Φ are closed called almost cosymplectic manifolds. Also, an almost contact metric manifold such that $d\eta = 0$ and $d\Phi = 2\eta \wedge \Phi$ is said to be an almost Kenmotsu manifold (Kenmotsu, 1972).

An almost contact metric manifold is said to be almost α -Kenmotsu if

$$d\eta = 0, d\Phi = 2\alpha(\eta \wedge \Phi). \quad (9)$$

Here, α is a non-zero real constant (Kim & Pak, 2005). It is obvious that a normal almost α -Kenmotsu manifold is said to be α -Kenmotsu manifold.

α -Kenmotsu Pseudo Metric Manifolds

This section is devoted to give fundamental concepts of α -Kenmotsu pseudo metric manifolds. In particular, basic curvature properties of α -Kenmotsu pseudo metric manifolds are presented. Here, α is given by a smooth function on M such that $d\alpha \wedge \eta = 0$.

A pseudo Riemannian metric g on M is said to be compatible with the almost contact structure (φ, ξ, η) if $g(\varphi X, \varphi Y) = g(X, Y) - \varepsilon \eta(X)\eta(Y)$ where $\varepsilon = \pm 1$. A smooth manifold M furnished with an almost contact structure (φ, ξ, η) and a compatible pseudo Riemannian metric g is called an almost contact pseudo metric manifold which is denoted by $(M, \varphi, \xi, \eta, g)$. It is obvious that $g(\varphi X, Y) = -g(X, \varphi Y)$, $\eta(X) = \varepsilon g(X, \xi)$ and $g(\xi, \xi) = \varepsilon$.

An almost contact pseudo metric manifold satisfying (9) is said to be an almost α -Kenmotsu pseudo metric manifold for $\alpha \neq 0, \alpha \in R$. When an almost α -Kenmotsu pseudo metric manifold M has a normal almost contact structure, we can say that it is an α -Kenmotsu pseudo metric manifold.

Proposition 1. Let $(M, \varphi, \xi, \eta, g)$ be a $(2n + 1)$ -dimensional almost contact metric manifold. If M is an α -Kenmotsu pseudo metric manifold, then we have

$$\nabla_X \xi = -\alpha \varphi^2 X = \alpha[X - \eta(X)\xi], \tag{10}$$

$$(\nabla_X \varphi)Y = \alpha[\varepsilon g(\varphi X, Y)\xi - \eta(Y)\varphi X] \tag{11}$$

for $X, Y \in \chi(M)$ (Öztürk & Öztürk, 2020).

Proposition 2. Let $(M, \varphi, \xi, \eta, g)$ be an α -Kenmotsu pseudo metric manifold. Then we have

$$R(X, Y)\xi = [\alpha^2 + \xi(\alpha)][\eta(X)Y - \eta(Y)X] \tag{12}$$

$$R(X, \xi)Y = -[\alpha^2 + \xi(\alpha)][-\varepsilon g(Y, X)\xi + \eta(Y)X] \tag{13}$$

$$R(X, \xi)\xi - \varphi R(\varphi X, \xi)\xi = 2[\alpha^2 + \xi(\alpha)][-X + \eta(X)\xi] \tag{14}$$

$$\eta(R(X, Y)Z) = \varepsilon[\alpha^2 + \xi(\alpha)][-\eta(X)g(Y, Z) + \eta(Y)g(X, Z)] \tag{15}$$

$$S(X, \xi) = -2n[\alpha^2 + \xi(\alpha)]\eta(X) \tag{16}$$

$$Q\xi = -2n\varepsilon [\alpha^2 + \xi(\alpha)] \tag{17}$$

$$(\nabla_X \eta)Y = \alpha[\varepsilon g(X, Y) - \eta(X)\eta(Y)] \tag{18}$$

$$S(\varphi X, \varphi Y) = [\alpha^2 + \xi(\alpha)](\varepsilon S(X, Y) - 2n[g(X, Y) - \varepsilon \eta(X)\eta(Y)]). \tag{19}$$

Here, α is defined by a smooth function such that $d\alpha \wedge \eta = 0$ and $\varepsilon = g(\xi, \xi)$ (Öztürk, 2017).

Definition 1. Let $(M, \varphi, \xi, \eta, g)$ be an α -Kenmotsu pseudo metric manifold. If the following condition holds

$$S(X, Y) = \lambda g(X, Y) + \varepsilon \mu \eta(X)\eta(Y) \tag{20}$$

for any $X, Y \in \chi(M)$, then M is said to be an η -Einstein α -Kenmotsu pseudo metric manifold. Here, λ and μ are the arbitrary functions on M . In particular, M becomes an Einstein manifold when $\mu = 0$ (Blair, 1976).

Proposition 3. Let $(M, \varphi, \xi, \eta, g)$ be an η -Einstein α -Kenmotsu pseudo metric manifold. Then we have

$$\lambda + \varepsilon\mu = -2n\varepsilon\alpha^2 \tag{21}$$

$$r = \lambda\varepsilon(2n + 1) + \varepsilon\mu, \lambda = \frac{r+2n\varepsilon\alpha^2}{(2n+1)\varepsilon-1}, \mu = \left[\frac{2n(\alpha^2+r)+r}{(2n+1)\varepsilon-1} \right]$$

for any $X, Y \in \chi(M)$ (Öztürk & Öztürk, 2022).

Definition 2. Let (M, g) be a $(2n + 1)$ -dimensional ($n \geq 2$) Riemannian manifold. Then the D -conformal curvature tensor field on M defined as follows:

$$\begin{aligned} B(X, Y)Z &= R(X, Y)Z + \frac{1}{2n-2} [S(X, Z)Y - S(Y, Z)X + g(X, Z)QY - g(Y, Z)QX \\ &- S(X, Z)\eta(Y)\xi + S(Y, Z)\eta(X)\xi - \eta(X)\eta(Z)QY + \eta(Y)\eta(Z)Q - \frac{k-2}{2n-2} [g(X, Z)Y - \\ &g(Y, Z)X] + \frac{k}{2n-2} [g(X, Z)\eta(Y)\xi - g(Y, Z)\eta(X)\xi + \eta(X)\eta(Z)Y - \eta(Y)\eta(Z)X]. \end{aligned} \tag{22}$$

Here, $k = \frac{r+4n}{2n-1}$ and r is a scalar curvature of M (Chuman, 1983).

Main Results

In this section, some curvature tensor fields are investigated on α -Kenmotsu pseudo metric manifolds depending on α such that $d\alpha \wedge \eta = 0$. Thus we state the following results:

Theorem 1. Let $(M, \varphi, \xi, \eta, g)$ be a $(2n + 1)$ -dimensional α -Kenmotsu D -conformal semi-symmetric pseudo metric manifold. If α is parallel along the characteristic vector field ξ and ξ is taken as time-like then M is an η -Einstein manifold. On the other hand, there exists no η -Einstein manifold if the characteristic vector field ξ is space-like.

Proof. According to the hypothesis, we assume that M is an α -Kenmotsu D -conformal semi-symmetric pseudo metric manifold. Now, let us introduce the D -conformal curvature tensor field B . If the D -conformal curvature tensor field B satisfies the following condition

$$R(X, Y) \cdot B = 0 \tag{23}$$

then M is said to be a D -conformal semi-symmetric manifold ($n \geq 2$) (Taleshian et al., 2011). In other words, we have

$$(R(X, Y) \cdot B)(Z, U)V = 0. \tag{24}$$

Then using the definition of (23), (24) can be written as

$$\begin{aligned} R(X, Y)B(Z, U)V - B(R(X, Y)Z, U)V \\ - B(Z, R(X, Y)U)V - B(Z, U)R(X, Y)V = 0. \end{aligned} \tag{25}$$

By the help of (13) and (25) with $X = \xi$, we deduce

$$\begin{aligned} [\alpha^2 + \xi(\alpha)][\eta(B(Z, U)V)Y - \varepsilon g(B(Z, U)V, Y)\xi - \eta(Z)B(Y, U)V] \\ + [\alpha^2 + \xi(\alpha)][\varepsilon g(Y, Z)B(\xi, U)V - \eta(U)B(Z, Y)V + \varepsilon g(Y, U)B(Z, \xi)V] \\ + [\alpha^2 + \xi(\alpha)][-\eta(V)B(Z, U)Y + \varepsilon g(V, Y)B(Z, U)\xi] = 0. \end{aligned} \tag{26}$$

Taking the inner product of both sides of (26) with respect to ξ , we have

$$\begin{aligned} [\alpha^2 + \xi(\alpha)][\varepsilon\eta(B(W, V)U)\eta(Z) - g(B(W, V)U, Z) - \varepsilon\eta(W)\eta(B(Z, V)U)] \\ + [\alpha^2 + \xi(\alpha)][g(Z, W)\eta(B(\xi, V)U) - \varepsilon\eta(V)\eta(B(W, Z)U) + g(Z, V)\eta(B(W, \xi)U)] \\ + [\alpha^2 + \xi(\alpha)][-\varepsilon\eta(U)\eta(B(W, V)Z) + g(U, Z)\eta(B(W, V)\xi)] = 0. \end{aligned} \tag{27}$$

Taking $Y = Z$ and $\xi(\alpha) = 0$ in (27), we get

$$\begin{aligned} & \varepsilon\eta(B(Z, U)V)\eta(Z) - g(B(Z, U)V, Z) - \varepsilon\eta(Z)\eta(B(Z, U)V) \\ & + g(Z, Z)\eta(B(\xi, U)V) - \varepsilon\eta(U)\eta(B(Z, Z)V) + g(Z, U)\eta(B(Z, \xi)V) \\ & - \varepsilon\eta(V)\eta(B(Z, U)Z) + g(V, Z)\eta(B(Z, U)\xi) = 0. \end{aligned} \tag{28}$$

Moreover, from (22) it follows that

$$\eta(B(Z, U)V = F\eta(U)g(Z, V) - F\eta(Z)g(U, V) \tag{29}$$

where F is defined by

$$F = \frac{1+\varepsilon\alpha^2(n-2)}{2n-2}. \tag{30}$$

Taking into account of (28) and (29), we obtain

$$\begin{aligned} g(B(Z, U)V, Z) &= \varepsilon g(Z, Z)[F\eta(U)\eta(V) - Fg(U, V)] + \varepsilon g(Z, U)[Fg(Z, V) - F\eta(Z)\eta(V)] \\ &\quad - \varepsilon\eta(V)[F\eta(U)g(Z, Z) - F\eta(Z)g(Z, V)]. \end{aligned} \tag{31}$$

Follows from (31) we have

$$g(B(Z, U)V, Z) = \varepsilon F[g(Z, U)g(Z, V) - g(Z, Z)g(U, V)]. \tag{32}$$

Now, we may take a local orthonormal φ -basis $E_j = \{e_1, \dots, e_n, \varphi e_1, \dots, \varphi e_n, \xi\}, j = 1, \dots, n$. Then taking contraction in (32) with respect to $Z = E_j$, we get

$$\sum_{j=1}^{2n+1} g(B(E_j, U)V, E_j) = \varepsilon F(1 - \varepsilon(2n + 1))g(U, V). \tag{33}$$

Also, considering (22), it follows that

$$\begin{aligned} & \sum_{j=1}^{2n+1} g(B(E_j, U)V, E_j) = S(U, V) \\ & + \frac{1}{2n-2} [2S(U, V) - \varepsilon(2n + 1)S(U, V) - rg(V, U) + \varepsilon S(U, V) + r\eta(V)\eta(U) + \\ & \quad 2n\alpha^2\eta(V)\eta(U)[\varepsilon + 1]] - \frac{k-2}{2n-2} [g(V, U) - \varepsilon(2n + 1)g(V, U)] \\ & \quad + \frac{k}{2n-2} [-\varepsilon g(V, U) + (1 - 2n\varepsilon)\eta(V)\eta(U)]. \end{aligned} \tag{34}$$

Finally, using (33) and (34), it yields

$$S(U, V) = F_1g(U, V) + F_2\eta(U)\eta(V) \tag{35}$$

where F_1 and F_2 are defined by

$$F_1 = \frac{-2r(n-1)+2(1-\varepsilon)+4n\varepsilon(k-1)-k(1+2\varepsilon)+(\varepsilon-1)(n\alpha^2-2\alpha^2-1)+2n(1-n\alpha^2\varepsilon)}{2n(\varepsilon-1)} \tag{36}$$

and

$$F_2 = \frac{r+2n\alpha^2(\varepsilon+1)+k(1-2n\varepsilon)}{2n(\varepsilon-1)}. \tag{37}$$

Thus it completes the proof by (36) and (37).

Theorem 2. Let $(M, \varphi, \xi, \eta, g)$ be a $(2n + 1)$ -dimensional α -Kenmotsu Ricci D -conformal semi-symmetric pseudo metric manifold. If α is parallel along the characteristic vector field ξ , then M is an Einstein manifold with constant scalar curvature $r = -2n\alpha^2(2n + 1)$.

Proof. We suppose that M is a Ricci D -conformal semi-symmetric pseudo metric manifold. It means that

$$B(X, Y) \cdot S(Z, U) = 0 \tag{38}$$

for $n \geq 2$. Thus (38) can be written as

$$S(B(X, Y)Z, U) + S(Z, B(X, Y)U) = 0. \tag{39}$$

Then putting $X = U = \xi$ in (39) we have

$$S(B(\xi, Y)Z, \xi) + S(Z, B(\xi, Y)\xi) = 0. \tag{40}$$

where $\xi(\alpha) = 0$.

Furthermore, in view of (29) we deduce

$$B(\xi, Z)U = F[\varepsilon\eta(U)Z - \xi g(Z, U)] \tag{41}$$

and

$$B(\xi, Z)\xi = F[Z - \varepsilon\eta(Z)\xi]. \tag{42}$$

Taking into account of (41) and (42) in (40) we obtain

$$S(Y, Z) = -2n\alpha^2\varepsilon g(Y, Z). \tag{43}$$

Lastly, taking contraction in (43) with respect to $Y = Z = E_j$, we get

$$r = -2n\alpha^2(2n + 1).$$

Here, E_j is a local orthonormal φ -basis such that $\{e_1, \dots, e_n, \varphi e_1, \dots, \varphi e_n, \xi\}$, $j = 1, \dots, n$. Thus the proof ends.

Theorem 3. Let M be a $(2n + 1)$ -dimensional D -conformal flat α -Kenmotsu pseudo-metric manifold. If α is parallel along the characteristic vector field ξ and ξ is time-like, then M is an η -Einstein manifold. Moreover, there exists no η -Einstein manifold where ξ is space-like.

Proof. According to the hypothesis, let us assume that M is a D -conformal flat α -Kenmotsu pseudo-metric manifold. Namely, we have

$$B(X, Y)Z = 0. \tag{44}$$

In view of (22) and (44), it follows that

$$\begin{aligned} R(X, Y)Z &= -\frac{1}{2n-2}[S(X, Z)Y - S(Y, Z)X + g(X, Z)QY - g(Y, Z)QX - S(X, Z)\eta(Y)\xi + \\ &S(Y, Z)\eta(X)\xi - \eta(X)\eta(Z)QY + \eta(Y)\eta(Z)QX] + \frac{k-2}{2n-2}[g(X, Z)Y - g(Y, Z)X] \\ &\quad - \frac{k}{2n-2}[g(X, Z)\eta(Y)\xi - g(Y, Z)\eta(X)\xi + \eta(X)\eta(Z)Y - \eta(Y)\eta(Z)X]. \end{aligned} \tag{45}$$

Then taking the inner product on both sides of (45) with respect to U , we get

$$\begin{aligned} g(R(X, Y)Z, U) &= -\frac{1}{2n-2}[S(X, Z)g(Y, U) - S(Y, Z)g(X, U) + g(X, Z)g(QY, U) \\ &\quad - g(Y, Z)g(QX, U) - \varepsilon S(X, Z)\eta(Y)\eta(U) + \varepsilon S(Y, Z)\eta(X)\eta(U) - \eta(X)\eta(Z)g(QY, U) + \\ &\quad \eta(Y)\eta(Z)g(QX, U)] + \frac{k-2}{2n-2}[g(X, Z)g(Y, U) - g(Y, Z)g(X, U)] \\ &\quad - \frac{k}{2n-2}[\varepsilon g(X, Z)\eta(Y)\eta(U) - \varepsilon g(Y, Z)\eta(X)\eta(U) + \eta(X)\eta(Z)g(Y, U) - \eta(Y)\eta(Z)g(X, U)] \end{aligned} \tag{46}$$

where $R(X, Y, Z, U) = g(R(X, Y)Z, U)$. From (15) and (16), (46) turns into

$$\begin{aligned} \eta(R(X, Y)Z) &= -\varepsilon[\alpha^2 + \xi(\alpha)][\eta(X)g(Y, Z) + \eta(Y)g(X, Z)] = \\ &\quad -\frac{\varepsilon}{2n-2}\{[(\varepsilon - 1)\eta(Y)S(X, Z) + (1 - \varepsilon)\eta(X)S(Y, Z)] \end{aligned} \tag{47}$$

$$-2n[\alpha^2 + \xi(\alpha)][\eta(Y)S(X, Z) - \eta(X)S(Y, Z)]\} \\ + \frac{k-2}{2n-2} [\eta(Y)g(X, Z) - \eta(X)g(Y, Z)] - \frac{\varepsilon k}{2n-2} [\eta(Y)g(X, Z) - \eta(X)g(Y, Z)]$$

for $U = \xi$. Putting $Y = \xi$ in (47) we have

$$-\frac{\varepsilon}{2n-2} [(\varepsilon - 1)\varepsilon S(X, Z) - 2n[\alpha^2 + \xi(\alpha)](\eta(X)\eta(Z) + \varepsilon g(X, Z))] \quad (48) \\ + \frac{(k-2)}{2n-2} \varepsilon [g(X, Z) - \eta(X)\eta(Z)] - \frac{k}{2n-2} [g(X, Z) - \eta(X)\eta(Z)] \\ = [\alpha^2 + \xi(\alpha)][g(X, Z) - \eta(X)\eta(Z)].$$

Next, simplifying (48) and $\xi(\alpha) = 0$, we obtain

$$S(X, Z) = \left(\frac{2n-2}{\varepsilon-1}\right) \left[\frac{\varepsilon(k-2)-k+2n\alpha^2}{2n-2} - \alpha^2\right] g(X, Z) \quad (49) \\ + \left(\frac{2n-2}{\varepsilon-1}\right) \left[\frac{-\varepsilon(k-2)+k+2n\varepsilon\alpha^2}{2n-2} + \alpha^2\right] \eta(X)\eta(Z).$$

So (49) becomes

$$S(X, Z) = \left[\frac{2(\alpha^2-\varepsilon)}{\varepsilon-1} + k\right] g(X, Z) \quad (50) \\ + \left[\frac{2(\varepsilon-\alpha^2+n\alpha^2(\varepsilon+1))}{\varepsilon-1} - k\right] \eta(X)\eta(Z).$$

Thus, considering (39), it is clear that the η -Einstein structure can not exist when the characteristic vector field ξ is chosen as space-like ($\varepsilon = g(\xi, \xi) = 1$). On the other hand, if the characteristic vector field ξ is chosen as time-like ($\varepsilon = g(\xi, \xi) = -1$), then we can state the following equation

$$S(X, Z) = \left[\frac{r+2n+1}{2n-1} - \alpha^2\right] g(X, Z) \quad (51) \\ + \left[-\frac{r+4n}{2n-1} + 1 + \alpha^2\right] \eta(X)\eta(Z)$$

which completes the proof.

Theorem 4. Let M be a $(2n + 1)$ -dimensional α -Kenmotsu pseudo-metric manifold. If α is parallel along the characteristic vector field ξ , then there exists no ξ - D -conformal flat manifold where ξ is space-like.

Proof. In accordance with the hypothesis, we suppose that M is an α -Kenmotsu pseudo metric manifold satisfying the ξ - D -conformal flat condition. In other words, we have

$$B(X, Y)\xi = 0. \quad (52)$$

Making use of (22), (52) becomes

$$R(X, Y)\xi + \frac{1}{2n-2} [S(X, \xi)Y - S(Y, \xi)X + g(X, \xi)QY - g(Y, \xi)QX - S(X, \xi)\eta(Y)\xi \\ + S(Y, \xi)\eta(X)\xi - \varepsilon\eta(X)QY + \xi\eta(Y)QX] - \frac{\varepsilon(k-2)}{2n-2} [g(X, \xi)Y - g(Y, \xi)X] \\ + \frac{\varepsilon k}{2n-2} [g(X, \xi)\eta(Y)\xi - g(Y, \xi)\eta(X)\xi + \eta(X)Y - \eta(Y)X] = 0. \quad (53)$$

Follows from (12), (13) (16) and taking the inner product on both sides of (53) with respect to V , we deduce

$$\begin{aligned}
 & [\alpha^2 + \xi(\alpha)][\eta(X)g(Y, V) - \varepsilon\eta(Y)g(X, V)] \\
 & + \frac{-2n[\alpha^2 + \xi(\alpha)]}{2n-2} [\eta(X)g(Y, V) - \eta(Y)g(X, V)] \\
 & - \left(\frac{(k-2)\varepsilon}{2n-2}\right) [\eta(X)g(Y, V) - \eta(Y)g(X, V)] \\
 & + \left(\frac{\varepsilon k}{2(n-1)}\right) [\eta(X)g(Y, V) - \eta(Y)g(X, V)] = 0.
 \end{aligned} \tag{54}$$

Then putting $Y = \xi$ and $\xi(\alpha) = 0$ in (54) we have

$$\left[\frac{\alpha^2\varepsilon-1}{n-1}\right] g(X, V) + \left[\frac{-\alpha^2\varepsilon+1}{n-1}\right] \eta(X)\eta(V) = 0. \tag{55}$$

Also, it is well known that

$$g(\varphi X, \varphi V) = g(X, V) - \varepsilon\eta(X)\eta(V). \tag{56}$$

Since $n \geq 2$ and $\alpha^2 \neq 0$, (55) takes the form

$$g(X, V) - \eta(X)\eta(V) = 0. \tag{57}$$

In view of (55) and (56) with $\varepsilon = 1$, it follows that

$$g(\varphi X, \varphi V) = 0. \tag{58}$$

However, (58) is a contradiction. Therefore, the ξ - D -conformal flat α -Kenmotsu pseudo-metric manifold does not exist when the characteristic vector field ξ is taken as space-like. Thus, the proof is completed.

Theorem 5. Let M be a $(2n + 1)$ -dimensional φ - D -conformal flat α -Kenmotsu pseudo-metric manifold. If α is parallel along the characteristic vector field ξ , then M is an η -Einstein manifold.

Proof. Let us assume that M is an α -Kenmotsu pseudo metric manifold satisfying the φ - D -conformal flat condition. Thus M holds the following equation:

$$g(B(\varphi X, \varphi Y)\varphi Z, \varphi V) = 0. \tag{59}$$

By the help of (22) and (59), we have

$$\begin{aligned}
 & g(R(\varphi X, \varphi Y)\varphi Z, \varphi V) + \frac{1}{2n-2} [S(\varphi X, \varphi Z)g(\varphi Y, \varphi V) - S(\varphi Y, \varphi Z)g(\varphi X, \varphi V) \\
 & + S(\varphi Y, \varphi V)g(\varphi X, \varphi Z) - S(\varphi X, \varphi V)g(\varphi Y, \varphi Z)] \\
 & - \frac{k-2}{2n-2} [g(\varphi X, \varphi Z)g(\varphi Y, \varphi V) - g(\varphi Y, \varphi Z)g(\varphi X, \varphi V)] = 0.
 \end{aligned} \tag{60}$$

Taking into account of (15), (19) and (57), (60) takes the form

$$\begin{aligned}
 & \varepsilon[\alpha^2 + \xi(\alpha)][g(\varphi X, \varphi W)g(\varphi Y, \varphi U) - g(\varphi Y, \varphi W)g(\varphi X, \varphi U)] \\
 & + \frac{[\alpha^2 + \xi(\alpha)]}{2n-2} [\varepsilon S(X, Z)g(Y, V) - 2ng(X, Z)g(Y, V) + 2n\varepsilon\eta(X)\eta(Z)g(Y, V) \\
 & - S(X, Z)\eta(Y)\eta(V) + 2n\varepsilon\eta(Y)\eta(V)g(X, Z) - S(Y, Z)g(X, V) \\
 & + 2ng(X, V)g(Y, Z) - 2n\varepsilon\eta(Y)\eta(Z)g(X, V) + S(Y, Z)\eta(X)\eta(V) \\
 & - 2n\varepsilon\eta(X)\eta(V)g(Y, Z) + \varepsilon S(Y, V)g(X, Z) - 2ng(X, Z)g(Y, V) \\
 & + 2n\varepsilon\eta(Y)\eta(V)g(X, Z) - S(Y, V)\eta(X)\eta(Z) + 2n\varepsilon\eta(X)\eta(Z)g(Y, V) \\
 & - \varepsilon S(X, V)g(Y, Z) + 2ng(X, V)g(Y, Z) - 2n\varepsilon\eta(X)\eta(V)g(Y, Z)
 \end{aligned}$$

$$\begin{aligned}
 & +S(X, V)\eta(Y)\eta(Z) + 2n\epsilon\eta(Y)\eta(Z)g(X, V)] \tag{61} \\
 & -\frac{\epsilon(k-2)}{2n-2} [\epsilon g(X, Z)g(Y, V) - g(X, Z)\eta(Y)\eta(V) - g(Y, V)\eta(X)\eta(Z) \\
 & -\epsilon g(Y, Z)g(X, V) + g(Y, Z)\eta(X)\eta(V) + g(X, V)\eta(Y)\eta(Z)] = 0.
 \end{aligned}$$

Now, we may choose a local orthonormal φ -basis $E_j = \{e_1, \dots, e_n, \varphi e_1, \dots, \varphi e_n, \xi\}, j = 1, \dots, n$. Then taking contraction in (61) with respect to $X = V = E_j$ and $\xi(\alpha) = 0$, we obtain

$$-S(Y, Z) = \frac{E_1}{E_3} g(Y, Z) + \frac{E_2}{E_3} \eta(Y)\eta(Z) \tag{62}$$

Here, the functions used in (62) are as follows:

$$\begin{aligned}
 E_1 &= \alpha^2[\epsilon + 2(n + 1)] + b(2n\epsilon - 1) - a\alpha^2(6n + \epsilon r) + 2na\alpha^2\epsilon(4n + 1) \\
 E_2 &= \alpha^2(2n\epsilon - 1) - b(2n - 1) + a[\alpha^2 r - 4n\alpha^4(2n - 1) + 2n\alpha^2(\epsilon + 1)] \\
 E_3 &= \left[\frac{\alpha^2(\epsilon - n)}{n - 1} \right], a = \frac{1}{2n - 2}, b = \frac{k - 2}{2n - 2}, k = \frac{r + 4n}{2n - 1}.
 \end{aligned}$$

As a result, the proof completes with the help of (62).

Theorem 6. Let M be a $(2n + 1)$ -dimensional α -Kenmotsu semi-symmetric pseudo-metric manifold. If α is parallel along the characteristic vector field ξ such that ξ is space-like, then M is a space of constant negative curvature $-\alpha^2$.

Proof. Note that (1) is equivalent to

$$R(\xi, Y) \cdot R = 0 \tag{63}$$

for all vector field Y on M , that is,

$$\begin{aligned}
 & R(\xi, Y)R(X, Z)U - R(R(\xi, Y)X, Z)U \\
 & -R(X, R(\xi, Y)Z)U - R(X, Z)R(\xi, Y)U = 0.
 \end{aligned} \tag{64}$$

Taking $X = \xi$ in (64) we get

$$\begin{aligned}
 & R(\xi, Y)R(\xi, Z)U - R(R(\xi, Y)\xi, Z)U \\
 & -R(\xi, R(\xi, Y)Z)U - R(\xi, Z)R(\xi, Y)U = 0.
 \end{aligned} \tag{65}$$

Making use of (13) and $\xi(\alpha) = 0$, (65) turns into

$$\begin{aligned}
 & -\alpha^2 R(Y, Z)U - \alpha^4 \epsilon g(Z, U)Y + \alpha^4 \epsilon g(Y, U)Z + \alpha^4 \epsilon \eta(Y)\eta(U)Z \\
 & + \alpha^4 \epsilon \eta(Z)g(Y, U)\xi - \alpha^4 \epsilon \eta(Y)\eta(U)Z - \alpha^4 \eta(Z)g(Y, U)\xi = 0.
 \end{aligned} \tag{66}$$

In particular, when the vector field ξ is taken as space-like, (66) can be written

$$-\alpha^2 R(Y, Z)U - \alpha^4 g(Z, U)Y + \alpha^4 g(Y, U)Z = 0. \tag{67}$$

Moreover, we have

$$R(Y, Z)U = c[g(Z, U)Y - g(Y, U)Z] \tag{68}$$

where c is constant curvature of M . Thus from (67) and (68), the proof is completed.

Example 1. Suppose that M is a 3-dimensional manifold defined by

$$M = \{(x, y, z): z \neq 0\}$$

where (x, y, z) are the standart coordinates. Let the vector fields be as follows:

$$e_1 = e^{z^2}(\partial/\partial x), e_2 = e^{z^2}(\partial/\partial y), e_3 = (\partial/\partial z).$$

Moreover, the metric tensor g is given by

$$g = e^{-2z^2}(\varepsilon_1 dx^2 + \varepsilon_2 dy^2) + \varepsilon dz^2, \quad \eta = dz.$$

Then the following relations are held:

$$\begin{aligned} \varphi(\xi) &= 0, \varphi(e_1) = e_2, \varphi(e_2) = -e_1, \\ \varphi^2 X &= -X + \eta(X)e_3, \eta(X) = \varepsilon g(e_3, X), \eta(e_3) = g(e_3, e_3) = \varepsilon = \varepsilon_3, \\ g(\varphi X, \varphi Y) &= g(X, Y) - \varepsilon \eta(X)\eta(Y), \varepsilon_i = g(e_i, e_i), i = 1, 2, 3. \end{aligned} \quad (69)$$

According to all the equations in (69), an almost contact pseudo metric structure $(M, \varphi, \xi, \eta, g)$ exists. To check whether it is almost α -Kenmotsu pseudo metric or not, we verify the condition $d\Phi = 2\alpha(\eta \wedge \Phi)$.

On the other hand, all Φ_{ij} 's vanish except for $\Phi(e_1, e_2) = -\varepsilon_i$, we deduce

$$\begin{aligned} \Phi\left(\left(\frac{\partial}{\partial x}\right), \left(\frac{\partial}{\partial y}\right)\right) &= -\varepsilon_i e^{-2z^2} \\ \Phi &= -\varepsilon_i e^{-2z^2} (dx \wedge dy) \\ d\Phi &= -\varepsilon_i 2ze^{-2z^2} (dx \wedge dy \wedge dz). \end{aligned}$$

Since $\eta = dz$, we obtain

$$d\Phi = -2\varepsilon_i 2z(\eta \wedge \Phi)$$

such that $\alpha = -2\varepsilon z$. Also, we remark that $N_\varphi = 0$. Thus M is α -Kenmotsu pseudo metric one.

Discussion and Conclusion

The main purpose of this study is to investigate α -Kenmotsu pseudo metric manifolds satisfying some tensor conditions. First, the central theme that draws attention to the study is the underlying differences and similarities between the Riemannian metric and pseudo-Riemannian tensors on α -Kenmotsu manifolds such that $d\alpha \wedge \eta = 0$. Our further studies will be related to nullity distributions, (κ, μ, ν) -spaces, D -homothetic deformations, local symmetry, semi-symmetric conditions, certain parallel tensors, and the other curvature tensor fields using soliton theory on almost α -Kenmotsu pseudo metric manifolds.

References

- Begawadi, C. S. & Kumar, E. G. & Venkatesha, V. (2005) On irrational D -conformal curvature tensor. *Novi Sad J. Math.*, 35 (2), 85-92.
- Blair, D. E. (1976). *Contact manifolds in Riemannian geometry*. Lecture Notes in Math., Vol. 509, New York: Springer-Verlag, Berlin-Heidelberg.
- Calvaruso, G. & Perrone, D. (2002). Semi-symmetric contact metric three-manifolds, *Yokohama Math. J.*, 49, 149-161.
- Calvaruso, G. & Perrone, D. (2010). Contact pseudo-metric manifolds. *Differential Geometry and its Applications*, 28, 615-634. Doi: <https://doi.org/10.1016/j.difgeo.2010.05.006>
- Calvaruso, G. (2011). Contact Lorentzian manifolds. *Differential Geometry and its Applications*, 29, 541-551. Doi: <https://doi.org/10.1016/j.difgeo.2011.04.006>
- Chuman, G. (1983). On the D -conformal curvature tensor. *Tensor*, 40 (2), 125-134.
- De, U. C. & Pathak, G. (2004). On 3-dimensional Kenmotsu manifolds. *Ind. J. Pure Applied Math.*, 35, 159-165.
- Dileo, G. & Pastore A. M. (2007). Almost Kenmotsu manifolds and local symmetry. *Bulletin of the Belgian Mathematical Society-Simon Stevin*, 14, 343-354. Doi: 10.36045/bbms/1179839227
- Hong, S. & Özgür, C. & Tripathi, M. M. (2006). On some special classes of Kenmotsu manifolds. *Kuwait J. Sci. Eng.*, 33, 19-32.
- Jun, J. B. & De, U. C. & Pathak, G. (2005). On Kenmotsu manifolds. *J. Korean Math. Soc.*, 42, 435-445. Doi: <https://doi.org/10.4134/JKMS.2005.42.3.435>
- Kenmotsu, K. (1972). A class of contact Riemannian manifold. *Tôhoku Math. J.*, 24, 93-103. Doi: 10.2748/tmj/1178241594
- Kim, T. W. & Pak, H. K. (2005). Canonical foliations of certain classes of almost contact metric structures. *Acta Math. Sinica, Eng. Ser. Aug.*, 21, 841-846. Doi: <https://doi.org/10.1007/s10114-004-0520-2>
- Naik, D. M. & Venkatesha, V. & Kumara, H. A. (2020). Some results on almost Kenmotsu manifolds, *Note di Matematica.*, 40 (1), 87-100. Doi: 10.1285/i15900932v40n1p87
- Nomizu, K. (1968). On hypersurfaces satisfying a certain condition on the curvature tensor, *Tôhoku Mat. J.*, 20, 46-69.
- Ogawa, Y. (1977). A condition for a compact Kählerian space to be locally symmetric, *Nat. Sci. Rep. Ochanomizu Univ.*, 28, 21-23.
- O'Neil, B. (1983). *Semi-Riemannian geometry with applications to relativity*. New York: Academic Press.
- Öztürk, H. (2017). On α -Kenmotsu manifolds satisfying semi-symmetric conditions, *Konuralp Journal of Mathematics*, 5, 192-206.

Öztürk, S. & Öztürk, H. (2020). On α -Kenmotsu pseudo metric manifolds, *AKU Journal of Science and Eng.*, 20, 975-982. Doi: 10.35414/akufemubid.803483

Öztürk, S. & Öztürk, H. (2021). Almost α -cosymplectic pseudo metric manifolds. *Journal of Mathematics*, 2021, Article ID 4106025, 10 pages. Doi: <https://doi.org/10.1155/2021/4106025>

Öztürk, S. & Öztürk, H. (2022). *D*-konformal eğrilik tensör alanına sahip α -Kenmotsu pseudo metrik manifoldlar. Fen ve Mühendislik Bilimlerinde Güncel Tartışmalar ve Araştırmalar 6, Ankara: Bilgin Kültür Sanat Yayınları (in press).

Perrone, D. (2014). Contact pseudo-metric manifolds of constant curvature and CR geometry. *Results in Mathematics*, 66, 213-225. Doi: <https://doi.org/10.1007/s00025-014-0373-7>

Szabó, Z. I. (1982). Structure theorem on Riemannian spaces satisfying $R.R = 0$, *Journal of Differential Geo.*, 17, 531-582.

Takahashi, T. (1969). Sasakian manifold with pseudo-Riemannian metric, *Tōhoku Mathematical Journal*, 21, 271-290.

Taleshian, A. & Hosseinzadeh, A. A. & Khaniani, F. (2011). On *D*-conformal curvature tensor Sasakian manifolds. *Journal of Nonlinear Analysis and Application*, 2011, 1-5. Doi: 10.5899/2011/jnaa-00088

Wang, Y. & Liu, X. (2016). Almost Kenmotsu pseudo-metric manifolds. *Analele Stiintifice ale Universitatii Al I Cuza din Iasi -Matematica*, 62, 241-256. Doi: [10.2478/aicu-2014-0030](https://doi.org/10.2478/aicu-2014-0030)

Yano, K. & Kon, M. (1984). *Structures on manifolds*, Series in Pure Math., Vol. 3, Singapore: World Scientific Publishing Co.

Adaptive Fuzzy Logic Based Vector Controlled Permanent Magnetic Synchronous Motor Speed Control

Mehmet . KARAYEL
Ç. ERSİN

1.Introduction

Permanent Magnet Synchronous Motors (PMSM) is one of the electric motors with the high power density and high efficiency. PMSMs are highly preferred in applications that require high speed/position accuracy and high torque/inertia. It is smaller in size and requires less maintenance than drive motors such as asynchronous motors. With these features, it is widely used in different fields [1].

Permanent Magnet Synchronous Motor (PMSM), three-phase windings in the stator; The rotor consists of surface-mounted permanent magnets. Due to the permanent magnets being inside (on the rotor surface), it provides advantages such as mechanical durability, and reduction of flux weakening and is suitable for high-speed applications.

The PMSM is driven by the rotor position-dependent synchronous sine voltage received from the position sensors. Along with the stator flux produced, the rotor flux produced by the magnets determines the torque and speed of the motor. To produce maximum torque, the phase difference between the stator flux and the rotor flux should be 90° and the sine wave voltage output should be applied to the three-phase stator windings. To achieve this, the motor must be controlled with driver circuits [2,3].

Conventional controllers are widely used in the speed/position control of PMSMs due to their simplicity of structure and sufficient efficiency in many industrial applications. However, the need for a model of the system to be controlled and the determination of the most appropriate gain values by trial and error method is the disadvantage of these controllers [4]. Conventional controllers such as proportional integral (OI) shouldn't cause overshoot and fluctuations in speed and load changes [5]. This situation has brought along more efficient searches in terms of performance and efficiency. In addition, the hardware difficulty of analogue control techniques and the necessity of complex mathematical modelling have led to the search for new approaches in control techniques. Among the developing control techniques, the fuzzy logic approach has become frequently used because it does not need complex mathematical modelling. In addition to the advantage of simple mathematical modelling, fuzzy logic control has advantages such as being flexible and conceptually easy to understand, which has increased its use in many process control systems [6,7].

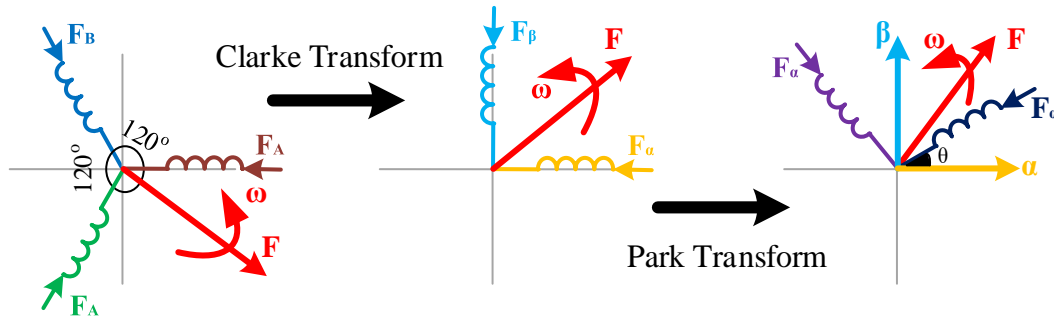
Conventional PI control, when subjected to changes or deterioration of motor parameters, cannot fundamentally resolve the conflict between dynamic and static performance, and cannot meet the fast-tracking requirements of the servo system [8]. Therefore, to compensate for the

disadvantages of PI control. In this study, PI control parameters were adjusted with adaptive fuzzy logic and applied in PMSM control and the simulation of the system was established in Simulink. The result shows that the dynamics of the system using the AF-PI control have been improved.

2. Modelling of Permanent Magnet Synchronous Motors

2.1. Reference Plane Transformations

While modelling three-phase AC motors, conversion between phase planes is performed. The phase transformation is usually from the three-phase plane to the reference two-phase fixed plane (Clarke transform) or from the reference two-phase fixed plane to the polyphase plane (Inverse Clarke transform), from the reference two-phase fixed plane to the two-phase rotor plane (Park transform) 90° perpendicular to each other and 90° to each other. the reference from the two-phase rotor plane to the two-phase fixed plane (Reverse Park transform). Figure 1 shows the reference plane transformations.



Şekil 1. Referans düzlem dönüşümleri.

2.2. Clarke Transform

When modelling three-phase AC motors, the conversion from a three-phase fixed plane to two-phase planes perpendicular to each other is called Clarke transform. With phase transformations, the number of variables in motor modelling is reduced and the solution is facilitated. Figure 2 shows the Clarke transform components. While the Clarke transform components are represented as vectorial, it is assumed that the plane of the motor phase A and the plane of the reference α phase are in the same direction. Clarke and Inverse Clarke transformation equations are given in Equations (1) and (2), respectively.

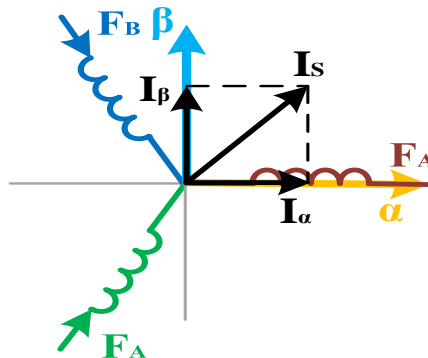


Figure 2. Components in Clarke transform.

$$\begin{bmatrix} F_\alpha \\ F_\beta \\ F_0 \end{bmatrix} = \frac{2}{3} \begin{bmatrix} 1 & -\frac{1}{2} & -\frac{1}{2} \\ 0 & \frac{\sqrt{3}}{2} & -\frac{\sqrt{3}}{2} \\ \frac{1}{2} & \frac{1}{2} & \frac{1}{2} \end{bmatrix} \begin{bmatrix} F_A \\ F_B \\ F_C \end{bmatrix} \quad (1)$$

$$\begin{bmatrix} F_A \\ F_B \\ F_C \end{bmatrix} = \frac{2}{3} \begin{bmatrix} 1 & 0 & 0 \\ -\frac{1}{2} & \frac{\sqrt{3}}{2} & 0 \\ -\frac{1}{2} & -\frac{\sqrt{3}}{2} & 0 \end{bmatrix} \begin{bmatrix} F_\alpha \\ F_\beta \\ F_0 \end{bmatrix} \quad (2)$$

2.3.Park Transform

The Park conversion method is used to convert from a two-phase fixed reference plane perpendicular to each other at 90o to a two-phase rotating rotor plane. Also the reverse of this situation, the reverse parking transform is used to convert from two phases rotating rotor plane to a two-phase fixed reference plane 90o to each other. Figure 3 shows the Park transform vector diagram. The Park and Inverse Park transform equations are given in (3) and (4), respectively.

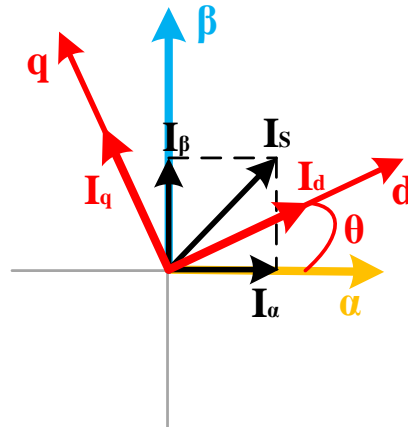


Figure 3. Components in the park transformation.

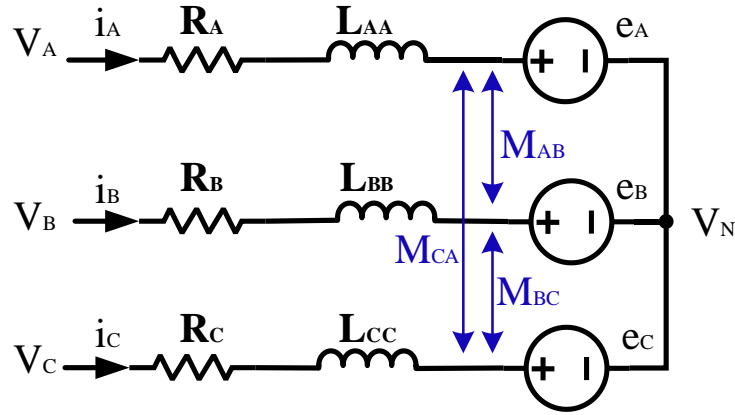
$$\begin{bmatrix} F_d \\ F_q \end{bmatrix} = \begin{bmatrix} \cos\theta_r & \sin\theta_r \\ -\sin\theta_r & \cos\theta_r \end{bmatrix} \begin{bmatrix} F_\alpha \\ F_\beta \end{bmatrix} \quad (3)$$

$$\begin{bmatrix} F_\alpha \\ F_\beta \end{bmatrix} = \begin{bmatrix} \cos\theta_r & -\sin\theta_r \\ \sin\theta_r & \cos\theta_r \end{bmatrix} \begin{bmatrix} F_d \\ F_q \end{bmatrix} \quad (4)$$

In equations (3) and (4), F_d and F_q denote the phasor components of the stator d-q in the rotor reference plane and θ_r the rotor angle. Here, the current and voltage variables of the d-q phasor components can be found using these equations.

2.4. Three-Phase Equivalent Circuit of Permanent Magnet Synchronous Motor

The three-phase ABC model of the PMSM is realized using the equivalent circuit shown in Figure 4. Equivalent active V_A, V_B, V_C instantaneous value of stator phase-neutral voltages, i_A, i_B, i_C instantaneous value of stator currents, R_A, R_B, R_C ohmic resistance values of stator phase windings, L_{AA}, L_{BB}, L_{CC} The total inductance values of the stator phase windings, M_{AB}, M_{BC}, M_{CA} It represents the mutual inductance values between phases of the stator phase windings.



Şekil 4. PMSM üç fazlı stator eşdeğer devresi.

The three-phase sinusoidal voltages applied to the motor are expressed as:

$$V_A = V_m \sin \omega_e t \quad (5)$$

$$V_B = V_m \sin (\omega_e t - 2\pi/3) \quad (6)$$

$$V_C = V_m \sin (\omega_e t + 2\pi/3) \quad (7)$$

If the stator resistance, self and mutual inductance values are considered equal;

$$R_A = R_B = R_C = R_S \quad (8)$$

$$L_{AA} = L_{BB} = L_{CC} = L_S \quad (9)$$

$$M_{AB} = M_{BC} = M_{CA} = M \quad (10)$$

stator voltages;

$$\begin{bmatrix} V_A \\ V_B \\ V_C \end{bmatrix} = R_S \begin{bmatrix} i_A \\ i_B \\ i_C \end{bmatrix} + \frac{d}{dt} \begin{bmatrix} \Psi_A \\ \Psi_B \\ \Psi_C \end{bmatrix} \quad (11)$$

phase winding currents;

$$\begin{bmatrix} \Psi_A \\ \Psi_B \\ \Psi_C \end{bmatrix} = \begin{bmatrix} L_{AA} & M_{AB} & M_{AC} \\ M_{BA} & L_{BB} & M_{BC} \\ M_{CA} & M_{CB} & L_{CC} \end{bmatrix} \begin{bmatrix} i_A \\ i_B \\ i_C \end{bmatrix} + \psi_m \begin{bmatrix} \cos\theta_e \\ \cos(\theta_e - 2\pi/3) \\ \cos(\theta_e + 2\pi/3) \end{bmatrix} \quad (12)$$

If equation (12) is substituted in equation (11) and the equations in equation (10) are applied;

$$\begin{bmatrix} v_A \\ v_B \\ v_C \end{bmatrix} = R_s \begin{bmatrix} i_A \\ i_B \\ i_C \end{bmatrix} + L_s \frac{d}{dt} \begin{bmatrix} i_A \\ i_B \\ i_C \end{bmatrix} + \omega_e \psi_m \begin{bmatrix} \cos\theta_e \\ \cos(\theta_e - 2\pi/3) \\ \cos(\theta_e + 2\pi/3) \end{bmatrix} \quad (13)$$

obtained from the equations. Here, ψ_A, ψ_B, ψ_C represents the total flux of the phase windings, ψ_m represents the magnetic flux formed by the permanent magnets, the reduced amplitude of the magnetic flux to the stator, R_s the stator resistance, L_s the synchronous inductance, and θ_e the electrical displacement of the rotor.

Motor's electrical output power and electromagnetic torque expression;

$$P_e = e_A I_A + e_B I_B + e_C I_C \quad (14)$$

$$T_e = P_e / \omega_e \quad (15)$$

$$T_e = p \left\{ \frac{1}{2} [i_{ABC}]^T \frac{\partial [L_{ABC}]}{\partial \theta_r} [i_{ABC}] + [i_{ABC}]^T \frac{\partial [\Psi_{ABC}]}{\partial \theta_r} \right\} \quad (16)$$

Here θ_r is the mechanical rotor position and p is the number of pairs of the motor.

The electrical moment equation can be expressed as:

$$T_e = T_m + J \frac{d\omega_e}{dt} + B_m \omega_e \quad (17)$$

where ω_m is the mechanical angular velocity, J is the moment of inertia, T_y is the load moment and B_m is the friction coefficient of the machine and the rotating system. The following relations can be written between θ_e electrical position and ω_e electrical angular velocity.

$$\omega_e = \frac{d\theta_e}{dt} \quad (18)$$

$$\theta_r = \frac{1}{p} \theta_e \quad (19)$$

$$\omega_e = \frac{1}{p} \omega_m \quad (20)$$

2.5.dq0 Equivalent Circuit and Model of Permanent Magnet Synchronous Motor

Another method used in the modelling of PMSMs is the d-q model, which is obtained by transferring the stator sizes to the rotor plane. Computing is easier and faster in this model, which is similar to the free-excited synchronous machine model. Current and voltage variables in the three-phase plane are transferred to the rotor reference plane by using the Clarke transform and park transform methods, respectively. Figure 5 shows the PMSM d-q equivalent circuit.

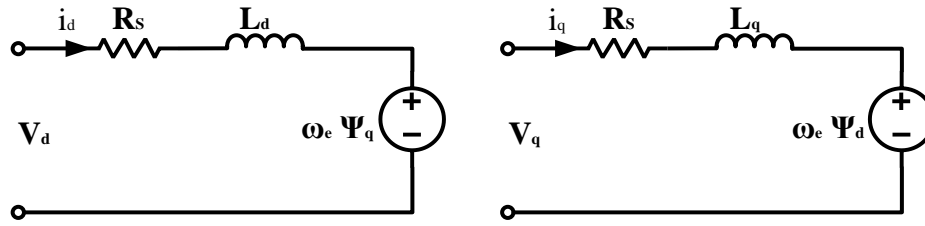


Figure 5. PMSM d-q equivalent circuit.

When Clarke and Park's transformations are applied to the voltage equations of the motor given in Equation (13);

$$V_d = r_s i_d + \frac{d}{dt} \psi_d - \psi_q \omega_e \quad (21)$$

$$V_q = r_s i_q + \frac{d}{dt} \psi_q - \psi_d \omega_e \quad (22)$$

Here, V_d and V_q show the d and q axis voltages, i_d and i_q show the d and q axis currents, and ψ_d and ψ_q show the d and q axis fluxes. D and q-axis flux expressions are given in equations (23) and (24).

$$\psi_q = L_i i_q \quad (23)$$

$$\psi_d = L_i i_d + \psi_m \quad (24)$$

If these expressions are substituted in equations (21) and (22);

$$V_d = r_s i_d + L_d \frac{d}{dt} i_d - L_q i_q \omega_e \quad (25)$$

$$V_q = r_s i_q + L_q \frac{d}{dt} i_q + L_d i_d \omega_e + \omega_e \psi_m \quad (26)$$

If necessary adjustments are made in Equations (25) and (26), the equations i_d and i_q are written as follows:

$$\frac{d}{dt} i_d = \frac{1}{L_d} \{V_d - r_s i_d + L_q i_q \omega_e\} \quad (27)$$

$$\frac{d}{dt} i_q = \frac{1}{L_q} \{V_q - r_s i_q + L_d i_d \omega_e - \omega_e \psi_m\} \quad (28)$$

The electromagnetic or induced moment expression is;

$$T_e = \frac{3}{2} p [\psi_m i_q + (L_d - L_q) i_d i_q] \quad (29)$$

After obtaining the electromagnetic torque expression, the velocity equation is obtained as follows:

$$\frac{d}{dt} \omega_m = \frac{3p}{2J} \{(L_d - L_q) i_d i_q + i_q \psi_m\} - \frac{B \omega_m}{J} - \frac{T_m}{J} \quad (30)$$

3.Establishment of Simulation Model of PMSM

The creation of the control model in the MATLAB/SIMULINK environment is discussed by making use of the mathematical equations of PMSM specified in the second chapter. By using the obtained control model of PMSM, its performances will be compared by making separate controls with both the traditional PI controller and the proposed AF_PI controller.

3.1.PMSM'un Alan Yönlendirmeli Kontrol (AYK) Modeli

AYK, which is used in electrical machines, allows Alternating Current (AC) motors to be controlled independently of each other, without any relationship between the excitation circuit and armature circuit, as in Direct Current (DC) motors. Thanks to this method, high dynamic performance obtained from DC motors can also be obtained from AC motors [10,11]. The basic principle of AYK is based on the separation of the machine current into two components, expressed as d-q, one that produces torque and the other that produces flux, and these components are controlled independently of each other. AYK is easier in PMSMs compared to other electrical machines. The reason for this is that permanent magnets placed in the rotor produce a constant magnetic flux in the rotor [12]. Using equations (18), (19), (27), (28), (29) and (30), the mathematical model of PMSM is respectively; Figure 6 shows the i_q axis model, Figure 7 shows the i_d axis model, and Figure 8 shows the induced torque T_e , θ_e electrical position and ω_e electrical angular velocity models. Figure 9 shows the final version of the PMSM mathematical model.

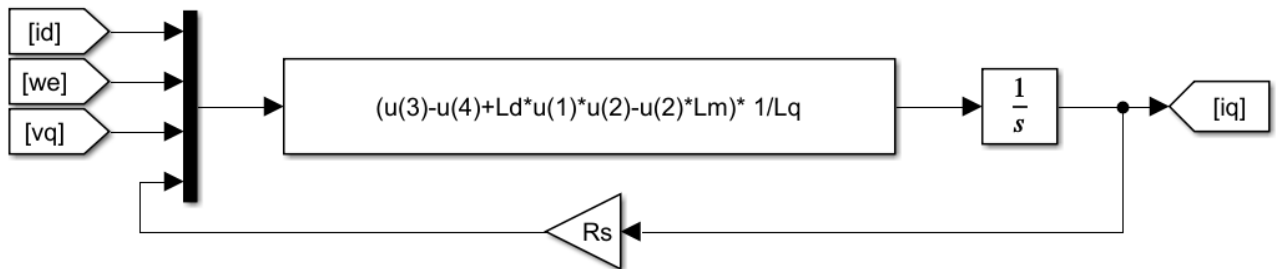


Figure 6. MATLAB/SIMULINK i_q axis model and block representation.

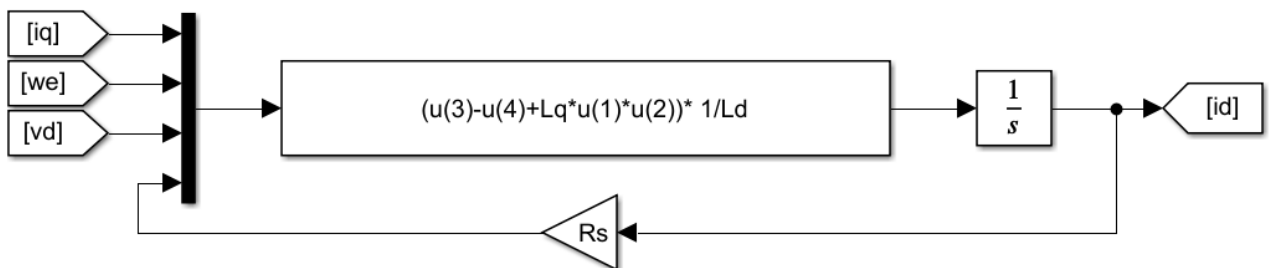


Figure 7. MATLAB/SIMULINK i_d axis model and block representation.

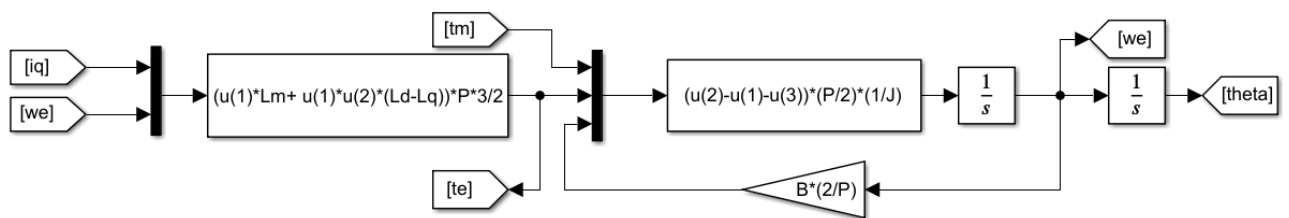


Figure 8. MATLAB/SIMULINK torque, electrical rotational speed and position model and block representation.

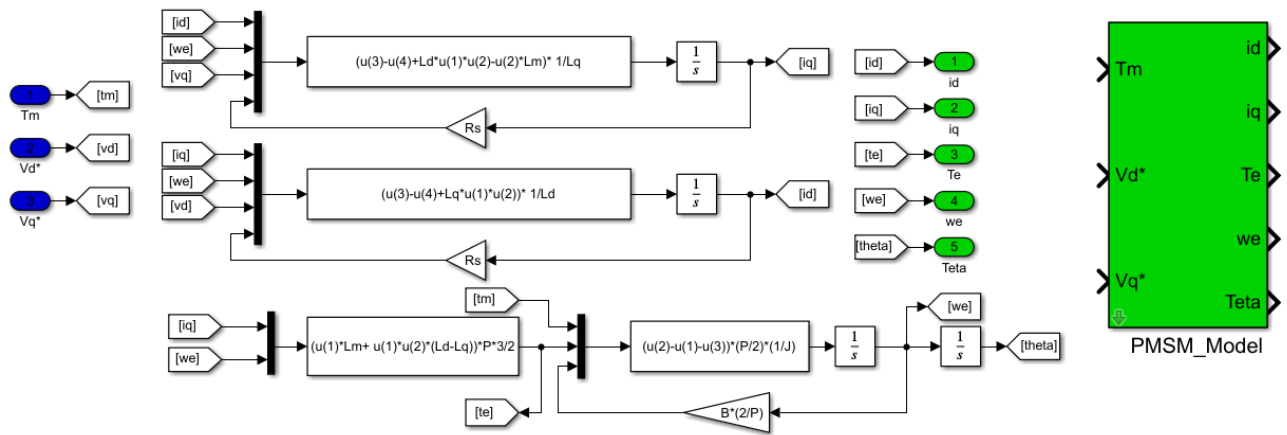


Figure 9. MATLAB/SIMULINK PMSM model and block representation.

3.2. Permanent Magnet Synchronous Motor Conversion Models

The simulations of the transformation expressions given above were performed in the MATLAB/SIMULINK environment. These transformations are shown respectively in Figure 10 Clarke transform, Figure 11 Park transform, Figure 12 Inverse Clarke transform and Figure 13 Inverse Park transform.

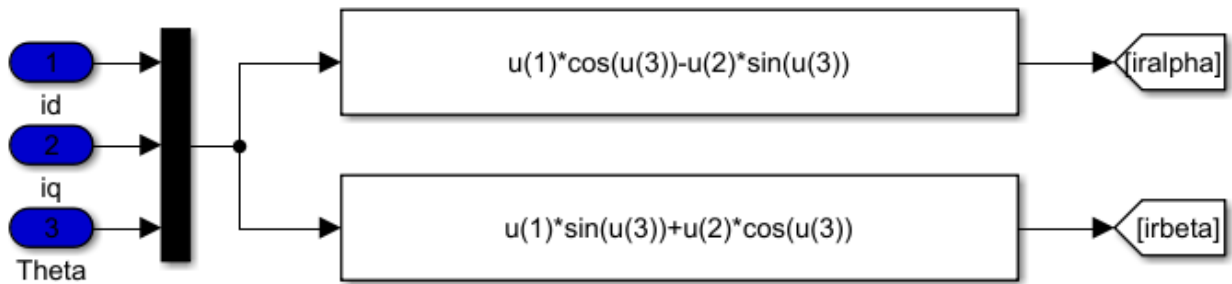


Figure 10. MATLAB/SIMULINK parking model and block representation

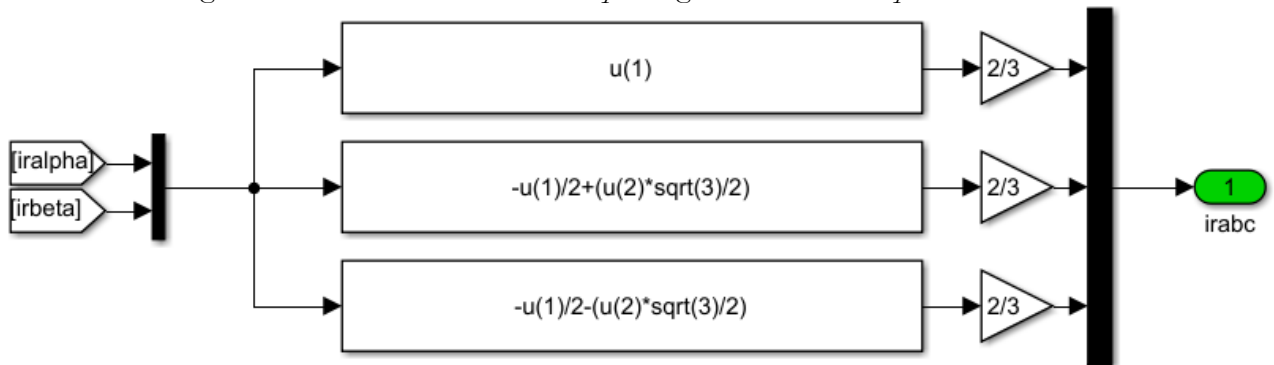


Figure 11. MATLAB/SIMULINK Clarke model and block representation.

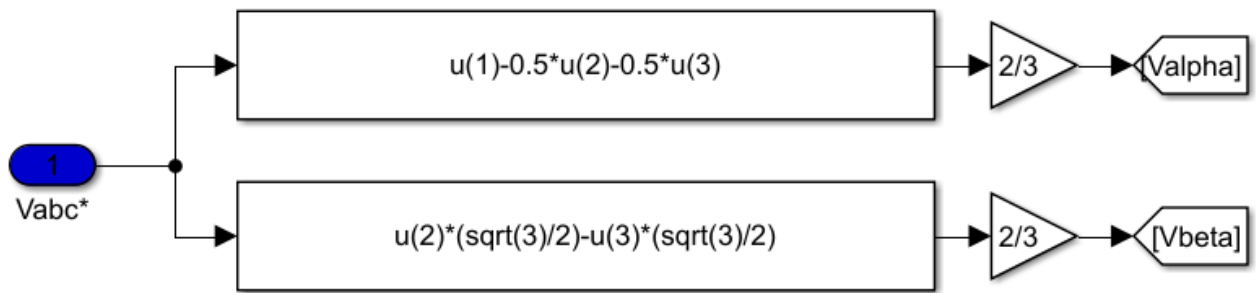


Figure 12. MATLAB/SIMULINK reverse Clarke model and block representation.

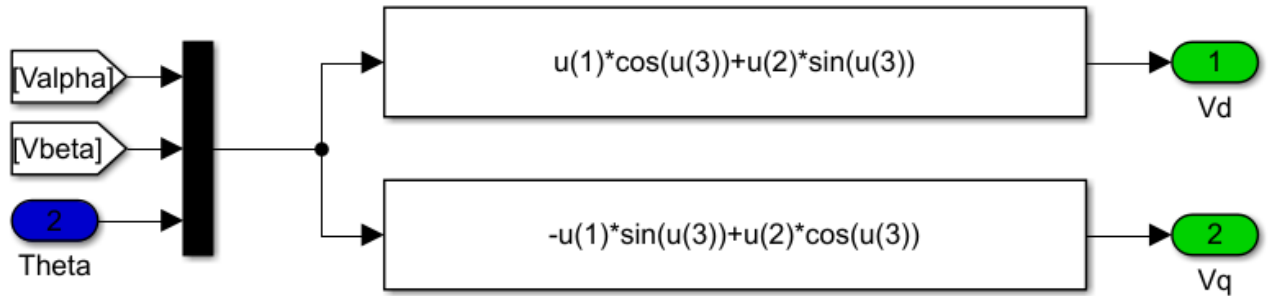


Figure 13. MATLAB/SIMULINK reverse parking model and block representation.

3.3. Inverter and Inverter Model

Current-controlled voltage source inverters have an important place in the control of AC motors. It is possible to improve the inverter performance and accordingly the performance of AC motors by improving current control methods and modulation techniques. Pulse width modulation is generally used as a modulation technique in voltage source inverters. The most commonly used current control techniques are hysteresis current control, ramp comparison control and space vector pulse width current control [13]. In this study, PMSM vector control was performed using the hysteresis current control technique, and its performance was examined under various operating conditions.

In hysteresis PWM control, it is permissible for the output to fluctuate within the predefined error band. This error band is called the hysteresis band. Figure 14 shows the hysteresis PWM control model.

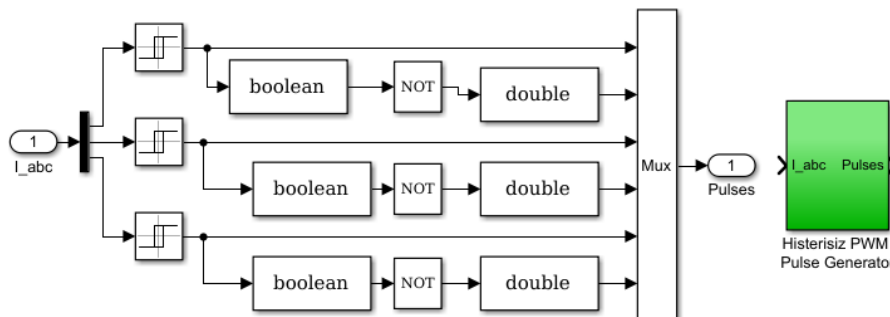


Figure 14. MATLAB/SIMULINK Hysteresis PWM control model and block representation.

A current or voltage with variable amplitude and frequency is required to supply the PMSM. This is formed by inverter circuits. A voltage source inverter is used as shown in Figure 15. The circuit is 300VDC DC voltage source and MOSFETs are used as inverter switches.

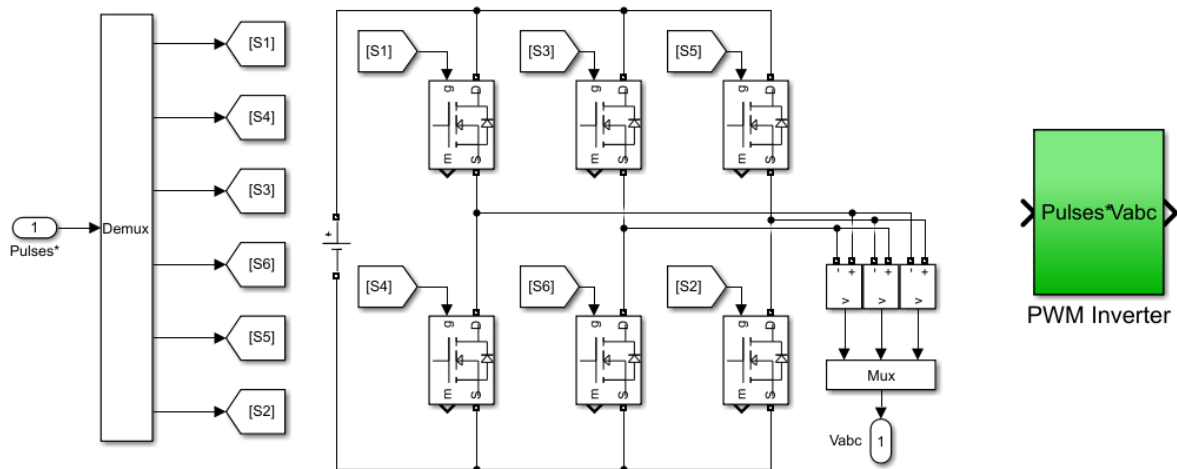


Figure 15. MATLAB/SIMULINK MOSFET switched inverter model and block representation.

The closed-loop PMSM controller model is obtained by combining the MATLAB/SIMULINK function blocks mentioned above. Figure 16 shows the traditional-PI controller applied model of PMSM. In closed loop conventional PI speed control of PMSM, the error value of the speed is obtained by taking the difference of the reference speed value and the measured speed value. The error value of the speed is applied to the conventional-PI controller and the output reference i_q produced by the conventional PI controller is accepted as the current value. An error signal is generated by taking the difference of this reference i_q value from the real i_q value obtained from the MATLAB model shown in Figure 6, and using this error signal, it is transferred to the PI controller and the q axis current controller. In the field-oriented control method, since the current i_d does not affect the torque, it is tried to keep the current value at zero to reduce the losses. However, flux weakening is required when operating at higher speeds than the rated speed of the motor. In this case, the current i_d needs to be set to a suitable negative value. In motor control, the value of i_d current obtained from the MATLAB model shown in Figure 7 is compared with the zero reference value and transferred to the d axis current controller by applying a PI control method [1].

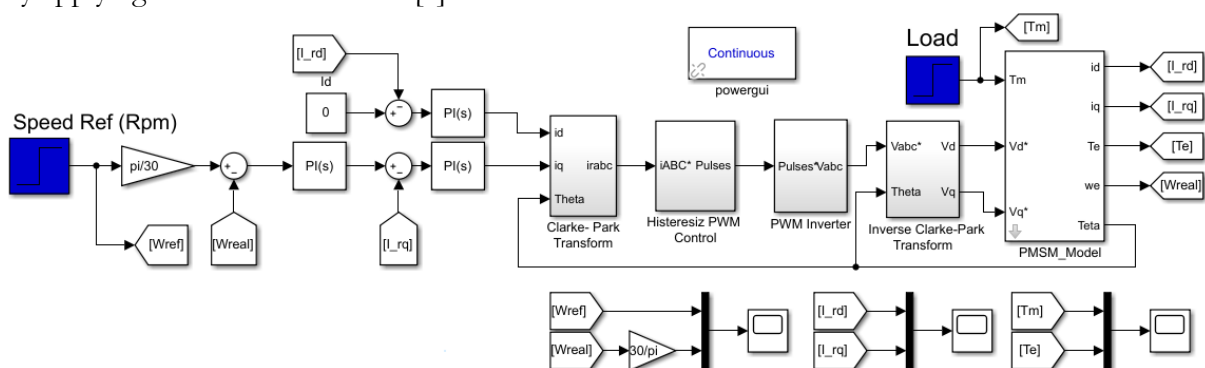


Figure 16. Field-oriented control model of MATLAB/SIMULINK PMSM with the traditional-PI controller.

4.Fuzzy Logic Control

Its basis is based on the simulation of human behaviour depending on thoughts and intuitions in controlling any system. Therefore, a person achieves the goal by applying a control strategy depending on his intuition and experience to take a system from the real situation to the desired state. Fuzzy control is based on such logical relations. For fuzzy logic, it can be called the application of mathematics to the real world [14].

When the traditional PI control is subject to the change or deterioration of the motor parameters, it cannot fundamentally resolve the conflict between dynamic and static performance, and cannot meet the fast-tracking requirements of the servo system. Therefore, to compensate for the disadvantages of PI control. As shown in the adaptive FUZZY-PI control scheme in Figure 17, the k_p and k_i parameters of the traditional PI controller were adjusted by adaptive fuzzy logic and implemented in the PMSM control.

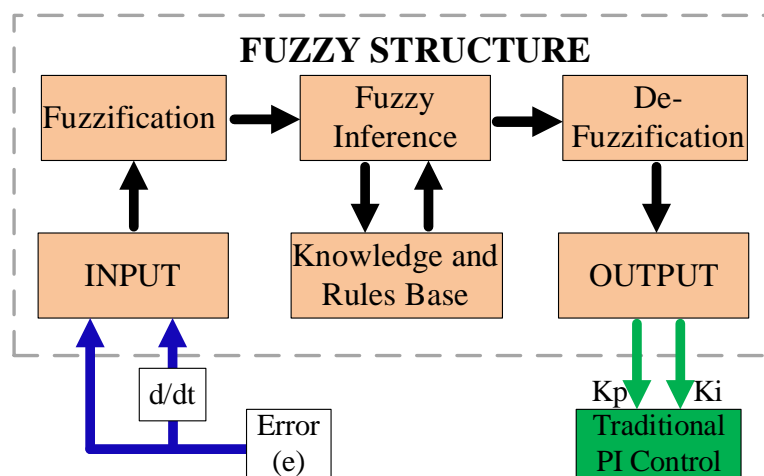


Figure 17. Adaptive FUZZY-PI control scheme.

Figure 18 shows the model of the adaptive FUZZY-PI control created in the MATLAB/SIMULINK environment. The adaptive FUZZY-PI controller consists of two separate fuzzy controllers. One of the fuzzy controllers changes the k_p parameter of the PI controller and the other fuzzy controller changes the k_i parameter of the PI controller depending on the speed error and the variation of the error.

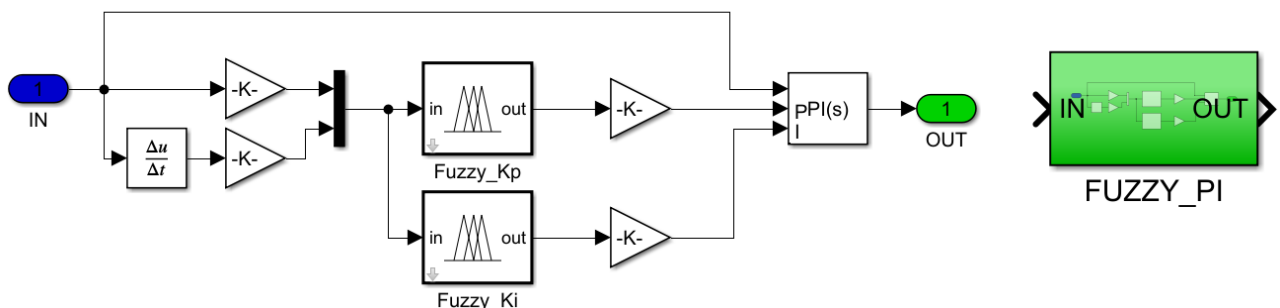


Figure 18. Adaptive FUZZY-PI controller MATLAB/SIMULINK model.

Depending on the defined rules of the fuzzy error and error variation data in fuzzy membership functions, the appropriate control output is obtained from the seven variable state

output membership function in Figure 19 for the K_p parameter of the PI controller. The rule table of the output membership function obtained for the K_p parameter is given in Table 1.

Table 1. Rule table of K_p parameter.

e / de	HN	MN	LN	ZE	LP	MP	HP
HN	HP	HP	MP	MP	LP	ZE	ZE
MN	HP	HP	MP	LP	LP	ZE	LN
LN	MP	MP	MP	LP	ZE	LN	LN
ZE	MP	MP	LP	ZE	LN	MN	MN
LP	LP	LP	ZE	LN	MN	MN	MN
MP	LP	ZE	LN	MN	MN	MN	HN
HP	ZE	ZE	MN	MN	MN	HN	HN

Triangle and trapezoidal functions are used while generating membership functions for Fuzzy- K_p and Fuzzy- K_i controllers. In the generated fuzzy membership functions, triangular and trapezoidal functions are shown with seven different symbolic values. These are HP (High Positive), MP (Medium Positive), LP (Low Positive), ZE (Zero), HN (High Negative), MN (Medium Negative), LN (Low Negative)

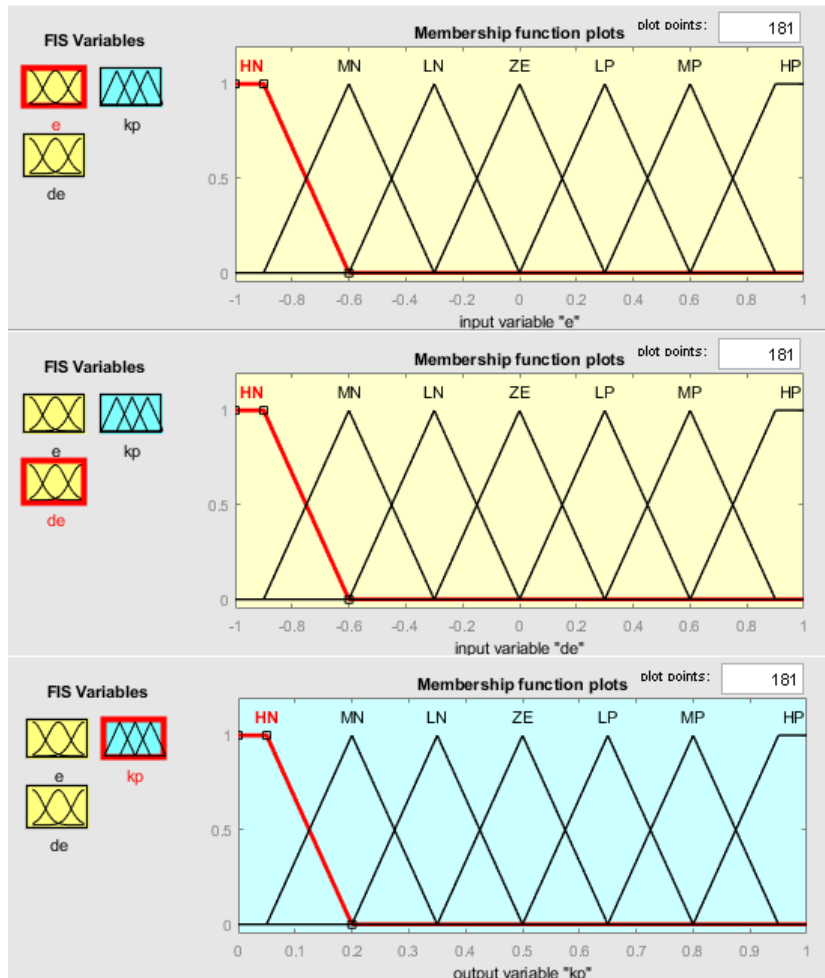


Figure 19. Input-output membership functions for the adaptive FUZZY- K_p parameter.

The appropriate control output is obtained from the seven variable state output membership function in Figure 20, the K_i parameter of the PI controller, depending on the defined rules of the blurred error and error variation data in the fuzzy membership functions. The rule table of the output membership function obtained for the K_i parameter is given in Table 2.

Table 2. Rule Table of Fuzzy K_i .

e / de	HN	MN	LN	ZE	LP	MP	HP
HN	HN	HN	MN	MN	LN	ZE	ZE
MN	HN	HN	MN	LN	LN	ZE	LP
LN	MN	MN	MN	LN	ZE	LP	LP
ZE	MN	MN	LN	ZE	LP	MP	MP
LP	LN	LN	ZE	LP	MP	MP	MP
MP	ZE	ZE	LP	MP	MP	MP	HP
HP	ZE	ZE	LN	MP	MP	HP	HP

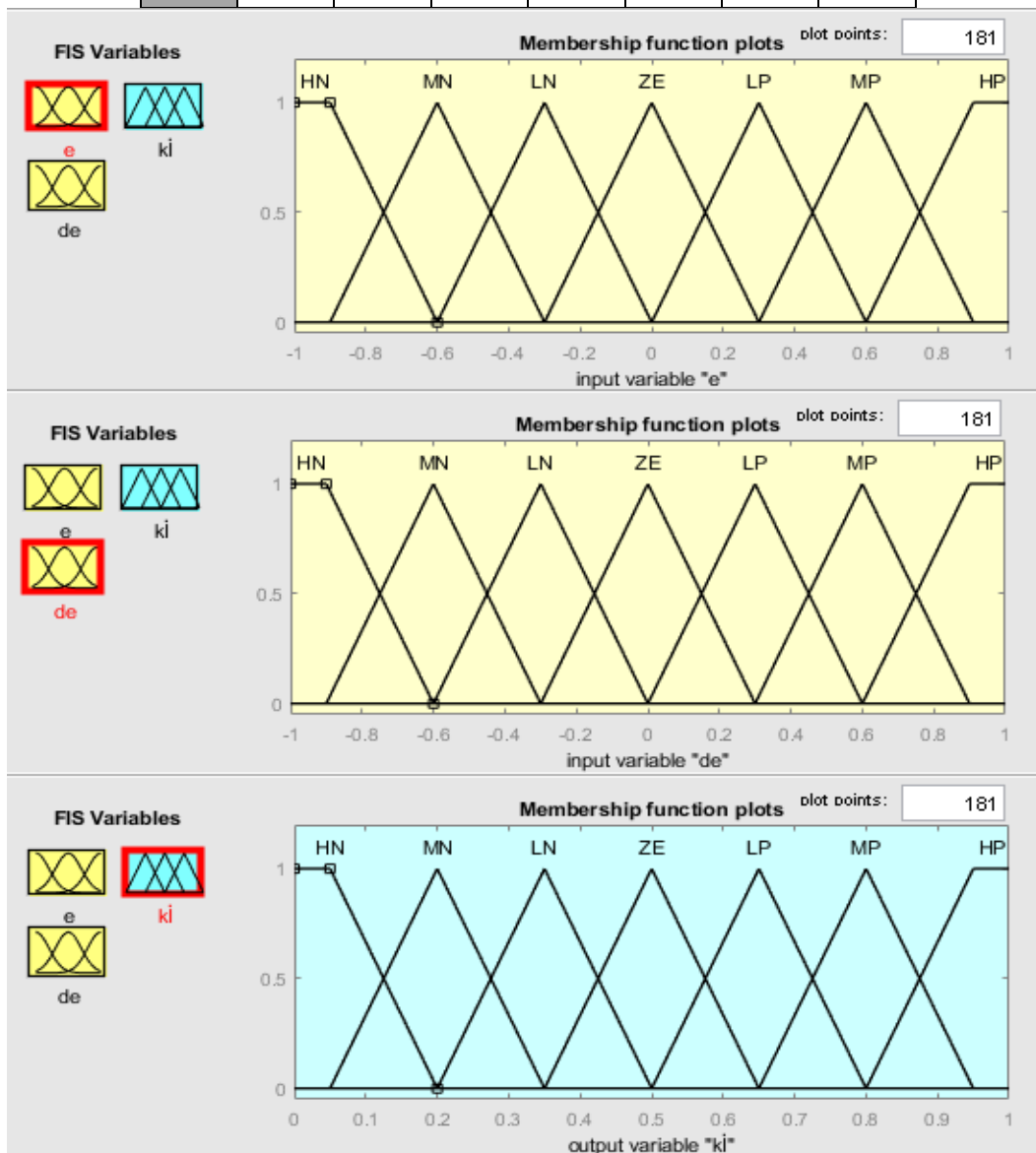


Figure 20. Input-output membership functions for the adaptive FUZZY- K_i parameter.

In Figure 21, there is a field-oriented control model of PMSM created in the MATLAB/SIMULINK environment with an adaptive FUZZY-PI controller.

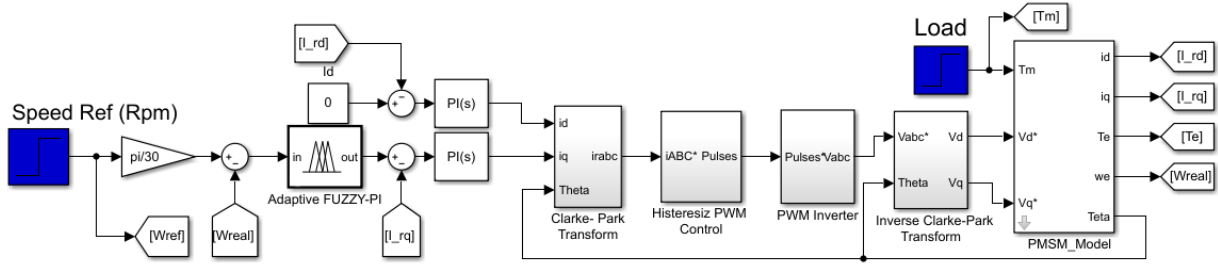


Figure 21. Field-oriented control model of MATLAB/ SIMULINK PMSM with adaptive FUZZY-PI controller.

5.Simulation Results

In the simulation, the parameters of the permanent magnet synchronous motor with 8 Nm torque, 300 VDC supply and 2000 RPM speed values, which are found as a package in the Matlab/Simulink program, are created as follows.

Stator Resistance, R_s : 0.9585 Ω

Stator Inductance, L_d : 5.25 mH

Moment of Inertia, J : 0.0006329 kgm²

Coefficient of Friction, B : 0.0003035 Nm.s

Magnet Flux, Ψ_M : 0.1827 Weber

Number of Poles, $2p$: 8

Simulation of PMSM was performed simultaneously with both conventional-PI controller and proposed adaptive FUZZY-PI controller under different speed and load conditions. I simulate. As shown in Figure 22, the reference speed value at the start time ($T=0$ ms) was determined as 1000rpm and the reference load value was determined as 2 Nm. The reference speed value was changed to 2000 rpm at $T=50$ ms. Finally, at $T=85$ ms, the reference load value was changed to 4 Nm. In Figure 22, the speed changes graph of conventional-PI and proposed adaptive FUZZY-PI controller in different operating states.

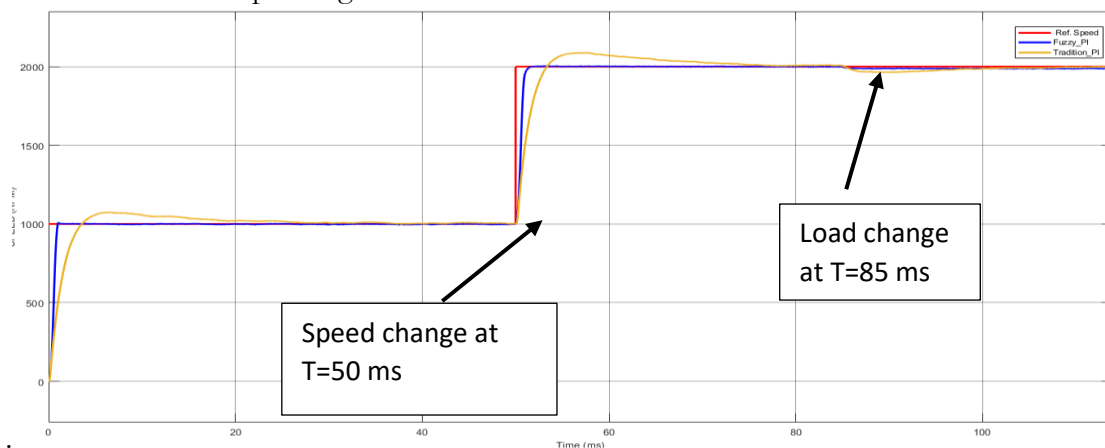


Figure 22. Graph of velocity changes of conventional-PI and proposed adaptive FUZZY-PI controllers in different states.

6.RESULT

In this study, speed control mathematical modelling and simulation of Permanent Magnet Synchronous Motor (PMSM) based on field-oriented vector control has been done using Matlab/Simulink program. In field-oriented vector control, the traditional-PI control model for speed controls and the adaptive FUZZY-PI control model are compared. The PMSM is powered by a current-controlled voltage source inverter. Hysteresis pulse-wide modulation is used to determine the current control and switching sequences of the inverter.

When the results are examined, it is seen that the proposed adaptive FUZZY-PI controller has a shorter transition time from unstable to steady state against speed and load changes compared to the traditional-PI controller, and the oscillations in the speed that occurs during the change are lower.

REFERENCES

- [1]. Erken, F., (2014). Sabit mıknatıslı senkron motorda moment dalgalanması azaltılması, Doktora Tezi, Fırat Üniversitesi Fen Bilimleri Enstitüsü, Elazığ.
- [2] Donsión, M. P., (2007). Parameters Influence On The Control Of A Pmsm”, ISEF 2007 - XIII International Symposium on Electromagnetic Fields in Mechatronics, Electrical and Electronic Engineering, Çek Cumhuriyeti, 13-15.
- [3] Akyazı, Ö., Küçükali, M., & Akpınar, A. S. (2011). Sürekli mıknatıslı senkron motorun hız denetiminin farklı bulanık üyelik fonksiyonları kullanılarak gerçekleştirilmesi. *Elektrik-Elektronik ve Bilgisayar Sempozyumu (FEEB)*.
- [4] Gençer, Ç, ve Gedikpınar, M., (2005). Sürekli Mıknatıslı Senkron Motorların Sayısal İşaret İşleme Tabanlı Konum Denetimi, F. Ü. Fen ve Mühendislik Bilimleri Dergisi, 17 (2), 216-223
- [5] C. Elmas, M.A. Akcayol, T. Yigit, (2007). Fuzzy PI Controller For Speed Control of Switched Reluctance Motor J.Fac.Eng. Arch. Gazi University, Vol 22, No 1, 65–72.
- [6] G.C.D. Sousa, B.K. Bose, (1994). A Fuzzy Set Theory Based Control of a Phase-Controlled Converter DC Machine Drive, IEEE Transactions on Industry Applications, Vol. 30, No. 1, pp. 34–44.
- [7] G. Feng, (2006). A Survey on Analysis and Design of Model-Based Fuzzy Control Systems, IEEE Transactions on Fuzzy Systems, Vol. 14, No. 5, pp. 676–697.
- [8] Du Changqing, Zeng Hongxia, Wu Dongmei, et al. (2018). Contrastive simulation study on the control strategy of permanent magnet synchronous motor [J]. Digital Manufacturing Science, 34-41.
- [9] Gu, D., Yao, Y., Zhang, D. M., Cui, Y. B., & Zeng, F. Q., (2020). Matlab/Simulink based modelling and simulation of fuzzy PI control for PMSM”. *Procedia Computer Science*, 166, 195-199.
- [10] Çelik, H., Kürüm, H., (2013). Sabit mıknatıslı Senkron motorun alan yönlendirmeli kontrolü, NWSA-Technological Applied Sciences, 1A0342, 8, (1), 67-85, Elazığ.
- [11] Dursun, M., Karayel, M., (2020). Sabit mıknatıslı senkron motorun alan yönlendirmeli hız kontrolü, 2. Uluslararası Avrasya Bilim, Mühendislik ve Teknoloji Konferansı, 621-632, Gaziantep/Türkiye,
- [12] Adam, A.A., (2007). Sabit mıknatıslı senkron motorda moment dalgalanması ve gürültünün azaltılması, Doktora Tezi, Yıldız Teknik Üniversitesi Fen Bilimleri Enstitüsü, İstanbul.
- [13] Bal, G., Özgenel, M. C. ve Demirbaş, Ş., (2007) Vektör denetimli kalıcı mıknatıslı senkron motorun uzay vektör darbe genişliği modülasyonu ile performans analizi, Politeknik Dergisi, Cilt: 10, Sayı: 1, Sayfa: 7-13, Ankara.
- [14] Karayel, M., Çelik, E., ve Yücedağ, İ., (2019). Bulanık Mantık Tabanlı Tek Bölge Yüklü Frekans Kontrolü, III. Uluslararası Bilimsel ve Mesleki Çalışmalar Kongresi-Mühendislik, 27-30 Haziran, Nevşehir/Türkiye,

Zinc Oxide (ZnO) – Fundamental Properties and Applications

E. Asikuzun Tokeser

Introduction

Zinc oxide (ZnO) is an inorganic compound. The powder form is widely used as an additive to such as many materials and products plastics, ceramics, glass, cement, rubber, oil, ointments, adhesives, leather sealants, dyestuffs, foods, batteries, ferrites, flame retardants. ZnO exists as a mineral zinc stone in the earth's crust. However, most of the commercially used ZnO is produced synthetically.

Since zinc and oxygen are in II. and VI. groups of the periodic table, respectively, ZnO is often referred to as a group II-VI semiconductor in materials science. This semiconductor has some advantageous properties. Good permeability, high electron mobility, wide band gap, effective room temperature luminescence are among the most important.

What is a semiconductor?

Semiconductors are materials whose resistivity is between $\rho = 10^{-2} - 10^9$ ohm.cm at room temperature. The electrical properties of semiconductors can be changed by methods such as optical excitation, doping, and heat treatment. For this reason, semiconductor materials are used in many devices such as transistors, switches, diodes, detectors, thermistors and sensors.

Pure Semiconductors

At absolute zero (at 0 K), the conduction band of semiconductors is empty, the valence band is full and these bands are separated by a forbidden energy gap (E_g). The semiconductor behaves like a complete insulator at this temperature. When the temperature rises from 0 K, the thermal energy of the electrons increases and if this energy reaches the forbidden energy value, the electrons pass from the valence band to the conduction band. When electrons are displaced, holes are formed.

The hole is an opposite sign with electron but the values are the same. These gaps in the valence band are filled by other electrons in the same band, and the displaced electrons form new holes. Thus, the hole moves in lattice. In this way, electrons and holes act as free carriers and contribute to electrical conductivity.

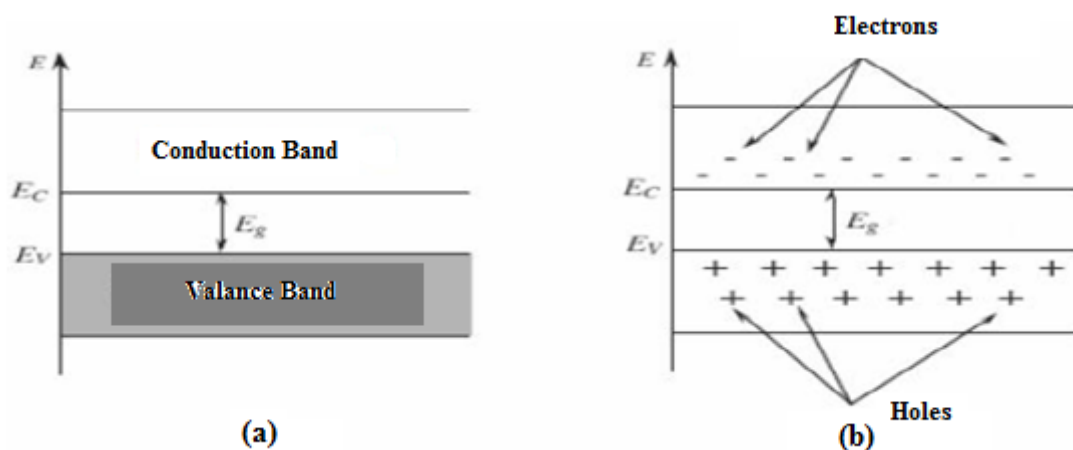


Figure 1. Energy band diagram for undoped semiconductors at different temperatures (a) $T = 0$ K, (b) $T > 0$ K

Doped Semiconductors

• n-Type Semiconductors

Silicon (Si) and germanium (Ge) in group IV A of the periodic table are semiconductors with four valence electrons. The electrons of the Si atom form covalent bonds with the electrons of other Si atoms. When VA group elements (P,As...) of the periodic table are added to this structure, impurities occur in the crystal structure. Four of the five electrons of these impurity atoms can form bonds with Si atoms. The binding energy of this non-bonding fifth electron is very low and thus begins to act as a free electron in the crystal.

Non-bonding electrons in the crystal create an energy level. This additional level is located just below the conduction band in the forbidden band gap. A very small amount of energy is needed to excite the electron from this level (for the movement of the nonbonding fifth electron). An electron moves into the conduction band with every excitation. These impurities are called donors.

Each donor electron is excited from the impurity level so that no gap is formed in the valence band. The heat energy at room temperature is sufficient to excite a large number of electrons from the donor level. In addition, transitions formed by the pure atom occur between the valence-conduction band, but this is neglected. Thus, there are more electrons in the conduction band than the number of holes in the valence band. Such materials are called n-type semiconductors.

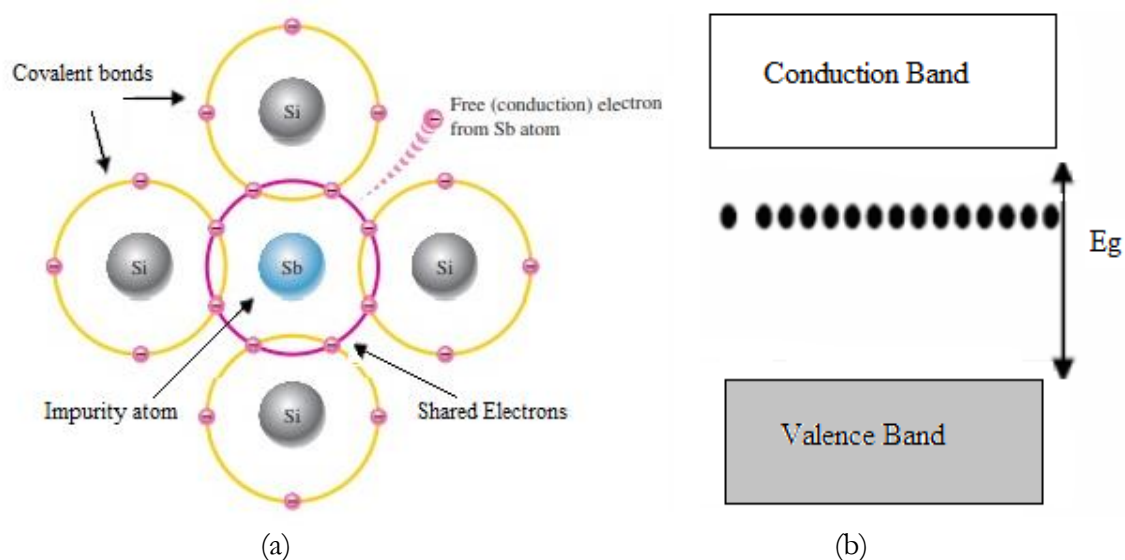


Figure 2. (a) Covalent bond formation for n-type semiconductor, (b) Impurity energy level for n-type

• p-Type Semiconductors

If impurities from group III A of the periodic table (such as Al, Ga...) are added to semiconductors such as Si or Ge, an electron will be deficient in the covalent bond formed. This deficiency can be seen as a void attached to the impurity atom. This vacancy can move within the impurity atom by electron transition. Such an impurity atom creates an energy level within the band gap, and this additional level is just above the valence band.

It can be thought that the gap is formed as a result of thermal excitation of an electron from the valence band to the impurity level. With this transition there is only a gap (a carrier) in the valence band. The free electron does not occur at either the impurity level or the conduction level. Such impurities are called acceptors and the additional level that occurs in the band gap is called the acceptor level. In this type of semiconductor, since the number of holes is more than the number of electrons, it is called a p-type semiconductor.

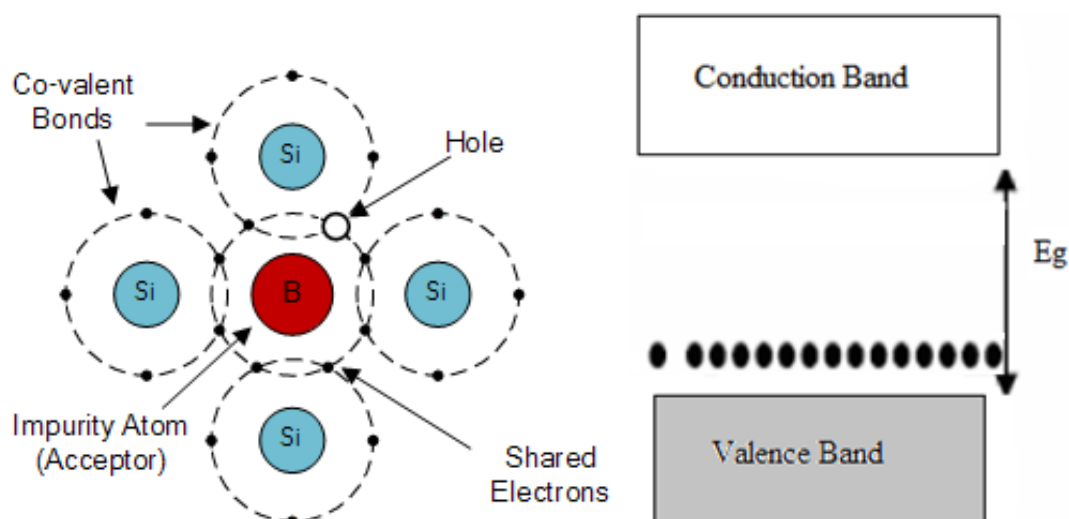


Figure 3. (a) Covalent bond formation for p-type semiconductor (b) impurity energy level for p-type

Physical and Chemical Properties of ZnO

Undoped ZnO is white at room temperature. When zinc oxide is heated up to 300°C, its color changes from white to yellow. When ZnO is heated to different temperatures, it can also take different colors such as yellow, green, brown and red. These color differences are due to the 0.02-0.03% gaps in the crystal structure.

In addition to the band gap, the carrier concentration in the structure significantly affects the surface properties of the particles. This effect has been proven by chemical sensor studies. Therefore, understanding the basic physical and chemical properties of zinc oxide samples is important for the development of future applications (Asikuzun, 2016).

Table 1. Various properties of ZnO

Properties	
Molecular Formula	ZnO
Density	5.606 g/cm ³
Melting Point	1975 °C
Boiling Point	2360 °C
Band Gap	3.3 eV (direct)
Crystal Structure	Wurtzite
Refractive Index	2.0041
Lattice Parameters (T=300 K)	
a_0	0.32495 nm
c_0	0.52069 nm
a_0/c_0	1.602
Static Dielectric Constant	8.656
Activation Energy	60 meV
Effective Electron Mass	0.24
Electron Mobility (T=300 K)	200 cm ² /V.s
Effective Void Mass	0.59

Crystal Structure

Semiconductor ZnO crystals, formed by the combination of zinc and oxygen, have a tetrahedral appearance formed by wrapping 4 oxygen atoms around each zinc atom. (Figure 2.1). The bonds that create to tetrahedral structure are typical sp³ covalent bonds. The crystal structure of ZnO may be in the wurtzite, zinc-blende or rock salt phases. Under normal conditions, the thermodynamically stable phase is the wurtzite phase. The zinc blende phase becomes durable with

the growth of cubic structures. The rock salt phase can be observed under high pressure (Ozgur & ark., 2005).

The lattice constants are $a = 3.250 \text{ \AA}$ and $c = 5.206 \text{ \AA}$. The c/a ratio is 1.60, just slightly less than the ideal 1.633. The distance between Zn and O is parallel to the c direction and is 1.992 \AA and 1.973 \AA in the other three directions. Its specific gravity is 5.72 gr/cm^3 (Bonnell, 1995).

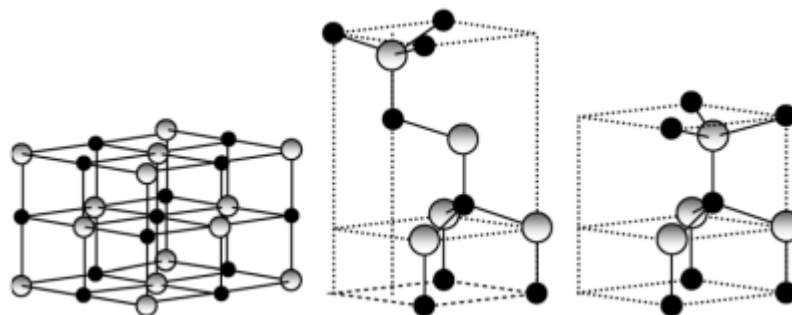


Figure 1. Representation of ZnO crystal structure (white spheres Zn atoms) (a) cubic rocksalt, (b) cubic zinc blende and (c) hexagonal wurtzite structure (Morkoc & Ozgur, 2009).

Lattice Parameters

The lattice parameters of a semiconductor generally depend on the following factors:

1. Mobility in free electron concentration with the degradation potential of the conduction band that is minimally occupied by these electrons.
2. Foreign atom and defect concentration and difference in ionic radii due to displacement with the host atom.
3. Temperature
4. External stresses (strain) can be created for example by the substrate. For many crystal materials, lattice parameters can be commonly and most accurately measured by high resolution x-ray diffraction (HRXRD) using the Bond method for symmetrical and asymmetrical reflections. Table 2.2 shows a , c and u parameters for the wurtzite structure of ZnO.

Table 2. Lattice and u parameters for ZnO

a (Å)	b (Å)	c (Å)	u
3,2496	5,2042	1,6018	0,3819
3,2501	5,2071	1,6021	0,3817
3,2860	5,2410	1,5950	0,3830
3,2498	5,2066	1,6021	
3,2475	5,2075	1,6035	
3,2497	5,5060	1,6020	

Electronic Band Structure

The most important point determined according to many studies is that zinc oxide (ZnO) has n-type character even in the undoped. It is seen that the forbidden energy range of zinc oxide changes with the doping of most oxides at different rates. The electronic structure of zinc oxide includes a fully filled $2p$ O^{2-} band and an empty $4s$ band (Zn^{2+}).

The width of the forbidden zone is approximately 3.37 eV . The character and use potential of a semiconductor is determined by its band structure. The accuracy of the information about the band structure of a semiconductor has great importance in order to be an accepted material for use in electronic circuits and device applications.

Literature Review

Transparent conductive oxides attract attention with their electrical conductivity and optical transmittance characteristics. ZnO, ITO, SnO and CdO are widely used for these applications (Akyuz, 2005).

Transparent conductive oxides find applications in many areas due to their properties. Transparent conductive oxide thin films; It is widely used in flat screen displays, laptop screens, gas sensors, solar cells. In addition, durability against environmental factors, low cost and suitability as an electronic circuit element are the factors that determine the usefulness of transparent conductive oxide material (Alexander, 2015).

Zinc oxide (ZnO) is also a very popular material in transparent conductive oxides. Zn is abundant in nature and is a non-toxic element. This has led to the widespread use of ZnO as a transparent conductive oxide material (Addonizio, 2014).

With the development of semiconductor technology, it has been seen that semiconductors such as Si and Ge are not sufficient in applications requiring high speed, high power and high frequency due to their indirect band gap structure, low mobility and conductivity. Because direct band gap semiconductors are required for optoelectronic devices. Direct band gap semiconductors are usually III-V or II-VI group compounds. III-V group semiconductors are limited to wavelengths of 500 nm and above in optoelectronic applications due to forbidden energy gaps (Singh, 1994).

II-VI group compounds have an energy band gap ranging from 1.7 to 4 eV. They are binary compounds formed between one of the II. group elements (Zn, Hg, Cd) and one of the VI. group elements (O, S, Te and Se) of the periodic table. II-VI compounds with wide band gap are used in optoelectronic devices, especially in light emitting devices. Because they have suitable direct band gap energy in the region where visible light has short wavelengths (Yuonesi & Pakdel, 2010).

Zinc oxide (ZnO) is a compound of group II-VI since zinc is in group II of the periodic table and oxygen is in group VI of the periodic table. ZnO can be found in wurtzite (hexagonal), cubic ZnS and cubic NaCl structures. The Wurtzite crystal structure is the most stable of these structures. The cubic ZnS structure can be stabilized by growing ZnO on cubic substrates. NaCl-structured ZnO can only be obtained under very high pressures (Steiner, 2004).

The wurtzite structure has a hexagonal unit cell. The lattice parameters of this structure are given as $a=0.3249$ nm, $c=0.5205$ nm (Berger, 1997). The c/a ratio of zinc oxide is 1.602 and it is close to the ideal tight-packed hexagonal structure (1,633 nm) (Steiner, 2004).

ZnO is a semiconductor that has a direct band structure and a very wide band gap (~ 3.3 eV) (Salam, 2013). Due to its wide band gap, it is accepted as a suitable material for LED production in the blue and ultraviolet region of the electromagnetic wave spectrum. The photoelectric, piezoelectric and thermoelectric properties of the ZnO semiconductor are very good and these are used in many applications due to these properties. These applications are; gas sensors, thin film transistors, photoelectric devices, optoelectronic devices, solar cells, UV detectors, piezoelectric transducers, surface acoustic circuits, thermoelectric devices, pH sensors, biosensors (Tsay, 2010). In addition, ZnO absorbs UV light and performs band transitions. Due to this feature, transparent conductive oxide is widely used as a thin film (Ashour & ark., 2006).

The properties of ZnO can be changed by heat treatment or by suitable doping. There are many application areas where Al, In, Ga, Li, Cu, Sn and Mg are used as doping atoms. The conductivity of zinc oxide can be increased with the contribution of ions such as Al, In, Ga. An increase in the transmittance and a decrease in the resistivity of Sn-doped ZnO thin films are observed. This is very advantageous for the construction of solar cells, on which many research

studies have been carried out recently. In addition, the forbidden energy gap value can be easily changed with the addition of Mg (Peker, Temel & Nebi, 2015).

Sol-gel method, which is one of the effective thin film forming techniques, has a wide area of use in that it can easily cover large areas and homogeneously form multi-layered films. Sol-gel method can be used in the production of most single-component or multi-component oxide films (Uhlmann & ark., 1997).

Nanostructured $Zn_{1-x}Gd_xO_\delta$ ($0 \leq x \leq 0,02$) powders were synthesized by combustion reaction method (CR) at room temperature in order to investigate its effect on structural, optical band gap, dielectric and magnetic properties. Oxygen vacancies and/or interstitial oxygen defects in Gd-doped ZnO samples play an important role in dielectric permittivity at room temperature. All Gd-doped ZnO samples exhibit typical paramagnetic behavior at room temperature (Franco & Pessoni, 2017).

The structural and thermoluminescence (TL) properties of Gd-doped ZnO nanoparticles were investigated. TL curves recorded in the 10-300 K range showed three overlapping peaks around 56, 110 and 155 K for the undoped ZnO nanoparticles (Isik & Gasanly, 2019).

Undoped, Gd-doped and (Gd, Mn) co-doped ZnO nanoparticles were produced by a hydrothermal method and their structural, morphological, optical and magnetic properties were investigated. Morphological studies showed that the synthesized nanoparticles were single and hexagonal in shape. When the diamagnetic ZnO sample is doped with Gd ions, it becomes ferromagnetic. However, this behavior was prevented with Mn ions (Poornaprakash & ark., 2017).

The structural, optical and gas sensing properties of undoped and Gd-doped ZnO nanoparticles were investigated. SEM images showed that particle diameters increased from a few nm to micrometers after Gd doping. 3% Gd-doped ZnO nanoparticles exhibited the best sensitivity (Noel & ark., 2014).

References

- Addonizio, M.L. (2014). Sol–gel synthesis of ZnO transparent conductive films: the role of pH. *Applied Surface Science*, 305, 194–202.
- Akyuz, İ. (2005). *Effects of Al doping and annealing on some physical properties of CdO Films*, PhD Thesis, Eskişehir Osmangazi University The graduate School of Natural and Applied Sciences, Department of Physics.
- Alexander, J.N. (2015). Development and characterization of transparent and conductive InZnO films by magnetron sputtering at room temperature. *J. of Alloys and Compounds*, 633, 157–164.
- Asikuzun, E. (2016). *Characterization of ZnO Based Diluted Magnetic Semiconductor Thin Films and Nano Particles Produced By Sol-Gel Method*, PhD Thesis, Abant İzzet Baysal University, The graduate School of Natural and Applied Sciences, Department of Physics.
- Ashour, M. A., Kaid, N. Z., El-Sayed and Ibrahim, A. A. (2006). Physical properties of ZnO thin films deposited by spray pyrolysis technique. *Applied Surface Science*, 252, 7844-7848.
- Bonnell, D. (1995). Physical Properties of Ceramics. *MSE*, 566.
- Franco, J., A., Pessoni, H. V. S. (2017). Effect of Gd doping on the structural, optical band-gap, dielectric and magnetic properties of ZnO nanoparticles. *Physica B*, 506, 145-151.
- Isik, M., Gasanly, N. M. (2019). Gd-doped ZnO nanoparticles: Synthesis, structural and thermoluminescence properties. *J. of Luminescence*, 207, 220-225.
- Morkoç, H., Ozgur, U. (2009). *Zinc Oxide: Fundamentals, Materials and Device Technology*. Copyright WILEY-VCH Verlag GmbH & Co. KGaA, Weinheim.
- Noel, J. L., Udayabhaskar, R., Renganathan et al. (2014). Spectroscopic and fiber optic ethanol sensing properties Gd doped ZnO nanoparticles. *Spectrochimica Acta Part A: Molecular and Biomolecular Spectroscopy*, 132, 634-638.
- Ozgur , U., Alivov, I., Liu , C., Teke, A. (2005). Comprehensive review of ZnO materials and devices. *J. of Applied Physics*, 98, 2-103.
- Peker, D., Temel, S., Nebi, M. (2015). Mg-doped ZnO films by sol-gel spin coating method, International. *J. of Scientific and Technological Research*, 1, 263- 269.
- Poornaprakash, B., Chalapathi, U., Babu, S., Park, Si-Hyun. (2017). Structural, morphological, optical, and magnetic properties of Gd-doped and (Gd, Mn) co-doped ZnO nanoparticles. *Physica E: Low-dimensional Systems and Nanostructures*, 93.
- Singh, J. (1994). *Semiconductor devices an introduction*. Mcgraw- Hill Inc. p87, 88.
- Steiner, T. (2004). *Nanostructures for optoelectronic applications*. Artech House Inc., London.
- Uhlmann, D.R., Suratwala, T., Davidson, K., Boulton, J.M., Teowee, G. (1997). Sol-gel derived coatings on glass. *J. of Non- Crystalline Solids*, 218, 113-122.
- Yuonesi, M., Pakdel, A. (2010). Effect of low concentration of nickel on structural and optical properties of ZnO nanofilms. *Physica B*, 405, 2083–2087.

The Story of a Superconductor

E. Asikuzun Tokeser

Introduction

Superconductivity is the properties of certain materials when they are cooled to extremely low temperatures in order to conduct direct current without encountering any resistance. In other words, materials that have zero electrical resistance under direct current when their temperature is lowered below a certain value are called superconductors. If the resistance is great, the applied voltage and the lost energy are large. But in some conductors, when the material is cooled below the critical temperature, the current carrying electrons lose their ability to convert their energy into heat and the resistance falls to zero. In this case, it is possible to create a current without applying any voltage and without losing energy. In other words, when the material is cooled below the critical temperature in an ideal metallic structure, the phonon effect disappears and the electrons move freely in the structure without any interaction with the lattice. In this case, the resistance of the structure suddenly drops to zero below the critical temperature. This material below the critical temperature is called superconducting material. In other words, in ordinary conductors, the lost energy arising from resistance and radiated as heat is prevented (between 3% and 10%). With the understanding that thousands of metal alloys can be superconducting under different conditions, new ones are added to these materials day by day.

Compared to a perfect lattice, electrons are scattered due to structural defects or impurities in the crystal. Also, lattice ions in normal modes have vibrations. These waves are called phonons. More phonons are formed in the lattice with increasing the temperature. As a result, an electron-phonon interaction, which scatters conduction electrons and causes greater resistance, occurs. Therefore, as the temperature decreases, the electrical resistance of the metal decreases. However, a residual resistance around absolute zero temperature is expected due to crystal defects. Therefore, the electrical resistivity of some solids disappears completely at sufficiently low temperatures. This situation seems extraordinary.

The behavior of electrons in a superconductor is quite different. There are impurities and lattice defects in this structure. However, the superelectrons in the conductor are not encounter any obstacles and move through the lattice. Because the electrons will not clash with any obstacle, no friction will occur, and as a result, current and energy will be transmitted without any loss.

The question of why electrons moving through the superconducting material do not encounter any obstacles has occupied scientists for years. When a material is heated, lattice vibrations increase, and when cooled, these vibrations decrease. Previous researchers believed that atomic vibrations in matter helped electrons pass more easily through the lattice. However, this was an indication that the resistance would decrease as the temperature increased. These and similar simple ideas were not sufficient to explain superconductivity. The state of superconductivity is too complex to be easily explained.

The first studies on superconductivity started with the liquefaction of helium by H. Kamerling Onnes in 1908 in Leiden. As a result of his studies in 1911, Onnes found that when solid mercury is cooled below a certain temperature called the T_c critical temperature, its electrical resistance drops to an immeasurably small value (Onnes, 1911; Kittel, 1986; Hwu & ark., 1987). As the temperature dropped below $T_c=4.2$ K, the mercury transitioned from the normal state to a

superconducting state. Since then, many other elements, compounds and alloys below critical temperatures as high as 30 K have been known as superconductors. But not all materials are superconductors. Figure 1 shows the variation of resistivity with temperature at very low temperatures for superconducting tin and non-superconducting silver. In a superconductor, current can flow for years without measurable reduction.

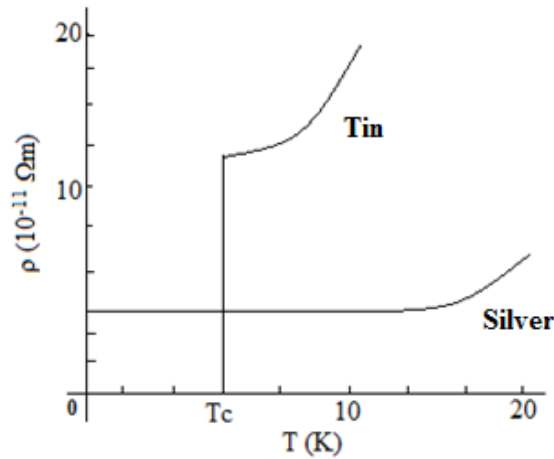


Figure 1. a) Finite resistivity curve of a normal metal at absolute temperature b) variation of resistivity ρ of a superconductor with respect to the critical temperature T_c

In 1933, Meissner and Oschenfeld found that when a superconducting material is cooled below its critical temperature under the influence of a magnetic field, it ejects all the magnetic flux from the interior of the superconductor (Meissner & Oschenfeld, 1933). If the magnetic field is applied after the material is cooled below its critical temperature, the magnetic flux is again ejected from the superconductor (Fig. 2). Therefore, we can say that a superconducting material behaves exactly like a diamagnet. Both of the Meissner events are shown in Figure 2.

According to Lenz's law, a reduced current occurs when the magnetic flux changes in a circuit. Orbital electrons in a diamagnetic atom regulate their rotational motion to create a net magnetic moment to oppose the externally applied magnetic field. We can explain it this way: An external magnetic field cannot penetrate inside a superconductor because the conduction electrons in the superconductor adjust their motion to create a magnetic field in the opposite direction to the external field. In this case, the superconducting material behaves like a single diamagnetic atom. Thus, the two main properties of superconductors, namely the exclusion of magnetic flux and the absence of resistance to resist current, are associated with each other.

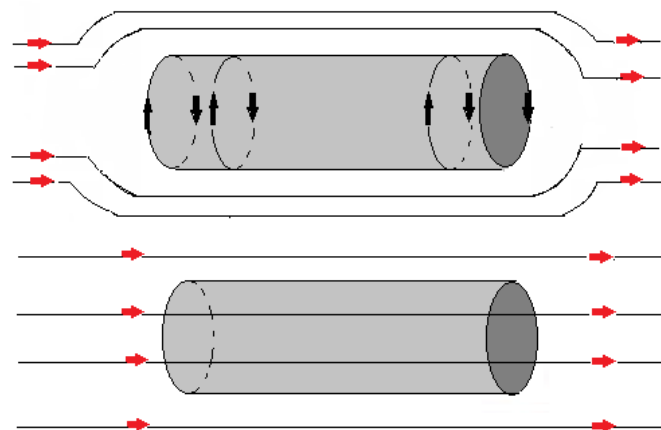


Figure 2. Schematic ejection of the magnetic field. Above is the Meissner event (Rose, 1978).

If the external field is increased above a certain value called critical B_c , it is seen that the material has no superconductivity and it becomes normal. The value of this critical magnetic field for a given metal depends on temperature (as shown for lead in Figure 3). As the external magnetic field increases, the critical temperature decreases until $B > B_c(0 K)$. There is no superconductivity at any temperature for this metal. We can understand it like this: Suppose a magnetic field is applied on a superconductor at a temperature below T_c . The superconductor will expel this magnetic field due to the Meissner effect. The energy reduction in the magnetic field occurs as the increased energy of the electrons that creates a superconducting current. As the strength of the external magnetic field increases, the energy gained by the superconductor increases. At the critical value of B_c , the energy of the superconducting state becomes more than the energy of the normal state, so the material becomes normal.

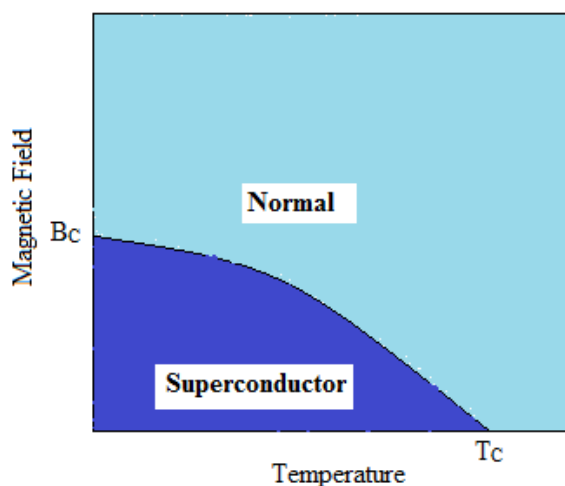


Figure 3. Change of critical B_c field with temperature (Rose, 1978)

There are many important applications of superconductivity. For example; The use of superconducting electromagnets, arising from non-resistive currents flowing inside the magnet windings, in electric motors and generators, is an obvious application. A small problem arises in this case; Magnetic fields are created in the winding wires to oppose superconductivity. This negative is eliminated using II. type superconducting materials.. There is no difference between the I. and II. types superconductors in terms of mechanism of superconductivity. Both types show similar thermal properties during the superconductor-normal transition at zero magnetic field. However, the Meissner effect is completely different. A I. type superconductor completely excludes the magnetic field, and as soon as the superconductivity disappears, the magnetic field completely penetrates. In a II. type superconductor, the magnetic field is completely ejected up to the value of H_{C1} . The field above H_{C1} is partially ejected, but the ambient is still superconducting. At a higher H_{C2} value, the flux completely enters the system and superconductivity disappears (Fig.4).

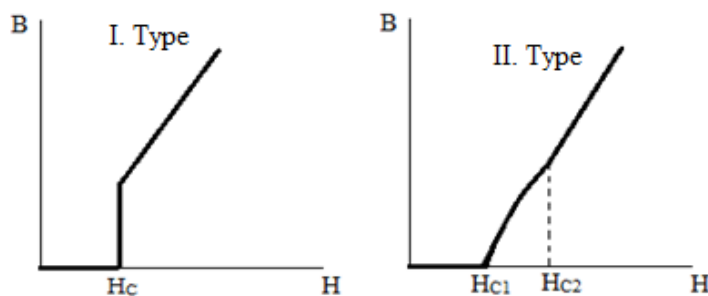


Figure 4. Behavior of I and II. type superconductors under magnetic field

Properties of Superconductors

The phenomenon of superconductivity is determined by the behavior of electrons: The interaction of free electrons in the crystal lattice of a superconducting metal with positive ions in vicinity of its causes defects in the lattice. As a result, an indirect force of attraction is created between the electrons that would normally repel each other and thus electron pairs are formed in the metal. These electron pairs, called Cooper pairs, are difficult to separate from each other by scattering. Moreover, these pairs have anti-scattering quantum properties. These pairs are responsible for the superconductivity. Because the electrical conductivity in metals basically depends on scattering. Less scattering means the metal is better electrically conductive. In addition, superconductors can carry large amounts of current. Small superconducting coil magnets can create strong magnetic fields without consuming too much energy. Such magnets can be used as particle deflectors in the construction of airborne trains, accelerator tunnels, and nuclear magnetic resonance scanners, thanks to the magnetic field (Mikio & ark., 1987; Grant & ark., 1987).

When a superconductor is cooled to low temperatures, it shows two different properties.

- 1- When the electric current collides with the ion lattice forming the material structure, the current is blocked. This phenomenon creates the resistance of the material against electric current. When the same material is made into a superconductor, the ion lattice, that creates matter, supports the electric current instead of blocking it. In this way, resistance drops to zero.
- 2- Superconductors exclude the magnetic field.

In 1933, two German physicists, Meissner and Ochsenfeld, observed that superconductors repel magnetic field lines and do not insert them. In other words, a magnet repels a superconductor that is below its critical temperature. his event is called the Meissner Event (Tokana & ark., 1987). Experiments were carried out with cylindrical superconductors. It was seen that the sample completely repulsed the magnetic field lines at below the critical temperature and was found to be superconducting. The fact that $B=0$ in the material is as natural as the zero resistance of superconductors. Superconductors are also excellent diamagnets.

Zero Resistivity

The most basic property used to determine the superconducting state is the zero resistance property. The zero resistance state of superconductors can be determined by measuring the resistance against temperature. Resistance of metals is caused by the scattering of electrons from phonons, impurities, and crystal defects. In perfectly pure metals, the resistance is due to the scattering of electrons by the temperature-dependent phonons. Therefore, in pure metals, the resistance will go to zero as the temperature reaches 0 K. However, any metal always has its impure atoms. Therefore, electrons are scattered regardless of temperature, and the metal exhibits resistance even at 0 K. However, in a superconducting material, the resistance of the material decreases continuously with decreasing temperature and at critical temperature the resistance suddenly goes to zero. In the superconducting state, the electrical resistance for direct current is zero, that is, in the superconducting state, there is no loss in current. Therefore, a current can flow in the superconducting ring without loss for a very long time (Ozturk, 2007).

Resistance and magnetic susceptibility measurements have aspects that are superior to each other. Resistance measurements are preferred by researchers since these are easier. Since the magnetic field can break the interparticle bonds in granular structures. In general, resistance measurements show higher critical temperatures and sharper transitions than susceptibility measurements. In contrast, susceptibility measurements explain the magnetic behavior of superconducting material. In addition, since magnetization is a thermodynamic state variable, it can provide information about the thermodynamic behavior of the superconducting state.

Susceptibility measurements can also give information about the ratio of the superconducting phase in the material. It should also be noted that if the sample is porous, resistivity measurements cannot be occur as desired due to the problems and gaps between the particles. In an ideal homogeneous superconductor, both measurements give the same transition temperature.

How is this possible?

A microscopic theory of superconductivity is as follows.

Let's consider a metal as a lattice of positive ions (Fig. 5). Single electrons moving towards the lattice create an electric current. Normally the electrons repel each other and are scattered by the lattice and are scattered by the lattice. That is, they oppose their movements.

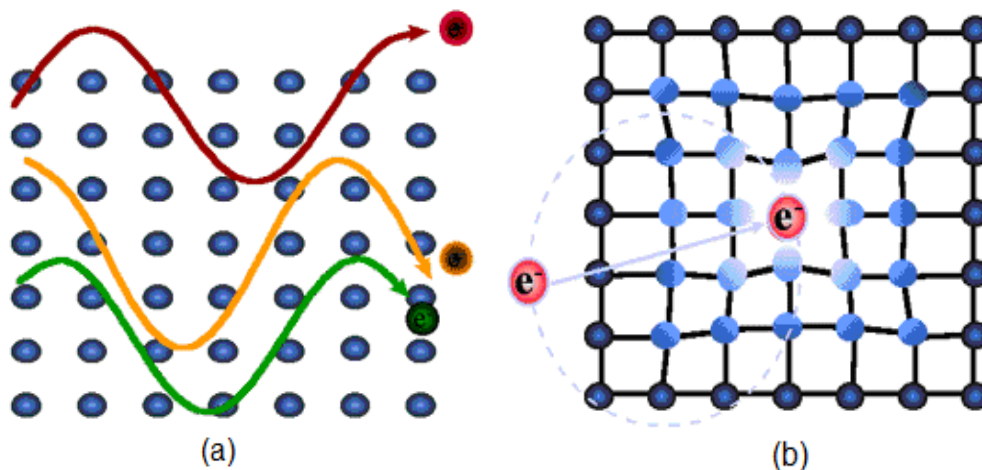


Figure 5. a) Conduction in metals and b) Formation of Cooper pairs

As an electron passes near the positive ions in the lattice, it enters the Coulomb interaction with the ions and moves slowly towards the lattice. After passing, the electrons are quickly scattered back to their original moves positions. When some samples and ions are cooled to low temperatures, they are not rapidly backscattered to their original positions and form a temporary positively charged local region and form a transient positively charged local region. A second passing electron is attracted towards this positive region and follows the first electron. Thus, the two electrons move together and cross the ion lattice as a pair (Asikuzun, 2010). Electrons do not scatter when acting as a couple and they encounter a small resistance, that is, the sample has zero resistance. The current passes through the sample without resistance (Figure 6).

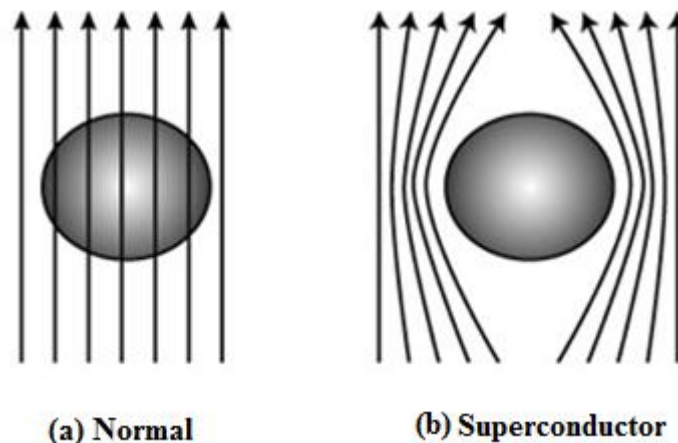


Figure 6. a) Normal and b) Magnetic flux distribution around a superconducting material

Excellent Diamagnetism

When a superconductor is cooled in a weak magnetic field, permanent currents at the surface increase at the transition temperature. These currents circulate inside and destroys the flux density. The situation is the same when a magnetic field is applied after cooling (Ibach & Luth, 1990) (Fig. 7). This phenomenon, that is, the absence of a flux density inside the superconductor, even in an applied magnetic field, is called the Meissner effect.

As is known, there are two types of superconductors that can be distinguished by their behavior under a magnetic field. These are called type I and type II. Except for Niobium (Nb) and Vanadium (V), which show superconductivity, all metallic elements are type I superconductors. Nb and V elements and all alloys and compounds showing superconductivity are II. type superconductor. All high temperature superconductors are also II. type superconductor. There is no difference in the superconductivity mechanism of I. and II. type metallic superconductors. Both have similar properties in the superconductor-normal transition at zero magnetic field. But the Meissner effect is completely different.

Type I Superconductors: After a certain magnetic field, the material recovers from the Meissner effect, returns to normal state and allows the magnetic flux to penetrate completely inside. Their critical magnetic fields are usually small.

II. Type Superconductors: In this type of materials, the material is the same as Type I until the subcritical magnetic field value called H_{c1} . Flux does not penetrate. From this value to the H_{c2} value, there is partial flux penetration. But the superconductivity continues. After the H_{c2} value, the material loses its superconductivity by transitioning to the normal phase.

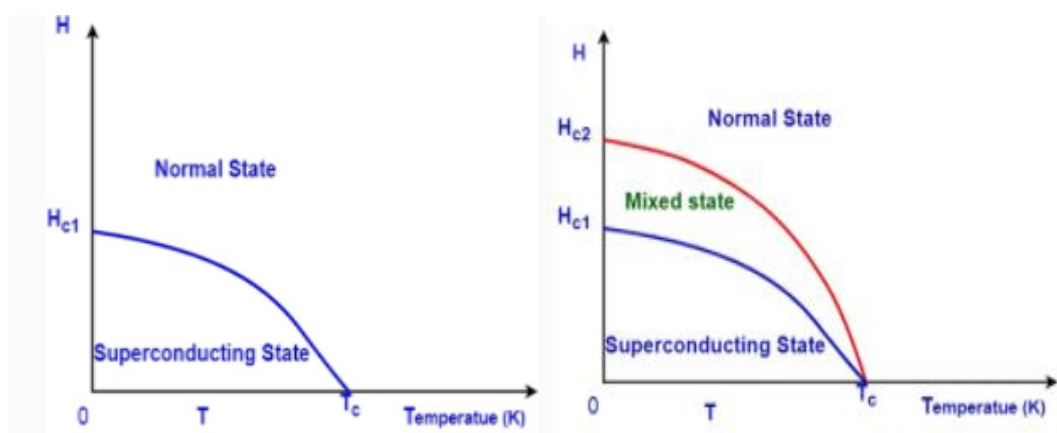


Figure 7. The magnetic behavior of a) I. type and b) II. type superconductor against the applied field.

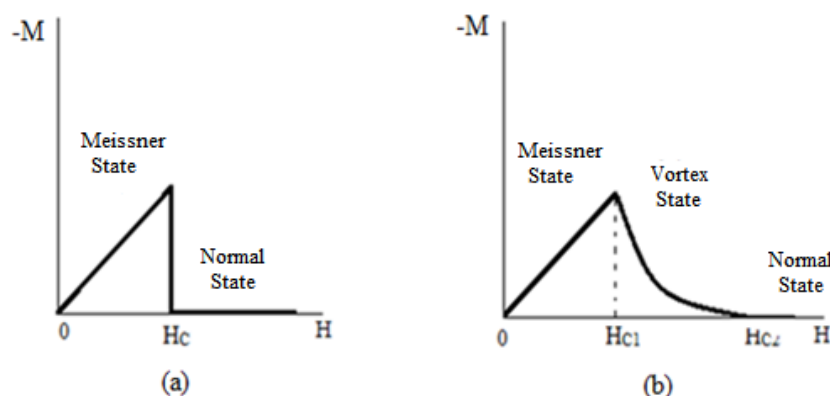


Figure 8. Magnetization of a) I. type and b) II. type superconductor

Figure 8a shows the magnetization of the I. type superconductor. The Meissner state is represented by a line with a slope of -1 in the (M,H) plane. When the transition to the normal state occurs, the slope suddenly becomes zero. Figure 8b shows the magnetization of the II. type superconductor. II. type superconductors behave completely like I. type superconductors when the applied external magnetic field value is below H_{C1} and show excellent diamagnetism.

References

Asikuzun, E. (2010). *The Investigation of Electrical and Mechanical Properties of Pr Doped Bi-2212 Superconductor*. Master Thesis, Kastamonu University Graduate School of Natural And Applied Sciences, Department of Physics.

Grant, P.M., Beyers, M.B., Engler, E.M., Lim, G., Parkin, S.S.P., Ramirez, M.L., Lee, V.Y., Nazzari, A., Vazquez, J.E., and Sovay, R.J. (1987). Superconductivity Above 90K in the Compound $\text{YBa}_2\text{Cu}_3\text{O}_{7-x}$. *Phys. Rev. B*, 35, 7242-7244.

Hwu, S.J., Song, S.N., Thiel, J., Poepelmeier, K.R., Ketterson, J.B., and Freeman, A.J. (1987). High T_c superconductivity in Regions of Possible Compound Formation. *Phys. Rev. B*, 35, 7119-7121.

Ibach, H., & Luth, H. (1990). *Festkörperphysik*. Third Edition.

Kittel, C. (1986). *Introduction to Solid State Physics*. John Wiley & Sons, Inc. New York, London, Sydney.

Meissner, W., Oschenfeld, R. (1933). Upper Critical Fields of High- T_c Superconducting Y-Ba-Cu-O. *Nature*, 132, 931-935.

Mikio T., Jun T., Kiichi O., Hitoshi K., Yoshinari M., Yasunori I., Yoichi T. and Hiromasa M. (1988). High- T_c Phase Promoted and Stabilized in the Bi, Pb-Sr-Ca-Cu-O System. *Japanese Journal of Applied Physics*, 27, L1041.

Onnes, H. K. (1911). Superconductivity and Magnetism. *Comm. Phys. Lab. Univ. Leiden*, 119-120.

Ozturk, O. (2007). *The effect of Au diffusion-doped on structural, superconducting and mechanical properties of $\text{Bi}_{1.8}\text{Pb}_{0.35}\text{Sr}_{1.9}\text{Ca}_{2.1}\text{Cu}_3\text{O}_y$* . Doktora Tezi, Abant İzzet Baysal Üniversitesi Fen Bilimleri Enstitüsü Fizik Anabilim Dalı.

Rose-Innes, A. C., & Rhoderic, E. H. (1978). *Introduction to Superconductivity*. New York: Pergamon, 5.

Tokana, K., et al. (1988). Properties of Pb-Doped Bi-Sr-Ca-Cu-O Superconductors. *Appl. Phys. Lett.*, 53, 1329-1331.

Effect of Volcanic Basalt Fiber on Physical and Mechanical Behaviors in Mg Alloy Produced by Powder Metallurgy

Bünyamin ÇİÇEK¹
Tuna AYDOĞMUŞ²

Introduction

Magnesium (Mg) metal is in the alkaline earth group in the periodic table. Being very light in terms of density increases the usage area. This metal is 1/4 times lighter than iron (Fe) and 1/2 times that of aluminum (Al). For this reason, it is frequently used in the aerospace, automotive, aviation and defense industries where lightness is at the forefront (Bamberger & Dehm, 2008; Huang, Subramani, & Chiang, 2021; Zengin, Turen, & Elen, 2019).

Many metals can be oxidized during production due to their reaction to free oxygen in the atmosphere. Mg metal has a high affinity for oxygen. For this reason, it is necessary to protect Mg metal with an atmospheric environment in production methods. While an atmosphere-controlled melting furnace is required at the casting stage, the use of an atmosphere-controlled heat treatment furnace is mandatory in powder metallurgy production. Otherwise, the reaction between Mg and oxygen develops very rapidly to form the MgO compound. Thus, the Mg element loses its known metal property (Akkaş & Boz, 2019; Bamberger & Dehm, 2008; Elen, Turen, & Koç, 2019; Matykina et al., 2016; Taleghani, 2014).

The pure Mg element, like many metals, lacks most properties while in its pure form. However, alloys produced within the framework of Hume-Rothery rules provide success in many properties. Mg element can form alloys with many elements within the framework of binary and triple phase diagrams. As a result of the alloy system, intermetallic structures and hard particles in microstructure can be formed. Thus, the alloy gains new properties with the effect of denser and harder formations than the α -Mg structure. Alloyed Mg metal is also exposed to mechanical forces, increasing many physical properties. For example, in an Mg alloy rolled for the effect of compression force, corrosion resistance shows a significant increase due to grain refinement. In a forged Mg alloy, the wear loss can decrease tens of times compared to the first sample. In addition to mechanical strength, Mg alloys give successful results in heat treatment processes and artificial aging stages. Thus, production, alloying, post-production mechanical effects and heat treatments are very important processes for Mg alloys. By applying some or all of these processes, a high-level Mg alloy can be obtained in terms of many properties (Bamberger & Dehm, 2008; B Çiçek, 2011; Elen et al., 2019; Gu et al., 2010; Yan, Bai, Liu, & Jin, 2017; Zhao, Liu, Song, & Atrens, 2008).

When Mg metal is used as a matrix, there is a letter-based proportional standard writing style for naming the alloys formed. In this writing style, the first letters are usually indicated by the initial letter of the symbol of the elements in the periodic table or by another letter. For example, the

¹ Dr. Lecturer, Hitit University, ORCID: 0000-0002-6603-7178

² Asist. Prof. Dr., Hitit University, ORCID: 0000-0002-8736-2949

letter A denotes aluminum metal, while the letter X. Integer numbers are used for the weight percentage ratio denotes calcium. For example, while the ratio of Al metal is 9 %wt and Zn metal is 1 %wt, this alloy is called AZ91 (Balasubramani, Srinivasan, Pillai, & Pai, 2007; Elen et al., 2019; Zengin et al., 2019; Zhu et al., 2021).

Apart from alloying, Mg metal can take place in a composite material as a matrix. Fiber, particle, layer etc. can create composite material with many external geometrical products. In recent years, carbon-based nanomaterials, carbides, ceramics and glassy forms can be added to the Mg matrix as additional products. Reinforcement products added to the composite material cause porosity and microstructure irregularities in the structure. For this reason, the weight percent and geometric conditions of the supplement products should be well analyzed (Sun & Ahlatci, 2011; Ye & Liu, 2004).

Density level is one of the important topics in composite materials. For this reason, the preference for the use of Mg metal is increasing. Thus, Mg metal takes its place as a matrix structure in many composite material studies. There are serious gains in the properties of composite materials with the effect of additional products. For example, by adding a Mg_2Si particle to the Mg matrix structure or forming it in the structure, the wear resistance can increase up to 40 times compared to pure Mg (B Çiçek, 2011; Lokesh, Ramachandra, Mahendra, & Sreenith, 2013; Sohag et al., 2020; Sun & Ahlatci, 2011).

One of the structures used as a composite material by-product is fiber-based products. In this context, glassy fibers, organic fibers and artificial fibers are frequently used. Fiber structures provide the composite material with an increase in yield and tensile strength. In addition, a significant increase in wear resistance is observed with the addition of certain proportions. Fiber structures are classified in terms of length, diameter and material type. Many fiber structures can be used, from the nanometer level to the millimeter level. Quartz fibers, basalt fibers (BF), fruit peel fibers, organic wood fibers, etc. products are used in composite materials (Akhlaghi, Eslami-Farsani, & Sabet, 2013; Hou et al., 2017; Rawal, 2001).

Basalt structures, one of the fiber reinforcement products added to composite materials, give successful results. BF obtained from volcanic rocks is preferred due to its high mechanical strength and wear resistance. The chemical composition differences of volcanic rocks according to geographical regions give the materials unique values. In basalt structures, Na, Al, Cl, P, Si and S elements exist in different proportions and the form of oxide compounds. In addition, structures such as Al_2O_3 and SiO_2 , which are oxidized compounds of the elements that make up basalt structures, are very hard and durable ceramic compounds. Thus, BF creates a difference in many properties of a composite material to which it is added (Jamshaid & Mishra, 2016; Khalili, Daghigh, & Eslami Farsani, 2011).

BF is produced industrially. It is frequently used in ceramic structures in the industry. In addition, it takes its place in concrete additives for micro reinforcement, insulation applications, linings and increasing the mechanical strength of polymer structures. An industrially supplied BF modulus of elasticity reaches 89 GPa, while tensile strength is measured at about 5000 MPa. By adding a structure with high mechanical strength at this level to the composite, high properties can be achieved (Fiore, Scalici, Di Bella, & Valenza, 2015; Jamshaid & Mishra, 2016).

In this study, the effect of BF on the mechanical process was investigated by adding different ratios of BF to an AZ91 alloy produced by powder metallurgy method. Since BF loses its properties at high temperatures, it is produced by powder metallurgy method. The sintering heat treatment was carried out at 550°C to prevent thermal change. Sintering was applied at this temperature for 360 minutes. Afterwards, the samples were examined both physically and mechanically. BF effect was tried to be revealed by hardness and dry wear tests. Scanning electron microscopy (SEM) was used in powder-fiber mixing, microstructure phase and post-abrasion surface examinations. Energy

dispersion X-ray spectrometry (EDX) was used for the elemental determination of the structures in the SEM stage. X-ray Fluorescence (XRF) was used in the initial analysis of the powders and fiber structure and the elemental analysis after sintering. X-ray diffraction (XRD) analysis was performed to follow the microstructure phases. Thus, the effect of BF on AZ91 alloy produced by powder metallurgy has been examined with a serious investigation process.

Material Preparation and Experiments

Powder metallurgy method and process were applied in this study to obtain AZ91 material, which is Mg alloy. Differences in properties were observed with BF added to AZ91 alloy. Mg, Al and Zn metals used in this study were obtained from Nanografi Turkey. Metal powders with 99.9% purity were used. The grain sizes of metal powders are listed as $D_{90} = 15.2 \mu\text{m}$, $7.1 \mu\text{m}$ and $11.3 \mu\text{m}$, respectively. The data obtained in the XRF (Rigaku Primus II) analysis applied before the experiments are listed in Table 1.

BF, which is used as a supplement, was purchased from Dost Kimya Turkey. The product specifications provided by the company are given in Table 2. The ready-made BF was ground in a rod mill for 1 hour for grain reduction before use. The basic SEM (Carl Zeiss Ultra Plus Gemini Fesem) images of the products used as raw materials are shown in Figure 1.

Table 1. XRF analyzes for metal powders

Elements	Mg (%wt)	Al (%wt)	Zn (%wt)	Other
Mg Powder	99.981	0.002	0.002	0.015
Al Powder	0.025	99.918	0.001	0.056
Zn Powder	0.009	0.001	99.925	0.065

Table 2. Catalogue parameters for basalt fiber

Tensile strength	4840 MPa
Elasticity module	89 GPa
Service temperatures	-260°C / +982°C
Melting Temperature	1450°C
Density	2.60-2.80 g / cm ³
Fiber diameter	9-23 micrometer
Fiber length	6-12 mm

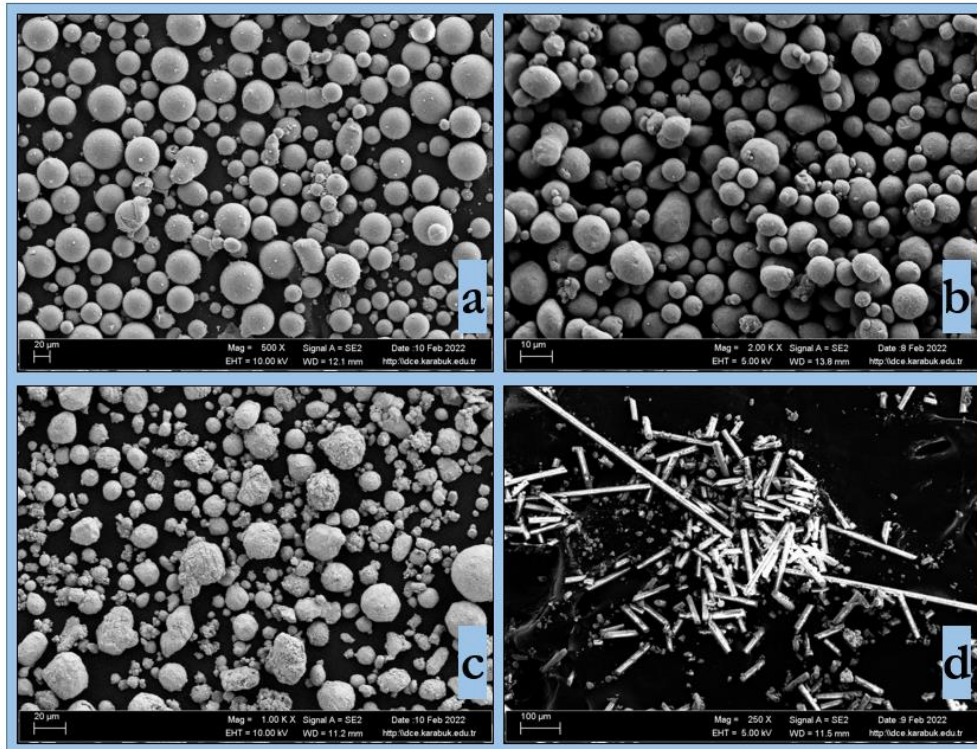


Figure 1. SEM images for raw materials; (a) Mg, (b) Al, (c) Zn, and (d) basalt fiber

Raw materials and materials were first taken into a homogeneous mixing process for the powder metallurgy process. During the mixing process, a mechanical mixing process was applied in the presence of ethanol. Mg, Al and Zn elements added to 200 ml of ethanol were mixed at 400 rpm / 1 hour. BF, on the other hand, is mixed primarily in the same details. In these initial mixing processes of powders and BF structure, agglomeration and static electrification, processes are minimized. In the mixing process applied in the magnetic stirrer, the containers were added to each other and the mixture was continued under the same conditions. After 3 hours, the liquid+powder mixture was placed on a *hydrophobic* filter paper and dried at 70°C/24h. The resulting mixtures were used as samples. The percentage wt powder ratios in the mixtures are given in Table 3. Also, the mixing process is illustrated in Figure 2.

Table 3. Element amounts for specimens

Specimen	Mg (%wt)	Al (%wt)	Zn (%wt)	BF (%wt)
AZ91-0	90	9	1	-
AZ91-1	90	9	1	+1
AZ91-2	90	9	1	+2
AZ91-3	90	9	1	+3

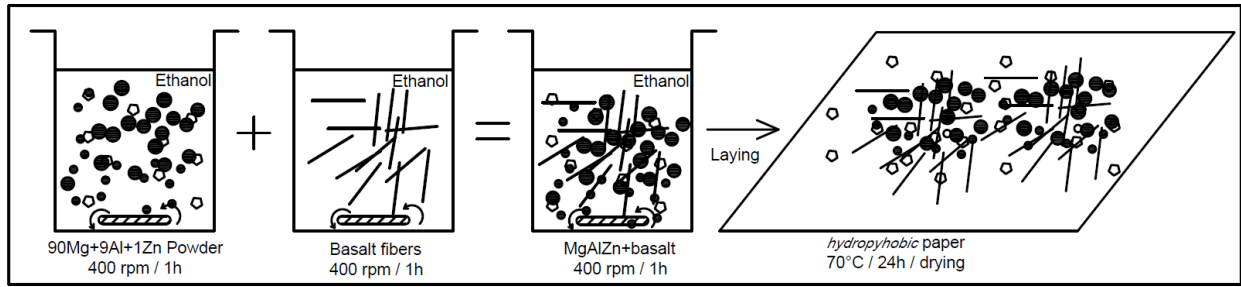


Figure 2. Powder mixing details

The powder samples obtained after the mixing process were taken into SEM analysis to control the mixing conditions. The powder samples were then taken to the pressing process. The samples were pressed in a 13 mm diameter die under a load of approximately 4 MPa/mm². The pressed samples were sintered in a Protherm brand heat treatment furnace, in a quartz glass tube with both ends blanked. In order to protect the samples placed in the glass tube from the atmosphere, the glass tube was melted with oxy-acetylene flame and the ends were blinded. The samples were sintered at 550°C for 6 hours. Photographs of the glass tube and sample after sintering were observed.

Metallic samples obtained after sintering were taken into microstructure analysis after classical metallographic preparations. A mixture of 5% picric acid+methanol was used as etching reagent in the metallographic process.

First, microstructure examinations of the samples were made under SEM microscope. In addition, EDX analysis was obtained from different structures in the AZ91-0 sample and reported. At the same time, XRD (Rigaku Ultima IV) and XRF analyzes applied for phases and elemental ratios were observed in the obtained AZ91-0 sample. For the follow-up of BF in the composite material, XRF analysis was applied to the AZ91-3 sample.

The samples were also examined by microhardness (QNESS Q10 A+) and dry wear (UTS Tribometer T10) tests. Vickers penetrating tip was used in the hardness test. The hardness test was carried out under a load of 1000 g and in five measurements. The average of the obtained values is reported.

In the dry abrasion test, the surfaces prepared with 1200 mesh sandpaper were abraded with a back-and-forth sliding motion. 316L quality 6 mm diameter balls were slid on the samples placed on a movable mechanism at a speed of 1500mm/min. A total of 100 m sliding distance was applied under 10N load. The difference between the first-last weight and the wear rate were followed. Finally, the worn surfaces were examined with SEM images.

Experimental Results and Discussions

A metal matrix composite material was obtained with the BF structure added to the AZ91 alloy produced by the powder metallurgy method during production. Composite material has been examined by many physical and mechanical based experiments and applications. SEM image analysis is given in Figure 3 for tracking the fibers added to the structure during the composite material creation process. Thus, the post-mixing process of the powder + fiber structure was monitored.

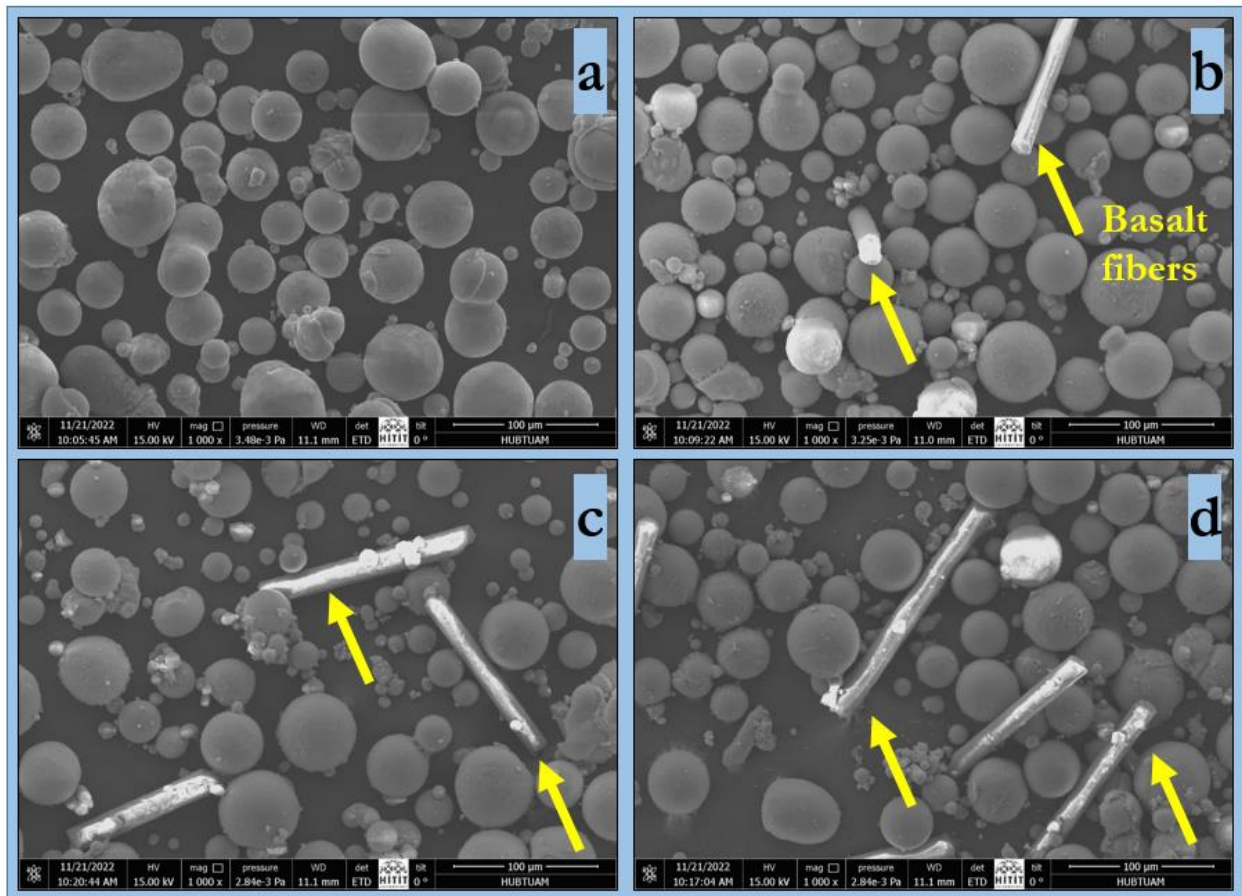


Figure 3. SEM images of mixed powder and fiber structures, (a) AZ91-0, (b) AZ91-1, (c) AZ91-2, and (d) AZ91-3

When Figure 3 is examined, it is observed that spherical powders preserve their geometric structure in all mixtures. No oxidation or deformation was observed on the surfaces with the mixing process in alcohol. Fibers are seen in blends with BF addition. The increased BF ratio was detected in the pictures.

Pressed powder mixtures were sintered in quartz tube with blunt ends. Samples in quartz tubes after sintering are shown in Figure 4.



Figure 4. Composite materials sintered in a quartz tube

When the sintered samples are examined, it is seen that the Mg alloy can be sintered in a quartz tube with both ends closed without atmospheric environment. No oxide structures were found on

the sample surfaces. Thus, a Mg sintering process has been developed, eliminating cost and application difficulties.

After sintering, samples of basic alloy AZ91-0 material were examined in SEM environment. In Figure 5, the microstructure image of the base alloy is observed.

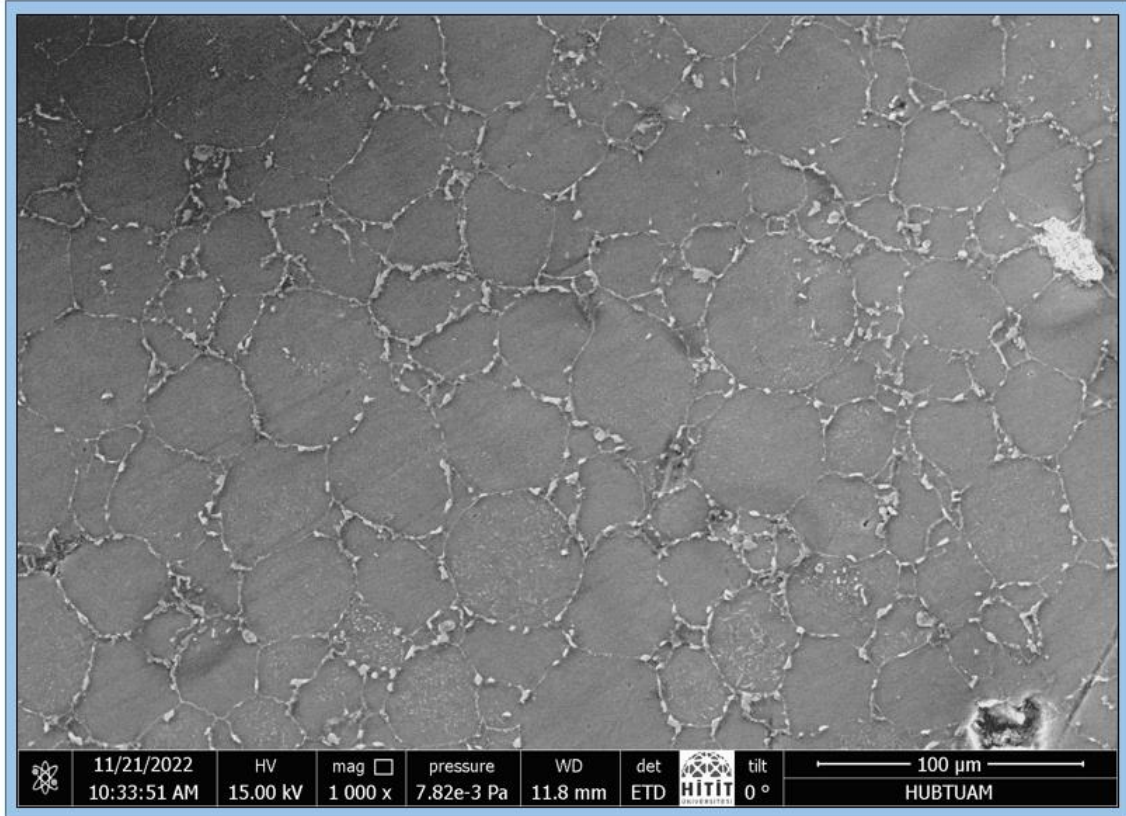


Figure 5. SEM image of AZ91-0 sintered alloy

When Figure 5 is examined, the requirements of the powder metallurgy production method are observed. Phase structures developing between dust grains are seen. Low porosity conditions have developed. Thus, the basic microstructure expected in a metallic alloy sintered without atmosphere was obtained.

In order to examine the phase structures observed between the powder grains in the AZ91-0 sample, SEM examination at high magnification was performed in Figure 6. In addition, the results of elemental EDX analysis of the phases detected in the microstructure are given in the picture.

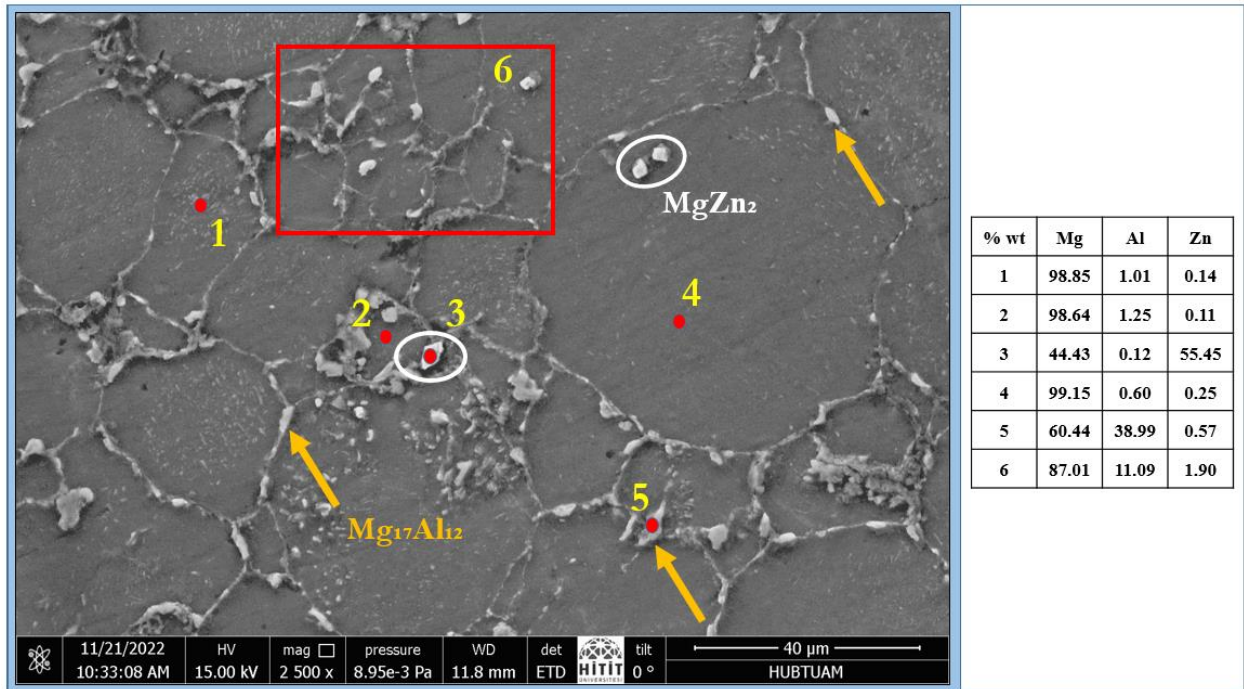


Figure 6. Microstructure analysis and EDX examination at high magnification for AZ91-0 alloy

Different phase structures observed in the microstructure were analyzed. It is seen that the expected phases in the AZ91 alloy are $Mg_{17}Al_{12}$ and $MgZn_2$, consistent with the literature. The result of the XRD analysis applied as well as the EDX analyzes of the formed phases are shown in Figure 7.

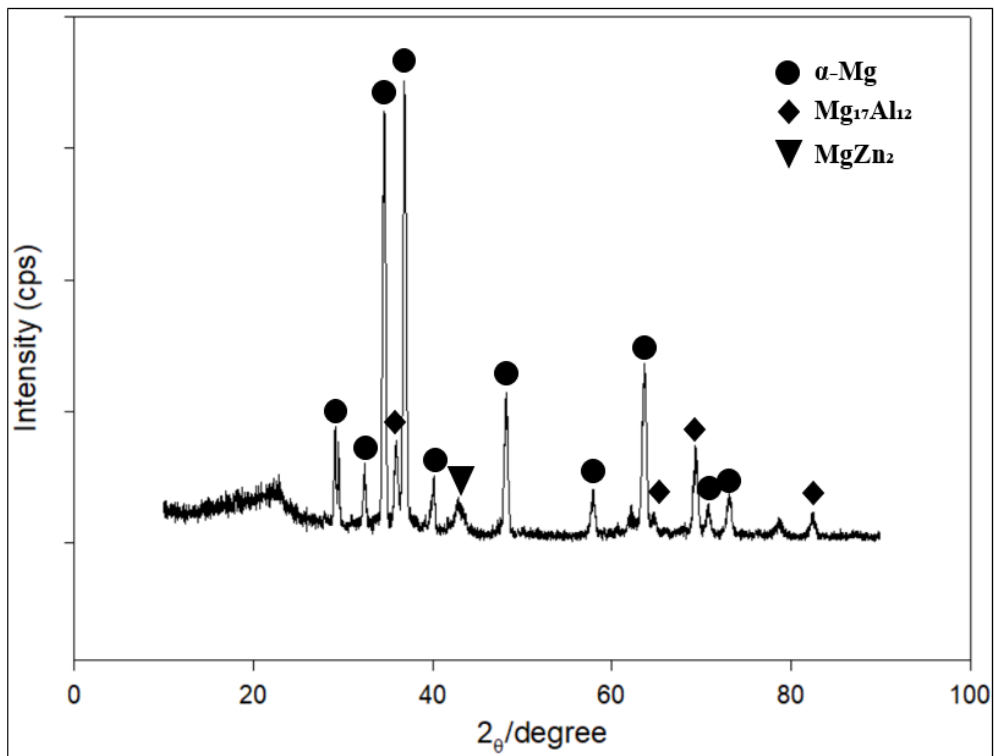


Figure 7. XRD peak for AZ91-0 alloy

When the XRD peaks given in Figure 7 were examined, the intermetallic structures shown in the microstructure were detected. Thus, it was observed that the phases expected in the AZ91 alloy were formed in the microstructure and the production method applied gave acceptable results.

The microstructure images of the composite structures obtained with the BF structure added to the AZ91-0 sample during production are given in Figure 8. Pictures are given at low and high magnification.

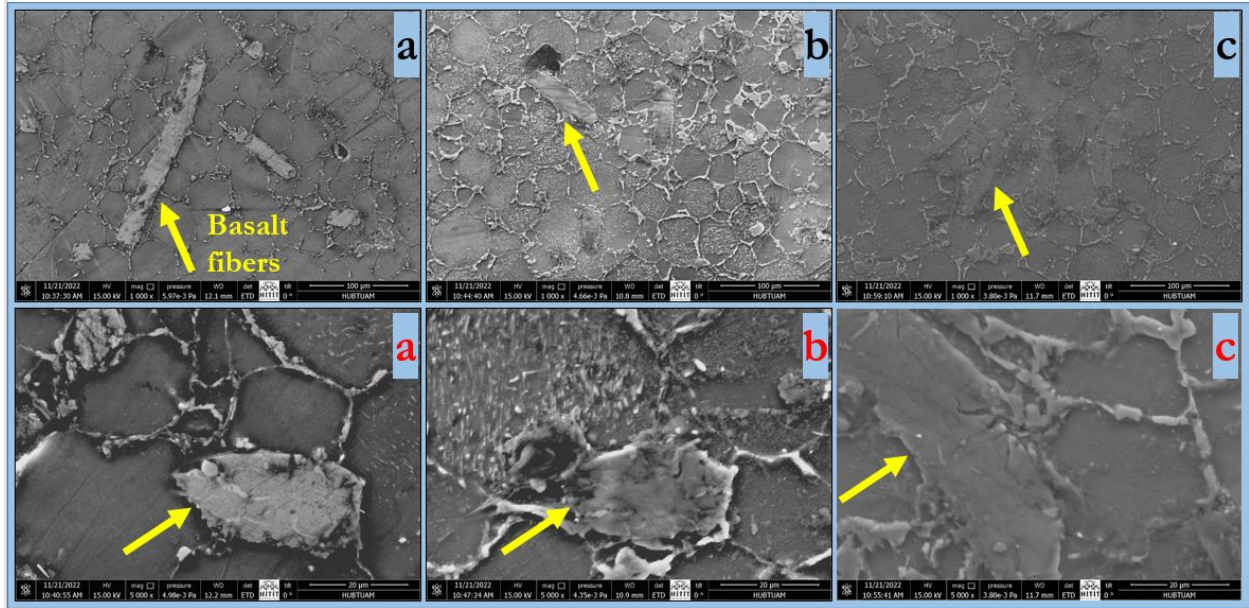


Figure 8. Microstructure images of composite materials

(a) AZ91-1, (b) AZ91-2, and (c) AZ91-3

BF structures are clearly observed in the microstructure examination of composite materials. As the BF ratio increased, the amount of detection increased. Low porosities are observed around the fiber structures. Thus, a successful metal matrix composite material was obtained with a fiber structure containing a high percentage of oxidized compounds.

XRF analyzes applied to determine the elemental ratios of alloy and composite materials are listed in Table 4.

Table 4. XRF analyzes for specimens

Specimen	Na (%wt)	Al (%wt)	Si (%wt)	S (%wt)	Cl (%wt)	Ca (%wt)	Zn (%wt)	P (%wt)	Mg (%wt)
AZ91-0	0.0083	9.5244	0.1292	0.0328	0.1187	0.0387	1.3739	0.0029	Balance
AZ91-3	0.1544	9.9093	1.9601	0.0176	0.7296	0.9378	1.0811	0.0129	Balance

According to XRF analysis, Al and Zn ratios of AZ91 alloy were found to be at the expected level. In the AZ91-3 composite material, the Al and Zn ratios were observed to be 9% and 1% by weight, respectively. In addition, Na, Si, Cl, Ca, and P elements detected in the composite material show the presence of basalt in the structure.

Vickers microhardness test was applied to the produced alloy and composite structures. The results obtained as a result of the hardness test are shown in Figure 9.

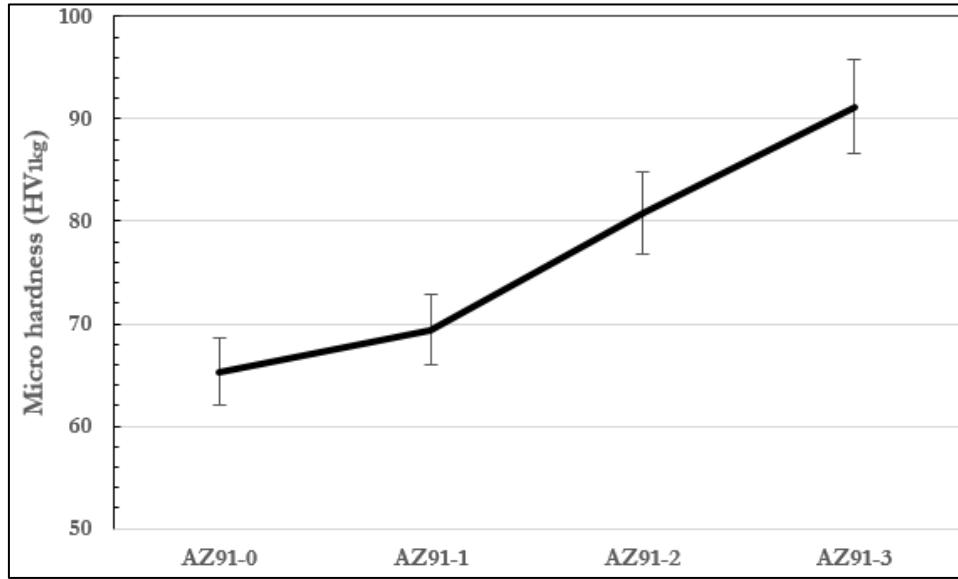


Figure 9. Hardness test results for all specimens

As a result of the hardness test, the hardness value of the composite materials increased with the addition of the BF structure to the alloy. The high strength value and modulus of elasticity of the BF structure are mainly effective in this process. In the AZ91-3 sample with the highest BF ratio, the hardness showed an increase of approximately 40% compared to the base alloy.

Worn surfaces formed as a result of the dry wear test applied to basic alloy and composite materials are shown in Figure 10 and Figure 11. Images are given at low and high magnification.

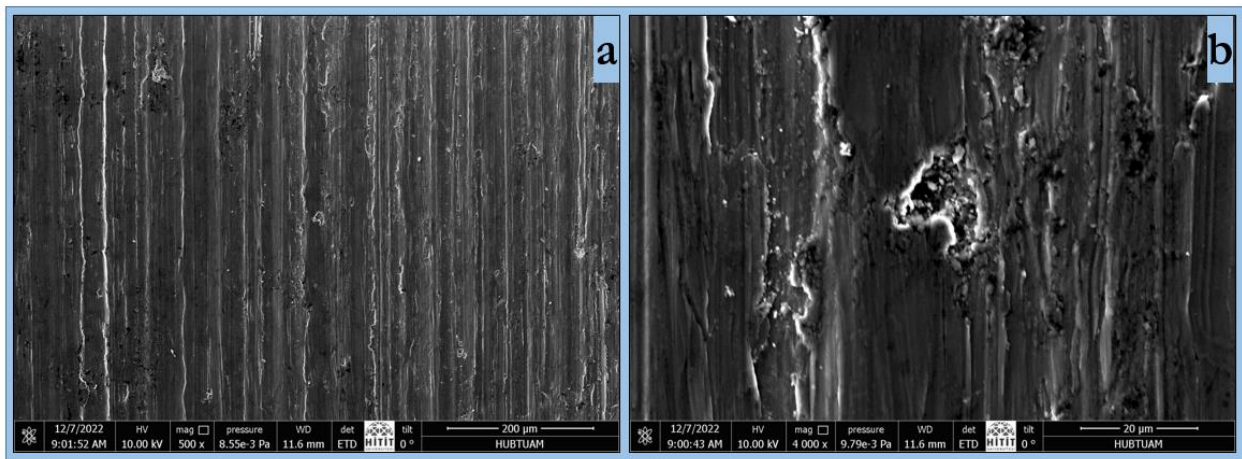


Figure 10. Worn surfaces in AZ91-0 alloy, (a) low and (b) high magnification

An adhesive wear mechanism is generally observed on the worn surface of the AZ91-0 alloy. A homogeneous image was observed on the worn surface. However, abrasive spots were detected at high magnification. The high hardness of the MgZn₂ particle is thought to form these abrasive spots.

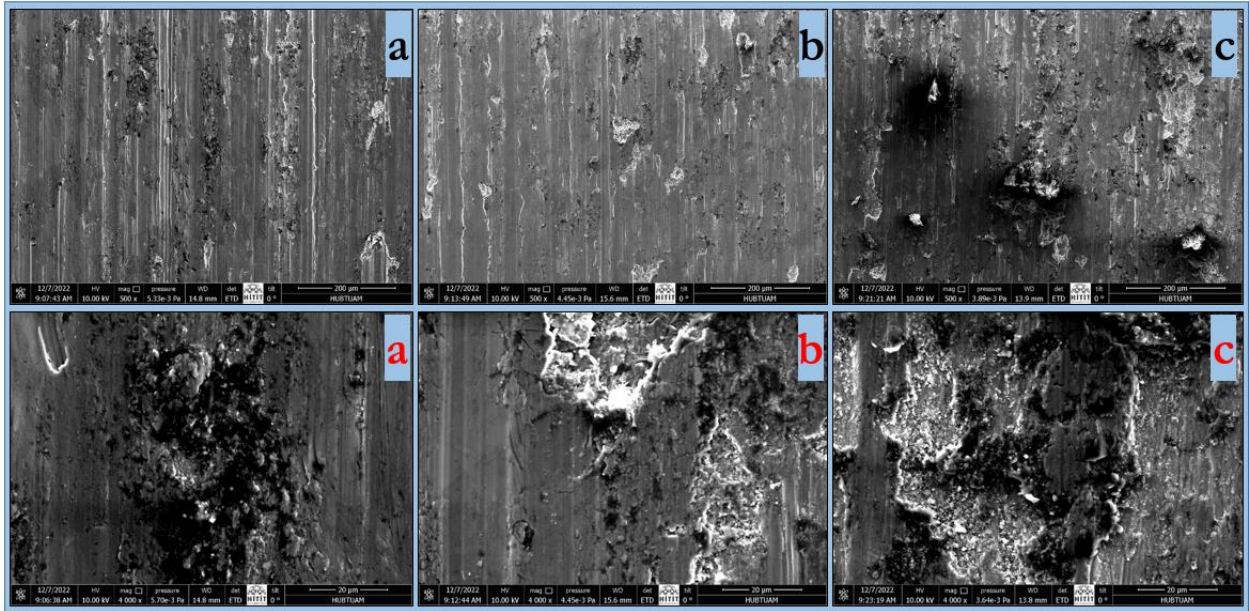


Figure 11. Worn surfaces for composite materials, (a) AZ91-1, (b) AZ91-2, and (c) AZ91-3

Worn surfaces formed in composite materials contain both wear mechanisms, adhesive and abrasive. Abrasive wear zones are observed in high magnification images. It can be said that the reinforcement fiber material causes the abrasive structure. Due to the high yield strength of the fiber material and therefore its high hardness value, the abrasive mechanism has developed. Due to the axial load applied during wear and the 316L stainless steel ball, the fiber structures are fragmented. The hard fiber particles resulting from the fragmentation deformed the softer alloy regions. Thus, as the BF ratio increased, the amount of abrasive mechanism increased.

The graph of the wear rates due to the weight loss obtained after the wear test is shown in Figure 12.

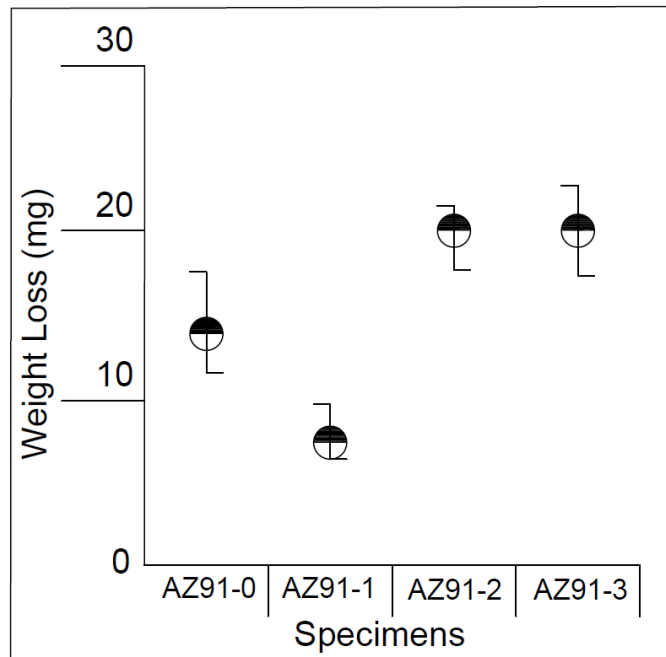


Figure 12. Weight loss rates for specimens

According to the weight loss results calculated after wear, an average of 14 mg loss occurred in the alloy sample. In the AZ91-1 composite structure, the weight loss was measured as 7 mg with an improvement rate of 50%. However, it was observed that the weight loss increased rapidly as the basalt ratio increased. In the AZ91-3 sample, the weight loss reached an average of 20 mg. Wear resistance increased with the effect of BF added at a low rate (1%). The wear rate of the structure increased with the addition of 3% BF. It is seen in Figure 11c that the fibers break and accelerate wear and develop an abrasive mechanism. Thus, while adding 1% of the BF structure was a successful result, increasing BF negatively affected the results.

According to the experimental results, the production of AZ91 Mg alloy by powder metallurgy method has been carried out successfully. General requirements for alloys produced by powder metallurgy method are provided (Cicek, Sun, Turen, & Ahlatci, 2022). In addition, it was observed that the Mg alloy, which was sintered with a unique method without atmosphere control, transitioned from oxidation to metallic form. In addition, composite materials obtained with basalt structure added to the alloy were produced.

Production of AZ91 alloy by powder metallurgy is a process that has been studied in many studies. Intermetallic phases and particles formed between dust grains were similar to the literature (Akkaş & Boz, 2019). However, atmosphere controlled sintering process is generally used in the production of Mg alloy (Akkaş & Boz, 2019; Taleghani, 2014). A new sintering step has been added to the literature with the atmosphereless method applied in this study.

The BF structure has been used frequently in the literature in recent years and has an effect on many features. It is a possible result that basalt has different chemical content depending on the geographical and volcanic region. Therefore, elemental ratios in all studies give different properties (Jamshaid & Mishra, 2016).

When the hardness test was examined, the high mechanical properties of the BF structure caused a serious increase in hardness in composite materials. This increase is an expected result with the effect of hard compounds in the BF structure. Hardness increase in BF added alloys showed similar results (Akhlaghi et al., 2013; Jamshaid & Mishra, 2016). Thus, the increase in hardness was confirmed.

The wear resistance of the composite materials formed by adding the BF structure to the alloys shows different values. As the fibers break during wear, the wear rate increases. However, fibers added at a low rate can break and fill into porosities. Thus, while the wear resistance increases at a low rate, the wear resistance decreases as the fiber content increases. The reason for this can be shown as more abrasion of the matrix alloy by the hard fibers (Bünyamin Çiçek & Aydoğmuş, 2022; Fiore et al., 2015; Jamshaid & Mishra, 2016). Finally, it has been stated in studies that abrasive wear mechanisms occur in fiber-reinforced composite materials (Amuthakkannan, Manikandan, Raja, & Rajesh, 2017; Chairman, Jayasathyakawin, Srinivasan, & Ravichandran, 2020; Guo et al., 2015). As a result, similar processes were followed in this study.

Conclusions

The production of AZ91 Mg alloy by powder metallurgy method and the process of making it into a composite material with basalt fiber addition were investigated in this study. In addition, microstructure, hardness and physical dry wear tests were applied to the samples. As a result, the following main results were obtained.

1. AZ91 alloy produced with powder forms of pure elements Mg, Al and Zn has been successfully obtained.
2. After sintering, intermetallic phases were observed among the metallic powder grains.
3. Metallic structure has been achieved without oxidation with the sintering process applied in a blanked quartz glass tube without atmosphere control.
4. Composite materials are produced with the basalt structure in the form of fiber added to the alloy.
5. With the effect of basalt fibers, the hardness level of composite materials increased by 40%.
6. In the dry wear test applied to alloy and composite materials, the structure containing 1% basalt fiber suffered the lowest weight loss.

Thus, this study was completed with both the use of a volcanic basalt fiber structure and the sintering process applied without atmospheric control. The effect of volcanic basalt fiber on wear and hardness properties has been brought to the literature. In addition, a new sintering method open to development for Mg alloys has been specifically investigated.

References

Akhlaghi, F., Eslami-Farsani, R., & Sabet, S. (2013). Synthesis and characteristics of continuous basalt fiber reinforced aluminum matrix composites. *J Compos Mater*, 47(27), 3379-3388. doi:<https://doi.org/10.1177/002199831246576>

Akkaş, M., & Boz, M. (2019). Investigation of the compressibility and sinterability of AZ91 powder production and particle production by gas atomisation method. *Journal of magnesium and alloys*, 7(3), 400-413.

Amuthakkannan, P., Manikandan, V., Raja, M. A., & Rajesh, S. (2017). Wear characterization of aluminium/basalt fiber reinforced metal matrix composites-A Novel Material. *Tribology in Industry*, 39(2), 219.

Balasubramani, N., Srinivasan, A., Pillai, U., & Pai, B. (2007). Effect of Pb and Sb additions on the precipitation kinetics of AZ91 magnesium alloy. *Materials Science and Engineering: A*, 457(1-2), 275-281.

Bamberger, M., & Dehm, G. (2008). Trends in the development of new Mg alloys. *Annu. Rev. Mater. Res.*, 38, 505-533. doi:10.1146/annurev.matsci.020408.133717

Chairman, C. A., Jayasathyakawin, S., Srinivasan, D., & Ravichandran, M. (2020). Abrasive wear characteristics of bio-based jatropha oil cake incorporated basalt fiber reinforced epoxy composites. *Materials Today: Proceedings*, 33, 3947-3950.

Cicek, B., Sun, Y., Turen, Y., & Ahlatci, H. (2022). Investigation of Microstructural Evolution of Gas-assisted Metal Injection Molded and Sintered Mg-0.5 Ca Alloy. *Sci Sinter*, 54(1), 25-37. doi:<https://doi.org/10.2298/SOS2201025C>

Çiçek, B. (2011). *Investigation of wear and corrosion properties of Mg alloys reinforced with Mg₂Si particle*. (M.Sc. Thesis), Karabuk University, Turkey.

Çiçek, B., & Aydoğmuş, T. (2022). The Effect of Basalt Fiber Addition on Physical Dry Wear in Al-Cu Alloy Used in the Automotive Industry. *International Journal of Automotive Science And Technology*, 6(4), 379-385.

Elen, L., Turen, Y., & Koç, E. (2019). AZ91 Mg alaşımına farklı oranlarda Sb ilavesi ile katılaşma hızının mikroyapı ve mekanik özelliklere etkisi. *International Journal of Engineering Research and Development*, 11(2), 451-463. doi:<https://doi.org/10.29137/umagd.507264>

Fiore, V., Scalici, T., Di Bella, G., & Valenza, A. (2015). A review on basalt fibre and its composites. *Composites Part B: Engineering*, 74, 74-94.

Gu, X., Zhou, W., Zheng, Y., Cheng, Y., Wei, S., Zhong, S., . . . Chen, L. (2010). Corrosion fatigue behaviors of two biomedical Mg alloys—AZ91D and WE43—in simulated body fluid. *Acta biomaterialia*, 6(12), 4605-4613. doi:<https://doi.org/10.1016/j.actbio.2010.07.026>

Guo, W., Guo, J., Wang, J., Yang, M., Li, H., Wen, X., & Zhang, J. (2015). Evolution of precipitate microstructure during stress aging of an Al-Zn-Mg-Cu alloy. *Materials Science and Engineering: A*, 634, 167-175.

Hou, L., Wu, R., Wang, X., Zhang, J., Zhang, M., Dong, A., & Sun, B. (2017). Microstructure, mechanical properties and thermal conductivity of the short carbon fiber reinforced magnesium matrix composites. *Journal of alloys and compounds*, 695, 2820-2826.

Huang, S.-J., Subramani, M., & Chiang, C.-C. (2021). Effect of hybrid reinforcement on microstructure and mechanical properties of AZ61 magnesium alloy processed by stir casting method. *Composites Communications*, 25, 100772.

Jamshaid, H., & Mishra, R. (2016). A green material from rock: basalt fiber—a review. *The Journal of The Textile Institute*, 107(7), 923-937.

Khalili, S., Daghigh, V., & Eslami Farsani, R. (2011). Mechanical behavior of basalt fiber-reinforced and basalt fiber metal laminate composites under tensile and bending loads. *Journal of Reinforced Plastics and Composites*, 30(8), 647-659.

Lokesh, G., Ramachandra, M., Mahendra, K., & Sreenith, T. (2013). Effect of Hardness, Tensile and Wear Behavior of Al-4.5 wt% Cu Alloy/Flyash/SiC Metal Matrix Composites. *Int J Mod Eng Res Technol*, 3(1), 381-385.

Matykina, E., Garcia, I., Arrabal, R., Mohedano, M., Mingo, B., Sancho, J., . . . Pardo, A. (2016). Role of PEO coatings in long-term biodegradation of a Mg alloy. *Appl. Surf. Sci.*, 389, 810-823.

Rawal, S. P. (2001). Metal-matrix composites for space applications. *JOM*, 53(4), 14-17.

Sohag, M. A. Z., Gupta, P., Kondal, N., Kumar, D., Singh, N., & Jamwal, A. (2020). Effect of ceramic reinforcement on the microstructural, mechanical and tribological behavior of Al-Cu alloy metal matrix composite. *Mater Today: Proc*, 21, 1407-1411. doi:<https://doi.org/10.1016/j.matpr.2019.08.179>

Sun, Y., & Ahlatci, H. (2011). Mechanical and wear behaviors of Al–12Si–XMg composites reinforced with in situ Mg₂Si particles. *Materials & Design*, 32(5), 2983-2987.

Taleghani, M. A. J. (2014). *Processing and properties of high performance 7075 Al and AZ91 Mg powder metallurgy alloys*. Universidad Carlos III de Madrid.

Yan, K., Bai, J., Liu, H., & Jin, Z.-Y. (2017). The precipitation behavior of MgZn₂ and Mg₄Zn₇ phase in Mg-6Zn (wt.%) alloy during equal-channel angular pressing. *Journal of magnesium and alloys*, 5(3), 336-339.

Ye, H. Z., & Liu, X. Y. (2004). Review of recent studies in magnesium matrix composites. *Journal of Materials Science*, 39(20), 6153-6171.

Zengin, H., Turen, Y., & Elen, L. (2019). A comparative study on microstructure, mechanical and tribological properties of A4, AE41, AS41 and AJ41 magnesium alloys. *Journal of Materials Engineering and Performance*, 28(8), 4647-4657. doi:<https://doi.org/10.1007/s11665-019-04223-8>

Zhao, M.-C., Liu, M., Song, G., & Atrens, A. (2008). Influence of the β -phase morphology on the corrosion of the Mg alloy AZ91. *Corrosion Science*, 50(7), 1939-1953. doi:<https://doi.org/10.1016/j.corosci.2008.04.010>

Zhu, L., Qiu, F., Zou, Q., Han, X., Shu, S.-L., Yang, H.-Y., & Jiang, Q.-C. (2021). Multiscale design of α -Al, eutectic silicon and Mg₂Si phases in Al-Si-Mg alloy manipulated by in situ nanosized crystals. *Materials Science and Engineering: A*, 802, 140627. doi:<https://doi.org/10.1016/j.msea.2020.140627>

Highway Vertical Curve Optimization with Meta- Heuristic Algorithm

Sina ASHERLOU¹
Aref YELGHİ²
Erhan Burak PANCAR³
Şeref ORUÇ⁴

Introduction

Due to the high cost of the road, it is required careful attention. Many studies have been carried out in the world generally due to the high cost of the highway superstructure and many methods have been developed and proposed for the design of the project. Since highway design is open to innovations, research is continuing at full speed today.

A highway project consists of infrastructure and superstructure. The ground floor, which is under the leveling surface created at the end of earthworks, that is, splitting and filling works, is called infrastructure works. The performance of the pavement is directly related to the physical properties of the infrastructure. In this regard, all conditions must always be met. The superstructure, on the other hand, has a layered structure and transfers the traffic loads directly to the subgrade. The superstructure is the part that can carry traffic loads without facing major deterioration and cracking throughout its economic life (Sütaş & Öztaş, 1983).

It is an undeniable fact that optimization is everywhere, from design to implementation of all engineering fields. Mathematical optimization or programming is used in all design planning problems. In this context, the experimental result with the most economical or highest achievable performance is obtained by considering all factors. The aim of using the optimization method is to maximize production efficiency (Yang & Press, 2010). In 1988, the cost calculation was realized by considering all the geometrical features of the road class and minimizing the amount of excavation (Easa, 1988). Later, a dynamic programming model was formulated to solve two-dimensional highway location problems as defined in 1988 (Goh, Chew & Fwa, 1988). Numerical studies have been carried out to find the optimum ground line and grade line by modeling a three-dimensional road route and subjecting it to a wide variety of possible constraints (Chew, Goh & Fwa, 1989). Fwa presents an optimization program developed in 1989 to produce an optimum vertical line profile for a preselected horizontal line (Fwa, 1989). To determine the cost of excavation in the highway application, studies have been carried out on the road class chosen by the designer. The designer has an almost infinite number of viable alternatives to choose from, all of which meet the geometrical properties of the road (Moreb, 1996).

With the aid of the artificial intelligence technique of genetic algorithms, it performs route optimization analyses by making complex mathematical solutions of slopes, fixed elevation points, and horizontal-vertical curves in highway design. Considering these three constraints, the relevant

¹ Department of Civil Engineering, Avrasya University, Trabzon, Turkey

² Department of Computer Engineering, İstanbul Topkapı University, İstanbul, Turkey

³ Department of Civil Engineering, Ondokuz Mayıs University, Samsun, Turkey

⁴ Department of Civil Engineering, Karadeniz Technical University, Trabzon, Turkey

construction costs were examined (Fwa, Chan & Fwa, 2002). There has been some work presented on being able to significantly reduce the cost of construction. In this study, in addition to minimizing excavation works, split-fill balancing was also taken into account (Goktepe & Lav, 2003).

Considering the cost, he presented a model of a route that integrates genetic algorithms with a geographic information system, examines the effects of various costs on route selection, and explores optimization in constrained areas that realistically reflects the limits of road improvement projects (Jha & Schonfeld, 2004). Since the elevation level on the axis line of the cross-section can be misleading, it is adjusted as close as possible to the ground level on a cross-section, using the weighted ground line method. In addition, due to the difference between the original volume in a cross-section and the post-compression volume in a fill, and accordingly, not all excavated material can be used as fill material, modified excavation and fill volumes are used in the calculation of weighted ground elevations (Goktepe & Lav, 2004).

By defining a methodology for the optimization of road grade lines, using the dynamic programming approach, an optimal grade line with minimum cost was found by considering various design constraints (Goktepe, Lav & Altun, 2005). The use of a genetic algorithm is recommended to increase the efficiency of the calculation and the quality of the solutions. It is observed that the load of the data to be calculated in the geographic information system (GIS) database will be an important problem during the optimization phase of the highway design. On the other hand, through GIS, it has worked on real-world maps (Kim, Jha & Son, 2005).

A three-dimensional optimization method has been developed to automatically determine whether bridges or tunnels are preferred to fill zones (Kim et al., 2007). Since the optimization of excavations related to highway optimization will play a very important role in the total cost of projects, an excavation optimization technique based on a ground line that balances the cut-fill volumes and minimizes the total amount of excavation by developing the weighted ground line method has been developed (Goktepe, Altun & Ahmedzade, 2009).

Designers of grade line prefer an intelligent optimization tool to offer genetic algorithms for highway optimization integrated with a geographic information system (GIS) (Kang, Jha & Schonfeld, 2012).

The development of algorithms for highway optimization is increasing rapidly. Since this topic is very complex and consists of many factors, engineers have to reach different and relevant targets. Minimizing the costs of construction and excavation, adapting to environmental restrictions, and increasing the safety and comfort of users should be considered very carefully at the same time. This complex calculation can be made simple by modern artificial intelligence techniques and can be simplified and extended. In this study, a search algorithm was proposed using the partial swarm optimization method (PSO) for road optimization (Bosurgi, Pellegrino & Sollazzo, 2013).

Some work has been performed on the determination of the grade line in excavation. In this study, the grade line design affects road costs, safety, and traffic performance. grade line optimization design meets the criteria as well as the total excavation quantity which allows minimizing. generally, determining the optimum grade line starts the process. In this context, the grade line segments are assumed to be equidistant. However, these equal distances will not result in low excavation. This statement is based on a numerical approach to equalizing debt. However, the proposed approach is only available on one part of the grade line (Al-Sobky, 2014).

A general formulation of tangential lengths and circular curves appropriately associated with transition curves is presented for optimization of the horizontal route (Casal, Santamarina & Vázquez-Méndez, 2017). GA and PSO methods related to the optimization of the grade line using meta-heuristic algorithms have been used as two smart optimization tools, to find an optimized

forest path by connecting the endpoints in the forest path Profile design and cost assessment (Babapour et al., 2018).

By formulating the optimization of the grade line, height and length are considered variables in the selection of a node. To solve this optimization problem was compared using genetic algorithm (GA) and particle swarm optimization (PSO) (Ghanizadeh & Heidarabadzadeh, 2018). In the first stage of the design of highway projects, several alternative horizontal routes are usually created, and the vertical route of that road is created for each alternative horizontal route selected. Since there can be an unlimited number of vertical routes in compliance with all design rules for a selected horizontal route, an optimization method was created by the designer to obtain the most economical design and focused on optimizing the vertical route (Ozkan, Tuydes-Yaman & Acar, 2021).

In finance and application engineering, optimization algorithms are used to solve complex problems. In other words, by solving these problems, it is possible to solve other real problems in a more stable and faster manner (Yelghi & Tavangary, 2022)

To obtain an optimum grade line design by considering earthworks on the profile, the upper heuristic methods PSO, FA, and ABC have been used and very satisfactory results have been obtained thanks to these methods (Asherlou et al., 2022). If a highway project is to be fully economical, the excavation operations of that project should be minimized and at the same time, the cut-fill volumes should be equalized. To summarize this situation, to make a highway project the most economical, studies should be done on the cut-fills of that project. In this context, optimization should be made on the Profile design to equalize and at the same time minimize excavation operations.

The data on the profile are ground line and grade line. However, it will not be possible to interfere with the ground line, which shows the natural state of the land. In this case, there is only one option left for us to intervene, and that is what we call the grade line or the project line. In this context, for a highway project to be economical, the grade line of that project must be optimized.

As can be seen from the literature, excavation cost is one of the most important problems when designing a highway project. In this context, it has become an undeniable fact that some optimization methods are used for grade line design to minimize the amount of excavation and to get the cut-fill amount equal. However, only some single-objective optimization algorithms from meta-heuristic algorithms have been used in the studies on grade line so far. The methods used in this context are generally only used for horizontal path optimization.

In this study, vertical curve optimization, which is one of the most important elements apart from the straight parts of the grade line, should also be done carefully. vertical curve optimization is an undeniable fact in optimum grade line design with minimum cost. Only in this way will it be possible to solve a grade line design with a multi-stage optimization technique. However, in the studies on the grade line until now, only single-purpose methods from the metaheuristic algorithms have been used. However, with multi-objective optimization methods, it will be possible to make more detailed analyzes and develop the grade line optimization algorithm, making calculations instantly.

In this study, vertical curve optimization is performed. In this context, grade line optimization can be done using a multi-objective meta-heuristic optimization algorithm. However, nowadays only single-objective methods are generally used in grade line optimization. Since the grade line design consists of extremely complex mathematical operations, it would be more logical to use multi-objective optimization algorithms than optimization methods.

Thus, by integrating the application prepared for the optimization of the grade line and multi-purpose optimization algorithms, a more detailed analysis will be made based on two factors or

two targets for less excavation amount and Cut-fill balancing. In this context, the results obtained are more stable and reliable due to the proposed algorithm. Of course, these processes with 2000 iterations and 30 times on the X-Y axis for the meta-heuristic optimization method and compared.

As it is known during the optimization of the grade line, the grade line does not consist of only the right parts. In other words, a vertical curve must be placed between these straight segments, that is, where the point of intersections are found. However, since thousands of vertical curves will be passed during optimization, the vertical curve with the most optimum Cut-fill should be selected. In this regard, vertical curves passed through the point of intersections of the grade line can be either a stream vertical curve or a peak vertical curve, depending on the situation. In the selection of the optimum vertical curve, where the vertical curve should be, only the vertical curve at the top, which is closest to the point of intersections, out of thousands of vertical curves passed by the application, and at the same time the vertical curve at the bottom, which is the closest to the point of intersections, where the stream vertical curve should be. should be selected. Thus, all vertical curves must be optimized throughout the project to optimize the entire project in the grade line design.

Material and Method

A highway project consists of design and implementation. The finer details of the implementation of highway projects, the more attention should be paid to the design phase. In other words, just as wrong practices create unacceptable results during implementation, in projects that are not designed following the required specifications during the project design phase, implementation costs will increase and cause it to be uneconomical. In this context, by choosing one of the multi-purpose optimization algorithms and adding some coding in addition to the existing application, we will develop this algorithm for more economical grade line design. Thus, the most optimum grade line will be designed by minimizing the amount of cut and fill.

Multi-Purpose Optimization Method MOPSO (Multiple Objective Particle Swarm Optimization)

We can solve single-objective optimization problems with the PSO method and multi-objective optimization problems with the MOPSO method by developing the PSO method. It is possible to convert to MOPSO by applying some modifications to the PSO algorithm. The most important reason for this change is that the problem is multi-purpose (Coello, Pulido & Lechuga, 2004). The basis of the Particle Swarm Optimization algorithm is swarming intelligence. Factors alone cannot be effective in herd intelligence. For this reason, they reach the result by taking part in the herd and cooperating. They can't reach the result they have achieved in the form of a flock alone. To find new answers in the search area, some rules must be defined. In this context, the most important concept is the concept of movement. The first movement is considered a kind of inertia. The second move counts as nostalgic and is useless on its own. The main core of the algorithm is considered the third stage. The difference between PSO and MOPSO is in the selection of the best particle, so multi-objective optimization is focused on the definition of the best option in the algorithm. According to multi-objective optimization algorithms, the first degree of quality and then the order of the option that is not defeated is important (De Oca al., 2009).

Profile Design

The most important stage of Profile design in highway projects is the part where grade line is determined. Profile design consists of ground line and grade line. In this context, we must minimize the amount of excavation to reduce the cost. In other words, optimizing each parameter of the grade line separately in Profile design, it will have a significant effect on reducing direct costs. Thus, it is an undeniable fact that the optimum design of Profile elements will directly affect the amount of excavation. In the profile design, first of all, ground elevations and cross-section

kilometers of the axis line will be determined. The distance will be displayed on the X-axis of the profile and high on the Y-axis. In this context, an example of black and grade line design is shown in figure 1. Today, grade line is passed by determining the point of intersections in the Profile design. However, the most important factor in grade line design is the peak points of the grade line. The amount of cut and fill between the ground line and the grade line should be the least and at the same time equal. The grade line design is shown on the example ground line, that is, in figure 1.

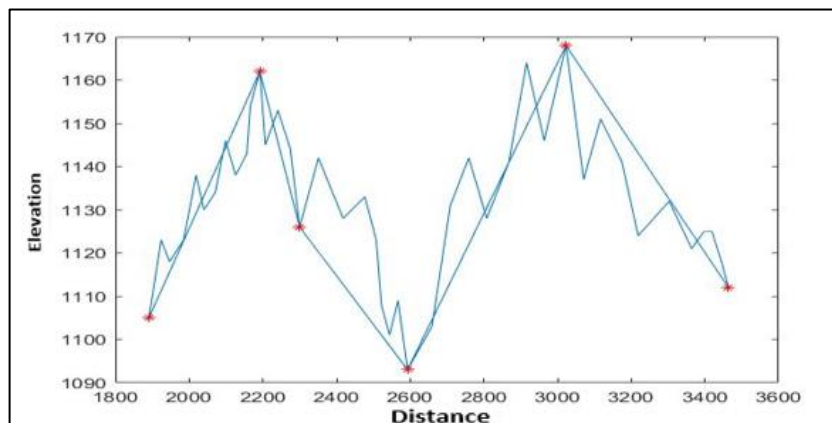


Figure 1. Profile design

Adding and Removing Points of Intersections

As shown above, it will not be entirely correct that only the intersection points along the way are selected automatically by the algorithm. In some projects, the mandatory intersection points must also be found within the scope of the project operation, as seen in figure 2, or on the contrary, there should not be any node points at certain distances for the project operation. In this context, to ensure that the application is not incomplete, at a certain stage of the design, the application designer will be asked whether there are fixed nodes, and the application will be interfered with by adding and subtracting unlimited nodes.

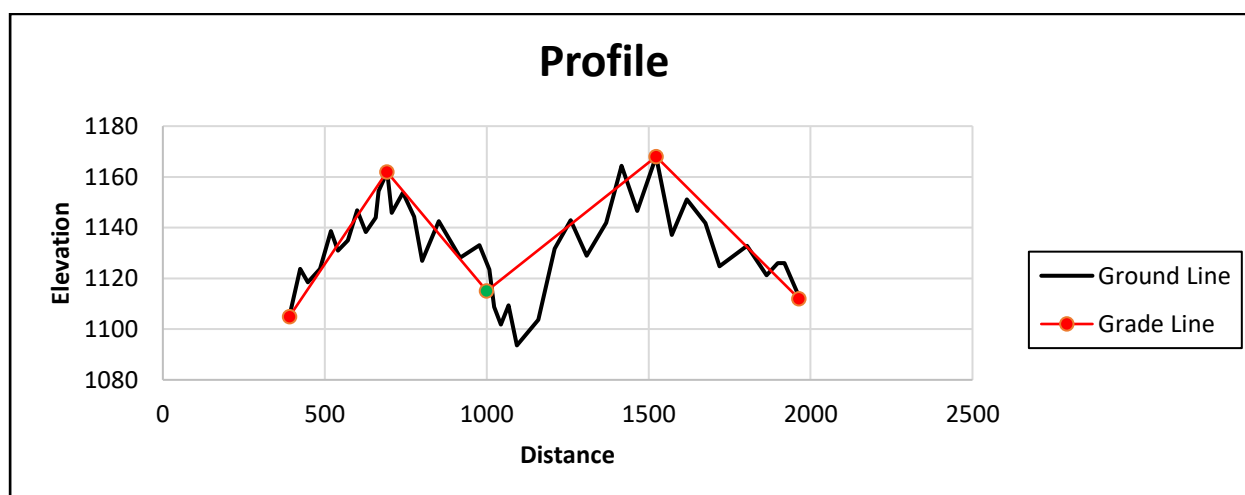


Figure 2. Addition and removal of the intersection points

Figure 3 shows only a part of this coding. With the aid of this coding, it is first asked by the application whether there is a mandatory node that should be added in addition to the automatic knuckles found about the grade line's nodes. If the answer to the question of the node to be added is yes, the application asks for the total number of nodes to be added within the scope of the

project. After entering the number of node points that need to be added to the total, the coordinates of those node points are requested. Of course, when the X axis is asked, the kilometer where the node is located in, and when the Y axis is asked, the height code of that node is requested. Thus, the coordinates of the point of intersection that we need to add extra will be given to the application, and now a mandatory point of intersection will be added in addition to the automatically found point of intersection.

```
prompt = 'Do you want to insert peak Y/N: ';
yesno = input(prompt, "s");
if yesno=='y'
number_range = input('Please input the insert number :', "s");
number_range=str2num(number_range);
user_range_insert=[];
for i=1:number_range
prompt = "please input x "+num2str(i)+" :";
number_range = input(prompt, "s");
number_rangex=str2num(number_range);
user_range_insert(i,1)=number_rangex;
prompt = "please input y "+num2str(i)+" :";
number_range = input(prompt, "s");
number_rangey=str2num(number_range);
user_range_insert(i,2)=number_rangey;
end
else
user_range_insert=[];
end
```

Figure 3. Application coding of mandatory point of intersections addition

As seen in Figure 4 by the application, the designer will be asked whether there are the point of intersections that need to be removed first. In this way, if there are intervals where the corner points should not exist due to the project, they will be entered by the designer. Of course, at this stage, the application will need the starting and ending kilometers of the intervals where there should not be a point, and if these intervals are entered, if there is a node, it will be removed.

```
prompt = 'Do you want to remove the range data for peak Y/N: ';
yesno = input(prompt, "s");
if yesno=='y'
number_range = input('please input the number of Range:', "s");
number_range=str2num(number_range);
user_range=[];
for i=1:number_range
prompt = "please input x start "+num2str(i)+" :";
number_range = input(prompt, "s");
number_rangex=str2num(number_range);
user_range(i,1)=number_rangex;
prompt = "please input x end "+num2str(i)+" :";
number_range = input(prompt, "s");
number_rangey=str2num(number_range);
user_range(i,2)=number_rangey;
end
else
user_range=[];
end
end
```

Figure 4. Application coding required for point of intersections removal

Grade Line Slopes

Slope limits are determined for each road class in the highway specification. In this study, the maximum and minimum slopes of the grade line up and down should be determined as shown in Figure 5. In other words, a road project should be designed according to the maximum and minimum slopes and the slope of the grade line should not exceed these limits throughout the project.

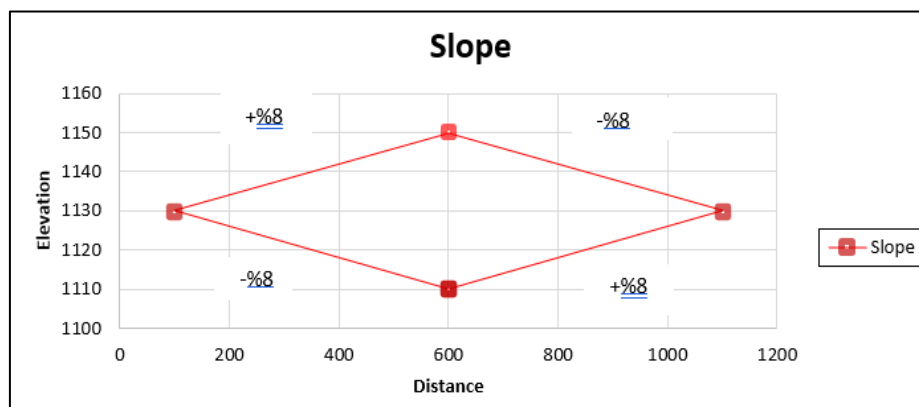


Figure 5. Maximum and minimum slope values

Maximum and minimum slopes will be asked from the designer by the designed application as shown in Figure 6. Within the scope of this study, 8% for the maximum slope of the project and 0.5% for the minimum slope will be accepted and the grade line design will be carried out between the determined slope limits. Accordingly, grade line parts outside the slope limits will be disabled and will not be included in the calculations.

```

slope_valuemax = input('please input the max slope:', "s");
% slope_valuemax=0.08;
slope_valuemax=str2num(slope_valuemax);

slope_valuemin = input('please input the min slope:', "s");
% slope_valuemin=0.005
slope_valuemin=str2num(slope_valuemin);
    
```

Figure 6. Application coding of maximum and minimum slopes

Cut-Fill Areas

Grade line generally consists of vertical Alignment and vertical curves. As explained above, if every element of the grade line is designed by optimizing, the amount of excavation can be minimized. In this context, the straight parts of the grade line will be passed according to the condition of the ground and the cut-fill amounts will be tried to be equal. In the red line design, first, the straight segments of the grade line will be passed in a way that equalizes the regions above and below the ground line. However, even if the correct parts to be passed at this stage are made with care, it is still almost impossible to equalize the cut fill amount exactly. Accordingly, the areas above (Cut) and below (Fill) the grade line will be calculated and equalized by the application. At the same time, we will minimize the amount of excavation by keeping the amount of these areas at

a minimum level. If the areas shown in Figure 7 are equal, it means that the most appropriate grade line design has been realized.

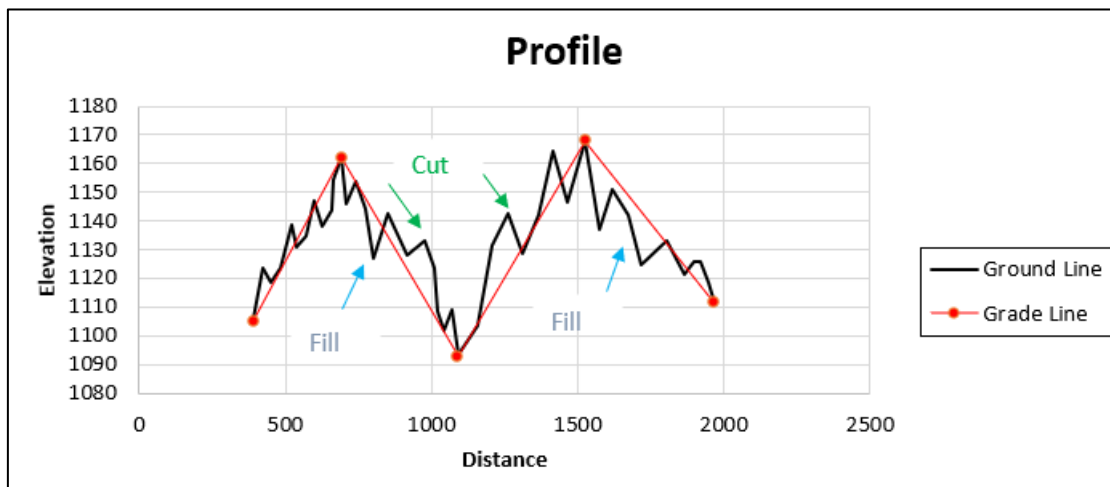


Figure 7. An example of the calculated area by using filling and cutting

Coordinate of Point of Intersections on the Ground Line

In the profile design, the places of the joint points are displaced thousands of times on both the X and Y axis, as seen in figure 8, thanks to the designed application. In this context, it becomes an undeniable fact that at every change of point of intersections, they will coincide with different places on the ground line. If we are to summarize this situation, there are different black jeans for each node. In this context, help will be taken from formula 1 in finding the black jeans for different points along the road.

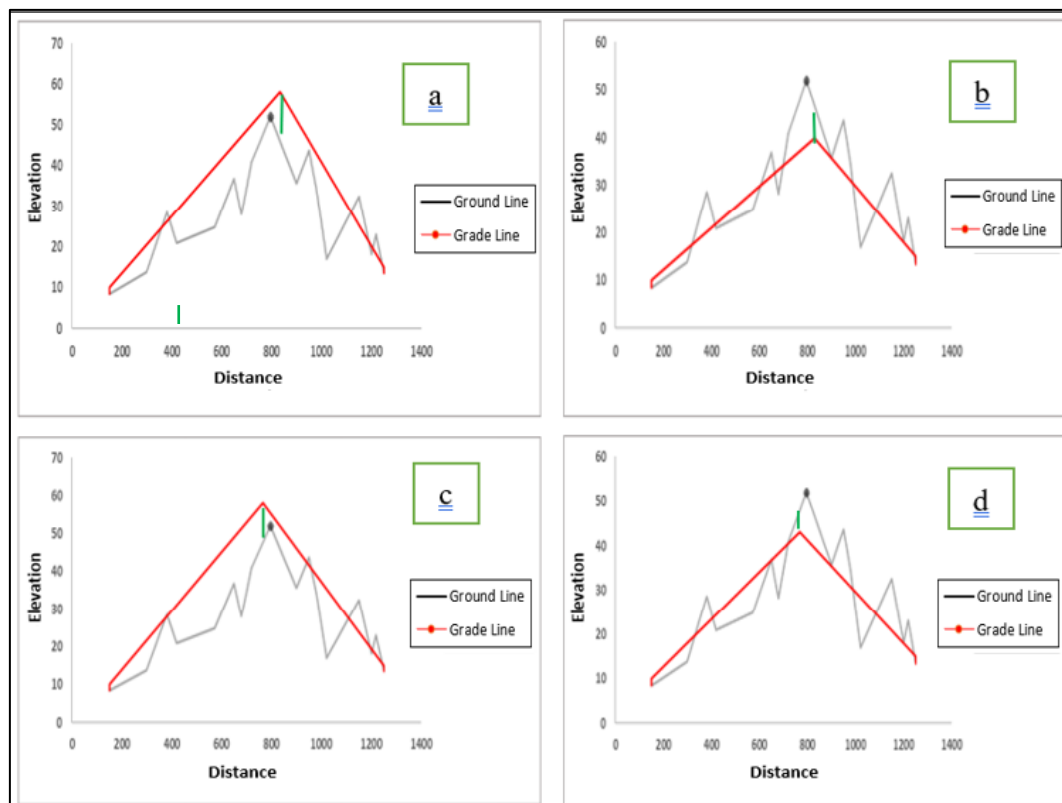


Figure 8. The situation of the point of intersection on the land

With aid of the formula 1 below, the coordinate of any node will be found on the ground line. Thus, the coordinate of the junction point on the land will be calculated as shown in Figure 9. Coordinates of points A (a, b) and B (c, d) are known from the beginning of the project as they are land elevations. Where the Point of the intersection will coincide on the ground line, that is, the X and Y coordinates are found from the formula below. Of course, at this stage, the X coordinate shows the kilometer on the Profile. In other words, the X coordinate is the same for the ground line and grade line for each node.

$$Y = \frac{X(d-b) - ad + cb}{c-a} \quad (1)$$

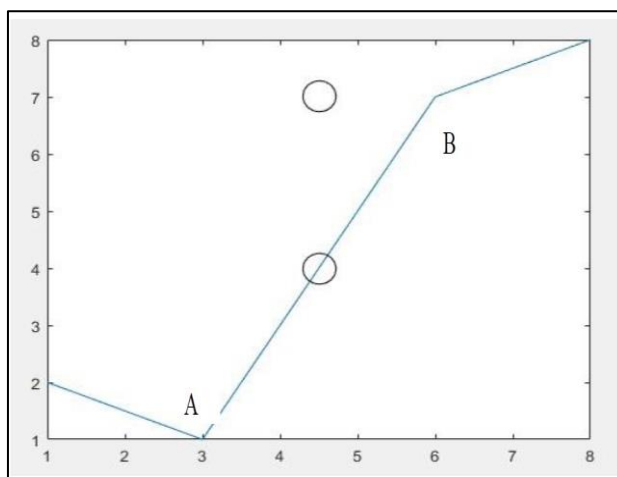


Figure 9. Ground line coordinates

Optimization of Point of Intersections of the Grade Line

Optimization over the areas described above examines the situation where the difference between the areas of the Cut-fills is zero, which is the most important point of the excavation, that is, using the excavated Cut amount in the fill areas and with almost zero excess material behind. Within the scope of this study, the intersection points of the designed grade line were examined on the X and Y axis of the coordinate system as seen in Figure 10.

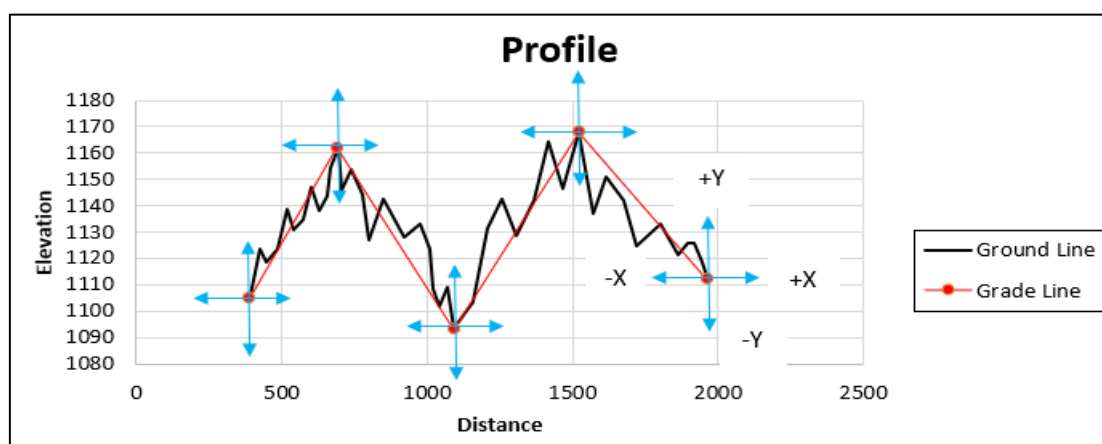


Figure 10. Controlling on the X and Y axis

For the optimization of points of intersections, examinations are made in the X and Y directions of the coordinate system by creating a matrix for each node. In other words, if we move the point of intersection up or down, maybe the Cut fill amounts will change and even cause us to

pass a more optimal grade line. In this context, since there are thousands of variables that can occur around it, points of intersections are accepted randomly by the algorithm. Of course, the higher the number of these random points, the more optimized our grade line will be designed. These areas that change in the X and Y directions will be calculated again because the Cut-fill areas change accordingly each time a change is made. Thus, it becomes an undeniable fact to use an optimization method to perform these complex calculations since there is a lot of mathematical operation involved in the realization of this method.

The application should define how much of an opening the matrix of a point of intersection will cover in the horizontal and vertical directions. In other words, a range of displacement must be specified at the point of intersections. In this coordinate system, the intervals on the X and Y axis for each node point in this coordinate system are shown with application coding in Figure 11. As seen in the application coding, the range of variability is entered separately at the start-end and mid-points. In this context, by adding a certain distance to the X and Y coordinates of each node automatically found by the application, an opening will be defined to the right, left, up, and down sides as much as that distance, and it will be possible to change the place of the node within these intervals.

```

VarMin(1)=y(1)-10;           % Lower Bound of Variables
VarMax(1)=y(1)+10;          % Upper Bound of Variables
VarMin(2)=y(cutterpeak_idx)-10; % Lower Bound of Variables
VarMax(2)=y(cutterpeak_idx)+10; % Upper Bound of Variables
VarMin(3)=y(end)-10;        % Lower Bound of Variables
VarMax(3)=y(end)+10;        % Upper Bound of Variables

VarMin(4)=x(1)-10;          % Lower Bound of Variables
VarMax(4)=x(1)+10;          % Upper Bound of Variables
VarMin(5)=x(cutterpeak_idx)-10; % Lower Bound of Variables
VarMax(5)=x(cutterpeak_idx)+10; % Upper Bound of Variables
VarMin(6)=x(end)-10;        % Lower Bound of Variables
VarMax(6)=x(end)+10;        % Upper Bound of Variables
    
```

Figure 11. Coding of the change interval for each point of intersection

Vertical Curve Optimization of Grade Line

In road projects, straight segments of the grade line are passed over the ground line and a vertical curve should be made at the intersections of these straight segments, that is, at the point of intersections. As seen in Figure 12, a vertical curve is placed at the intersection of the line segments that cut the ground line.

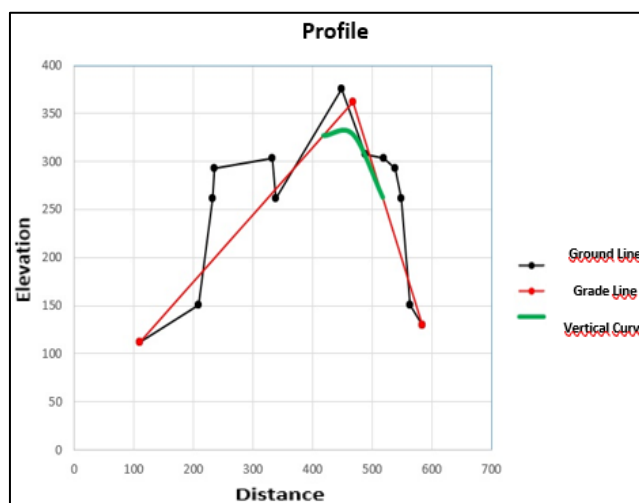


Figure 12. Placing the vertical curve at the point of intersection

The grade line visible above, as well as the vertical curve present at the nub, is more clearly shown in Figure 13.

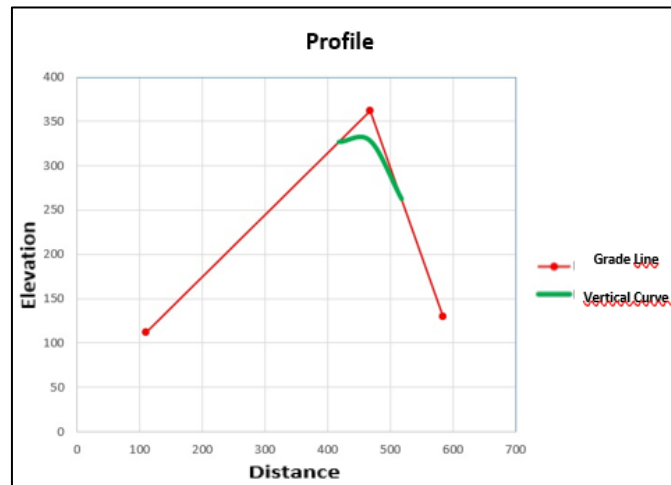


Figure 13. Vertical curve placement at the point of intersection

Vertical Curve Coding

In this context, hundreds of lines of coding must be written to integrate the same vertical victim with complex mathematical operations into the application. In Figure 14, some application related to this coding is shown in order. In this coding, which is made as an example, first, a coordinate is given to the grade line as a hypothetical. Then the slopes of this grade line will be calculated. After the slope calculation is made, the vertical curb length will be entered into the application by asking the designer. With these data, Vertical curve calculation operations will be performed very quickly by the application, even if it consists of complex operations.

```

xa=110,70
ya=111,80
xb=468,10
yb=361,40
xc=584,40
yc=130,20

x=[xa;xb;xc];
y=[ya;yb;yc];
plot(x,y)

g1=(yb-ya)/(xb-xa);
g2=(yc-yb)/(xc-xb);

G=abs(g1-g2);
prompt = 'What is the original value? ';
L = input(prompt);
T=L/2
E=(L*G)/8
KMT1=xb-T
KMT2=xb+T
KOTT1=yb-(g1*T)
KOTT2=yb+(g2*T)
KOTS=yb-E
xy=[KMT1 KOTT1;xb KOTS;KMT2 KOTT2];

hold on
fplot(cscvn(xy),'r',2)
hold off
    
```

Figure 14. Vertical curve application coding

Findings and Discussion

Vertical Curve Optimization Using Meta-Heuristics Algorithms

In road projects, straight segments of the grade line are passed over the ground line and a vertical curve should be made at the intersections of these straight segments, that is, at the point of intersections. As seen in Figure 15, a vertical curve is drawn at the point where the line segments intersecting the ground line intersect.

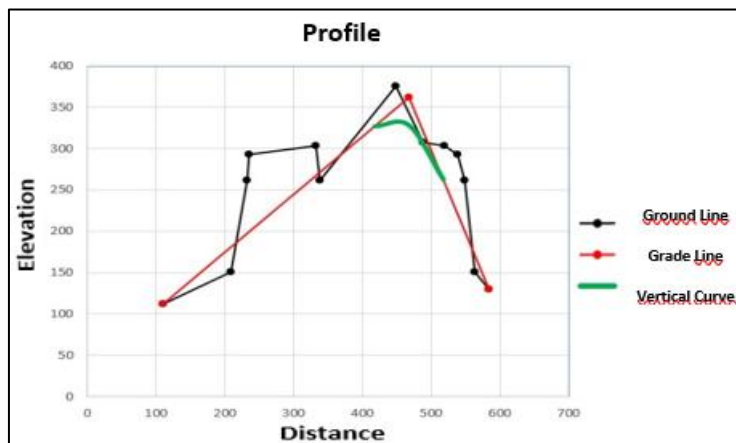


Figure 15. Placing the vertical curve at the point of intersection

Vertical Curve Implementation with Meta-Heuristics Algorithms

The grade line visible above and also the vertical curve present at the apex are shown in Figure 16 alone. In this context, lines of coding are required to integrate the vertical victim into meta-heuristic optimization algorithms.

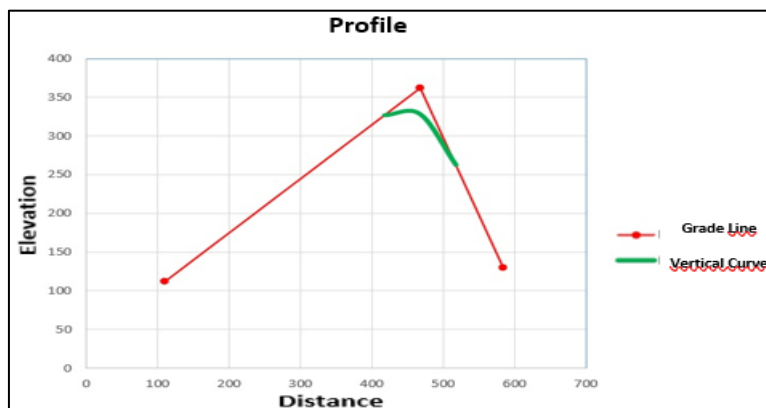


Figure 16. Vertical curve placement at the point of intersection

Vertical Curve Optimization

If vertical curve coding is integrated into the straight parts of the above-mentioned grade line, a vertical curve is passed to the grade line, which is shown in Figure 17 and exactly in Figure 18. With the aid of the application, it was possible to place a vertical curve between the straight parts of the grade line.

One vertical curve is made by the application for the grade lines drawn during the design with any optimization method, and thanks to this application, a vertical curve is passed separately for each node, despite the thousands of displacements of the node in the X and Y directions. In Figure 19, it is observed that the displacement of the junction point and the vertical curves change accordingly.

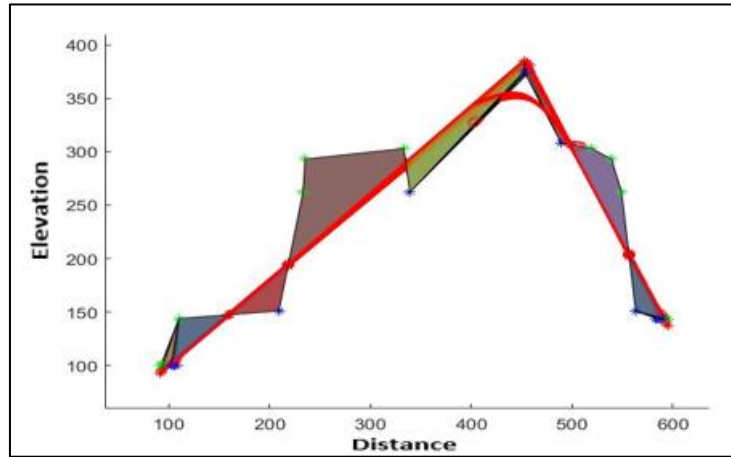


Figure 17. Vertical curves applied to grade lines

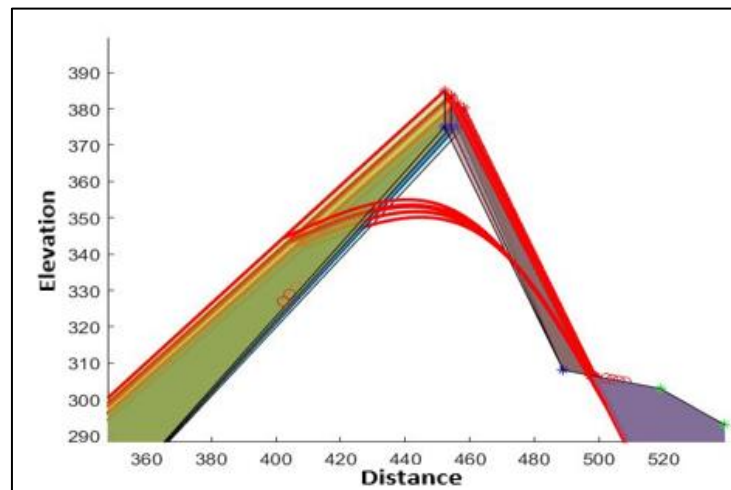


Figure 18. A separate vertical curve application for each point of intersection

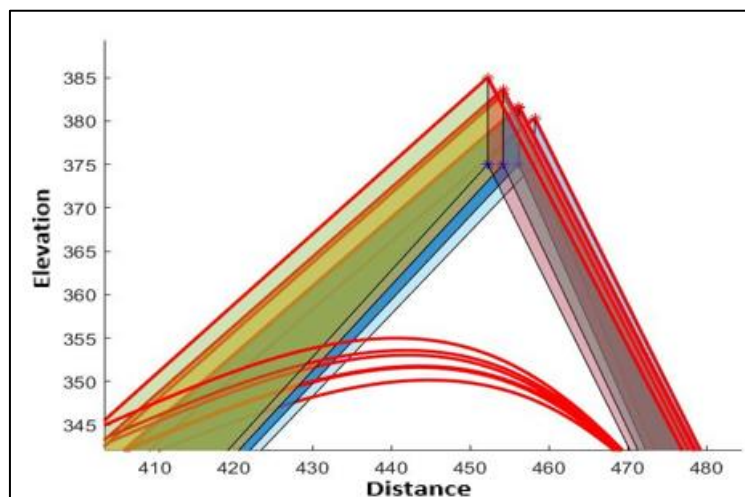


Figure 19. Displacement of the axes on the X and Y axis and the vertical curve

Elevations on the Ground Line of the Vertical Curve

In highway design, while optimizing the grade line, the vertical victim should create closed zones with the ground line. Of course, for the formation of these closed areas, this situation should be ensured by lowering the verticals from the curve start and end points to the ground line. The

height elevations of the points where these vertical lines and the ground line intersect will be found by the coding shown in Figure 20. Also, the locations of these intersection points are shown in Figure 21.

```
[KMT1,KOTT1,xs,KOTS,KMT2,KOTT2]=curve3point(xyvector(4),xyvector(1),xyvector(5),xyvector(2),xyvector(6),xyvector(3))

[pointyhat1,pointx1]=ziyaafn(y,x,[KOTT1 KMT1])
[pointyhat2,pointx2]=ziyaafn(y,x,[KOTT2 KMT2])
plot(pointx1,pointyhat1,'or')
plot(pointx2,pointyhat2,'or')

lx=x((pointx1<x) & (x<pointx2))
ly=y((pointx1<x) & (x<pointx2))

point_curv_x=[pointx1,pointx2]
point_curv_y=[pointyhat1,pointyhat2]

plot(point_curv_x,point_curv_y,'or')
```

Figure 20. Application coding of vertical curve and ground line relationship

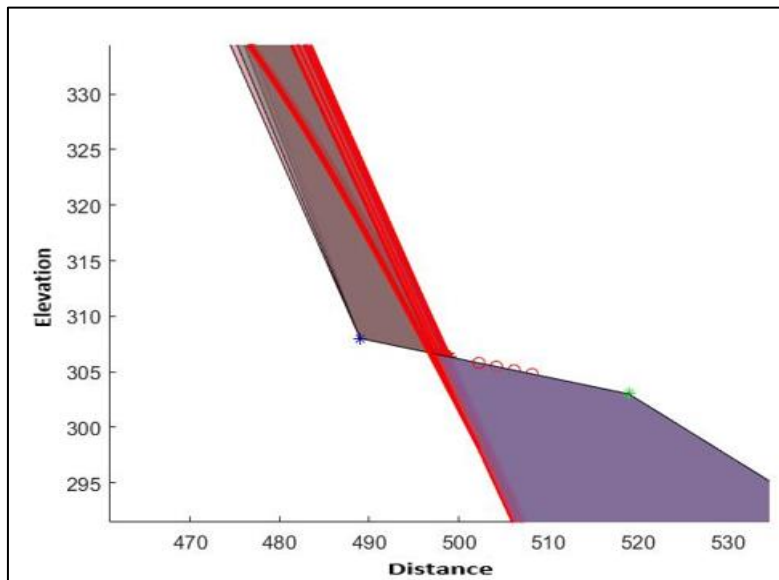


Figure 21. Height of vertical curve above ground line

Selecting the Optimum Vertical Sacrifice

As it is known during the optimization of the grade line, the grade line does not consist of just the right parts. In other words, a vertical curve must be placed between these straight segments, that is, where the point of intersections are found. However, since thousands of vertical curves will be passed during optimization, the vertical curve with the most optimum Cut fill should be selected. In this context, vertical curves passed through the point of intersections of the grade line can be either a stream vertical curve or a peak vertical curve, depending on the situation. In the selection of the optimum vertical curve, where the vertical curve should be, only the vertical curve at the top, which is closest to the point of intersection, out of thousands of vertical curves passed by the application, and at the same time, the vertical curve at the bottom, which is the closest to the point of intersection, where the stream should be vertical curve. should be selected. Thus, all vertical curves must be optimized throughout the project to optimize the entire project in the grade line design. An optimum peak vertical curve is shown in Figure 22 as an example.

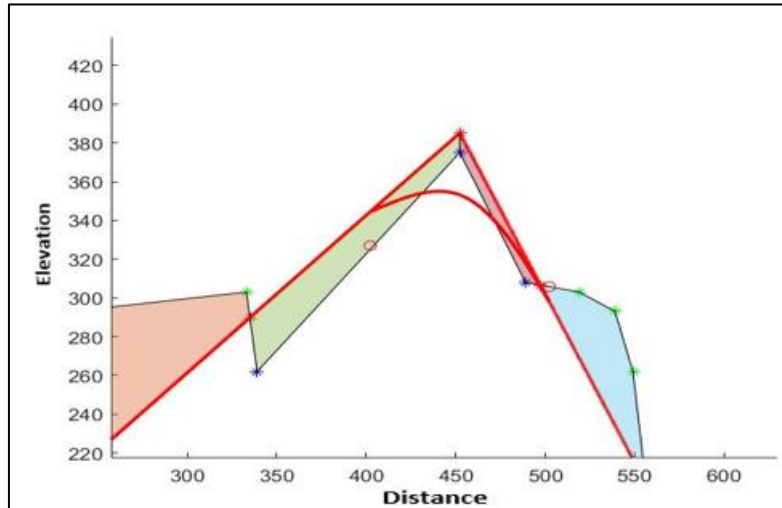


Figure 22. An example of an optimum peak vertical curve

Conclusion

In the implementation, a coordinate was given to the grade line as a hypothetical. Then, the optimization of the correct parts of this grade line has been performed. However, vertical curves must be added between these straight segments. In this context, the vertical curve length must be entered into the application. With these data, vertical curve calculation operations were performed very quickly by the application, even if it consisted of complex operations. Thus, in vertical curves, the vertical curve closest to the curve should be selected, and at the same time, the vertical curve, which is closest to the curve, is selected by the application as the most optimal vertical curve in places where there is a creek vertical curve.

References

- Al-Sobky, A. S. (2014). An optimization approach for highway vertical alignment using the earthwork balance condition. *World Applied Sciences Journal*, 29(7), 884-891.
- Asherlou, S., Yelghi, A., Pancar, E. B., & Oruç, Ş. (2022). An optimization approach for highway alignment using metaheuristic algorithms. *Meta-heuristic Optimization Techniques: Applications in Engineering*, 10, 11.
- Babapour, R., Naghdi, R., Ghajar, I., & Mortazavi, Z. (2018). Forest road profile optimization using meta-heuristic techniques. *Applied Soft Computing*, 64, 126-137.
- Bosurgi, G., Pellegrino, O., & Sollazzo, G. (2013). A *PSO* highway alignment optimization algorithm considering environmental constraints. *Advances in Transportation Studies*, (31).
- Casal, G., Santamarina, D., & Vázquez-Méndez, M. E. (2017). Optimization of horizontal alignment geometry in road design and reconstruction. *Transportation Research Part C: Emerging Technologies*, 74, 261-274.
- Chew, E. P., Goh, C. J., & Fwa, T. F. (1989). Simultaneous optimization of horizontal and vertical alignments for highways. *Transportation Research Part B: Methodological*, 23(5), 315-329.
- Coello, C. A. C., Pulido, G. T., & Lechuga, M. S. (2004). Handling multiple objectives with particle swarm optimization. *IEEE Transactions on evolutionary computation*, 8(3), 256-279.
- De Oca, M. A. M., Stutzle, T., Birattari, M., & Dorigo, M. (2009). Frankenstein's PSO: a composite particle swarm optimization algorithm. *IEEE Transactions on Evolutionary Computation*, 13(5), 1120-1132.
- Easa, S. M. (1988). Selection of roadway grades that minimize earthwork cost using linear programming. *Transportation Research Part A: General*, 22(2), 121-136.
- Fwa, T. F. (1989). Highway vertical alignment analysis by dynamic programming. *Transportation Research Record*, 1239(1-9), 2-3.
- Fwa, T. F., Chan, W. T., & Fwa, Y. P. (2002). Optimal vertical alignment analysis for highway design. *Journal of transportation engineering*, 128(5), 395-402.
- Ghanizadeh, A. R., & Heidarabadizadeh, N. (2018). Optimization of vertical alignment of highways in terms of earthwork cost using colliding bodies optimization algorithm. *دانشگاه علم و صنعت ایران*, 8(4), 657-674.
- Goh, C. J., Chew, E. P., & Fwa, T. F. (1988). Discrete and continuous models for computation of optimal vertical highway alignment. *Transportation Research Part B: Methodological*, 22(6), 399-409.
- Goktepe, A. B., & Lav, A. H. (2003). Method for balancing cut-fill and minimizing the amount of earthwork in the geometric design of highways. *Journal of transportation engineering*, 129(5), 564-571.
- Goktepe, A. B., & Lav, A. H. (2004). Method for optimizing earthwork considering soil properties in the geometric design of highways. *Journal of surveying engineering*, 130(4), 183-190.

- Göktepe, A. B., Altun, S., & Ahmedzade, P. (2009). Optimization of vertical alignment of highways utilizing discrete dynamic programming and weighted ground line. *Turkish Journal of Engineering and Environmental Sciences*, 33(2), 105-116.
- Goktepe, A. B., Lav, A. H., & Altun, S. (2005). Dynamic optimization algorithm for vertical alignment of highways. *Mathematical and Computational Applications*, 10(3), 341-350.
- Jha, M. K., & Schonfeld, P. (2004). A highway alignment optimization model using geographic information systems. *Transportation Research Part A: Policy and Practice*, 38(6), 455-481.
- Kang, M. W., Jha, M. K., & Schonfeld, P. (2012). Applicability of highway alignment optimization models. *Transportation Research Part C: Emerging Technologies*, 21(1), 257-286.
- Kim, E., Jha, M. K., & Son, B. (2005). Improving the computational efficiency of highway alignment optimization models through a stepwise genetic algorithms approach. *Transportation Research Part B: Methodological*, 39(4), 339-360.
- Kim, E., Jha, M. K., Schonfeld, P., & Kim, H. S. (2007). Highway alignment optimization incorporating bridges and tunnels. *Journal of Transportation Engineering*, 133(2), 71-81.
- Moreb, A. A. (1996). Linear programming model for finding optimal roadway grades that minimize earthwork cost. *European Journal of Operational Research*, 93(1), 148-154.
- Ozkan, E., Tuydes-Yaman, H., & Acar, S. O. (2021, February). Vertical alignment optimisation in highway design by means of mesh adaptive direct search. In *Proceedings of the Institution of Civil Engineers-Transport* (pp. 1-12). Thomas Telford Ltd.
- Sütaş, İ., & Öztaş, G. (1983). *Karayolu inşaatında uygulama ve projelendirme*. Teknik Kitaplar Yayınevi.
- Yang, X. S., & Press, L. (2010). *Nature-inspired metaheuristic algorithms second edition*.
- Yelghi, A., & Tavangari, S. (2022). Features of metaheuristic algorithm for integration with ANFIS model (No. 7594). EasyChair.

Liquid Chromatography Methods for the Determination of Beta-Carotene in Vegetable and Fruit Samples- an Evaluation of the Last Decade

F. A. Özdemir Olgun¹

Introduction

Carotenoids are compounds that cannot be synthesized by human-beings and animals, but are synthesized only by plants and microorganisms. An important carotenoid, β -carotene is a natural pigment found in many fruits and vegetables and also widely used in the food industry. By definition, natural pigments are pigments derived from living organisms or cells. Color can be obtained in nature from fruits, roots, seeds of plants, insects and other biological species. Beta-carotenes are high in colorful fruits and vegetables such as broccoli, brussels sprouts, bell peppers, tomatoes, spinach, carrots, sweet potatoes, zucchini, paprika, apricots, pink grapefruit, cherries, mangoes, papayas and peaches. They are also used as a coloring agent for foodstuffs such as margarine, butter and many soft drinks, as they also have natural pigment properties.

Besides being a natural colorant, β -carotene is an important antioxidant compound that acts as a precursor to vitamin A. For this reason, it has an important role in the human body as an antioxidant that can reduce the risk of cardiovascular diseases and certain types of cancer. People, low in vitamin A show histopathological changes in the pulmonary epithelium and lung parenchyma, resulting in an increased risk of lung dysfunction and respiratory disease. Various studies have reported that fruits and vegetables containing micronutrients can increase immune function. These micronutrients, such as vitamin E, vitamin C, and β -carotene (vitamin A), are antioxidants. In the COVID-19 disease, which affects the world, it has been determined that apart from the social measures taken, the nutritional habits of the people also play an important role in the course of the disease (Topuz, 2020).

Considering all the above-mentioned properties of β -carotene, it is important to determine the rates of presence in vegetables and fruits, both in terms of dietary intake of this antioxidant type, which cannot be synthesized by our body, and its use as a colorant in the food industry. Within the scope of this chapter, the chromatographic methods used for the determination of β -carotene in fruit and vegetable samples were examined and evaluated in line with the studies in the literature. I hope that this study will shed light and provide insight for future studies for researcher readers working with β -carotene.

Carotenoids

Carotenoids constitute one of the most important pigment groups found in nature with their wide distribution, structural differences, wide range of effects and functions, which function as an auxiliary pigment in photosynthesis in plants and photosynthetic bacteria, giving colors ranging from yellow to red (Olson, 2006). They also protect against photosensitization (light sensitivity) in animals, plants and bacteria. Animals store carotenoids in their tissues by modifying them because they cannot synthesize them (Rodriquez et. al., 2001). Carotenoids act only as Vitamin A

(Provitamin A) in the human body. At the same time, they can have different effects such as antioxidant activity, strengthening of the immune system, inhibition of cell mutation and transformation, non-photochemical fluorescence quenching (Olson, 1999). In adults, dietary carotene intake and blood carotene concentration provide positive health outcomes such as reduced cancer risk, prevention of cardiovascular disease, elimination of age-related stains, and improved conceptual understanding (Von Elbe et. al., 1996).

There are 600 different types of carotenoids derived from natural sources (Olson, 2006). These molecules are found in all green leafy vegetables as well as in red, yellow and orange colored fruits and vegetables. However, the chlorophyll molecule found in green leafy vegetables masked the yellow to red color of the carotenoids (Von Elbe, 1996).

Carotenoids are the molecules that belong to the isoprenoid group and have a skeletal structure of 40 carbons, which are formed as a result of covalent bonding of eight isoprene units (Figure 1) (Morrison, 1954).

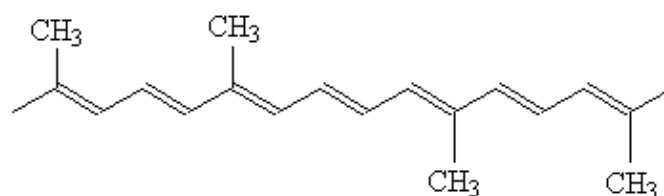


Figure 1. Polyisoprenoid structure of carotenoids

According to their chemical composition, carotenoids are divided into two main classes: "carotenes" consisting of only hydrocarbon chains and "xanthophylls", which are defined as carotenoids containing oxygen. The main ones of the carotene group consisting of hydrocarbon chains with nonpolar properties are; α -carotene, β -carotene and lycopene. Xanthophylls, on the other hand, are more polar and contain oxygen in the form of methoxy, hydroxy, keto, carboxy and epoxy 4. Examples of xanthophylls are β -cryptoxanthin, zeaxanthin, and lutein. Figure 2 shows the structure of carotenoids commonly found in foods.

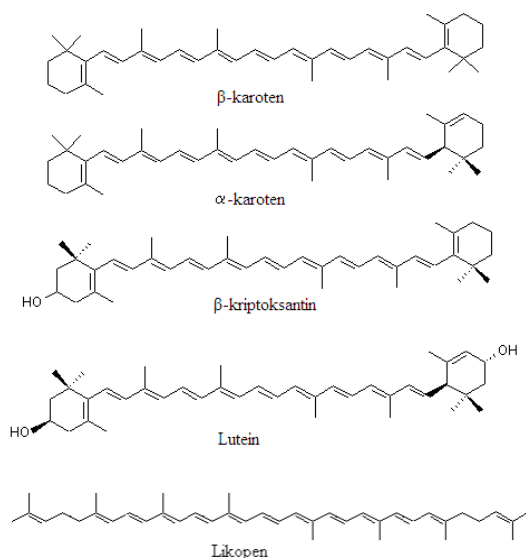


Figure 2. Some carotenoids found in foods

Different pigments are formed as a result of the cyclization of the hydrocarbon skeleton in the isoprene structure or the oxidation of the end points. Thanks to the conjugated double bond in the structure of almost all carotenoids, they absorb light in the visible region of the spectrum, and it is easy to determine their biological functions such as energy transfer and protection of cells from the harmful effects of light (Deming et. al., 1999; Krinsky, 1990). This means that they show maximum absorption at wavelengths of about 430–480 nm (Von Elbe et. al., 1996). They may be found in free form (crystalline or amorphous) or dissolved in oil in plant tissues (Von Elbe et. al., 1996) and have a boiling point varying between 130-220 °C (Britton et. al., 1995)

Of the approximately 600 different carotenoid molecules identified in nature, only 50 of those containing β -rings show provitamin A activity. All-trans- β -carotene, which has two β -rings in its structure, has the highest provitamin A activity since it is degraded to 2 molecules of retinal in the intestine. In contrast, 13-cis- β -carotene (53%) and 9-cis- β -carotene (38%) have lower provitamin A activity. Apart from provitamin A activity, isomerization also affects the antioxidant activity of carotenoids (Schieber et. al., 2005)

Tablo 1. Vitamin A Activity of β -carotene Isomers

Isomer	Activity of Vitamin A (%)
All-trans- β -carotene	100
9-cis- β -carotene	38
13-cis- β -carotene	53

The historical development of β -carotene began with its isolation from carrots by Wachenroder in 1820. After Willstaetin's molecular formula of β -carotene was determined in 1906, its chemical formula was elucidated between 1939 and 1941. After it was synthesized in the laboratory in 1953, it was produced synthetically. Since 2010, it has started to be used as a functional food additive with its antioxidant properties that support the immune system, its anticarcinogenic function against some cancers and its efficiency-enhancing effects in animals, and it still maintains its importance by today's researchers.

Beta-carotene is the precursor of vitamin A and is the most important of the provitamin A molecules. As a result of its degradation, two molecules of retinol are formed, which are then metabolized to retinol and retinoic acid. It has a skeleton containing C40 atoms in its β -carotene structure, this skeleton structure contains carbon and hydrogen atoms but no oxygen atoms. β -carotene, with the general formula $C_{40}H_{56}$ (Figure 3), consists of two beta-ionone rings at both ends of an aliphatic isoprenoid chain symmetrically linked to methyl groups (Olson, 2006).

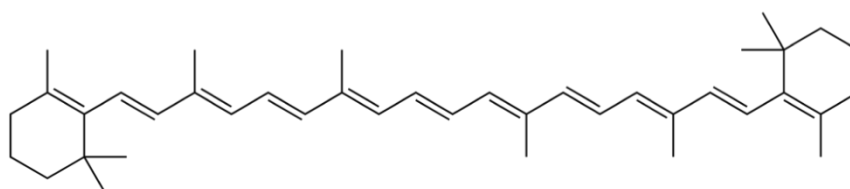
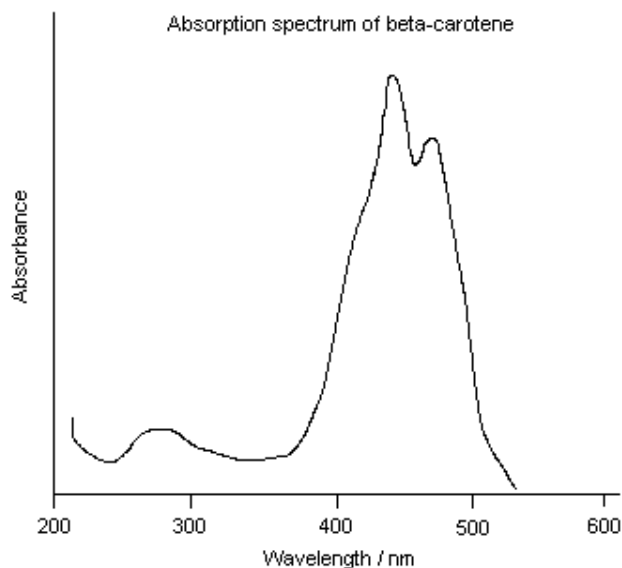


Figure 3. Chemical Structure of β -carotene

The double bond system ensures that the colors of the carotenoids are formed and the light absorbed during photosynthesis is transferred to the chlorophyll. Thanks to this feature, beta carotene reflects a bright orange-red color. In the figure below, the UV-visible molecular absorption spectrum of the β -carotene molecule is displayed, and it is obvious to see a shouldered peak between 400-500 nm. The reason for this is that the green-blue color in this region is absorbed by the molecule and reflects the red-orange color.



Graphic 1. UV-Visible Spectrum of beta-carotene

It also contributes to photosynthesis by transferring energy and protecting cells from the harmful effects of light (Deming et. al.,1999) Factors such as oxygen, temperature, light, pH, sulfites, water activity are effective in the oxidative breakdown of carotenoids.

With all these efficient properties, β -Carotene takes place in the food industry as a precursor to vitamin A, a natural colorant and a strong antioxidant (Shishi et. al., 2016).

Beta-Carotene

Beta carotenes are the most widely consumed plant-derived pigments. They are usually found on plants with bright orange and green colours. These include carrots, sweet potatoes, pumpkin, broccoli, even red palm oil and vitamin supplements. The amount of vitamin A obtained from beta carotenes is directly related to the source from which they are obtained. β -carotenes from citrus and vegetables are more absorbed and more biocompatible than leafy greens.

α -and β -carotenes constitute approximately 90% of the total carotenoid content present in plants. Although the amount in plants varies according to the plant species, its leaves contain 5-10 times more carotenoids than their stems (Giuffrida et. al., 2012).

As a plant source of β -carotene, there are fruits such as apricots, melons, peaches, dates, vegetables such as carrots, pumpkins, spinach, peppers, and green plants that grow naturally in meadows and pastures.

Crustaceans such as shrimp, crabs, lobsters, and fish such as salmon are sources of animal sourced carotenoids (Shahidi et. al., 1998). It is also commonly found in milk and dairy products, meat, eggs, and liver (Simpson et. al., 1985).

Functions of Beta-Carotene

Effect of Provitamin

Among the 600 carotenoids identified in nature, there are approximately 50 carotenoids that show provitamin A activity, that is, contain a β -ring. Some known carotenoids with provitamin A activity; Alpha Carotene, Beta Carotene, Betaoxide Carotene, Semi beta Carotene, Gamma Carotene..)

Since there is a β -ion ring on each side of the β -carotene molecule, theoretically, one molecule of β -carotene has the potential to break through the middle to form two molecules of vitamin A. Two molecules of vitamin A are formed when one molecule of β -carotene is broken down in the organism by means of a special enzyme (β -carotene 15.15' dioxygenase) and other hydrolases, especially found in the intestine and liver. Therefore, the synthesis of vitamin A generally takes place in the small intestine mucosa and liver (Morrison et. al., 1954).

Antioxidant Effect

The antioxidant effect is generated by protecting cells and organisms against oxidation. In this process, as a result of the reaction with free radicals, singlet oxygen ($1O^{2*}$) decomposes as a result of direct interaction with peroxide radicals. Thus, superoxide and peroxide radicals are scavenged (Jinshi et. al., 2016).

While β -carotene shows singlet oxygen scavenging properties, it also binds free radicals. Although the chemical structure is effective in this feature of carotenoids, the most important thing is the increase in the number of conjugated double bonds.

Health Effects of Beta-Carotene

Many epidemiological studies have reported that consumption of carotenoid-rich fruits and vegetables reduces the risk of cancer (Ziegler et. al., 1989; Mc Keith et. al. 2005), cardiovascular diseases and eye diseases. (Dietmar et. al., 2001; Kalt et. al., 1999; Sulaeman et. al., 2001). It was determined that the risk of lung and stomach cancers decreased especially with β -carotene intake. In addition, it is reported that β -carotene increases lymphocyte proliferation, prevents macrophage receptor loss caused by free oxygen radicals (SOR), increases the ability of natural killer cells to kill tumor cells, and prevents the transformation of cancer cells. Since the last month of 2019, the world has faced a major public health crisis with the Covid-19 epidemic caused by the SARS-CoV-2 virus. More than 77 million cases of COVID-19 have been seen worldwide, and more than one million cases have resulted in death. Apart from social precautions, people's eating habits also play an important role in the course of the disease.

The general health status and immune system of the patients are adversely affected. This diet causes metabolic diseases such as obesity and hypertension, which are risk factors for Covid-19 infection.

With the Corona virus, quarantine has become widespread to reduce the spread of the virus all over the world. During quarantine, increased macronutrient intake may be accompanied by micronutrient deficiencies, as in obesity, which is commonly associated with impaired immune systems. Therefore, during this period, it is important to pay attention to eating habits by following a healthy and balanced diet with high amounts of minerals, antioxidants and vitamins.

Various studies have reported that fruits and vegetables containing micronutrients can increase immune function. These micronutrients, such as vitamin E, vitamin C, and B-carotene (vitamin A), are antioxidants. Beta Carotene is most commonly found in sweet potatoes, carrots and green leafy vegetables. Vitamin A deficiency has been associated with an increased risk of infection. People low in vitamin A, show histopathological changes in the pulmonary epithelium and lung parenchyma, resulting in an increased risk of lung dysfunction and respiratory disease. This is especially important considering the negative effects of COVID19 on lung function (Topuz, 2020).

Beta-Carotene in Food Processing

Uses of β -carotene in the food industry may be listed as confectionery products, beverage products, bakery products, processed cheese, butter and clarified butter obtained from cow's milk, dried fruits and vegetables, fruits and vegetables in vinegar-oil-brine, fruit and vegetable preparations and breakfast cereals. According to the Turkish Food Codex Communiqué on Colorants Used in Food, the codes in which carotenoids are used as food dyes; E160, E160b, E160c, E160d, E160e and E160f.

High Performance Liquid Chromatography (HPLC) Methods of Last Decade To Determine Beta-Carotene in Fruit and Vegetable Samples

The principle behind HPLC and the chromatographic methods, in general, is the separation between different components in a sample. This separation is performed according to a series of equilibrium stages where the injected sample components interact by partitioning or adsorption between stationary and mobile phase during movement through the system. Depending on the chemical and physical properties, the components in the sample exhibit different affinities for the mobile and stationary phase and migrate along the column at different rates.

Carotene determination studies are carried out using a High Performance Liquid Chromatography (HPLC) device. The HPLC method, which is very sensitive, gives extremely sensitive results in the separation of non-volatile or easily degradable compounds at a fixed temperature.

Many studies have been conducted to identify β -carotene contents in foods by HPLC. During the analysis of β -carotene, many different techniques with different mobile phases and column properties were used according to the compatibility of the medium. The successful findings of the last decade was tabulated in Table 2 as a summary.

Table 2. HPLC Parameters for the Determination of β -carotene in Vegetable and Fruit Samples

Sample	Column Properties	Mobile Phase	Detection	Beta Carotene Concentration	Reference
Banana (Thailand)	C18 column (250 × 4.6mm, 5 μ m)	Using isocratic run of 10% Ethylacetate :Methanol (1:1, v/v) in Acetonitrile Flow rate : 1 mLmin ⁻¹	UV-Vis Dedector 450 nm	645.9- 5222.6 μ g 100g ⁻¹	(Tongspoodsomjit et. al., 2020)
Corn	C18 column for UPLC	methanol/acetonitrile (9 : 1 v/v),flow rate of 0.5 mLmin ⁻¹	UV-Vis Dedector 448nm	0.08-2.14 mgkg ⁻¹	(Satarova et. al., 2019)
Animal Feed	Venusil C8 column (250 mm × 4.6 mm, 5 μ m)	The mobile phase consisted of 0.1% ammonium acetate, acetonitrile, methanol and water.	UV-Vis Dedector (450 nm)	0.12–0.2 mg kg ⁻¹	(Chen et. al., 2019)
Carrot	C18 column (250.0 × 4.6 mm, 5 μ m)	The mobile phase was composed of 980mL of methanol and 20mL of trichloromethane Flow rate: 0.9 mL min ⁻¹	UV-Vis Dedector (454 nm)	41.06 μ g g ⁻¹	(Dai and Row, 2019)
Fruit Juice	SB- C18 column (250 mm × 4.6 mm, 5 μ m)	The mobile phase was composed of 60% acetonitrile and 40% tetrahydrofuran. Flow rate : 1.0 mL min ⁻¹	UV-Vis Dedector (445 nm)	1-5 μ g mL ⁻¹	(Li et. al., 2019)

Özdemir Olgun, F., A.; Liquid Chromatography Methods for the Determination of Beta-Carotene in Vegetable and Fruit Samples- an Evaluation of the Last Decade

Fruit Juice	C18 column (4.6 × 250 mm, 5 µm)	Mobile phase isocratic elution using dichloromethane –methanol– acetonitrile at (45 :45 : 10) Flow rate : 1mL min ⁻¹	UV-Vis Dedector (450 nm)	0.3-46 mg L ⁻¹	(Simpson et. al., 1985)
Water-melon	C18 column (4.6 × 250 mm, 5 µM)	Mobile phase consisted of acetonitrile l (solvent A)/dichlorometh ane (solvent B) and methanol (solvent C) at a Flow rate of 1 mL min ⁻¹	UV-Vis Dedector (450 nm)	121.6- 454.4 µg g ⁻¹	(Whong et. al., 2017)
Outer Skin of Strawberry	C18 column (200 mm ×4.6 mm, 3 lm)	binary-gradient elution using an initial composition of 75% acetone and 25% deionised water Flow rate : 1 mL min ⁻¹	UV-Vis Dedector (450 nm)	10.5-14.6 µg g ⁻¹	(Delgado et. al., 2016)
Raw/ Cooked Sweet Potato	C18 column (200 mm ×4.6 mm, 5µm)	Mobile phase (acetonitrile : methanol : 2- propanol in the ratio of 85:15:33 with 0.01% ammonium acetate) Flow rate : 1.7mL min ⁻¹	UV-Vis Dedector (450 nm)	3.50-95.29 µg g ⁻¹	(Islam et. al., 2016)

Özdemir Olgun, F., A.; Liquid Chromatography Methods for the Determination of Beta-Carotene in Vegetable and Fruit Samples- an Evaluation of the Last Decade

Various Types of Apples	C18 column (200 mm × 4.6 mm, 3 μm)	Acetone: Water (75: 25) Flow rate : 1 mL min ⁻¹	UV-Vis Dedector (450 nm)	Flesh: 2.34- 0.17 μg g ⁻¹ Peel: 1-35 μg g ⁻¹	(Delgado et. al., 2014)
Soy-milk	C18 column (250mm × 4.60 mm, 5 μm)	Mobile phase used was methanol: THF: water 67:27:6 (v/v/v) Flow rate : 0.8 mL min ⁻¹	UV-Vis Dedector (440 nm)	20-700 μg 100mL ⁻¹	(Andres et. al., 2014)
Commercial Agricultural Products	(UHPLC) C18 column (100 mm, 1.8 μm)	The solvent system consisted of (Solvent A) 75:23:2 acetonitrile, water, and hexane (v/v/v; 0.1% acetic acid v/v) and B 90:8:2 acetonitrile, butanol, and hexane (v/v/v, 0.1% acetic acid v/v). Flow rate : 0.5ml min ⁻¹	UV-Vis dedector (450 nm)	1.5-55μg g ⁻¹	(Mc Kevith et. al., 2005)
Food Additives	C18 (30mm × 4.6 mm, 2.7μm) Precolumn GuardCartridge RP-18e (10mm × 4.6 mm)	Washing mobile phase (methanol : water; 92:8) mobile phase consisting of 100% methanol. Flow rate: 1.5 mL min ⁻¹	UV-Vis Dedector (450 nm)	6.00-30.00mg	(Brabcova et. al., 2013a)
Water-melon	C30 Column (4.6 × 150 mm, 5 μm)	1:1 (v/v) mixture of MTBE and methanol.	UV-Vis Dedector (450 nm)	12-250 μg g ⁻¹	(Giuffrida et. al., 2012)

Özdemir Olgun, F., A.; Liquid Chromatography Methods for the Determination of Beta-Carotene in Vegetable and Fruit Samples- an Evaluation of the Last Decade

					Flow rate: 1.8mL min ⁻¹
Peach (Juice/ marmalade/ jam)	C30 column (250 mm × 4.6 mm, 5 µm)	Methanol / MTBE / water (83:15:2, v / v / v; eluent A) and methanol / MTBE / water (8:90:2, v / v / v; eluent B),	UV-Vis Dedector (450 nm)	1.96-1.42 µg g ⁻¹	(Brabcova et. al., 2013b)
					Flow rate: 0.8 mL min ⁻¹
Products from tomato paste	C18 column (75 × 2.00 mm)	A methanol-water (95:5, v/v) and component B acetonitrile-dichlormethane (90:10, v/v).	UV-Vis Dedector (450 nm)	1.5-4mg 100g ⁻¹	(Radu et. al., 2012)
					Flow rate : 1mL min ⁻¹
Red Bell Pepper, Tomatoes, Strawberry	u-HPLC C18 column (2 mm × 50 mm, 2 µm)	Mobile phase was ethylacetate: acetonitrile: acetic acid (30:68:2, v/v/v)	UV-Vis Dedector (450nm)	0.5 – 140 µg mL ⁻¹	(Shim et. al., 2019)
					Flow rate: 0.2 mL min ⁻¹
Tomato and its by-products	C30 column (3.0 mm × 150mm, 5 µm)	The mobile phase consisted of solvent A (methanol) and B (methyl- tertbutyl ether (MTBE), v/v).	UV-Vis Dedector (450nm)	20-125 µg g ⁻¹	(Salomon et. al., 2020)
					Flow rate: 0.5 mL min ⁻¹

Cladenia Species	C18 column (4.6mm ×250mm, 5 µm)	Methanol: Water: Phosphoric Acid (75: 25: 0.9 v/v/v) Flow rate: 1mL min ⁻¹	PDA Dedector (200-500nm)	-	(Kocakaya et. al., 2021)
Pink grapefruit, tomato paste, fresh kiwi, apricot nectar,	C30 column (250 × 4.6 mm, 5.0 µm)	Water: Methanol: Methyl tetrabutyl ether (MTBE) Flow Rate: 1mL min ⁻¹	DAD Dedector	-	(Achir et. al., 2022)
Soybean Seeds	C18 column (250 × 4.6 mm, 5.0 µm)	Gradient Elution Methanol (10mM Ammonium Acetate: MTBE)	UV-Vis Dedector (450 nm)	0.10-10 µgmL ⁻¹	(Gebreziabher et. al., 2021)
Carrots, Sweet Potato	R-P HPTLC (10cm × 20 cm) glass plates precoated with silica gel	Ternary Mobile Phase Ethanol: Cyctohexane: Acetone	UV-Vis Dedector	25-1000 ng band ⁻¹	(Alqarni et. al., 2021)

Conclusions And Recommendations

Carotenoids are difficult molecules to analyze due to their complex structures and isomers, especially if they had been through a food process. As far as it is known, beta-carotene which is an important member of this family generally stands together with the other carotenoid compounds. Therefore, the accurate analysis of beta-carotene may be challenging due to this similarity among the family members. In this study, the chromatographic methods for the determination of beta carotene (which is an important type of carotenoid molecules) that were proposed at the last decade were surveyed carefully, for the first time in literature, to give a basic idea for the future studies.

As it is already known, development of a HPLC method that is suitable to separate carotenoids with good linearity, accuracy and precision is significant. Mobile phases and the analytical columns used in the determination of beta carotene generally depends on the matrix including other molecules that are to be co-analyzed with beta carotene or the ones that may be found just as interferences. The reports and studies on HPLC method for this specific analysis is infinite and it is hardly possible to make a general standardization since it depends on several factors such as matrix effect, solvent, flow rate, temperature e.t.c. But it should be indicated that, the following parameters such as limit of detection (LOD), limit of quantification (LOQ), linearity, accuracy, repeatability and recovery should be evaluated carefully in case of method validation.

Among the suggested methods searched in this study, we may conclude that the issues like analytical duration, installation of less hazardous chemicals, reproduction and similar chemistry consideration should be evaluated and highlighted at the installation of a chromatographic technique for the determination of beta carotene in vegetable and fruit samples.

References

- Achir N., Sevent A., Soto M., Mayer C. (2022). Feasibility of Individual Carotenoid Quantification in Mixtures Using UV-Vis Spectrophotometry with Multivariate Curve Resolution Alternating Least Squares (MCR-ALS). *Hindawi Journal of Spectroscopy*, 1, 1-13. DOI: 10.1155/2022/4509523.
- Alqarni M. H., Alam P., Alam A., Ali A., Foudah A., Alshehri S., Ghoneim M., Shakeel F. (2021). A Greener HPTLC Approach for the Determination of β -Carotene in Traditional and Ultrasound-Based Extracts of Different Fractions of *Daucus carota* (L.), *Ipomea batatas* (L.), and Commercial Formulation, *Argonomy*, 11, 2443-2457.
- Andrés V., Villanueva M. J., Tenorio M. D. (2014). Simultaneous determination of tocopherols, retinol, ester derivatives and β -carotene in milk- and soy-juice based beverages by HPLC with diode-array detection, *Food Science Technology*, 58 (2), 557-562.
- Brabcová I., Hlavackova M., Satinsky D., Solich P. (2013). A rapid HPLC column switching method for sample preparation and determination of β -carotene in food supplements, *Food Chemistry* 141(2), 1433-1437. DOI: 10.1016/j.foodchem.2013.04.063.
- Britton, G. (1995). Structure and properties of carotenoids in relation to function, *FASEB Journal*, 9, 1551-1558.
- Chen D., Wu M., Xie S., Li X., Tao Y., Wang Z., Huang L., Pan Y., Peng D., Zonghui Y. (2019). Determination of Tartrazine, Lutein, Capsanthin, Canthaxanthin and β -Carotene in Animal Derived Foods and Feeds by HPLC Method, *Journal of Chromatographic Science*, 57 (5), 462-468, DOI: [10.1093/chromsci/bmz019](https://doi.org/10.1093/chromsci/bmz019).
- Dai Y., Row K. H. (2019). Isolation and Determination of Beta- Carotene in Carrots by Magnetic Chitosan Beta-Cyclodextrin Extraction and High-Performance Liquid Chromatography (HPLC), *Analytical Letters*, 52(11), 1828-1843. DOI: [10.1080/00032719.2019.1570245](https://doi.org/10.1080/00032719.2019.1570245).
- Delgado-Pelayo R., Gallardo- Guerrero L., Horrero-Mendez D. (2014). Chlorophyll and carotenoid pigments in the peel and flesh of commercial apple fruit varieties, *Food Research International*, 65, 272- 281.
- Delgado-Pelayo R., Gallardo- Guerrero L., Horrero-Mendez D. (2016). Carotenoid composition of strawberry tree (*Arbutus unedo* L.) fruits, *Food Chemistry*, 199, 165-175. DOI: 10.1016/j.foodchem.2015.11.135.
- Deming, D.M. and Erdman, J.W. (1999). Mammalian carotenoid absorption and metabolism, *Pure and Applied Chemistry*, 71, 2213-2223.
- Dietmar, E.B. and Bamedi, A. (2001). Carotenoid esters in vegetables and fruits: A screening with emphasis on β -cryptoxanthin esters, *Journal of Agricultural and Food Chemistry*, 49, 2064-2067.
- Fleshman M., Lester G. E., Riedl K. M., Kopec R. E., Narayanasmy S., Curley R. W., Schwartz S. J., Harrison E. H. (2011). Carotene and Novel Apocarotenoid Concentrations in Orange-fleshed Cucumis melo Melons: Determinations of β -Carotene Bioaccessibility and Bioavailability, *Agricultural Food Chemistry*, 59 (9), 4448-4454. DOI: [10.1021/jf200416a](https://doi.org/10.1021/jf200416a).

Gebreziabher B. S., Zhang S., Qi J., Azam M., Ghosh F., Feng Y., Huai Y., Li B., Sin J. (2021). Simultaneous Determination of Carotenoids and Chlorophylls by the HPLC-UV-VIS Method in Soybean Seeds, *Agronomy*, 11, 758. DOI: 10.3390

Giuffrida D., Torne G., Dugo P., Dugo G. (2012). Determination of the carotenoid profile in peach fruits, juice and jam, *Fruits, Journal of Tropical and Subtropical Horticulture*, 68, 39-44. DOI: 10.1051/fruits/2012049.

Ha. J., Shim. Y., Teo H., Nam H., Ito M., Nakagawa H. (2010). Rapid Method for Determination of β -Carotene in Foods Using Ultra High Performance Liquid Chromatography, *Food Science and Biotechnology*, 19, 1199-1204.

Huang X., Liu Y., Di D., Liu J., Li C. (2010). An Improved LC-DAD Method for Simultaneous Determination of Lutein, β -Carotene and Lycopene in Tomato and Its Products, *Chromatographia*, 71 (3), 331-334. DOI:10.1365/s10337-009-1417-0.

Islam S. N., Nusrat T., Begum P., Ahsan M. (2016). Carotenoids and β -carotene in orange fleshed sweet potato: A possible solution to vitamin A deficiency, *Food Chemistry*, 199, 628-631. DOI: 10.1016/j.foodchem.2015.12.057.

Jacop R. A., Burri B. J. (1996). Oxidative damage and defense, *American Journal of Clinical Nutrition*, 63(6), 985-990.

Kalt W., Forney C.F., Martin A., Prior R.L. (1999). Antioxidant capacity, vitamin C, phenolics and anthocyanins after fresh storage of small fruits, *Journal of Agricultural and Food Chemistry*, 47, 4638-4644.

Kocakaya Z., Kocakaya M., Karatoprak G. Ş. (2021). Comparative Analyses of Antioxidant, Cytotoxic, and Anti-inflammatory Activities of Different Cladonia Species and Determination of Fumarprotocetraric Acid Amounts, *KSU J. Agric Nat*, 24 (6), 1196-1207.

Kongaphisith Tongpoolsomjit K., Grandmottet F., Boonruangrod R., Krueajan A., Viyoch J. (2020). Determination of β -carotene content in Musa AA pulp (Kluai Khai) at different ripening stage and harvest period in Thailand, *Emirates Journal of Food and Agriculture*. 32(6), 443-452. DOI: 10.9755/ejfa.2020.v32.i6.2114.

Krinsky, N.I., Russet, M.D., Hendelman, G.J. and Snadderly, D.M. (1990). Structural and geometrical isomers of carotenoids in human plasma, *Journal of Nutrition*, 120, 1654-1661.

Lehman R. W. (1967). *Methods of vitamin assay*. (3rd Ed.). New York: John Wiley & Sons.

Li H., Zhao C., Tian H., Yang Y., Li W. (2019). Liquid-Liquid Microextraction Based on Acid-Base- Induced Deep Eutectic Solvents for Determination of β -Carotene and Lycopene in Fruit Juices, *Food analytical Methods*, 12 (12), 2777-2784.

Maurer M. M., Mein J. R., Chaudhuri S. K., Constant H. L. (2014). An improved UHPLC-UV method for separation and quantification of carotenoids in vegetable crops, *Food Chemistry*, 165, 475-482. DOI: 10.1016/j.foodchem.2014.05.038.

McKevith, B. (2005). A carrot a day to keep cancer away, *Nutrition Bulletin*, 30, 117- 119.

Morrison F. B. (1954). *Feeds and Feeding—A Handbook for the Student and Stockman*. (21). New York, USA: The Morrison Publishing Company.

Olson, J.A. (1993). Vitamin A and carotenoids as antioxidants in a physiological context. *Journal of Nutritional Science Vitaminol*, 39, 57-65.

Radu G. L., Litescu S. C., Albu C., Teodor C., Truica G. (2012). Beta-carotene and lycopene determination in new enriched bakery products by HPLC-DAD method, *Romanian Biotechnological Letters*, 17 (1), 7005-7012.

Rodriguez-Amaya, D.B. (2001). *A guide to carotenoid analysis in foods*, USA: ILSI Press.

Salamon M. V., Piccoli P., Fontana A. (2020). Simultaneous determination of carotenoids with different polarities in tomato products using a C₃₀ core-shell column based approach. *Microchemical Journal*, 159, 105-309.

Satarova T. M., Semenova V. V., Zhang J., Jin H., Dzubetskii B. V. Cherchel V. Y. (2019). Differentiation of maize breeding samples by β -carotene content, *Regulatory Mechanisms in Biosystems*, 10(1), 63–68. DOI:10.15421/021910.

Schieber, A. and Carle, R. (2005). Occurrence of carotenoid cis-isomers in food: Technological, analytical and nutritional implications, *Trends in Food Science and Technology*, 16, 416–422.

Shaidi F., Metusalach A., Brown J. A. (1998). Carotenoid pigments in seafoods and aquaculture. *Critical Reviews on Food Science*. 38 (1), 1- 67. DOI: 10.1080/10408699891274165.

Sulaeman, A., Keeler, L., Giraud, D.W., Taylor, S.L., Wehling, R.L. and Driskell, J.A. (2001). Carotenoid content and physicochemical and sensory characteristics of carrot chips deep fried in different oils at several temperatures, *Food and Chemical Toxicology*, 66, 1257–1264.

Topuz, H. S. (2020). Covid-19 Enfeksiyonunda Beslenme, *Medical Research Reports* ;3(1), 176-180.

Whong P., Songsri P., Suriharn B., Lomthaisong K., Lertrat K. (2017). Rapid assesment of lycopene and β -carotene in spiny bitter gourd (*momordica cochinchinensis* (lour.) spreng), *Pakistan Journal of Botany*, 49(2), 493-497.

Von Elbe, J.H. and Schwartz, S.J. (1996). *Colorants In "Food Chemistry"*. (O.R. Fennema Ed). New York: Marcel Dekker Incoporation.

Ziegler, R.G. (1989). A review of epidemiologic evidence that carotenoids reduce the risk of cancer, *Journal of Nutrition*, 119, 116–122.

Data: Concepts and Processing

Ahmet YÜCEL¹

Introduction

The field of processing data concepts is growing exponentially. New methods are being developed to process this data and make it useful for the future of education, health technology, and other fields. Data is being generated faster than ever before. The amount of data produced in a single day today is greater than the amount of data produced in all of human history before 1900s. In the future, this may change the way we live and learn in everything from education to healthcare. As technology advances, there are more and more data concepts that need to be processed. New methods are being developed to process Big Data. The future of education and healthcare will be greatly impacted by this new technology.

Big Data is a term used to describe large amounts of data that can be difficult to manage. As with the oil mines discovered before the Industrial Revolution, it can be difficult for societies of our time, confronted for the first time with the data phenomenon, the most important mine of this age, to understand how Big Data is used or what it is used for. In this regard, it is of great importance to developing new methods both for using data and for explaining its meaning and potential. The importance of data concepts in dealing with Big Data has never been greater. Data can be collected from many sources such as social media, mobile devices, internet searches, and more. This data is then analyzed to find patterns and trends that can be used in different areas. Big Data is a term that refers to data sets that are too large or too complex to be processed by traditional database management tools. Big Data processing is the process of analyzing Big Data and extracting useful information from it. Big Data processing requires many resources such as storage space and network speed. In addition, data processing requires knowledge of coding and programming languages such as Java and Python.

In this study, we will discuss data concepts and data processing approaches. We will explain some current concepts for each phase of these critical processes of generating, transmitting, and processing data and obtaining meaningful results.

What is Data

Data are collection or metrics expressed as written documents, numerical quantities, or multimedia content. Often the concept of data is thought to consist only of numbers, but data can also be audio recordings, images, videos, or documents. Depending on the research area, the data will have different forms. For example, if you're researching the impact of global warming on polar ice caps, your data might be satellite images. But if you're researching the proportions of graduate college students who find employment after school, your data might be the number of graduates per year and the number of students finding employment. The data will be different depending on the subject studied. There are many different approaches to categorize data. However, in general, data are expressed in two categories, either qualitative or quantitative. Quantitative data are collected on a numerical scale such as temperature, density, and length, and can be compared on this scale. Qualitative data are obtained from concepts such as verbal descriptions, photographs,

¹ Dr. Öğr. Üyesi, Finans ve Bankacılık Bölümü, Ankara Yıldırım Beyazıt Üniversitesi, orcid.org/0000-0002-2364-9449

maps, etc. Analyzing data correctly and interpreting results will help us understand patterns and trends in data, provide solutions to data-related problems, or better understand scientific facts. For example, Andrić et al. examined the qualitative data of cultural heritage works and applied pattern recognition techniques to determine the details of the origin of these cultural works (Andrić, Gajić-Kvašček, Crkvenjakov, Marić-Stojanović, and Gadžurić, 2021). Also, Villez compared two qualitative trend analyzes based on two different data sets (Villez, 2014). Data will provide us with a powerful resource in our effort to understand the physical and sociological phenomena in our environment. For example, Gantala and Balasubramaniam simulated the propagation of ultrasound waves by applying a special data-driven physical learning model using the deep neural network method (Gantala and Balasubramaniam, 2022). Also, Chabert-Liddell et al. propose a stochastic model for the analysis of multi-level networks in the context of organizational sociology (Chabert-Liddell, Barbillon, Donnet, and Lazega, 2021).

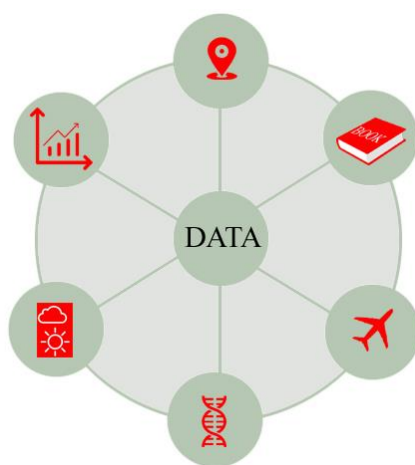


Figure 1. Data Sources

The content of data is expressed in two basic categories, quantitative and qualitative. Besides, the data can be divided into two sub-categories as structural and unstructured, depending on whether the data content is ready or not ready to be analyzed by statistical methods. Also, according to the source of the data, it can be referred to as biometric data, metadata, etc.

Structured and unstructured Data

Structured data is also known as tabular data and can be found in databases, spreadsheets, and text files. Unstructured data is any type of data that does not fall into a predefined format or classification scheme.

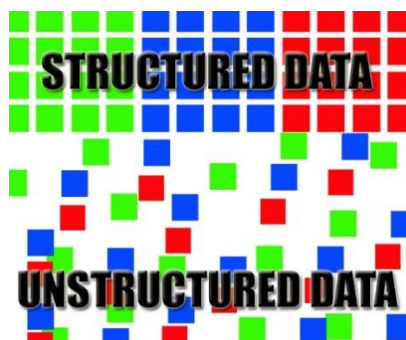


Figure 2. Structured and unstructured data

The two types of data have their own benefits and drawbacks. For example, structured data can be easily manipulated by computers. It is in a ready-to-analyze format. This can mean an

advantage or a shortened processing time. On the other hand, unstructured data provides a more natural representation of reality.

Metadata

Metadata is data that describes other data. It describes the content and format of a document. Metadata is important for many reasons. Metadata has a format that is easy to understand and interpret (McGilvray, 2008). If a person knows what metadata they are looking for, it can help them find the right document quickly and easily. Metadata also has other uses in an organization. For example, metadata helps people know when to update documents, when to archive, or where to store them (Eicken and Salganek, 2009).



Figure 3. Metadata

Biometric Data

Biometric technology, in addition to many uses, is mainly used for authentication through data based on human biometrics. Fingerprint, palm, face, etc. such that the biological characteristics of the human body are used as data. In addition, behavioral features such as voice, posture, gait, handwriting and signature are also used in biometric technology. Since each human biological characteristics are unique, unchangeable and portable, automatic biometric authentication, in particular, provides higher trust and speed compared to classical authentication. Biometric technologies scan biometric features in all their details and convert them into digital data. These data are called digital biometric codes. Produced biometric codes are transferred to microprocessors and electronic components and used for authentication purposes in system access.



Figure 4. Biometric Data

Biometric technologies, image processing, sensors, etc. are all built on digital components and artificial intelligence. Artificial intelligence is the stage that detects and interprets biometric data collected over digital components. Biometric technologies have the ability to constantly improve themselves thanks to machine learning algorithms based on artificial intelligence. Hao et al. propose an SVM-based biometric authentication system that integrates face and fingerprint data to improve the accuracy of personal identification detection (Hao et al., 2005). Machine learning processes are

basically based on big data analysis and deep learning algorithms. In this respect, biometric technologies can be thought of as a composite approach that brings together digital technologies and data science.

All over the world, countries have been investing in biometric technologies for more than 60 years (Küfeoğlu, 2022) in order to increase their market share and to be one of the pioneers of technology. Thanks to these investments, the sector continues to grow continuously and rapidly. In parallel with the development of IoT and M2M technologies, it is clear that in the coming decades, every industry based on artificial intelligence will experience significant developments and as a natural result, new investment opportunities will emerge. It is also quite clear that the market potential of the biometric technology sector, which has artificial intelligence at its center, will grow with an increasing momentum (Fairhurst, Fierrez, and Campisi, 2011).

People use the brain to see, hear, feel. It analyzes the data it collects through the senses and transforms this data into information. This information is used by the brain in decision stages, mainly for human survival. In this respect, biometric technologies produce information by imitating the methods of data collection of human senses and subsequent analysis of the brain. This process is referred to as “multi-modal biometrics” (Kumari and Thangaraj, 2020). The main goal of these technologies, based on multi-modal sensing, is for human survival and for living in safety, away from dangers. For example, the multimodal biometric approach proposed by Rajasekar et al. for smart cities, which uses biometric features such as fingerprint and iris, shows that it increases the accuracy of biometric authentication, which is critical for security (Rajasekar et al., 2022). Security is at the forefront of the use of biometric data-based technologies, but its use for purposes that facilitate human life is becoming more common day by day. From drivers’ attention detection (Abate, Bisogni, Castiglione, and Nappi, 2022) to the smart city concept (Ross, Banerjee, and Chowdhury, 2020), many biometric technology application areas have begun to integrate into daily life.

What is Data Source?

Database and data warehouse

Data warehouses are a collection of databases that store the data for long periods of time. They are used to store data from different sources and provide a centralized location for analyzing and accessing the data.

A database is a set of files that stores information in tables. A table can have one or more columns, which represent fields in the database, and one or more rows, which represent records in the database. The tables are linked together by unique identifiers called keys.

Data warehouses use relational databases to store their data. These databases use SQL commands, which allow users to perform queries on their data using various clauses such as select, update, insert, delete and join.

Relational and Non-Relational Databases

Relational Databases are tables of data which are related to one another. Non-Relational Databases are not related to each other in any way and they can be easily updated.

Relational databases are the most common type of database. The data is stored in tables with rows and columns. It's organized as a series of related tables, which can be accessed by joining the tables together.

Non-relational databases don't use table-based organization to store data. They store data in a single file or document, which may contain several different types of information. This often makes them more flexible than relational databases, but they're less efficient and take up more space on the hard drive.

Data Source

Data source is a defined connection to a database, and contrary to popular belief, there is no real data in the data source. In the data source, only the database information and connection method and form are included. A database can have multiple data source connections. The available data source in the server or processor is used for data storage. The stored data can be a database or files containing tables (Oracle, 2011).

The data source is responsible for all processes from activating database connections and assigning them to the relevant database, managing them and deactivating them again. The structure in which all these connections take place is called the database connection pool. Data connection pool, which is used for effective management of database connections, which is a limited and costly tool, is widely used especially in web applications (Oracle, 2011).

Although classical approaches based on the analysis of stored data have been widely used in recent years, real-time analysis and modeling of data streams have become an urgent need in many sectors because they cannot meet the needs at the speed point. Finance, telecommunications, advertising, etc. These real-time data analysis and modeling applications are used in many industries. The ability to react quickly to rapid changes in the sectors, as well as to predict future changes, is of vital importance for every sector player.

Although data is always valuable in science, in some industries data loses its value over time. In such sectors, instead of storing and analyzing the data afterward, it is necessary to analyze the data as soon as it is formed and to use the obtained information quickly. For example, online shopping platforms such as Amazon, eBay, etc. should direct users' queries to the right products very quickly or channel the customers according to their needs by showing the right ads. At the same time, more detailed information about the needs of the customer can be produced by taking and examining the data that customers have recently created on other online platforms such as Twitter, Facebook, Instagram, Youtube, Whatsapp, etc. The data created by the same users on different platforms, user feedback, clicks, past queries, gender, age, etc. all data will be an important source of information for online commercial enterprises to meet both current customer expectations and potential customer expectations in the future. The data is analyzed quickly and the results are matched with the customer profile and used exactly when the customer needs it. For this reason, data collection and processing must be done in real-time and synchronized. Classical databases are sufficient to quickly store single-source data streams, but most of them do not support the most critical feature of data flow, "real-time data analysis".

Especially for high accuracy rates, non-real-time data analysis models are used on smaller sizes of data. In this way, guiding models and qualified information are produced to be used in real-time models. Real-time data analytics is often applied to big data, in industries where timing is critical, analyzes are performed within seconds, and results are used. Especially in the internet industry, real-time data analysis should be a source that produces uninterrupted and real-time information. For this reason, real-time data flow should occur both in parallel and simultaneously from the internet to the data source (data storage) and from the data source to the sectoral use (information based on analysis results). One of the most critical elements of the ongoing data flow, such as a circular infinite sequence, is the data recording time information. Data recording time information will allow an analysis of data by dividing it into periods, such as minute, hour, certain hours of the day, daily, weekly, monthly, certain periods of the month, annual, and certain periods of the year.

In order to meet the real-time data needs, there is a need for low-latency connection speeds, simple and reliable distributed systems (Galić, 2016) that will enable real-time data flow, and qualified application interfaces (Bornschlegl, Engel, Bond, and Hemmje, 2016) to be used in data collection. Operating in the internet industry, Facebook, LinkedIn, Cloudera, Hadoop, etc. key applications are using Scribe, Kafka, Cloudera, etc. data collection tools (Ljubenović, Pantelić, and

Simović, 2018). Many of these tools continue to operate as open sources. In classical data analysis processes, data is first stored in specified databases and then information is extracted from the data based on user interaction. In these processes, user interaction is kept passive while the database storage system actively collects data. However, this method, in which user interaction is kept passive, is used in finance, communication, trade, etc. sectors will not be enough. The “flow” management, in which calculations are made on the data as soon as the data is created, will provide higher benefits (Ke et al., 2022). System requirements for flow calculation; data collection tools compatible with data flow rate, secure and uninterrupted data query engines, maintainability (alternative systems), distributed systems, parallel computing capability.



Figure 5. Data flow

A data flow diagram (DFD) is used to represent the data flow in a computing system and refers to the process of transmitting data in the system, from storing it in a database to reporting analysis results. In DFD, abstract tasks and concrete components are expressed synchronously. DFD based on tasks (actions to be done) expresses at what stage a task should be completed, its inputs related to the task, and the expected outputs to be used in the next stage. DFD based on tangible components refers to internal and external components to perform tasks. DFD, which should be simple and understandable, supported by visuals, is also used in the processes of classifying data and distributing data according to tasks. The most common mistakes made in a DFD task step are defining the input but not defining the output, defining the output but not defining the input, or having the input and output unrelated. In this respect, DFD operates to facilitate communication between users and system designers. DFD is designed to be open to detecting deficiencies or new needs of the system and correcting or improving it by system developers, based on observations and analyses. In general, DFD is used to monitor information flow and determine system requirements.

In DFD, the initial connection must be made between the datastore and task 1. Apart from the DFD, the data store must also have a new-input connection. This external port is called an external entity. The external entity point also performs output collection tasks from the DFD. In this way, the accuracy of the system data source and new input needs are determined. The external entity connection point can be an autonomous system, as well as real people who are experts in the field. In cases where the external entity is a natural person, data entry into the system is usually done manually. The external point of existence can also be expressed as the interaction of the information system with the outside world. The background diagram shows the data flow from all external entity points and the overall concept of the system. For this reason, in the DFD drawing, the background image should not exceed one page, and the program name and the information system name should not be the same.

DFDs can be designed in different ways according to the subjects to which they will be applied. In a subject with a lot of detail, a distinction can be made from very intense to less intense, according to the task intensity. This will reveal more details. This process is called designing a DFD by flattening. In the smoothing process, first, the target system is holistically expressed in the DFD. Next, each task is broken down into possible sub-detail tasks until all sequential steps are defined

by different tasks. The most common mistake made in this process, which requires adding more layers to the DFD, is mismatching the input and output values. For consistency between DFD layers, the input and output values of each level must be equal and related. If there are many external entity points in a system, it may be necessary to first express the system and related external points in a separate DFD and then edit the remaining parts of the system's base DFD. This practice will make it easier to ensure consistency between layers.

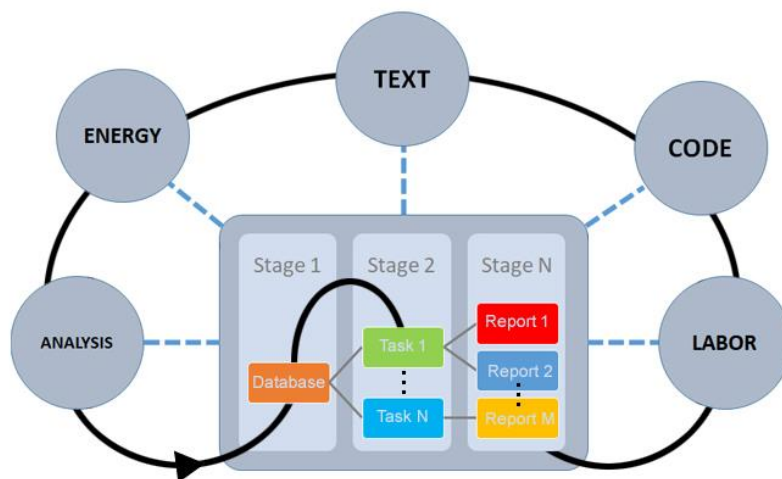


Figure 6. Data Flow Diagram

A DFD consists of tasks and concrete components. Task-based DFD essentially represents the system operation but does not say how the system will be set up and run technically. Processes such as data storage, analyzing data and transforming it into information, and reporting the results are shown in the DFD based on Tasks. Based on tangible components, DFD demonstrates the setup and operation of the system, including technical tools, computer software, files, and personnel assigned to the system. For the system to achieve its goals, DFD based on tasks and DFD based on concrete components must be implemented in a synchronized and accurate manner.

Task-based DFD shows task distributions. Therefore, it is effectively used in communication with system users. In addition, this DFD model is drawn according to the task distributions and thus determined independently of the physical components. This ensures a more stable application of the system flow. Task-based DFD enables systems analysts to better understand systemic tasks and consequently to make more solid decisions (Sutcliffe, 1989). This ensures that the task descriptions do not change frequently and thus the system is easier to maintain. While task-based DFD systems require detailed documentation, Concrete component-based DFD systems require the development of computer software.

Transactional Database

Transactional database is a real-time, dynamic, and applied database that requires high reaction speed (Cuzzocrea et al., 2015). A transactional database consists of tables in which each record represents a financial or trading transaction. As a concept, each transaction contains an original and unique ID number and a list of the transaction's stakeholders. In the transactional database, product name, transaction date, seller/buyer ID numbers, institution address, etc., can also be found in some additional tables related to the transaction content. Transactional database, which product is preferred more according to customer profile, which products' sales are related to each other, how much a product will be needed in the future, etc. It provides important product and customer-based operational information. Traditional databases do not present this information without data analysis. The way of storing datasets gives transactional databases this capability.



Figure 7. Transactional data

In a transactional database, attribute categories of data can be used for different purposes. From a statistical point of view, classification of data, content analysis and weighting of data according to content analysis are done by using attribute categories. In this way, the importance of the items can be measured. The weights of the items are formed spontaneously according to the data universe without any artificial intervention. For example, while using the customer's shopping history and profile information to identify customers in a store, some customer-specific details (inquiry history in the search engine, wedding anniversary, birthday, depending on education level, school term, etc.) might help. To determine the importance of these qualitative elements, some statistical analysis methods such as generalized linear models (GLM) are applied. In their study, Xie and Luo measured the effects of variables in the data set on insurance pricing by applying GLM (Xie and Luo, 2022).

Data mining is a dynamic research process based on data storage and the use of artificial intelligence algorithms. The “coexistence rule”, which reveals the coexistence pattern of any two attributes, is one of the main purposes of data mining. For example, selling phone and phone screen protector products together can be expressed by the association rule. For example, the information that 75% of customers who buy phones also purchase screen protectors can be easily detected in the transactional database. Thanks to the association rules provided by the transactional database, determination of product variety, production planning, determination of target customer profiles, etc. Important steps can be taken in many areas. Producing association rules that about the important items is one of the most important contributions of data mining in transactional database creation processes. In their study, Yen and Lee proposed an association rule to observe the distribution of benefits and costs of products. To this end, they developed a data mining algorithm to identify useful product clusters that could be purchased (Yen and Lee, 2007).

Distributed Information Systems

Distributed systems are a collection of autonomous computers that work together to perform a task. The autonomous computers can be geographically distributed, and they are connected through a network.

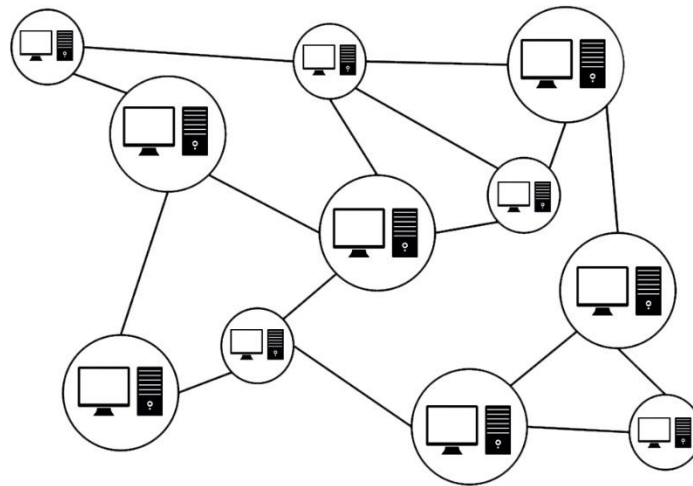


Figure 8. Distributed Information Systems

The system is designed to be tolerant of the failure of some of its components, so that it can still operate in the event that any number of its components fail. This is achieved by dividing the tasks amongst all the computer nodes in such a way that each node only performs one type of task, and each type of task is performed at least once by every node.

Extract, Transform and Load (ETL)

ETL is a process that extracts, transforms and loads data from one system to another. This process is used to extract data from a source system, transform it into the desired format and load it into a target system.

There are many software platforms available in the market that can be used for ETL processes. These platforms have different features and prices which depend on the number of users in an organization.

What is Data Science?

Data science is a set of predictive calculations that generate valuable information from existing data. It is also a multidisciplinary set of instruments and procedures that transform any data into qualified information by coordination strategies based on data science and computer science. Thanks to today's digital infrastructure, huge amounts of data are created every second. Some of this data flows in vain like a river, some of it is stored in different databases. Unfortunately, it is not possible to say that all this data is used to its full potential. Having data science will give you a unique strength and advantage in transforming data into useful and strategic information and in the ongoing competition in all sectors of real life. Thanks to data science, it will be possible to reach reliable information and decisions based on this data, produced with an approach based on facts and science, rather than just intuition and guesswork.

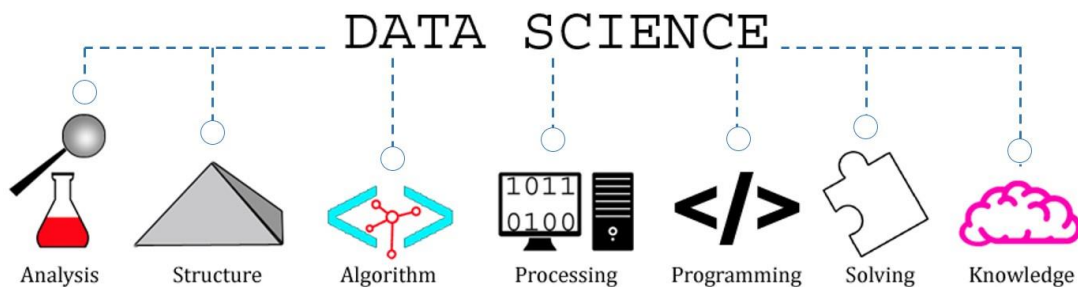


Figure 9. Data Science

Data science, one of the sub-branches of statistical theory, has been prominent for many years. However, technological advances in the last 20 years have also made industrial applications of data science possible. These new possibilities have stimulated interest and prospects in data science. This interest, the rise of big data, and its expectations can be grouped under the headings of the Internet of Things (IoT). The adoption of digital technology in business brings a wealth of information on competitors, clients, tendency of markets, and other critical factors that affect company performance. Extracting information from data is a challenging task, as this information is obtained from different structured and unstructured sources. Data can come from many sources and in different formats. Since the data may be unstructured (text, code, symbol, etc.), it is difficult or impossible for the data to be interpreted intuitively, or for industry stakeholders to manage and use the relevant data on their own.

Artificial intelligence (AI) and machine learning (ML), which were previously just science fiction concepts, have now become a part of everyday life to solve big data challenges. With the exponential growth in the amount, variety, and rate of occurrence of data, the need for data pattern detection, analysis, and prediction has gone beyond human cognitive abilities and conventional statistical methods. Today, AI and ML are a 'must' for reliable data analysis. Therefore, advanced data analytics is not possible without significant advances in computational computing power. The realization that computer processors designed to create game graphics are also very suitable for machine learning and artificial intelligence applications have triggered this development to a great extent. These advanced computer chips can handle highly complex computational algorithms, giving fast results even under the considerably tricky challenges, making them advantageous for data science applications.

Developing data storage technologies, including cloud technology, offer the ability to store all types of data at low cost and high speeds. Companies can reasonably store petabytes of data through a hybrid platform of physical and cloud storage memories. Because data science connects all aspects of an enterprise, tight integration of high-speed processes is critical. Technologies and methods designed to deliver information in real time must be able to integrate seamlessly with computational modeling capabilities that use ML algorithms to predict outcomes. These results are then used with little or no delay to decide on a topic.

There are three fields in that data scientists are proficient: statistics, computer science, and industry domain expertise. The core role of a data scientist is to control and interpret all data associated with a problem, construct and test models to provide insights and predictions, present the results to stakeholders, and then report on the computational details, including coding. In addition, data scientists are also responsible for analyzing and reporting concrete business results. Due to the many specialized skills involved, finding qualified data scientists can be overwhelming. Data science has become such a natural part of every industry that industry stakeholders and basically customers expect to receive technical support based on data analysis in product selection without demanding it. Companies that receive data science support want to understand their customers better and increase customer satisfaction and ultimately increase their sales rates and industry market shares. In addition, companies try to control costs by increasing efficiency in all processes in which the company operates and obtaining information about future trends for strategic planning. The most important aspect of this process is that decisions are based on facts rather than intuitive guesswork.

Actively investing in data science has become a necessity, not a choice, in the age of artificial intelligence and data. Data science can provide enormous financial and strategic benefits, depending on the strategic goals of companies. Boehmke et al. explain how data science can be used to meet an organization's analytical and strategic needs (Boehmke, Hazen, Boone, and Robinson, 2020). Also, using algorithms to analyze data, Yang et al. has developed a financial risk management model required for an online supply chain (Yang, Wang, and Ren, 2019). For example,

a bank can rely on real-time in-house transaction size and operating cost models to optimize online data transfer and transaction speed, thereby minimizing operating costs and energy consumption. Manufacturers may use data science to predict future demand and determine product assortment. In their study, Thomitzek et al. predict the future destinations of battery cell demand used in battery manufacturing with simulation-based modeling (Thomitzek, von Drachenfels, Cerdas, Herrmann, and Thiede, 2019). Besides, automakers are actively using data science to collect real-world driving behavior data and design autonomous driving methods through ML. Industrial factories are using data science to minimize waste and equipment downtime (França, Monteiro, Arthur, and Iano, 2020).

Overall, data science and artificial intelligence drive innovation, improvement, and efficiency in all industries. Data science can be effectively used to optimize the supply chain, streamline workforce use, understand and meet customer needs, accurately predict business metrics, monitor and improve product design and performance. Regardless of companies' strategic goals, data scientist experts can rationally gather and research available information, integrate necessary third-party data streams, apply cutting-edge analytics, and ultimately recommend actions that will lead to a forward-planning strategy relevant to companies. In addition, data scientists can help predict future results and compare confirmed outcomes by building a culture of constant learning and progress. All these data analysis capabilities will commercially secure companies both today and tomorrow.

Data science is becoming more and more automated, and it is clear that this will continue to accelerate in the future. Today, a data scientist can build an automated data analysis model on all potential varieties of thousands of data parameters, discovering the most suitable solution to an existing problem in real-time. In the past, statisticians had to manually design and adjust predictive models over a long period, combining statistical experience and their creativity. But nowadays, with the enormous increase in data volume and complexity of business problems, such tasks are extremely complex with conventional methods. Therefore, this issue needs to be addressed with AI, ML, and other digital computational techniques. While these techniques are often associated with eliminating human work, in reality, they exclusively lift the significance of data scientists and corresponding fields. When these technologies are used for the benefit of all humanity, they will offer advantages that make life easier in every field, from trade to health, and will encourage continuous innovation and development. This will require data scientists to introduce new theories and approaches to meet next-generation needs.

Big Data Analysis

To fully understand the importance and applications of big data analysis, it is necessary to first understand the concept of big data. Big data can be expressed as recorded data collected in large sizes from various sources, based on a specific goal. With the advancement of science and technology, it has become the sociological norm of the digital age to collect large-scale data to observe, analyze and extract information from all kinds of changes and new developments from social sciences to natural sciences, where human and human benefit are at the center. Big data applications are used in many areas from ordinary human life to all kinds of activities of companies or governments.

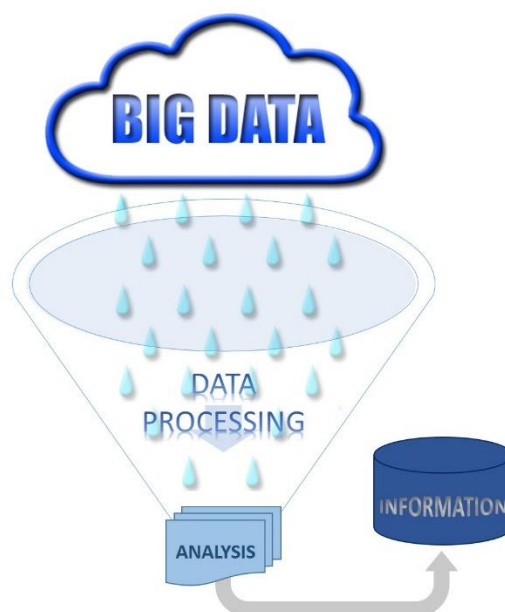


Figure 10. Big Data Analysis

Big data applications are widely used in the business world. Many large companies employ dedicated big data analysts to analyze various behaviors of customers. A company that can analyze customer data well can better understand its customers' needs and purchasing behavior (Zulu and Nkuna, 2022). This information will be a critical foundation for the company to develop strategies for both the present and the future. Through many social media and phone applications, target customers are identified, access to their phone or browser records is provided for these people to be understood more comprehensively, and very detailed and qualified data is collected. Thanks to these data, the steps to develop advertising strategies for product development for needs, to identify the deficiencies of the current product, and to market the product correctly can be taken correctly. For example, chain retail stores gain valuable insights through the analysis of big data and formulate relevant strategies to accurately predict what customers want to buy. Based on this information, they determine personalized campaigns or product prices. Based on the analysis of big data, telecommunication companies can better predict the customers and take preventive steps. Iwashita et al. propose a semantic analysis method based on information about customer requests for telecommunications services (Iwashita, Shimogawa, and Nishimatsu, 2011). With big data analysis, politicians can better understand the preferences of the voters and prepare their election propaganda according to this information.

Besides analyzing user preferences, big data can optimize the entire business process, reduce cost and accurately identify more efficient working or business models for businesses and companies Zolnowski et al. present a new approach to the cost-benefit analysis of data-driven business models (Zolnowski, Anke, and Gudat, 2017). Big data analysis is also effectively applied in processes such as the optimization of internal workflows, integration and connection of network data, optimization of logistics distribution destinations and routes, and effective management of human resources. Lucci et al. present a workflow modeling based on artificial intelligence in his study. Thanks to this model, it can provide the management and control of robotic applications (Lucci, Monguzzi, Zanchettin, and Rocco, 2022). In their study, Zheng et al. put forward an analysis approach that uses big data on traffic flow and the economic associations that cause traffic flow (Zheng, Lu, and Li, 2022). Giménez-Palacios et al. develop strategies based on data analysis for the solution of dynamic route problems that arise due to the number of vehicles or new customer demands in the distribution of logistic products (Giménez-Palacios et al., 2022). Hamilton and Sodeman presented a study on how Big Data algorithms can be used in simultaneously solving human resource management problems and determining strategies (Hamilton and Sodeman, 2020).

Big data applications can be used by large businesses or governments as well as ordinary individuals. For example, data collected by wearable technologies such as smartwatches or smart glasses are transmitted to large online databases (data clouds). Calorie intake/expenditure, duration of sleep, number of steps taken, blood pressure, etc. The data is analyzed and helps people to observe and manage their physical condition. In addition, thanks to the personal data produced during the use of both wearable and other communication technologies, artificial intelligence support can be obtained in personal decision processes. For example, in choosing a birthday gift, artificial intelligence tools will choose the most suitable options for you from the large product catalog and put them in front of you. By analyzing regional traffic data, the problems experienced in traffic and the sources of the problems can be determined. Dokuz presents an approach that scores each area of the city in terms of traffic speed, thus aiming to predict regional traffic speed, using the New York taxi trajectory dataset and the Weighted spatiotemporal trajectory and velocity big data mining approach (Dokuz, 2022). Every day, many new big data applications that aim to optimize the quality of human life come into our lives.

Another sector where the analysis of big data is used effectively is health. Diseases have very similar characteristics periodically according to the course of the disease, from the preliminary symptoms in the formation process to the effects after they appear. Understanding the data of these processes in full detail will make a contribution that increases the success both in preventive treatment and in the treatment of the disease (Chaochao et al., 2018). Thanks to the new developments in the field of biostatistics, the genetic predisposition of people to certain diseases or the duration and probability of the disease can be calculated by examining the DNA. Some big data analysis studies examine the situation of premature babies and babies born with certain genetic diseases. We can name these studies on DNA as the deciphering of DNA with big data analysis.

Sports competitions are of great importance both nationally and internationally. The sociological and economic dimensions of sportive activities, which drag large fan bases behind them, make the sport more critical than just sport. All countries and sports clubs that want to achieve success in this field apply all kinds of technical support to increase the performance of their athletes. In this way, it is possible to reach new records and new achievements. Especially football, basketball, etc. where large budgets are used. sports branches have become an industry on their own. This situation reveals that it is necessary to deal with the issue not only with sports concepts but also with scientific and technological concepts. Apart from the classical methods to achieve success, many athletes now apply big data analysis technology during training (Fury, Oh, and Berkson, 2022). For example, with the sensor technology worn on the athlete or sports equipment, the athlete's body data, performance, physical posture, and technique can be understood, and various improvement suggestions are made for better performance.

Big data analytics can make devices smarter and more autonomous. For example, Tesla uses big data collections obtained from consumers to develop self-driving cars (Kerschner and Somare, 2017). Autonomous cars are working on navigation services and artificial intelligence (AI) that collects both in-vehicle and out-of-vehicle data including other vehicles on the traffic via cameras, lidars, sensors, and internet network (Huang, 2018). The AI system processes them with simultaneous big data analysis methods. Data processing continues instantaneously and uninterruptedly, and thus, it has gained a form that constantly improves itself by debugging errors. This makes autonomous driving increasingly safe and comfortable.

Especially in recent years, the instant processing of images collected by unmanned aerial vehicles and security cameras with big data analysis methods and transforming them into intelligence information has become a very common practice in the field of security. In particular, China has installed cameras with facial recognition technology in almost every street (Chan, 2018). In addition, instant analysis of digital data such as credit card usage is used effectively in the physical tracking of suspects in some criminal investigations all over the world (Wacks, 2013). On the other

hand, there are some criticisms that in these AI supported security concepts, personal privacy is violated.

Another sector where big data algorithms are used extensively is the finance sector. Institutional or individual investors operating in the financial sector use big data models for the analysis of financial transactions (OECD, 2021). By analyzing the historical transaction records and the current data, they can make predictive, fast, and reliable investment choices that make the risks clear to a certain extent. In most of the stock buying/selling transactions, before the official buys or sells decision, it is artificial intelligence (AI) supported big data analysis algorithms, not a real financial expert, that simulates the possible decision and performs an active information flow to the investor based on the analysis.

Big Data Technologies

Collecting, storing, analyzing, and interpreting Big Data requires a range of Big Data technologies. Distributed computing methods, clustering, real-time data analysis, etc. may also be used and are also required. By using Big Data and Big Data analytics, companies can optimize costs, increase efficiency, develop new products that meet customer expectations, make smarter investment decisions, and take more accurate and risk-mitigating actions. The applications and importance of Big Data extend far beyond these examples. Examples of Big Data can be observed from all stages of life.

The ability to analyze Big Data has already passed the petabyte-second mark in real-time, and reaching the exabyte-second mark when the 6G data transmission infrastructure is ready is not a distant goal. With today's technologies, it is impossible to store and process such large amounts of data in a single database. Data of this scale should be stored in different databases, divided into subsets, and processed on different devices, and then the results should be combined. Big Data storage systems store the same data in multiple locations to ensure data security. Analyzing subsets of the same data on different devices and storing them in different repositories is called a distributed system. Some algorithms help organize how data can be stored and processed most efficiently and quickly in a distributed system.

The first step in the Big Data processing cycle is data collection. In the classical understanding of data, data is treated under three basic headings: structured, semi-structured, and unstructured. Audio, video, etc. However, data is not included in the classical understanding of data. Also network, system, device, hardware, etc. The data generated by the components are also not included in the scope of classical data. All these new forms of data are stored in the Big Data concept and analyzed together with other forms of data. Network data, links, text, images, etc. comprise the content. Device data is usually collected using devices equipped with sensors. In some cases, information related to the mechanical operation of the device (temperature level, signal strength, etc.) can also be considered device data. The collected data is transmitted and stored through data sources. During data transmission, information such as the queue ID, data subscription, data source ID, time, and serialization is used for message queue software of relevant data and synchronization of subsets collected in other sources.

Message queue middleware is mostly used in distributed big data systems. The main purpose of this software is to increase the performance of distributed data systems. In the processes from data collection to data analysis, it aims to facilitate the selection of data collected for specific purposes among other data, i.e. to ensure communication between the user and the data, thus ensuring the most effective use of the data. It also performs tasks such as scaling data, organizing new data entries, transferring data to applications, and combining data from different sources. Data subscription is a system that provides users with cumulative, uninterrupted, real-time data. Thanks to this system, users can realize business scenarios such as determining and applying asynchronous systemic task distributions and accessing data with similar content collected in different sources

and asynchronous times. Serialization, then, is the serial connection of data systems during data transmission, as in power models. In this process, objects working in the phases of data collection and production communicate through a serial connection. In the transmission of Big Data, serialized communication systems between objects provide speed, performance, and efficiency-enhancing effects in data-based workflows.

Big Data storage systems provide performance-optimized, secure storage and access to large structured and unstructured heterogeneous data. As technology and data forms change, so does the architecture of data storage. The classic physical storage points, computer main memory, flash disks, etc. are well known. But data storage (cloud databases) at different physical data storage points over the network can also be counted among the classic methods. Data storage can be classified according to the server type of the system whose data is being collected. Closed systems such as mainframe and open systems such as Windows and Linux. Open systems are divided into internal and external storage points. Distributed storage systems, such as object, block, and file storage systems, which should be used depending on the different storage points, are diversified. Distributed data storage systems, such as HDFS, Swift, Luster, etc., allow multiple users to access and share Big Data simultaneously based on multiple storage nodes.

As the size and scope of data increase, database technology continues to evolve to meet current and potential needs. The development of network technologies is an important factor that has a positive impact on the development of database technology. The access and usage methods provided by network and database technology have paved the way for more effective user activities in database processes. This database concept, in which users are as actively involved as objects, is called a relational database. Greenplum, Mycat, Aurora, etc. are well-known examples of relational databases. In a relational database, existing data is recalculated through mathematical methods based on user interaction. The weaknesses of this approach include low performance due to user speed and difficulty in scaling. In addition to storing data, the analytic database provides users with the ability to perform statistical data analysis on existing data. AnalyticDB, Clickhouse, and LucidDB are some popular analytical databases. Since the entire process is performed online in this database concept, users do not need physical components and the value of existing data can be determined without an external platform.

Big Data users use search engines to quickly and accurately find the data they need. A search engine can scale distributed data. Thus, when scanning data with specific content, the user is presented with the target data in order of importance. This feature helps optimize database performance. Elasticsearch and OpenSearch are examples of distributed search engines.

Big Data computing is the process of dividing large amounts of data into discrete subsets and computing the results by analyzing each subset synchronously with multiple computer programs. Since almost the entire process is independent of software, the application of data computing and distributed task management is maintained with high performance and reliability. In large distributed systems, when a hardware component is added to the system, the automatic operation of this physical device must be coordinated. The distributed coordination system provides coordination of all processes related to hardware components, such as commissioning replacement components, ensuring communication between components, and synchronous operation of components when a malfunction or change occurs in physical components. Examples of popular distributed coordination systems include ConfigServer, Eureka, and Chubby.

Resource management is the process of creating clusters and data centers that ensure the management and allocation of resources to ensure the most efficient use of all data sources to which the system is connected. Resource management works on the principle of dynamic allocation when there are multiple users. Ambari and Hue are examples of data resource management tools.

As the size of the system increases, so does the complexity of the workflows of the system participants and the number of problems that arise due to the complexity. This results in the need to monitor, audit, and troubleshoot workflow processes. If the definitions of the roles and responsibilities of stakeholders are not clear, this ambiguity leads to some technical problems, such as transaction deletion on metadata. At this point, the Directed Acyclic Graph (DAG) workflow management application provides important support in identifying and resolving issues. Complex workflows can be visually represented using DAG. Thanks to this graphical representation, workflows can be processed step-by-step and irreversibly from start to finish. In this workflow model, the data contained in the flow cannot be re-entered at the end of the process, and the output of each stage is treated as the input of the next stage. Airflow and Azkaban are examples of tools that provide the DAG application service.

With the development and proliferation of technology-based management systems, traditional enterprise management processes no longer meet expectations. New systems not only speed up tedious processes but also convert data generated in workflows into information. It is also possible to convert external data submitted to the system into commercial value thanks to the new approach. For example, classic database systems can provide basic services such as storing data and inserting/deleting/changing/checking data but cannot provide good decision support. For decision support, the integration of various data and historical flow structures should be considered. This highlights the importance of timing and speed. Traditional databases do not provide predictive support for future data while exploring existing data. Therefore, new information processing systems that provide decision support are gradually being deployed and their penetration is increasing.

References

Abate, A. F., Bisogni, C., Castiglione, A., and Nappi, M. (2022). Head pose estimation: An extensive survey on recent techniques and applications. *Pattern Recognition*, 127, 108591. doi:<https://doi.org/10.1016/j.patcog.2022.108591>

Andrić, V., Gajić-Kvašćev, M., Crkvenjakov, D. K., Marić-Stojanović, M., and Gadžurić, S. (2021). Evaluation of pattern recognition techniques for the attribution of cultural heritage objects based on the qualitative XRF data. *Microchemical Journal*, 167, 106267. doi:<https://doi.org/10.1016/j.microc.2021.106267>

Boehmke, B., Hazen, B., Boone, C. A., and Robinson, J. L. (2020). A data science and open source software approach to analytics for strategic sourcing. *International Journal of Information Management*, 54, 102167. doi:<https://doi.org/10.1016/j.ijinfomgt.2020.102167>

Bornschlegl, M. X., Engel, F. C., Bond, R., and Hemmje, M. L. (2016). *Advanced Visual Interfaces. Supporting Big Data Applications : AVI 2016 Workshop, AVI-BDA 2016, Bari, Italy, June 7-10, 2016, Revised Selected Papers*. Bari, Italy: Springer International Publishing. doi:10.1007/978-3-319-50070-6

Chabert-Liddell, S.-C., Barbillon, P., Donnet, S., and Lazega, E. (2021). A stochastic block model approach for the analysis of multilevel networks: An application to the sociology of organizations. *Computational Statistics and Data Analysis*, 158, 107179. doi:<https://doi.org/10.1016/j.csda.2021.107179>

Chan, T. F. (2018, February 13). Business Insider. Business Insider: <https://www.businessinsider.com/how-china-uses-facial-recognition-technology-surveillance-2018-2> adresinden alındı

Chaochao, Y., Li, W., Lihong, K., Feng, S., Chaoyang, M., Yanjun, D., and Hua, Z. (2018). Acupoint combinations used for treatment of Alzheimer's disease: A data mining analysis. *Journal of Traditional Chinese Medicine*, 38(6), 943-952. doi:[https://doi.org/10.1016/S0254-6272\(18\)30995-6](https://doi.org/10.1016/S0254-6272(18)30995-6)

Cuzzocrea, A., Jiang, F., Leung, C. K., Liu, D., Peddle, A., and Tanbeer, S. K. (2015). Mining Popular Patterns: A Novel Mining Problem and Its Application to Static Transactional Databases and Dynamic Data Streams. A. Hameurlain, J. Küng, R. Wagner, A. Cuzzocrea, and U. Dayal içinde, *Transactions on Large-Scale Data- and Knowledge-Centered Systems XXI: Selected Papers from DaWaK 2012* (s. 115-139). Springer Berlin Heidelberg. doi:10.1007/978-3-662-47804-2_6

Dokuz, A. S. (2022). Weighted spatio-temporal taxi trajectory big data mining for regional traffic estimation. *Physica A: Statistical Mechanics and its Applications*, 589, 126645. doi:<https://doi.org/10.1016/j.physa.2021.126645>

Eicken, H., and Salganek, M. (2009). *Field Techniques for Sea-Ice Research*. University of Alaska Press.

Fairhurst, M., Fierrez, J., and Campisi, P. (2011). Future Trends in Biometric Processing. *Computer Vision IET*, 5, 335-337. doi:10.1049/iet-cvi.2011.0241

França, R. P., Monteiro, A. C., Arthur, R., and Iano, Y. (2020). An Overview of the Internet of Things Technologies Focusing on Disaster Response. I. Rahimi, A. H. Gandomi, S. J. Fong, and

M. A. Ülkü içinde, Big Data Analytics in Supply Chain Management: Theory and Applications (s. 158-159). CRC Press. doi:<https://doi.org/10.1201/9780367816384>

Fury, M. S., Oh, L. S., and Berkson, E. M. (2022). New Opportunities in Assessing Return to Performance in the Elite Athlete: Unifying Sports Medicine, Data Analytics, and Sports Science. *Arthroscopy, Sports Medicine, and Rehabilitation*, 4(5), 1897-1902. doi:<https://doi.org/10.1016/j.asmr.2022.08.001>

Galić, Z. (2016). *Spatio-temporal data streams*. Springer. doi:10.1007/978-1-4939-6575-5

Gantala, T., and Balasubramaniam, K. (2022). DPAI: A Data-driven simulation-assisted-Physics learned AI model for transient ultrasonic wave propagation. *Ultrasonics*, 121, 106671. doi:<https://doi.org/10.1016/j.ultras.2021.106671>

Giménez-Palacios, I., Parreño, F., Álvarez-Valdés, R., Paquay, C., Oliveira, B. B., Carravilla, M. A., and Oliveira, J. F. (2022). First-mile logistics parcel pickup: Vehicle routing with packing constraints under disruption. *Transportation Research Part E: Logistics and Transportation Review*, 164, 102812. doi:<https://doi.org/10.1016/j.tre.2022.102812>

Hamilton, R. H., and Sodeman, W. A. (2020). The questions we ask: Opportunities and challenges for using big data analytics to strategically manage human capital resources. *Business Horizons*, 63(1), 85-95. doi:<https://doi.org/10.1016/j.bushor.2019.10.001>

Hao, Y., Liu, J., Wang, Y.-P., Cheung, Y.-m., Yin, H., Jiao, L., . . . Jiao, Y.-C. (2005). *Computational Intelligence and Security : International Conference, CIS 2005, Xian, China, December 15-19, 2005, Proceedings, Part II*. Xian, China: Springer-Verlag Berlin Heidelberg. doi:10.1007/11596981

Huang, B. (2018). *Comprehensive geographic information systems*. Amsterdam, Netherlands: Elsevier.

Iwashita, M., Shimogawa, S., and Nishimatsu, K. (2011). Semantic analysis and classification method for customer enquiries in telecommunication services. *Engineering Applications of Artificial Intelligence*, 24(8), 1521-1531. doi:<https://doi.org/10.1016/j.engappai.2011.02.016>

Iwashita, M., Shimogawa, S., and Nishimatsu, K. (2011). Semantic analysis and classification method for customer enquiries in telecommunication services. *Engineering Applications of Artificial Intelligence*, 24(8), 1521-1531. doi:<https://doi.org/10.1016/j.engappai.2011.02.016>

Ke, C., Zhang, M., Zuo, Y., Xiang, F., Zhang, D., and Tao, F. (2022). Data-driven real-time control method for process equipment in flow shop towards product quality improvement. *Procedia CIRP*, 908-913. doi:<https://doi.org/10.1016/j.procir.2022.05.083>

Kerschner, I., and Somare, M. (2017). *Taxation in a global digital economy*. Wien: Linde. <https://worldcat.org/title/1014019256> adresinden alındı

Kumari, P., and Thangaraj, P. (2020). A fast feature selection technique in multi modal biometrics using cloud framework. *Microprocessors and Microsystems*, 79, 103277. doi:<https://doi.org/10.1016/j.micpro.2020.103277>

Küfeoğlu, S. (2022). *Emerging technologies : value creation for sustainable development*. Springer. doi:10.1007/978-3-031-07127-0

Ljubenović, J., Pantelić, O., and Simović, A. P. (2018). BIG DATA ANALYSIS IN SOCIAL MEDIA. N. J. Žarkić, and S. Marinković içinde, Doing business in the digital age challenges, approaches and solutions (s. 135-142). Symorg 2018.

Lucci, N., Monguzzi, A., Zanchettin, A. M., and Rocco, P. (2022). Workflow modelling for human–robot collaborative assembly operations. *Robotics and Computer-Integrated Manufacturing*, 78, 102384. doi:<https://doi.org/10.1016/j.rcim.2022.102384>

McGilvray, D. (2008). *Executing Data Quality Projects: Ten Steps to Quality Data and Trusted Information™*. San Francisco,, USA: Morgan Kaufmann Publishers Inc.

O. C. (2011). JD Edwards EnterpriseOne Tools Configurable Network Computing Implementation Guide Release 8.98 Update 4, Chapter 5.1. https://docs.oracle.com/cd/E17984_01/index.htm adresinden alındı

OECD. (2021). Artificial Intelligence, Machine Learning and Big Data in Finance: Opportunities, Challenges, and Implications for Policy Makers. OECD: <https://www.oecd.org/finance/artificial-intelligence-machine-learningbig-data-in-finance.htm> adresinden alındı

Rajasekar, V., Predić, B., Saracevic, M., Elhoseny, M., Karabasevic, D., Stanujkic, D., and Jayapaul, P. (2022). Enhanced multimodal biometric recognition approach for smart cities based on an optimized fuzzy genetic algorithm. *Scientific Reports*, 12(1), 622. doi:10.1038/s41598-021-04652-3

Ross, A., Banerjee, S., and Chowdhury, A. (2020). Security in smart cities: A brief review of digital forensic schemes for biometric data. *Pattern Recognition Letters*, 138, 346-354. doi:<https://doi.org/10.1016/j.patrec.2020.07.009>

Sutcliffe, A. (1989). *Human-computer interface design*. New York: Springer-Verlag New York Inc. doi:10.1007/978-1-4899-6749-7

Thomitzek, M., von Drachenfels, N., Cerdas, F., Herrmann, C., and Thiede, S. (2019). Simulation-based assessment of the energy demand in battery cell manufacturing. *Procedia CIRP*, 80, 126-131. doi:<https://doi.org/10.1016/j.procir.2019.01.097>

Villez, K. (2014). Qualitative trend analysis for process monitoring and supervision based on likelihood optimization: state-of-the-art and current limitations. (1. I. Congress, Dü.) IFAC Proceedings Volumes, 47(3), 7140-7145. doi:<https://doi.org/10.3182/20140824-6-ZA-1003.01596>

Wacks, R. (2013). *Privacy and media freedom*. Oxford: Oxford University Press.

Xie, S., and Luo, R. (2022). Measuring Variable Importance in Generalized Linear Models for Modeling Size of Loss Distributions. *Mathematics* 2022. doi:10, 1630. <https://doi.org/10.3390/>

Yang, Q., Wang, Y., and Ren, Y. (2019). Research on financial risk management model of internet supply chain based on data science. *Cognitive Systems Research*, 56, 50-55. doi:<https://doi.org/10.1016/j.cogsys.2019.02.001>

Yen, S.-J., and Lee, Y.-S. (2007). Mining High Utility Quantitative Association Rules. I. Y. Song, J. Eder, and T. M. Nguyen (Dü.), *Data Warehousing and Knowledge Discovery içinde* (s. 283-292). Berlin: Springer Berlin Heidelberg. doi:10.1007/978-3-540-74553-2_26

Zheng, Y., Lu, M., and Li, J. (2022). Internal circulation in China: Analyzing market segmentation and integration using big data for truck traffic flow. *Economic Modelling*, 115, 105975. doi:https://doi.org/10.1016/j.econmod.2022.105975

Zolnowski, A., Anke, J., and Gudat, J. (2017). Towards a Cost-Benefit-Analysis of Data-Driven Business Models. *Wirtschaftsinformatik und Angewandte Informatik*, 181-195.

Zulu, V. M., and Nkuna, A. M. (2022). Data modelling of subsistence retail consumer purchase behavior in South Africa. *Data in Brief*, 42, 108094. doi:https://doi.org/10.1016/j.dib.2022.108094

DNA Sequencing Methods: From Past to Present

K. Eren¹
N. Taktakoğlu²
İ. Pirim³

Introduction

DNA double helix structure was first explained by Watson and Crick. The first natural polynucleotide DNA sequence was announced in 1953. Due to the development of many sequencing techniques, the entire human genome was sequenced in 2003 as a result of the Human Genome Project (Behjati & Tarpey, 2013). The goal of the Genome Project, a large-scale scientific initiative, is to investigate and evaluate the chemical sequence of the 50.000–100.000 genes that make up the human genome, or the entire collection of all genetic material. The separation and examination of the genetic code included in DNA provides the basis for this huge project. Considering the size of the human genome, scientists must have developed new techniques for DNA analysis that can quickly, cheaply, and reliably analyze massive amounts of data. DNA sequencing methods requiring large-scale application have driven technology to both enhance capacity and decrease instrument size. This demand has prompted the creation of automated equipment that speeds up and lowers the cost of biochemical processes connected to sequencing, enhances the analysis of these reactions, and makes it simpler to enter the resulting data into databases (Collins et al., 1998). It was not possible for scientists at the time to sequence nearly a full gene because they could only sequence a few base pairs per year. There was a flurry of RNA and DNA sequencing that improved procedures and provided new data, although there were difficulties in the sequencing process, the first complete genome sequencing was completed after a while. This eventually gave rise to the Maxam and Gilbert chemical degradation DNA sequencing method, which physically separates terminally tagged DNA fragments by electrophoresis and chemically cleaves specific bases of those pieces (Doğan et al., 2017). Maxam-Gilbert, called the first generation sequencing method, is based on chemical fragmentation of DNA and imaging with electrophoresis (Behjati & Tarpey, 2013). Later, a new technique with higher simplicity, reliability, and a lower hazardous level was developed. It was simply called the Sanger sequencing method. When the Human Genome Project was completed in 2003, automated Sanger DNA sequencing with fluorescent dye labels was the dominant technology (Zhong et al., 2021). Sanger technique, which uses fewer chemicals and is less harmful, is still regarded as the gold standard today.

Sequencing methods should be inexpensive, fast, accurate, and easy to implement. The inability of first-generation sequencing to meet these demands has led to new searches. The demand for less expensive and quicker sequencing techniques has grown since the first human genome sequence was completed. Massively parallel sequencing techniques avoid the scalability issues with standard Sanger sequencing by constructing micro-reactors and/or anchoring the DNA molecules to be sequenced to solid surfaces or beads. This enables millions of sequencing operations to occur simultaneously (Behjati & Tarpey, 2013). After Sanger sequencing, NGS

¹ Master Student, Izmir Katip Celebi University,

² Master Student, Izmir Katip Celebi University,

³ Prof. Dr., Izmir Katip Celebi University

represents a real revolution in sequencing technology. A whole human genome may now be sequenced in a couple of days for less than \$1,000, compared to many years and billions of dollars for the first human genome's Sanger sequencing (Zhong et al., 2021). Second-generation sequencing methods, also referred to as next-generation sequencing (NGS), were developed in response to this demand. The quality of genome assemblies were greatly enhanced by the use of third-generation sequencers, which generate reads of previously unprecedented sequence lengths. Field sequencing is additionally made possible by quick sequencing and simple sample preparation (Bleidorn, 2015). Massively parallel sequencing is a technique used by NGS systems in which millions of DNA fragments from a single sample are sequenced (Reis-Filho, 2009). Third-generation single molecule sequencing has been developed to lower the cost of sequencing and simplify the preparation. The procedures involved in generating libraries, amplifying DNA, and sequencing that are part of the second-generation sequencing method are not necessary in the third-generation sequencing approach.

As a result, in this review, the evolution of DNA sequencing methods from the beginning to the present were discussed in detail. It was focused on how NGS methods referring to modern high-throughput sequencing processes sequencing methods actually developed and how they carried sequencing methods forward.

1. First-Generation DNA Sequencing

First-generation DNA sequencing methods consist of two methods: Maxam-Gilbert (Chemical degradation) and Sanger (Chain termination) methods which are based on the amplification of template DNA and gel electrophoresis, emerged at approximately the same time, but the completion times differ from each other. These techniques that are crucial for sequencing the human genome, currently have a disadvantage in terms of cost and time.

Maxam-Gilbert Method

The Maxam-Gilbert method is a method based on chemical degradation introduced by Maxam and Gilbert in the late 1970s. The first step is to convert the DNA sample into a single strand. The phosphate group in the DNA sequence is removed with the help of alkaline phosphatase (Maxam & Gilbert, 1977). Polynucleotide kinase then adds a radioactive phosphate group (P^{32}) to the single helical chain's 5' end (Heather & Chain, 2016). Millions of copies of the template DNA are produced by polymerase chain reaction (PCR). The replicated template DNA is cut into pieces by cutting on the base with base-specific chemicals (Hardin, 2001). Four different chemicals are used for each base (A, G, T and C). As a result, the reaction is conducted in four different tubes, one for each base. All tubes consist of base-specific chemical and radioactively labeled template DNA. The reading of the DNA sequences can be observed by placing the reactions on different strips on the gel with the help of electrophoresis. The negatively charged DNA samples are run on the gel with an electric current. To see the bands, the gel is placed on an X-ray film. The part with the radio-labeled sequences darkens on the X-ray film. The position of the bands that become visible will differ due to the chemical cut of the DNA samples. Since the sequence with a short base length will run fast, the sequence is read from the bottom to the up (Figure 1) (Hardin, 2001).

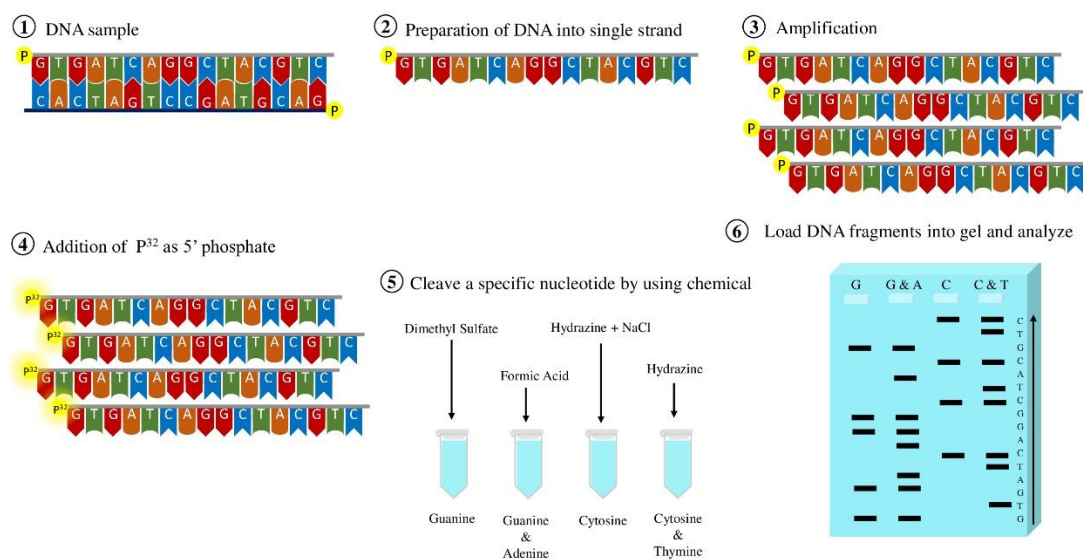


Figure 8. The basic principle of Maxam-Gilbert sequencing method. G: Guanine, A: Adenine, C: Cytosine, T: Thymine, P³²: Radioactive isotope of phosphorus.

In the Maxam-Gilbert procedure, the guanine base is cut using dimethyl sulfate, the cytosine base is cut using hydrazine and sodium chloride, the guanine and adenine bases are cut together using formic acid, and the cytosine and thymine bases are cut together using hydrazine (Hardin, 2001; Maxam & Gilbert, 1977; Rubin & Schmid, n.d.). The chemicals mentioned above methylate their specific bases. Only in high salt (NaCl) environment, hydrazine prevents methylation of the thymine base, thus making the distinction between thymine and cytosine bases easier. In addition, hot piperidine added to the medium breaks the chain of methylated DNA (Rubin & Schmid, n.d.).

The Maxam-Gilbert method isn't routinely used in the laboratory due to various disadvantages (Hardin, 2001) such as high toxicity because of the phosphate isotope and cutting chemical usage, difficulties analyzing sequences longer than 500 bp, and errors during cleavage (Franc et al., 2003).

Sanger Method

The Sanger method, which was introduced by F. Sanger in 1977, is a method based on chain elongation termination, which is used in DNA sequencing with the help of polymerase and special nucleotides (McCombie et al., 2019; Sanger et al., 1977). The elongation of the chain is terminated by synthetic ddNTPs (dideoxynucleoside triphosphate; ddCTP, ddTTP, ddGTP, ddATP), which are the monomers of the DNA chain added to the reaction (Bruijns et al., 2018; Garrido-Cardenas et al., 2017; Heather & Chain, 2016). The only difference between these ddNTPs and dNTPs (deoxynucleotide triphosphate; dCTP, dTTP, dGTP, dATP) is that they lack a hydroxyl group on the deoxyribose sugar's third carbon (Garrido-Cardenas et al., 2017). Lack of hydroxyl causes polymerization to stop, and thus, chain elongation is stopped because it cannot establish a bond with the 5' phosphate of the following dNTP (Heather & Chain, 2016). ddNTPs are designed for each nucleotide separately. Since each base corresponds to a different ddNTP reaction, the Sanger method of DNA sequencing creates a total of 4 distinct reactions for each base (Figure 2). Template DNA, polymerase, primer, ddNTP, and dNTP are all included in each tube (Bruijns et al., 2018; Hardin, 2001). Unlike dNTPs added to the reaction, the concentration of ddNTPs should be lower (Bruijns et al., 2018). When the polymerase adds one ddNTP to the elongated thread, no additional

base can be added and the elongation stops (Hardin, 2001). In this reaction carried out in parallel, loading is made into a separate well (4 different lanes) for each ddNTP on the polyacrylamide gel (Heather & Chain, 2016). In electrophoresis, the negative property of DNA is used and the positions of the DNA strands are determined (Hardin, 2001). DNA strands transferred onto the gel form a ladder image when exposed to X-rays due to their different base lengths. Since the shortest thread will advance first, the reading is performed from the bottom up (McCombie et al., 2019).

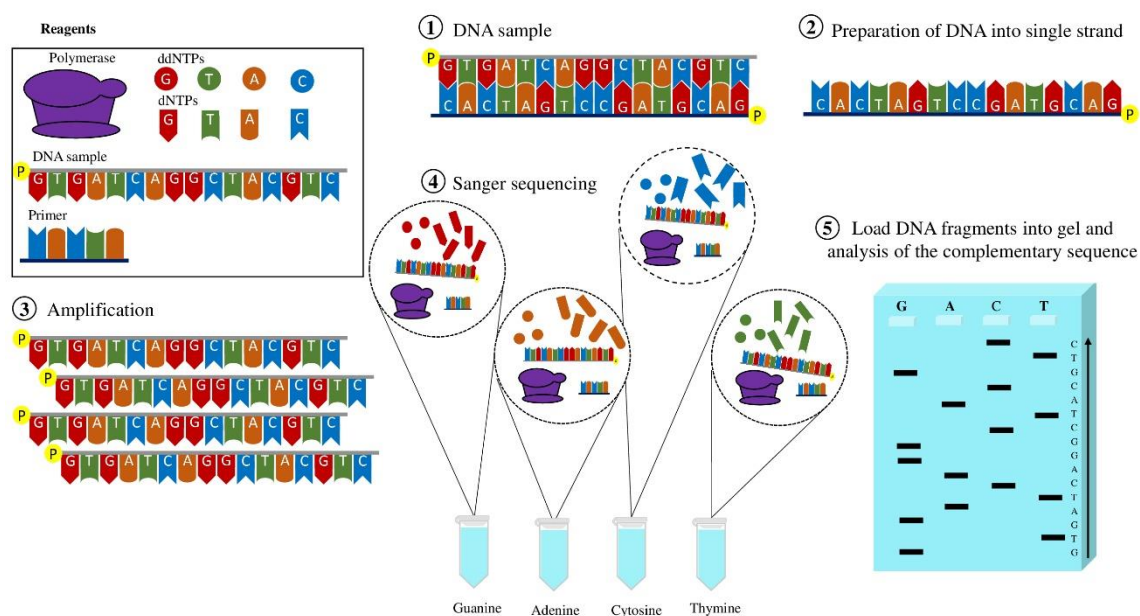


Figure 9. Schematic representation of the old Sanger method. G: Guanine, A: Adenine, C: Cytosine, T: Thymine, P: Phosphate, ddNTPs: Dideoxynucleoside triphosphate, dNTPs: Deoxyribonucleotide triphosphate.

With the advancement of technology, the Sanger method has begun to be performed with fluorescently labeled ddNTPs and capillary electrophoresis (Bruijns et al., 2018). While it was necessary to set up four different reactions for each base with the old method, the reaction is carried out only in a single tube with fluorescently labeled ddNTPs. Each ddNTP is labeled with four different base-specific fluorescent dyes (McCombie et al., 2019). These fluorescently labeled ddNTPs provide information about the last added base to the DNA strand. By capillary gel electrophoresis, DNA fragments are sorted by size difference. The fluorescent dye at the terminator of ddNTPs on the last bases of the DNA sequences undergoing electrophoresis glows with a laser. Fluorescent detection occurs through spectral detectors called CCD (Charge-Coupled Device) (Garrido-Cardenas et al., 2017). Software is required to interpret and analyze sequences (Figure 3)(Slatko et al., 2018).

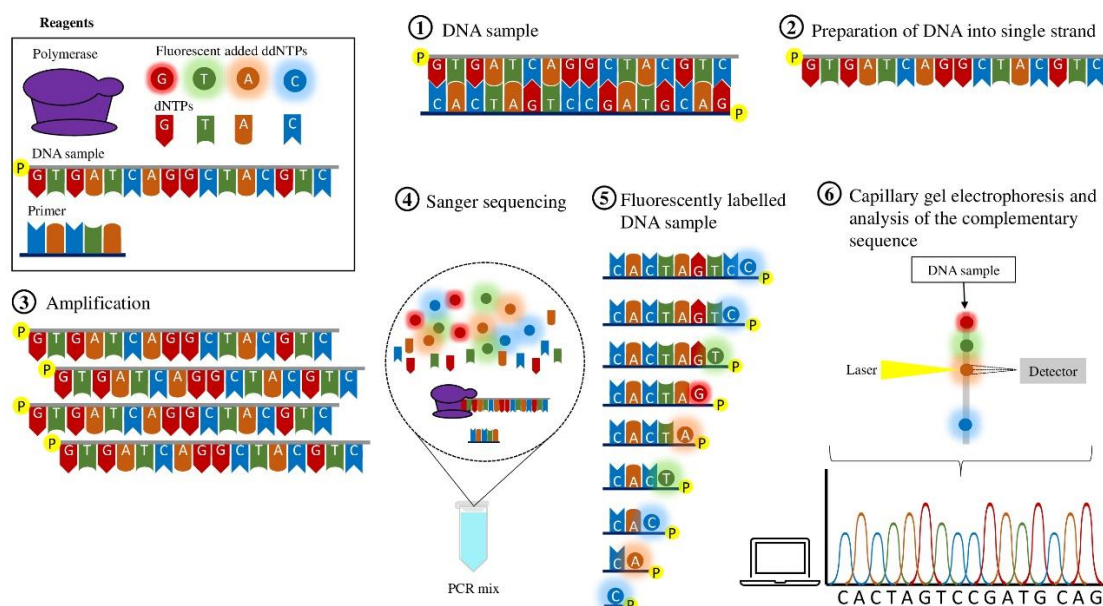


Figure 10. The new Sanger method in its simple form. G: Guanine, A: Adenine, C: Cytosine, T: Thymine, P: Phosphate, ddNTPs: Dideoxynucleoside triphosphate, dNTPs: Deoxyribonucleotide triphosphate, PCR: Polymerase chain reaction.

The Sanger sequencing method is still valid today. According to the Maxam-Gilbert method, the use of hazardous chemicals and radioactive materials is limited. Therefore, it is a less toxic method. The automated Sanger method is the most commonly used one among DNA sequencing methods (Dönmez et al., 2015). The sequence synthesized in this method constitutes the complement of the target sequence.

2. Second-Generation Sequencing

Second-generation sequencing technology allows for the rapid sequencing of whole genome. For this next-generation sequencing, there are several different kits and equipment possibilities. These tools and kits are designed to make the procedures cost-effective and time-saving. As second-generation novel sequencing techniques, it makes use of the Roche 454, Illumina, SOLiD, and Ion Torrent platforms.

Roche 454 Method

The Roche/454 GLS FLX Titanium instrument uses a platform known as pyrosequencing. Emulsion PCR and the subsequent pyrophosphate detection technique are the foundations of Roche/454 pyrosequencing (Salmaninejad et al., 2019). Nyren et al. introduced the pyrosequencing concept for the first time in 1997 (Nyren, 2007). It is a continuing procedure that combines magnetic beads covered with streptavidin, 3'-deficient recombinant DNA polymerase, and luciferase. 5' exonuclease activity (read-out evidence) and luminescence detection bring the process to a close (Liu et al., 2012).

The 400-600 bp DNA fragments from the sequencing sample should be divided into libraries by adding adapter sequences to both ends (Escalante et al., 2014). During the library-building process, PCR amplification by DNA polymerase lengthens each DNA fragment in the sample as nucleotides are added (Balzer et al., 2010). In this method, each nucleotide must be added one by

one to the reaction. Each amplification reaction occurs in a well containing a single DNA molecule in the form of a nanosphere or bead, oligonucleotides or probes attached to its surface, a polymerase, and other essential elements (dNTPs, buffer, $MgCl_2$, primers). The adapter sequences on the DNA fragments are complementary to the sequence of the probes. Only one DNA molecule can exist in each well for there to be a clonal amplification associated to each well. After library creation, the finished emulsion is placed in a PTP (Picotiter plate). In each of the 100,000 wells that are individually observed during the pyrosequencing procedure, PTP only supplies one bead. Each well's data will be produced for a different DNA sequence. This procedure is called Emulsion PCR (Figure 4).

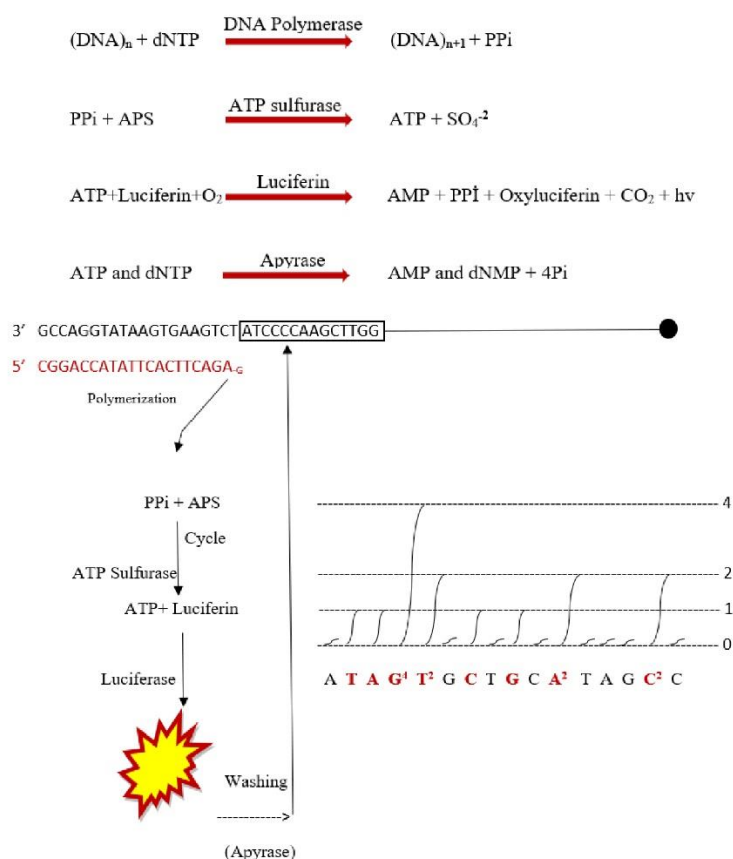


Figure 11. Principle of Roche 454 method. G: Guanine, A: Adenine, C: Cytosine, T: Thymine, dNTPs: Deoxyribonucleotide triphosphate, ATP: Adenosine triphosphate, AMP: Adenosine monophosphate, dNMP: deoxyribonucleoside monophosphate, APS: Adenosine 5'-phosphosulfate sodium salt, PPI: Pyrophosphate, Pi: Phosphatase, hv: Emission of light.

Illumina Method

Illumina acquired the Solexa Genome Analyzer and commercialized it in 2007, and today, the HiSeq and MiSeq platforms in particular are the most successful sequencing system on the market. The amplified template DNA for sequencing creates miniature colonies called colonies by bridging PCR (Slatko et al., 2018).

In order to sequence data, Illumina uses reversible dyes. When added to DNA strands, these colors make it possible to recognize nucleotides. The blocking group and fluorescence with a distinct color for each nucleotide are revealed when the nucleotide binds. To create DNA fragment clusters, the adaptor segments are joined to single strands and put in the flow cell. Bridge

amplification is then carried out (Liu et al., 2012). The four types of nucleotides (A/T/C/G) are introduced, and each is fluorescently labeled with a different color. The unincorporated nucleotides are washed away as the four nucleotides compete for binding sites on the template DNA to be sequenced. Each synthesis is followed by the use of a laser to eliminate the fluorescent probe and blocking group. The subsequent cycle starts when one of the four bases develops a measurable fluorescent color distinct to it that allows for sequence identification. Up until the DNA molecule is sequenced, this process continues (Figure 5).

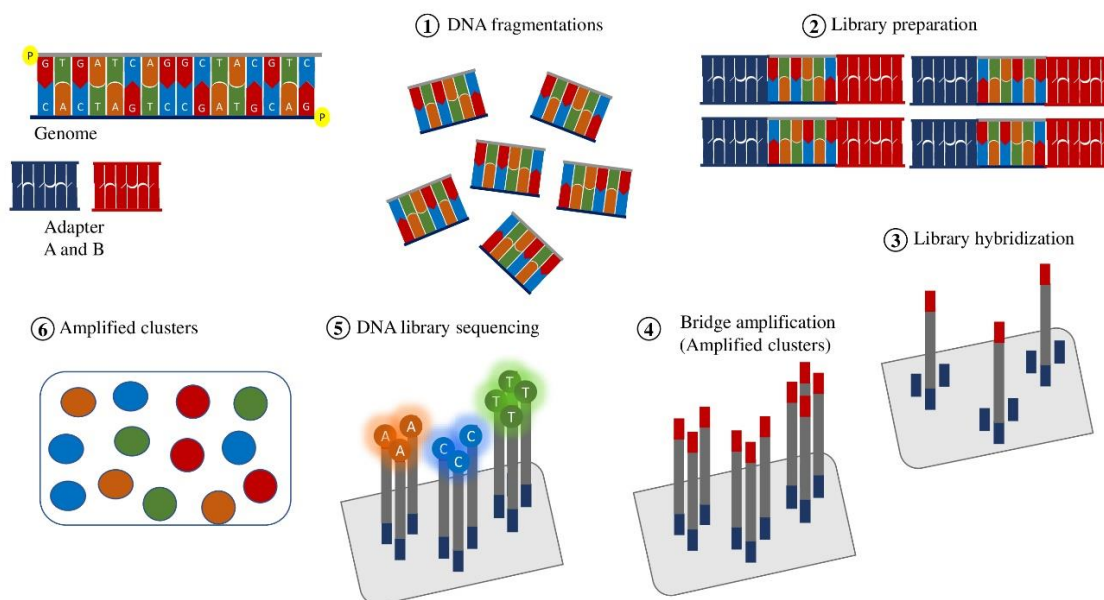


Figure 12. Library preparation and Illumina method. G: Guanine, A: Adenine, C: Cytosine, T: Thymine.

Scale differences between HiSeq and MiSeq technologies are substantial. In 10.8 days run, the HiSeq2000 produces more than 50 Gb of data and 1.6 billion base 100 dual-ended reads. MiSeq, in comparison, generates 1.5 Gb every day from 5 million 150-base paired-end reads and is intended for trials that last only one day (Slatko et al., 2018).

Compared to conventional sequencing techniques like Sanger sequencing, the Illumina approach has some advantages. Multiple sequences can be quickly sequenced at once using Illumina sequencing. Furthermore, unlike pyrosequencing, which requires expensive enzymes, this approach just employs DNA polymerase (Slatko et al., 2018). With a 0.1% error rate, Illumina's reversible terminator technology and paired-end sequencing make it the most accurate base-by-base sequencing method available (Hu et al., 2021). Sequence data outperforms most other systems in terms of throughput, read length, cost, and run time.

Solid Method

The ligation sequencing-based platform Solid Method was purchased by Applied Biosystems in 2006. A high rating of 99.85% indicates that the data collected through this platform's filtering is accurate (Liu et al., 2012).

This technique also uses the Roche 454 emulsion PCR method, which uses tiny magnetic beads. When the DNA library is finished using PCR, the magnetic beads are affixed to a glass flow cell plate. The amplified fragments are sequenced using DNA ligase. These base pairs are found on two-base coded probes that have been specially created. These sensors are a mixture composed of

an identifier base pair, a fluorescent molecule, and certain base components. Four distinct colors are defined to symbolize each base pair. The probe with the correct base pair is added to the sequence and bound to the primer by the ligase during the first cycle after the primer has been connected to the adaptor. The fluorescent lights and the camera shows the light as a result of binding. Following the removal of unbound probes, imaging of the fluctuating fluorescence that distinguishes the bound probe is completed. The sequential ligation cycle is restarted when the fluorescent dye has been removed (Escalante et al., 2014).

The newly generated sequence, together with the primer, is entirely discarded, and the preceding procedures are started over with a new primer. New primer is attached to the main adaptor that was previously handed to the medium one base back. The binding order in their detectors have been changed this time, which have result in various glow colors, because all of these other identifying base pairs bind one base back (n-1). During this time, the fluorescent color have been changing due to the new base pair. The nucleic acids determine according to this alteration. The known sequence is gradually completed with each cycle by shifting back a main base, and after five cycles, there is enough data to make up for any gaps in the sequence (Figure 6).

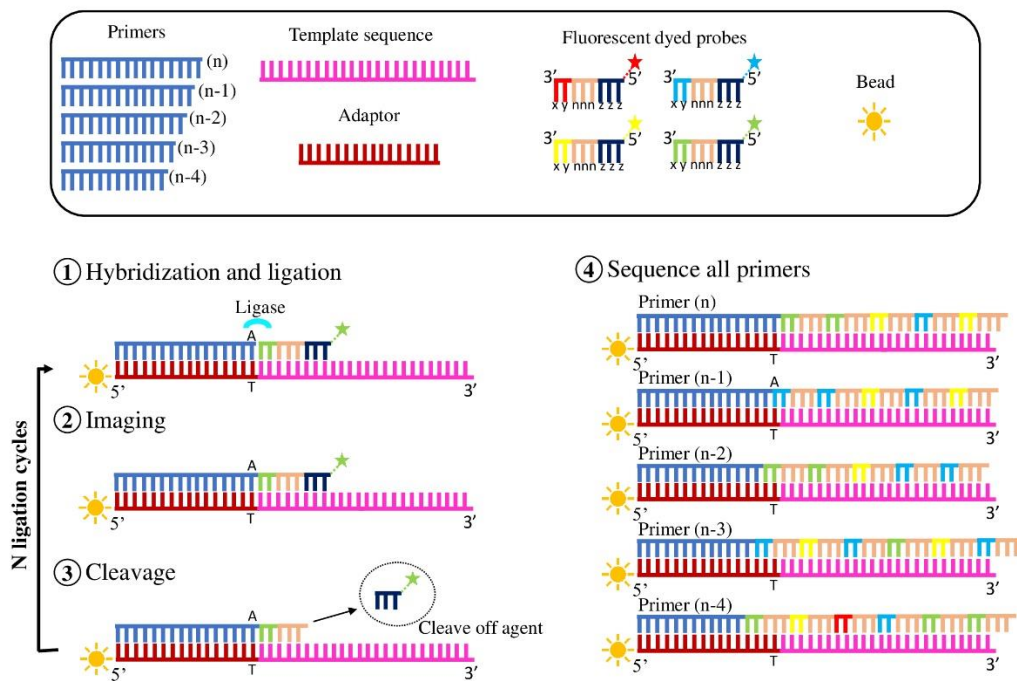


Figure 13. Stages of Solid method. G: Guanine, A: Adenine, C: Cytosine, T: Thymine, x: First base, y: Second base, n: Degenerate bases, z: Universal bases, Primer(n): GCGTAACGTAATGCTA.

5 different primers are used in the solid method. The base at the end of the primer is reduced by one, completing the sequence in 5 cycles. The reason why there are five cycles is for the detection of degenerate bases in the prepared probes in other cycles. While designing the primer, the first base of the sequence is determined by the last base of the primer. It is known that the last base of the primer is A. Considering at the color scale table, the 2nd base is determined by looking at the base corresponding to the color of the 1st base (A). The 1st base of the other probe, which is in line with with the 2nd base, is determined. The same process continues for the others, and the DNA sequence is completed (Figure 7). Solid sequencing method can be used in whole genome sequencing, targeted region sequencing, and analysis of gene expressions and small RNAs.

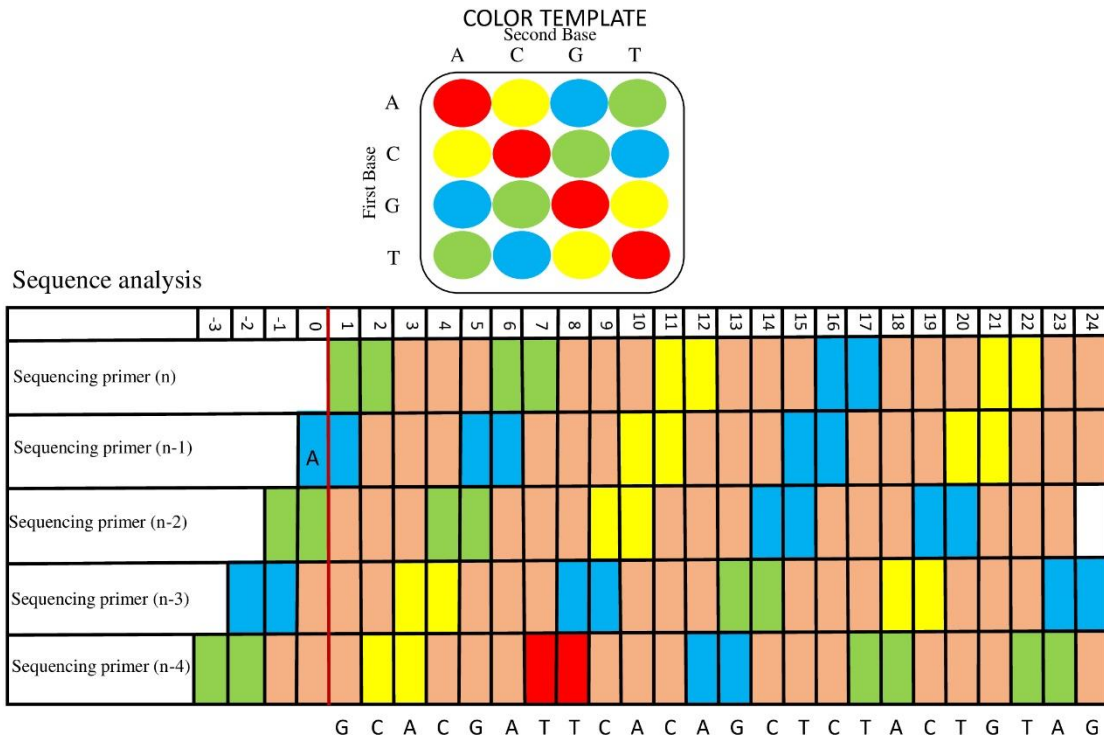


Figure 14. Analysis of DNA sequence with Solid method. G: Guanine, A: Adenine, C: Cytosine, T: Thymine, Primer(n): GCGTAAACGTAATGCTA.

Solid method can complete a single run in 7 days and generate 30 Gb of data in that time. Unfortunately, its main drawback is that read lengths are short and unsuitable for many applications.

Ion Torrent Method

A primary base is shifted back in this method in each cycle, making the known sequence a little bit more complete at each step. After five cycles, there are enough information to fill in any gaps in the sequence. There are five ligation cycles in total. A reliable approach for sequencing; it can be applied to small RNA and gene expression analyses, whole genome sequencing, and targeted region sequencing (Üstek et al., n.d.).

This optics-based technique gathers photons from genome sequences and information on the appearance of the genome's base pairs. Conductive metals and software are combined in Ion Torrent (CMOS). Thus, the surface potential change of the metal oxide sensitive layer is stimulated and the potential of the terminal changes (Escalante et al., 2014).

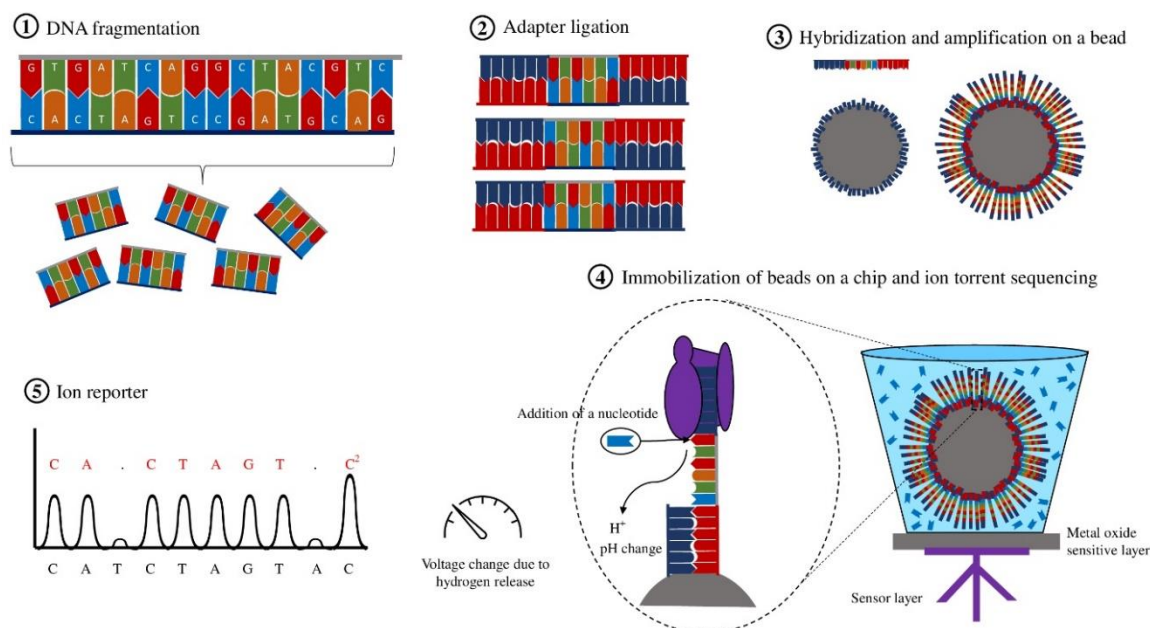


Figure 15. Ion Torrent sequencing and ion reporter. G: Guanine, A: Adenine, C: Cytosine, T: Thymine.

With the help of particular adapter sequences, fragmented DNA is joined to microbeads. Emulsion PCR beads are placed in a "chip" that has a million micro-wells, one bead in each one. A microchip with flow cells and electrical sensors below the cells hosts the sequencing reaction. Each nucleotide is incorporated and turned into an electrical signal. Protons are found using a semiconductor sensor that is ion sensitive. A voltage signal proportional to pH is created from the sensor. Protons are found using a semiconductor and ion sensitive semiconductor sensor. The sensor converts the pH fluctuations in the well into a voltage signal. Each well is integrated into the ion sensitive layer of the chip and the ion sensor, allowing for the recording of very minute voltage changes caused by nucleotide addition during DNA synthesis sequencing. One by one, dNTPs are inserted into the wells. Unlabeled dNTPs are cleaned one after the other. Hydrogen ions are released as dNTP, which is complementary to the incoming nucleotide and is added to the chain. The pH of the solution varies as the H protons are released in direct proportion to the quantity of nucleotides (Figure 8) (Escalante et al., 2014).

The major disadvantage of the system is the problems in reading homopolymer extensions and repeats. Its main advantages seem to be relatively longer read lengths, more flexible workflow, more reduced time, and a more affordable price than those provided by other platforms.

3. Third-Generation DNA Sequencing

With the increasing use of DNA sequencing methods, new technological developments are needed. Although first- and second-generation sequencing methods are revolutionary for DNA sequencing, they need to be improved in many aspects such as time, cost, and error rate. As a result of these searches, third-generation sequencing methods with longer read length, low cost and faster sequencing have been developed (Mohammadi & Bavi, 2022; Rhoads & Au, 2015). The distinguishing features of the method are the fact that it doesn't need amplification and allows real-time analysis without fragmenting the DNA (as a single molecule) (Athanasopoulou et al., 2022; Bruijns et al., 2018; Liu et al., 2012). Third-generation DNA sequencing methods are divided into two techniques as Pacific Bioscience and Oxford Nanopore Technology.

Pacific Bioscience (PacBio) Method

Pacific Biosciences' PacBio method, which was released at the end of 2010, is an SMRT-based method (Single Molecule Real Time) (Bruijns et al., 2018; Garrido-Cardenas et al., 2017; Slatko et al., 2018). It is a method used to read long-dimensional DNA sequences by making use of the components necessary for DNA synthesis (Athanasopoulou et al., 2022). In addition, the duration of preliminary preparation method is shorter than the other methods. The method involves inserting hairpin-shaped sequences known as "SMRTbell" at the beginning and end of a double-stranded DNA sample. Thanks to these sequences, the DNA becomes a circular sequence and minimizes base errors with long repetitive readings. The SMRTbell embedded DNA binds to polymerases that are immobilized to the base of a chip made of ZMW (Zero Mode Waveguides) technology (Garrido-Cardenas et al., 2017; Pareek et al., 2011). In contrast to conventional DNA sequencing techniques, which sequence DNA by wrapping the polymerase around the DNA, this technique sequences DNA by immobilizing the polymerase to the well's bottom (Athanasopoulou et al., 2022). There are thousands of picoliter ZMW wells on the chip and each well contains only one polymerase. Thus, a single DNA molecule is attached to only one well and can be analyzed in real-time. As the fluorescently labeled dNTP is incorporated into the DNA, a different colored glow appears for each base (Garrido-Cardenas et al., 2017; Liu et al., 2012; Pareek et al., 2011). The signal ends with the cleavage of the nucleotide-bound fluorescent dye pyrophosphate by the polymerase (Rhoads & Au, 2015). Imaging takes place instantaneously for each base added to the DNA (Slatko et al., 2018). An optical system with green and red lasers at the bottom of the ZMW continuously observes the radiations in milliseconds. This process takes place in other wells simultaneously and in parallel. ZMW ensures that the light is distorted exponentially. As a result, fluorescent light only illuminates the well's bottom and doesn't diffuse into neighboring wells (Figure 9) (Garrido-Cardenas et al., 2017; Slatko et al., 2018).

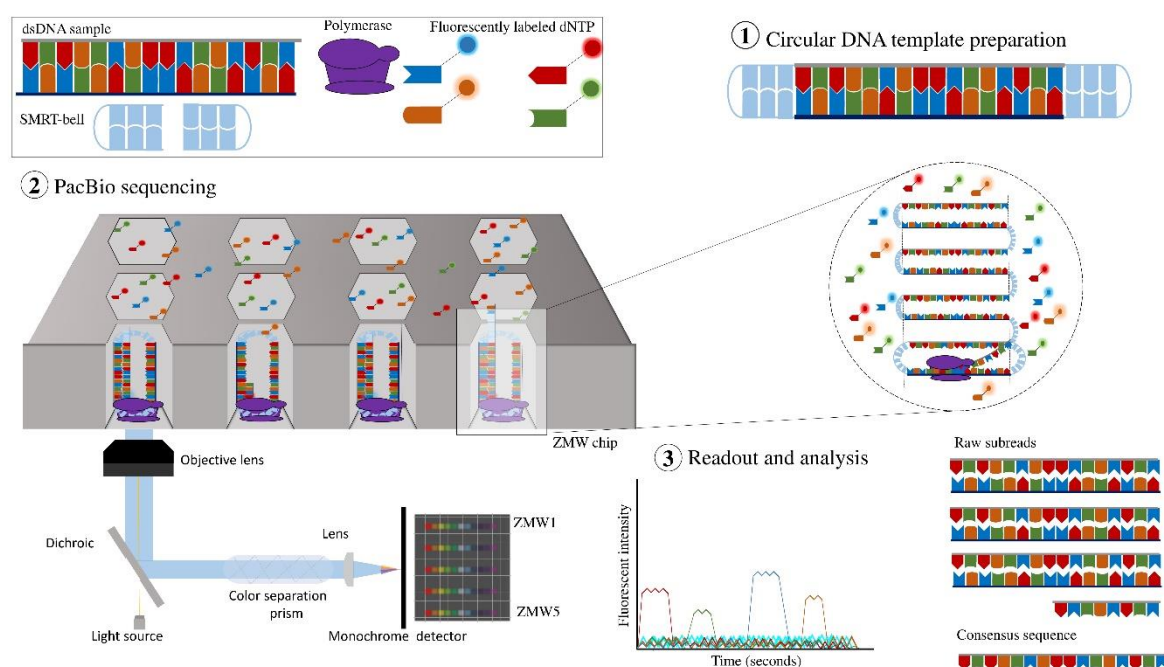


Figure 16. The basic principle of PacBio sequencing method. dsDNA: Double-stranded DNA, SMRT: Single molecule real-time, ZMW: Zero mode waveguide.

In addition to DNA sequencing, this method can detect epigenetic modifications and structural changes in the DNA sequence (Liu et al., 2012; Slatko et al., 2018). SMRT sequencing,

which is still in development, is the most commonly used platform among third-generation sequencing methods (Heather & Chain, 2016). With the use of SMRTbell, the PacBio method showed its difference compared to other methods. While this method sorts quickly, it has a high error rate. The control of this problem is provided by reading the same sequence more than once and evaluating similar templates (Slatko et al., 2018). The reading time varies depending on the length of the DNA but ranges from 0.5 to 4 hours (Rhoads & Au, 2015).

Oxford Nanopore Technology (ONT) Method

Another of the third-generation DNA sequencing methods is the ONT method developed by Oxford Nanopore Technologies. Despite the fact that this concept was first proposed in 1990, it has just recently been commercially available (Athanasopoulou et al., 2022). This technique theoretically has a much lower mistake rate because it does not involve the use of enzymes, amplification, or fluorescently tagged nucleotides. For this method, an artificial nanopore embedded in the membrane with an electric current (100 pA – 100 mV) is needed (Liu et al., 2012). This nanopore is formed by alpha-hemolysin (α HL), a 33 kD protein derived from *Staphylococcus*

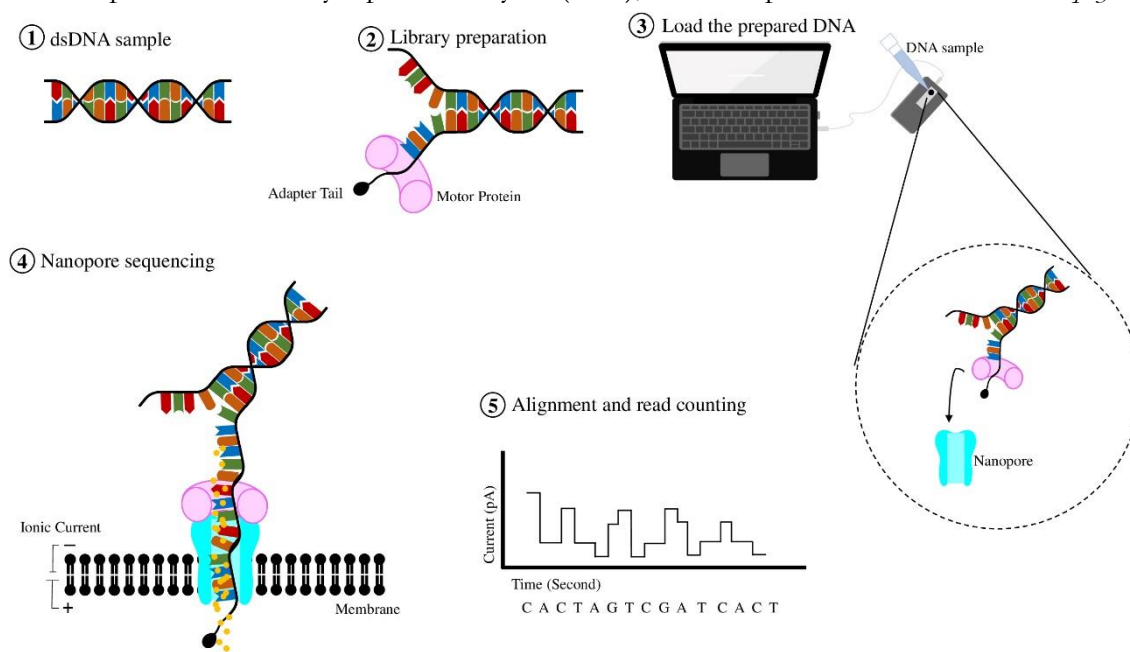


Figure 17. The Oxford nanopore technology method in its simple form. dsDNA: Double-stranded DNA, G: Guanine, A: Adenine, C: Cytosine, T: Thymine, pA: Picoampere.

aureus (Dönmez et al., 2015). Before the DNA can be sequenced, the polyA tail-containing adapter sequence needs to be introduced into it. The adapter sequence is recognized and transported to the nanopore by a motor protein. Once the nanopore detects the adapter sequence, DNA begins to pass through the nanopore as a single strand. Since DNA is negatively charged, DNA moves through the nanopore with the ionic current passing through the membrane. Each of the bases that make up the genetic material will create a different interruption on the ionic current. The characterization of the molecule passing through the nanopore according to the interruption of the current is carried out by the algorithm (Figure 10) (Feng et al., 2015).

The advantage of ONT over other methods is that it can read in a short time. In this method, analysis takes place without a secondary signal such as fluorescence, pH, or color. Since it does not need an enzyme like polymerase, it can sequence without the exposure to high temperatures. In addition, since it does not require amplification, there is no long sample preparation step (Liu et

al., 2012). In addition to being crucial for DNA sequencing, ONT is also crucial for characterizing RNAs, proteins, peptides, polymers, medicines, and macromolecules (Feng et al., 2015).

Future Approaches

Many complex diseases, including cancer, have been diagnosed and treated using sequencing techniques. Although methods such as RT-PCR, FISH, and immunohistochemistry are used in the diagnosis of diseases, sequencing methods have a greater advantage. Sequencing methods can pave the way for new perspectives in disease diagnosis and treatment. Genetic variants that are currently unknown can be identified by sequencing. In order to find alternative treatment methods, changes in DNA, RNA, or protein levels can be examined by sequencing methods, mutations in cancer signaling pathways or repair mechanisms can be detected, and genetic profiles of individuals can be narrowed by comparing transcriptome readings of genetic materials obtained from patients and healthy individuals. As a result, the disease can be diagnosed early on, paving the way for personalized treatment methods.

Multiple sequencing methods have been introduced to date. These sequencing methods differ in terms of read speed, accuracy and cost. Since DNA is a long material, the time, cost and required storage space of the sequencing method increase proportionally.

Reference

- Athanasopoulou, K., Boti, M. A., Adamopoulos, P. G., Skourou, P. C., & Scorilas, A. (2022). Third-Generation Sequencing: The Spearhead towards the Radical Transformation of Modern Genomics. *Life*, 12(1). <https://doi.org/10.3390/LIFE12010030>
- Balzer, S., Malde, K., Lanzén, A., Sharma, A., & Jonassen, I. (2010). Characteristics of 454 Pyrosequencing Data-enabling Realistic Simulation with Flowsim. *Bioinformatics*, 26(18), i420–i425. <https://doi.org/10.1093/BIOINFORMATICS/BTQ365>
- Behjati, S., & Tarpey, P. S. (2013). What is next generation sequencing? *Archives of Disease in Childhood. Education and Practice Edition*, 98(6), 236–238. <https://doi.org/10.1136/ARCHDISCHILD-2013-304340>
- Bleidorn, C. (2015). Third generation sequencing: technology and its potential impact on evolutionary biodiversity research. *Systematics and Biodiversity*, 14(1), 1–8. <https://doi.org/10.1080/14772000.2015.1099575>
- Bruijns, B., Tiggelaar, R., & Gardeniers, H. (2018). Massively parallel sequencing techniques for forensics: A review. *Electrophoresis*, 39(21), 2642. <https://doi.org/10.1002/ELPS.201800082>
- Collins, F. S., Patrinos, A., Jordan, E., Chakravarti, A., Gesteland, R., & Walters, L. R. (1998). New goals for the U.S. Human Genome Project: 1998-2003. *Science*, 282(5389), 682–689. <https://doi.org/10.1126/science.282.5389.682>
- Doğan, M., Eröz, R., Yüce, H., & Özmerdivenli, R. (2017). *Yeni Nesil Dizileme (YND) Hakkında Bilinenler (Literatür Taraması) The Known about Next-Generation Sequencing (NGS) (Review of the Literature)*. 19(1), 27–30.
- Dönmez, D., Şimşek, Ö., & Aka Kaçar, Y. (2015). Yeni Nesil DNA Dizileme Teknolojileri ve Bitkilerde Kullanımı. *Türk Bilimsel Derlemeler Dergisi*, 8(1), 30.
- Escalante, A. E., Barbolla, L. J., Ramírez-Barahona, S., & Eguiarte, L. E. (2014). The study of biodiversity in the era of massive sequencing. *Revista Mexicana de Biodiversidad*, 85(4), 1249–1264. <https://doi.org/10.7550/RMB.43498>
- Feng, Y., Zhang, Y., Ying, C., Wang, D., & Du, C. (2015). Nanopore-based Fourth-generation DNA Sequencing Technology. *Genomics, Proteomics & Bioinformatics*, 13(1), 4. <https://doi.org/10.1016/J.GPB.2015.01.009>
- Franc, L. T. C., Carrilho, E., & Kist, T. B. L. (2003). A review of DNA sequencing techniques. *Quarterly Reviews of Biophysics*, 35, 169–200. <https://doi.org/10.1017/S0033583502003797>
- Garrido-Cardenas, J. A., Garcia-Maroto, F., Alvarez-Bermejo, J. A., & Manzano-Agugliaro, F. (2017). DNA Sequencing Sensors: An Overview. *Sensors (Basel, Switzerland)*, 17(3). <https://doi.org/10.3390/S17030588>
- Hardin, S. H. (2001). DNA Sequencing. *Encyclopedia of Life Sciences*.
- Heather, J. M., & Chain, B. (2016). The sequence of sequencers: The history of sequencing DNA. *Genomics*, 107(1), 1. <https://doi.org/10.1016/J.YGENO.2015.11.003>

Hu, T., Chitnis, N., Monos, D., & Dinh, A. (2021). Next-generation sequencing technologies: An overview. *Human Immunology*, 82(11), 801–811. <https://doi.org/10.1016/J.HUMIMM.2021.02.012>

Liu, L., Li, Y., Li, S., Hu, N., He, Y., Pong, R., Lin, D., Lu, L., & Law, M. (2012). Comparison of Next-Generation Sequencing Systems. *Journal of Biomedicine and Biotechnology*, 2012, 11. <https://doi.org/10.1155/2012/251364>

Maxam, A. M., & Gilbert, W. (1977). A new method for sequencing DNA (DNA chemistry/dimethyl sulfate cleavage/hydrazine/piperidine). *Biochemistry*, 74(2), 560–564.

McCombie, W. R., McPherson, J. D., & Mardis, E. R. (2019). Next-Generation Sequencing Technologies. *Cold Spring Harbor Perspectives in Medicine*, 9(11). <https://doi.org/10.1101/CSHPERSPECT.A036798>

Mohammadi, M. M., & Bavi, O. (2022). DNA sequencing: an overview of solid-state and biological nanopore-based methods. *Biophysical Reviews*, 14(1), 99. <https://doi.org/10.1007/S12551-021-00857-Y>

Nyrén, P. (2007). 1-The History of Pyrosequencing ®. In M. Sharon (Ed.), *Pyrosequencing Protocols* (Vol. 373). Humana Press. <http://link.springer.com/10.1385/1597453773>

Pareek, C. S., Smoczynski, R., & Tretyn, A. (2011). Sequencing technologies and genome sequencing. *Journal of Applied Genetics*, 52(4), 413. <https://doi.org/10.1007/S13353-011-0057-X>

Reis-Filho, J. S. (2009). Next-generation sequencing. *Breast Cancer Research: BCR*, 11(Suppl 3), S12. <https://doi.org/10.1186/BCR2431>

Rhoads, A., & Au, K. F. (2015). PacBio Sequencing and Its Applications. *Genomics, Proteomics & Bioinformatics*, 13(5), 278. <https://doi.org/10.1016/J.GPB.2015.08.002>

Rubin, C. M., & Schmid, C. W. (n.d.). *Nucleic Acids Research Pyrimidine-specific chemical reactions useful for DNA sequencing*. 5, 1980.

Salmaninejad, A., Motae, J., Farjami, M., Alimardani, M., Esmailie, A., & Pasdar, A. (2019). Next-generation sequencing and its application in diagnosis of retinitis pigmentosa. *Ophthalmic Genetics*, 40(5), 393–402. <https://doi.org/10.1080/13816810.2019.1675178>

Sanger, F., Nicklen, S., & Coulson, A. R. (1977). *DNA sequencing with chain-terminating inhibitors (DNA polymerase/ nucleotide sequences/ bacteriophage 4X174)*. 74(12), 5463–5467.

Slatko, B. E., Gardner, A. F., & Ausubel, F. M. (2018). Overview of Next Generation Sequencing Technologies. *Current Protocols in Molecular Biology*, 122(1), e59. <https://doi.org/10.1002/CPMB.59>

Üstek, D., Abacı, N., Sırma, S., & Çakiris, A. (n.d.). Yeni Nesil DNA Dizileme. *Deneyisel Tıp Araştırmalar Dergisi*, 1(1), 11.

Zhong, Y., Xu, F., Wu, J., Schubert, J., & Li, M. M. (2021). Application of Next Generation Sequencing in Laboratory Medicine. *Ann Lab Med*, 41, 25–43. <https://doi.org/10.3343/alm.2021.41.1.25>

CURRENT DEBATES ON NATURAL AND ENGINEERING SCIENCES

5

